Pulse Rate Variability for the Assessment of Cardiovascular Changes

Elisa Mejía-Mejía

A thesis submitted in partial fulfilment for the degree of Doctor in Philosophy

Research Centre for Biomedical Engineering
School of Mathematics, Computer Science and Engineering
City, University of London

January 2023

Contents

Contents iii

List of Figures xi

List of Tables xxxvii

Abbreviations liii

Acknowledgements lxi

Declaration lxiii

Abstract lxv

1 Introduction 1

1.1 Outline 2

2 Anatomy and Physiology of the Cardiovascular System 5

2.1 The heart 5

2.1.1 Anatomy of the heart 5

2.1.2 Mechanical activity of the heart 7

2.1.3 Electrical activity of the heart 9

2.2 Blood vessels 11

2.2.1 Anatomy of the vessels 12

2.2.2 Circulation of blood 15

2.3 Haemodynamics and vascular mechanics 16

2.3.1 Blood and blood flow 16

2.3.2 Pressure and flow in arteries 20

2.4 Abnormal conditions 23

2.4.1 Hyper- and hypotension 23
2.4.2 Arterial stiffness 25
2.5 Summary 26

3 Anatomy and Physiology of the Autonomic Nervous System 27
3.1 The Nervous System 27
3.2 Structure of the Autonomic Nervous System 29
3.2.1 Sympathetic Nervous System 30
3.2.2 Parasympathetic Nervous System 30
3.3 Physiology of the Autonomic Nervous System 31
3.4 Cardiovascular Autonomic Activity 32
3.4.1 Autonomic control of the heart 34
3.4.2 Autonomic control of the vessels 35
3.4.3 Autonomic activity and changes in blood pressure and arterial stiffness 36
3.5 Summary 37

4 Heart Rate Variability in the Assessment of Cardiovascular Autonomic Nervous System 39
4.1 Electrocardiography 39
4.2 Heart Rate Variability 41
4.2.1 Time-domain analysis 43
4.2.2 Frequency-domain analysis 45
4.2.3 Non linear analysis 47
4.3 Heart Rate Variability and cardiovascular changes 51
4.4 Limitations of heart rate variability 54
4.5 Summary 56

5 Photoplethysmography and Pulse Rate Variability 59
5.1 Photoplethysmography 59
5.1.1 The origin of photoplethysmography 61
5.1.2 The photoplethysmographic waveform 63
5.1.3 Applications of photoplethysmography 64
5.2 Pulse rate variability 65
5.2.1 Analysis and characteristics of pulse rate variability 65

5.2.1.1 Fiducial point detection and pulse rate variability . 66
5.2.1.2 Effects of noise and pre-processing of the photoplethysmogram on pulse rate variability assessment 70
5.2.1.3 Minimal sampling rate for pulse rate variability analysis 72
5.2.1.4 Non-linear indices from pulse rate variability 75
5.2.1.5 Pulse rate variability derived from video photoplethysmography 76
5.2.2 Applications of pulse rate variability 78
5.2.2.1 Mental health 78
5.2.2.2 Pharmaceutical research 79
5.2.2.3 Sleep studies 80
5.2.2.4 Somatic and cardiovascular diseases 85
5.2.3 Relationship between pulse rate variability and heart rate variability 90
5.2.4 Advantages and limitations of pulse rate variability 139
5.3 Summary 143

6 Effects of technical aspects on the assessment of pulse rate variability from photoplethysmographic signals 145
6.1 Aims and objectives 145
6.2 Methods and materials 146
6.2.1 Data simulation 146
6.2.2 Experiments 148
6.2.2.1 Experiment 1: Interbeat interval detection algorithms and fiducial points 153
6.2.2.2 Experiment 2: Sampling rate 156
6.2.2.3 Experiment 3: Spectral analysis 156
6.2.2.4 Experiment 4: Duration of signal 158
6.2.2.5 Experiment 5: Outlier management 159
6.2.2.6 Experiment 6: Noise management 161
6.3 Results 164
6.3.1 Experiment 1: Interbeat interval detection algorithms and fiducial points 164

6.3.2 Experiment 2: Sampling rate 175
6.3.3 Experiment 3: Spectral analysis 176
6.3.4 Experiment 4: Duration of signal 201
6.3.5 Experiment 5: Outlier management 204
6.3.6 Experiment 6: Noise management 207
6.4 Discussion 233
6.4.1 Signal simulation 234
6.4.2 Experiment 1: Interbeat interval detection algorithms and fiducial points 235
6.4.3 Experiment 2: Sampling rate 238
6.4.4 Experiment 3: Spectral analysis 239
6.4.5 Experiment 4: Duration of signal 242
6.4.6 Experiment 5: Outlier management 244
6.4.7 Experiment 6: Noise management 245
6.4.8 Limitations of the study 247
6.5 Summary 248

7 Investigation of pulse rate variability and heart rate variability in conditions of whole-body cold exposure 249

7.1 Aims and objectives 249
7.2 Methods and materials 250
7.2.1 Experimental protocol 250
7.2.2 Signal acquisition and processing 251
7.2.2.1 Signal acquisition 251
7.2.2.2 PPG and ECG signal processing 252
7.2.2.3 HRV and PRV analysis 253
7.2.3 Statistical analysis 255
7.3 Results 256
7.3.1 Selection of fiducial points 256
7.3.2 Changes in PRV and HRV during cold exposure 256
7.3.2.1 Time-domain indices 257
7.3.2.2 Frequency-domain indices 258
7.3.2.3 Non-linear indices 259
7.3.3 Behaviour of PRV and HRV indices 259

7.3.4 Agreement between PRV and HRV 268
7.3.4.1 Friedman rank sum tests 268
7.3.4.2 Correlation analysis 268
7.3.4.3 Bland-Altman analysis 270
7.4 Discussion 272
7.4.1 Effects of cold exposure in peripheral and core vasculature . . 272
7.4.2 Relationship between PRV and HRV during whole-body cold exposure 285
7.4.3 Limitations of the study 288
7.5 Summary 289

8 Relationship between pulse rate variability and heart rate variability under different blood pressure states in critically-ill subjects 291
8.1 Aims and objectives 291
8.2 Methods and materials 292
8.2.1 Signal selection 292
8.2.2 Signal processing 293
8.2.2.1 Arterial blood pressure signals 294
8.2.2.2 Heart rate variability 294
8.2.2.3 Pulse rate variability 295
8.2.2.4 Pulse rate and heart rate variability indices 296
8.2.3 Statistical analysis 300
8.3 Results 304
8.3.1 Signal selection and segmentation 304
8.3.2 Correlation between PRV and HRV indices 304
8.3.3 Comparison between HRV and PRV using the Friedman rank sum test 304
8.3.4 Comparison between blood pressure states using Kruskal-Wallis tests 305
8.3.5 Bland-Altman analysis to assess agreement 307
8.4 Discussion 311
8.4.1 Selection of signals using Signal Quality Indices 313
8.4.2 Linear correlation between PRV and HRV 313
8.4.3 Comparison between PRV and HRV under each BP state . . 314

8.4.4 Agreement between PRV and HRV 315
8.4.5 Limitations of the study 316
8.5 Summary 316

9 Pulse rate variability for the classification and estimation of blood pressure states using machine learning algorithms 319

9.1 Aims and objectives 319
9.2 Methods and materials 321
9.2.1 Critically-ill patients 321
9.2.1.1 Signal selection 321
9.2.1.2 Signal processing 321
9.2.1.3 Feature extraction 323
9.2.1.4 Classification of blood pressure states 324
9.2.1.5 Estimation of blood pressure values 327
9.2.2 Healthy volunteers 327
9.2.2.1 Signal acquisition 327
9.2.2.2 Arterial blood pressure analysis 328
9.2.2.3 Pulse rate variability analysis 328
9.2.2.4 Estimation of blood pressure values 329
9.3 Results 329
9.3.1 Critically-ill patients 329
9.3.1.1 Feature extraction 330
9.3.1.2 Five-minute segments 331
9.3.1.3 One-minute segments 341
9.3.2 Healthy volunteers 344
9.3.2.1 Feature extraction 344
9.3.2.2 Estimation of blood pressure values 344
9.4 Discussion 348
9.4.1 Classification of blood pressure states 349
9.4.2 Estimation of blood pressure values 353
9.4.3 Limitations of the study 356
9.5 Summary 357

10 In-vitro Study to Assess Pulse Rate Variability in the Absence of Heart Rate Variability **359**

10.1 Aims and objectives . . . 359

10.2 Materials and methods . . . 361

10.2.1 In-vitro setup . . . 361

10.2.1.1 Upper body circulatory rig . . . 361

10.2.1.2 Radial and deep-palmar arch phantoms . . . 361

10.2.1.3 Artificial blood . . . 363

10.2.1.4 Pressure and photoplethysmography measurements 363

10.2.1.5 Setup validation . . . 364

10.2.2 In-vitro experiment . . . 365

10.2.2.1 Experimental protocol . . . 365

10.2.2.2 Data processing . . . 365

10.2.2.3 Statistical analysis . . . 366

10.3 Results . . . 366

10.3.1 In-vitro setup . . . 366

10.3.2 Pressure and Pulse Rate Variability measurements . . . 369

10.3.3 Linear regression between PRV and arterial blood pressure . 371

10.3.4 Relationship between PRV and cardiac output changes . . . 374

10.4 Discussion . . . 393

10.4.1 In-vitro setup . . . 393

10.4.2 Behaviour of pressure measurements and PRV indices with haemodynamic changes . . . 394

10.4.3 Linear regression between PRV and arterial blood pressure . 396

10.4.4 Relationship between PRV and cardiac output changes . . . 397

10.4.5 Limitations of the study . . . 398

10.5 Summary . . . 399

11 Discussion, Conclusions and Future Work **401**

11.1 Standardisation of pulse rate variability extraction from PPG signals 402

11.2 Relationship between cardiovascular changes and pulse rate variability 404

11.3 Conclusion . . . 407

Appendices **409**

A Behaviour of Pulse Rate Variability indices against Blood Pressure 409

B Confusion matrices 419

Contributions 451

Bibliography 455

List of Figures

2.1 Anatomy of the heart (*Heart: function and structure - access revision* n.d.) 6

2.2 Summary of the cardiac cycle. The atria contract and the blood is transferred to the ventricles via the atrioventricular (AV) valves. Then, the ventricles contract and pump the blood to the minor and major circulation circuits. Finally, the atria and ventricles fill with blood again during diastole to restart the cycle. 8

2.3 Pressure and volume changes in the left ventricle and arteries, where each numbered phase of the cycle refers to (1) the isovolumetric contraction of the heart; (2) the ejection of blood from the heart; (3) the isovolumetric relaxation; (4) the rapid filling of the ventricles; and (5) the atrial contraction. (Fox 2016) 10

2.4 Electrical system of the heart (Cypressvine 2019). The coordinated electrical stimulation of the different tissue allows for the correct execution of the cardiac cycle. 11

2.5 Schematic diagram of the distribution of blood vessels (Ostadfar 2016). Oxygenated blood travels through arteries and arterioles to capillaries, where oxygen is diffused to the tissue. Contaminated blood travels back to the heart through venules and veins. 12

2.6 Composition of the arterial wall of large elastic (top) and muscular (bottom) arteries (Ostadfar 2016). In most arteries, the arterial wall is composed of the tunica intima, the tunica media and the tunica adventitia. 14

2.7 Structure of blood vessels (Fox 2016) 16

2.8 Simplified model of the cardiovascular system (Conti 2011*a*). In this model, the cardiovascular system is simulated as two cylindrical tubes that connect two mechanical pumps (left and right ventricles) in series. 17

2.9 The Windkessel model of the arteries. In this model, the vessel is pictured as a compliant chamber of volume V proportional to the pressure p_{ea}. The flow rate Q is proportional to the pressure difference p_{ea} - p_{ev}, and may be different to the flow rate getting into the system, Q_H (Rangayyan 2002) 21

3.1 Structure of (a) a motor neuron, and (b) a sensory neuron (Fox 2016). In both cases, the three distinct parts of the neuron, i.e., the cell body, the dendrites and the axon, are present. 28

3.2 Distribution of the Autonomic Nervous System (Fox 2016). Red lines indicate sympathetic nerves, while parasympathetic fibres are depicted in blue. Preganglionic and postganglionic fibres are represented by solid and dashed lines, respectively. 29

3.3 Origin and pathways of ANS fibres that innervate the cardiovascular system (Drew & Sinoway 2012). The heart is innervated both from fibres from the vagus nerve and postganglionic sympathetic fibres, while blood vessels are only innervated by sympathetic fibres. 33

3.4 Effects of the autonomic nervous system activity on the heart (Drew & Sinoway 2012). 34

4.1 Electrocardiography waveform and its different characteristic waves during one cardiac cycle. A normal cycle shows the P wave, related to the atrial depolarization; a QRS complex, which is an indication of the rapid depolarization of the ventricles; and a T wave, related to the repolarization of the ventricles (Rangayyan 2002). 40

4.2 Derivation of heart rate variability from an electrocardiogram by extracting the duration of cardiac cycles using the R peaks. (a) Identification of R peaks from an electrocardiogram and the subsequent measurement of RR intervals; (b) Tachogram extracted by plotting the RR intervals against time. 43

4.3 Number of publications per year (up to 2021) in Scopus with the term "heart rate variability" in title, abstract or keywords. The number of publications related to heart rate variability has increased exponentially in the last decades. 54

5.1 Absorbed and transmitted light in living tissue. Adapted from (Wieben 1997). This behaviour of the light results in the photoplethysmographic signal, which has a pulsatile component, also known as AC component, and a quasi-DC component. 60

5.2 Optical pathways in skin: Relationship between light wavelength and depth of penetration in skin (mm) (Njoum 2017). The longer the wavelength, the deeper the penetration of the light. 62

5.3 Example of a healthy PPG pulse waveform with its different components, the anacrotic and catacrotic phases. The morphology of the waveform also depends on the site of measurement. 63

6.1 Framework for the simulation of photoplethysmographic (PPG) signals with randomly-generated Pulse Rate Variability (PRV) information. 149

6.2 Behaviour of the different types of noise on the simulated PPG signals.150

6.3 Photoplethysmographic cardiac cycles generated using the proposed mode, using ratios of value (a) $r = 2$ (excellent quality), and (b) $r = 4$ (acceptable quality). The blue and orange dotted lines illustrate the two Gaussian functions generated, while the black continuous line shows the result of summing these two Gaussian functions, i.e., z. . . 150

6.4 Example of photoplethysmographic (PPG) signals simulated using the proposed model and randomly generated pulse rate variability (PRV) information. (a) PPG signal with excellent quality ($r = 2$). (b) PPG signal with acceptable quality ($r = 4$). (c) PRV information used for the generation of these signals. 151

6.5 Flow diagram of experiments performed to understand the effects of technical aspects on pulse rate variability analysis 152

6.6 Fiducial points extracted from each inter-beat interval detected from the photoplethysmographic signals (continuous line), its second derivative (dashed line) and third derivative (dotted line). Red circle: Systolic peak (PKS); blue circle: Onset (ONS); yellow circle: Tangent intersection point (TI); orange circle: Maximum slope point (M1D); purple diamond: a point from the second derivative (A); green diamond: b point from the second derivative (B); white star: p_1 point from the third derivative (P1); black star: p_2 point from the third derivative (P2). 155

6.7 Example of noise-corrupted, excellent quality photoplethysmographic signals simulated for experiment 6. RES: Respiratory noise; BW: Baseline wandering; EM: Electromagnetic noise; MA: Movement artifact. 161

6.8 Example of noise-corrupted, acceptable quality photoplethysmographic signals simulated for experiment 6. RES: Respiratory noise; BW: Baseline wandering; EM: Electromagnetic noise; MA: Movement artifact. 163

6.9 Summary of the absolute differences (mean ± standard deviation) between indices measured from gold standard and extracted pulse rate variability from excellent quality PPG signals. 165

6.10 Summary of the absolute differences (mean ± standard deviation) between indices measured from gold standard and extracted pulse rate variability from acceptable quality PPG signals. 166

6.11 Results obtained from the factorial analyses both with (a) excellent quality PPG signals and (b) acceptable quality PPG signals. Blue bars: Standardised effects of the algorithm. Orange bars: Standardised effects of the fiducial points. Grey bars: Standardised effects of the interaction between the two factors. Yellow line: Reference value; higher standardised effects imply significance of the factor or the interaction. 167

6.12 Mean value of the absolute differences between SDNN measured from gold standard and extracted pulse rate variability (PRV), measured from excellent (top) and acceptable (bottom) quality photoplethysmographic signals. Left axis (black, continuous line): Difference to gold standard before Box-Cox transformations. Right axis (orange, dashed line): Difference to gold standard after Box-Cox transformation. 168

6.13 Mean value of the absolute differences between RMSSD measured from gold standard and extracted pulse rate variability (PRV), measured from excellent (top) and acceptable (bottom) quality photoplethysmographic signals. Left axis (black, continuous line): Difference to gold standard before Box-Cox transformations. Right axis (orange, dashed line): Difference to gold standard after Box-Cox transformation. 169

6.14 Mean value of the absolute differences between pNN50 measured from gold standard and extracted pulse rate variability (PRV), measured from excellent (top) and acceptable (bottom) quality photoplethysmographic signals. Left axis (black, continuous line): Difference to gold standard before Box-Cox transformations. Right axis (orange, dashed line): Difference to gold standard after Box-Cox transformation. 170

6.15 Mean value of the absolute differences between S measured from gold standard and extracted pulse rate variability (PRV), measured from excellent (top) and acceptable (bottom) quality photoplethysmographic signals. Left axis (black, continuous line): Difference to gold standard before Box-Cox transformations. Right axis (orange, dashed line): Difference to gold standard after Box-Cox transformation. 171

6.16 Mean value of the absolute differences between SD1 measured from gold standard and extracted pulse rate variability (PRV), measured from excellent (top) and acceptable (bottom) quality photoplethysmographic signals. Left axis (black, continuous line): Difference to gold standard before Box-Cox transformations. Right axis (orange, dashed line): Difference to gold standard after Box-Cox transformation. 172

6.17 Mean value of the absolute differences between SD1/SD2 measured from gold standard and extracted pulse rate variability (PRV), measured from excellent (top) and acceptable (bottom) quality photoplethysmographic signals. Left axis (black, continuous line): Difference to gold standard before Box-Cox transformations. Right axis (orange, dashed line): Difference to gold standard after Box-Cox transformation. 173

6.18 Mean and standard deviation of time-domain and Poincaré plot indices extracted from pulse rate variability (PRV), both from excellent and acceptable quality simulated photoplethysmographic (PPG) signals, with varying sampling rates. Blue bars: values obtained from gold standard PRV; orange bars: values obtained from PRV extracted from excellent quality PPG signals; yellow bars: values obtained from PRV extracted from acceptable quality PPG signals. Red stars indicate statistically significant difference to gold standard. 177

6.19 Mean and standard deviations of the differences obtained by comparing pulse rate variability absolute power frequency-domain indices obtained from extracted and gold standard trends. Differences are greater when Lomb-Scargle algorithm is used. 196

6.20 Mean and standard deviations of the differences obtained by comparing pulse rate variability relative power frequency-domain indices obtained from extracted and gold standard trends. Differences are greater when Lomb-Scargle or Welch algorithms are used. 197

6.21 Mean and standard deviations of the differences obtained by comparing pulse rate variability centroid-related frequency-domain indices obtained from extracted and gold standard trends.Differences are greater mostly when Lomb-Scargle algorithm is used. 198

6.22 Mean and standard deviations of the correlation results obtained by comparing pulse rate variability spectra obtained from extracted and gold standard trends. Maximum correlations were obtained when Lomb-Scargle, FFT and Welch algorithms were used. 199

6.23 Mean and standard deviations of the differences between indices extracted from measured and gold standard pulse rate variability trends with varying lengths of excellent photoplethysmographic signals. Differences tended to stabilise with durations longer than 120 s. 203

6.24 Mean and standard deviations of the differences between indices extracted from measured and gold standard pulse rate variability trends with varying lengths of acceptable photoplethysmographic signals. Differences tended to stabilise with durations longer than 120 s. . . . 204

6.25 Mean and standard deviation of absolute differences between pulse rate variability (PRV) indices extracted from excellent quality photoplethysmographic (PPG) signals contaminated with different noises and filtered using the best combination of factors obtained, against indices obtained from gold standard PRV trends. RES: Respiratory noise. BW: Baseline wandering. EM: Electromagnetic noise. MA: Movement artifact. 230

6.26 Mean and standard deviation of absolute differences between pulse rate variability (PRV) indices extracted from acceptable quality photoplethysmographic (PPG) signals contaminated with different noises and filtered using the best combination of factors obtained, against indices obtained from gold standard PRV trends. RES: Respiratory noise. BW: Baseline wandering. EM: Electromagnetic noise. MA: Movement artifact. 231

7.1 Measurement protocol for the whole-body cold exposure study. . . . 251

7.2 Example of photoplethysmographic (PPG) and electrocardiographic (ECG) signals used for the extraction of pulse rate variability and heart rate variability, respectively. From top to bottom, the PPG signals correspond to the signals obtained from the finger, the toe, the ear canal and the earlobe. The black stars show the R peaks detected from the ECG signal, while the white, black, red and green circles show the detected onsets, peaks, maximum slope points and tangent intersection points, respectively. 254

7.3 Behaviour (mean value and standard deviation) of heart rate variability (HRV) and pulse rate variability (PRV) indices extracted during the whole duration of basal measurement (BM, blue), cold exposure (CE, orange) and cold recovery (CR, yellow) stages. PRV indices were extracted from photoplethysmograms acquired from the finger (F), toe (T), ear canal (EC) and earlobe (EL). HRV was obtained from electrocardiograms. 257

7.4 Behaviour of indices measured from HRV (blue line) and PRV from the finger (orange line), toe (yellow line), ear canal (purple line) and earlobe (green line). BM: Baseline measurement; CE (1): Cold exposure between the start of the stage and the second minute of this stage; CE (2): Cold exposure between the 4th and 6th minutes of this stage; CE (3): Cold exposure between the 8th and 10th minutes of this stage; CR (1): Cold recovery between the start of the stage and the second minute of this stage; CE (2): Cold recovery between the 4th and 6th minutes of this stage; CE (3): Cold recovery between the 8th and 10th minutes of this stage.
. 260

7.5 Correlation coefficients (ρ) between HRV and PRV from each location during each stage (BM: baseline measurement, white bars; CE: cold exposure, black bars; CR: cold recovery, grey bars) and with each index. Stars over bars indicate statistically significant correlations (p-value < 0.05).
. 270

7.6 Bland-Altman ratios (BAR's) between HRV and PRV from each location (finger: blue line; toe: orange line; ear canal: grey line; earlobe: yellow line), during each stage (BM: baseline measurement; CE: cold exposure; CR: cold recovery) and with each index. Agreements were considered as good (BAR $\leq$ 10%), moderate (10% $\leq$ BAR $\leq$ 20%) or insufficient (BAR $\geq$ 20%).
. 271

7.7 Bland-Altman analysis for the assessment of agreement between SDNN indices extracted from HRV and PRV, measured during the three stages of the study. Differences and averages are shown in seconds. From left to right: Basal measurement, cold exposure and cold recovery. From top to bottom, SDNN was obtained from the finger, the toe, the earlobe and the ear canal. Continuous line: Mean value of the difference. Dashed lines: Limits of agreement. Dotted lines: Confidence intervals. Black line: Zero difference. 273

7.8 Bland-Altman analysis for the assessment of agreement between RMSSD indices extracted from HRV and PRV, measured during the three stages of the study. Differences and averages are shown in seconds. From left to right: Basal measurement, cold exposure and cold recovery. From top to bottom, RMSSD was obtained from the finger, the toe, the earlobe and the ear canal. Continuous line: Mean value of the difference. Dashed lines: Limits of agreement. Dotted lines: Confidence intervals. Black line: Zero difference. 274

7.9 Bland-Altman analysis for the assessment of agreement between pNN50 indices extracted from HRV and PRV, measured during the three stages of the study. From left to right: Basal measurement, cold exposure and cold recovery. From top to bottom, pNN50 was obtained from the finger, the toe, the earlobe and the ear canal. Continuous line: Mean value of the difference. Dashed lines: Limits of agreement. Dotted lines: Confidence intervals. Black line: Zero difference. 275

7.10 Bland-Altman analysis for the assessment of agreement between LF indices extracted from HRV and PRV, measured during the three stages of the study. Differences and averages are shown in squared seconds (s^2). From left to right: Basal measurement, cold exposure and cold recovery. From top to bottom, LF was obtained from the finger, the toe, the earlobe and the ear canal. Continuous line: Mean value of the difference. Dashed lines: Limits of agreement. Dotted lines: Confidence intervals. Black line: Zero difference. 276

7.11 Bland-Altman analysis for the assessment of agreement between HF indices extracted from HRV and PRV, measured during the three stages of the study. Differences and averages are shown in squared seconds (s^2). From left to right: Basal measurement, cold exposure and cold recovery. From top to bottom, HF was obtained from the finger, the toe, the earlobe and the ear canal. Continuous line: Mean value of the difference. Dashed lines: Limits of agreement. Dotted lines: Confidence intervals. Black line: Zero difference. 277

7.12 Bland-Altman analysis for the assessment of agreement between TP indices extracted from HRV and PRV, measured during the three stages of the study. Differences and averages are shown in squared seconds (s^2). From left to right: Basal measurement, cold exposure and cold recovery. From top to bottom, TP was obtained from the finger, the toe, the earlobe and the ear canal. Continuous line: Mean value of the difference. Dashed lines: Limits of agreement. Dotted lines: Confidence intervals. Black line: Zero difference. 278

7.13 Bland-Altman analysis for the assessment of agreement between nLF indices extracted from HRV and PRV, measured during the three stages of the study. From left to right: Basal measurement, cold exposure and cold recovery. From top to bottom, nLF was obtained from the finger, the toe, the earlobe and the ear canal. Continuous line: Mean value of the difference. Dashed lines: Limits of agreement. Dotted lines: Confidence intervals. Black line: Zero difference. 279

7.14 Bland-Altman analysis for the assessment of agreement between nHF indices extracted from HRV and PRV, measured during the three stages of the study. From left to right: Basal measurement, cold exposure and cold recovery. From top to bottom, nHF was obtained from the finger, the toe, the earlobe and the ear canal. Continuous line: Mean value of the difference. Dashed lines: Limits of agreement. Dotted lines: Confidence intervals. Black line: Zero difference. 280

7.15 Bland-Altman analysis for the assessment of agreement between LF/HF indices extracted from HRV and PRV, measured during the three stages of the study. From left to right: Basal measurement, cold exposure and cold recovery. From top to bottom, LF/HF was obtained from the finger, the toe, the earlobe and the ear canal. Continuous line: Mean value of the difference. Dashed lines: Limits of agreement. Dotted lines: Confidence intervals. Black line: Zero difference. 281

7.16 Bland-Altman analysis for the assessment of agreement between SD1 indices extracted from HRV and PRV, measured during the three stages of the study. Differences and averages are shown in seconds. From left to right: Basal measurement, cold exposure and cold recovery. From top to bottom, SD1 was obtained from the finger, the toe, the earlobe and the ear canal. Continuous line: Mean value of the difference. Dashed lines: Limits of agreement. Dotted lines: Confidence intervals. Black line: Zero difference. 282

7.17 Bland-Altman analysis for the assessment of agreement between SD2 indices extracted from HRV and PRV, measured during the three stages of the study. Differences and averages are shown in seconds. From left to right: Basal measurement, cold exposure and cold recovery. From top to bottom, SD2 was obtained from the finger, the toe, the earlobe and the ear canal. Continuous line: Mean value of the difference. Dashed lines: Limits of agreement. Dotted lines: Confidence intervals. Black line: Zero difference. 283

7.18 Bland-Altman analysis for the assessment of agreement between SD1/SD2 indices extracted from HRV and PRV, measured during the three stages of the study. From left to right: Basal measurement, cold exposure and cold recovery. From top to bottom, SD1/SD2 was obtained from the finger, the toe, the earlobe and the ear canal. Continuous line: Mean value of the difference. Dashed lines: Limits of agreement. Dotted lines: Confidence intervals. Black line: Zero difference. 284

8.1 Signal quality assessment algorithm. The arterial blood pressure (ABP) signals are segmented into cardiac cycles and signal quality indices are extracted for each cardiac cycle. Then, these indices are used as features to group the cycles in two clusters, using a k-Means algorithm. Then, signals are classified as good or poor-quality cycles using the ratio between the number of points grouped in each cluster. 293

8.2 Example of the analysis of a 5 -min arterial blood pressure (ABP, gray line) signal, with the trends for systolic (SBP, continuous line) and diastolic (DBP, dotted line) blood pressure, as well as the determination of blood pressure state (BP State, dashed line). Each 5-min segment is classified as hypotension (hypo), normotension (normo) or hypertension (hyper) according to the most frequent state during the 300 seconds. 294

8.3 Example of (a) an electrocardiographic (ECG) and (b) a photoplethysmographic (PPG) signal. R peaks (black circles on the ECG signal) were detected from ECG signals to measure heart rate variability (HRV) as the time interval between consecutive R peaks (RR intervals). Onsets (black circles on the PPG signal) were detected from PPG signals to measure pulse rate variability (PRV) as the time interval between consecutive onsets (PP intervals). 295

8.4 Spearman correlation coefficients (ρ) between indices obtained from pulse rate variability and heart rate variability in each blood pressure state. Most indices showed good correlation regardless of blood pressure state, although some, such as SpEn and BSE, showed lower correlations during normotension. 305

8.5 Bias between indices obtained from pulse rate variability and heart rate variability in each blood pressure state. Pulse rate variability tends to overestimate most indices, while the differences between these variables is more notorious during normotension. 309

8.6 Differences between upper ($\mathrm{LoA_U}$) and lower ($\mathrm{LoA_L}$) limits of agreement obtained from Bland-Altman analysis comparing indices measured from pulse rate variability and heart rate variability in each blood pressure state. Most indices related to short-term changes showed insufficient agreement, and the state of agreement was generally not affected by blood pressure. 310

9.1 Example of the analysis of a 5-min arterial blood pressure signal (light gray line), with the trends for systolic (red, dotted line) and diastolic (blue, dotted line) blood pressure, as well as the determination of the instantaneous blood pressure state (dark gray line). Each cycle was classified as hypertensive, normotensive or hypotensive according to the thresholds for hypertension (green, discontinuous lines) and hypotension (yellow discontinuous lines), and the most common state in the segment. For instance, this 5-min segment was labelled as hypertension since this was the most common state for the individuals pulses. 322

9.2 Example of a photoplethysmography (PPG) signal. Onsets (black circles) were detected from PPG signals to measure pulse rate variability (PRV) as the time interval between consecutive onsets (PP intervals). 323

9.3 Definition of true positives (TP-2), true negatives (TN), false positives (FP) and false negatives (FN) from (a) the confusion matrix for the i-th class of a multi-class problems; (b) the confusion matrix of this study for the hypotension class; (c) the confusion matrix of this study for the normotension class; (d) the confusion matrix of this study for the hypertension class. 326

9.4 Filtering of features obtained from (a) 5-min and (b) 1-min segments of pulse rate variability. Features with separability criterion $S(j)$ lower than the median value of S's (dashed lines) were discarded. . . 333

9.5 Accuracy (mean ± standard deviation) of the machine learning algorithms for the classification of hypotension (red lines), normotension (blue lines) and hypertension (yellow lines), as well as the average performance for all three classes (green lines), using all, filtered (ranked) and forward-selected features extracted from 5-min (left column) and 1-min (right column) segments. Results are presented as the average performance and its standard deviation after a 10-fold cross-validation. KX: k-NN algorithms with X nearest neighbors; NX: Feed-forward networks with X n neurons; SX(Y): Support vector machines with X kernel functions using a one-vs-all (Y = A) or one-vs-one scheme (Y = O). Accuracy tends to be higher for hypertension classification, especially with 5 min segments and using support vector machines. 336

9.6 True Positive Rate (TPR, mean ± standard deviation) of the machine learning algorithms for the classification of hypotension (red lines), normotension (blue lines) and hypertension (yellow lines), as well as the average performance for all three classes (green lines), using all, filtered (ranked) and forward-selected features extracted from 5-min (left column) and 1-min (right column) segments. Results are presented as the average performance and its standard deviation after a 10-fold cross-validation. KX: k-NN algorithms with X nearest neighbors; NX: Feed-forward networks with X n neurons; SX(Y): Support vector machines with X kernel functions using a one-vs-all (Y = A) or one-vs-one scheme (Y = O). TPR tends to be higher for hypertension classification, and is higher using all features extracted from 1-min segments and one-vs-one SVM. 337

9.7 True Negative Rate (TNR, mean ± standard deviation) of the machine learning algorithms for the classification of hypotension (red lines), normotension (blue lines) and hypertension (yellow lines), as well as the average performance for all three classes (green lines), using all, filtered (ranked) and forward-selected features extracted from 5-min (left column) and 1-min (right column) segments. Results are presented as the average performance and its standard deviation after a 10-fold cross-validation. KX: k-NN algorithms with X nearest neighbors; NX: Feed-forward networks with X n neurons; SX(Y): Support vector machines with X kernel functions using a one-vs-all (Y = A) or one-vs-one scheme (Y = O). TNR is higher than other performance metrics, which could indicate a good capacity to detect false cases for all classification models. 338

9.8 Positive Predictive Value (PPV, mean ± standard deviation) of the machine learning algorithms for the classification of hypotension (red lines), normotension (blue lines) and hypertension (yellow lines), as well as the average performance for all three classes (green lines), using all, filtered (ranked) and forward-selected features extracted from 5-min (left column) and 1-min (right column) segments. Results are presented as the average performance and its standard deviation after a 10-fold cross-validation. KX: k-NN algorithms with X nearest neighbors; NX: Feed-forward networks with X n neurons; SX(Y): Support vector machines with X kernel functions using a one-vs-all (Y = A) or one-vs-one scheme (Y = O). PPV tends to be higher for hypertension classification with support vector machines. 339

9.9 F1 Score (F1S, mean ± standard deviation) of the machine learning algorithms for the classification of hypotension (red lines), normotension (blue lines) and hypertension (yellow lines), as well as the average performance for all three classes (green lines), using all, filtered (ranked) and forward-selected features extracted from 5-min (left column) and 1-min (right column) segments. Results are presented as the average performance and its standard deviation after a 10-fold cross-validation. KX: k-NN algorithms with X nearest neighbors; NX: Feed-forward networks with X n neurons; SX(Y): Support vector machines with X kernel functions using a one-vs-all (Y = A) or one-vs-one scheme (Y = O). F1 Scores tend to be higher for when using 5 min segments, and performance is better for hypertension classification. 340

9.10 Results of the estimation of blood pressure values measured using regressive support vector machines (rSVM's) and fitting neural networks (fNN's). Mean absolute errors and standard deviations were measured from models obtained using all (red bars) and filtered features (yellow bars) extracted from 5-min (left column) and 1-min (right column) segments of pulse rate variability. SX_n: Support vector machine with linear kernel (X = L), radial-basis kernel (R) with varying scale n, or polynomial kernel (P) with varying polynomial order n. NX: Neural network with X n neurons. 342

9.11 Bland-Altman plots for the assessment of agreement between real (R) and estimated (E) values of mean arterial pressure (MAP), systolic blood pressure (SBP) and diastolic blood pressure (DBP). Estimated values were obtained using support vector machines with radial-basis kernel function, and using the best combination of features measured from 5-min pulse rate variability segments. Dashed lines: Limits of agreement. Solid line: Bias. In all cases, agreement between predicted and target values was good, indicated by low biases and limits of agreement, although a better agreement was observed for estimation of MAP and DBP. 343

9.12 Bland-Altman plots for the assessment of agreement between real (R) and estimated (E) values of mean arterial pressure (MAP), systolic blood pressure (SBP) and diastolic blood pressure (DBP). Estimated values were obtained using support vector machines with radial-basis kernel function, and using the best combination of features measured from 1-min pulse rate variability segments. Dashed lines: Limits of agreement. Solid line: Bias. The agreement was better for MAP and DBP, indicated by tighter limits of agreement. 346

9.13 Bland-Altman plots for the assessment of agreement between real (R) and estimated (E) values of mean arterial pressure (MAP), systolic blood pressure (SBP) and diastolic blood pressure (DBP) from healthy subjects. Estimated values were obtained using support vector machines with radial-basis kernel function, and using the best combination of features measured from 5-min pulse rate variability segments. Dashed lines: Limits of agreement. Solid line: Bias. Dotted lines: Linear model. Left column: Scatter plot of estimated and target values. Right column: Bland-Altman plots. Bland-Altman plots show good agreement, indicated by low biases and limits of agreement, and a tendency to increase the error as the mean value of the estimated and target values increase. It can also be observed that most predicted values follow the behaviour of targets. 350

9.14 Bland-Altman plots for the assessment of agreement between real (R) and estimated (E) values of mean arterial pressure (MAP), systolic blood pressure (SBP) and diastolic blood pressure (DBP) from healthy subjects. Estimated values were obtained using support vector machines with radial-basis kernel function, and using the best combination of features measured from 1-min pulse rate variability segments. Dashed lines: Limits of agreement. Solid line: Bias. Dotted lines: Linear model. Left column: Scatter plot of estimated and target values. Right column: Bland-Altman plots. Bland-Altman plots show good agreement, although limits of agreement are larger than those obtained with 5 min segments. Most predicted values follow the behaviour of targets, especially during normotension. . . . 351

10.1 Diagram of designed rig for the simulation of upper-body circulatory system, which consists of a commercial pump that replicates heart activity; aorta, subclavian, brachial, radial and deep-palmar arch arterial segments; a venous reservoir; and a single vein replicating the venous return. Pressure sensors are placed to measure the pressure of the fluid flowing through the system, and silicon, custom-made phantoms are used for the placement of photoplethysmography (PPG) sensors. 361

10.2 Design of phantoms for replicating tissue and positioning photoplethysmographic sensors 362

10.3 Constructed rig for the in-vitro experiment. This consists of a commercial pump that replicates heart activity, tubing that mimics arteries and veins from the upper-body circulatory system, and a fluid that have similar optical properties as blood. Pressure sensors and photoplethysmographic (PPG) probes were used to measure the pressure in the tubes and the optical pulsatile signals from two developed phantoms, that model the skin. PPG signals are acquired and processed using a custom-made system (ZenPPG) while pressure information is acquired directly from a data acquisition card. 367

10.4 Pattern used for controlling the pumping activity of the pulsatile pump. The ejected volume is larger as target flow increases, while it becomes smaller as stroke rate increases. 368

10.5 Spectrum obtained from the spectrophotometer and the artificial blood. The maximum absorbance was obtained with a wavelength of 610 nm. 368

10.6 Pressure and photoplethysmographic (PPG) signals acquired from the constructed rig when stroke rate was set to 60 beats per minute and target flow was set to 3 L/min. DPA: Deep palmar arch. 369

10.7 Behaviour of mean pressure measured from the aorta, subclavian, brachial, radial and deep palmar arch (DPA) locations while changing stroke rate and target flow. The measured pressure increases as target flow increases within the same stroke rate. At lower target flows and greater stroke rates, pressure values decrease. 370

10.8 Behaviour of pulse rate measured from the radial (left) and deep palmar arch (right) phantoms using photoplethysmographic sensors while changing stroke rate and target flow. As stroke rate increases, the measured pulse rate increases as well. With greater stroke rates and lower target flows, i.e., lower pulse pressure, the quality of the signals obtained from the deep palmar arch phantom is lowered, increasing the errors in the measurement of pulse rate. 370

10.9 Example of photoplethysmographic (PPG) signals acquired from the constructed rig under different stroke rates and target flows. The amplitude of the signals become larger as the target flow increases and the stroke rate decreases, and when measured from the radial PPG phantom. 371

10.10 Example of pressure signals acquired from the constructed rig under different stroke rates and target flows. The amplitude of the signals become smaller as the pulse travels further away from the pump, and as the target flow decreases and the stroke rate increases. 372

10.11Mean and standard deviation of pressure measurements acquired under different stroke rates (SR) and target flows (TF) conditions. MAP: Mean arterial pressure. SBP: Systolic blood pressure. DBP: Diastolic blood pressure. Pressure measurements are higher with lower stroke rates and higher target flows, while the difference between SBP, DBP and MAP become unsignificant as stroke rates increase. 373

10.12Mean and standard deviation of time-domain indices extracted from pulse rate variability under different stroke rates (SR) and target flows (TF) conditions, and measured from the radial (blue) and deep palmar arch (orange) phantoms. Most indices show larger variability when measured from the deep palmar arch phantom, while some indices show clear differences due to changes in stroke rate and target flow. 374

10.13Mean and standard deviation of absolute frequency-domain indices extracted from pulse rate variability under different stroke rates (SR) and target flows (TF) conditions, and measured from the radial (blue) and deep palmar arch (orange) phantoms. Most indices show larger variability when measured from the deep palmar arch phantom. . . . 375

10.14Mean and standard deviation of relative frequency-domain indices extracted from pulse rate variability under different stroke rates (SR) and target flows (TF) conditions, and measured from the radial (blue) and deep palmar arch (orange) phantoms. Most indices show larger variability when measured from the deep palmar arch phantom. There are notable differences due to target flow within each stroke rate level. 376

10.15Mean and standard deviation of the x-coordinates of the centroid-related indices extracted from pulse rate variability under different stroke rates (SR) and target flows (TF) conditions, and measured from the radial (blue) and deep palmar arch (orange) phantoms. Most indices show larger variability when measured from the deep palmar arch phantom, although this variability is lower than other type of indices. 377

10.16Mean and standard deviation of the y-coordinates of the centroid-related indices extracted from pulse rate variability under different stroke rates (SR) and target flows (TF) conditions, and measured from the radial (blue) and deep palmar arch (orange) phantoms. Most indices show larger variability when measured from the deep palmar arch phantom. There is notorious differences in the behaviour of the indices due to stroke rate. 378

10.17Mean and standard deviation of Poincaré plot indices extracted from pulse rate variability under different stroke rates (SR) and target flows (TF) conditions, and measured from the radial (blue) and deep palmar arch (orange) phantoms. Most indices show larger variability when measured from the deep palmar arch phantom. As the stroke rate increases, indices become lower with increasing target flow. . . . 379

10.18Mean and standard deviation of detrended fluctuation analysis indices extracted from pulse rate variability under different stroke rates (SR) and target flows (TF) conditions, and measured from the radial (blue) and deep palmar arch (orange) phantoms. The variability of these indices measured from either phantom is similar. 380

10.19Mean and standard deviation of entropy-related indices extracted from pulse rate variability under different stroke rates (SR) and target flows (TF) conditions, and measured from the radial (blue) and deep palmar arch (orange) phantoms. Most indices show larger variability when measured from the deep palmar arch phantom. Some indices show increasing values as target flow increases within the same stroke rate. 381

10.20Cross-correlation coefficients (ρ) between systolic, diastolic and mean pressure signals measured from the aorta, subclavian, brachial, radial and deep palmar arch (DPA), and pulse rate variability indices extracted from photoplethysmographic signals acquired from the radial (left column) and DPA (right column) phantoms. Some of the indices showed a relatively high inverse relationship (ρ closer to -1), and there was higher correlation between indices extracted from the radial PPG and pressure values. The three pressure measures have a similar tendency. 382

10.21 Adjusted coefficient of determination (R^2) for linear models between systolic, diastolic and mean pressure values measured from the aorta, subclavian, brachial, radial and deep palmar arch (DPA), and pulse rate variability indices obtained from red photoplethysmographic signals acquired from the radial and DPA phantoms. The relationship between pressure measures and pulse rate variability indices seems to be stronger when radial-related indices are considered. The behaviour of the linear regression results was very similar regardless of the location of measurement of pressure information. 383

10.22 Akaike's Information Criteria (AIC) for linear models between systolic, diastolic and mean pressure values measured from the aorta, subclavian, brachial, radial and deep palmar arch (DPA), and pulse rate variability indices obtained from red photoplethysmographic signals acquired from the radial and DPA phantoms. A lower AIC implies a better fit of the linear model. Better results were observed with the x-coordinates of centroid-related indices. 384

10.23 Bayesian Information Criteria (BIC) for linear models between systolic, diastolic and mean pressure values measured from the aorta, subclavian, brachial, radial and deep palmar arch (DPA), and pulse rate variability indices obtained from red photoplethysmographic signals acquired from the radial and DPA phantoms. A lower BIC implies a better fit of the linear model. Better results were observed with the x-coordinates of centroid-related indices. 385

10.24 Effect estimates for stroke rate (SR), target flow (TF) and their interaction on each of the indices extracted from pulse rate variability (PRV) measured from the radial phantom. Red stars on top of the bars indicate statistically significant effects. All indices showed statistically significant effects from each factor and their interaction. . . 386

10.25 Effect estimates for stroke rate (SR), target flow (TF) and their interaction on each of the indices extracted from pulse rate variability (PRV) measured from the deep palmar arch phantom. Red stars on top of the bars indicate statistically significant effects. All indices showed statistically significant effects from each factor and their interaction. 386

10.26Post-hoc comparisons for target flow (TF) levels when pulse rate variability indices are measured from the radial phantom. The appearance of a circle indicates a significant difference between the corresponding levels for each of the indices. There were more statistically significant differences for time domain, Poincaré plot, DFA and entropy-related indices, while relative and centroid-related frequency-domain indices were less affected by TF changes. 387

10.27Post-hoc comparisons for target flow (TF) levels when pulse rate variability indices are measured from the deep palmar arch phantom. The appearance of a circle indicates a significant difference between the corresponding levels for each of the indices. Absolute, relative and centroid-related frequency-domain indices were less affected by TF changes as TF increased. 388

10.28Post-hoc comparisons for stroke rate (SR) levels when pulse rate variability indices are measured from the radial phantom. The appearance of a circle indicates a significant difference between the corresponding levels for each of the indices. Most significant differences were observed as stroke rate increased. 389

10.29Post-hoc comparisons for stroke rate (SR) levels when pulse rate variability indices are measured from the deep palmar arch phantom. The appearance of a circle indicates a significant difference between the corresponding levels for each of the indices. Most significant differences were observed as stroke rate increased. 390

10.30Post-hoc comparisons for the interaction between stroke rate (SR) and target flow (TF) when pulse rate variability indices are measured from the radial phantom. The appearance of a circle indicates a significant difference between the corresponding levels for each of the indices. Time-domain, centroid-related frequency-domain and non-linear indices are largely affected by the changes in target flow and stroke rate. There were more significant differences as SR and TF increased. 391

10.31 Post-hoc comparisons for the interaction between stroke rate (SR) and target flow (TF) when pulse rate variability indices are measured from the deep palmar arch phantom. The appearance of a circle indicates a significant difference between the corresponding levels for each of the indices. Absolute and relative frequency-domain indices showed less significant differences among possible combinations. There were more significant differences as SR and TF increased. 392

11.1 Comparison between AVNN and SDNN indices extracted from pulse rate variability (PRV) and heart rate variability (HRV) from subjects with different blood pressure values. 406

A1 Behaviour of time domain indices extracted from pulse rate variability, compared to systolic blood pressure (BP, left column), diastolic BP (centre column) and mean arterial BP (right column). 410

A2 Behaviour of absolute frequency domain indices extracted from pulse rate variability, compared to systolic blood pressure (BP, left column), diastolic BP (centre column) and mean arterial BP (right column). . 411

A3 Behaviour of relative frequency domain indices extracted from pulse rate variability, compared to systolic blood pressure (BP, left column), diastolic BP (centre column) and mean arterial BP (right column). . 412

A4 Behaviour of the x-coordinate of centroid-related frequency domain indices extracted from pulse rate variability, compared to systolic blood pressure (BP, left column), diastolic BP (centre column) and mean arterial BP (right column). 413

A5 Behaviour of the y-coordinate of centroid-related frequency domain indices extracted from pulse rate variability, compared to systolic blood pressure (BP, left column), diastolic BP (centre column) and mean arterial BP (right column). 414

A6 Behaviour of Poincaré plot indices extracted from pulse rate variability, compared to systolic blood pressure (BP, left column), diastolic BP (centre column) and mean arterial BP (right column). 415

A7 Behaviour of entropy-related indices extracted from pulse rate variability, compared to systolic blood pressure (BP, left column), diastolic BP (centre column) and mean arterial BP (right column). . . . 416

A8 Behaviour of phase-related indices extracted from pulse rate variability, compared to systolic blood pressure (BP, left column), diastolic BP (centre column) and mean arterial BP (right column). 417
A9 Behaviour of detrended fluctuation analysis related indices extracted from pulse rate variability, compared to systolic blood pressure (BP, left column), diastolic BP (centre column) and mean arterial BP (right column). 418

List of Tables

2.1 Approximate characteristics of human blood vessels (Ostadfar 2016). 12

2.2 Main human arteries and veins (Ostadfar 2016). 13

2.3 Components of blood (Hoskins & Hardman 2017). 18

4.1 Time-domain indices for analysing HRV data (Shaffer & Ginsberg 2017). 44

4.2 Frequency-domain indices for analysing HRV data (Shaffer & Ginsberg 2017). 46

4.3 Commonly used non-linear indices for analysing HRV data (Shaffer & Ginsberg 2017). 48

5.1 Summary of previous studies comparing HRV and PRV. T: Time-domain indices. F: Frequency-domain indices. NL: Nonlinear indices. ICC: Intra-class correlation. CS: Cubic Spline Interpolation. AR: Autoregressive models. FFT: Fast Fourier transform. Welch: Welch's periodogram. Lomb-Scargle: Lomb-Scargle periodogram. 92

6.1 Ranges for the Pulse Rate Variability (PRV) parameters and the generation of PRV gold standard values. 147

6.2 Sample sizes selected for the different experiments. 152

6.3 Combinations of parameters used for the extraction of frequency spectra from pulse rate variability trends. Frequency resolution: number of samples used to calculate spectrum (nFFT) divided by the sampling rate of the signal. 158

6.4 Outlier detection methods 159

6.5 Outlier management methods 160

6.6 Parameters used for the simulation of noise corrupted photoplethysmographic (PPG) signals. RES: Respiratory noise; BW: Baseline wandering; EM: Electromagnetic noise; MA: Movement artifact. A_n: Proportion of the noise amplitude with respect to the PPG signal amplitude; f: Fundamental frequency of the noise. x: Indicates the inclusion of the specific type of noise in the resulting signal. 162

6.7 Results of the post-hoc comparisons between the combination of algorithms and fiducial points with the five lowest differences to the gold standard for each time-domain index extracted from excellent and acceptable quality photoplethysmographic (PPG) signals. (-): Non-significant difference. (+): Significant differences. 174

6.8 Results of the post-hoc comparisons between the combination of algorithms and fiducial points with the five lowest differences to the gold standard for each Poincaré-plot index extracted from excellent and acceptable quality photoplethysmographic (PPG) signals. (-): Non-significant difference. (+): Significant differences. 176

6.9 Summary of results from factorial analyses performed to evaluate the effects of interactions among factors altered for spectral analysis of pulse rate variability obtained from excellent quality photoplethysmographic signals. A: Type of interpolation used; B: Number of data points used for obtaining the spectrum; C: Sampling rate used for interpolation; D: Order of the model. $\star$: Significant interaction or factor. -: Non-significant interaction or factor. 178

6.10 Summary of results from factorial analyses performed to evaluate the effects of interactions among factors altered for spectral analysis of pulse rate variability obtained from acceptable quality photoplethysmographic signals. A: Type of interpolation used; B: Number of data points used for obtaining the spectrum; C: Sampling rate used for interpolation; D: Order of the model. ⋆: Significant interaction or factor. -: Non-significant interaction or factor. 181

6.11 Combinations of factors that delivered the lowest differences between indices or the maximal cross-correlation between gold-standard and measured spectra, from pulse rate variability extracted from excellent quality photoplethysmographic signals. A: Type of interpolation used; B: Number of data points used for obtaining the spectrum; C: Sampling rate used for interpolation; D: Order of the model. 185

6.12 Combinations of factors that delivered the lowest differences between indices or the maximal cross-correlation between gold-standard and measured spectra, from pulse rate variability extracted from acceptable quality photoplethysmographic signals. A: Type of interpolation used; B: Number of data points used for obtaining the spectrum; C: Sampling rate used for interpolation; D: Order of the model. 190

6.13 Summary of results obtained from the Kruskal-Wallis one-way analysis of variance and post-hoc comparisons. ⋆: Significant differences. -: Non-significant differences. 195

6.14 Best parameters found for spectral analysis using fast Fourier transform (FFT) for pulse rate variability (PRV) frequency-domain indices and for achieving maximal correlation between measured and gold standard spectra. 200

6.15 Best parameters found for spectral analysis using the multiple signal classification (PMUSIC) spectral analysis method for pulse rate variability (PRV) frequency-domain indices, and for achieving maximal correlation between measured and gold standard spectra. 202

6.16 Post-hoc comparisons results for differences between indices extracted from measured and gold standard pulse rate variability trends that showed statistically significant differences among photoplethysmographic signal duration, both with excellent and acceptable quality. 205

6.17 Combination of factors with the lowest difference to indices extracted from the gold standard. 206

6.18 Average difference to gold standard for indices that showed significant differences between applying or not applying outlier management strategies 207

6.19 Summary of results from factorial analyses performed to evaluate the effects of interactions among factors altered for the filtering of excellent quality, noise contaminated photoplethysmographic signals and pulse rate variability analysis. A: Type of filter; B: Low cutoff frequency; C: High cutoff frequency. $\star$: Significant interaction or factor. - : Non-significant interaction or factor. 208

6.20 Summary of results from factorial analyses performed to evaluate the effects of interactions among factors altered for the filtering of acceptable quality, noise contaminated photoplethysmographic signals and pulse rate variability analysis. A: Type of filter; B: Low cutoff frequency; C: High cutoff frequency. $\star$: Significant interaction or factor. - : Non-significant interaction or factor. 218

6.21 Best combination of factors for filtering excellent quality photoplethysmographic signals with different types of noise. FIR: Finite impulse response filters. IIR: Infinite impulse response filters. RES: Respiratory noise. BW: Baseline wandering. EM: Electromagnetic noise. MA: Movement artifact. fc_{low}: Low cut-off frequency. fc_{high}: High cut-off frequency. 232

6.22 Best combination of factors for filtering acceptable quality photoplethysmographic signals with different types of noise. FIR: Finite impulse response filters. IIR: Infinite impulse response filters. RES: Respiratory noise. BW: Baseline wandering. EM: Electromagnetic noise. MA: Movement artifact. fc_{low}: Low cut-off frequency. fc_{high}: High cut-off frequency. 233

7.1 Signal quality indices (SQI) extracted from finger, toe, ear canal and ear lobe PPG signals.
. 252

7.2 P-values obtained from the repeated-measures ANOVA and its post hoc analyses, when applied to time-domain and Poincaré plot-derived indices of PRV and HRV. Values in red indicate statistical significance (p-value < 0.05). Sphericity corrections using Greenhouse-Geisser correction were applied when Mauchly's test showed statistically significant results, and p-values shown are after these corrections. BM: baseline measurement; CE: cold exposure; CR: cold recovery.
. 258

7.3 P-values obtained from the repeated-measures ANOVA and its post hoc analyses, when applied to frequency-domain indices of PRV and HRV. Values in red indicate statistical significance (p-value < 0.05). Sphericity corrections using Greenhouse-Geisser correction were applied when Mauchly's test showed statistically significant results, and p-values shown are after these corrections. Normalised frequency-domain indices did not show statistical differences between stages from any of the signals. BM: baseline measurement; CE: cold exposure; CR: cold recovery.
. 259

7.4 Results from repeated-measures ANOVA for the comparison among indices extracted from 2-min segments of data, during basal measurement, cold exposure and cold recovery. BM: Baseline measurement; CE (1): Cold exposure between the start of the stage and the second minute of this stage; CE (2): Cold exposure between the 4th and 6th minutes of this stage; CE (3): Cold exposure between the 8th and 10th minutes of this stage; CR (1): Cold recovery between the start of the stage and the second minute of this stage; CE (2): Cold recovery between the 4th and 6th minutes of this stage; CE (3): Cold recovery between the 8th and 10th minutes of this stage. $\star$: Significant differences. -: Non-significant differences. 262

7.5 P-values obtained from the Friedman rank sum test and the multiple comparison tests performed between HRV and PRV from each location (F: Finger; T: Toe; EC: Ear canal; EL: Earlobe), during each stage (BM: baseline measurement; CE: cold exposure; CR: cold recovery) and with each index. Values in red indicate statistically significant differences (p-value < 0.05). 269

8.1 Indices extracted from pulse rate variability (PRV) and heart rate variability (HRV). 298

8.2 Mean $\pm$ standard deviation of indices measured from pulse rate variability (PRV) and heart rate variability (HRV) under each blood pressure state. $*$ Values multiplied by 1×10^{-3}. $**$ Values divided by 1×10^{6}. $***$ Values divided by 1×10^{9}. 301

8.3 Friedman rank sum tests results for the comparison between pulse rate variability and heart rate variability in the different blood pressure states. 306

8.4 Kruskal-Wallis and post-hoc multiple comparisons p-values for the comparison among blood pressure states from indices measured from pulse rate variability. 307

8.5 Kruskal-Wallis and post-hoc multiple comparisons p-values for the comparison among blood pressure states from indices measured from heart rate variability. 308

8.6 Ratio of agreement (BAR, %) derived from Bland-Altman analysis 311

9.1 Machine learning algorithms applied for the classification of blood pressure states. 325

9.2 Time-domain and Poincaré plot indices extracted from 5-min and 1-min segments of pulse rate variability. Values are shown as Mean ± Standard Deviation. 330

9.3 Frequency-domain indices extracted from 5-min and 1-min segments of pulse rate variability. Values are shown as Mean ± Standard Deviation. 331

9.4 Entropy, phase and detrended-fluctuation analysis indices extracted from 5-min and 1-min segments of pulse rate variability. Values are shown as Mean ± Standard Deviation. 332

9.5 Results of the sequential forward selection scheme to identify the best combination of features for each machine learning algorithm using 5 min segments. Bullets indicate the features selected as part of the best combination for each algorithm. 334

9.6 Results of the sequential forward selection scheme to identify the best combination of features for each feed forward neural network using 5 min segments. Bullets indicate the features selected as part of the best combination for each algorithm. 335

9.7 Mean absolute errors ± standard deviation of the estimation of blood pressure values measured using regressive support vector machines (rSVM's) with radial-basis functions after obtaining the best combinations of features using sequential forward selection, extracted from 5-min and 1-min segments of pulse rate variability. 341

9.8 Results of the sequential forward selection scheme to identify the best combination of features for each machine learning algorithm using 1 min segments. Bullets indicate the features selected as part of the best combination for each algorithm. 344

9.9 Results of the sequential forward selection scheme to identify the best combination of features for each feed forward neural network using 1 min segments. Bullets indicate the features selected as part of the best combination for each algorithm. 345

9.10 Pulse rate variability indices extracted from 5-min and 1-min segments. Values are shown as mean ± standard deviation. 347

9.11 Mean absolute errors ± standard deviation of the estimation of blood pressure values measured using regressive support vector machines (rSVM's) with linear, radial-basis (RBF, different scales σ) and polynomial (different orders n) Kernel functions, with all, filtered and sequentially forward selected (SFS) features, extracted from 5-min pulse rate variability segments. 348

9.12 Mean absolute errors ± standard deviation of the estimation of blood pressure values measured using regressive support vector machines (rSVM's) with linear, radial-basis (RBF, different scales σ) and polynomial (different orders n) Kernel functions, with all, filtered and sequentially forward selected (SFS) features, extracted from 1-min pulse rate variability segments. 349

9.13 Comparison of the obtained results to results found in the literature. SBP: Systolic blood pressure. DBP: Diastolic blood pressure. MAP: Mean arterial pressure. 354

10.1 Characteristics of arterial and venous segments replicated on the in-vitro setup. 362

A1 Confusion matrices obtained for the k-Nearest Neighbors algorithms evaluated using all features extracted from 5- and 1-min segments. Values are presented as the mean percentage ± the standard deviation, obtained after the 10-fold cross-validation. Hypo: hypotension. Normo: normotension. Hyper: hypertension. 420

A2 Confusion matrices obtained for the neural networks evaluated using all features extracted from 5- and 1-min segments. Values are presented as the mean percentage ± the standard deviation, obtained after the 10-fold cross-validation. Hypo: hypotension. Normo: normotension. Hyper: hypertension. N: number of neurons in the hidden layer. 421

A3 Confusion matrices obtained for the neural networks evaluated using all features extracted from 5- and 1-min segments. Values are presented as the mean percentage ± the standard deviation, obtained after the 10-fold cross-validation. Hypo: hypotension. Normo: normotension. Hyper: hypertension. N: number of neurons in the hidden layer. 422

A4 Confusion matrices obtained for the neural networks evaluated using all features extracted from 5- and 1-min segments. Values are presented as the mean percentage ± the standard deviation, obtained after the 10-fold cross-validation. Hypo: hypotension. Normo: normotension. Hyper: hypertension. N: number of neurons in the hidden layer. 423

A5 Confusion matrices obtained for the neural networks evaluated using all features extracted from 5- and 1-min segments. Values are presented as the mean percentage ± the standard deviation, obtained after the 10-fold cross-validation. Hypo: hypotension. Normo: normotension. Hyper: hypertension. N: number of neurons in the hidden layer. 424

A6 Confusion matrices obtained for the one-vs-all linear support vector machine evaluated using all features extracted from 5- and 1-min segments. Values are presented as the mean percentage ± the standard deviation, obtained after the 10-fold cross-validation. Hypo: hypotension. Normo: normotension. Hyper: hypertension. 425

A7 Confusion matrices obtained for the one-vs-all radial basis support vector machines evaluated using all features extracted from 5- and 1-min segments. Values are presented as the mean percentage ± the standard deviation, obtained after the 10-fold cross-validation. Hypo: hypotension. Normo: normotension. Hyper: hypertension. σ: Scale of kernel. 426

A8 Confusion matrices obtained for the one-vs-all polynomial support vector machines evaluated using all features extracted from 5- and 1-min segments. Values are presented as the mean percentage ± the standard deviation, obtained after the 10-fold cross-validation. Hypo: hypotension. Normo: normotension. Hyper: hypertension. n: Order of the polynomial kernel. 427

A9 Confusion matrices obtained for the one-vs-one linear support vector machine evaluated using all features extracted from 5- and 1-min segments. Values are presented as the mean percentage ± the standard deviation, obtained after the 10-fold cross-validation. Hypo: hypotension. Normo: normotension. Hyper: hypertension. 427

A10 Confusion matrices obtained for the one-vs-one radial-basis support vector machines evaluated using all features extracted from 5- and 1-min segments. Values are presented as the mean percentage ± the standard deviation, obtained after the 10-fold cross-validation. Hypo: hypotension. Normo: normotension. Hyper: hypertension. σ: Scale of kernel. 428

A11 Confusion matrices obtained for the one-vs-one polynomial support vector machines evaluated using all features extracted from 5- and 1-min segments. Values are presented as the mean percentage ± the standard deviation, obtained after the 10-fold cross-validation. Hypo: hypotension. Normo: normotension. Hyper: hypertension. n: Order of the polynomial kernel. 429

A12 Confusion matrices obtained for the k-Nearest Neighbors algorithms evaluated using ranked features extracted from 5- and 1-min segments. Values are presented as the mean percentage ± the standard deviation, obtained after the 10-fold cross-validation. Hypo: hypotension. Normo: normotension. Hyper: hypertension. 430

A13 Confusion matrices obtained for the neural networks evaluated using ranked features extracted from 5- and 1-min segments. Values are presented as the mean percentage ± the standard deviation, obtained after the 10-fold cross-validation. Hypo: hypotension. Normo: normotension. Hyper: hypertension. N: number of neurons in the hidden layer.
. 431
A14 Confusion matrices obtained for the neural networks evaluated using ranked features extracted from 5- and 1-min segments. Values are presented as the mean percentage ± the standard deviation, obtained after the 10-fold cross-validation. Hypo: hypotension. Normo: normotension. Hyper: hypertension. N: number of neurons in the hidden layer.
. 432
A15 Confusion matrices obtained for the neural networks evaluated using ranked features extracted from 5- and 1-min segments. Values are presented as the mean percentage ± the standard deviation, obtained after the 10-fold cross-validation. Hypo: hypotension. Normo: normotension. Hyper: hypertension. N: number of neurons in the hidden layer.
. 433
A16 Confusion matrices obtained for the neural networks evaluated using ranked features extracted from 5- and 1-min segments. Values are presented as the mean percentage ± the standard deviation, obtained after the 10-fold cross-validation. Hypo: hypotension. Normo: normotension. Hyper: hypertension. N: number of neurons in the hidden layer.
. 434
A17 Confusion matrices obtained for the one-vs-all linear support vector machine evaluated using ranked features extracted from 5- and 1-min segments. Values are presented as the mean percentage ± the standard deviation, obtained after the 10-fold cross-validation. Hypo: hypotension. Normo: normotension. Hyper: hypertension.
. 435

A18 Confusion matrices obtained for the one-vs-all radial basis support vector machines evaluated using ranked features extracted from 5- and 1-min segments. Values are presented as the mean percentage ± the standard deviation, obtained after the 10-fold cross-validation. Hypo: hypotension. Normo: normotension. Hyper: hypertension. σ: Scale of kernel. 436

A19 Confusion matrices obtained for the one-vs-all polynomial support vector machines evaluated using ranked features extracted from 5- and 1-min segments. Values are presented as the mean percentage ± the standard deviation, obtained after the 10-fold cross-validation. Hypo: hypotension. Normo: normotension. Hyper: hypertension. n: Order of the polynomial kernel. 437

A20 Confusion matrices obtained for the one-vs-one linear support vector machine evaluated using ranked features extracted from 5- and 1-min segments. Values are presented as the mean percentage ± the standard deviation, obtained after the 10-fold cross-validation. Hypo: hypotension. Normo: normotension. Hyper: hypertension. 437

A21 Confusion matrices obtained for the one-vs-one radial-basis support vector machines evaluated using ranked features extracted from 5- and 1-min segments. Values are presented as the mean percentage ± the standard deviation, obtained after the 10-fold cross-validation. Hypo: hypotension. Normo: normotension. Hyper: hypertension. σ: Scale of kernel. 438

A22 Confusion matrices obtained for the one-vs-one polynomial support vector machines evaluated using ranked features extracted from 5- and 1-min segments. Values are presented as the mean percentage ± the standard deviation, obtained after the 10-fold cross-validation. Hypo: hypotension. Normo: normotension. Hyper: hypertension. n: Order of the polynomial kernel. 439

A23 Confusion matrices obtained for the k-Nearest Neighbors algorithms evaluated using forward selected features extracted from 5- and 1-min segments. Values are presented as the mean percentage ± the standard deviation, obtained after the 10-fold cross-validation. Hypo: hypotension. Normo: normotension. Hyper: hypertension. 440

A24 Confusion matrices obtained for the neural networks evaluated using forward selected features extracted from 5- and 1-min segments. Values are presented as the mean percentage ± the standard deviation, obtained after the 10-fold cross-validation. Hypo: hypotension. Normo: normotension. Hyper: hypertension. N: number of neurons in the hidden layer. 441

A25 Confusion matrices obtained for the neural networks evaluated using forward selected features extracted from 5- and 1-min segments. Values are presented as the mean percentage ± the standard deviation, obtained after the 10-fold cross-validation. Hypo: hypotension. Normo: normotension. Hyper: hypertension. N: number of neurons in the hidden layer. 442

A26 Confusion matrices obtained for the neural networks evaluated using forward selected features extracted from 5- and 1-min segments. Values are presented as the mean percentage ± the standard deviation, obtained after the 10-fold cross-validation. Hypo: hypotension. Normo: normotension. Hyper: hypertension. N: number of neurons in the hidden layer. 443

A27 Confusion matrices obtained for the neural networks evaluated using forward selected features extracted from 5- and 1-min segments. Values are presented as the mean percentage ± the standard deviation, obtained after the 10-fold cross-validation. Hypo: hypotension. Normo: normotension. Hyper: hypertension. N: number of neurons in the hidden layer. 444

A28 Confusion matrices obtained for the one-vs-all linear support vector machine evaluated using forward selected features extracted from 5- and 1-min segments. Values are presented as the mean percentage ± the standard deviation, obtained after the 10-fold cross-validation. Hypo: hypotension. Normo: normotension. Hyper: hypertension. 445

A29 Confusion matrices obtained for the one-vs-all radial basis support vector machines evaluated using forward selected features extracted from 5- and 1-min segments. Values are presented as the mean percentage ± the standard deviation, obtained after the 10-fold cross-validation. Hypo: hypotension. Normo: normotension. Hyper: hypertension. σ: Scale of kernel. 446

A30 Confusion matrices obtained for the one-vs-all polynomial support vector machines evaluated using forward selected features extracted from 5- and 1-min segments. Values are presented as the mean percentage ± the standard deviation, obtained after the 10-fold cross-validation. Hypo: hypotension. Normo: normotension. Hyper: hypertension. n: Order of the polynomial kernel. 447

A31 Confusion matrices obtained for the one-vs-one linear support vector machine evaluated using forward selected features extracted from 5- and 1-min segments. Values are presented as the mean percentage ± the standard deviation, obtained after the 10-fold cross-validation. Hypo: hypotension. Normo: normotension. Hyper: hypertension. 447

A32 Confusion matrices obtained for the one-vs-one radial-basis support vector machines evaluated using forward selected features extracted from 5- and 1-min segments. Values are presented as the mean percentage ± the standard deviation, obtained after the 10-fold cross-validation. Hypo: hypotension. Normo: normotension. Hyper: hypertension. σ: Scale of kernel. 448

A33 Confusion matrices obtained for the one-vs-one polynomial support vector machines evaluated using forward selected features extracted from 5- and 1-min segments. Values are presented as the mean percentage ± the standard deviation, obtained after the 10-fold cross-validation. Hypo: hypotension. Normo: normotension. Hyper: hypertension. n: Order of the polynomial kernel.
. 449

Abbreviations

A1	Short-term slope, α_1, from Detrended Fluctuation Analysis
A2	Long-term slope, α_2, from Detrended Fluctuation Analysis
AAMI	Association for the Advancement of Medical Instrumentation
ABP	Arterial Blood Pressure
AC	Pulsatile component of the photoplethysmogram
ACC	Accuracy
ADT	Adaptive Threshold
AF	Atrial Fibrillation
AIC	Akaike's Information Criterion
AMIF	Automutual Information Function
AMPD	Automatic Multiscale-based Peak Detection
ANN	Artificial Neural Network
ANOVA	Analysis of Variance
ANS	Autonomic Nervous System
ApEn	Approximate Entropy
AR	Autoregressive
ATP	Adenosyl Triphosphate
AUC	Area Under the Curve
AV	Atrioventricular
AVNN	Mean value of normal-to-normal intervals
BAR	Bland-Altman Ratio

BIC	Bayesian Information Criterion
BM	Baseline Measurement
BP	Blood Pressure
bpm	Beats per minute
BSE	Basic Scale Entropy
BW	Baseline Wandering noise
CDM	Complex Demodulation Method
CE	Cold Exposure
CO	Cardiac Output
COM	Compaction
CR	Cold Recovery
CSD	Correntropy Spectral Density
D2	Correlation dimension
DAP	Decrease in Amplitude of the Pulse
DBP	Diastolic Blood Pressure
DC	Non-pulsatile component of the photoplethysmogram
DFA	Detrended Fluctuation Analysis
DP	Diastolic Points
DPA	Deep Palmar Arch
EC	Ear Canal
ECG	Electrocardiography
EDV	End-Diastolic Volume
EL	Earlobe
EM	Electromagnetic noise
EMB DIM	Embedded Dimension
EMD	Empirical Mode Decomposition
ESV	End-Systolic Volume
ET	Electroconvulsive Therapy
F1	F1 Score

FDR	Fisher Discriminant Ratio
FFT	Fast Fourier Transform
FIR	Finite Impulse Response
FIRCLS	Constrained Least Squares Filter
FIREQR	Equiripple Filter
FIRLS	Least Squares Filter
FIRPM	Praks-McClellan Filter
FIRWIN	Hamming Window Filter
FN	False Negative
fNN	Fitting Neural Network
FP	False Positive
GQ	Good Quality
HF	High-frequency band (0.15 – 0.40 Hz)
HHT	Hilbert Huang Transform
HR	Heart Rate
HRV	Heart Rate Variability
IBIs	Interbeat Intervals
ICA	Independent Component Analysis
ICU	Intensive Care Unit
IIR	Infinite Impulse Response
IIRBUT	Butterworth Filter
IIRELL	Elliptic Filter
kNN	k-Nearest Neighbors
LagPD	Lag of the first local maxima from the Automutual Information Function
LagT	Lag at which the Automutual Information Function reaches a value of $\frac{1}{e}$
LBNP	Low-body Negative Pressure
LEDs	Light Emitting Diodes

LF	Low-frequency band (0.04 – 0.15 Hz)
LF/HF	Ratio of the low-frequency band power to the high-frequency band power
LoA	Limits of Agreement
LSTM	Long- and Short-Term Memory
LYA	Lyapunov Exponent
M1D	Maximum point from the first derivative of the photoplethysmogram
MA	Movement Artefact
MACE	Major Adverse Cardiac Events
MAE	Mean Absolute Error
MAP	Mean Arterial Pressure
MDD	Major Depressive Disorder
ML	Machine Learning
MLP	Multi-Layer Perceptron
MSD	Maximum Second Derivative point
MSE	Multi-Scale Entropy
nFFT	Number of points used to calculate the Fast Fourier Transform
nHF	Relative high-frequency band (0.15 – 0.40 Hz)
NIR	Near Infrared Spectroscopy
nLF	Relative low-frequency band (0.04 – 0.15 Hz)
NN	Normal-to-normal
NN50	Number of successive normal-to-normal intervals that differ by more than 50 ms
NREM	Non-Rapid-Eye Movements
OH	Orthostatic hypotension
ONS	Onsets from the photoplethysmogram
OSA	Obstructive Sleep Apnea

P1	First point from the third derivative of the photoplethysmogram
P2	Second point from the third derivative of the photoplethysmogram
PBS	Phosphate-buffered Saline
PBURG	Burg's method to obtain the power spectral density
PCOV	Covariance method to obtain the power spectral density
PDMS	Polydimethylsiloxane
PFDM	Pulse Frequency Demodulation Method
PKS	Peaks from the photoplethysmogram
PLOMB	Lomb-Scargle algorithm to obtain the power spectral density
PMCOV	Modified covariance method to obtain the power spectral density
PMUSIC	Multiple Signal Classification method to obtain the power spectral density
pNN50	Percentage of successive normal-to-normal intervals that differ by more than 50 ms
PNS	Parasympathetic Nervous System
PPG	Photoplethysmography
PPI	Pulse-to-Pulse Intervals
PPV	Positive Predictive Value
PR	Pulse Rate
PRV	Pulse Rate Variability
PSD	Power Spectral Density
PSG	Polysomnography
PTSD	Post-Traumatic Stress Disorder
PTT	Pulse Transit Time
PWELCH	Welch's method to obtain the power spectral density
PYULEAR	Yule-Walker's method to obtain the power spectral density

RBF	Radial Basis Function
REM	Rapid-Eye Movements
RES	Respiratory noise
RF	Random Forest
RMSE	Root-Mean-Square Error
RMSSD	Root mean square of successive normal-to-normal interval differences
ROC	Receiver Operating Characteristic
RRI	R-to-R Intervals
rSVM	Regressive Support Vector Machine
S	Area of the ellipse formed on the Poincaré plot
SA	Sino-atrial
SampEn	Sample Entropy
SBP	Systolic Blood Pressure
SD1	Poincaré plot standard deviation perpendicular to the line of identity
SD1/SD2	Ratio of SD1-to-SD2
SD2	Poincaré plot standard deviation along the line of identity
SDANN	Standard deviation of the average normal-to-normal intervals for each 5 min segment of a 24 h recording
SDB	Sleep Disordered Breathing
SDNN	Standard deviation of normal-to-normal intervals
SDSD	Standard deviation of successive normal-to-normal interval differences
SFS	Sequential Forward Selection
SLO	Maximum slope point
SNR	Signal-to-Noise Ratio
SNS	Sympathetic Nervous System
SpEn	Spectral Entropy

SQI	Signal Quality Index
SR	Stroke Rate
SSE	Sign-Series Entropy
SSEA	Sign Series Entropy Analysis
SV	Stroke Volume
SVM	Support Vector Machine
SVR	Support Vector Regressor
TF	Target Flow
TI	Tangent Intersection
TINN	Baseline width of the RR interval histogram
TN	True Negative
TNR	True Negative Rate
TP	Total power of spectrum (0.003 – 0.40 Hz)
TP-2	True Positive
TPR	True Positive Rate
ULF	Ultra-low-frequency band ($\leq$ 0.003 Hz)
UV	Ultraviolet
VHF	Very High Frequency
VI	Virtual Instrument
VIS	Visible
VLF	Very-low-frequency band (0.003 – 0.04 Hz)
VVI	Valley-to-Valley Intervals
XC	Cross-correlation

Acknowledgements

This thesis is a result of many years of work which would not have been possible without the help and support of many people. First of all, I want to thank my supervisor Professor P.A. Kyriacou for all the guidance, support and understanding during this time. He was always present and always conscious of the circumstances, and always had the appropriate ideas to solve any issue encountered.

Secondly, I wish to thank Dr Robinson Torres, who has always been an inspiration and a guide to always become not only a better professional but a better human being. Gracias por ser la personificación de un maestro.

To all my colleagues at the Research Centre for Biomedical Engineering at City, University of London, thank you. You have been an amazing support during this time. A special thanks to Ms María Roldán, Ms Mahsa Sheikh, Mr Abdullah Al-Aishan and Mr Karthik Budidha. This journey has been even more enjoyable and manageable having you here.

Also, I would like to acknowledge all the people that have become my support system in London. Ms Rosana Marrero and Mrs Lorraine Doubrere, you have made this experience even more valuable.

And last and most importantly, to my parents, my sister and my niece, and all my family back home, thank you for cheering for me even when I didn't think this was possible. Mami, papi, esto es de ustedes.

Declaration

I, Elisa Mejía-Mejía, declare that this thesis titled, 'Pulse Rate Variability for the Assessment of Cardiovascular Changes' and the work presented in it are my own. I confirm that:

- This work was done wholly or mainly while in candidature for a research degree at this University.
- Where I have consulted the published work of others, this is always clearly attributed.
- Where I have quoted from the work of others, the source is always given. With the exception of such quotations, this thesis is entirely my own work.
- I have acknowledged all main sources of help.
- Where the thesis is based on work done by myself jointly with others, I have made clear exactly what was done by others and what I have contributed myself.

Abstract

Pulse rate variability (PRV) describes the way pulse rate changes through time and is measured from pulsatile signals such as the photoplethysmogram (PPG). It has been proposed as a surrogate for heart rate variability (HRV). Nonetheless, the relationship between these variables is not entirely clear, probably due to both physiological and technical aspects involved in the extraction of PRV. Moreover, the effects of cardiovascular changes on PRV have not been elucidated. In this thesis, four studies were performed to (1) determine the best combination of some technical aspects for the extraction of PRV from PPG signals; (2) evaluate the relationship between PRV and HRV under different cardiovascular conditions; and (3) explore the effects of cardiovascular changes on PRV.

First, PRV extraction gave lower errors when (1) signals were acquired for at least 120 s with a 256 Hz sampling rate and filtered with lower low cut-off frequencies and elliptic, equiripple or Parks-McClellan filter; (2) cardiac cycles were determined using the D2max algorithm and the *a* fiducial points; and (3) the Fast Fourier Transform was applied to obtain frequency spectra. Secondly, the relationship between HRV and PRV was found to be affected by cold exposure and changes in blood pressure, while PRV was found to be different at different body sites. Finally, PRV was affected by haemodynamic changes, such as target flow, stroke rate and blood pressure, both in an in-vitro model and in-vivo data. Additionally, PRV was found to be a potential tool for the estimation of blood pressure, with errors as low as 1.54 ± 0.17 mmHg, 1.07 ± 0.06 mmHg and 1.22 ± 0.09 mmHg for the estimation of systolic, diastolic and mean arterial pressure.

Although more studies are needed to fully understand PRV and its clinical potential, PRV should not be regarded as the same as HRV, and it could be consider as a potential valuable biomarker for cardiovascular health.

Chapter 1

Introduction

Pulse Rate Variability (PRV) refers to the changes in pulse rate (PR) overtime, when measured from pulse waves such as the photoplethysmogram (PPG), and has been widely used in recent decades as an alternative to heart rate variability (HRV) (Schäfer & Vagedes 2013). HRV assesses the changes of heart rate (HR) measured from the electrocardiogram (ECG) and has been used in different scenarios for evaluating the cardiac autonomic nervous system (ANS) and its regulation (Huikuri et al. 1999, Quintana 2017, Malik et al. 2017). The assessment of PRV from PPG signals is increasingly gaining attention due to the widespread use of PPG sensors and their capability for obtaining cardiovascular information in a non-invasive, non-intrusive manner, in addition to the cost-effectiveness of the PPG devices (Allen 2007, Kyriacou 2021).

Although HRV and PRV originate from similar processes, and pulse rate (PR) have been found to be a good surrogate of heart rate (HR) (Schäfer & Vagedes 2013), the relationship between HRV and PRV is not straightforward, and there is still no consensus regarding the validity of using PRV as a surrogate of HRV. Some researchers argue that the differences between HRV and PRV are mainly due to physiological aspects, such as changes of haemodynamics due to stress or disease (Giardino et al. 2002, Charlot et al. 2009, Khandoker et al. 2011), the different nature of PPG and ECG signals (Schäfer & Vagedes 2013), and the effects on PRV of pulse transit time and other factors, e.g. external forces on the arterial vessels (Chen et al. 2015, Gil, Orini, Bailón, Vergara, Mainardi & Laguna 2010, Trajkovic et al. 2011). Moreover, PRV has been found to be present in the absence of HRV, as shown by Constant et al. (1999) and Pellegrino et al. (2014), and there are

reports of differences in PRV due to measurement site (Yuda, Yamamoto, Yoshida & Hayano 2020). All of these suggest there are different processes affecting PRV that are not related to HRV.

Besides physiological differences, other studies have concluded that the agreement between PRV and HRV may be affected by technical aspects in the extraction of PRV from pulse waves, such as the selection of fiducial points for the measurement of pulse-to-pulse intervals (Posada-Quintero, H.F., Delisle-Rodríguez, D., Cuadra-Sanz, M.B., & Fernández de la Vara-Prieto, R.R. 2013, Hemon & Phillips 2016, Alqaraawi et al. 2016*a*) and the sampling rate used for the acquisition of the pulse wave signals (Choi et al. 2017, Hejjel 2017, Baek et al. 2017). Moreover, there are no published guidelines for the extraction of PRV from pulse waves and the standardisation of the related analyses. Therefore, most methodologies for PRV studies are based on the guidelines for HRV assessment from ECG signals, published in 1996 (Task Force of the European Society of Cardiology and The North American Society of Pacing and Electrophysiology 1996).

Hence, studies aiming to better characterise PRV and its relationship with HRV, as well as attempting to standardise the procedure to obtain PRV from PPG signals are needed. In this thesis, the aim was to understand how PRV and its relationship with HRV are affected by cardiovascular changes, as well as to determine the appropriate technical aspects that need to be considered for the extraction of PRV from PPG signals.

1.1 Outline

A brief summary of the chapters contained in this thesis is as follows.

Chapter 2 describes the anatomy and physiology of the cardiovascular system of the human body with emphasis on describing haemodynamics and vascular mechanics, as well as some common disorders that can appear in the cardiovascular system. **Chapter 3** introduces the anatomy and physiology of the autonomic nervous system of the human body and describes its relationship with cardiovascular homeostasis. These two chapters are the physiological basis of this thesis.

Chapter 4 describes the origin, extraction, and application of heart rate variability (HRV), as well as its limitations and relation with cardiovascular disorders. Then, in **Chapter 5**, photoplethysmography (PPG) and pulse rate variability (PRV)

are introduced. This chapter provides a profound review of the current literature on PRV and its applications, as well as its relationship with HRV. Also, this chapter describes the current state-of-the-art and the areas of interest for PRV analysis. This is the last theoretical chapter of this thesis.

Chapter 6 focuses on the analysis of technical aspects for the assessment of PRV from PPG signals. In this chapter, a computational model for simulating PPG signals with varying PRV information is proposed, and six independent experiments are described, and their results presented in order to determine the best combination of factors for the extraction of PRV from PPG signals.

Chapter 7 presents the results of an in-vivo study, developed to understand how whole-body cold exposure affects PRV and its relationship with HRV. This was done to evaluate if cardiovascular changes, especially vasoconstriction, could affect PRV in a different manner to HRV, as a model of arterial stiffening.

Chapter 8 and **Chapter 9** evaluate the effect of hypo- and hypertension on PRV and its relationship with HRV, as well as the capability of PRV to classify blood pressure states and estimate blood pressure values using machine learning algorithms.

Chapter 10 describes the development of an in-vitro system for the simulation of the upper-limb circulatory system and the measurement of PPG and pressure signals from this model. Also, a study is presented in which PRV was assessed from PPG signals acquired from this model under different haemodynamic conditions and in the absence of HRV.

Although a complete discussion of the results found in Chapters 6 to 10 is given at the end of these chapters, the last chapter of this thesis, **Chapter 10**, contains a summary of these discussions, as well as the main conclusions of this work and suggestions for future studies.

Chapter 2

Anatomy and Physiology of the Cardiovascular System

2.1 The heart

Blood is a connective tissue constituted by plasma and a corpuscular portion, which includes gases, electrolytes, metabolites, proteins and specialized cells, among others (Conti 2011*b*). This element is of vital importance in every tissue of the human body, and needs to be transported so it can reach every portion of the body. The heart, a four-chambered pump, is the organ which controls and carry out the movement of the blood throughout the body (Rangayyan 2002), and is essential for the correct functioning of every organ and for understanding the physiology of the cardiovascular system.

2.1.1 Anatomy of the heart

The heart is a four-chambered pump with two top chambers, named atria, and two bottom chambers, called ventricles (Rangayyan 2002). The principal function of the heart is to pump the heart to the circulatory system, which consists of both the cardiovascular and the lymphatic system, and its pumping action creates the pressure needed by the blood to circulate through the vessels spread around the body (Fox 2016). Figure 2.1 illustrates the anatomy of the heart.

The blood reaches the heart from various vessels. The right atrium receives it via the superior and inferior vena cava, and the left atrium gets the blood from the pulmonary veins. Atria and ventricles communicate with each other via atrioven-

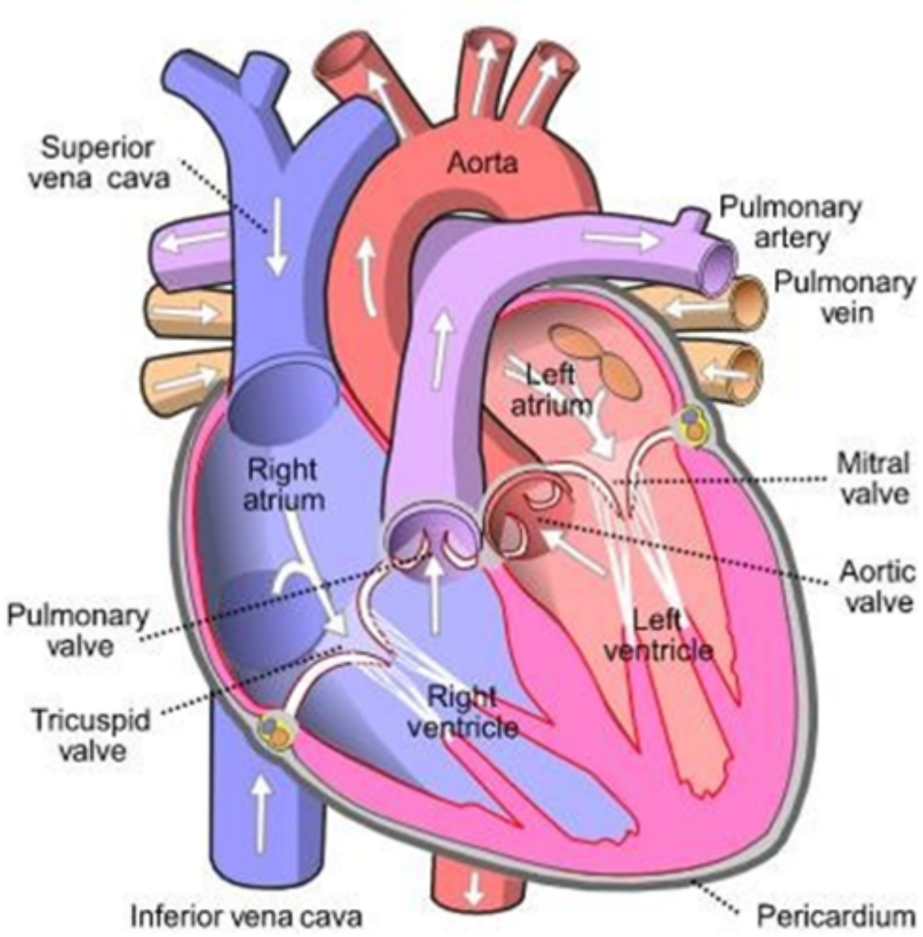

Figure 2.1: Anatomy of the heart (*Heart: function and structure - access revision* n.d.)

tricular valves. The mitral valve communicates the left atria and ventricle, whereas the tricuspid valve serves as a channel between the right chambers. These valves serve as a gateway for the blood to pass from the atria to the ventricle, and prevent the blood to return from the ventricle to the atria (*Heart: function and structure - access revision* n.d.).

With each cardiac beat the blood is ejected from the ventricles via the aorta (left) and the pulmonary artery (right) (Conti 2011*c*). Once again, there are specialized valves that prevent the backflow of the blood from the vessels to the heart, called semilunar valves (*Heart: function and structure - access revision* n.d.). Specifically, the pulmonary valve is located between the right ventricle and the pulmonary artery, and the aortic valve prevents backflow from the aorta to the left ventricle (Conti 2011*c*).

The heart is constituted by involuntary, cardiac muscle, which contracts in a

rhythmic pattern (Conti 2011*c*). This muscle is composed of striated fibres called myocytes, which feature an irregular structure with a single nucleus, high numbers of mitochondria, diameters from 10 to 15 μm and lengths of around 50 μm (Conti 2011*c*). The fibres are connected by intercalated discs, which improve the contact between fibres for a proper distribution of electrical potentials, and form sarcomeres similar to those observed in skeletal muscle (Conti 2011*c*).

2.1.2 Mechanical activity of the heart

The cardiovascular system is composed of the heart and the vessels, and transport blood from the centre to the periphery and from the periphery to the centre. Hence, the four-chambered pump, i.e. the heart, can be divided into two main pumps, right and left, which are in charge of the systemic or major circulation, and the pulmonary or minor circulation, respectively (Conti 2011*c*).

The major circulation circuit has the principal function of delivering fundamental nutrients, such as glucose, fatty acids, amino acids and mineral salts, along with oxygen, to the tissue cells, while removing from the cellular interstitium the carbon dioxide (the main product of the cellular metabolism) and other catabolites. On the other hand, the main objective of the minor circulation is to ensure the oxygenation of blood and the removal of carbon dioxide, which takes place in the lungs through the gas exchange performed by the alveoli (Conti 2011*c*).

To accomplish these, the right and left pumps are connected in a serial manner that assures the transportation of blood. The right atrium receives contaminated blood, which comes from the systemic circulation and has collected metabolic waste, from the inferior and superior vena cava. This blood is pumped from the right atrium to the right ventricle, passing through the tricuspid valve, from where it goes to the pulmonary circulation via the pulmonary valve, where the blood is oxygenated again for its recirculation through the body tissue. From the pulmonary system, the oxygenated blood reaches the left atrium via the pulmonary vein. The left atrium expels the oxygenated blood to the left ventricle via the mitral valve, from where blood is pumped to the systemic circulation via the aortic valve and the aorta, from where it is distributed to the different arterial branches (Rangayyan 2002).

This process is known as the cardiac cycle (Figure 2.2), which refers to the repeating pattern of contraction and relaxation of the heart tissue (Fox 2016). The cardiac cycle can be separated in two main phases, the ventricular systole (contrac-

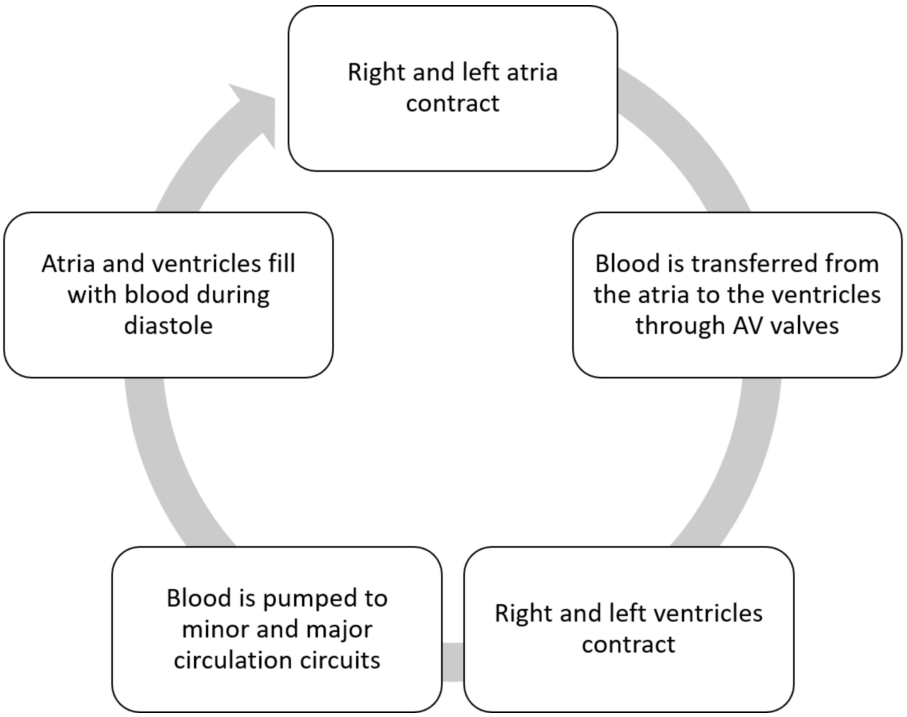

Figure 2.2: Summary of the cardiac cycle. The atria contract and the blood is transferred to the ventricles via the atrioventricular (AV) valves. Then, the ventricles contract and pump the blood to the minor and major circulation circuits. Finally, the atria and ventricles fill with blood again during diastole to restart the cycle.

tion) and diastole (relaxation) (Rangayyan 2002). Although the atria also contract and relax during the cardiac cycle, and hence present an atrial systole and diastole, the terms systole and diastole are usually used to denote the ventricle activity, due to the importance and magnitude of the contraction of these chambers (Fox 2016).

The cardiac cycle is repeated continuously, depending on the heart rate determined by the amount of times the blood needs to be pumped from the heart to the vessels. This rate is determined according to the needs of the body in each moment and is controlled by the firing rate of specialised pacemaker cells that constitute the sino-atrial (SA) node (Rangayyan 2002). At an average heart rate of 75 beats per minute (bpm), the cardiac cycle has a mean duration of 0.8 seconds, from which around 0.5 seconds are spent in diastole and the remaining 0.3 seconds are used in the systole (Fox 2016).

The duration of the cardiac cycle, along with the stroke volume, i.e., the amount of blood that is pumped by the heart in a single contraction, determine the cardiac output, which is the volume of blood pumped per minute (*Heart: function and structure - access revision* n.d.). An average heart rate (70 bpm) and an average

stroke volume (70 mL) imply an average cardiac output at rest of around 5 L/min (*Heart: function and structure - access revision* n.d.).

During the systole, the ventricles have an isovolumetric contraction, which cause the AV valves to close and the blood to be ejected. The diastole has several processes: first, the ventricles present an isovolumetric relaxation and the semilunar valves are closed; this is followed by a rapid filling phase in which both atria and ventricles are relaxed and the blood starts filling the heart chambers; finally, the atrial contraction takes part while the ventricles are relaxed, finalising the filling of the ventricles before a new systole begins (Fox 2016).

These processes have pressure and volume changes related with them, both in the left and the right side of the heart. The main differences between the two pumps (right and left) are the magnitudes of the pressures and volumes needed to pump the blood: since the left ventricle pumps the blood to the systemic circulation, it needs higher pressures and volumes to ensure that it reaches every tissue in the body, whereas the right pump needs lower magnitudes due to the lower complexity of the system it infuses (Conti 2011*c*). Figure 2.3 illustrates the pressure and volume changes that take place in the left ventricle, and their effects during the cardiac cycle.

2.1.3 Electrical activity of the heart

As mentioned above, the muscle fibres present in the heart muscle are specialised fibres known as myocytes. Although they share the basic myosin-actin contraction mechanism with skeletal muscle fibres, cardiac muscle fibres are highly specialised and its membrane structure makes it autorhythmic, so the heart contracts on its own without the impulses from the nervous system (*Heart: function and structure - access revision* n.d.).

The heart comprises several types of tissues composed of myocytes: the SA and the atrioventricular (AV) nodal tissue, atrial, Purkinje, and ventricular tissue (Webster 2010). Each of these types of cell exhibit a different, characteristic action potential and they are all electrically excitable (Webster 2010), constituting the main effectors of the electrical activity of the heart. These specialised tissues are illustrated in Figure 2.4.

A proper functioning of the cardiac conduction system plays a major role in the contractile activity of the heart and, hence, in the proper development of the cardiac cycle. The electrical activity of the heart starts in the SA node, which acts as the

natural cardiac pacemakers and triggers the action potential. Once the SA node fires, the electrical activity propagates through the atrial musculature at low rates, causing the depolarization and contraction of the atria. The excitation wave reaches the AV node, where it is delayed to assure the completion of the transfer of blood from the atria to the ventricles. From there, the His bundle, the bundle branches, and the Purkinje fibres propagate the stimulus to the ventricles at a higher rate, so the wave of stimulus travels fast from the apex of the heart upwards, causing the ventricles to rapidly depolarize and contract. Once the blood is pumped from the ventricles, these repolarize and relax, before a new action potential is sent by the SA node (Rangayyan 2002).

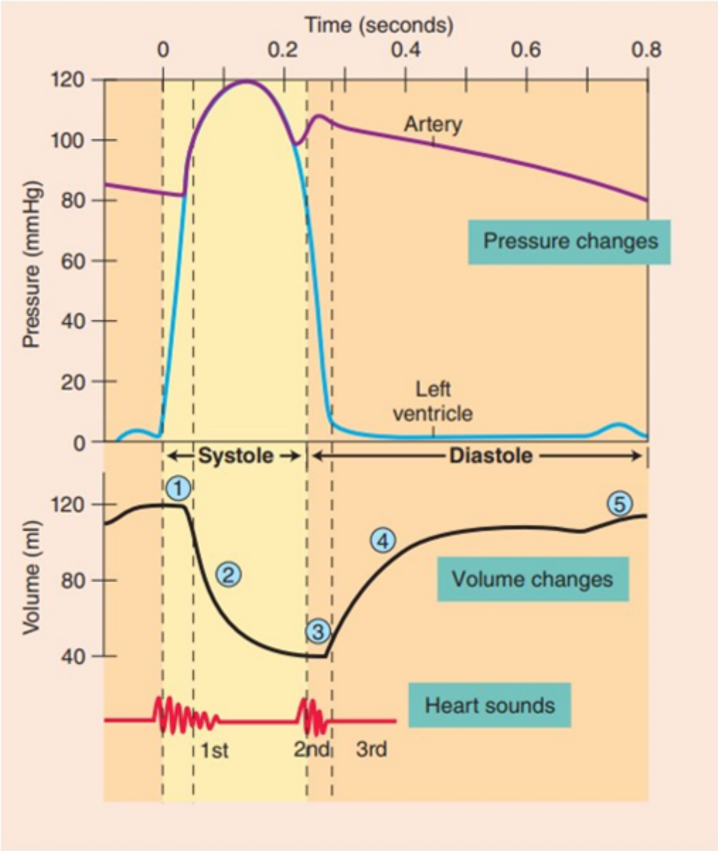

Figure 2.3: Pressure and volume changes in the left ventricle and arteries, where each numbered phase of the cycle refers to (1) the isovolumetric contraction of the heart; (2) the ejection of blood from the heart; (3) the isovolumetric relaxation; (4) the rapid filling of the ventricles; and (5) the atrial contraction. (Fox 2016)

2.2 Blood vessels

Blood vessels are the organs that transport the blood pumped by the heart to the rest of the body, both in the major and the minor circulation. There are 3 major types of blood vessels: the arteries, which carry blood and metabolic substrates from the heart; the capillaries, which transport metabolic substrates and waste products to living tissue; and the veins, which carry blood back to the heart (Ostadfar 2016). Figure 2.5 shows a schematic of the distribution of blood vessels.

The blood vessels can be classified as arteries, arterioles, capillaries, venules, and veins, and each of these types have different morphological and physiological characteristics (Table 2.1). These organs are distributed around the body to form, along with the heart, the pulmonary, systemic and coronary circulation systems (Ostadfar 2016). In general, the vascular system executes two essential tasks: the distribution

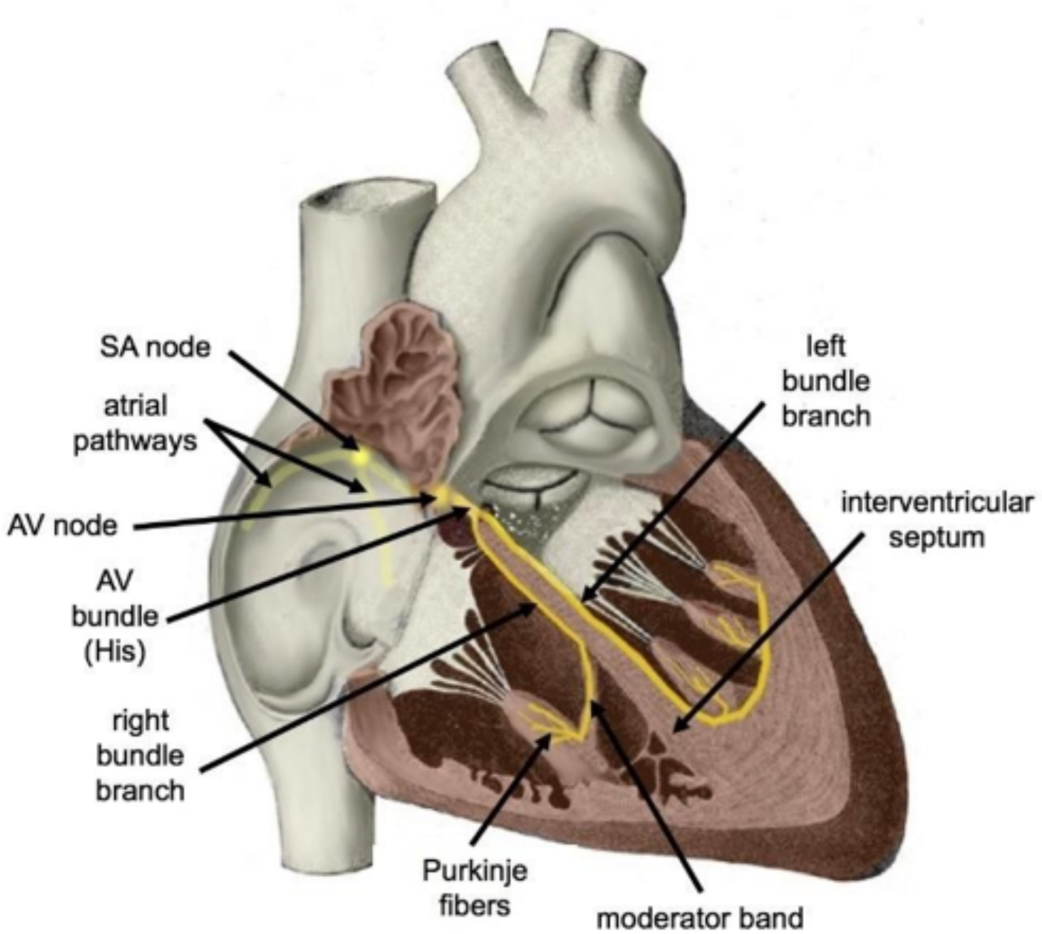

Figure 2.4: Electrical system of the heart (Cypressvine 2019). The coordinated electrical stimulation of the different tissue allows for the correct execution of the cardiac cycle.

Table 2.1: Approximate characteristics of human blood vessels (Ostadfar 2016).

Vessel type	Internal diameter (mm)	Wall thickness (mm)	Length (cm)	Average blood velocity (cm/s)	Function
Aorta	25	2	50	45	Distribution Pulse damping
Arteries	4	1	25	30	Distribution Resistance
Arterioles	0.03	0.02	1	0.5	Resistance
Capillaries	0.006	0.001	0.1	0.03	Exchange
Venules	0.02	0.002	0.2	0.2	Collection Capacitance
Veins	5	0.5	2.5	1	Capacitance
Vena Cava	30	1.5	50	14	Collection

of blood and the exchange of nutrients between the blood and the tissues, which is mainly performed by the capillaries. In addition, vessels help regulate blood pressure and blood volume by creating and modifying resistance and capacitance in the vascular system (Ostadfar 2016).

2.2.1 Anatomy of the vessels

The anatomy of each type of blood vessel differs, due to the different actions they perform in the circulatory system. The arteries, which are in charge of transporting blood from the heart to the body tissues, are known as the higher-pressure part of the cardiovascular system. Veins, on the contrary, are in charge of collecting blood

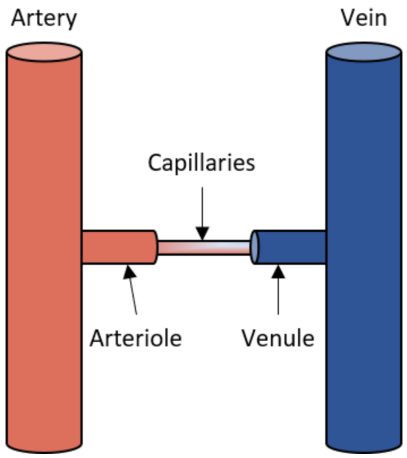

Figure 2.5: Schematic diagram of the distribution of blood vessels (Ostadfar 2016). Oxygenated blood travels through arteries and arterioles to capillaries, where oxygen is diffused to the tissue. Contaminated blood travels back to the heart through venules and veins.

Table 2.2: Main human arteries and veins (Ostadfar 2016).

Main Arteries	Main Veins
Aorta	Vena Cava
Pulmonary artery	Jugular veins
Subclavian artery	Pulmonary vein
Carotid artery	Femoral vein
Femoral artery	Subclavian vein
Brachial artery	Brachial vein
Renal artery	Renal veins
Anterior tibial artery	Anterior tibial vein
Common iliac artery	Iliac veins
Ulnar artery	Saphenous vein
Radial artery	Radial vein
Posterior tibial artery	Posterior tibial vein
Hepatic artery	Hepatic vein
Mesenteric artery	Mesenteric vein
Lateral circumflex artery	Axillary vein
Popliteal artery	Popliteal vein

and taking it back to the heart (Ostadfar 2016). Since nearly 60% of the total blood volume is housed within the veins, these vessels also act as a reservoir for blood (Rubenstein et al. 2016). Table 2.2 summarizes the main arteries and veins that are found in a human body.

There are three main types of arteries in the human body: Elastic arteries, which receive blood directly from the heart (i.e. aorta and pulmonary artery), have a high wall thickness to diameter ratio in order to maintain blood pressure during both systole and diastole, and contain greater number of elastic fibres on their walls to allow for the elasticity behaviour needed by these vessels; muscular or distributing arteries, which are in charge of distributing blood to various tissues and organs and are mainly constituted by smooth muscle in their walls; and arterioles, which are the smallest arteries, with only one or two layers of smooth muscle in their walls, and allow for a drop in the blood pressure (Ostadfar 2016).

The arterial wall is composed of three layers: the tunica intima, the tunica media, and the tunica adventitia (Figure 2.6) (Ostadfar 2016, Rubenstein et al. 2016). Under normal conditions, the tunica intima is the only layer in contact of blood and is composed of endothelial cells and a small connective tissue layer, primarily built of elastic fibres that helps secure the endothelial cells in place (Rubenstein et al. 2016). The tunica media, composed of smooth muscle cells, is responsible of changing the arterial diameter in response to neural and humoral control, and helps maintain the

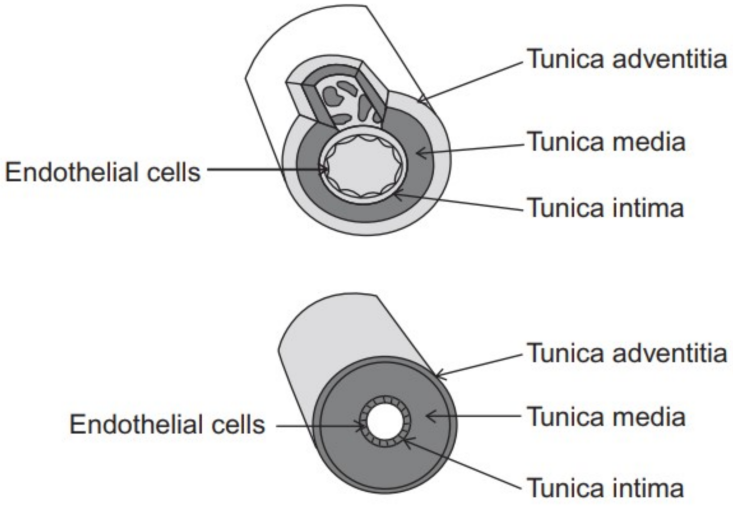

Figure 2.6: Composition of the arterial wall of large elastic (top) and muscular (bottom) arteries (Ostadfar 2016). In most arteries, the arterial wall is composed of the tunica intima, the tunica media and the tunica adventitia.

integrity of the blood vessel while it is exposed to higher pressures (Rubenstein et al. 2016). Finally, the tunica adventitia, also known as tunica externa (Ostadfar 2016), is responsible for anchoring the blood vessel to adjacent tissue (Rubenstein et al. 2016). This layer is mainly composed of collagen (Ostadfar 2016). The thickness of each of these layers depends on the type or artery; nonetheless, the tunica media is, in general, the thickest layer in the arterial wall (Rubenstein et al. 2016).

Veins, in contrast to the arteries, transport blood under much lower pressures, usually below 5 mmHg; therefore, their walls are thinner than in the arteries, but still are mainly composed of muscular tissue (Rubenstein et al. 2016). Also, the inner diameters of the veins are smaller but comparable to that of the arteries in similar locations (Rubenstein et al. 2016).

The venous wall is also composed of the three layers: Tunica intima, tunica media and tunica adventitia, and although they have the same general anatomy, there are some differences: the endothelial layer within the tunica intima is smooth because veins are not usually significantly contracted or dilated, as occurs with arteries; the tunica media is thinner and composed of smooth muscle cells and collagen; and the tunica adventitia is the thickest layer, composed of collagen, elastin, and smooth muscle cells (Rubenstein et al. 2016). Lastly, the veins differ from the arteries in that the former contain valves that prevent the backflow of blood toward the capillary beds, and that can act as a pump to help blood flow from the lower limbs back to

the heart (Rubenstein et al. 2016).

The thickness and sizes of vessels' layers differ according to the size of the vessel (Fox 2016). Moreover, the venules, arterioles and capillaries have different structures. Arterioles are mainly formed by endothelium, which contains precapillary sphincters; venules, on the other hand, are formed by endothelium wrapped by tunica externa similar to that of medium-sized veins (Fox 2016). Unlike most of the other vessels, capillaries are composed of one cell layer (endothelium), which permits the rapid transfer of materials between the blood and the tissues; according to the organ they are infusing, the endothelial lining of the capillaries change, so they are classified as continuous, in which adjacent cells are closely joint together; fenestrated, located in the kidneys, endocrine glands, and intestines, and in which the main characteristic is the presence of wide intercellular pores that are covered by a layer of mucoprotein; and discontinuous capillaries, in which the distance between endothelial cells is greater, and are usually found in bone marrow, liver, and spleen (Fox 2016). Figure 2.7 illustrates the structure of blood vessels.

2.2.2 Circulation of blood

Once the blood is pumped by the left ventricle, it goes through the aorta, which makes a 180° turn in the aortic arch to take the blood to the descending aorta. This arch contains branches that lead blood to the head and the arms, via the carotid and subclavian arteries, respectively. The descending aorta goes to the pelvis, and on its way there it distributes blood to the main arteries that infuse the major abdominal organs, i.e., renal, hepatic, bronchial arteries, among others. Once in the pelvis, the descending aorta branches into the left and right iliac arteries, and the sacral artery (Rubenstein et al. 2016).

After the blood travels through the arteries, it enters the arterioles, the final branch of the arterial system before entering the microcirculation and an important player in the regulation and control of blood flow throughout the entire body (Rubenstein et al. 2016).

After passing through the capillaries, the blood reaches the venules, which converge into the veins, and then travels back to the heart via the inferior and superior vena cava (Rubenstein et al. 2016).

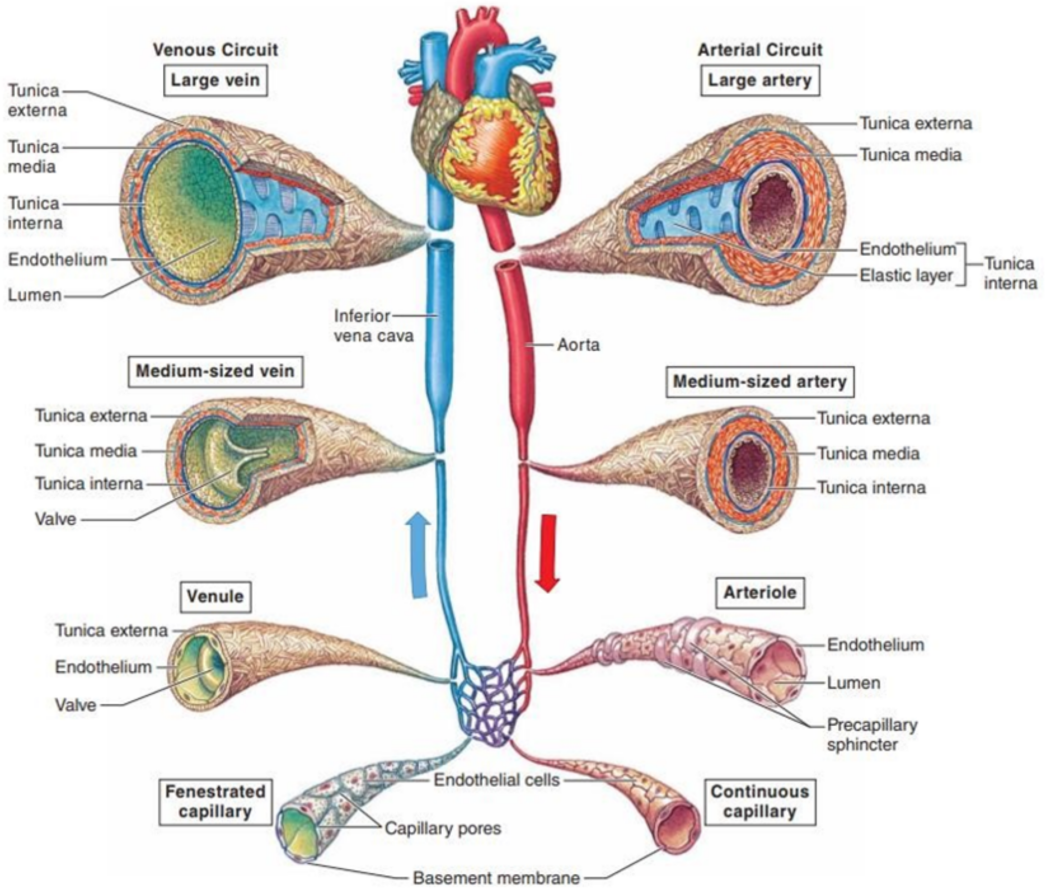

Figure 2.7: Structure of blood vessels (Fox 2016)

2.3 Haemodynamics and vascular mechanics

The cardiovascular system can be modelled as two cylindrical tubes that connect two mechanical pumps in series, as shown in Figure 2.8 (Conti 2011*a*). Since the two pumps are connected in series, it is expected that the volume of blood that is pumped by the left ventricle is the same volume that is received by the right atrium, and vice versa; also, it is assumed that the flow rate remains constant, meaning that the mean velocity of blood decreases as the cross-sectional area of vessels increases (Hoskins 2017). This behaviour has important consequences on the cardiovascular function (Conti 2011*a*) and helps to understand the laws that govern the flow within the arterial and venous systems.

2.3.1 Blood and blood flow

Blood is not a pure fluid, but a suspension of particles in a fluid base, known as plasma. The particles that are suspended in plasma are red and white cells, platelets,

macromolecules, especially proteins, and fragments of cells (Hoskins & Hardman 2017). Table 2.3 summarises some properties of the main components of blood.

Several forces act on blood and its particles in order to generate and sustain blood flow, including forces related to gravity, velocity and shear, and chemical and electrical forces (Hoskins & Hardman 2017). Although these forces apply to every particle in the fluid, the viscosity and flow of blood is mainly affected by the behaviour of red cells, or erythrocytes (Hoskins & Hardman 2017).

The rate of blood that flows to an organ is related to the resistance to flow in the small arteries and arterioles of such organ (Fox 2016). In the simplest model, the flow through a blood vessel, Q, is determined by the pressure difference across the vessel, ΔP, and the resistance to flow throughout the vessel, R, as shown in (2.1) (Rubenstein et al. 2016).

$$Q = \frac{\Delta P}{\Delta R} = \frac{P_1 - P_2}{R} \tag{2.1}$$

This behaviour is analogous to that of an electrical circuit governed by Ohm's law, in which a driving force (the changes in pressure) is proportional to the flow through the system (Rubenstein et al. 2016, Conti 2011*a*). Resistance to flow cannot be measured, but can be derived from (2.1), assuming that the fluid flow and fluid properties have no temporal variation and that there is a constant uniform

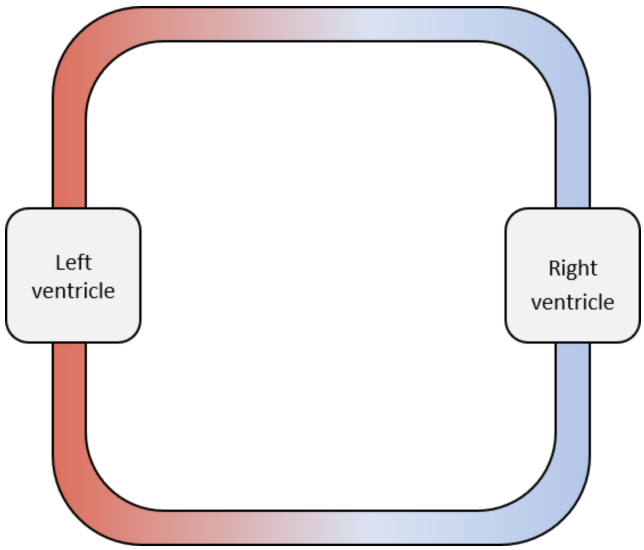

Figure 2.8: Simplified model of the cardiovascular system (Conti 2011*a*). In this model, the cardiovascular system is simulated as two cylindrical tubes that connect two mechanical pumps (left and right ventricles) in series.

cross-section within a rigid blood vessel (Rubenstein et al. 2016). The resistance is important to maintain the same flow rate: At a higher-pressure head, resistance to flow must also increase (Rubenstein et al. 2016).

A more appropriate approximation to this behaviour is given by Hagen-Poiseuille's law, which takes into account the geometry of the vessel and calculates the volumetric flow of blood (2.2) (Rubenstein et al. 2016, Conti 2011*a*). The flow depends on the dimensions of the conduct (its radius R and length L), the difference in the pressures between the ends of the segment (ΔP), and the fluid viscosity (μ) (Conti

Table 2.3: Components of blood (Hoskins & Hardman 2017).

Blood component	**Percentage (by volume)**	**Principle function**	**Low concentration**	**High concentration**
Red cells	40-50	Carrying oxygen.	Blood loss, sickle cell anemia, enlarged spleen, cancer.	Polycythaemia, chronic hypoxia, blood doping, dehydration.
White cells	0.7	Immune system.	Medication and radiation treatment, immune dysfunction, toxins (including alcohol), major surgery.	Infection, genetic disorders, leukaemia, spleen removal.
Platelets	0.3	Clotting of blood.	Medication and chemotherapy, haemolytic-uremic syndrome, snakebite.	Thrombocytosis.
Albumin	2	Maintenance of osmotic pressure.	Reduced production (various diseases).	Dehydration.

2011*a*).

$$Q = \frac{\pi \Delta P R^4}{8 \mu L} \tag{2.2}$$

It can be seen that vasodilation decreases the resistance of the vessel and increases the flow, while vasoconstriction increases resistance and decreases flow (Fox 2016). Remarkably, the flow varies in direct proportion to the fourth power of the ratio, meaning that small variations of the ratio generate important variations of flow; this is the main explanation to the fact that small changes in the diameter of arterioles can induce notable variations of peripheral resistance and blood flow in microvascular level (Conti 2011*a*). As stated in (Rubenstein et al. 2016), if changes in diameter did not generate rapid changes in flow rate, blood vessels would have to dilate or constrict significantly to respond to demands in tissue oxygenation levels, which would be associated with important energy demands that would ultimately deplete the smooth muscle cell of energy.

In the systemic circulation, the blood pressure reduces from 80-120 mmHg in the aorta to near 2-4 mmHg in the arterioles, where the maximum pressure fall occurs; therefore, the maximal peripheric resistance is given by these vessels, which regulate the capillary flow to assure the proper behaviour of oxygen exchange (Conti 2011*a*).

Using (2.2), it is possible to estimate the average velocity of the blood, by dividing the volumetric flow by the cross-sectional area of the vessel (2.3), and its maximum velocity, which occurs at the axis of the tube (2.4) (Nichols et al. 2011).

$$\bar{V} = \frac{R^2 \Delta P}{8 \mu L} \tag{2.3}$$

$$V_{axial} = \frac{R^2 \Delta P}{4 \mu L} \tag{2.4}$$

These equations can be considered as an approximation of the flow dynamics in the veins and venules as well, although these vessels are generally not cylindrical, and hence do not meet all the assumptions made for the derivation of the Hagen Poiseuille's law (Rubenstein et al. 2016).

There is a relationship between the flow and viscosity of blood, as is shown in (2.2) (Nichols et al. 2011). Viscosity is a fundamental property of liquids that represent the friction between the different liquid layers (Conti 2011*a*), and is defined

as the ratio of shear stress (the force applied to the liquid layer) and shear rate (the velocity gradient obtained between adjacent layers of the liquid) (Nichols et al. 2011).

Blood viscosity varies due to flow velocity, diameter of the vessels, and the quantity and quality of the blood cells suspended on plasma (Conti 2011*a*). Although blood is a non-Newtonian fluid, in the larger vessels the blood has a Newtonian-like behaviour, showing a parabolic velocity profile and a laminar flow, and shows a behaviour similar to that expected from (2.2) (Conti 2011*a*). On the other hand, if (2.2) is applied to a capillary, the hydrodynamic analysis of blood flow will present several differences, not only due to viscosity changes but also because some parameters of the vessel cannot be measured accurately in the living vessel (Nichols et al. 2011).

2.3.2 Pressure and flow in arteries

Blood pressure is affected by three main factors: Blood volume, total peripheral resistance, and cardiac rate (Fox 2016). However, it is different across the arterial system, in which arterioles and capillaries have smaller pressures due to their diameter and the resistance of flow; these smaller blood pressures allow for a proper nutrient exchange in capillary level (Fox 2016).

Blood pressure is maintained within limits due to the measurement of pressure levels performed by baroreceptors located in the aortic arch and in the carotid sinuses (Fox 2016). Once these sensors measure the levels of pressure, parasympathetic or sympathetic activity is stimulated according to the needs: If blood pressure is low, sympathetic nerve activity increase, generating a compensatory increase in cardiac output and total peripheral resistance; conversely, a high blood pressure generates an increased activity in parasympathetic nerves which evoke a reduction in cardiac output and total peripheral resistance (Fox 2016). The levels of blood pressure are essential to assure a proper blood flow through the whole circulatory system.

Each time the heart pumps, the blood circulates through the arterial tree and the pressure propagates from the aorta to the other arteries. This is due to the arteriovenous pressure differences, which comes from the aorta (around 100 mmHg) to the vena cava (which is close to 0) (Caro et al. 2012).

As mentioned by Caro et al (2012), if the vascular system consisted of a single, long, straight, rigid tube, the volume flow rate Q would be uniform at all times and directly proportional to the pressure difference between the two ends. Hence, the

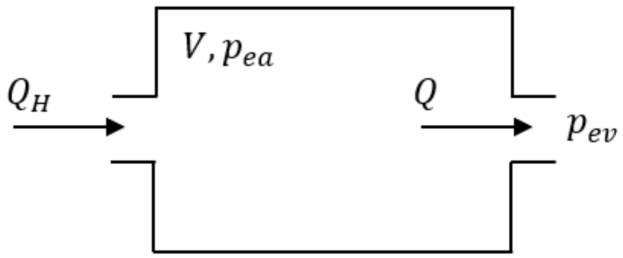

Figure 2.9: The Windkessel model of the arteries. In this model, the vessel is pictured as a compliant chamber of volume V proportional to the pressure p_{ea}. The flow rate Q is proportional to the pressure difference p_{ea} - p_{ev}, and may be different to the flow rate getting into the system, Q_H (Rangayyan 2002)

pressure waveform at any point of the tube would be synchronous and similar to that of the aorta, but with a different amplitude (Caro et al. 2012). However, this does not occur in an in-vivo model due to the elasticity of blood vessels: When the pressure passes through an artery, the vessel expands with the increase in pressure, and when the pressure falls again it contracts again (Caro et al. 2012). This is known as Frank's or the Windkessel model (Figure 2.9).

From this model, it can be concluded that the rate of increase of volume of the chamber must be equal to the difference between the two flows, Q_H and Q (2.5) (Caro et al. 2012). Nonetheless, this model has an important shortcoming: It assumes that all arteries are distended simultaneously, and hence fails to describe the dynamic events in the cardiovascular system adequately and the wave propagation feature of the cardiovascular system (Caro et al. 2012, Hoskins & Hose 2017). In fact, when the blood is pumped to the aorta, this disturbance is propagated along the arterial system in the form of a pressure wave, which generally originates at the heart and travels distally, although it can propagate in either direction and is modified by the reflection of components from the periphery (Caro et al. 2012).

$$\frac{dV}{dt} = Q_H - Q \tag{2.5}$$

The speed with which this pressure waves propagates through the arterial system can be estimated by considering the arterial system to behave as a stretched string, in which the velocity of propagation of a wave is given by the tension of the string and its inertia; in the case of a blood vessel, the inertia term is supplied primarily by the mass of the blood and can be characterized by the blood density (ρ), and the tension of the string is dependent on the elasticity of the vessel walls (D), i.e. a more

distensible wall will diminish the wave speed, while a stiffened wall will increase it (Caro et al. 2012). Equation (2.6) shows a simplified relationship between the wave speed, c, and these two factors, in which two assumptions are made: The blood viscosity has no effect on the motion, and the elastic wall properties and the fluid mechanics are linear; neither blood viscosity and the non-linear aspects of blood flow affect the wave speed in a relevant manner in human arteries, especially large arteries, although the latter influence the shape of the pressure and flow waveforms (Caro et al. 2012).

$$c = \frac{1}{\sqrt{\rho D}} \tag{2.6}$$

The shape changes are associated with wave reflections from terminations and branches of the vessels, as well as with the continuous tapering of individual vessels and the different frequency components of the wave, which may travel at different speed and being attenuated in a different manner (Caro et al. 2012). In fact, in any point in which the properties of the vessel change, there will be partial reflection of the wave (Caro et al. 2012); e.g., in a bifurcation, the parent branch not only contains the incident wave but also contains a portion of the wave that is reflected backwards into the parent branch (Rubenstein et al. 2016). Reflections are the source of the greatest modification of pulse wave shape as it travels to the periphery (Caro et al. 2012). Due to the way the wave propagates, there are also differences in the pressure and flow waveforms at different distances from the heart, with an increased pulse pressure with distance from the heart in young adults (Hoskins & Hose 2017).

The flow in arteries depends mainly on the Reynolds number (Re) of the fluid. The mean Re in the arterial system decreases from around 2000 in the aorta during systole to very small Re in the microcirculation (Hoskins & Hose 2017). The larger Re in the aorta means there is turbulent flow in the post-systolic phase, but in healthy subjects the flow can be considered laminar in the remainder of the arterial tree (Hoskins & Hose 2017). Although flow in long, straight tubes, such as arteries in legs and arms, is mainly axial, there are also segments of the arterial system in which rotational flow occurs, mainly due to curvature and bifurcations in arteries. This rotational flow is also actively induced by twists of the left ventricle during contraction, and is thought to serve as a way to stabilise flow in the arterial system

and to mix blood to assure a more uniform distribution of red cells in arteries (Hoskins & Hose 2017).

The understanding and measurement of the pressure and flow behaviour of blood in arteries is essential to improve the diagnosis and treatment of diseases and abnormal conditions related to the cardiovascular system.

2.4 Abnormal conditions

Abnormal conditions may lead to several chronic cardiovascular diseases, such as hypertension, heart failure, and diabetes mellitus (Sheng & Zhu 2018). Therefore, understanding the complex processes that contribute to a normal activity of the cardiovascular system may lead to new and effective strategies for prevention, diagnosis and treatment of cardiovascular diseases (Sheng & Zhu 2018).

As was discussed above, the arterial blood pressure and the elasticity of the vessels are crucial for obtaining a proper blood flow throughout the arterial tree and for ensuring the transport of nutrients and oxygen through all the tissues in the body. Hence, changes in these properties may generate diseases that can lead to serious health conditions. The measurement of physiological data that could help identify these changes is of invaluable interest and have been shown to aid in the diagnosis and treatment of some important cardiovascular disorders such as hyper and hypotension, and arterial stiffness.

2.4.1 Hyper- and hypotension

An arterial blood pressure of 120/80 mmHg (systolic/diastolic pressure) is considered as the normal and healthy value for arterial blood pressure (National Health Service 2019*a*). Blood pressure values may vary around 120/80 mmHg throughout the day but tend to be very close to these in healthy subjects (National Health Service 2019*a*). Blood pressure is primarily regulated, in a beat-to-beat basis, by the sympathoadrenal system, when changes in the pressure measured by baroreceptors need to be balanced (Fox 2016). However, sustained increased or decreased values of blood pressure, both during systole and diastole, are considered as abnormal conditions that may affect the blood flow to tissues and, hence, the homeostasis of the circulation.

Hypotension refers to blood pressure values that are equal to or less than 90/60

mmHg, and is related to light-headedness, blurred vision, weakness, confusion, and fainting; although in fit subjects, a lower arterial pressure is expected, a lower blood pressure can be related to pregnancy, some medicines, and some medical conditions, such as diabetes mellitus (National Health Service 2017). Although it has not been as studied as its counterpart, i.e. high blood pressure, some kinds of hypotension are now clinically significant and recognized as a cause of impairment of quality of life and potentially of worse outcomes (Magkas et al. 2019). One of the most studied causes of low pressure is known as Orthostatic Hypotension (OH), and refers to the pressure fall when changing from a supine position to a standing position; this condition is considered as a cardiovascular disorder, which is highly prevalent in elderly and frail subjects, as well as in patients with certain comorbidities (Magkas et al. 2019). OH is defined as a sustained reduction of at least 20 mmHg or 10 mmHg in systolic and diastolic blood pressure, respectively, within 3 minutes of standing or head-up tilt to at least 60° on a tilt table (Magkas et al. 2019). OH is considered as a major cause of syncope, and is related to loss of consciousness due to severe hypotension and cerebral hypoperfusion (Magkas et al. 2019). In many cases, the origin of OH is related to inadequate autonomic regulation of heart rate, venous return, cardiac contractility, and vascular tone (Magkas et al. 2019).

Hypertension, on the other hand, is a condition in which the blood pressure values are persistently raised from the normal values, causing an increase in the force applied by the heart to pump the blood throughout the circulatory system (World Health Organization 2019). Although it usually does not have noticeable symptoms, hypertension increases the risk of different serious disorders, such as heart attacks and strokes (National Health Service 2019*a*). In hypertensive patients, the arterial blood pressure is equal to or higher than 140/90 mmHg (National Health Service 2019*a*). Blood pressure can be increased due to a higher total peripheral resistance as a result of vasoconstriction of arterioles, or due to an increase in cardiac output, whether it is because of elevations on heart rate or in stroke volume (Fox 2016).

When hypertension generates as a result to a known disease, it is called secondary hypertension, while when it is the result of complex processes, it is regarded as primary or essential hypertension, which is the most common source of hypertension (Fox 2016). It is estimated that 1.13 billion people in the world have hypertension (World Health Organization 2019); however, more patients are asymptomatic and hypertension is usually not identified until substantial vascular damage has occurred

(Fox 2016).

Some of the physiological effects of hypertension are: (1) large- and medium-sized arteries become thickened, rigid, dilated, and tortuous, generally with atheroma, and smaller arteries have thickened tunica media, intimal expansion, and a narrowing lumen; (2) in the heart, coronary artery atheroma is common, as well as long-term cardiac functional impairment with left ventricular systolic dysfunction, and hypertension may result in coronary artery disease, heart attacks and strokes; (3) intracerebral haemorrhage and cerebral infarction are often related with hypertension due to microaneurysms of the small arteries deep within the brain; (4) there is thickening, irregularity and tortuosity in the retinal artery even with mild hypertension, and emboli is often present in this artery due to hypertension; and (5) malignant hypertension is often related with extensive and progressive fibrinoid necrosis of afferent glomerular arterioles, glomerular infarction, and consequent renal impairment (Beevers & Robertson 2007).

2.4.2 Arterial stiffness

The velocity of the pulse wave propagation throughout the circulatory system is related to the elasticity of the vessel wall (Messas et al. 2013). The elasticity of the vessel, also referred to as the arterial stiffness, has been considered as a precursor for peripheral vascular disease and as an independent risk marker of cardiovascular disease and atherosclerosis (Messas et al. 2013). The stiffening and thickening of the arterial wall is called arteriosclerosis, and is manifested in two main forms: Calcification of the arterial wall, associated with the deposition of calcium salts between the tunica media and the tunica intima, or atherosclerosis, which refers to the deposition of lipids within the arterial wall (Rubenstein et al. 2016). The latter is the most common form of arteriosclerosis (Fox 2016) and is a risk factor for most cardiovascular diseases, with increased prevalence in recent years (Roth, G.A., et al. 2020).

As stated by Rubenstein et al (2016), arteriosclerosis is an inflammatory disease that originates due to altered fluid dynamic forces, which injures the wall of the vessel or causes the oxidation of lipoproteins. It is a more general disease than atherosclerosis, as it only requires the thickening and stiffening of blood vessels, and tends to occur in concentric and diffuse patterns, whereas atherosclerosis usually occurs asymmetrically at particular points (Rubenstein et al. 2016).

Arteriosclerosis is highly related with aging and is a problem spread all around the world but can be seen as a disease condition when occurs prematurely (Nichols et al. 2011). It is directly related with increased systolic and diastolic blood pressure (Izzo 2007). With aging, the arterial elastic lamellae fractures and the artery is stiffened and dilated, causing and increased impedance and increased, early reflection; this generates isolated systolic hypertension, which derives in left ventricle hypertrophy and impaired myocardial supply/demand, eventually leading to myocardial ischemia, which later causes arrhythmias, ventricular enlargement, cardiac failure and end-stage heart disease (Nichols et al. 2011).

Arterial stiffness is usually found in the aorta and the larger arteries, mainly due to the effects of pressure and the stress they are subjected to during each cardiac cycle, and the changes in diameter of the vessels due to blood flow; increased heart rates and blood pressures are therefore related to premature aging arteries, since larger pressures and an increase in the number of repetitions in which the artery wall needs to expand will diminish the lifespan of the elastic fibres of the wall of the vessel (Nichols et al. 2011).

2.5 Summary

The cardiovascular system mainly comprises the heart and blood vessels. These organs have the vital role of transporting blood around the body, in order to carry nutrients and oxygen to the tissue, and to help extract metabolic waste such as carbon dioxide. Several features such as pressure, flow and viscosity of blood are essential to allow for a proper functioning of the cardiovascular system, and of the oxygenation of tissue.

Hence, the understanding of these features allow for a proper comprehension of cardiovascular dynamics and abnormal conditions that may arise from changes in blood pressure and flow. Some of the most studied conditions are the sustained increase or decrease of pressure, i.e. hyper- and hypotension, and the stiffening of arteries, that may lead to changes in flow and to critical pathologies such as atherosclerosis.

Chapter 3

Anatomy and Physiology of the Autonomic Nervous System

3.1 The Nervous System

The human body features several control systems which are in charge of maintaining the constancy of the internal environment, which is also known as homeostasis (Fox 2016). The concept of homeostasis has been of paramount importance for understanding several disorders that may be seen as a general failure of body systems but that may be especially related to a single measurement that deviates significantly from the normal range of values (Fox 2016).

Usually, these control systems are based on negative feedback loops: Changes in the body stimulate sensors that send information to an integrating centre, such as a particular region of the brain or spinal cord, or an endocrine gland, which is in charge of directing the responses of muscles or glands in order to normalise the values that are being measured by the sensors (Fox 2016).

The endocrine and nervous systems are the principal control systems in the human body, and they regulate the activities of most of the other systems (Fox 2016). Specifically, the nervous system activity is based on nerve fibres which innervate the organs that they regulate, called target organs, and stimulate them using electrochemical nerve impulses (Fox 2016).

The nervous system is divided into the central nervous system and the peripheral nervous system. The former includes the brain and spinal cord, while the latter includes the cranial nerves that arise from the brain and the spinal nerves that

originate in the spinal cord (Fox 2016).

The nervous tissue is composed of nerve cells called neurons, which are specialised cells for the generation and conduction of electrical events, and supporting cells, which assist the functions of neurons and are known as neuroglia or glial cells (Fox 2016). Neurons have three distinct parts: A cell body, which contains the nucleus and in which all metabolic activity of the cell takes place; dendrites, which are highly branched cytoplasmic extensions of the cell body and which receive input from other neurons or from receptor cells; and an axon, a large single cytoplasmic extension which is in charge of conducting nerve impulses from the cell body to another neuron or to an effector cell (Fox 2016) (Figure 3.1).

Neurons can be classified according to their function or their structure. Their functional classification is based on the direction of conduction of the impulses: Sensory (afferent) neurons conduct impulses from sensory receptors located in the periphery to the central nervous system, while motor (efferent) neurons conduct impulses from the central nervous system to the effector organs, whether they are

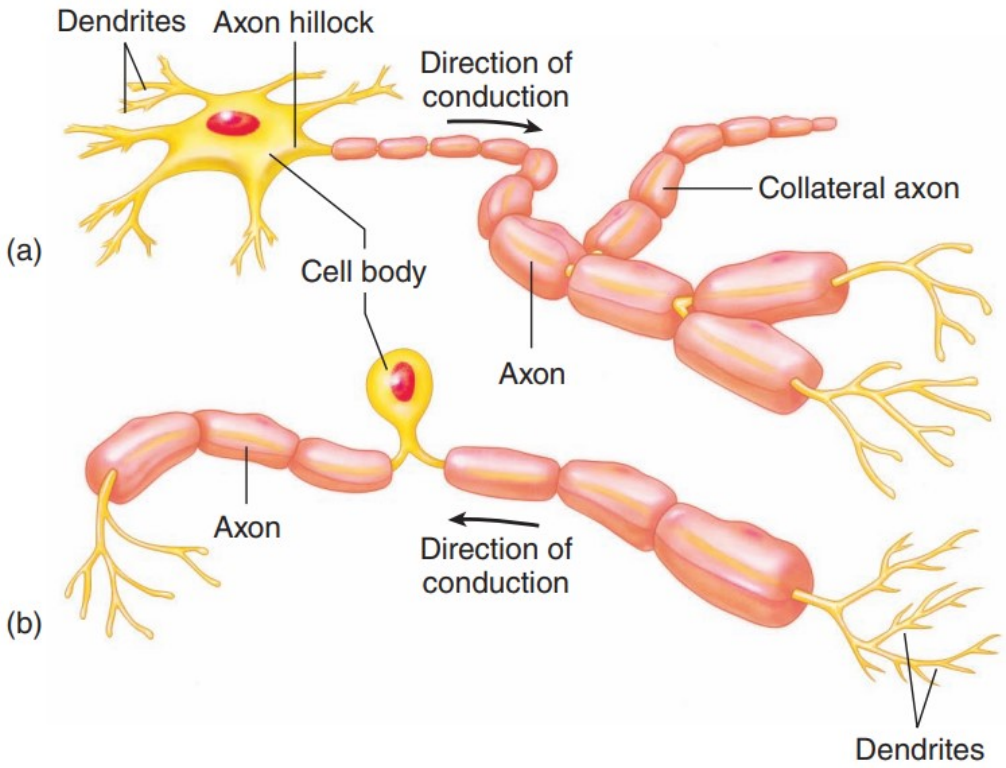

Figure 3.1: Structure of (a) a motor neuron, and (b) a sensory neuron (Fox 2016). In both cases, the three distinct parts of the neuron, i.e., the cell body, the dendrites and the axon, are present.

muscles or glands (Fox 2016). Motor neurons can also be classified in two groups: Somatic motor neurons, which are in charge of both reflex and voluntary control of skeletal muscles; and autonomic motor neurons, which innervate involuntary effectors such as smooth muscle, cardiac muscle and glands (Fox 2016). These autonomic motor neurons, along with their central control centres, constitute the Autonomic Nervous System (ANS), and play a vital role in regulating the activity of involuntary muscles (Fox 2016). The ANS has the ultimate task of ensuring the survival and procreation of species (Hamill et al. 2012).

3.2 Structure of the Autonomic Nervous System

Figure 3.2 illustrates the distribution of the ANS within the human body. Autonomic motor nerves innervate organs, such as the heart, blood vessels, and visceral organ, and are characterised by the involvement of two neurons in the efferent pathway: A

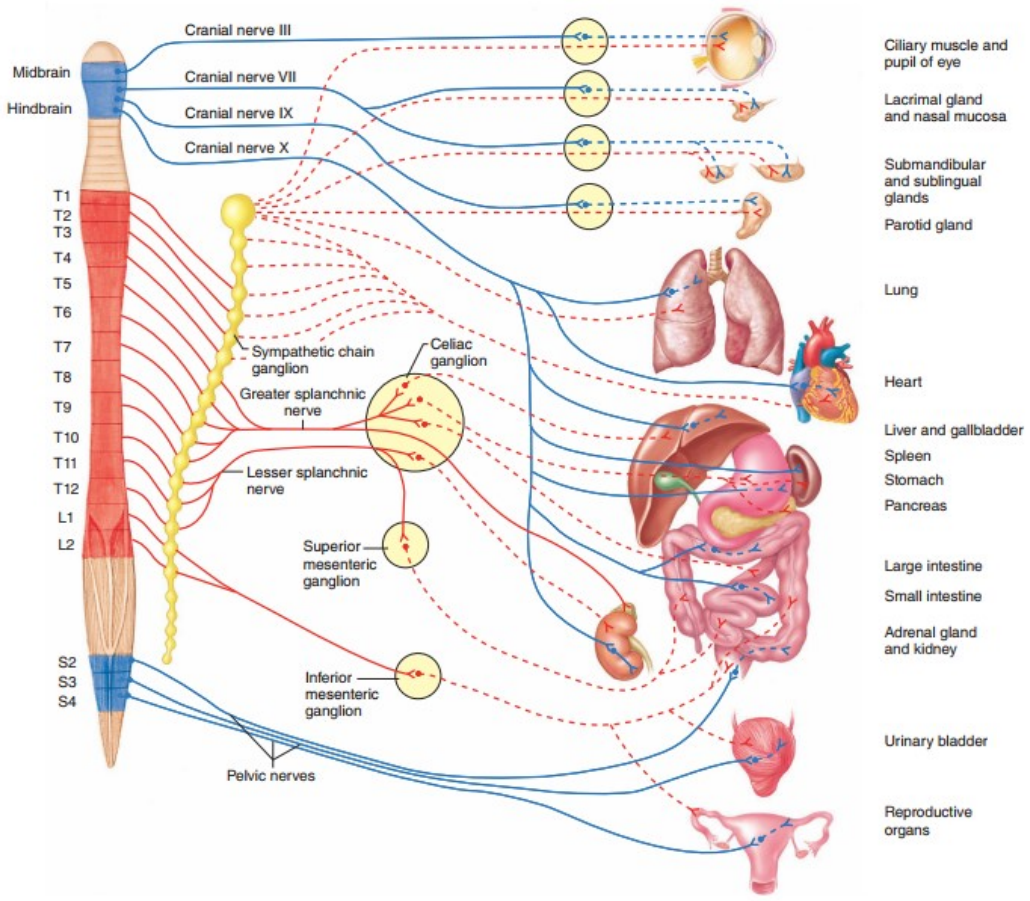

Figure 3.2: Distribution of the Autonomic Nervous System (Fox 2016). Red lines indicate sympathetic nerves, while parasympathetic fibres are depicted in blue. Preganglionic and postganglionic fibres are represented by solid and dashed lines, respectively.

preganglionic neuron, a first neuron that originates in the grey matter of the brain or spinal cord, which synapses in an autonomic ganglion with a second neuron, called postganglionic neuron, whose axon extends from the ganglion to the effector organ, where it synapses with the target tissue (Fox 2016).

The origin of the preganglionic autonomic fibres (midbrain and hindbrain, and the upper thoracic to the fourth sacral levels of the spinal cord) and the location of the autonomic ganglion (head, neck, abdomen and parallel the right and left sides of the spinal cord) help classify between the sympathetic and parasympathetic divisions of the ANS (Fox 2016), which along the enteric nervous system constitute the three major subdivisions of the autonomic system (Kim & Kim 2012).

The sympathetic nervous system (SNS) regulates the flight-or-fight response during emergencies, by increasing the sympathetic outflow to effector organs such as the heart and other viscera, while the parasympathetic nervous system (PNS) is responsible of maintaining basal autonomic functions under normal conditions; the enteric system, on the other hand, regulates peristalsis and modulates the activity of secretary glands (Kim & Kim 2012).

3.2.1 Sympathetic Nervous System

The SNS, also known as the thoracolumbar division of the ANS, features preganglionic neurons that originate in the thoracic and lumbar levels of the spinal cord, and the sympathetic ganglia is located parallel the spinal cord (paravertebral ganglia) (Fox 2016). Since the sympathetic nerves form a component of spinal nerves, they are distributed along most of the skeletal muscles and skin in the body, where they innervate blood vessels and other involuntary effectors (Fox 2016). The widespread distribution of these neurons is important for the mass activation of almost all the postganglionic sympathetic neurons, allowing for the entire SNS to be tonically active and to increase its activity in response to emergency situations (Fox 2016).

3.2.2 Parasympathetic Nervous System

Unlike the SNS, preganglionic neurons from the PNS (craniosacral division of the ANS) originate in the brain (i.e., in the midbrain, pons and medulla oblongata) and in the sacral level of the spinal cord, from where axons travel to ganglia located in or near the effector organs, which in turn supply the postganglionic fibres that synapse with the effector cells (Fox 2016).

The oculomotor, facial, glossopharyngeal, and vagus cranial nerves contain preganglionic parasympathetic fibres. Those fibres within the first three of these nerves synapse in ganglia located in the head, while fibres located in the vagus nerve synapse in ganglia located in several regions of the body; the latter provides the major parasympathetic innervation in the body, which includes parasympathetic innervation to the heart, lungs, oesophagus, stomach, pancreas, liver, small intestine, and the upper half of the large intestine (Fox 2016). Preganglionic fibres that originate from the sacral levels of the spinal cord provide parasympathetic innervation to the lower half of the large intestine, the rectum, and the urinary and reproductive systems (Fox 2016).

3.3 Physiology of the Autonomic Nervous System

The effects of the SNS and PNS on visceral organs are thought to be different. While the SNS prepares the body for intense physical activity in emergencies, by increasing heart rate, blood glucose levels, and blood flow to the skeletal muscles, the PNS is usually considered to act in an opposite way by slowing heart rate, dilating visceral blood vessels, and increasing activity of the digestive tract (Fox 2016). The difference in the responses from visceral organs to sympathetic and parasympathetic nerve activity is due to the release of different neurotransmitters from each of the two divisions, with the SNS primarily stimulating the release of epinephrine and norepinephrine, and the PNS generating the release of acetylcholine (Fox 2016). Interestingly, the SNS displays tonic activity, and as a result sympathetic nerves tonically regulate the heart, blood vessels and other organs, while the PNS is not normally activated as a whole and stimulation of parasympathetic nerves occurs in a separate manner (Fox 2016).

Most visceral organs receive dual innervation (i.e., both sympathetic and parasympathetic fibres innervate the organs), and usually they reflect an antagonistic effect, in which the increased activity of one of the branches of the ANS is accompanied by a decreased activity from the other branch. Nonetheless, in a few cases, the SNS and PNS activity display complementary (stimulation from SNS and PNS produce similar effects) or cooperative (stimulation from PNS and SNS produce different effects that work together to promote a single action) behaviour. The effects of SNS and PNS activity on salivary gland secretion and on the reproductive system are

complementary and cooperative, respectively (Fox 2016). Other organs, such as the adrenal medulla, the arrector pili muscles in the skin, the sweat glands in the skin, and most blood vessels receive only sympathetic innervation; in these cases, regulation is achieved by increasing or decreasing the firing rate of sympathetic fibres (Fox 2016).

Most autonomic reflexes originate from neural centres influenced by higher brain areas and sensory input, which is in turn transmitted to brain centres that integrate the received information and generate responses by modifying the activity of preganglionic neurons (Fox 2016). The main brain structure involved in the regulation of ANS activity is the medulla oblongata, located on the brain stem, to which most sensory input travels in afferent fibres from the vagus nerve and where centres for the regulation of cardiovascular, pulmonary, urinary, reproductive, and digestive systems can be found (Fox 2016). The medula oblongata is also responsive to regulation from other higher brain structures, such as the hypothalamus, which contains centres for the control of body temperature, hunger and thirsts; the regulation of the pituitary gland; and for various emotional states, making it one of the major regulatory centres of the ANS (Fox 2016).

Along the hypothalamus, the limbic system plays an important role in regulating visceral responses to emotional states. This system corresponds to a fibre tract and nuclei located around the brain stem, and includes the cingulate gyrus of the cerebral cortex, the hypothalamus, the fornix, the hippocampus, and the amygdaloid nucleus (Fox 2016).

Finally, impulses from the cerebellum to the medulla oblongata also influence ANS activity related to motion sickness, whereas the frontal and temporal lobes of the cerebral cortex influence the response of lower brain areas as part of their involvement in emotion and personality (Fox 2016).

3.4 Cardiovascular Autonomic Activity

The regulation of the cardiovascular system is mostly in charge of the ANS. Specifically, this system helps regulate cardiac output and promotes constriction and dilation of blood vessels, for the regulation of blood flow and blood pressure (Fox 2016). Especially, the sympathetic branch of the ANS plays a major role in maintaining cardiovascular homeostasis and in regulating physiological functions (Sheng & Zhu

2018). Figure 3.3 illustrates the origin and pathways of ANS fibres that innervate the cardiovascular system. It can be seen that the PNS innervation, performed by fibres from the vagus nerve, occurs only in the heart, whereas sympathetic fibres that originate in the spinal cord innervate both the heart and blood vessels.

The ANS system mostly affects vasomotor tone and cardiac function, but also has an effect on the systemic volume and the peripheral resistance by modulating the release of certain hormones (Castillo & Adams 2012). Three areas of the brain constitute an integrated functional system that coordinates the vasomotor status of the cardiovascular system: The upper anterolateral medulla, the lower anterolateral medulla, and the nucleus tractus solitarii. The first one of these areas is in charge of vasoconstrictor stimuli, while the second one is in charge of vasodilation. The nucleus tractus solitarii integrates both vasoconstrictor and vasodilator stimuli (Castillo & Adams 2012). These areas are located in the thealamus, hypothalamus, and dorsal

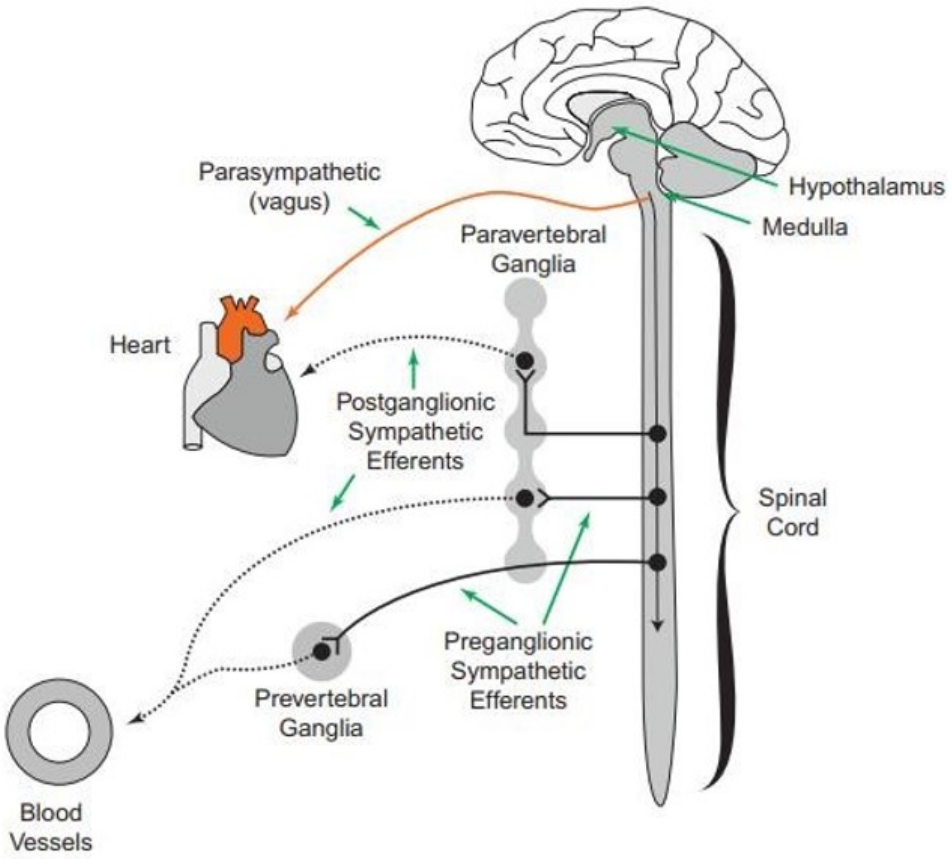

Figure 3.3: Origin and pathways of ANS fibres that innervate the cardiovascular system (Drew & Sinoway 2012). The heart is innervated both from fibres from the vagus nerve and postganglionic sympathetic fibres, while blood vessels are only innervated by sympathetic fibres.

region of the medulla oblongata (Castillo & Adams 2012).

Changes in SNS activity perform a powerful control over the peripheral circulation, with vascular nerves that terminate on small arteries, arterioles, venules and veins, and adjust vascular resistance, volume capacity, and heart pacing (Castillo & Adams 2012). In contrast, the PNS plays an insignificant role in regulating arterial pressure; however, it is crucial in the modulation of heart rate, due to the parasympathetic fibres of the vagus nerve which innervate both the sinoatrial and atrioventricular nodes, as well as the atrium myocardium, providing chronotropic control (Castillo & Adams 2012).

3.4.1 Autonomic control of the heart

The heart, as most visceral organs, has a dual innervation from the ANS, which means that it has both sympathetic and parasympathetic fibres, and the effects of the PNS and SNS are mainly antagonistic (Fox 2016). Figure 3.4 summarizes the effects of the ANS on the heart.

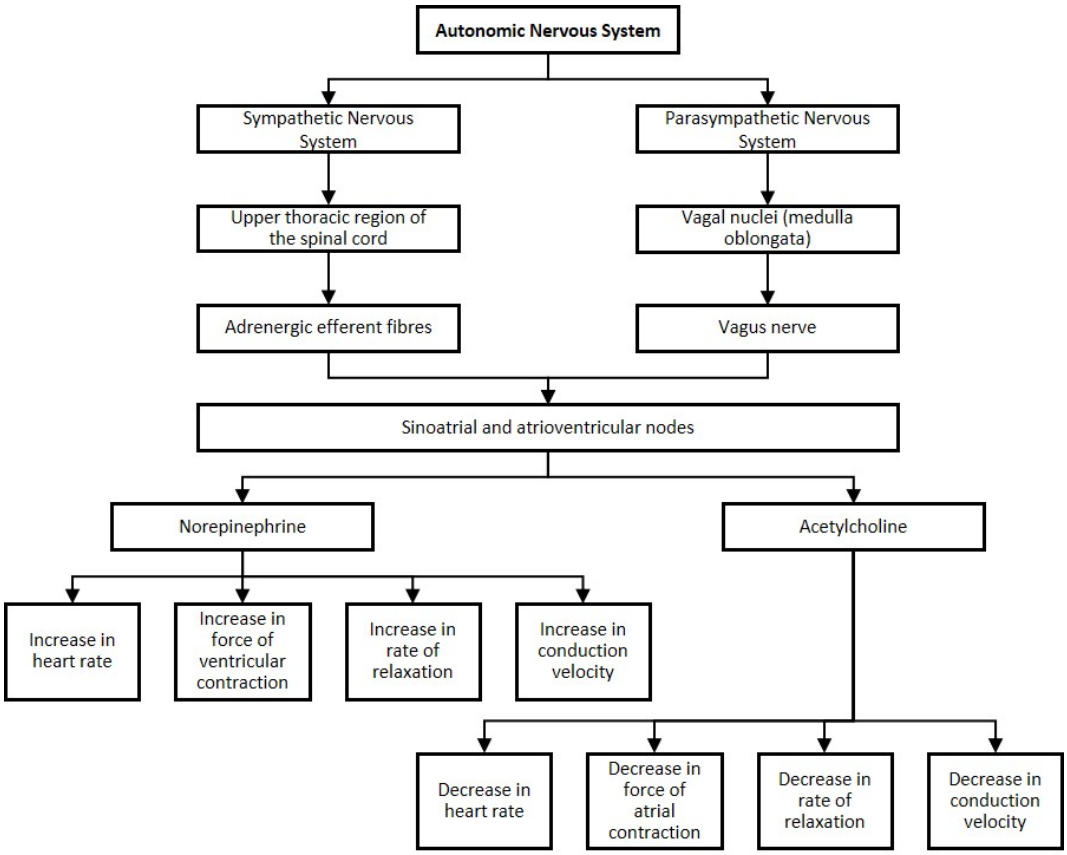

Figure 3.4: Effects of the autonomic nervous system activity on the heart (Drew & Sinoway 2012).

PNS control of the heart arises from the vagal nuclei within the medulla oblongata in the brainstem, with the tenth cranial nerve, the Vagus nerve, as the way for efferent nervous outflow; on the other hand, SNS control arises from the upper thoracic region of the spinal cord, where preganglionic efferent nerve fibres synapse with postganglionic sympathetic fibres that reach the sinus and atrioventricular nodes in the heart (Drew & Sinoway 2012). The main effects of the SNS are the increase in heart rate, in force of ventricular contraction, in rate of relaxation, and in conduction velocity; on the contrary, the PNS activity decreases all these properties (Drew & Sinoway 2012).

One of the main regulation tasks of the ANS in the heart is the control it performs upon heart rate. The SNS increases HR mainly due to the right sympathetic fibres that innervate mainly the sinus node, while the right fibres from the Vagus nerve exercise the contrary action upon this node (Conti 2011*c*).

3.4.2 Autonomic control of the vessels

Unlike the heart, most blood vessels do not have dual innervation, and their regulation is mainly achieved by increases and decreases in the firing rate of sympathetic fibres (Fox 2016). The ANS control of blood vessels is essential to maintain and regulate blood pressure within the arteries, and for regulating the distribution of blood flow between and within individual vascular beds (Lombard & Cowley 2012). The sympathetic regulation of cutaneous blood vessels also has an important role in thermoregulation (Lombard & Cowley 2012).

Activation of the SNS elicits a vasoconstriction mediated by three main neurotransmitters: Norepinephrine, adenosyl triphosphate (ATP), and neuropeptide Y (Lombard & Cowley 2012). In general, the postganglionic efferent nerves of the SNS ramify into small bundles, which form a plexus located in the tunica adventitia of the vessel; the terminal effector plexus is located near the tunica media where adrenergic fibres establish neuromuscular contact; finally, these nerves end in varicosities that have Schwann cell sheaths, which release the transmitters in response to the action potential of the nerves (Lombard & Cowley 2012).

One of the main tasks of ANS regulation of blood vessels is the control of blood flow. The sympathetic nerves produce an increase in the cardiac output and an increase in the peripheral resistance; even under resting conditions, the adrenergic sympathetic fibres help maintain the tone of the vascular smooth muscles and during

an stimulation of its fibres, the SNS produces vasoconstriction in the digestive tract, kidneys, and skin; on the contrary, cholinergic sympathetic fibres cause vasodilation during the "fight or flight" reaction in the arterioles of skeletal muscle, promoting a higher blood flow in this tissue (Fox 2016).

Although the ANS control on the blood vessels is achieved mainly by the SNS, the cranial and sacral nerves, which belong to the PNS, also help regulate vascular tone; nonetheless, the contribution of PNS in the regulation of vascular tone and haemodynamics is small (Lombard & Cowley 2012). The PNS fibres that end in arterioles are always cholinergic and, hence, always promote vasodilation; the PNS innervation of blood vessels is limited to the digestive tract, external genitalia, and salivary glands, and it is considered that the PNS is less important than the SNS in the regulation and control of the total peripheral resistance (Fox 2016).

It is important to clarify that major arteries and precapillary arterioles are innervated mainly by the SNS, but other vessels, such as venules, capillaries, and veins are rarely innervated (Sheng & Zhu 2018).

3.4.3 Autonomic activity and changes in blood pressure and arterial stiffness

The SNS is the principal system that controls changes in blood pressure that originate from the brain, and along with the adrenal medulla it becomes a powerful control mechanism that cause rapid changes in arterial pressure (Northcott & Haywood 2007). It is controlled by different central nervous system pathways, which are activated by chemical, hormonal and neural stimuli (Northcott & Haywood 2007). As mentioned by Sheng and Zhu ((2018)), autonomic cardiovascular control is impaired in hypertensive subjects, and the SNS activity is increased both in the heart and the peripheral vessels, leading to increased cardiac output and vasoconstriction. Moreover, autonomic dysfunction has already been associated with the appearance of essential hypertension (Carthy 2014).

As mentioned by Grassi and Seravalle (2012), the control that ANS exerts over the cardiovascular system undergoes important changes in hypertension, with resultant sympathetic activation and parasympathetic inhibition, and these alterations are related to the severity of the hypertensive state; and are potentiated when hypertension is complicated by cardiac, metabolic or renal disease.

The regulation of ANS over arterial stiffness is still a matter of debate: Although

it is thought that the main regulators of arterial stiffness are the structural components of the arterial wall, the distending pressure, and smooth muscle, animal and human experiments have shown that the autonomic activity controls the stiffness of muscular brachial and carotid arteries (Mäki-Petäjä et al. 2016).

3.5 Summary

The proper functioning of the human body depends in the maintenance of proper values and behaviour of the different systems that integrate it. This is called homeostasis. There are two main control systems that communicate and regulate activity of the other systems in order to maintain homeostasis: The endocrine and the nervous system. The nervous system, which tissue is made of specialised cells called neurons, regulates the activity of the body systems using electrical energy, and generating the liberation of neurotransmitters for controlling the activity of tissues.

One of the subdivisions of the nervous system is the Autonomic Nervous System (ANS), which is "in charge" of controlling and regulating the activity of involuntary tissue such as visceral organs and glands. It has a crucial role in regulating the performance of systems such as the cardiovascular, pulmonary and reproductive systems.

There are two branches in the ANS, the sympathetic and parasympathetic branches, which originate from different locations in the brain and spinal cord, and generate the excretion of different neurotransmitters in order to modify the behaviour of the systems. Usually, the sympathetic nervous system is related with the liberation of norepinephrine, whereas the parasympathetic nervous system controls the liberation of acetylcholine. Most of the organs have dual innervation, and this dual innervation is usually antagonistic, i.e., the sympathetic and parasympathetic activity act in an opposite manner in order to obtain the expected results. However, the activity of the two branches can be complementary or cooperative in certain systems, and some organs do not exhibit dual innervation but are only innervated by sympathetic fibres.

The cardiovascular system is largely regulated by the ANS, with the heart having dual innervation, whereas the blood vessels feature only sympathetic innervation. In the heart, the ANS is in charge of controlling heart rate, cardiac output and conduction velocity, with the sympathetic activity generating an increase in these

variables, while parasympathetic activity decreases them. The blood vessels, on the other hand, are regulated by sympathetic fibres which control the vasoconstriction and vasodilation, having an important role in regulating blood pressure and peripheral resistance. Since the ANS regulates cardiovascular performance, abnormal activity of any of its branches can be related to diseases such as hypertension, diabetes, and arterial stiffening.

Chapter 4

Heart Rate Variability in the Assessment of Cardiovascular Autonomic Nervous System

4.1 Electrocardiography

As mentioned in section 3.4, the cardiac cycle follows a pattern and has a duration that can be used to derive important information related to cardiac health. The recording of this electrical behaviour is known as electrocardiography (ECG) and is routinely used in clinical practice for monitoring the heart activity and diagnosing cardiovascular diseases (Rangayyan 2002). An electrocardiogram can be understood as the recording of the electrical potentials generated by the electrical activation of the ventricles and excitatory cells in the cardiac muscle, measured in the body surface (Webster 2010).

An electrocardiogram features a characteristic waveform from which the different stages of the cardiac cycle can be identified (Figure 4.1): (1) The depolarization of the atria result in the P wave, which is a slow, low-amplitude wave; (2) once the electrical stimulus reaches the AV node, there is an iso-electric segment after the P wave, known as the PQ interval; (3) afterwards, the rapid contraction of the ventricles take place, generating a sharp biphasic or triphasic wave known as the QRS complex; (4) since the ventricular cells have a relatively long action potential duration, there is an iso-electric segment after the QRS segment, known as the ST interval; (5) finally, the repolarization of the ventricles generate a slow wave called

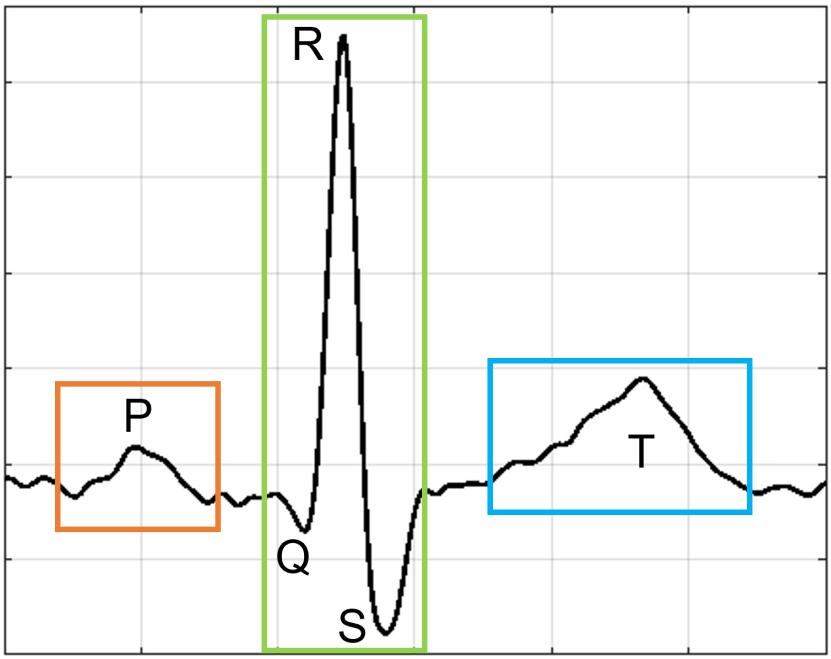

Figure 4.1: Electrocardiography waveform and its different characteristic waves during one cardiac cycle. A normal cycle shows the P wave, related to the atrial depolarization; a QRS complex, which is an indication of the rapid depolarization of the ventricles; and a T wave, related to the repolarization of the ventricles (Rangayyan 2002).

the T wave (Rangayyan 2002). After the T wave, sometimes is possible to identify another wave called the U wave, which has very low amplitude and is often absent or masked by the next cardiac cycle (Reisner et al. 2006). This process repeats itself in each cardiac cycle, generating a quasi-periodic signal from which important information regarding the health status can be derived (Rangayyan 2002).

The idea to acquire the ECG from the body surface arises from the assumption that the electrical activity of the heart can be represented by a current dipole, located at the electrical centre of the heart, and whose magnitude and orientation can change with time (Webster 2010). The net dipole at one particular moment of time is called the heart vector, and as the depolarization of tissue spreads through the heart, this vector changes in magnitude and direction as a function of time (Reisner et al. 2006). For measuring ECG, then, it is necessary to obtain the voltage difference between two points that are related to the cardiac vector, using biopotential electrodes located in the skin (Webster 2010). In clinical practice, a standard 12-channel ECG using four limb leads and chest leads in six positions is usually acquired (Rangayyan 2002).

Each of these leads reveals the magnitude of the cardiac vector in a specific direction at a given time (Reisner et al. 2006). The chest leads, known as precordial leads, report activity in the transverse plane of the body, whereas the limb leads, give information regarding the frontal plane of the body (Webster 2010). Hence, each of the leads can illustrate at any time the behaviour of the cardiac vector, and form a two-dimensional graph that represents the distribution of the electrical potential in any instant (Reisner et al. 2006).

The ECG is an extremely useful and largely used tool for clinical assessment of electrical pathologies, which usually come in two forms: Bradycardias, in which the heart pumps too slowly or infrequently, and tachycardias, in which the cardiac cycle is too short, implying a high pumping rate (Reisner et al. 2006). These are regarded as heart rate abnormalities and can be detected from multi- and single lead ECG traces. Some of these abnormalities have their origin in the ANS (Reisner et al. 2006), which, as mentioned previously, is the control system for heart rate. Therefore, ECG is a useful tool for measuring heart rate and obtaining valuable information regarding the ANS activity over the cardiac cycle.

4.2 Heart Rate Variability

The term "Heart Rate" refers to the number of heart beats that occur in a certain time interval, usually a minute (Shaffer & Ginsberg 2017), and, therefore, is the inverse value of the mean duration of cardiac cycles in that time. However, the duration of each cardiac cycle is not the same and varies around that mean value. This variation between adjacent cardiac cycle duration is called Heart Rate Variability (HRV) (Shaffer & Ginsberg 2017) and is a reflection of changes in the balance between the cardiac sympathetic and parasympathetic branches of the ANS, regarded as the sympathovagal balance (Clifford 2006).

HRV has been largely explored in the last 40 years due to its simplicity and non-invasive nature to evaluate changes in the cardiac ANS and related diseases (Xhyheri et al. 2012). Since the rate at which the heart pumps blood to the circulatory system is determined by the sinus node in the heart, and this is controlled by the sympathetic (SNS) and parasympathetic (PNS) branches of the ANS (Rangayyan 2002), changes in heart rate indirectly reflect the behaviour of the cardiac control exercised by this system (Kleiger et al. 2005). The measurement of the variability of the heart rate has

been shown to reflect regulation of autonomic balance, blood pressure, gas exchange, and gut, heart, and vascular tone, among others; and an optimal level of variation in heart rate has been related with health and self-regulatory capacity, and adaptability to different and changing environment conditions (Clifford 2006).

In 1996, the Task Force for the European Society of Cardiology and the North American Society of Pacing and Electrophysiology published standards of measurement, physiological interpretation, and clinical use for HRV (Task Force of the European Society of Cardiology and The North American Society of Pacing and Electrophysiology 1996). Guidelines were proposed in this document, including the use of R peaks as fiducial point for segmenting the ECG into cardiac cycles, the minimum length of measurements for obtaining valid HRV data, and the acquisition and processing conditions needed to consider when analysing ECG data to extract HRV information. Nonetheless, in recent years some of these standards have been questioned and other aspects regarding HRV analysis have been established. For instance, HRV has been traditionally extracted from short-term and long-term measurements, i.e., from ECG signals recorded during at least 5 min or recorded for a time period of 24 hours, respectively. In the case of short-term measurements, HRV is usually analysed in the laboratory and different protocols are applied for the modification of autonomic activity; on the contrary, 24 h analysis is based on extracting HRV information while the subject is performing usual daily activities (Kleiger et al. 2005). However, ultra-short term HRV analysis have now been proposed as an alternative to short-term measurements, although further validation is needed (Pecchia et al. 2018). As explained by Li et al. (2019), the selection of the appropriate time window is essential to understand the obtained results, given that short-term HRV analysis is useful for tracking dynamic changes of cardiac autonomic function, while long-term HRV is a more stable tool for assessing autonomic function and can be more reliable for disease prognosis.

HRV is obtained by measuring the duration of each cardiac cycle from an ECG, i.e., by identifying the QRS complexes, specifically the R peaks, and measuring the time difference between consecutive cycles. This results in a time series of intervals, also known as RR intervals, which when plotted against time delivers a graph known as the tachogram (Clifford 2006). Figure 4.2 illustrates this process. It is important to indicate that, for HRV analysis, only heart beats that originate from the sinus node should be taken into account, which are referred to as normal-to-normal (NN)

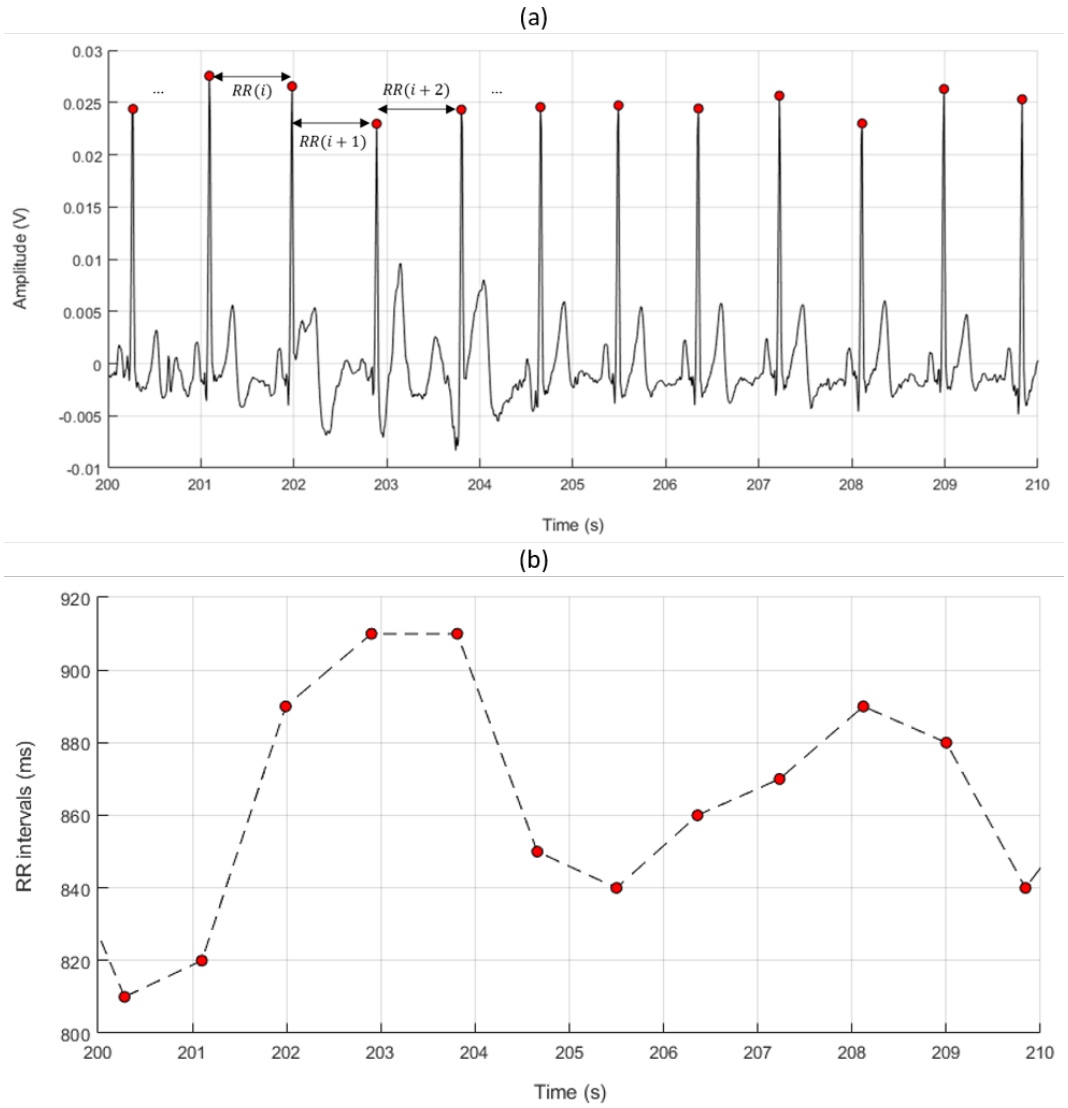

Figure 4.2: Derivation of heart rate variability from an electrocardiogram by extracting the duration of cardiac cycles using the R peaks. (a) Identification of R peaks from an electrocardiogram and the subsequent measurement of RR intervals; (b) Tachogram extracted by plotting the RR intervals against time.

intervals (Clifford 2006). Once the NN intervals are obtained, different indices are extracted to characterise the changes in their duration. In general, these indices can be classified in three groups, time-domain, frequency-domain and non-linear indices (Shaffer & Ginsberg 2017).

4.2.1 Time-domain analysis

Time-domain indices quantify the amount of variability in the NN intervals, using mainly statistical measures (Shaffer & Ginsberg 2017). Table 4.1 summarises some of the most usually used time-domain indices. The most widespread indices used in

Table 4.1: Time-domain indices for analysing HRV data (Shaffer & Ginsberg 2017).

Index	Unit	Description
AVNN	ms	Mean value of NN intervals
SDNN	ms	Standard deviation of NN intervals
SDANN	ms	Standard deviation of the average NN intervals for each 5 min segment of a 24 h HRV recording
SDNN index	ms	Mean of standard deviations of all NN intervals for each 5 min segment of a 24 h HRV recording
pNN50	%	Percentage of successive RR intervals that differ by more than 50 ms
HR max - HR min	bpm	Average difference between the highest and lowest HR during each respiratory cycle
RMSSD	ms	Root mean square of successive RR interval differences
SDSD	ms	Standard deviation of successive RR interval differences
HRV triangular index	-	Integral of density of the RR interval histogram divided by its height
TINN	ms	Baseline width of the RR interval histogram

the literature are AVNN, SDNN, RMSSD and pNN50.

Some researchers have, as well, proposed modification to these indices. For example, authors have suggested that using 35 ms as the difference in time for measuring pNN50, instead of 50 ms, gives better results for detecting atrial fibrillation (Conroy et al. 2017). Changing the time threshold for pNN50 has been applied by other researches as well, in an attempt to achieve a generalisation of the technique (Clifford 2006). Most of time-domain indices can be extracted either from short- and long-term recordings, or from both, and some of the statistical indices have been proposed for ultra-short term recording with windows lasting between 60 and 240 S(Shaffer & Ginsberg 2017).

The mathematical derivation of some of these indices can be done as shown in (4.1) to (4.5), in which RRI refers to the peak-to-peak intervals detected from ECG signals; N is the number of intervals detected in the PPG; and δ takes values of 1 when the condition is met, or 0 in any other case.

$$AVNN = \frac{1}{N}\sum_{i=1}^{N} RRI(i) \tag{4.1}$$

$$SDNN = \sqrt{\frac{1}{N-1}\sum_{i=1}^{N}|RRI(i) - AVG|^2} \tag{4.2}$$

$$RMSSD = \sqrt{\frac{1}{N-1}\sum_{i=1}^{N-1}|RRI(i+1) - RRI(i)|^2} \tag{4.3}$$

$$NN50 = \sum_{i=1}^{N-1}\delta(RRI(i+1) - RRI(i) \geq 50ms) \tag{4.4}$$

$$pNN50 = \frac{NN50}{N-1} \tag{4.5}$$

4.2.2 Frequency-domain analysis

Frequency-domain measurements are based on the estimation of absolute or relative powers into four separated frequency bands: ultra-low frequency (ULF), very-low frequency (VLF), low frequency (LF), and high frequency (HF) (Shaffer & Ginsberg 2017). The most commonly-used frequency-domain measurements for analysing HRV are shown in Table 4.2. These indices are obtained after applying a frequency transformation to the time-domain RR intervals tachogram, by applying a Fast Fourier Transform (FFT) or autoregressive (AR) modelling (Shaffer & Ginsberg 2017). However, both FFT and AR models introduce non-linear distortion to data, and need the data to be uniformly sampled for obtaining the frequency spectra, so the RR intervals need to be resampled employing linear or cubic approaches and using a sampling rate from 2 to 10 Hz, which could lead to overestimation of the frequency-domain indices (Clifford 2006). It is usually accepted that using a sampling rate of 4 Hz is appropriate for human beings (Berntson et al. 1997). To overcome some of the difficulties related to the resampling of data, the Lomb-Scargle periodogram has also been proposed as an alternative to obtained a frequency spectrum without uniformly sampled data (Clifford 2006).

Depending on the duration of the recordings, certain bands of the frequency spectrum can or cannot be obtained. The ULF band includes fluctuations in RR intervals with a period from 5 min to 24 h; the VLF is comprised of intervals ranging from 25 to 300 S; the LF band includes RR intervals with duration between 7 and 25 S; and the HF band, also regarded as the respiratory band, in influenced by breathing from 9 to 24 bpm (Shaffer & Ginsberg 2017). Therefore, for measuring

Table 4.2: Frequency-domain indices for analysing HRV data (Shaffer & Ginsberg 2017).

Index	Unit	Description
ULF power	ms^2	Absolute power of the ultra-low-frequency band ($\leq$ 0.003 Hz)
VLF power	ms^2	Absolute power of the very-low-frequency band (0.003 – 0.04 Hz)
LF peak	Hz	Peak frequency of the low-frequency band (0.04 – 0.15 Hz)
LF power	ms^2	Absolute power of the low-frequency band (0.04 – 0.15 Hz)
	nu	Relative power of the low-frequency band (0.04 – 0.15 Hz) in normalised units
	%	Relative power of the low-frequency band (0.04 – 0.15 Hz)
HF peak	Hz	Peak frequency of the high-frequency band (0.15 – 0.40 Hz)
HF power	ms^2	Absolute power of the high-frequency band (0.15 – 0.40 Hz)
	nu	Relative power of the high-frequency band (0.15 – 0.40 Hz) in normalised units
	%	Relative power of the high-frequency band (0.15 – 0.40 Hz)
LF/HF	%	Ratio of the LF-to-HF power

reliable information from the ULF and the VLF, recording periods of at least 24 h and 5 min are needed, respectively, while LF and HF bands can be estimated from shorter recordings of at least 2 and 1 minute duration, respectively (Shaffer & Ginsberg 2017). The LF/HF ratio has been proposed usually as an indicator of sympathovagal balance; however, recent studies have shown this is not accurate since, unlike originally thought, LF does not reflect solely sympathetic activity, while it is affected both by parasympathetic and sympathetic components (Ackermann et al. 2021). Therefore, frequency-domain indices extracted from HRV should mainly be considered as indicators of vagal activity.

The mathematical derivation of some of the absolute frequency-domain indices is shown in (4.6) to (4.9), in which P refers to the power of the frequency spectrum, while (4.10) to (4.12) describe the mathematical expressions for the measurement of nLF, nHF and LF/HF.

$$VLF = \sum_{f=0.0033}^{0.04} P(i) \tag{4.6}$$

$$LF = \sum_{f=0.04}^{0.10} P(i) \tag{4.7}$$

$$HF = \sum_{f=0.10}^{0.40} P(i) \tag{4.8}$$

$$TP = \sum_{f=0.0033}^{0.40} P(i) \tag{4.9}$$

$$nLF = \frac{LF}{TP} \tag{4.10}$$

$$nHF = \frac{HF}{TP} \tag{4.11}$$

$$LF/HF = \frac{LF}{HF} \tag{4.12}$$

4.2.3 Non linear analysis

The oscillations of a healthy heart are complex and non-linear, and usually are best described by mathematical chaos (Shaffer & Ginsberg 2017, Quintana 2017). This non-linearity is determined by complex interactions of hemodynamic, electrophysiological, and humoral variables, and the autonomic and central nervous systems (Task Force of the European Society of Cardiology and The North American Society of Pacing and Electrophysiology 1996). Poincaré plots, low-dimension attractor plots, singular value decomposition, Lyapunov exponents, Kolmogorov entropy, among others, have been used to describe the non-linear processes occurring in HRV (Task Force of the European Society of Cardiology and The North American Society of Pacing and Electrophysiology 1996). In general, these non-linear indices aim to quantitatively assess the quality, scaling, and correlation properties of HRV (de Godoy 2016). In other words, they are related with the unpredictability, fractability and complexity of the signal. Table 4.3 summarises some of the most used non-linear parameters measured from HRV data. Although non-linear indices from HRV are potentially powerful tools with the capability of accurately reflecting autonomic regulation and the complexity of this system (Stein & Reddy 2005, Pernice et al. 2019*a*), standards for their measurement are lacking (Task Force

Table 4.3: Commonly used non-linear indices for analysing HRV data (Shaffer & Ginsberg 2017).

Index	Unit	Description
S	ms	Area of the ellipse which represents total HRV
SD1	ms	Poincaré plot standard deviation perpendicular to the line of identity
SD2	ms	Poincaré plot standard deviation along the line of identity
SD1/SD2	%	Ratio of SD1-to-SD2
ApEn	-	Approximate entropy (measures the regularity and complexity of a time series)
SampEn	-	Sample entropy (measures the regularity and complexity of a time series)
DFA α_1	-	Detrended fluctuation analysis (describes short-term fluctuations)
DFA α_2	-	Detrended fluctuation analysis (describes long-term fluctuations)
D2	-	Correlation dimension (estimates the minimum number of variables required to construct a model of system dynamics)

of the European Society of Cardiology and The North American Society of Pacing and Electrophysiology 1996) and their physiological explanation and utility are not entirely elucidated (Germán-Salló & Germán-Salló 2016).

Some of the most used non-linear indices in HRV analysis are those extracted from the Poincaré plot. This is a geometrical representation of a time series in a Cartesian plane, which plots the actual data against the data occurring in the future (Khandoker et al. 2013). For HRV, it is usually done by plotting the i-th RR interval against the $(i+1)$-th interval, although Poincaré analysis using larger lags have demonstrated interesting results in several applications (Khandoker et al. 2013, Shi et al. 2009). The indices SD1, SD2 and SD1/SD2 are usually used for quantifying the dynamics on the Poincaré plot, and are comparable to time- and frequency-domain indices (Khandoker et al. 2013).

The extraction of Poincaré plot indices is usually done using the ellipse-fitting method (Khandoker et al. 2013) and applying equations (4.13) to (4.16), where N is the number of intervals analysed, $RRI(i)$ corresponds to i-th peak-to-peak interval, and $\overline{RRI}$ represents the mean value of the inter-beat intervals.

$$S = \pi(SD1)(SD2) \tag{4.13}$$

$$SD1 = \sqrt{\frac{1}{N-1}\sum_{i=1}^{N-1}\frac{(RRI(i+1) - RRI(i))^2}{2}} \tag{4.14}$$

$$SD2 = \sqrt{\frac{1}{N-1}\sum_{i=1}^{N-1}\frac{(RRI(i+1) - RRI(i) - 2(\overline{RRI}))^2}{2}} \tag{4.15}$$

$$SD1/SD2 = \frac{SD1}{SD2} \tag{4.16}$$

Entropy measures, e.g. ApEn, SampEn, have been used to quantify the regularity and complexity of HRV time series (Shaffer & Ginsberg 2017, Task Force of the European Society of Cardiology and The North American Society of Pacing and Electrophysiology 1996). In HRV analysis, high ApEn implies low predictability of the fluctuations, whereas small ApEn is related with a regular and predictable signal. This measure was designed for brief time series in which some noise may be present, while SampEn has been proposed as a less biased and more reliable measure of regularity and complexity, even when calculated from shorter time series (Shaffer & Ginsberg 2017).

The approximate and sample entropy (ApEn and SampEn, respectively) can be measured using a pattern length, m, and a criterion of similarity, r (Semmlow & Griffel 2014). In both cases, the RRIs are first adjusted according to their standard deviation and the patterns with length m and $m+1$ extracted. Then, the number of patterns that lie within a radius r are denoted as B_n (4.17) and A_n (4.18), for the patterns of length m and $m+1$, respectively.

$$B_n = \sum_{k=1}^{N-m}\delta(\|x_n^m - x_k^m\| < r) \tag{4.17}$$

$$A_n = \sum_{k=1}^{N-m}\delta(\left\|x_n^{m+1} - x_k^{m+1}\right\| < r) \tag{4.18}$$

Then, ApEn can be measured as (4.19). SampEn is an unbiased version of ApEn, in which the template match between the current template and itself is not counted. It can be measured as shown in (4.20). The multi-scale entropy of HRV trends can assessed using one of the entropy measurements, usually SampEn, with varying scales of the time series, and then characterising it as the area under the curve of

the resulting function (Semmlow & Griffel 2014).

$$ApEn(x, m, r, N) = \frac{\sum_{n=1}^{N-m+1} - \ln A_n}{N - m + 1} - \frac{\sum_{n=1}^{N-m} - \ln B_n}{N - m} \tag{4.19}$$

$$SampEn = -\ln \frac{A}{B} = -\ln \frac{\frac{\sum_{n=1}^{N-m+1} A_n}{N-m+1}}{\frac{\sum_{n=1}^{N-m} B_n}{N-m}} \tag{4.20}$$

Using detrended fluctuation analysis, DFA, it is possible to obtain the correlations between successive RR intervals, resulting in slopes α_1 and α_2, which describe brief and long-term fluctuations, respectively. DFA indices can be extracted from HRV trends as explained by Golińska (2012), integrating the signal of the interpolated inter-beat intervals and segmenting it in segments of varying lengths, n, according to the original length of the time series. Then, using least squares fit, each segment is linearly approximated, denoted as y_n. The average fluctuation $F(n)$ of the signal around the trend of each segment is computed as shown in (4.21), where N is the length of the signal and n is the corresponding length.

$$F(n) = \sqrt{\frac{1}{N} \sum_{k=1}^{N} (y(k) - y_n(k))^2} \tag{4.21}$$

Then, a plot of $\ln F(n)$ against $\ln n$ is produced and two linear models from this plot can be extracted. The first linear model is obtained using the $F(n)$ related to lower values of length, while the second linear model is obtained using $F(n)$ related to longer n. A1 and A2 are finally assigned as the slopes of these models, respectively.

Finally, correlation dimension and Lyapunov exponents estimate the minimum number of variables needed for constructing a model of the system dynamics: The more variables required the more complex the system (Shaffer & Ginsberg 2017). Lyapunov exponents can be computed by determining an embedded dimension of the system and calculating trajectory divergence; a linear model can be fitted to the resulting function and the value of the Lyapunov exponent assigned as the value of the slope of the model (Semmlow & Griffel 2014). The correlation dimension, D2, is obtained from the correlation sum as shown in 4.22, where N is the number of points to analyse, Θ is the Heaviside operator (i.e. 1 for all positive values, 0 for all other values), R is a radius of a hypersphere and x is the attractor of the

interpolated time series of inter-beat intervals. Values of R used in the subsequent analyses presented in this thesis range from e^{-1} to e^{1}, in steps of 0.1. Then, D2 is calculated as the slope of the linear model derived from the function shown in (4.23) (Semmlow & Griffel 2014).

$$Cd(R) = \frac{1}{N(N-1)} \sum_{i=1}^{N} \sum_{j=1, j \neq i}^{N} \Theta(R - |x(i) - x(j)|) \tag{4.22}$$

$$D2 = \frac{d \ln Cd(R)}{d \ln R} \tag{4.23}$$

4.3 Heart Rate Variability and cardiovascular changes

HRV has been largely studied as a marker of cardiac autonomic activity (Quintana 2017, Huikuri et al. 1999, Malik et al. 2017) and its major clinical applications have been in risk-stratifying patients for arrhythmic death after myocardial infarction and in the evaluation of autonomic neuropathy in diabetic patients (Villareal et al. 2002). The sinus node of the heart, modulated by both sympathetic (SNS) and parasympathetic (PNS) branches of the Autonomic Nervous System (ANS), is the main controller of heart rate, along with hormonal and mechanical factors (Constant et al. 1999). As explained by Weatherred and Pruett, HRV can be considered as an indicator of cardiac adrenergic receptor sensitivity, postsynaptic signal transduction, and multiple neural reflexes, in addition to its main interpretation as an end-organ response determined by nerve firing and electrochemical coupling (Weatherred & Pruett 1995). A proper analysis of the variations in heart rate is therefore thought to reflect the activity of cardiac SNS and PNS, and has been proposed as a potential marker of common cardiovascular physiological and pathological conditions (Xhyheri et al. 2012), such as atherosclerosis (Xhyheri et al. 2012), peripheral arterial disease (Goernig et al. 2008), hypertension, diabetes mellitus, myocardial infarction, and heart failure (Takase 2010), among others. Moreover, since most HRV results can be related to changes in the interaction between baroreceptors, the cardiorespiratory unit, and the autonomic nervous system, the dysfunction in any of these systems impacts normal homeostatic mechanisms that are reflected in HRV indices (Weatherred & Pruett 1995).

HRV has been proposed as a diagnostic and prognostic tool, and low values of HRV indices relate to cardiac events, such as myocardial infarction; progression of

atherosclerosis; and heart failure (Huikuri et al. 1999, Weatherred & Pruett 1995). Some studies relate HRV values with pathologies and conditions such as coronary artery disease and sudden death (Xhyheri et al. 2012, Thayer et al. 2010, Moridani et al. 2015), diabetes mellitus (da Silva et al. 2016), pain (Broucqsault-Dédrie et al. 2016), acute (Castaldo et al. 2015) and chronic stress (Murray 2012), metabolic syndrome (Stuckey et al. 2014), depression (Liang et al. 2015, Vazquez et al. 2016, Koenig et al. 2016, Hamilton & Alloy 2016), and bipolar disorders (Bassett 2016). Furthermore, HRV has been used as a marker of social interaction (Shahrestani et al. 2015), sports performance (Gavrilova 2016, Dong 2016), and emotional states (Torres-Valencia et al. 2017, Choi et al. 2017).

Cardiovascular diseases and its relationship with HRV, especially, have gain important attention, with some results that encourage for further studies. In general, it has been found that lower HRV indices may be related with a wide range of cardiovascular diseases, such as acute myocardial infarction, hypertension, heart failure, and arrhythmia (Takase 2010, Souza et al. 2021). Furthermore, it has been suggested that lowering cardiovascular risk profiles is associated with an increased HRV (Thayer et al. 2010), and that interventions such as physical training in cardiovascular and elderly patients result in an increased HRV, usually accompanied by a reduction in hemodynamic and metabolic parameters (Souza et al. 2021). In a review published in 2012, Xhyheri et al. summarised the relationship between cardiovascular health and HRV, and concluded that: (1) All HRV parameters were reduced by aging in 24 h recordings; (2) diabetes affects HRV measurements, both in time- and frequency-domain indices, when compared between healthy and diabetic populations, which may be explained by an inadequate metabolic control and the occurrence of diabetic neuropathy; (3) atherosclerosis generates a reduction in HRV parameters, probably associated with the lipid accumulation in the tunica intima and coronary narrowing, and a depressed HRV is associated with the occurrence of stroke and increased risk of mortality; (4) HRV is related with several cardiovascular risk factors, such as cholesterol serum levels, hyperlipidaemia, hypertension, and smoking; (5) reduced HRV can be used to identify an increment in cardiac mortality after myocardial infarction, as well as heart failure and ischemic sudden death in apparently healthy people prior to death; and (6) HRV is related with coronary instability (Xhyheri et al. 2012).

Special attention has been given to the relationship between HRV and diabetes.

França da Silva et al. (2016) concluded that HRV is a good tool to discriminate cardiac autonomic neuropathy in diabetic subjects, especially using non-linear indices such as SampEn, SD1/SD2, ApEn, recurrence plot, DFA, Lyapunov exponents, and correlation dimension, and using SDANN and HF information; moreover, it was suggested that HRV indices could be used along with automatic classifiers to discriminate between healthy and diabetic subjects. In line with these results, other studies concluded that subclinical cardiac autonomic neuropathy is related with a reduction in HRV, allowing for an early detection of the syndrome even before it becomes symptomatic (Fisher & Tahrani 2017, Vinik et al. 2018). Metabolic syndrome, i.e., a clustering of risk factors that increase the risk of developing cardiovascular diseases and type 2 diabetes mellitus, has also been related with HRV (Souza et al. 2021). It has been found that there were reduced HRV parameters in women with metabolic syndromes, but men results were inconsistent, concluding that HRV is altered differently in men and women with metabolic syndrome, but that results were inconclusive (Stuckey et al. 2014).

Hypertension has also received important attention, in an attempt to identify increased blood pressure using HRV. Researchers from the Framingham Heart Study, which has been going on in United States since 1948 (*Framingham Heart Study* 2021), have shown that HRV was reduced both in men and women with systemic hypertension, and that the LF power was associated with the development of this disease in men (Carthy 2014). Moreover, it has been established that there is a direct relationship between higher blood pressure values and the activation of SNS (Mancia & Grassi 2014), and that lower HRV can be used to predict hypertension onset (Hill & Thayer 2019). These conclusions are in line with the findings reported by Weatherred and Pruett (1995), who concluded that HRV changes can be used for the differentiation among normotensive, borderline hypertensive and mildly hypertensive patients.

Finally, hemodynamic variables have also been related with HRV. In a study performed with 59 type 1 diabetic patients, it was observed that HRV was directly related with arterial stiffness: Lower frequency-domain parameters extracted from HRV were observed in patients with stiffer arteries (Jensen-Urstad et al. 1999). Similarly, in a study performed with 382 healthy and young Japanese men, a relationship between arterial stiffness and HRV was observed: LF/HF ratio was found to be an independent predictor of the brachial-ankle pulse wave velocity, a simple

and reliable marker of arterial stiffness (Nakao et al. 2004). Interestingly, in a study published in 2013, it was found that lower HRV is associated with increased arterial stiffness in both central and peripheral vascular beds in young subjects with type 1 diabetes, but there were no associations between HRV and arterial stiffness in the control, non-diabetic group, except for an association between SDNN and peripheral stiffness (Jaiswal et al. 2013). In patients with essential hypertension, a relationship between HRV and arterial stiffness has also been observed (Carthy 2014). Finally, Kyrlagkitsis et al (2016) found that, in healthy subjects, age was negatively associated with non-linear HRV indices, such as entropy measurements, implying that complexity is reduced in aged systems, i.e. in stiffer vessels.

4.4 Limitations of heart rate variability

However promising, HRV results have been found to be contradictory and inconclusive, mainly due to the lack of standardisation of methodologies (Souza et al. 2021). Thus, HRV has not yet been accepted as a reliable clinical tool by physicians for supporting their diagnosis and monitoring of diseases (Kranjec et al. 2014, Veloza et al. 2019). Amongst the research community, on the other hand, HRV is still popular with a large volume of publications produced on an annual basis, as shown in Figure 4.3.

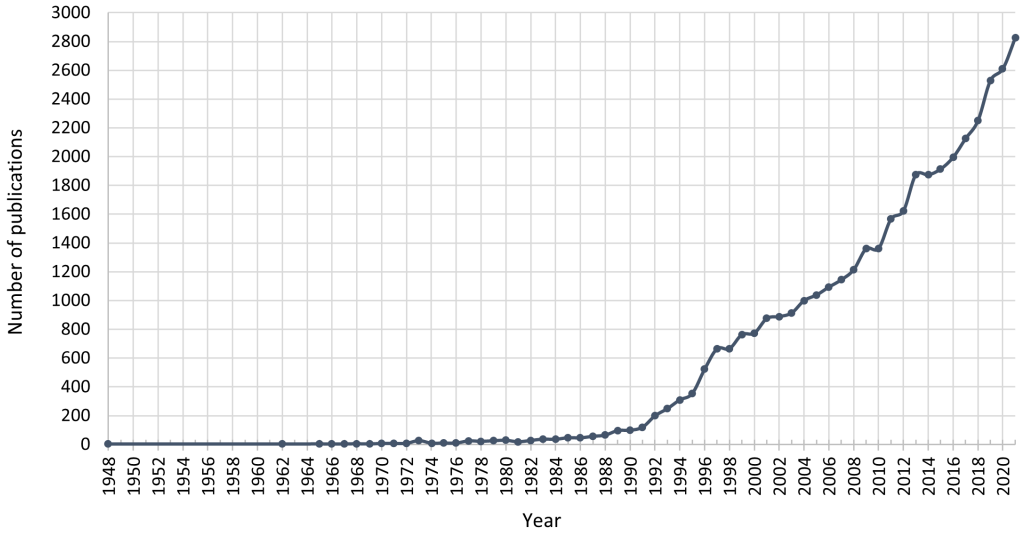

Figure 4.3: Number of publications per year (up to 2021) in Scopus with the term "heart rate variability" in title, abstract or keywords. The number of publications related to heart rate variability has increased exponentially in the last decades.

Although HRV has attracted a lot of attention due to its potential applications, its clinical use is still restricted. First of all, different factors, which include physiological, procedural, and technical factors can affect HRV measurements, which preclude the generalisation of the results of studies specially in critically ill patients (Karmali et al. 2017). Moreover, the methodology and design of the studies affect the results grandly, and need to be taken into account when reporting and analysing the outcomes of a study (Karmali et al. 2017, Souza et al. 2021, Quintana 2017). Finally, it is important to notice that there is still debate regarding the capability of HRV to provide information about sympathetic mechanisms, which could imply a deficiency in the technique for assessing ANS activity (Owens 2020).

As mentioned, standards of measurement and guidelines for HRV research were published in the late nineties in an attempt to have more comparable and generalizable results (Task Force of the European Society of Cardiology and The North American Society of Pacing and Electrophysiology 1996). These standards include recommendations regarding sample rate, extraction of frequency- and time-domain parameters, and signal processing for the assessment of HRV. For instance, it has been recommended in these guidelines that HRV measurements should be derived from ECG signals acquired at least with a 250-Hz sampling rate, by identifying R peaks as the initial point of each cardiac cycle. Nonetheless, other latter studies have recommended different parameters, such as using higher sampling frequencies, i.e. 500-1000 Hz, to assure that time resolution for identification of the location of the R peaks does not affect the HRV data (Berntson et al. 1997). In addition, several issues remain to be resolved in HRV research. One of the main confounders is the fact that usually relevant co-variables are not reported, such as Body Mass Index, physical status, ethnicity, or social background, all of which can alter HRV results, along with age and gender (Hill & Thayer 2019, Souza et al. 2021, Ernst 2017). Other variables, such as position, movement, recency of physical activity, tasks performed during recording, and relationship variables, can affect HRV measurements by changing ANS mechanisms, breathing mechanics or emotions (Shaffer & Ginsberg 2017). Likewise, most of these confounding variables are rarely controlled, although they have the potential to substantially alter between- and within-subject variability (Heathers 2014). The selection of the parameters to measure when analysing HRV data is also important. Although time- and frequency-domain indices are more standardised and validated, the increased use of non-linear measurements make the

comparison among HRV studies more difficult. As mentioned by Ernst (2017), the relevance of most of the non-linear indices that have been introduced in HRV analysis is still unclear, and there are no standardised norms for their measurement. Moreover, the meta-analysis of the results reported in the literature is difficult and some statistical considerations regarding the effect sizes of the studies should be taken into consideration (Quintana 2017).

Finally, it is important to consider the equipment needed to obtain reliable HRV information, which is based on the processing of good-quality ECG signals, which need to be acquired during long-term (24-hour) or short-term (5-minute) recordings (Shaffer & Ginsberg 2017, Xhyheri et al. 2012, Task Force of the European Society of Cardiology and The North American Society of Pacing and Electrophysiology 1996). However, ECG signals acquisition needs cumbersome instrumentation including the use of at least three skin-contact electrodes, and many cables (Webster 2010). Moreover, the frequency components of an ECG signal spam from nearly 0 Hz to frequencies above 100 Hz (Rangayyan 2002), which imply a higher sampling rate needed for a reliable ECG recording. Trying to overcome the issues related to ECG acquisition for HRV estimation, some researchers have proposed alternatives to this signal, such as blood pressure (Constant et al. 1999, Ahmad et al. 2009), photoplethysmography (Gil, Orini, Bailón, Vergara, Mainardi & Laguna 2010, Jeyhani et al. 2015, Rauh et al. 2003), ballistocardiography (Pinheiro et al. 2009), and near-infrared spectroscopy (Holper et al. 2016). Heart rate modulates these signals as well, and their quasi-periodic nature relates to the rhythm of blood travelling through the vessels. However, unlike ECG, their frequency content is more limited (meaning that lower sampling rates are enough for acquiring a reliable signal), and some of them need only one probe in order to obtain the signal. Hence, they may be easier to apply in a regular manner both in clinical settings and in daily life using wearable devices (Georgiou et al. 2018). Nonetheless, accurate fiducial point identification in most of these signals can be problematic and require further validation for its use in HRV analysis (Berntson et al. 1997).

4.5 Summary

Heart rate variability (HRV) describes the changes through time in the duration of cardiac cycles. It is usually measured from electrocardiographic (ECG) signals

by detecting the R peaks and measuring the duration of the time interval between consecutive R peaks. Then, from the series of these intervals, several time-domain, frequency-domain and non-linear indices can be extracted to characterise HRV.

These indices have been used to identify and monitor diseases, especially cardiovascular and metabolic disorders. Although promising, several factors have impacted HRV deployment for clinical use, but it has been increasingly used in research and has been proposed as a good, noninvasive biomarker of cardiac autonomic activity.

Chapter 5

Photoplethysmography and Pulse Rate Variability

5.1 Photoplethysmography

Photoplethysmography (PPG) is a simple, low-cost, non-invasive, optical measurement technique which serves for the detection of blood volume changes in peripheral tissues, and is probably the most used signal in wearable devices nowadays, mostly to detect volume changes in the microvascular bed of tissue using light scattering properties (Kyriacou 2021). Therefore, a device that obtains the reflected or transmitted light when this interacts with tissue allows for the assessment of the pulse wave in the periphery. In each cardiac cycle, the diameter of the arteries varies, modifying the optical pathlength (reaching minimum and maximum transmittance values in the systole and the diastole, respectively) and, hence, the light detected by an optical sensor (Budidha & Kyriacou 2021). Figure 5.1 shows the components of a PPG signal, i.e., the pulsatile component (AC) and a quasi-DC component (DC) (Mejía-Mejía, Allen, Budidha, El-Hajj, Kyriacou & Charlton 2021). The DC component, a quasi-static component varies slowly due to respiration, vasomotor activity, and vasoconstrictor waves, and is related with the tissues and average blood volume, as well as the blood stores in the veins; Traube Hering Mayer waves and thermoregulation also modify this component (Mejía-Mejía, Allen, Budidha, El-Hajj, Kyriacou & Charlton 2021, Allen 2007). Superimposed to the DC component, the AC component of the PPG signal is a quasi-periodic waveform with a fundamental frequency that is usually around 1 Hz, which depends on heart rate (Mejía-Mejía, Allen, Bu-

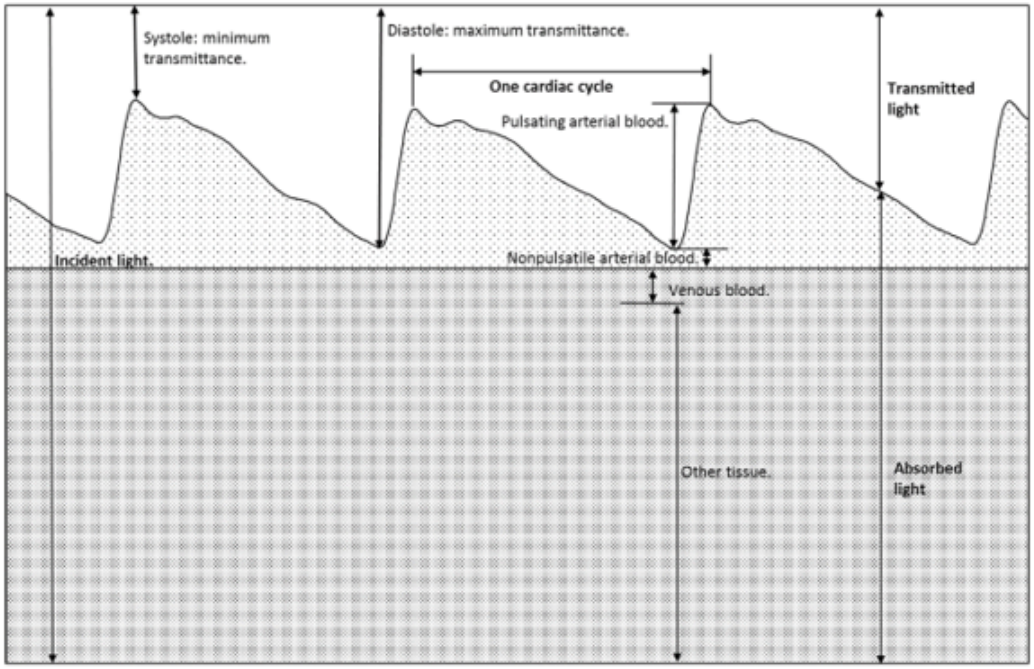

Figure 5.1: Absorbed and transmitted light in living tissue. Adapted from (Wieben 1997). This behaviour of the light results in the photoplethysmographic signal, which has a pulsatile component, also known as AC component, and a quasi-DC component.

didha, El-Hajj, Kyriacou & Charlton 2021, Allen 2007). This component reflects the changes in the blood volume due to the cardiac cycle and is mainly explained by changes in the volume of pulsatile arterial blood (Mejía-Mejía, Allen, Budidha, El-Hajj, Kyriacou & Charlton 2021, Sun & Thakor 2016). The AC component is around 1 to 2% of the total amplitude of the PPG signal (Budidha 2016) but important information can be extracted from it, such as the changes in pulse rate through time, also known as Pulse Rate Variability, which has been proposed as an alternative option to HRV (Schäfer & Vagedes 2013).

Several aspects may affect the PPG signal. Some of these factors are: (1) the periodic increase and decrease in the tissue blood fraction, due to the cardiac activity; (2) the distensibility of the skin vessels; (3) the distance between the light source and detector, and the depth of the pulsing vasculature; (4) the extinction coefficient of the blood volume at the measurement wavelength; (5) the scattering of the light due to the erythrocytes; (6) venous pulsatile blood; and (7) the autonomic function and the vasoconstriction and vasodilation processes (Njoum 2017, Allen 2007). Furthermore, the PPG signal can be highly affected by factors such as the ambient temperature and the contact pressure of the sensor against the tissue

(Middleton et al. 2011, May et al. 2021).

5.1.1 The origin of photoplethysmography

There are several theories that explain the origin of the PPG signal (Kyriacou & Chatterjee 2021). However, they are mostly based on the optical processes that take place when light penetrates tissue. These are scattering, absorption, reflection, transmission, and fluorescence, and their behaviour also depend on the type of tissue irradiated and its different layers (Kyriacou 2021, Chatterjee & Kyriacou 2019). Since tissue has several heterogeneous layers, the propagation of light in tissue depends on the scattering and absorption properties of each component of the tissue (Njoum 2017).

Light absorption is one of the primordial processes that occur when tissue is illuminated. It has been described by the Beer-Lambert's law, as shown in (5.1), which describes the logarithmic attenuation of light travelling through an absorbing medium (Kyriacou & Chatterjee 2021). When monochromatic light penetrates a uniform medium, a part of the original intensity of the light, I_0, is transmitted through the medium, while some of it is absorbed, reflected and scattered; the intensity of the light decreases exponentially with distance and depends on the extinction coefficient (absorptivity) of the absorbing substance in the medium at a specific wavelength, $\epsilon(\lambda)$; on the concentration of the absorbing substance, c; and on the optical path length through the medium, d (Njoum 2017, Kyriacou & Chatterjee 2021).

$$I = I_0 e^{-\epsilon(\lambda)cd} \tag{5.1}$$

From Beer-Lambert's law, it is possible to obtain an estimation of the properties of transmittance, T, and unscattered absorbance, A, of the illuminated medium, as shown in (5.2) and (5.2), respectively. These equations can be generalised to mediums in which more than one substance absorbs light, by considering that the total absorbance of light is the sum of the independent absorbances from each absorbing substance (Kyriacou & Chatterjee 2021, Chatterjee & Kyriacou 2019). Although applying Beer-Lambert's law requires certain assumptions, such as the use of monochromatic and collimated light or considering pure and uniform absorption properties in the irradiated medium, it can be used as an estimation of the absorp-

tion of light in tissue (Njoum 2017).

$$T = \frac{I}{I_0} = e^{(-\epsilon(\lambda)cd)} \tag{5.2}$$

$$A = -\ln T = \epsilon(\lambda)cd \tag{5.3}$$

When light penetrates skin, it crosses different pathways in each layer of the tissue, which allow to estimate the optical properties of each skin layer, and which depend highly on the wavelength used when illuminating the tissue, as illustrated in Figure 5.2. The light that is absorbed by tissue is mostly related by the concentration of its natural chromophore, melanin, hence the transmission of the light varies according to the skin type (Njoum 2017). When it reaches connective tissue with nerves and blood vessels, light interacts mainly with the chromophores and especially with the erythrocytes, which carry haemoglobin, the strongest absorber of visible light in the human body (Kyriacou & Chatterjee 2021). The number of erythrocytes present in tissue in a certain instant of time vary; hence, the light absorbed by haemoglobin is constantly changing: The amount of light absorbed, scattered, and reflected by tissue depends then on the volume of blood circulating through

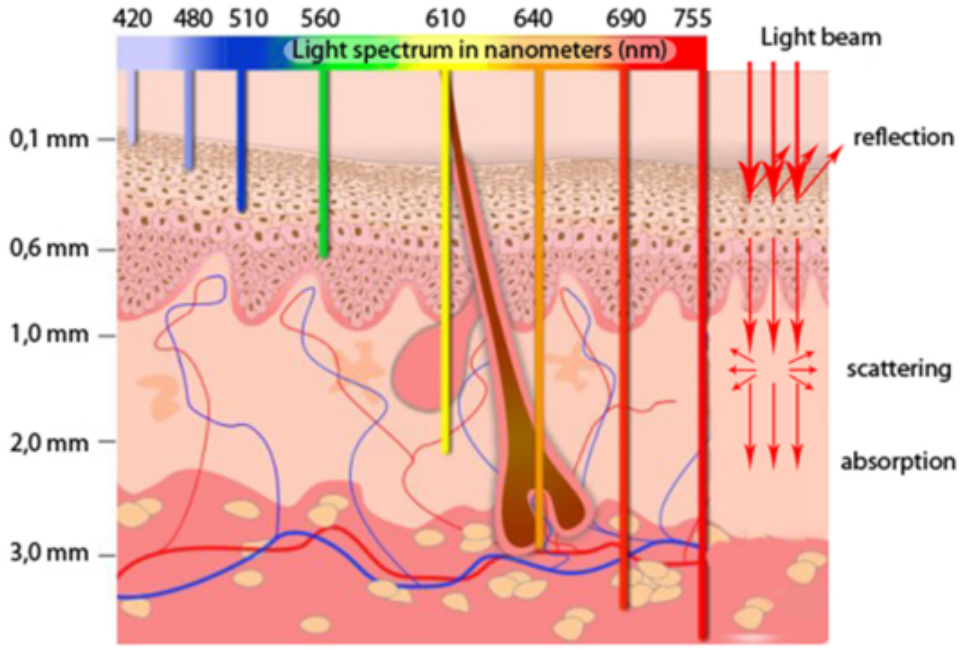

Figure 5.2: Optical pathways in skin: Relationship between light wavelength and depth of penetration in skin (mm) (Njoum 2017). The longer the wavelength, the deeper the penetration of the light.

the vessel of interest in a given time, resulting in the photoplethysmographic signal, which describes the blood volume as a function of time (Kyriacou & Chatterjee 2021).

5.1.2 The photoplethysmographic waveform

Although the origin of the PPG signal and its features is still an active area of research, the cardiac component of the PPG signal, i.e., the AC component, is thought to originate from the site of maximum pulsation within the arteriolar vessels (Alian & Shelley 2014). The PPG waveform resembles an arterial blood pressure pulse wave, although with some important differences in its contour (Mejía-Mejía, Allen, Budidha, El-Hajj, Kyriacou & Charlton 2021).

Figure 5.3 shows an example of the phases of the PPG pulse obtained from a healthy subject. Each pulse wave from the AC component of the PPG signal can be defined by two phases, the anacrotic phase (the rising edge of the pulse) and the catacrotic phase (the falling edge of the pulse), which correspond to the rising and

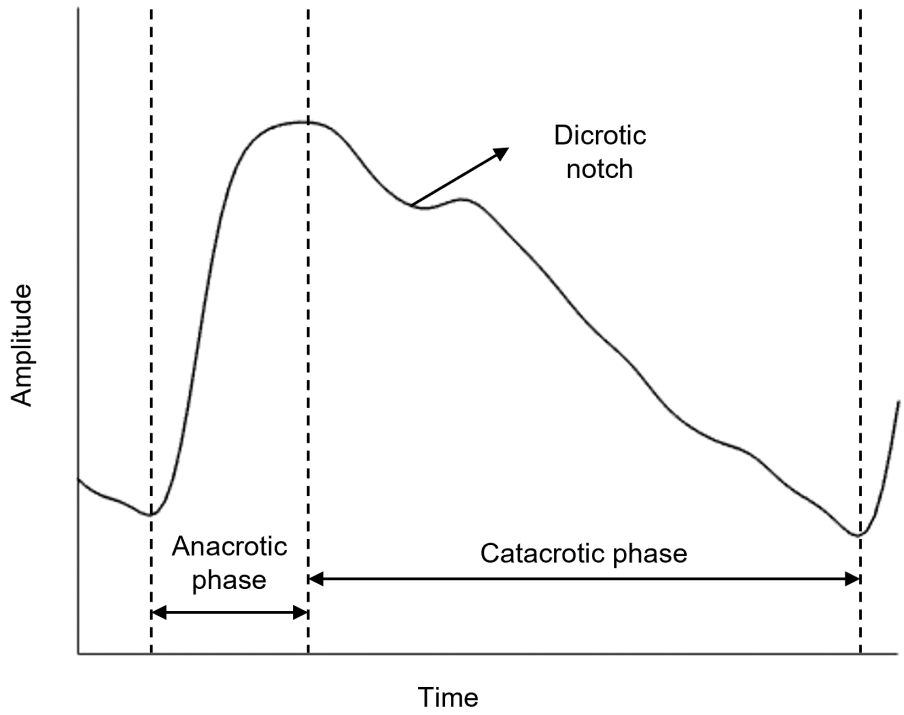

Figure 5.3: Example of a healthy PPG pulse waveform with its different components, the anacrotic and catacrotic phases. The morphology of the waveform also depends on the site of measurement.

falling limbs of the pulse wave (Mejía-Mejía, Allen, Budidha, El-Hajj, Kyriacou & Charlton 2021). These phases are related to the systole and the diastole of the heart, respectively, as well as to wave reflections from the periphery; in healthy subjects, with compliant arteries, a dicrotic notch is usually observed during the catacrotic phase (Allen 2007).

Although the pulsatile PPG signal is very similar to the blood pressure pulse and it has been found to be altered similarly by vascular diseases (Allen 2007), venous pressure waveform characteristics can affect PPG, which would be observed as large peaks during diastole (Alian & Shelley 2014). The morphology of the pulsatile PPG component is influenced by characteristics of cardiac ejection; circulatory changes, such as arterial stiffness and blood pressure; respiratory and autonomic activity; and several diseases (Mejía-Mejía, Allen, Budidha, El-Hajj, Kyriacou & Charlton 2021). This variety of factors that can affect PPG morphology make it challenging to analyse the signal, making the extraction of reliable information from the PPG signal a complex task (Elgendi 2020). Moreover, different kind of noises, including moving artefacts and probe-tissue interface disturbance, tend to affect PPG morphology, and hence affect the information obtained from it (Mejía-Mejía, Allen, Budidha, El-Hajj, Kyriacou & Charlton 2021).

5.1.3 Applications of photoplethysmography

Currently, the most accepted application of PPG is pulse oximetry, which refers to the measurement of SpO_2, an estimation of the amount of oxygen in blood (Budidha 2016, Abay & Kyriacou 2021). However, this signal has been employed for various applications, such as the assessment of vascular mechanics, blood pressure, blood viscosity, and pulse transit time; and the measurement of pulse rate (PR) and pulse rate variability (PRV) (Allen 2007, Alian & Shelley 2021), among others. Besides, it is currently available in most clinical environments and its potential uses are still under investigation (Kyriacou & May 2021).

Clinically and in research, PPG is currently used for real-time monitoring of physiological parameters such as SpO_2, PR, blood pressure, respiration, and cardiac output (Alian & Shelley 2021, Sun & Thakor 2016). Since PR has been shown to serve as a good estimate of heart rate (HR) (Schäfer & Vagedes 2013), the estimation of HRV indices from PRV is being used indistinctly by several researchers, although the relationship between HRV and PRV is still not clear. Even if PR and HR can

be used alternatively, they both refer to the mean value of the behaviour of heart rhythm during certain period of time, whereas PRV and HRV refer to the changes around this mean, and are not necessarily an estimate of each other (Schäfer & Vagedes 2013, Constant et al. 1999). The relationship between HRV and PRV has been investigated by several studies, but there is still no consensus: While some researchers claim that PRV can be used as a surrogate of HRV (Bolanos et al. 2006, Gil, Orini, Bail, Vergara, Mainardi & Laguna 2010, Vescio et al. 2018), some indicate that HRV and PRV may not be the same, especially during non-stationary conditions or when measured from unhealthy subjects (Constant et al. 1999, Georgiou et al. 2018, Schäfer & Vagedes 2013, Rapalis et al. 2018). Nonetheless, due to the wide range of applications of HRV, its relationship with several physiological and mental diseases, and the easiness of pulse wave signals acquisition using PPG technology, this signal has been largely used for the extraction of PRV information.

5.2 Pulse rate variability

5.2.1 Analysis and characteristics of pulse rate variability

As explained above, PPG has been used in recent years for the extraction of PRV as an alternative to measure HRV dynamics. This has been mainly because of the easiness and widespread use of PPG devices, and its capability to be included in everyday, wearable devices (Schäfer & Vagedes 2013, Georgiou et al. 2018). In a study performed by Natarajan et al. (2020), in which data from 8 million users of Fitbit devices was considered, it was concluded that analysing the data acquired from these wearable devices opens the door for large scale, longitudinal studies with the aim to describe and standardise PRV values in healthy population, and for research focused on its potential use in health promotion.

PRV analysis from the PPG is based on the detection of cardiac cycles from the pulsatile component of the signal. And, as with HRV analysis from the ECG, time-domain, frequency-domain and nonlinear indices are extracted from the time series built from the duration of cardiac cycles. Several studies have also proposed novel methods for the analysis of PRV and its characteristics, and some attention has been given to the effects of acquisition and processing techniques applied for the analysis of PRV, especially given how prone the PPG signal is to artefacts (Dobbs et al. 2019, Mejía-Mejía, Allen, Budidha, El-Hajj, Kyriacou & Charlton 2021, Fine

et al. 2021).

5.2.1.1 Fiducial point detection and pulse rate variability

One of the areas with more studies regarding the analysis of PRV from pulsatile signals has been the selection of fiducial points to use for the segmentation of cardiac cycles, given the pulse wave morphology, how it is affected by several environmental and physiological disturbances, and the slowly changing nature of the signal. In an attempt to understand the differences of PRV and HRV when obtained from several fiducial points from the PPG, Chen et al. (2013) compared HRV indices obtained from the ECG R peaks (RRI) to indices extracted from PRV traces obtained both from the peak-to-peak (PPI) and the valley-to-valley (VVI) intervals. ECG and finger PPG signals were obtained from 20 healthy subjects while seated, and RRI, PPI, and VVI time series were measured. From these time series, SDNN, RMSSD, pNN50, nLF, nHF, SD1, and SD2 indices were extracted, and their correlation was evaluated. As reported, VVI and RRI were more strongly correlated than PPI and RRI, especially for short-term analysis of PRV. Similarly, Posada-Quintero, H.F., Delisle-Rodríguez, D., Cuadra-Sanz, M.B., & Fernández de la Vara-Prieto, R.R. (2013) evaluated the interchangeability between PRV and HRV frequency-domain indices when inter-beat intervals (IBIs) from the PPG were determined using three different fiducial points, i.e. diastolic points (DP), maximum second derivative points (MSD) and tangent intersection points (TI), which is determined by the intersection of the tangent to the maximum slope point and the tangent of the minimum value (Hemon & Phillips 2016). Using concordance correlation coefficients and Bland-Altman analysis, they found that TI points were the most suitable to compute PRV indices as surrogates of HRV, with the highest accuracy, precision and reproducibility. Similar results were found by Hemon & Phillips (2016) who concluded that TI gave the best accuracy for extracting SDNN and pNN50 indices, while both TI and the valley points of the cycle are equally accurate for measuring RMSSD. Interestingly, they found that using the systolic peak of the cycle for PRV analysis resulted in the poorest correlation between HRV and PRV indices.

Parasnis et al. (2015) used data from the MIMIC-II database (Saeed et al. 2011, Goldberger et al. 2000) to compare non-linear indices obtained from HRV and PRV information acquired from 20 ICU patients. They extracted IBIs from the PPG by detecting systolic peaks, valleys, maximum point of the first derivative, and max-

imum point from the second derivative, and extracted multi-scale entropy (MSE), SD1 and SD2 to characterize PRV and HRV traces. These indices were compared between HRV and PRV using Pearson correlation coefficients and Concordance correlation coefficients. The authors concluded that neither of these fiducial points give reliable results for these non-linear indices when compared to HRV-derived indices. Their conclusion could be observed from two perspectives: PRV information obtained from PPG signals is not reliable to assess HRV dynamics, or PRV contains different non-linear information to what is present in HRV.

In 2016, Pinheiro et al. (2016) compared HRV and PRV parameters with subjects under three experimental settings, i.e. healthy subjects at rest, healthy subjects after physical exercise, and subjects with cardiovascular diseases. PRV was obtained from PPG signals by detecting the onsets, the time instants corresponding to 20% of the pulse amplitude; the maximum points of the first derivative; the time instants corresponding to 50% of the pulse amplitude; the time instants corresponding to 80% of the pulse amplitude; and the systolic peaks, and HRV and PRV indices were compared using Spearman's rank correlation coefficients, the normalised root mean squared error and Wilcoxon's rank sum test. It was found that for subjects at rest the agreement between PRV and HRV indices was good, although this was not the case for any of the other two experimental settings; and found that the lower error between HRV and PRV were obtained when PRV was extracted using the time instants when 50% or 80% of the amplitude was reached, or using the systolic peaks. However, these authors suggest that the selection of the best fiducial point for PRV analysis should be dependent on physiological conditions and the analysis context.

More recently, Peralta et al. (2019) investigated which fiducial points gave better results for PRV analysis when compared to ECG-derived HRV indices, with PPG signals acquired from the forehead and the finger. PPG and ECG signals were recorded simultaneously while participants took part on a tilt-table test, and time and frequency-domain indices were extracted from PRV and HRV traces. From both forehead and finger PPG signals, systolic peaks, onsets, middle-amplitude points, maximum slope points, and TI points were extracted for PRV analysis. It was found that PRV derived from the middle amplitude points, the maximum slope points and TI points gave the best results, with lower relative errors and higher correlation coefficients and reliability indices, while the dependency of the performance of the fiducial points on the morphology of the wave was also observed, with more reliable

PRV information extracted from forehead PPG signals.

While most of these studies are based on evaluating traditional fiducial points that can be visualised in the PPG signal or its derivatives, Wan-Hua et al. (2022) proposed a technique for detecting the pulse wave forward peak and investigated how reliable are time- and frequency-domain indices extracted from PRV traces measured using this novel fiducial point when compared to traditional fiducial points. They found that estimating PRV indices using the forward peak from the PPG signal is more reliable than most of the other fiducial points, especially for PPG signals acquired from elderly subjects and from different body sites.

Given the difficulties for reliable identification of fiducial points in the pulse waveform, some authors have also aimed to develop new methods for the detection of these points even when the quality of the signal is not great. Such is the case of Ricardo Ferro, B.T., Ramírez Aguilera, A., & Fernández de la Vara Prieto, R.R. (2015), who proposed a new methodology for the automatic detection of onsets and peaks in the PPG signal using the Hilbert Huang Transform (HHT), which was evaluated by comparing results to records annotated by trained experts and to results provided by other widely used methods, i.e., foot approximation and adaptive threshold methods. Good accuracy and precision of the method were observed when compared to the annotated records, and it outperformed the foot approximation and adaptive threshold methods. However, it was only tested in data obtained from 10 healthy subjects at rest, thus further validation of this methodology should be performed. Alqaraawi et al. (2016) proposed the use of a Bayesian classification in order to detect peaks in PPG signals. Although tested only with 3 subjects during rest, the algorithm was found to have a high positive predictivity, good sensitivity, and outperforms other algorithms available in the literature. These same authors developed another algorithm based on linear prediction analysis and Wavelet analysis for estimating PRV from PPG signals acquired by wearable devices (Alqaraawi et al. 2016*b*). The algorithm was tested in 3 subjects, both during rest (5 minutes) and while subjects were walking (5 minutes) and was compared to 2 different algorithms available in the literature, i.e., adaptive threshold (ADT) and automatic multiscale-based peak detection (AMPD), in terms of sensitivity and positive predictive value. It was found that the proposed algorithm outperformed ADT and AMPD both in stationary and non-stationary conditions.

Novel methods for obtaining PRV information without the need of the identifi-

cation of fiducial points have also been proposed. Hayano et al. (2005) proposed the method of Pulse Frequency Demodulation (PFDM) for the assessment of PRV. They simulated and acquired PPG signals (from the wrist of 33 healthy subjects) and tested the PFDM method to obtain PRV traces. PFDM is based on complex demodulation (CDM), a non-linear method that provides amplitude and frequency of non-stationary, oscillatory signals as a continuous function of time. PFDM is a customized CDM, in which the algorithm is modified so it delivers good results with pulse signals. In order to evaluate the performance of the PFDM method, an ECG signal was simulated or obtained simultaneously, and RR intervals were extracted to use as gold standard. Both from the PFDM-derived PRV and the ECG-based HRV, frequency-domain indices (LF and HF) of 5-min segments were extracted, and their agreement was evaluated. It was found that PFDM provides a reliable assessment of PRV information, and that its accuracy is not dependent on the time resolution of the data, i.e. the sampling rate for acquiring the PPG signals could be lower without compromising the results. Although it seems as a promising technique, it was only tested in resting, sleeping subjects; hence, its applicability in other circumstances should be evaluated in further studies. Chang, Hsiao & Hsu (2014) aimed to estimate the instantaneous PRV by applying HHT, and to explore a new frequency band with higher time precision in the frequency domain. As the authors claim, PRV could contain further information related to the peripheral circulation, due to the small oscillations of the arterial pulse waves that result from the regulation performed by the cardiac pumping function, the respiratory movement, and the vascular tone. A good correlation was found between PRV obtained using HHT and empirical mode decomposition (EMD), and ECG-derived HRV spectra. Results led the authors to propose the measurement of a very-high frequency (VHF) band as an index related to baroreflex and HF power, which could serve as an indicator of parasympathetic activities and can only be obtained from pulse wave signals that feature a sinusoid-like pattern. In a second study, these same researchers examined the potential of the VHF band and interpreted its physiological meaning during different non-stationary conditions, due to their hypothesis that PRV is influenced by volumetric and oxygenation changes, and contains more complex information than HRV (Chang, Hsu & Hsiao 2014). According to their findings, VHF was influenced by respiration and head-up tilt experiments, but its dominant frequency is neither the respiratory rate nor its combination with pulse rate, although is a potential in-

dicator of self-regulation. As authors concluded, the relationship and usefulness of this novel index still need further examination, but could have useful information for cardiovascular disease diagnosis. Recently, this technique was applied for the identification of gaming disorder in college students (Chi & Hsiao 2021).

Xu et al. (2019) also proposed the utilisation of machine learning algorithms for the extraction of PRV from PPG signals contaminated with noise due to finger movement. These authors applied a deep recurrent neural network for accurate segmentation of PPG cardiac cycles. Using three state-of-the-art methods and the proposed neural network, three indices were extracted, i.e. the peak-to-peak intervals, onset-to-onset intervals and instantaneous heart rates, from PRV traces measured from PPG signals acquired from right and left hand fingers, with the left finger kept static while the right finger was performing different movements to introduce movement artefact to these signals. It was concluded that the proposed method was more robust for the detection of cardiac cycles from PPG signals contaminated with motion artefacts, even when shallow neural networks were used. Similarly, Wittenberg et al. (2020) applied neural networks to estimate the duration of cardiac cycles from PPG signals. Their approach was based on the automatic detection of a fiducial point in the PPG signal that represents the location of R peaks on ECG signals. Signals from two publicly available databases were used, and time and frequency domain indices from ECG-based HRV and PRV obtained applying the proposed methodology were compared. It was found that applying neural networks may improve the accuracy of PRV indices, although they observed important discrepancies between PRV and HRV parameters. Finally, Kechris & Delopoulos (2021) developed a deep convolutional network framework for the measurement of RMSSD from PRV without detecting fiducial points from the PPG signal. The model was trained and tested using three publicly available databases, with simultaneously acquired ECG and PPG signals. When compared to RMSSD values estimated from HRV the results showed low errors, even improving the performance of traditional algorithms for fiducial point detection available in the literature.

5.2.1.2 Effects of noise and pre-processing of the photoplethysmogram on pulse rate variability assessment

The effects of pre-processing techniques applied to obtain PRV indices were initially analysed by Akar et al. (2013). They compared the indices extracted from PRV time

series after filtering (using a linear Butterworth filter or a non-linear weighted Myriad filter) and detrending (using linear least-squares fitting and smoothness priors), and using several power spectrum density (PSD) estimation techniques for extracting frequency-domain indices, namely periodogram, Welch's periodogram, and Burg method. PPG data was obtained from the middle finger for two minutes, using a sampling rate of 250 Hz, from each of the 15 healthy adults that volunteered for the study. According to the results, the periodogram does not provide an effective solution for each frequency band, probably due to spectral leakage, whereas Welch's periodogram results are more reliable. Moreover, it can be concluded that detrending affects the spectral components of the signal, and that the detrending method needs to be further investigated. However interesting, these results were not compared to an ECG-derived HRV, which would allow for further analysis of the effects of pre-processing on PRV data estimation. In the same line, Kim & Ahn (2019) evaluated the effects of filtering strategies on PRV from PPG signals, and found that Butterworth bandpass filters are more robust than Elliptic filters for the assessment of PRV time- and frequency-domain indices. As shown by Liu ET. al. (2021), there is an increasing need for standardising and defining the filters used for PPG pre-processing in PRV analysis, given the effects these processes may have in the time location of the fiducial points measured from the PPG signals acquired from different body sites.

Chou et al. (2014) also proposed an alternative method for deriving frequency related information from PRV, but with the aim of diminishing the computational complexity of the available methods. The method used the sliding window iterative discrete Fourier transform and the Hilbert transform, and was tested both with simulated and with real data, obtained from 30 subjects at rest. The results obtained showed a very small maximum relative error when compared to indices measured from time-domain-extracted PRV (measuring the pulse-to-pulse intervals), and was found to have a good noise immunity.

Recently, more importance have been given to the capability of extracting reliable PRV information from contaminated PPG signals. Baek & Cho (2019) proposed a frequency-tracking algorithm for the measurement of instantaneous heart rate from motion-artefact contaminated PPG signals obtained from the wrist. They suggested a novel index similar to SDNN, but more reliable and which could be used as an alternative for noisy PPG signals. Similarly, Haddad et al. (2020) developed an

algorithm for the detection of ectopic beats from wrist PPG signals, for the discrimination of sinus rhythm and atrial fibrillation based on PRV. The application of their algorithm allowed for a sensitivity of 93.08 ± 3.83% and a specificity of 97.80 ± 2.12% for detecting subjects with atrial fibrillation, meaning an increased specificity without significantly decreasing sensitivity when compared to other methods available in the literature. Also, Zanon et al. (2020) proposed the measurement of a quality index for PRV data, which is related to PRV accuracy and can be used as an indication of reliability of PRV information. This method is based on the measurement of the difference between HRV and PRV indices for the estimation of an error and quality of the extracted parameters. Similarly, Vila et al. (2021) showed importantly reduced error levels for the estimation of PRV indices when quality indices were applied directly to the PRV trace in real-time, using data acquired from wearable devices, while several authors have demonstrated the utility of assessing and correcting the quality of the PPG signal before PRV analysis in order to obtain more reliable results (Neshitov et al. 2021, Wang et al. 2021, Cosoli et al. 2021).

5.2.1.3 Minimal sampling rate for pulse rate variability analysis

Another important aspect in the extraction of PRV information is the effect of sampling rate in the analysis of PRV. Choi & Shin (2017) aimed to assess this matter by obtaining finger PPG and ECG simultaneously from 28 healthy volunteers. Data was obtained for 20 minutes while participants were resting, and both signals were acquired using 10 kHz sampling rate. PPG was then down-sampled to 5 kHz, 2.5 kHz, 1 kHz, 500 Hz, 250 Hz, 100 Hz, 50 Hz, 25 Hz, 15 Hz, 10 Hz and 5 Hz. The agreement between HRV and PRV derived from all down-sampled PPGs was analysed by extracting time- and frequency-domain indices. Significant differences, especially in time-domain indices, were observed once the sampling rate was below 20 Hz, indicating that PRV information can be reliably obtained from signals with a low sampling rate, allowing for a simpler analysis of this data in wearable and portable devices, mostly based on microcontrollers. However, this low sampling rate could affect PRV when different population is considered, such as people suffering cardiovascular diseases (Hejjel 2017).

In an attempt to better understand this matter, Béres et al. (2019) simulated PPG signals using cosine waves and evaluated how different sampling rates, and the utilisation of cubic spline interpolation to increase sampling rate, affected time-

domain, frequency-domain and Poincaré plot PRV parameters. They found that different indices required different sampling rates, and that cubic spline interpolation could be used for improving the results in case of lower sampling rates. Although interesting, their study was based on a small sample of master PPG signals with a original sampling rate of 1 kHz. These signals were decimated to simulate lower sampling rates, but it is not clear how this decimation may have affected PRV indices as well. The authors concluded that RMSSD, frequency-domain indices and the shape of the Poincaré plot are more susceptible to lower sampling rates, and the latter shows important differences due to interpolation. In a follow-up study with 57 PPG signals acquired from healthy volunteers at 1 kHz sampling rate, Béres & Hejjel (2021) aimed to validate the results obtained with simulated signals, and evaluated as well the differences between cubic-spline and parabola interpolated signals. Their results showed a similar trend, with different minimal sampling rates needed according to the index of interest, with AVNN being particularly robust regardless of sampling rate, while both interpolation techniques allowed for a reduced error due to sampling rate, with a better performance when parabola interpolation was applied. These results are based on the comparison of PRV indices extracted from the master, 1-kHz PPG signals and indices obtained from the decimated and interpolated PPG signals. In a similar study, Pelaez-Coca et al. (2022) investigated how reducing the sampling rate of PPG signals by decimation affects PRV indices extracted using several fiducial points. Their results, obtained by comparing PRV to HRV indices using signals simultaneously acquired from 57 subjects, showed that a novel fiducial point referred to as the interpolated medium point, gave the best results when sampling rate was lowered down to 50 Hz. Their analysis was based on time- and frequency-domain indices and PPG signals were acquired from the finger and the forehead.

Given the applicability of low-sampled PPG signals in wearable devices and video-based PRV, several authors have proposed methodologies for improving the reliability of PRV analysis from low-sampled PPG signals. Baek et al. (2017) evaluated the reliability of the parabola approximation method for analysis of PRV when PPG was acquired using low sampling rates. When low sampling rates are used for obtaining PPG data, a usual alternative is to interpolate the signals to obtain a higher-sampling-rate representation of them (Panganiban, F.C. & de Leon, F.A. 2019). Due to the morphology of the PPG signal, cubic spline interpolation has

been widely used for increasing its sampling rate. However, this methodology has a large computational load and requires higher power consumption. Hence, this study aimed to evaluate a simpler methodology, the parabola approximation method, for estimating PRV from low-sampling-rate PPG signals. The results of comparing HRV to PRV measured from 20-Hz sampled PPGs indicate that there was no significant difference between the parabolic and spline interpolation methods, whereas the difference between HRV and the 20-Hz-sampled-PPG-derived PRV was higher in all cases. In concordance with the results from Choi & Shin (2017), the HF band is more influenced by low sample rates than the LF and VLF components. However, the correlation analysis between non-linear indices indicate a special sensitivity of these parameters to sampling rate.

Yoshida et al. (2019) aimed to improve the accuracy of PRV indices by estimating the error between ECG-derived RR intervals and PPG-based IBIs, using a multiple linear regression model. With a sample of only three healthy subjects, the authors concluded that, by applying their proposed model, the mean absolute error between RR intervals and PPG IBIs was reduced from 5.49 ms to 3.83 ms, with an average improvement of the meant absolute percentage error of 17% on LF/HF ratio, being reduced from 26.7% to 9.7%. Similarly, Watanabe et al. (2020) proposed an error compensation method based on linear interpolation and autocorrelation measurements for improving PRV measurements obtained from low-sampled PPG signals. Applying their proposed method, the authors found that the mean absolute percentage error of LF/HF was only degraded by 3.3% with PPG signals sampled at 10 Hz. Liu et al. (2020) also proposed a methodology for improving the extraction of PRV information from smartphone-based PPG signals, which are usually sampled at a maximum of 30 Hz, based on a sum of sinusoidal functions for fitting and estimating the quality of the PPG. Their main conclusion was that applying the proposed signal quality index can increase the accuracy of PRV information obtained using a smartphone application, while they also found the TI point to give the best results when PRV was compared to ECG-based HRV. These methodologies open the door for the extraction of reliable PRV information from PPG signals acquired using low sampling rates, especially useful for wearable devices.

5.2.1.4 Non-linear indices from pulse rate variability

As explained by Hayano & Yuda (2021), the use of non-linear indices and novel approaches for their determination from PRV analysis can provide useful insights regarding autonomic function and may contain useful information that is not readily available from the classical time- and frequency-domain indices.

In terms of measurement of entropy-related indices from the PRV, Chou, Zhang, Feng, Lu, Lu & Xu (2017) proposed a low-computational algorithm for the measurement of basic scale entropy (BSE) with the theory of sliding window iterative, which they called SWIBSEA, in order to allow a real-time analysis of BSE in wearable and portable systems. When compared to the measurement of BSE using the traditional analysis, SWIBSEA results were very similar and the computational load was much lower. In a similar manner, some authors proposed the measurement of SWISSEA instead of SSEA for the analysis of sign series entropy, using a similar sliding window iterative analysis (Chou, Zhang & Yang 2017). Once again, results between SWISSEA and SSEA were similar and the computational needs of the latter were much lower, allowing for a real-time application of the method. As a proof of concept, SWISSEA was evaluated for identifying age-related changes in PRV indices, successfully classifying between young and old subjects. Pernice et al. (2019*c*) computed the complexity of PRV trends using a linear Gaussian approximation method for the extraction of Conditional Entropy Measures and found that PRV-based indices had a positive bias when compared to those extracted from HRV measured from the ECG, most likely attributable to differences between HRV and PRV than to the novel methodology proposed. Also, they found that these entropy measures could be used to discriminate among three conditions: subjects in supine position, at 45° upright position after head-up tilt, and during a mental arithmetic task in supine position, with increased differences when measured from PRV than from HRV.

In terms of detrended fluctuation analysis (DFA), Molkkari et al. (2019) used this non-linear analysis for classifying among sleep stages. Although classification results are not particularly good, these were obtained by using only DFA-related indices, which showed visible differences among sleep stages although with high variance within the same sleep phase. Other non-linear measurements have been extracted for PRV analysis. For instance, Nardelli et al. (2020) proposed a cross-mapping method to assess the quality of PRV trends obtained from the wrist and finger of

healthy volunteers, with respect to HRV information. It was concluded that, using cross-mapping for assessing PRV quality, the information obtained from finger PPG was more reliable for PRV assessment than that obtained from the wrist.

Perhaps one of the main drawbacks of non-linear analysis for PRV and HRV is the lack of standardisation of these measurements. Hence, the appearance of tools for the extraction of these indices in a more guided and standard manner, such as that proposed by Mayor et al. (2021), may increase their applicability and the comparability among studies using these indices.

5.2.1.5 Pulse rate variability derived from video photoplethysmography

A special interest has arisen for the measurement of PRV from non-contact, image based PPG signals. Non-contact PPG signals can be obtained by applying image processing techniques to images obtained from a subject skin. The changes in blood volume can be detected by filtering and segmenting the image obtained from the camera while a light, such as the white, flash light available in most Smartphone cameras, illuminates the body of a subject (Sun & Thakor 2016). One of the first attempts to obtain PRV data from non-contact, image PPG (iPPG) was presented in by Poh et al. (2011), who used a low-cost webcam for obtaining PRV data applying an Independent Component Analysis (ICA) strategy for the acquisition of PPG signals from the images, obtained using a camera speed of 15 frames per second. A good agreement between the PPG and iPPG signals was observed, as well as between both PRV frequency spectra, and a high correlation between indices. These results led the authors to conclude that iPPG could be used to obtain PRV information. However, some limitations emerged from this first approach: The low sampling rate (15 frames per second) established for the camera, and the short measurements performed (1-min long) which are not enough to measure the spectral indices of PRV and HRV (Task Force of the European Society of Cardiology and The North American Society of Pacing and Electrophysiology 1996). Based on this study, Sun et al. (2012) aimed to assess the feasibility of iPPG for measuring PRV, and investigated the influence of different sample rates on PRV analysis, since a low sampling frequency could modify the PPG morphology and thus the derived PPI series, which in turn could alter the frequency representation of PRV. The agreement between indices obtained from iPPG- and PPG-derived PRV was assessed using Bland-Altman analysis, and their correlation was evaluated using Pearson's

correlation coefficients. Significant correlations were found in the estimated results, while the Bland-Altman analysis showed that none of the biases differed significantly from zero. Importantly, no significant influence of the sampling rate was observed on any of the measured indices.

In 2014, McDuff et al. (2014) continued the work reported by Poh et al. (2011) by evaluating the use of a 5-band digital camera for the acquisition of PRV data in subjects at rest and under cognitive stress. A special camera, capable of obtaining red (R), green (G), blue (B), cyan (C) and orange (O) channels, was used for acquiring images from 10 healthy volunteers at rest (2-min) and under cognitive stress (2-min). It was found that the most correlated indices obtained from iPPG with respect to those obtained using contact PPG, were those measured from iPPG signals that contained images taken using the orange channel, with the greater correlation obtained from the GCO combination. Hence, the authors propose to include colour channel sensors closer to the orange, cyan, and green wavelengths.

Other studies have aimed to increase and analyse the effects of different factors on the acquisition of image-based PRV: Guede-Fernández et al. (2015) found significant differences among PRV traces and indices measured using different Smartphone models and cameras, as well as an effect on PRV due to changes in posture; Blackford et al. (2016) demonstrated that non-contact PPG can be measured from video images taken 25 meters apart from the object, and that PRV can be estimated from the obtained signal; Alghoul, K., Alharthi, S., Al Osman, H. & El Saddik, A. (2017) compared two methods, i.e. ICA and Eulerian Video Magnification for extracting iPPG signals from video, analysing the differences between the estimated PRV indices and HRV indices obtained from ECG signals; and Melchor Rodríguez, A., & Ramos-Castro, J. (2018) aimed to evaluate the effects of motion on iPPG-based PRV analysis, and proposed a robust tracking method for improving results during motion conditions. Similar attempts have been performed with the aim of improving the extraction of PRV information from video-based PPG (Cho et al. 2021).

Video PPG is a promising technique and the potential of acquiring PRV from these signals is immense. However, the acquisition of the PPG signals, as well as the processing of this data for PRV analysis, is different to contact PPG. Hence, further analysis of this technique is out of the scope of this work.

5.2.2 Applications of pulse rate variability

Since the PPG signal is easier to acquire than the ECG, several researchers have used PRV instead of HRV in different applications. These include the detection, characterisation and monitoring of somatic diseases; the assessment of mental health; research related with effects of drugs and medication on the ANS; and sleep studies.

5.2.2.1 Mental health

Several studies have related HRV with mental health conditions, such as depression (Liang et al. 2015, Vazquez et al. 2016, Koenig et al. 2016, Hamilton & Alloy 2016), bipolar disorders (Bassett 2016), and stress (Murray 2012, Tazarv et al. 2021, Beh et al. 2021). Hence, PRV has been proposed as an alternative to HRV to detect, assess, and investigate several mental health conditions and pathologies.

There has been an increasing interest in understanding how stress and emotions are reflected in the ANS, and several studies have focused on measuring PRV indices for assessing the effect of different techniques that allow for a better stress and emotional management, such as Mindfulness-based stress reduction programs (Geary & Rosenthal 2011), HRV biofeedback (Sakakibara et al. 2013), hypnosis (Kekecs et al. 2016), Taoist meditation (Volodina et al. 2021) and Baduanjin exercises (Cai et al. 2021). Moreover, PRV has been proposed as a technique for detecting stress in a continuous manner, achieving promising results (Choi et al. 2017, Hao et al. 2017, Jobbágy et al. 2017, Zangróniz et al. 2018, Can et al. 2019), and for classifying among different emotional states (Park et al. 2012, Martínez-Rodrigo et al. 2019, Cho et al. 2017, Suzuki et al. 2021, Bastos et al. 2021).

In an interesting study, an emotion recognition system based on the fusion of features obtained from lagged Poincaré plots from both HRV and PRV was proposed (Goshvarpour et al. 2017). The authors used finger PPG and ECG obtained from 35 college students while listening to musical excerpts selected to invoke 4 emotional states (peacefulness, happiness, sadness, and fear). Using the R peaks from the ECG and the systolic peaks from the pulse waveform, HRV and PRV were measured respectively, and Poincaré plots with lags from 1 to 10 were obtained. It was found that the emotional stimuli affected HRV and PRV Poincaré plots in a different way, and that the Poincaré measures were significantly different between lag 1 and the other lags in all emotional states, showing smaller p-values for PRV measures than

for HRV measures. Moreover, using support vector machines, the authors reported accuracy values higher than 70% when using PRV and HRV features separately or when fusing the features. Interestingly, the better results were obtained using PRV features solely, with an accuracy of 84.1%, which was 8% higher than what was obtained using only HRV-derived features.

The relationship between other psychiatric disorders and PRV has also been studied. Minassian et al. (2014) aimed to assess the relationship between posttraumatic stress disorder (PTSD) and HRV (measured as PPG-derived PRV) in 2430 male active-duty Marines. It was found that even when Traumatic Brain Injury is accounted for, lower PRV is significantly associated with PTSD. This same group of researchers evaluated if PRV indices before trauma were associated with the development of PTSD in Marines and Sailors after their return from combat (Minassian et al. 2015). Their findings imply that the measurement of PRV before deployment of Marines and Sailors could help identify those subjects that are more vulnerable for developing PTSD after combat, and thus that may be monitored during and after deployment to prevent the development of PTSD or related conditions. Recently, Cakmak et al. (2021) developed machine learning algorithms based on PRV and actigraphy features for the extraction of circadian rhythm patterns and the determination of PTSD outcome, finding relatively good accuracy values for classifying among different outcomes after a traumatic incident. Major depressive disorder (MDD) has also been related with PRV, and has been proposed as a technique for the self-assessment and screening of MDD. It has been observed that PRV reactivity is lowered in patients with MDD, as compared to control subjects (Kobayashi et al. 2017), and that frequency-domain indices could be employed for the identification of MDD patients, with high sensitivity (83%) and specificity (93%) (Dagdanpurev et al. 2018). Schizophrenia (Akar et al. 2015), psychosis (Clamor et al. 2014) and suicidal behaviour (Sheridan et al. 2021) have also been studied, in an attempt to use PRV for the assessment and management of these conditions, while Cainelli et al. (2022) used PRV information for predicting psychopathology and determining social skills in children.

5.2.2.2 Pharmaceutical research

Due to the relationship between HRV and the ANS, and the information related to cardiac regulation provided by HRV, some studies have tried to identify the effects

of pharmacological drugs using HRV. Mueck-Weymann et al. (2002) investigated the effects of atypical antipsychotics, namely Olanzapine and Clozapine upon PRV, with the aim of comparing their effects upon neurocardiac control in schizophrenic patients and healthy controls. Authors found a greater decrement in PRV values in the clozapine-treated patients than those observed in the olanzapine-treated group. This last group also exhibited a similar LF/HF ratio to that observed in healthy controls, implying a nearly equal reduction of modulation from both branches of ANS. Authors implied that PRV could be used as a clinically relevant tool in the rational use of drug therapies in patients with psychiatric disorders.

Later on, Arya et al. (2008) compared the Thiopentone sodium, propofol, and midazolam for Electroconvulsive Therapy (ET), finding a lower variability when midazolam or propofol were used, whereas thiopentone sodium generated an increase in pulse rate; with these results, authors recommended the use of propofol as anaesthetic agent during ET. In 2016, Sluyter et al. (2016) examined the relationship between pattern of statin use and brachial blood pressure (BP), measures of arterial function and cardiovascular autonomic function. Results indicate that the duration of the statin-based treatment is inversely related to PRV parameters in people with diagnosed or suspected cardiac arrhythmias, which could imply a reduction of the risk of adverse cardiovascular outcomes.

5.2.2.3 Sleep studies

Researchers have applied PPG-derived PRV to analyse different sleep disorders and conditions, and to study the role of ANS in the resting function of sleep. Many of these studies attempted to diminish the instrumentation and costs related to sleep studies based on polysomnography (PSG), and several researchers have studied the relationship of PRV with different sleep disorders. Special attention has been paid to the study of Obstructive Sleep Apnea (OSA), both in adults and in children, due to the difficulties in the instrumentation and experimental setup that needs to be applied during a PSG examination, which is the primary diagnostic tool for this disorder.

Restorative function of sleep has been studied by means of PRV and other physiological signals in postmenopausal women (Takahara et al. 2008), college students (Sakakibara et al. 2008), children having different chronic conditions (Krivec et al. 2012), and subjects with OSA (Fujimoto et al. 2018, Constantin et al. 2008). Results

from these studies indicate that PRV indices are related to subjective sleep reports, and to sleep efficiency and fragmentation.

The relationship between Periodic Limb Movement Disorder (PLMD) and PRV was studied by Krishnaswamy et al. (2010) who assessed whether the presence of increased PRV without overnight desaturation was suggestive of occurrence of periodic limb movements. It was concluded that isolated, increased PRV in overnight oximetry could serve as an indicator of the occurrence of periodic limb movements during sleep. PRV was also employed to determine how oximetry findings affect night maternal cardiac ANS modulation during uncomplicated pregnancy, in women with and without sleep-disordered breathing (SDB); findings suggest that the parasympathetic activity is attenuated in pregnant women with SDB, even in cases in which low saturation episodes were sparse (Watanabe et al. 2015).

The identification of OSA episodes and the segmentation of sleep stages has been of primary interest in the study of sleep. Hence, PRV has been proposed for enhancing the current techniques available for performing these tasks. Lazaro et al. (2012) evaluated PPG-derived PRV instead of ECG-derived HRV to discriminate between apnoeic and non-apnoeic decreases in amplitude fluctuations of the PPG signal (DAP) events. The number of DAP events per hour has been used as discriminator of children suffering from OSA and healthy children, so a HRV-based algorithm to discriminate apnoeic from non-apnoeic DAP events was initially proposed, in order to improve the determination of OSA in children. However, as these researchers state, HRV requires the acquisition of ECG signal. Hence, they proposed to replace HRV with PRV obtained from PPG, to decrease the system complexity. The DAP events classifier (a linear discriminant) improved its performance using PRV (70.4% accuracy) instead of HRV (67.9%), while the classification of subjects as OSA or non-OSA achieved an accuracy of 86.7% while using PRV, compared to the 80% obtained when using HRV information. This suggests that PRV not only can be used to discriminate DAP events, but that it carries more information than HRV for this purpose.

Following these results, these same authors analysed the discrimination of sleep apnoea-related DAP in children, by comparing HRV and PRV as discriminators of the same set of DAP events (Lázaro et al. 2014). PSG records from 21 children were analysed in their study, with a total 268 DAP events, which were clustered as apnoea-related and non-apnoea-related events according to their physiological

characteristics. Moreover, they classified 1-hour segments of data as normal or pathological based on the DAP events per hour ratio. It was found that this ratio, which was obtained both with a previous published algorithm based in PPG and SpO_2 (Gil et al. 2008) and with the proposed algorithm using PRV for classifying DAP events, had a better discriminant power between normal and pathological fragments when PRV was used. Since the features selected for PRV were different from those selected in a previous study which used HRV instead of PRV (Gil et al. 2009), authors concluded that the correlation between HRV and PRV may be affected by the respiratory abnormalities occurring during OSA episodes. Interestingly, DAP events were more accurately classified using the PRV-extracted features (70.37%), whereas the classification accuracy of subjects reached an 86.67% accuracy, which was a better result than that obtained using HRV information, as well as when only PPG and SpO_2 information was applied.

Dehkordi et al. (2013*b*) investigated the effects of sleep disordered breathing (SDB) and of different sleep stages on PPG-derived PRV, using the Phone Oximeter, an oximeter sensor connected to a mobile phone. A large database containing PSG and Phone Oximeter records from 142 children was used in this study. It was found that during both rapid eye movement (REM) and non-rapid eye movement (NREM) sleep, the mean pulse-to-pulse intervals appeared shorter for children with SDB in respect to children in the non-SDB group, which may indicate higher sympathetic activity in these subjects. Moreover, in the frequency domain, the LF component and the LF/HF ratio were higher in the SDB group, which presented a lower HF component as well, both during REM and NREM sleep; these results confirmed the feasibility of using PRV in monitoring ANS regulation during different sleep stages in both healthy and SDB children. Recently, Wulterkens et al. (2021) further demonstrated the feasibility of using PRV information, alongside accelerometry, for the classification of sleep stages using wrist-worn wearables, reaching accuracy values of 76.4% and 77.9% for the classification of four sleep stages in adults and children, respectively.

The combination of PRV and other physiological markers has been proposed for classifying OSA patients. Garde et al. (2014) proposed to classify SDB and healthy children using both oxygen desaturation (SpO_2) patterns and time- and frequency domain PRV indices using the Phone Oximeter. Using a linear classifier and the extracted features, an accuracy of 85% was obtained for the classification between

SDB and non-SDB subjects. Similarly, Then, these same authors evaluated the combination of SpO_2 and PRV features for identifying OSA events that occurred with and without oxygen desaturation (Garde et al. 2015). It was determined that one-minute long non-OSA and OSA segments with and without desaturation differed in PRV-based features such as mean PPI, SDNN, nLF, and nHF, along with other SpO_2-based features that were found to discriminate the three classes, and authors concluded that combining PRV and SpO_2 information, the discrimination between OSA and non-OSA patients was better than that obtained using solely SpO_2-based features, reaching an accuracy of 78.9% using a multiple logistic regression model. These authors also reported a multivariate logistic model based on PRV- and SpO_2-based features for the classification of OSA and non-OSA segments lasting just 30 seconds, which provided an accuracy above 73% (Garde et al. 2016), while Lazazzera et al. (2021) used PRV, PPG amplitude and SpO_2 information for the classification of sleep disordered breathing events, with an accuracy of 75.1% for the detection of apnoeas and hypoapnoeas, and high accuracy values for the discrimination of central and obstructive apnoeas.

In other study, PPG- and PRV-based features (46 and 40, respectively) where combined for the discrimination of respiratory arrests in OSA patients, reaching success rates above 80% when using different classifiers, such as k-Nearest Neighbours (kNN), multi-layer artificial neural networks (ANN), and support vector machines (SVM) (Bozkurt et al. 2019); whereas Aksahin et al. (2015) used synchronisation measurements between HRV and PRV time series to discriminate OSA patients, reporting good results when ANN were employed. Interestingly, the synchronisation between HRV and PRV during OSA differed from the synchronisation of these time series in healthy patients, which could be indicative of a difference between HRV and PRV due to respiratory pathologies.

Non-linear indices have also been proposed for classifying apnoeic and non-apnoeic subjects. Dehkordi et al. (2016) examined the cardiac modulation in children in response to apnoea/hypopnea events, using spectral analysis and Detrended Fluctuation Analysis (DFA), which determines the short- and long-range correlations in a time series. Findings indicate that cardiac sympathetic indices of PRV were higher at apnoea/hypopnea events for most children suffering from SDB, and that short- and large-range fluctuations of pulse rate were shown to be more correlated in children with SDB. Authors considered this last result as a sign of the

effects of breathing in pulse rate control: The control of pulse rate in the range of respiratory-related time scales seems to be much tighter in children with SDB. Garde et al. (2017) explored the usefulness of other non-linear indices, i.e., correntropy spectral density (CSD), for the identification of apnoea/hypopnea events in children. Authors compared the results of multivariate models based on CSD and spectral density (PSD) of PRV. All features obtained from CSD were significantly different to those obtained from PSD analysis, and the models implemented using CSD- and PSD based features obtained an area under the ROC curve of at least 0.72 and 0.67, respectively, indicating a better classification performance when CSD based features were used. Authors concluded that the performance improved using non-linear features, which may preserve non-linear characteristics and high-order moments of PRV data. More recently, Garde et al. (2019) recommended the use of different thresholds for OSA screening in children, in order to enhance the performance of a classifier by including an expression of uncertainty; their results showed good accuracy, specificity and sensitivity, and illustrate the utility of a screening tool for OSA that could be used at home before PSG examinations.

Regarding the classification of sleep stages, Dehkordi et al. (2014) classified sleep and wake states with a 77% accuracy, and NREM and REM sleep with an 80% accuracy, using time- and frequency-domain indices measured from PRV in children. Fonseca et al. (2017) aimed to validate a PPG-based sleep stage classification methodology in healthy adults by comparing the results to PSG-based sleep stage classification. Using a combination of time-, frequency-domain and non-linear indices obtained from PRV, they found that the algorithm proposed underestimated sleep onset latency and wake after sleep onset time by less than 10 minutes, and total wake time by less than 15 minutes; while it overestimated total sleep time by less than 15 minutes and sleep efficiency by less than 5%, in comparison with results obtained from PSG, leading the authors to conclude that PPG-based PRV may be a potential tool for evaluating sleep in healthy adults. Finally, Beattie et al. (2017) aimed to classify sleep stages in healthy subjects by using motion-based, PRV-based, and breathing based features. Using leave-one-out cross-validation, they achieved an overall accuracy of 69% when trying to classify sleep stages into 4 categories: wake, light sleep, deep sleep, and REM. These results demonstrate the utility of PRV information for a simple assessment of sleep quality and the screening of sleep-related disorders.

5.2.2.4 Somatic and cardiovascular diseases

Several somatic diseases have been related with changes in HRV. Hence, numerous studies have applied PPG for the acquisition of PRV information instead of ECG for the measurement of HRV, due to the ease of the PPG technique. Progressive supranuclear palsy (Brefel-Courbon et al. 2000), rehabilitation of spinal cord injured patients (Gal-On et al. 2005), syncope (Kamiya et al. 2005), traumatic brain injury (Melinosky et al. 2018), obstructive lung diseases (Rahman et al. 2020), smoking (Shi et al. 2009), and concussion (Coffman et al. 2021) are only a few examples of diseases in which PRV has been analysed. The relationship between PRV and certain cardiovascular changes have been of special interest, probably due to the origin of the PPG signal and the nature of HRV information. Additionally, researchers have aimed to understand the relationship between PRV and other cardiovascular biomarkers.

- Blood pressure (BP): The continuous, non-invasive, ubiquitous measurement of BP has been largely studied in the last decades due to the growing population with BP-related diseases, and due to the importance of this variable in the assessment of health condition in all patient populations (Mukkamala et al. 2015, El-Hajj & Kyriacou 2020). The relationship between BP and PRV has, thus, attracted attention, mainly focusing on evaluating the feasibility of using PRV information for estimating blood pressure values, and could be considered as one of the main research areas in PRV.

  Using the second-derivative of the PPG, PRV information, and the frequency content of the PPG signal, Fukushima et al. (2013) developed a regression model for the estimation of cardiovascular parameters, such as cardiac output, total peripheral resistance, and BP, achieving a 0.71 correlation with measured BP using conventional techniques. In (2016), Gaurav et al. reported mean absolute errors of 4.47 and 3.21 mmHg when estimating systolic and diastolic BP values, respectively, using PPG and PRV features, including RMSSD, pNN50, pNN20, mean NN, SDNN, the ratio between SDNN and mean NN, SDSD, SD2, LF, HF, and LF/HF, and a machine learning model based on artificial neural networks. Radha et al. (2019) employed PPG and PRV information for estimating the nocturnal systolic BP dip from a wrist-worn sensor using PPG data obtained from 110 healthy volunteers. PRV information was ob-

tained along with morphological features of the signal. Multi-scale entropy analysis, using scales from 6 to 10, was used to characterize the PRV information. Linear regression, random forest regression (RF), multi-layer perceptron neural networks (MLP), and long- and short- term memory networks (LSTM) were used as models for estimating BP values. The lowest root-mean squared errors were obtained from the RF model with 32 trees, the MLP model with 8 perceptrons, and the LSTM with 32 cells, for the relative diastolic BP, the relative systolic BP, and the systolic BP dip, respectively. For estimating the systolic BP and its dip, RF with 32 trees featured errors of -1.17 $\pm$ 8.01 mmHg and 3.77 $\pm$ 4.43 mmHg, whereas the LSTM with 32 cells showed errors of -2.60 $\pm$ 9.82 mmHg and 0.13 $\pm$ 3.88 mmHg, respectively. These results indicate the capability of PPG and PRV information to obtain relatively precise information regarding systolic BP during sleep. Similarly, Fong et al. (2019) proposed the estimation of BP values using a multi-channel PPG system and ensemble support vector regression machines (SVR). With PPG probes located in the fingertip, the wrist, and the arm, the authors measured morphological features, time- and frequency-domain PRV indices, and pulse wave velocity, and fed the ensemble SVR model with these, reporting mean errors of 7.29 $\pm$ 5.3 mmHg and 5.01 $\pm$ 4.1 mmHg in the estimation of systolic and diastolic BP, respectively. Results showed that better results were achieved using ensemble SVR and multiple PPG signals, when compared with SVR models using only pulse wave velocity; pulse wave velocity and pulse amplitude; and pulse wave velocity and heart rate information.

The identification of hypotension and hypertension from PRV analysis have also been investigated. Bolea et al. (2017) aimed to predict hypotensive events in pregnant women after spinal anaesthesia during programmed caesarean labour. They found that differences of ApEn values between supine and lateral decubitus positions had the best performance for identifying between the control and prophylactic groups, while this index did not show differences between the groups when computed from HRV, leading the authors to suggest that hemodynamic changes may affect peripheral regulation more than heart regulation, hence generating differences in PRV that are absent from HRV. The main conclusion from this study was that PRV analysis could help to predict hypotensive events in pregnant women during caesarean section. On

the other hand, Lan et al. (2018) aimed to predict hypertensive events during sleep using data acquired with a ring PPG probe. They found that, from the time- and frequency-domain indices extracted, SDNN has the highest accuracy rate for hypertension prediction, as well as a high recall rate and specificity, and concluded that PRV could have potential as a pre-filtering mechanism for hypertension prediction.

- Diabetes: Nitzan et al. (1998) evaluated some indices related to the variability of pulse rate and the PPG morphology in diabetic and healthy patients, using infrared PPG acquired from left and right index fingers. They found that the standard deviation and average values of the amplitude of the pulse and the duration of the IBIs were similar for males and females, and that the average values of these indices are significantly decreased in diabetic subjects. Moreover, they reported lower correlation coefficients between indices extracted from the right and left fingers, which could be attributed to diabetic neuropathy. In 2013, Wu et al. extracted frequency-domain and Poincaré plot indices from PRV trends obtained from pulse waves of 75 subjects (healthy young, healthy middle aged, and diabetic subjects) during 20 minutes while changing the occlusion performed with a wrist cuff. Their results showed that, compared with the values in healthy young individuals, LF and HF were significantly reduced in elderly subjects with diabetes both before and after RH induction and compared with the values in healthy subjects of the same age, these indices were significantly reduced in subjects with diabetes after RH induction, which means that both ageing and diabetes result in the reduction of autonomic function. Also, they concluded that Poincaré plot indices were capable of showing changes due to reactive hyperaemia in diabetic subjects, while frequency-domain indices did not show these differences. In 2017, Reddy et al. investigated the use of PRV features for classification of diabetic and healthy subjects, with excellent results, while this same year, Moreno et al. (2017) proposed the use of random forest and gradient boosting decision trees, with several PRV indices and PPG features, for the screening of type 2 diabetes, and found that the receiver operating characteristic (ROC) curve area reached a mean value of 70% across different groups of subjects for detecting diabetic patients, with sensitivity and specificity values close to those consid-

ered as valid for the gold standard method for the detection of type 2 diabetes. In this same direction, Guzman et al. (2021) proposed a machine learning approach for the detection of glycaemic level using mostly PRV features, reaching a mean absolute error of 16.24 mg/dL for the measurement of blood glucose concentration.

Chon et al. (2014) proposed a method for quantitatively assessing cardiac autonomic neuropathy in type 1 diabetic mice, based on time domain, frequency domain and non-linear parameters measured from PRV. They found that the non-linear Principal Dynamic Mode analysis was capable of separating the dynamics associated with the sympathetic and parasympathetic nervous systems, and showed depressed sympathetic activity and autonomic imbalance after 3 months of the study when the onset of diabetic neuropathy was detected in some of the mice. However, they found that, by using PPG for PRV analysis, other diabetic confounders, like arterial stiffness, microvascular dysfunction and poor peripheral circulation, were present, different to what could be expected from ECG-derived HRV analysis.

Theodorakopoulou et al. (2021) investigated cardiac autonomic activity in women with gestational diabetes compared to women with uncomplicated pregnancies. They found that there is an impaired ability to adapt to exercise in women with gestational diabetes, which was observed in RMSSD and SD1.

- Atrial fibrillation (AF) and cardiac arrhythmias: Several attempts have been proposed for the detection of cardiac arrhythmias using PRV. Couderc et al. (2015) compared the behaviour of PRV and HRV indices for the detection of AF, and found that, probably due to differences between the electrical and mechanical nature of ECG and PPG, the difference between time-domain and Poincaré plot indices measured during AF and non-AF periods were larger when obtained from the HRV. Nonetheless, McManus et al. (2016) used PRV indices for the classification of several types of arrhythmias and found a sensitivity of 0.97, a specificity of 0.94 and an accuracy of 0.95 for the discrimination between an irregular pulse and AF. In 2017, Conroy et al. aimed to detect AF using an earlobe PPG sensor and time-domain PRV indices, finding an accurate automatic AF detection method, and suggesting that pNN35 was

the index with the best performance for this task. Similarly, Krivoshei et al. (2017) used time-domain and non-linear indices to detect AF using PRV derived from video PPG. Their proposed methodology achieved a sensitivity and sensitivity of nearly 95%, with the combination of normalized RMSSD and SD1/SD2 indices giving the best results.

The interest in identifying and classifying AF using PRV has grown in the last couple of years. Sluyter et al. (2019) used PRV indices to predict AF and related cerebrovascular events. In their study, based on a large cohort study with a sample size of 5000 adults and a median follow up of 4.6 years, they found that using RMSSD and irregularity index were associated with a higher risk of AF and associated cerebrovascular events, even among those adults without prior AF diagnosis. Similarly, Millán et al. (2020) found the best features for AF classification from PRV based on a systematic review, and that sensitivity, specificity and accuracy above 98% can be achieved using machine learning algorithms and these features, while Väliaho et al. (2021) proposed the use of a combination of PRV and PPG features for the classification of AF, and achieved an area under the ROC curve of 0.982. In this same year, Ding et al. (2021) proposed a novel measurement from PRV based on time synchronous averaging and the measurement of Euclidean distance among segments of PPG signals, and achieved nearly perfect accuracy, sensitivity and specificity, while Ramesh et al. (2021) evaluated how classification algorithms trained with ECG-derived HRV data performed when PPG-derived PRV indices were used instead, and concluded that these models could be seamlessly adapted for their use with ambulatory wearable devices based on PPG.

- Other cardiovascular conditions: Ahn & Kong (2011) explored the correlations of PRV with Pulse Wave Velocity and Ankle-Brachial Pressure Index in 117 male adults, in order to evaluate if PRV could be related to atherosclerosis and arterial stiffness. They found a positive correlation between this index and SDNN, indicating that PRV seems to be associated with Peripheral Arterial Disease. Similarly, Chen et al. (2021) found that PRV indices, measured using a modified air-pressure-sensing system instead of PPG, were capable of discriminating between young adults with low- and high-risk of developing atherosclerosis.

In 2015, Jans et al. characterised PRV during early postoperative mobilisation and related its changes to orthostatic impairment. They observed that the mean NN, SDNN, RMSSD and TP indices reduced progressively in the supine position from baseline values to 6 h and 24 h after surgery, while LF decreased during standing from baseline to 6 h and 24 h. HF increased during standing from baseline to 6 h and 24 h and SampEn reduced in the supine position from baseline, but returned at 24 h. The authors concluded that PRV could be used to detect impairment of baroreflex control during postural change in the early postoperative period, either caused by central (attenuated sympathetic response or increased parasympathetic response) or peripheral mechanisms (by delayed vascular reactivity).

Muhadi et al. (2016) proposed the use of time- and frequency-domain PRV indices to predict Major Adverse Cardiac Events (MACE) in patients with Acute Coronary Syndrome, and found that both LF and LF/HF showed the best performance for classifying subjects with and without MACE, even considering the small percentage of subjects that showed MACE from the sample.

5.2.3 Relationship between pulse rate variability and heart rate variability

Several authors have investigated the relationship between HRV and PRV, trying to validate the use of PRV instead of HRV in different applications and as an alternative approach, which could be more viable to perform in a regular basis than ECG-derived HRV, especially due to the widespread use of PPG sensors in wearable devices (Georgiou et al. 2018). Nonetheless, results from these studies are inconclusive and contradictory, and several methodological aspects make it difficult to compare the findings. In 2013, Schäfer & Vagedes published a review study in which they aimed to summarise the studies reported, and to conclude whether PRV could serve as an estimate of HRV. Their revision of the literature allowed them to conclude that PRV is a good surrogate of HRV only for studies involving healthy, young, resting subjects, and that further studies regarding the differences between HRV and PRV are needed. In a more recent review, the authors aimed to compare HRV and PRV obtained from wearable devices, and this same conclusion was reached: PRV could serve as a surrogate of HRV only during resting scenarios, whereas in any other circumstances,

it should not be considered as a good estimator of HRV information (Georgiou et al. 2018). In a meta-analysis performed by Dobbs et al. (2019), it was concluded that HRV information acquired using portable devices based on different techniques, including PPG, had a small amount of absolute error when compared to ECG-derived HRV, which could be considered acceptable under certain circumstances given the improved practicality and compliance of HRV measurements when acquired using portable devices in everyday scenarios. Table 5.1 summarises some of the studies that aimed to compare pulse-wave-derived PRV to HRV information, with a total of 26 out of 60 studies (43.3%) concluding that HRV and PRV should not be interchangeable, and that PRV could be affected differently by both physiological and technical aspects when compared to HRV.

Table 5.1: Summary of previous studies comparing HRV and PRV. T: Time-domain indices. F: Frequency-domain indices. NL: Nonlinear indices. ICC: Intra-class correlation. CS: Cubic Spline Interpolation. AR: Autoregressive models. FFT: Fast Fourier transform. Welch: Welch's periodogram. Lomb-Scargle: Lomb-Scargle periodogram.

Reference	**Participants**	**Protocol**	**Pulse wave acquisition**		**Data processing**						**Conclusion**
			Sensor placement	**Sampling rate (Hz)**	**Fiducial points**	**Spectral analysis**	**Indices**			**Statistical analysis**	
							T	**F**	**NL**		
Constant et al. (1999)	20, 10 healthy children, 10 children with pacemakers	Seated and standing, controlled breathing. 5 min each position	3rd finger, right hand, Finapres	500	Systolic peaks	- (10 Hz)	x	x	-	Comparisons	Not a surrogate

Continued on next page

Table 5.1 – continued from previous page

Reference	Participants	Protocol	Pulse wave acquisition		Data processing					Conclusion
			Sensor placement	Sampling rate (Hz)	Fiducial points	Spectral analysis	Indices			Statistical analysis	
							T	F	NL		
Giardino et al. (2002)	26, Experiment E1: healthy young adults (16); Experiment E2: healthy adults (10)	E1: Seated, quiet, breathing normally. E2: Vanilla baseline task and Stroop test. 5 min each condition	3rd finger, left hand	E1: 1000; E2: 991	Systolic peaks	FFT (4 Hz)	-	x	-	Correlation, comparisons, Bland-Altman	Not a surrogate

Continued on next page

Table 5.1 – continued from previous page

Reference	Participants	Protocol	Pulse wave acquisition		Data processing						Conclusion
			Sensor placement	Sampling rate (Hz)	Fiducial points	Spectral analysis	Indices			Statistical analysis	
							T	F	NL		
Rauh et al. (2003)	44 healthy subjects	Seated in armchair, during spontaneous and controlled breathing. 3 min each condition	Earlobe	400	Maximum 1st derivative	-	x	x	-	Correlation, Bland-Altman	Surrogate

Continued on next page

Table 5.1 – continued from previous page

Reference	Participants	Protocol	Pulse wave acquisition		Data processing						Conclusion
			Sensor placement	Sampling rate (Hz)	Fiducial points	Spectral analysis	Indices			Statistical analysis	
							T	F	NL		
Bolanos et al. (2006)	2, 1 male, 1 female, healthy	Subjects relaxed. 5 min, 3 times the same day	-	196	Dicrotic notch	AR	x	x	x	Correlation, comparisons	Surrogate
Shi et al. (2008)	14 healthy, young adults	Supine position, breathing spontaneously. 10 min	Left earlobe and index finger	1000	Onsets	Welch	x	x	x	Correlation, comparisons, Bland-Altman	Surrogate

Continued on next page

Table 5.1 – continued from previous page

Reference	Participants	Protocol	Pulse wave acquisition		Data processing					Conclusion
			Sensor placement	Sampling rate (Hz)	Fiducial points	Spectral analysis	Indices			Statistical analysis	
							T	F	NL		
Selvaraj et al. (2008)	10, 9 males; healthy, young adults	5 min	Right middle finger	1000	Systolic peaks	- (CS 4 Hz)	x	x	x	Comparisons, Bland-Altman	Surrogate
Lu et al. (2008)	10 healthy subjects	Standing and supine. 10 min each position	Finger	400	Maximum 1st derivative in diastolic phase	- (CS)	x	x	x	Correlation, comparisons	Surrogate
Lu et al. (2009)	42 healthy subjects	Semi-recumbent. 7 min	Earlobe	100	Systolic peaks	FFT (CS 4 Hz)	x	x	x	Correlation, comparisons, regression	Surrogate

Continued on next page

Table 5.1 – continued from previous page

Reference	Participants	Protocol	Pulse wave acquisition		Data processing					Conclusion
			Sensor placement	Sampling rate (Hz)	Fiducial points	Spectral analysis	Indices			Statistical analysis	
							T	F	NL		
Charlot et al. (2009)	9 healthy young men	Active orthostatic test, slow walk, moderate and exhaustive cycling. 10 min each position	Left fingertip	1000	Systolic peaks	Welch (CS 2 Hz)	x	x	-	Correlation, comparisons, Bland-Altman	Not a surrogate
Lu & Yang (2009)	36 healthy young adults	Subjects remained still. 7 min	Finger	1000	Systolic peaks	FFT (CS 4 Hz)	x	x	x	Linear regression	Surrogate

Continued on next page

Table 5.1 – continued from previous page

Reference	Participants	Protocol	Pulse wave acquisition		Data processing					Statistical analysis	Conclusion
			Sensor placement	Sampling rate (Hz)	Fiducial points	Spectral analysis	Indices				
							T	F	NL		
Gil, Orini, Bailón, Vergara, Mainardi & Laguna (2010)	17 healthy young adults	Supine (4 min), tilt table (70°, 5 min), supine (4 min)	Index finger	250, interpolated to 1000	Systolic peaks	FFT	x	x	x	Correlation, comparisons, coherence	Not a surrogate

Continued on next page

Table 5.1 – continued from previous page

Reference	Participants	Protocol	Pulse wave acquisition		Data processing					Conclusion
			Sensor placement	Sampling rate (Hz)	Fiducial points	Spectral analysis	Indices			Statistical analysis	
							T	F	NL		
Khandoker et al. (2011)	51, 22 with Obstructive Sleep Apnea, 29 healthy	While sleeping, during NREM sleep. 2 min (1222 with OSA, 1502 without OSA)	-	128, resampled to >2092	Systolic peaks	Welch (1 Hz)	x	x	x	Comparisons	Not a surrogate

Continued on next page

Table 5.1 – continued from previous page

Reference	Participants	Protocol	Pulse wave acquisition		Data processing						Conclusion
			Sensor placement	Sampling rate (Hz)	Fiducial points	Spectral analysis	Indices			Statistical analysis	
							T	F	NL		
Trajkovic et al. (2011)	11 healthy adults	Standing, seating, seating and moving legs and arms. 5 min each position	NIRS from the forehead	100	Diastolic maxima points	-	x	-	-	Correlation, comparisons, Bland-Altman	Surrogate

Continued on next page

Table 5.1 – continued from previous page

Reference	Participants	Protocol	Pulse wave acquisition		Data processing					Conclusion
			Sensor placement	Sampling rate (Hz)	Fiducial points	Spectral analysis	Indices			Statistical analysis	
							T	F	NL		
Bulte et al. (2011)	20 healthy young males	Supine position, breathing spontaneously. 5 min, 2 times	Middle finger of right hand	200	-	FFT	-	x	-	Correlations, Bland-Altman, ICC	Surrogate
Wong et al. (2012)	31 healthy adults	Supine position. 10 min	Fingertips of both hands	400	Systolic peaks	FFT	x	x	-	Correlation, comparisons, Bland-Altman	Not a surrogate

Continued on next page

Table 5.1 – continued from previous page

Reference	Participants	Protocol	Pulse wave acquisition		Data processing						Conclusion
			Sensor placement	Sampling rate (Hz)	Fiducial points	Spectral analysis	Indices			Statistical analysis	
							T	F	NL		
Posada-Quintero, H.F., Delisle-Rodríguez, D., Cuadra-Sanz, M.B., & Fernández de la Vara-Prieto, R.R. (2013)	37 healthy subjects	Supine position, breathing spontaneously. 5 min	Right index finger	1000	Diastolic point, maximum second derivative, tangent intersection	Welch (CS)	-	x	-	Concordance, Bland-Altman	Surrogate

Continued on next page

Table 5.1 – continued from previous page

Reference	Participants	Protocol	Pulse wave acquisition		Data processing					Conclusion
			Sensor placement	Sampling rate (Hz)	Fiducial points	Spectral analysis	Indices			Statistical analysis	
							T	F	NL		
Dehkordi et al. (2013*a*)	63 children, 36 and 27 without and with sleep disordered breathing	While sleeping. 1 min, 50% overlap	-	256	Systolic peaks	AR (CS 4 Hz)	x	x	-	Correlation, Bland-Altman	Surrogate

Continued on next page

Table 5.1 – continued from previous page

Reference	Participants	Protocol	Pulse wave acquisition		Data processing					Conclusion
			Sensor placement	Sampling rate (Hz)	Fiducial points	Spectral analysis	Indices			Statistical analysis	
							T	F	NL		
Heathers (2013)	10 healthy young adults	2 experiments: Seated (E1, 5 min); reaction time task and basic exercise task (E2, 5 min each task)	Finger	500	Largest negative derivative	Welch (4 Hz)	x	x	-	Correlation, comparisons, Bland-Altman	Surrogate

Continued on next page

Table 5.1 – continued from previous page

Reference	Participants	Protocol	Pulse wave acquisition			Data processing					Conclusion
			Sensor placement	Sampling rate (Hz)	Fiducial points	Spectral analysis	Indices			Statistical analysis	
							T	F	NL		
Keet et al. (2014)	26 sujects with type 2 diabetes	Autonomic function test battery under standardised and non-standardised test conditions. 5 min	-	200	-	FFT	-	x	-	Correlations, Bland-Altman, ICC	Surrogate

Continued on next page

Table 5.1 – continued from previous page

Reference	Participants	Protocol	Pulse wave acquisition			Data processing					Conclusion
			Sensor placement	Sampling rate (Hz)	Fiducial points	Spectral analysis	Indices			Statistical analysis	
							T	F	NL		
Lin et al. (2014)	8 healthy and young	Seated before and after running on treadmill. 5 min	Finger	1000	Systolic peaks	FFT (CS 2.5 Hz)	-	x	-	Coherence	Not a surrogate

Continued on next page

Table 5.1 – continued from previous page

Reference	Participants	Protocol	Pulse wave acquisition		Data processing						Conclusion
			Sensor placement	Sampling rate (Hz)	Fiducial points	Spectral analysis	Indices			Statistical analysis	
							T	F	NL		
Pellegrino et al. (2014)	Male New Zealand white rabbits	Baseline measurement, ventricular pacing, cardiac autonomic blockade. 5 min each condition	Catheter into abdominal aorta	1000	Maximum of first derivative, zero before and after maximum of first derivative	Welch (8 Hz)	x	x	x	Correlation, comparisons, Bland-Altman, coherence	Not a surrogate

Continued on next page

Table 5.1 – continued from previous page

Reference	Participants	Protocol	Pulse wave acquisition		Data processing						Conclusion
			Sensor placement	Sampling rate (Hz)	Fiducial points	Spectral analysis	Indices			Statistical analysis	
							T	F	NL		
Chen et al. (2015)	33 healthy young adults	Supine and performing different breathing manoeuvres. 3 min	Left index finger	1000	Systolic peaks	-	x	x	x	Correlation, comparisons, Bland-Altman	Not a surrogate
Vasconcellos et al. (2015)	14 obese adolescents	Supine position. 25 min, repeated after 48 h	Finapres, left middle finger	1000	-	Welch	x	x	-	Comparisons, ICC, regression	Surrogate

Continued on next page

Table 5.1 – continued from previous page

Reference	Participants	Protocol	Pulse wave acquisition		Data processing						Conclusion
			Sensor placement	Sampling rate (Hz)	Fiducial points	Spectral analysis	Indices			Statistical analysis	
							T	F	NL		
Parasnis et al. (2015)	20 ICU patients (MIMIC III)	5 min	-	-	Systolic peaks, valleys, maximum 1st derivative, maximum 2nd derivative	-	-	-	x	Correlation, concordance	Not a surrogate

Continued on next page

Table 5.1 – continued from previous page

Reference	Participants	Protocol	Pulse wave acquisition		Data processing					Statistical analysis	Conclusion
			Sensor placement	Sampling rate (Hz)	Fiducial points	Spectral analysis	Indices				
							T	F	NL		
Shin (2016)	28 healthy young adults	Seated in low, moderate and high temperature rooms. 10 min each room	-	-	Systolic peaks	FFT (4 Hz)	x	x	-	Comparisons	Not a surrogate

Continued on next page

Table 5.1 – continued from previous page

Reference	Participants	Protocol	Pulse wave acquisition		Data processing						Conclusion
			Sensor placement	Sampling rate (Hz)	Fiducial points	Spectral analysis	Indices			Statistical analysis	
							T	F	NL		
Pinheiro et al. (2016)	29 healthy young adults (G1), 33 with cardiovascular disease (G2)	G1 in supine position, G1 after moderate exercise, G2 in supine. At least 3 min	Index finger	125	Onsets, time instants corresponding to 20%, 50% and 80% of pulse amplitude, maxima of 1st derivative, systolic peaks	-	x	x	-	Comparisons, correlation	Surrogate

Continued on next page

Table 5.1 – continued from previous page

Reference	Participants	Protocol	Pulse wave acquisition		Data processing						Conclusion
			Sensor placement	Sampling rate (Hz)	Fiducial points	Spectral analysis	Indices			Statistical analysis	
							T	F	NL		
Hemon & Phillips (2016)	12 healthy young adults	Seated. 15 min	Right earlobe	1000	Systolic peaks, valleys, maximum 1st derivative, maximum 2nd derivative, tangent intersection, diastole patching	-	x	-	-	Comparisons, correlation	Surrogate

Continued on next page

Table 5.1 – continued from previous page

Reference	Participants	Protocol	Pulse wave acquisition		Data processing					Conclusion
			Sensor placement	Sampling rate (Hz)	Fiducial points	Spectral analysis	Indices			Statistical analysis	
							T	F	NL		
Logier et al. (2016)	10 healthy adults	Supine and seated. 5 min each position	Finger	250	Diastolic onsets	Wavelet (8 Hz)	x	x	-	Correlation, Bland-Altman	Not a surrogate
Weinschenk et al. (2016)	343 adults, mostly women	Resting (5 min) and during deep breathing test (1 min)	Earlobe	500	Onsets	FFT (8 Hz)	x	x	x	Correlation, Bland-Altman	Surrogate

Continued on next page

Table 5.1 – continued from previous page

Reference	Participants	Protocol	Pulse wave acquisition			Data processing					Conclusion
			Sensor placement	Sampling rate (Hz)	Fiducial points	Spectral analysis	Indices			Statistical analysis	
							T	F	NL		
Okkesim et al. (2016)	10 healthy adults	Supine position, prior (50 min), during (80 - 120 min) and after (50 min) insulin-induced hypoglycaemia test	Ring finger	1000	Systolic peaks	Welch (4 Hz)	x	x	-	Correlation, comparisons, Bland-Altman	Surrogate

Continued on next page

Table 5.1 – continued from previous page

Reference	Participants	Protocol	Pulse wave acquisition		Data processing						Conclusion
			Sensor placement	Sampling rate (Hz)	Fiducial points	Spectral analysis	Indices			Statistical analysis	
							T	F	NL		
Liu et al. (2017)	75 adults with sleep apnea	While sleeping, 5 min windows	-	1000	Systolic peaks	-	x	x	x	Comparisons, correlation	Surrogate
Mohapatra et al. (2018)	20 healthy young adults	Supine, pelvic upright while sitting, standing. 5 min each position	Wrist	500	Onsets	Welch (CS 4 Hz)	x	x	-	Correlation, Bland-Altman, comparisons, regression	Surrogate

Continued on next page

Table 5.1 – continued from previous page

Reference	Participants	Protocol	Pulse wave acquisition		Data processing						Conclusion
			Sensor placement	Sampling rate (Hz)	Fiducial points	Spectral analysis	Indices			Statistical analysis	
							T	F	NL		
Ye et al. (2018)	37 chronic myofascial pain syndrome patients	Before and after pain therapy. 10 min each condition	Right-hand forefinger	-	Systolic peaks	FFT	x	x	-	Comparisons, correlation	Surrogate

Continued on next page

Table 5.1 – continued from previous page

Reference	Participants	Protocol	Pulse wave acquisition		Data processing						Conclusion
			Sensor placement	Sampling rate (Hz)	Fiducial points	Spectral analysis	Indices			Statistical analysis	
							T	F	NL		
Hernando et al. (2019)	26 healthy young adults	Inside a hyperbaric chamber, with pressure at 1 atm, 3 atm, 5 atm, 3 atm and 1 atm. 5 min each condition	Finger	1000	Medium point of the systolic phase	Welch (PFDM)	x	x	-	Comparisons, correlation	Surrogate

Continued on next page

Table 5.1 – continued from previous page

Reference	Participants	Protocol	Pulse wave acquisition			Data processing					Conclusion
			Sensor placement	Sampling rate (Hz)	Fiducial points	Spectral analysis	Indices			Statistical analysis	
							T	F	NL		
Rapalis et al. (2018)	54 adults with various cardiovascular diseases	Regular lifestyle during 24 h recordings. 5 min segments during 1 h	Fitbit Charge 2	-	-	Welch (4 Hz)	x	x	x	Bland-Altman	Not a surrogate

Continued on next page

Table 5.1 – continued from previous page

Reference	Participants	Protocol	Pulse wave acquisition			Data processing					Conclusion
			Sensor placement	Sampling rate (Hz)	Fiducial points	Spectral analysis	Indices			Statistical analysis	
							T	F	NL		
Vescio et al. (2018)	2 groups of 10 different healthy volunteers	Group 1: Rest (10 min). Group 2: Daily activities (24 h)	Earlobe	-	-	Lomb-Scargle	x	x	x	Comparisons, correlation, Bland-Altman, regression	Surrogate
Pernice et al. (2018)	76 healthy young adults	Supine and 45° upright position	Finger	1000	Systolic peaks	AR	x	x	x	Comparisons, correlation, Bland-Altman	Not a surrogate

Continued on next page

Table 5.1 – continued from previous page

Reference	Participants	Protocol	Pulse wave acquisition		Data processing					Conclusion
			Sensor placement	Sampling rate (Hz)	Fiducial points	Spectral analysis	Indices			Statistical analysis	
							T	F	NL		
Jan et al. (2019)	30 young (G1) and senior (G2) healthy subjects	Sitting while spontaneous breathing and controlled breathing. 5 min each condition	Left index finger, right index finger, left big toe, right big toe	1250	Maxima of 2nd derivative	-	x	-	-	Coherence, comparisons, Bland-Altman	Not a surrogate

Continued on next page

Table 5.1 – continued from previous page

Reference	Participants	Protocol	Pulse wave acquisition		Data processing						Conclusion
			Sensor placement	Sampling rate (Hz)	Fiducial points	Spectral analysis	Indices			Statistical analysis	
							T	F	NL		
Pernice et al. (2019*b*)	76 healthy young adults	Supine (15 min), head-up tilt test (8 min), supine (10 min), mental arithmetic task while supine (6 min), supine (10 min)	Finometer pro device	1000	Systolic peaks	AR	x	x	x	Comparisons, regression, correlation, Bland-Altman	Surrogate

Continued on next page

Table 5.1 – continued from previous page

Reference	Participants	Protocol	Pulse wave acquisition		Data processing						Conclusion
			Sensor placement	Sampling rate (Hz)	Fiducial points	Spectral analysis	Indices			Statistical analysis	
							T	F	NL		
Barrios et al. (2019)	14 healthy adults	Resting on stationary bike, biking at 60 W, biking at 120 W, walking, jogging, running. 5 min each activity, 2 times on different days	Empatica E4 on each wrist, Everion devices on each arm	1	Derived by devices	Welch (CS)	x	x	-	Bland-Altman, ICC, correlation, comparisons	Surrogate

Continued on next page

Table 5.1 – continued from previous page

Reference	Participants	Protocol	Pulse wave acquisition		Data processing						Conclusion
			Sensor placement	Sampling rate (Hz)	Fiducial points	Spectral analysis	Indices			Statistical analysis	
							T	F	NL		
Verma et al. (2019)	41 subjects with ischemic stroke history, 29 healthy age-matched controls	Sit-to-stand test. 10 min	Finapres	500	Systolic peaks with R peaks as reference	Welch (CS 10 Hz)	x	x	-	Comparisons, correlation	Not a surrogate

Continued on next page

Table 5.1 – continued from previous page

Reference	Participants	Protocol	Pulse wave acquisition		Data processing						Conclusion
			Sensor placement	Sampling rate (Hz)	Fiducial points	Spectral analysis	Indices			Statistical analysis	
							T	F	NL		
Schrödl et al. (2019)	10 healthy young adults	Upright seated position, three respiratory phases: normal (5 min), deep (30 s), voluntary apnea (40-60 s)	Earlobe	1000	Systolic peaks	-	x	-	-	Correlation, Bland-Altman	Surrogate

Continued on next page

Table 5.1 – continued from previous page

Reference	Participants	Protocol	Pulse wave acquisition		Data processing						Conclusion
			Sensor placement	Sampling rate (Hz)	Fiducial points	Spectral analysis	Indices			Statistical analysis	
							T	F	NL		
Nakamura & Tagawa (2019)	15 healthy young adults	Supine, resting, standing, in random order. 5 min each position	Left middle finger	3000	Systolic peaks	- (1 Hz)	-	x	x	-	Not a surrogate

Continued on next page

Table 5.1 – continued from previous page

Reference	Participants	Protocol	Pulse wave acquisition		Data processing						Conclusion
			Sensor placement	Sampling rate (Hz)	Fiducial points	Spectral analysis	Indices			Statistical analysis	
							T	F	NL		
Sun et al. (2019)	Healthy and overweight young adults (20, 13); healthy and overweight upper middle-aged adults (21, 14); diabetic patients (19)	Supine position, 30-min recording. First 5 min	Left index finger	500	Systolic peaks	FFT	x	x	x	Comparisons, correlation	Not a surrogate

Continued on next page

Table 5.1 – continued from previous page

Reference	Participants	Protocol	Pulse wave acquisition		Data processing						Conclusion
			Sensor placement	Sampling rate (Hz)	Fiducial points	Spectral analysis	Indices			Statistical analysis	
							T	F	NL		
Morresi et al. (2020)	12 healthy young adults	Sitting while spontaneous breathing. 15 min	Wrist	100	Systolic peaks	-	-	-	-	Regression, correlation	Surrogate
Kinnunen et al. (2020)	60 healthy adults	Whole night recordings. 5 min segments	Ring probe	250	Local maxima and minima	-	x	-	-	Regression, Bland-Altman, comparisons	Surrogate

Continued on next page

Table 5.1 – continued from previous page

Reference	Participants	Protocol	Pulse wave acquisition		Data processing						Conclusion
			Sensor placement	Sampling rate (Hz)	Fiducial points	Spectral analysis	Indices			Statistical analysis	
							T	F	NL		
Yuda, Yamamoto, Yoshida & Hayano (2020)	5 healthy young adults	Supine and sitting. 10 min each position	Wrist and forearms of both arms	200	Pulse frequency demodulation	FFT	-	x	-	Comparisons	Not a surrogate
Correia et al. (2020)	18 healthy adults	Sitting while resting and performing Stroop test. 5 min each condition	Earlobe James One PPG sensor	1000	Maximum 1st derivative	Lomb-Scargle	x	x	x	Comparison, correlation, concordance, Bland-Altman	Not a surrogate

Continued on next page

Table 5.1 – continued from previous page

Reference	Participants	Protocol	Pulse wave acquisition		Data processing						Conclusion
			Sensor placement	Sampling rate (Hz)	Fiducial points	Spectral analysis	Indices			Statistical analysis	
							T	F	NL		
Diehl et al. (2021)	96 ethnically-diverse young subjects	Watching a relaxation video; relaxing and breathing spontaneously; sitting trying to modify heart rate; arithmetic task. 5 min each condition	Middle finger of nondominant hand	2048	Systolic peaks	FFT	x	x	-	Concordance, Bland-Altman	Not a surrogate

Continued on next page

Table 5.1 – continued from previous page

Reference	Participants	Protocol	Pulse wave acquisition		Data processing						Conclusion
			Sensor placement	Sampling rate (Hz)	Fiducial points	Spectral analysis	Indices			Statistical analysis	
							T	F	NL		
Antink et al. (2021)	29 subjects who underwent vascular surgery or endovascular treatment	Long-term recordings during day and night activities. 5 min segments	PulseOn, wrist	25, upsampled to 200	Continuous local interval estimation	-	x	x	x	Comparisons	Not a surrogate

Continued on next page

Table 5.1 – continued from previous page

Reference	Participants	Protocol	Pulse wave acquisition		Data processing						Conclusion
			Sensor placement	Sampling rate (Hz)	Fiducial points	Spectral analysis	Indices			Statistical analysis	
							T	F	NL		
Killian et al. (2021)	14 healthy adults	Seated resting (10 min), Paced Auditory Serial Addition task (8), seated resting (10), paced breathing (5), orthostatic challenge (5). Twice, > 24 h apart	emWave 2 in both earlobes	200	Systolic peaks	- (4 Hz)	x	x	-	Bland-Altman, ICC, minimal detectable difference, regression	Surrogate

Continued on next page

Table 5.1 – continued from previous page

Reference	Participants	Protocol	Pulse wave acquisition		Data processing						Conclusion
			Sensor placement	Sampling rate (Hz)	Fiducial points	Spectral analysis	Indices			Statistical analysis	
							T	F	NL		
kumar et al. (2021)	50 healthy young females	Sitting while breathing spontaneously. 10 min	Finger	-	Systolic peaks	-	x	x	-	Comparisons, Bland-Altman, correlation	Surrogate
Singstad et al. (2021)	21 healthy young adults, mainly male	Sitting, cyclig with low intensity, mental stress. 5 min each condition	Middle finger	1000	Onsets, maximum slope	-	x	-	-	Comparisons, Bland-Altman	Not a surrogate

Continued on next page

Table 5.1 – continued from previous page

Reference	Participants	Protocol	Pulse wave acquisition		Data processing						Conclusion
			Sensor placement	Sampling rate (Hz)	Fiducial points	Spectral analysis	Indices			Statistical analysis	
							T	F	NL		
Umair et al. (2021)	32 healthy young adults	Baseline measurement while seated (10 min), mental stress (10 min), resting (5 min), cycling (5 min), resting (5 min)	Empatica E4 (wrist), Samsung Gear S2 (wrist), Polar OH1 (arm)	64, 100, 1	Maxima of 1st derivative	-	x	x	-	Correlation, Bland-Altman	Surrogate

Continued on next page

Table 5.1 – continued from previous page

Reference	Participants	Protocol	Pulse wave acquisition		Data processing						Conclusion
			Sensor placement	Sampling rate (Hz)	Fiducial points	Spectral analysis	Indices			Statistical analysis	
							T	F	NL		
Antali et al. (2021)	45 healthy subjects (33) and type 2 diabetic patients (12)	Seated and resting, cold pressor cardio-vascular challenge. 2 min each condition	Left index finger	200, upsampled to 1000	Systolic peaks	Welch	x	x	x	Bland-Altman	Surrogate
Bellenger et al. (2021)	6 healthy young adults	5 min during slow-wave sleep	Whoop (wrist)	-	-	-	x	-	-	Bland-Altman, ICC	Surrogate

Continued on next page

Table 5.1 – continued from previous page

Reference	Participants	Protocol	Pulse wave acquisition		Data processing						Conclusion
			Sensor placement	Sampling rate (Hz)	Fiducial points	Spectral analysis	Indices			Statistical analysis	
							T	F	NL		
Schumann et al. (2021)	79 healthy adults, two times for 24 subjects	Resting in supine position (10 min), and during functional magnetic resonance imaging (fMRI, 15 min)	Right index finger	1000 at rest, 500 during fMRI	Onsets	-	x	-	-	ICC	Not a surrogate

Continued on next page

Table 5.1 – continued from previous page

Reference	Participants	Protocol	Pulse wave acquisition		Data processing						Conclusion
			Sensor placement	Sampling rate (Hz)	Fiducial points	Spectral analysis	Indices			Statistical analysis	
							T	F	NL		
Nardelli et al. (2021)	57 healthy young (41) and healthy elderly (16) subjects	Supine position, 10 min	Finger	500	Systolic peaks	-	-	-	x	Comparisons	Not a surrogate

Continued on next page

Table 5.1 – continued from previous page

Reference	Participants	Protocol	Pulse wave acquisition		Data processing						Conclusion
			Sensor placement	Sampling rate (Hz)	Fiducial points	Spectral analysis	Indices			Statistical analysis	
							T	F	NL		
Królak & Pilecka (2022)	Dataset D1: Wrist PPG during exercise, 8 healthy young adults. Dataset D2: BIDMC, 10 critically ill patients	D1: Walking, jogging, cycling low load, cycling high load; 10 min each condition, first 3 min analysed. D2: Supine; 8 min, first 3 min analysed	D1: Left wrist. D2: Not specified	D1: 256. D2: 125	Systolic peaks	-	x	x	x	Comparisons	Not a surrogate

Continued on next page

Table 5.1 – continued from previous page

Reference	Participants	Protocol	Pulse wave acquisition		Data processing					Conclusion
			Sensor placement	Sampling rate (Hz)	Fiducial points	Spectral analysis	Indices			Statistical analysis	
							T	F	NL		
Nuuttila et al. (2022)	41 healthy active subjects	Awake while supine in controlled setting (5 min), during sleep at home (4 h, 5 min segments)	Polar Vantage V2 (wrist)	-	-	-	x	-	-	Comparisons, correlation, ICC, concordance, Bland-Altman	Surrogate

5.2.4 Advantages and limitations of pulse rate variability

As has been already mentioned, PRV has been derived for the analysis of ANS changes under different conditions, such as the presence of mental or somatic diseases, during sleep, or for evaluating the effects of pharmacological drugs. Most of these studies were performed considering PRV as a valid surrogate of HRV derived from ECG signals, and some results were indeed similar to those obtained in comparable studies performed using HRV data. Moreover, some of them even improved the performance of classification systems when using PRV instead of HRV. For instance, Lazaro et al. (2012) and Lázaro et al. (2014) demonstrated that PRV showed a better performance than HRV in identifying decreases in amplitude fluctuations of the PPG signal (DAP) events, when trying to classify them as apnoeic- and non-apnoeic-related. Although encouraging, almost none of the results presented on these studies included a comparison between HRV and PRV under the studied circumstances, and with the same subjects. Additionally, some researchers have tried to generate novel methods and techniques for the analysis of PRV. Hayano et al. (2005) proposed the Pulse Frequency Demodulation Method with which it is possible to eliminate the need of identifying fiducial points in the pulse wave in its time-domain representation, allowing for a less noise-sensitive extraction of frequency-domain parameters from PRV; while Chang, Hsiao & Hsu (2014) and Ricardo Ferro, B.T., Ramírez Aguilera, A., & Fernández de la Vara Prieto, R.R. (2015) developed strategies for obtaining PRV information from PPG by applying Hilbert Huang transform. The former even proposed a novel frequency band present in PRV, which they concluded, was related with the vascular effects involved in the changes of PRV, meaning that this information should not be available on HRV derived from ECG. This is probably one of the first studies aiming to obtain further information from PRV than what could be measured from traditional HRV parameters. This hypothesis has been further analysed by Yuda, Shibata, Ogata, Ueda, Yambe, Yoshizawa & Hayano (2020), who concluded that PRV contains additional information not available in HRV, and should be treated as an independent biomarker rather than a surrogate of HRV.

PRV seems like a logic alternative to HRV since PPG signals carry very valuable information regarding cardiovascular parameters and is very easy to acquire in a long-term manner in real-life scenarios. However, many factors may affect PPG and could probably alter PRV. One important aspect that has been studied is the

effect of the fiducial point used for determining each cardiac cycle. This issue is not remarkable when discussing HRV: R peaks are easily identified in most ECG traces, and due to its magnitude, physical origin, and frequency content, they are ideal marks for segmenting cardiac cycles and deriving HRV data (Clifford 2006). PPG, on the other hand, is a smooth signal, with slow changes and relatively constant frequency content. Identifying the fiducial point of the pulse wave may present an interesting challenge and an important pitfall for PRV. As mentioned by Pinheiro et al. (2016), the best fiducial point to be used in the analysis of PRV depends on the physiological conditions of each subject and on the analysis to be performed, making it crucial to have an automatic algorithm to select which fiducial point to use in each case. It is worth mentioning that most of the studies evaluating differences between PRV parameters measured from several fiducial points found the lowest agreement between PRV and HRV when systolic peaks from PPG are detected and used for segmenting cardiac cycles. This is troublesome, since most of the available studies in the literature nowadays have analysed PRV obtained from these systolic peaks, as an analogy to the detection of R peaks for the analysis of HRV. As shown by Peng et al. (2015) and Hemon & Phillips (2016), systolic peaks are more sensitive to environmental changes, such as temperature, and to movement artefacts, and the algorithms to detect them may be less accurate, yielding less reliable PRV information. Future studies regarding PRV should aim to compare HRV and PRV using fiducial points different from the systolic peaks, especially when vascular changes and movement artefacts are to be considered.

Also, the way PPG signals are acquired and processed for measuring PRV needs to be regarded. PPG, being an optical technique, is based on the interaction between tissue and light (Kyriacou & Chatterjee 2021). The wavelength at which the tissue is illuminated affect the depth at which light penetrates, with larger wavelengths reaching deeper tissue (Ash et al. 2017). It is still not clear if this could imply a difference in PRV measured from several wavelengths, although PRV has been measured indistinctly using red, infrared, green and even orange light. Another important aspect is the sampling frequency used for measuring PRV. As mentioned, Choi & Shin (2017) aimed to evaluate the effect of low sampling rates on the parameters derived from PRV and found no significant differences between PRV and HRV parameters at sampling rates as low as 20 Hz. However, as noted by Hejjel (2017), the results obtained during their study could have been influenced by the

health status of the subjects and by the study design, and other studies have found diminished similarity between HRV and PRV when PPG sampling rate was lower. More research in this field should be performed to find the ideal sampling rate for PRV analysis.

Processing of PPG and frequency domain analysis techniques could affect PRV results as well, as shown by Akar et al. (2013), who found differences between PRV estimation when frequency spectra is calculated differently and when different detrending methods are applied. It is important to remark the methodological issues that preclude a direct comparison between PRV studies. Some facts make it harder to have a strong conclusion regarding the relationship between PRV and HRV, as well as the capability of the former to yield more or different information than the latter. Small sample sizes, uneven gender and age distribution in most studies, different location of sensors and processing approaches, unclear estimation strategies for the different time- and frequency-domain and non-linear indices; and the lack of statistical validation, including agreement analysis in several studies, difficult the comparison between studies and the development of novel and reliable conclusions regarding the relationship between HRV and PRV, and the effects of cardiovascular and autonomic changes on PRV. This lack of standardisation for PRV analysis has recently been flagged by Dobbs et al. (2019), as a confounding factor in their systematic review and meta-analysis. It is urgent to establish techniques and methodological guidelines for PRV studies, such as those established for HRV, especially when PPG is becoming the most widely used technique for obtaining health information in real-life scenarios.

As concluded by Schäfer & Vagedes (2013) in their review, PRV is different from HRV not only due to errors in the fiducial points or due to the processing and acquisition methods applied, but also due to the nature of PPG and ECG signals, and the physiological factors that affect each of these. PPG, being of a mechanical nature, can be affected by other factors different to those that affect HRV. The most renowned differential factor is pulse transit time (PTT), the time the blood takes to travel from the heart to the peripheral site where the pulse wave is being measured (i Caros 2011). As demonstrated by Constant et al. (1999) and Gil, Orini, Bailón, Vergara, Mainardi & Laguna (2010), PTT has an important role in explaining the differences between HRV and PRV, especially in parameters such as HF and RMSSD. Therefore, the location of the sensor used for acquiring PPG could

affect the relationship between PRV and HRV, and thus it is possible to hypothesise that PRV measured from different body sites may yield different information regarding the vascular path that the blood had to travel. Moreover, the relationship between PRV and PTT allows for the arising of several conclusions regarding the relationship between PRV and cardiovascular health. Lu & Yang (2009) indicated that three factors (electromechanical coupling in the cardiomyocyte, pre-ejaculation period, and PTT) are subject to variations independent from heart rate and may be influenced by cardiovascular and ANS diseases, which could affect the relationship between HRV and PRV in diseased subjects; Gil, Orini, Bailón, Vergara, Mainardi & Laguna (2010) and Nardelli et al. (2021) also pointed out the effects of aging and blood pressure on PRV, suggesting that differences between PRV and HRV could be also due to vascular ageing; Trajkovic et al. (2011) concluded that not only PTT may affect PRV, but also other factors such as external forces on the arterial vessels, pathologies, movement artefacts and methodological issues; Heathers (2013) indicated that PRV from different body locations could allow to differentiate local and systemic vasoconstrictive responses; Parasnis et al. (2015), after evaluating non-linear parameters in cardiovascular patients both from HRV and PRV, concluded by raising a question: Could cardiovascular disorders be responsible for altering the behaviour of PRV differently to that of HRV?; Shin (2016) concluded that differences between PRV and HRV were mainly due to physiological processes affecting vascular behaviour; and as Vasconcellos et al. (2015) pointed out, there is not a profound explanation yet for the physiological or technical aspects that may affect the relationship between HRV and PPG-derived PRV, nor there is a clear hypothesis regarding the relationship between PRV and cardiovascular diseases, or the enhanced capability of PRV to detect cardiovascular changes over HRV. In conclusion, PRV has been used largely as a validated surrogate of HRV. However, their relationship is still not clear, although in healthy, young and resting subjects, PRV could be used as an alternative to HRV. Its application in cardiovascular disease diagnosis and monitoring should be further evaluated, since previous studies indicate that cardiovascular factors such as blood pressure and ageing may affect the parameters obtained from PRV.

5.3 Summary

Photoplethysmography (PPG), the measurement of blood volume changes using optical means, is the most commonly used physiological signal both in clinical and wearable devices, and contains a myriad of information valuable for assessing cardiovascular health. Pulse rate variability has been largely measured from it, and has been proposed by several authors as a valid surrogate of heart rate variability, especially in healthy, young, resting subjects. Nonetheless, several technical and physiological aspects seem to affect PRV in a different manner than HRV, leading several authors to conclude that PRV may contain additional information not readily available in HRV regarding cardiovascular and autonomic health. Given the effects of technical aspects on PRV analysis, there is an urgent need to standardise the assessment of this variable from PPG signals. This and further studies regarding the effects of changes in cardiovascular variables, such as blood pressure and arterial stiffness, are needed in order to better understand the relationship between PRV and HRV and, even more importantly, the role of PRV role in the diagnosis, monitoring and assessment of cardiovascular changes.

Chapter 6

Effects of technical aspects on the assessment of pulse rate variability from photoplethysmographic signals

6.1 Aims and objectives

The extraction of PRV information from PPG signals have become increasingly used given the widespread availability of these signals in wearable devices and in clinical setups. However, as explained in Chapter 5, there is still no standard regarding the analysis of PPG signals for assessing PRV information, which makes it difficult to compare and validate results from different studies. The aim of this analysis was to determine the combination of parameters for PRV assessment from PPG signals that gave the lower errors in the extraction of PRV indices when compared to indices extracted from simulated PRV trends, considered as gold standard, using a large database of simulated signals. The use of simulated PPG signals and PRV information allows for the direct comparison of the expected results to the extracted PRV information, instead of using HRV information as gold standard. Thus, this allows for a direct analysis of how the different technical aspects affect PRV analysis, and controls for the physiological differences that may be included in the comparison against ECG-derived HRV indices.

The simulation and processing of photoplethysmographic signals, as well as the

figures, were performed in MATLAB (version 2020b), while statistical analyses were done in RStudio (version 1.4.1717) and Minitab (version 19.1).

6.2 Methods and materials

6.2.1 Data simulation

PPG signals were simulated using a modified version of the model proposed by Tang et al. (Tang, Chen, Ward & Elgendi 2020, Tang, Chen, Allen, Alian, Menon, Ward & Elgendi 2020). In their model, a single cardiac cycle was simulated using the sum of two Gaussian functions with parameters set to simulate excellent and acceptable quality PPG signals. The values they proposed for the parameters describing the Gaussian functions, i.e. a_i, b_i and μ_i, were found by determining the optimal values when comparing the simulated cardiac cycle to annotated PPG signals from the MIMIC III database (Moody et al. 2020, Johnson et al. 2016, Goldberger et al. 2000). In the modified version of this model, used for this study, instead of altering the quality of the PPG waveform it is possible to determine the ratio of the a parameters, r, from the two Gaussian functions, which alters the amplitude of the Gaussian functions and, therefore, the quality of the PPG cycle, determined by the presence or absence of a dicrotic notch, and its amplitude. The b and μ parameters were selected according to what has been suggested in the original model for the excellent quality PPG. The resulting model for the PPG cycle is shown in (6.1), where θ corresponds to the four quadrant inverse tangent of the cosine and sine functions of the duration of the cycle.

$$z(t) = a(e^{-\frac{(\theta(t)-\mu_1)^2}{2b_1^2}}) + \frac{1}{r}a(e^{-\frac{(\theta(t)-\mu_2)^2}{2b_2^2}}) \tag{6.1}$$

Then, the simulated cardiac cycles were appended and the resulting signal was detrended and low-pass filtered using a second-order Butterworth filter with a cut-off frequency of 15 Hz. The duration of each of the appended cardiac cycles was modified in order to include PRV information on the PPG signal. This was done by simulating PRV information as a sum of sinusoidal waves with randomly generated parameters that fall inside plausible physiological values for PRV. The ranges for these parameters are shown in Table 6.1.

Table 6.1: Ranges for the Pulse Rate Variability (PRV) parameters and the generation of PRV gold standard values.

Parameter	Range	Units
Low frequency peak location (LF)	0.04 - 0.15	Hz
High frequency peak location (HF)	0.15 - 0.40	Hz
Average pulse rate (PR)	40 - 200	Beats per minute (bpm)
Standard deviation of pulse rate (SD)	0.05 - 0.08	s

The resulting function for the randomly generated PRV information is shown in (6.2). As can be seen, a total of 4 sinusoidal waves are summed, each of them with different fundamental frequencies, 2 for each of the main frequency bands in PRV analysis. This was done to increase the variability of the frequency spectrum and to alter the area of each of the frequency bands. Further studies should aim to better simulate these components using alternative models, such as the integral pulse frequency modulation model (Candia-Rivera et al. 2021).

$$PRV = PR + SD \sum_{i=1}^{2} (\sin(2\pi LF(i)t) + \sin(2\pi HF(i)t)) \tag{6.2}$$

Finally, the simulation framework allows for the inclusion of four different types of noise to the PPG signal. These noises are respiratory noise, baseline wandering, electromagnetic noise and movement artifact, and they can be added to the signal either independently or as a combination of noises, and their parameters can be modified accordingly. The mathematical model for the respiratory noise follows an amplitude modulation method, and is shown in (6.3), where $x(t)$ and $y(t)$ represent the clean and noisy PPG signals. There are two parameters that can be modified for this type of noise, the proportion of noise amplitude with respect to the amplitude of the PPG signal, A_n, and the fundamental frequency for the respiratory noise, $f[Hz]$.

$$y(t) = \max(x(t))[1 + A_n(\sin(2\pi ft))]x(t) \tag{6.3}$$

The mathematical model for baseline wandering noise is similar, as shown in (6.4), but allows for the selection of N frequency components for the noise. In this case, the parameters are also the proportion of amplitudes, A_n, and the fundamental

frequencies of each of the sinusoidal waves to add as noise.

$$y(t) = \max(x(t))[1 + A_n \sum_{i=1}^{N} (\sin(2\pi f(i)t))]x(t) \tag{6.4}$$

The electromagnetic noise is added as shown in (6.5), and the same two parameters, A_n and f, can be modified accordingly.

$$y(t) = x(t) + A_n[\max(x(t))] \sin(2\pi f t) \tag{6.5}$$

Finally, the model for the movement artifact is shown in (6.6). It consists on the summation of N sinusoidal waves, each of them with a fundamental frequency f within 1 and 10 Hz. The proportion of amplitudes A_n allows for the modification of the signal-to-noise ratio, as with the previously described types of noise.

$$y(t) = x(t) + A_n[\max(x(t))] \sum_{i=1}^{N} \sin(2\pi f(i)t) \tag{6.6}$$

Figure 6.1 summarises the simulation process, while Figure 6.2 illustrates the resulting PPG signals when simulated without and with each of the described noise types.

In this study, two groups of PPG signals were simulated, according to the ratio r used to simulate the amplitude of the Gaussian function. Excellent quality PPG signals were simulated with ratios of $r = 2$, while acceptable quality PPG signals were considered as those with $r = 4$. The base cardiac cycles for these two values of r are illustrated in Figure 6.3. The main difference between these signals can be observed in the notoriety of the dicrotic notch, i.e. its amplitude when compared to the amplitude of the systolic peak.

In general, using the proposed framework, PPG signals with varying qualities, signal-to-noise ratio and signal quality, and with specific PRV content can be simulated. Figure 6.4 depicts excellent and acceptable PPG signals simulated using the model with the specified r values, and with randomly-generated PRV information.

6.2.2 Experiments

Six sequential experiments (Figure 6.5) were performed using PPG signals simulated with the model described in the previous section. These experiments were performed in order to understand the effect of some technical aspects on the extraction of PRV

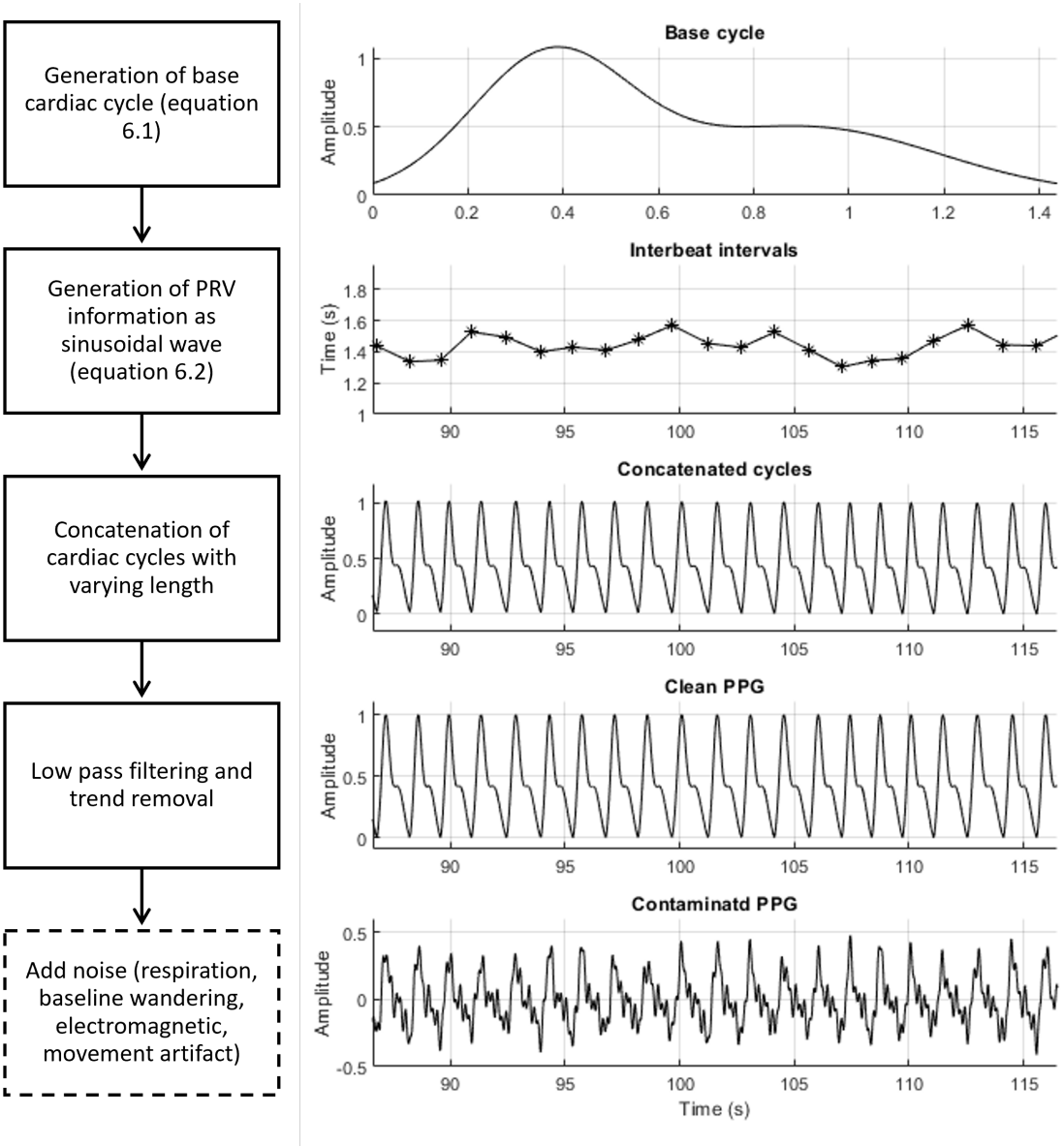

Figure 6.1: Framework for the simulation of photoplethysmographic (PPG) signals with randomly-generated Pulse Rate Variability (PRV) information.

information from PPG signals, considering the randomly generated PRV information as gold standard. The technical aspects of interest in these experiments were the algorithms and fiducial points used for the extraction of PRV, the sampling rate used for the acquisition of PPG signals, the techniques used for the extraction of spectral information from PRV trends, the duration of the PPG signal used to measure PRV indices, the management of outliers from PRV trends, and the effects of different type of noises and filters on PRV assessment from PPG signals.

In all cases, a pilot test was performed to determine the sample size needed to observe enough differences in the results. This was done as recommended in the

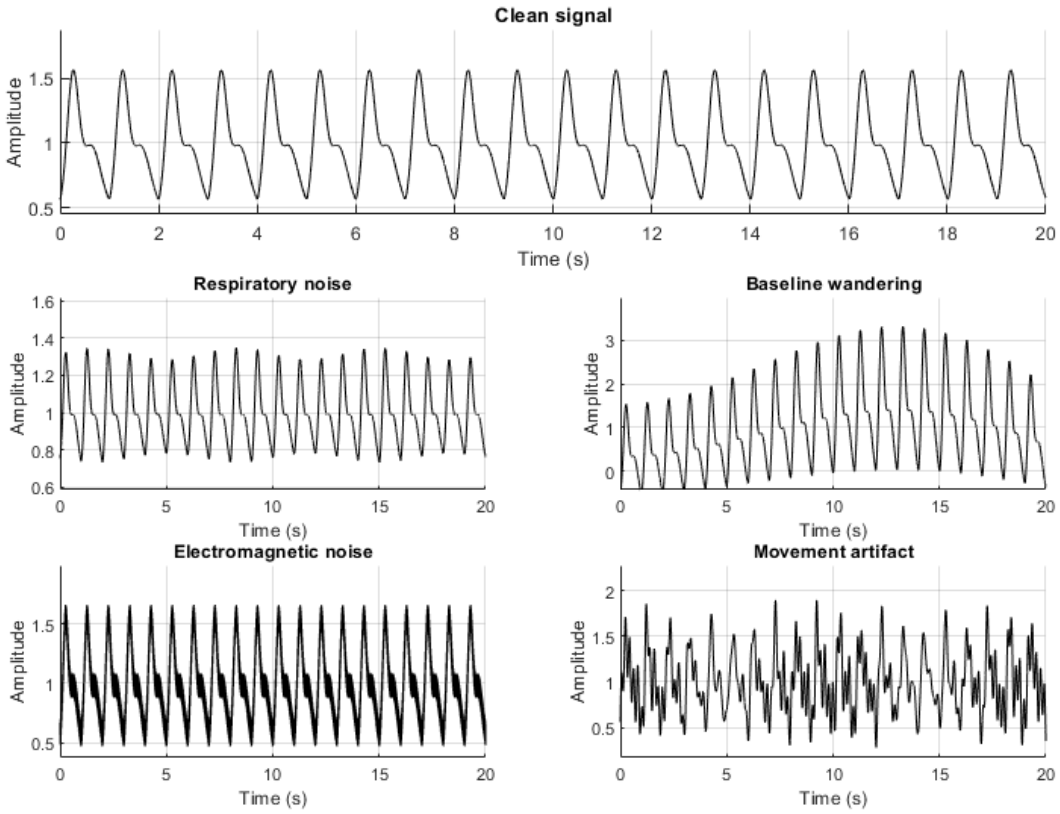

Figure 6.2: Behaviour of the different types of noise on the simulated PPG signals.

literature (Alvarado Orellana 2014). A total of 384 PRV trends were randomly generated and different PRV indices, specific to each experiment, were extracted

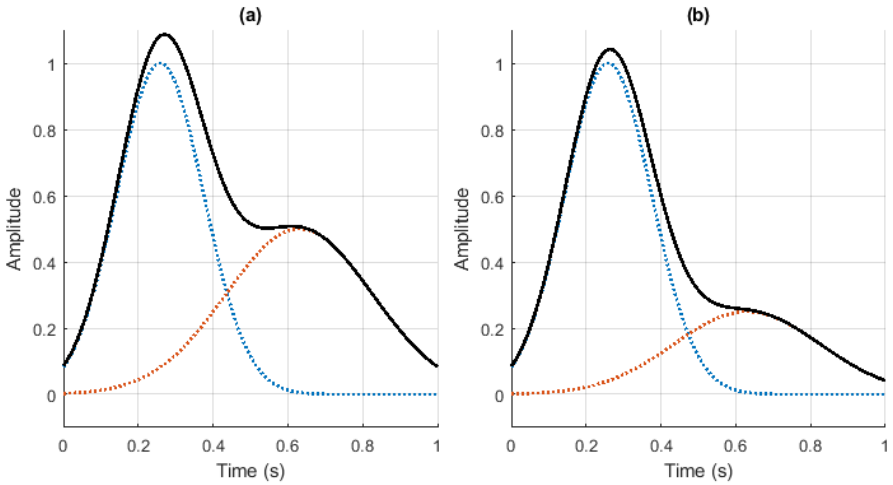

Figure 6.3: Photoplethysmographic cardiac cycles generated using the proposed mode, using ratios of value (a) $r = 2$ (excellent quality), and (b) $r = 4$ (acceptable quality). The blue and orange dotted lines illustrate the two Gaussian functions generated, while the black continuous line shows the result of summing these two Gaussian functions, i.e., z.

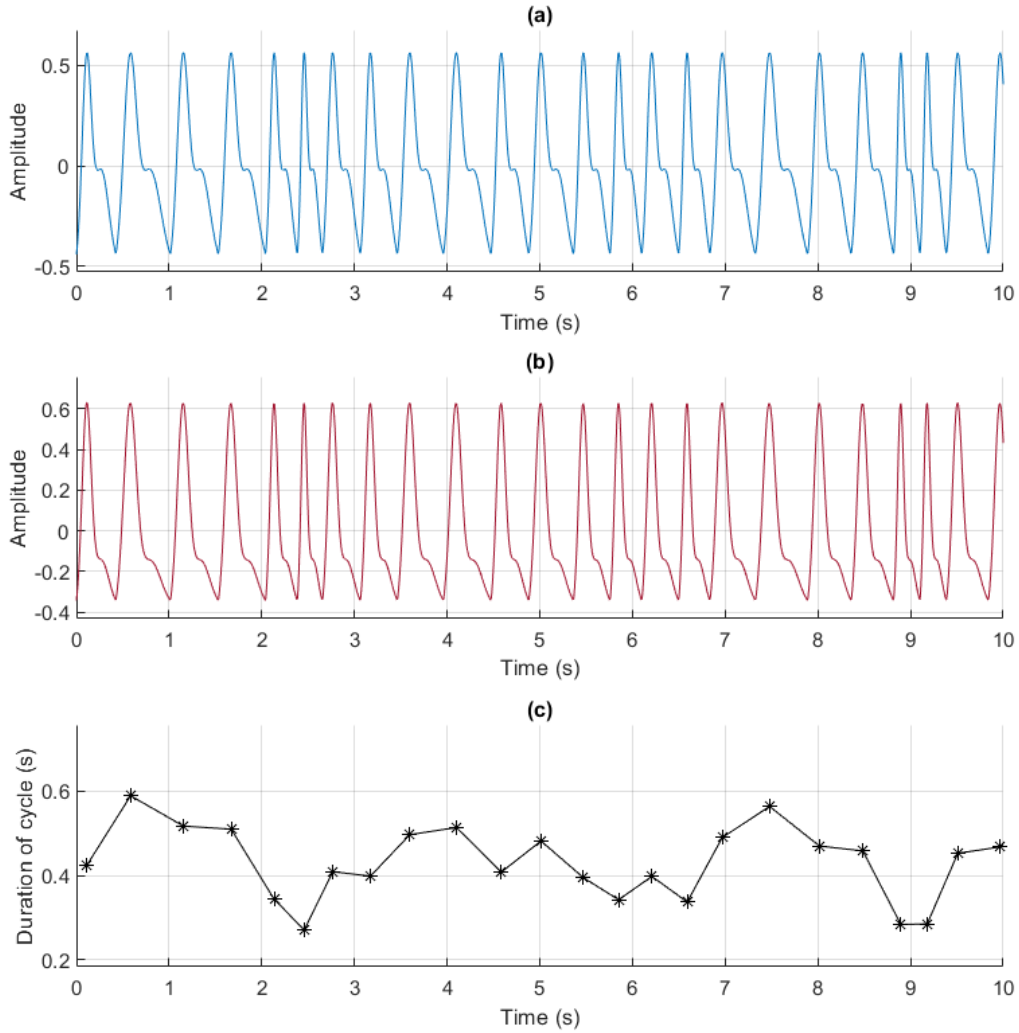

Figure 6.4: Example of photoplethysmographic (PPG) signals simulated using the proposed model and randomly generated pulse rate variability (PRV) information. (a) PPG signal with excellent quality ($r = 2$). (b) PPG signal with acceptable quality ($r = 4$). (c) PRV information used for the generation of these signals.

from the generated PRV information, considered as gold standard. Then, the sample size needed for the identification of differences as low as 2% of the mean value obtained for each of the extracted indices was calculated applying (6.7) or (6.8) for differences of means (used for AVNN, SDNN, RMSSD, VLF, LF, HF, TP, centroid-related indices, S, SD1 and SD2) or for differences of proportions (used for pNN50, nLF, nHF, LF/HF and SD1/SD2), respectively (Colimon 2018).

$$n = \frac{2(Z_{\frac{\alpha}{2}} - Z_{\beta})S}{(\mu_1 - \mu_2)^2} \tag{6.7}$$

$$n = \frac{(Z_{\frac{\alpha}{2}}\sqrt{2p_2(1-p_2)} - Z_{\beta}\sqrt{p_1(1-p_1) + p_2(1-p_2)})^2}{(p_1 - p_2)^2} \tag{6.8}$$

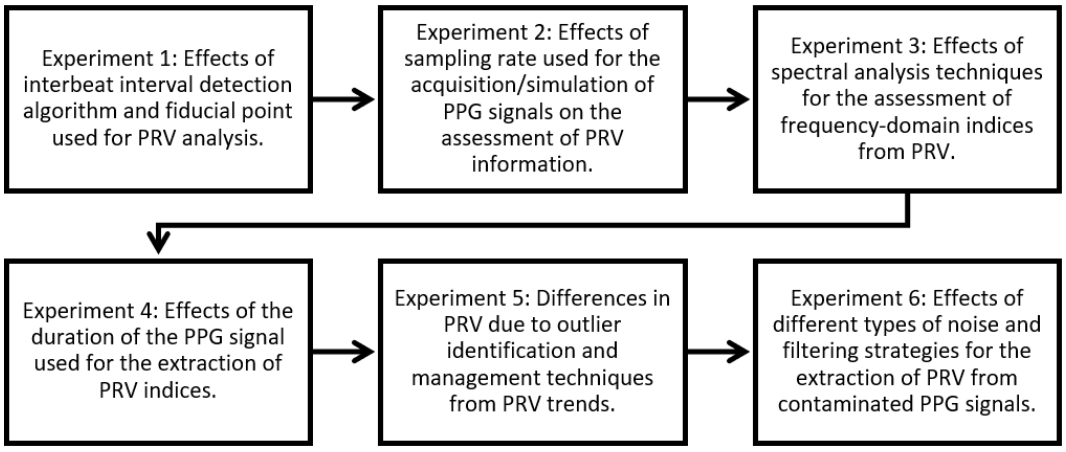

Figure 6.5: Flow diagram of experiments performed to understand the effects of technical aspects on pulse rate variability analysis

A sample size was obtained for each index with type I and II errors of $\alpha = 0.05$ and $\beta = 0.2$, respectively, and with S estimated as the standard deviation of each index extracted from the PRV gold standard; μ_1 as the mean value of each index extracted from the PRV gold standard; μ_2 as 1.02 times μ_1; p_1 as the mean value of the proportions obtained from the PRV gold standard; and p_2 as 1.02 times p_1. The final resulting sample sizes for each of the experiments are shown in Table 6.2. These were determined by selecting a value near the minimum of the resulting sample sizes obtained for the different indices, since a larger sample size can also lead to unreliable results in the statistical analyses (Khalilzadeh & Tasci 2017, Kaplan et al. 2014). Both excellent and acceptable quality PPG signals, each of the signals with different and randomly-generated PRV content, were simulated for the subsequent analyses according to these calculated sample sizes.

Table 6.2: Sample sizes selected for the different experiments.

Experiment	Number of signals
Experiment 1: Interbeat interval detection algorithms and fiducial points	125
Experiment 2: Sampling rate	125
Experiment 3: Spectral analysis	200
Experiment 4: Duration of signal	110
Experiment 5: Outlier management	117
Experiment 6: Noise management	117

6.2.2.1 Experiment 1: Interbeat interval detection algorithms and fiducial points

The aim of this experiment was to determine the interbeat intervals (IBIs) detection algorithm and fiducial point that provided the best performance for assessment of PRV from the simulated PPG signals, when compared to indices extracted from the gold standard PRV trends. Therefore, several algorithms and fiducial points were used for the extraction of PRV information, and time-domain (AVNN, SDNN, RMSSD and pNN50) and Poincaré plot indices (S, SD1, SD2 and SD1/SD2) were considered for this analysis. PPG signals with 1200 cycles were simulated, and random PRV information was added to them. This resulted in PPG signals with around 20-min duration, which is longer than what is usually used for short-term PRV analysis, and was considered sufficient to observe changes, especially in the analysed indices. A sampling rate of 2048 Hz was used, in order to diminish the effects of a low sampling rate in the detection of the fiducial points.

Five algorithms available in the literature were implemented for the extraction of IBIs from the simulated PPG signals, both with excellent and acceptable quality. The first of these algorithms, HeartPy, was proposed by van Gent et al. (van Gent et al. 2019). In this algorithm systolic peaks are detected using an adaptive threshold based on a moving average and the determination of regions of interest. The threshold is adapted according to the instantaneous heart rate and the standard deviation of peak-to-peak intervals. At the end, detected peaks are corrected based on outlier detection and rejection using the ±30% of the mean duration of peak-to-peak intervals. The algorithm is robust against signal clipping and has low computational load.

The second implemented algorithm was called D2max (Elgendi et al. 2013). The first steps of this algorithm involve filtering, clipping and squaring the signal, before generating blocks of interest based on two moving averages, which are designed based on the expected duration of cardiac cycles and the a point in the second derivative of the PPG signal. The location of the systolic peak from the PPG signal is determined as the location of the maximum point in each block of interest. This algorithm has been shown to be robust against movement artifacts.

The algorithm proposed by Argüello Prada and Serna Maldonado has also been implemented in this study (Prada & Maldonado 2018). This algorithm, referred

to as Upslopes, detects systolic upslopes instead of systolic peaks, since this is a constant feature of the PPG morphology regardless of the subject from which the signal is acquired or the body-site. The approach consists in identifying when there is an upslope in the signal, which is easily determined by checking if the amplitude of i-th sample of the signal is higher than the amplitude of the previous sample, $i-1$. A counter is updated until the condition is not met, and the value of the counter determines if the portion of the signal corresponds to a new pulse or not, depending on a comparison threshold. If the counter is smaller than the threshold, the algorithm determines that the current upslope does not occur due to a new cardiac cycle and starts counting again from zero. This is a simple algorithm which could be applied in real-time embedded applications.

Another of the applied algorithms is based on the work proposed by Conn and Borkholder (Conn & Borkholder 2013), which aims to identify the onset of the cardiac cycles using Wavelet transform. This method applies a fifth-scale quadratic spline Wavelet to the PPG, in which distinct peaks appear at the start of each beat. Using these peaks, a threshold is generated for identifying the valid range for the PPG onset, instead of the systolic peaks. Then, the third derivative of the PPG is obtained, and the first zero-crossing of this signal within the valid range is assigned as the onset of each pulse. Since it applies a Wavelet transform, this algorithm is robust to noise and shows high performance for the identification of PPG onsets.

Finally, the algorithm proposed by Li and Dong (Li et al. 2010) for the detection of cardiac cycles from arterial blood pressure waveforms has been applied. The first stage of this algorithm applies a low pass filter and obtains the derivative of the signal. Thresholds are also estimated from the filtered signal. Using the first derivative of the signal, zero-crossings are detected, and beats are evaluated according to the estimated thresholds and the detected zero-crossings. Then, peaks and onsets are detected from each beat, and dicrotic notches are also detected using inflection detection. In this study, the resulting onsets from this algorithm were used to segment the interbeat intervals.

IBIs longer than 1.25 times the median duration of all the IBIs were corrected by looking for additional cardiac cycles in each of these longer windows. IBIs shorter than 0.75 times the median duration of IBIs were also detected and discarded. Then, eight fiducial points were obtained from each segmented cycle. The extracted fiducial points were the systolic peak (PKS); the onset, considered as the minimum

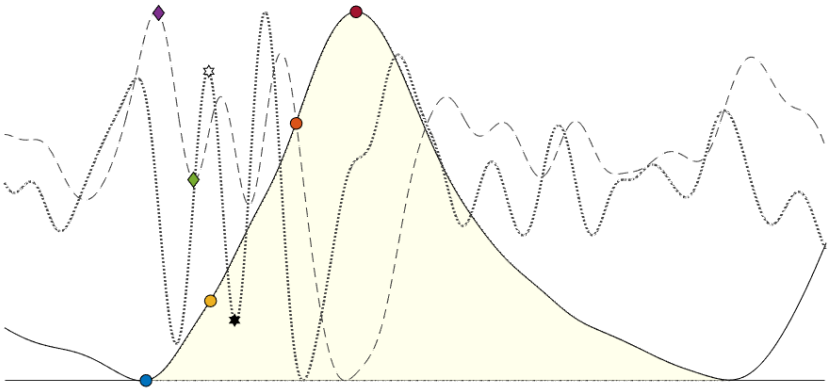

Figure 6.6: Fiducial points extracted from each inter-beat interval detected from the photoplethysmographic signals (continuous line), its second derivative (dashed line) and third derivative (dotted line). Red circle: Systolic peak (PKS); blue circle: Onset (ONS); yellow circle: Tangent intersection point (TI); orange circle: Maximum slope point (M1D); purple diamond: a point from the second derivative (A); green diamond: b point from the second derivative (B); white star: p_1 point from the third derivative (P1); black star: p_2 point from the third derivative (P2).

point before the systolic peak (ONS); the onset determined as the intersection point between the tangent line crossing the onset and the tangent line crossing the maximum slope point (TI); the location of the maximum point in the first derivative of the PPG cycle (M1D); the a and b points from the second derivative of the PPG cycle (A and B, respectively); and the p_1 and p_2 points obtained from the third derivative of the PPG cycle (P1 and P2, respectively). These fiducial points have been previously described in the literature (Mejía-Mejía, Allen, Budidha, El-Hajj, Kyriacou & Charlton 2021). Figure 6.6 illustrates the identification of these fiducial points in a segmented PPG cycle and its second and third derivatives.

PRV trends were obtained as the duration of IBIs extracted from each of the fiducial points, which were in turn obtained from the cycles segmented using each of the IBIs detection algorithms. Both time-domain and Poincaré plot indices were obtained from each of the trends. Extracted time-domain indices were AVNN, SDNN, RMSSD and pNN50, while S, SD1, SD2 and SD1/SD2 were measured from the 1-lag Poincaré plot, obtained applying the ellipse-fitting technique (Khandoker et al. 2013). These indices were also extracted from the gold standard PRV trends, and the differences between the indices assessed from detected and gold standard PRV were

calculated. A factorial analysis was then applied to determine which differences were minimal. Since the data did not follow a normal distribution, a Box-Cox transformation (Box & Cox 1964) was applied before the analysis of variance (ANOVA) for each extracted index. In the cases in which the ANOVA showed a difference among factors, post-hoc analyses were performed using Bonferroni pairwise comparisons.

Lastly, to determine which combination of algorithms and fiducial points gave the lower differences between measured and gold standard PRV, the combinations of factors that delivered minimal differences were obtained for each index after determining which indices showed a significant interaction between algorithms and fiducial points.

6.2.2.2 Experiment 2: Sampling rate

This experiment was conducted to evaluate the effects of lowering the PPG sampling rate in PRV extracted using the best combination of IBIs detection algorithms and fiducial points, as determined from the previous experiment. PPG signals with 1200 cardiac cycles were simulated using sampling rates of 32 Hz, 64 Hz, 128 Hz, 256 Hz, 512 Hz, 1024 Hz and 2048 Hz. PPG signals were generated independently for each sampling rate, instead of resampling a single set of PPG signals simulated with a larger sampling rate.

The combination of IBIs detection algorithm and fiducial point that performed the best in the previous experiment for excellent and acceptable PPG signals was used for extracting PRV trends and, as in the first experiment, time domain (AVNN, SDNN, RMSSD and pNN50) and Poincaré plot indices (S, SD1, SD2 and SD1/SD2) were calculated from these trends, and from the gold standard PRV. Student t-tests and Mann-Whitney tests were used for comparing the indices measured from the extracted and gold standard PRVs, for normally and non-normally distributed data, respectively, while normality was assessed using Lilliefors tests, which is a normality test suitable when the parameters of the null distribution are unknown and must be estimated (Mathworks 2022).

6.2.2.3 Experiment 3: Spectral analysis

The goal in this third experiment was to determine the best combination of parameters for the extraction of frequency-domain indices from PRV, considering PPG signals simulated with a properly selected sampling rate and applying the best per-

forming combination of IBIs detection algorithm and fiducial points, resulting from the previous experiments.

PRV trends were randomly generated, and their power spectra were calculated using the fast Fourier transform (FFT) with 2^{16} number of points (nFFT). Then, frequency-domain indices were extracted. The indices considered in this experiment were: The power of the very low frequency band (VLF); the absolute and relative power of the low frequency band (LF and nLF); the absolute and relative power of the high frequency band (HF and nHF); the total power of the spectrum between 0.0033 and 0.4 Hz (TP); the ratio between LF and HF (LF/HF); and the coordinates of the centroid of LF, HF and TP (cLF_x, cLF_y, cHF_x, cHF_y, cTP_x and cTP_y).

Using these PRV trends, excellent and acceptable PPG signals with 1200 cycles and a proper sampling rate were simulated, and IBIs were extracted using the best performing combination of IBIs detection algorithm and fiducial points. Then, different strategies for obtaining frequency spectra from the extracted PRV information were used to assess frequency-domain indices. Several algorithms were applied to extract the spectral content of PRV signals. FFT and Welch's power spectral density (PWELCH) were used as classical methods. Yule-Walker's (PYULEAR), Burg's (PBURG), covariance (PCOV), and modified covariance (PMCOV) autoregressive models were used to obtain model-based methods, as well as the multiple signal classification (PMUSIC) algorithm was used to obtain a pseudo-spectrum. Finally, the Lomb-Scargle algorithm (PLOMB) was also applied. In the case of classical and model-based algorithms, the parameters presented in Table 6.3 were optimised. From the different combinations of parameters and the different methods for spectral analysis, the mentioned frequency-domain indices were extracted.

As was performed in the first experiment, the difference between the indices extracted from measured and gold standard PRV trends were obtained. These differences were then used for the statistical analysis, in which independent factorial analysis were first performed in order to obtain the combination of factors that gave the lowest differences when spectra was obtained using each of the different methods, except for the Lomb-Scargle periodogram, in which no parameters need to be modified. Then, the best combination of factors was identified for each of the methods and these were compared using a Kruskal-Wallis test, since data did not follow a normal distribution according to the Lilliefors test of normality of data. Using Wilcoxon rank sum tests with Bonferroni correction, post-hoc analyses were

Table 6.3: Combinations of parameters used for the extraction of frequency spectra from pulse rate variability trends. Frequency resolution: number of samples used to calculate spectrum (nFFT) divided by the sampling rate of the signal.

Methods	**Interpolation**		**Frequency**	**Order**
	Technique	**Sampling rate (Hz)**	**resolution (Hz)**	
Classical	Linear or cubic spline	4, 8, 16, 32, 64, 128, 256	0.01, 0.001, 0.0001	-
Model-based	Linear or cubic spline	4, 8, 16, 32, 64, 128, 256 Hz	0.01, 0.001, 0.0001	5, 10, 15, 20, 25, 30, 35, 40, 45, 50

performed for the indices in which the Kruskal-Wallis analysis showed statistically significant differences among methods. The best combination of method, interpolation technique, frequency resolution and model order was then identified. A similar analysis was performed using cross-correlation and Pearson (XC Pearson) and Spearman (XC Spearman) correlation measured frequency spectra obtained from measured and gold standard PRV. This was done to assess the similarity among spectra extracted with the different combinations of parameters and with the different methods. The cross-correlation was characterised using the maximum value of cross-correlation found (XC max), and the lag at which this maximum occurred (XC lags).

6.2.2.4 Experiment 4: Duration of signal

The aim of this experiment was to evaluate how the length of the PPG signal affected the assessment of time-domain, frequency-domain and Poincaré plot indices. Therefore, excellent and acceptable quality PPG signals with randomly generated PRV information and different lengths were simulated. Sufficiently long PRV trends were generated, and PPG signals were simulated using the same trend. The length of the signals increased in steps of 30 s starting from 30 s up to 20 min (1200 s). IBIs were obtained using the best combination of algorithm and fiducial point obtained from experiment 1, and using the minimum proper sampling rate as found in experiment 2. Then, PRV indices were assessed, and for the case of frequency domain indices, the best strategy for spectral analysis found in experiment 3 was applied.

Table 6.4: Outlier detection methods

Name	Outlier definition
Median	IBIs with values more than three scales median absolute deviations from the median
Mean	IBIs with values more than three standard deviations from the mean
Quartiles	IBIs with more than 1.5 interquartile ranges above the upper quartile or below the lower quartile
Grubb's test	IBIs are detected in an iterative manner, assuming the sample as normally distributed. IBIs are classified as outliers using the largest absolute deviation from the sample mean in units of the sample standard deviation as the statistic
Generalized extreme Studentized deviate (GESD) test	Similar to the Grubb's test but optimised for multiple outliers
Moving mean	IBIs with values more than three standard deviations from the mean over a window of 5 consecutive samples
Moving median	IBIs with values more than three scales median absolute deviations from the median over a window of 5 consecutive samples

The differences between indices obtained from extracted PRV trends and from gold standard trends were measured, and Friedman rank sum tests were done to evaluate the differences between duration of the signals. This was considered as an appropriate non-parametric alternative to a 2-way ANOVA, where the utilisation of long PRV trends for the generation of PPG signals with different duration was considered as blocking factor and controlled for. Wilcoxon rank sum tests with Bonferroni correction were used for post-hoc comparisons.

6.2.2.5 Experiment 5: Outlier management

The main objective of this experiment was to establish guidelines for outlier management in PRV analysis, after the detection of interbeat intervals. IBIs were extracted from acceptable and excellent quality simulated PPG signals and different outlier detection and management techniques were used to determine the effects of these methods in PRV indices. The sampling rates and duration of the simulated PPG signals was set according to the results from experiments 2 and 4, respectively.

Cardiac cycles were identified from the simulated PPG signals using the best performing algorithm and fiducial point found from experiment 1. Outliers in these IBIs traces were detected and corrected applying the methods described in Tables

6.4 and 6.5, respectively. From the extracted IBIs, the corrected IBIs, and gold standard PRV traces, time-domain, frequency-domain and Poincaré plot indices were extracted. Frequency-domain analysis was performed using the best performing strategy found from experiment 3.

The differences between indices extracted from the gold standard and the original and corrected IBIs were calculated and used for the statistical analyses. Factorial analyses were performed to evaluate the effects of the detection and correction methods, as well as their interaction on the differences of each of the PRV indices. Since the data did not follow a normal distribution, as checked using the Lilliefors test, Box-Cox transformations were applied to the differences, after finding the optimal lambda for each case. Then, the combination of factors that gave the lowest difference for each index was compared to the differences obtained if no outlier detection and management strategy was applied, using Wilcoxon rank sum tests. A 95% significance value was used for all the analyses.

Table 6.5: Outlier management methods

Name	Description
Mean $k = 5$	Replaces each outlier for the mean value of the 5 previous IBIs
Median $k = 5$	Replaces each outlier for the median value of the 5 previous IBIs
Mean	Replaces each outlier for the mean value of the IBIs
Median	Replaces each outlier for the median value of the IBIs
Clip	Replaces each outlier with the lower or upper threshold value for elements smaller than or higher than three scaled median absolute deviations from the median
Previous	Replaces each outlier with the previous non-outlier value
Next	Replaces each outlier with the next non-outlier value
Nearest	Replaces each outlier with the nearest non-outlier value
Linear	Replaces each outlier after linearly interpolating neighbouring, non-outlier values
Spline	Replaces each outlier after applying a cubic spline interpolation with neighbouring, non-outlier values
Piecewise Spline	Replaces each outlier after applying a shape-preserving piecewise cubic spline interpolation with neighbouring, non-outlier values
Makima	Replaces each outlier after applying a modified Akima cubic Hermite interpolation with neighbouring, non-outlier values

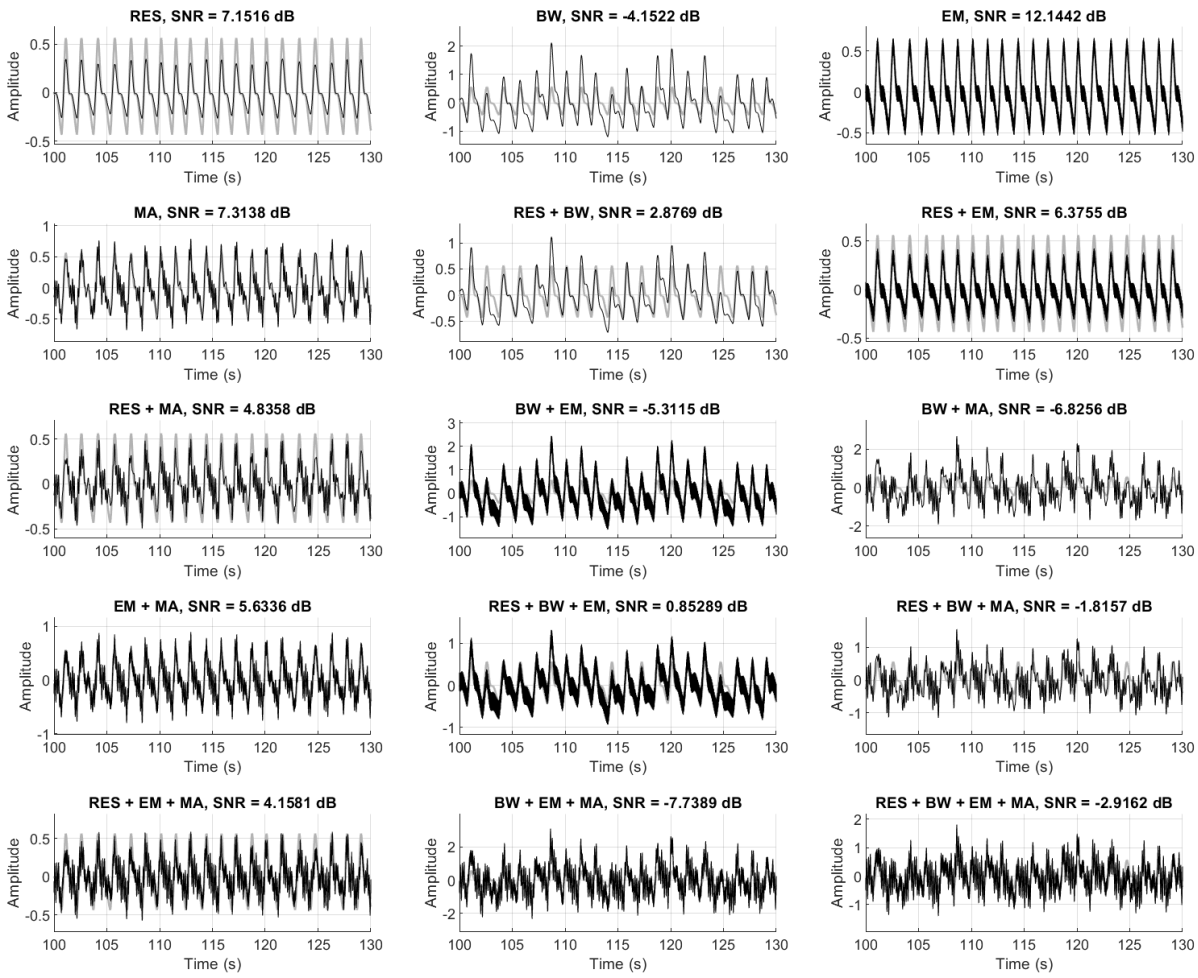

Figure 6.7: Example of noise-corrupted, excellent quality photoplethysmographic signals simulated for experiment 6. RES: Respiratory noise; BW: Baseline wandering; EM: Electromagnetic noise; MA: Movement artifact.

6.2.2.6 Experiment 6: Noise management

The aim of this final experiment was to understand how different filtering techniques applied to PPG signals corrupted with different types of noise affected PRV indices, to determine the best performing filter to apply in PRV analysis. Therefore, PPG signals were simulated with 15 different types of noise reached by applying all possible combinations of the 4 types of noise that can be simulated with the proposed framework. Table 6.6 summarises these combinations and the parameters used for the generation of noise, while Figure 6.7 and 6.8 exemplify the excellent and acceptable signals simulated with these noises, respectively. These signals were simulated considering the more appropriate duration and sampling rate found in previous analyses.

Additionally, different types of filters were designed in order to evaluate which

Table 6.6: Parameters used for the simulation of noise corrupted photoplethysmographic (PPG) signals. RES: Respiratory noise; BW: Baseline wandering; EM: Electromagnetic noise; MA: Movement artifact. A_n: Proportion of the noise amplitude with respect to the PPG signal amplitude; f: Fundamental frequency of the noise. x: Indicates the inclusion of the specific type of noise in the resulting signal.

Combination	**Types of noise**				**Parameters**	
	RES	**BW**	**EM**	**MA**	A_n	f **(Hz)**
C1	x	-	-	-	0.1	0.15
C2	-	x	-	-	0.5	[0.08, 0.18]
C3	-	-	x	-	0.1	60
C4	-	-	-	x	0.07	[1.02, 7.31, 5.06]
C5	x	x	-	-	RES: 0.1	RES: 0.15
					BW: 0.5	BW: [0.08, 0.18]
C6	x	-	x	-	RES: 0.1	RES: 0.15
					EM: 0.1	EM: 60
C7	x	-	-	x	RES: 0.1	RES: 0.15
					MA: 0.07	MA: [1.02, 7.31, 5.06]
C8	-	x	x	-	BW: 0.5	BW: [0.08, 0.18]
					EM: 0.1	EM: 60
C9	-	x	-	x	BW: 0.5	BW: [0.08, 0.18]
					MA: 0.07	MA: [1.02, 7.31, 5.06]
C10	-	-	x	x	EM: 0.1	EM: 60
					MA: 0.07	MA: [1.02, 7.31, 5.06]
C11	x	x	x	-	RES: 0.1	RES: 0.15
					BW: 0.5	BW: [0.08, 0.18]
					EM: 0.1	EM: 60
C12	x	x	-	x	RES: 0.1	RES: 0.15
					BW: 0.5	BW: [0.08, 0.18]
					MA: 0.07	MA: [1.02, 7.31, 5.06]
C13	x	-	x	x	RES: 0.1	RES: 0.15
					EM: 0.1	EM: 60
					MA: 0.07	MA: [1.02, 7.31, 5.06]
C14	-	x	x	x	BW: 0.5	BW: [0.08, 0.18]
					EM: 0.1	EM: 60
					MA: 0.07	MA: [1.02, 7.31, 5.06]
C15	x	x	x	x	RES: 0.1	RES: 0.15
					BW: 0.5	BW: [0.08, 0.18]
					EM: 0.1	EM: 60
					MA: 0.07	MA: [1.02, 7.31, 5.06]

filtering strategy was related to more reliable PRV indices extracted from these corrupted signals. Both finite (FIR) and infinite impulse response (IIR) filters were considered, with different orders and low and high cut-off frequencies.

For FIR filters, 5 design methods were considered: Equiripple filter (FIREQR), Hamming window (FIRWIN), constrained least squares (FIRCLS), least squares (FIRLS) and Parks-McClellan (FIRPM). For FIREQR and FIRPM, the optimal order was determined using MATLAB functions, whereas for the remaining FIR filters,

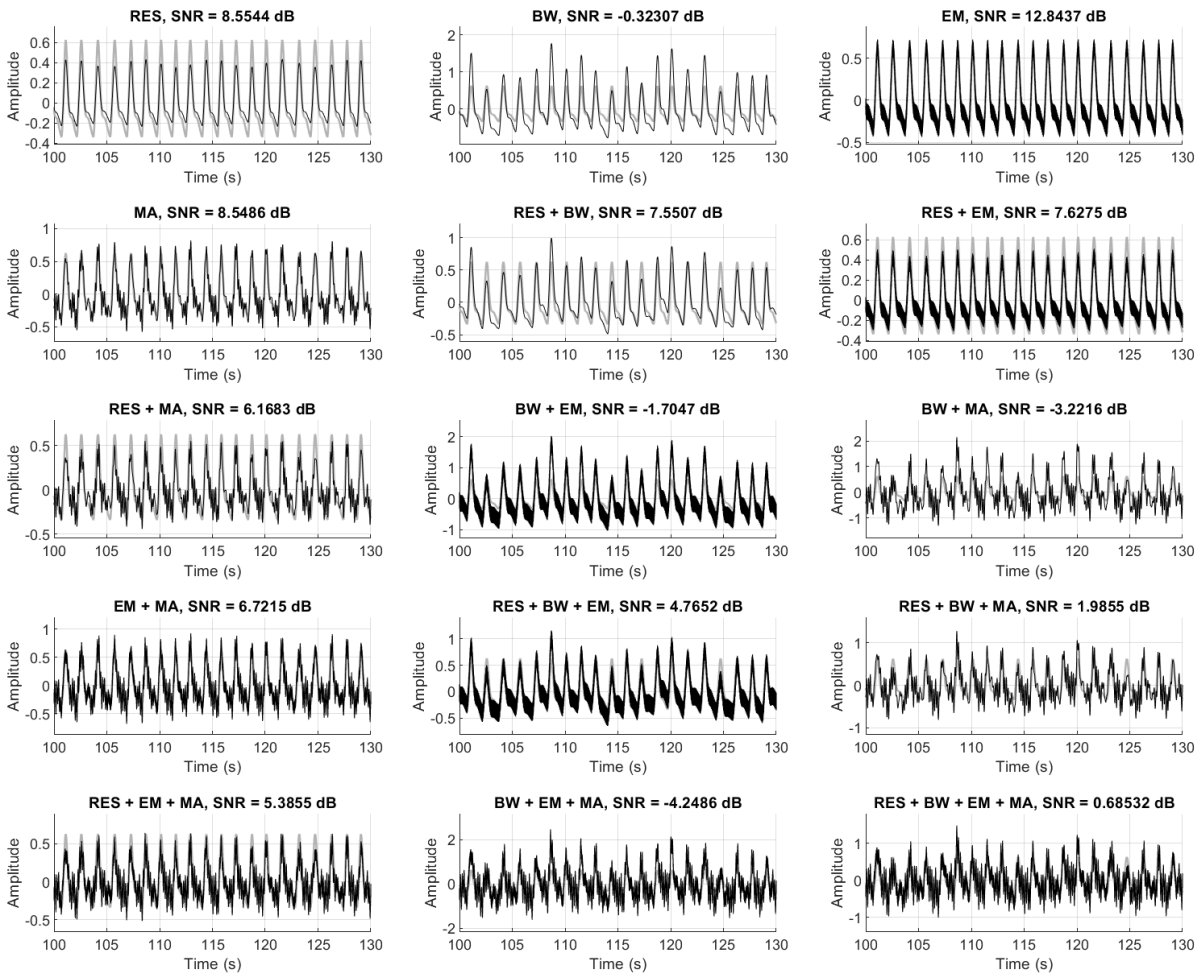

Figure 6.8: Example of noise-corrupted, acceptable quality photoplethysmographic signals simulated for experiment 6. RES: Respiratory noise; BW: Baseline wandering; EM: Electromagnetic noise; MA: Movement artifact.

the sampling rate f_s was used as order of the filter. In all cases, a 3 dB passband ripple and a 40 dB stopband attenuation were considered. Similarly, two design methods were considered for IIR filters, i.e., Butterworth (IIRBUT) and Elliptic (IIRELL) filters. For these filters, the order was also optimised using MATLAB functions and 3 dB and 40 dB for passband ripple and stopband attenuation. A total of 210 filters were designed by combining these parameters and the investigated values of low and high cut-off frequencies. Low cut-off frequencies considered were $f_{c,low} \in [0.0, 0.1, 0.2, 0.5, 1.0, 2.0]$ Hz, while high cut-off frequencies were $f_{c,high} \in [8, 10, 12, 15, 20]$ Hz.

These filters were then applied with zero-phase to the noise-corrupted simulated PPG signals, and PRV trends were extracted from filtered signals, using the best performing interbeat intervals detection algorithm and fiducial point. Outliers were

detected and managed as found appropriate from the previous experiment, and time domain, frequency domain and Poincaré plot indices were estimated from PRV trends. Spectral analysis was performed according to results from experiment 3.

The difference between the extracted indices and the indices obtained from gold standard PRV trends was measured, and the results obtained from applying the different filters within each of the combination of noises were compared using a factorial analysis, in order to evaluate which combination of cut-off frequencies, filter type and filter topology gave the most accurate results. Since these differences did not follow a normal distribution, a Box-Cox transformation was applied in each case, and the factorial analyses results were derived after these transformations.

6.3 Results

6.3.1 Experiment 1: Interbeat interval detection algorithms and fiducial points

A summary of the differences between indices obtained from measured and gold standard PRV is presented in Figures 6.9 and 6.10, for excellent and acceptable PPG signals, respectively. Some of the extracted indices behave differently due to the algorithms used. For instance, there are differences in pNN50 and S among algorithms and signal quality. This needs to be considered when deciding what kind of algorithm to use for a specific analysis involving these two indices. On the other hand, differences among fiducial points within the same algorithm are not very significant for AVNN and SD2.

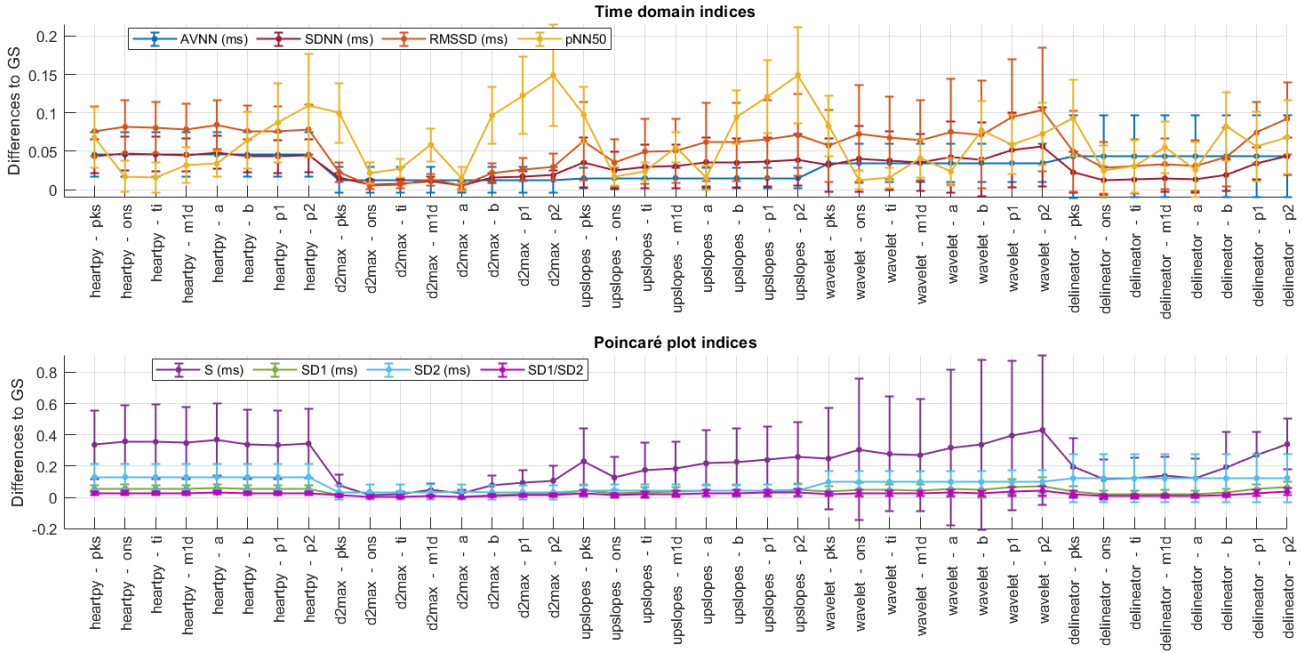

Figure 6.9: Summary of the absolute differences (mean ± standard deviation) between indices measured from gold standard and extracted pulse rate variability from excellent quality PPG signals.

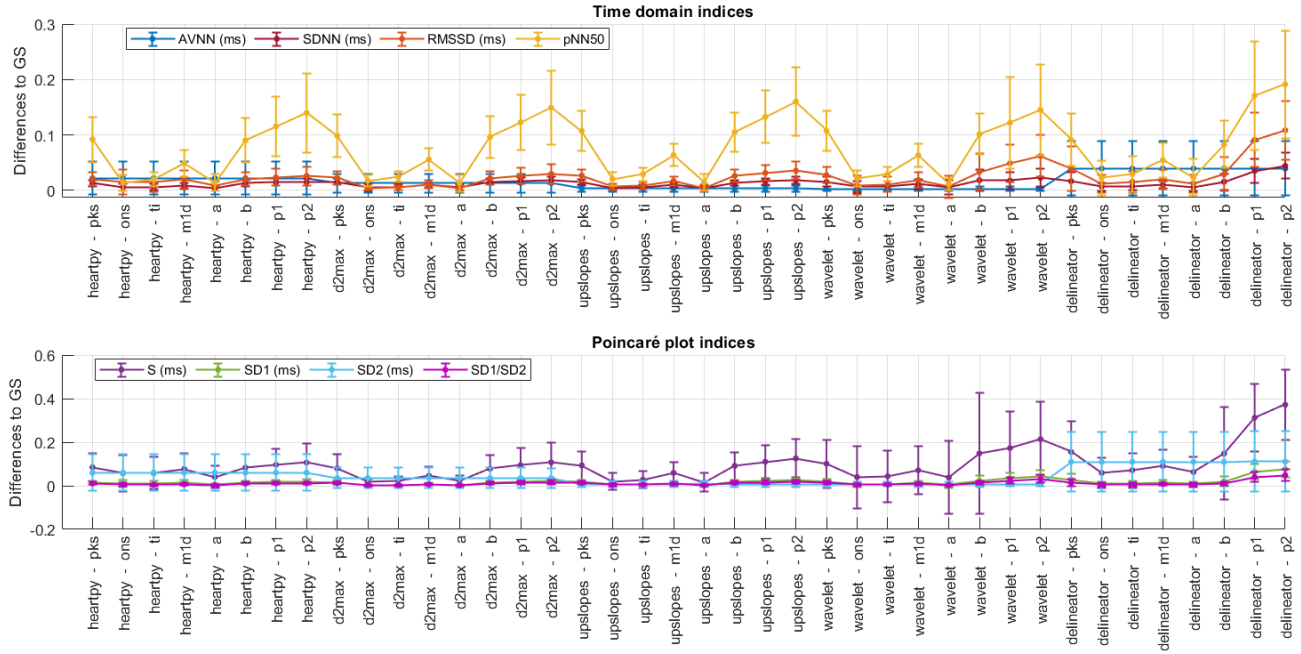

Figure 6.10: Summary of the absolute differences (mean ± standard deviation) between indices measured from gold standard and extracted pulse rate variability from acceptable quality PPG signals.

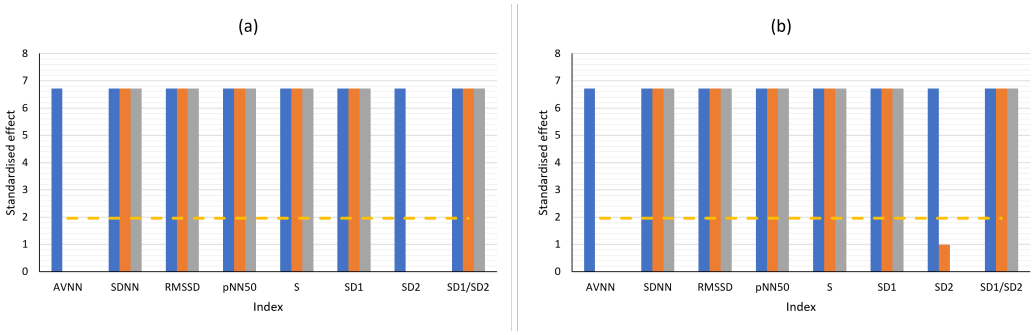

Figure 6.11: Results obtained from the factorial analyses both with (a) excellent quality PPG signals and (b) acceptable quality PPG signals. Blue bars: Standardised effects of the algorithm. Orange bars: Standardised effects of the fiducial points. Grey bars: Standardised effects of the interaction between the two factors. Yellow line: Reference value; higher standardised effects imply significance of the factor or the interaction.

As explained, a factorial analysis was performed for each index, to identify if there were differences among algorithms and fiducial points, and to assess whether the interaction between algorithm and fiducial point showed any statistical significance. Figure 6.11 summarises the results obtained from these factorial analyses. It can be observed that AVNN and SD2 are the only indices in which the fiducial points or the interaction between algorithms and fiducial points are not statistically significant, while all indices have similar behaviour regardless of the quality of the signal, which could be due to the fact that all the fiducial points extracted in this study belong to the systolic phase of the cardiac cycle, and this is not highly affected by the difference in quality in the proposed model. Only fiducial points from the systolic phase were considered in this experiment due to the smooth changes and varying morphologies of the diastolic phase of the cardiac cycle obtained from PPG signals, and because the absence of a very distinct point in this phase could introduce additional errors in the analysis. Moreover, most of the PRV-related studies reported in the literature make use of the fiducial points included in this experiment.

Since the aim of this experiment was to determine the best combination of fiducial points and algorithms used for PRV assessment, the differences between indices measured from gold standard and extracted PRV that did show significant interactions were determined and organised in ascending order (Figures 6.12 to 6.17).

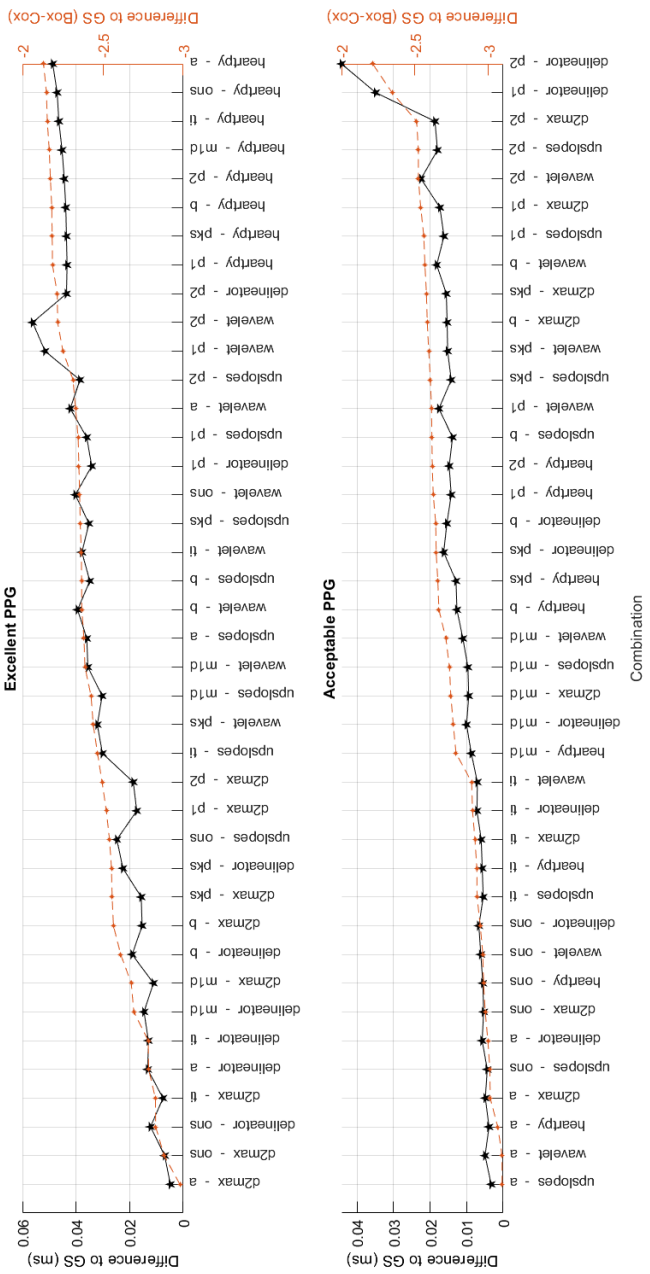

Figure 6.12: Mean value of the absolute differences between SDNN measured from gold standard and extracted pulse rate variability (PRV), measured from excellent (top) and acceptable (bottom) quality photoplethysmographic signals. Left axis (black, continuous line): Difference to gold standard before Box-Cox transformations. Right axis (orange, dashed line): Difference to gold standard after Box-Cox transformation.

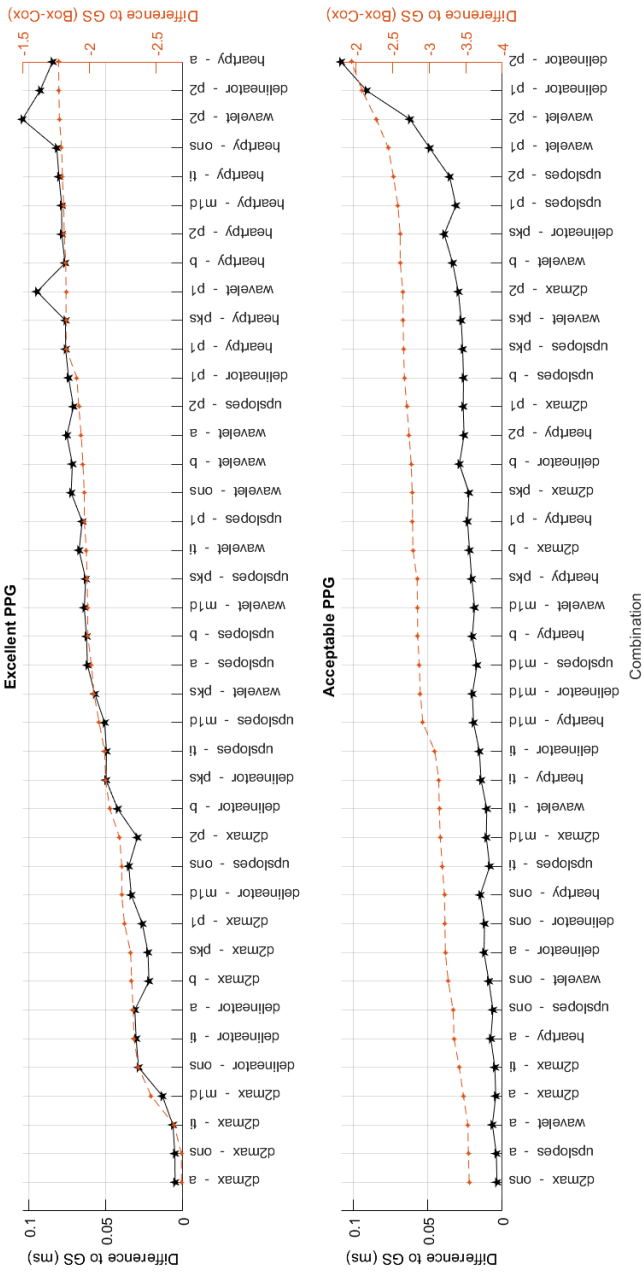

Figure 6.13: Mean value of the absolute differences between RMSSD measured from gold standard and extracted pulse rate variability (PRV), measured from excellent (top) and acceptable (bottom) quality photoplethysmographic signals. Left axis (black, continuous line): Difference to gold standard before Box-Cox transformations. Right axis (orange, dashed line): Difference to gold standard after Box-Cox transformation.

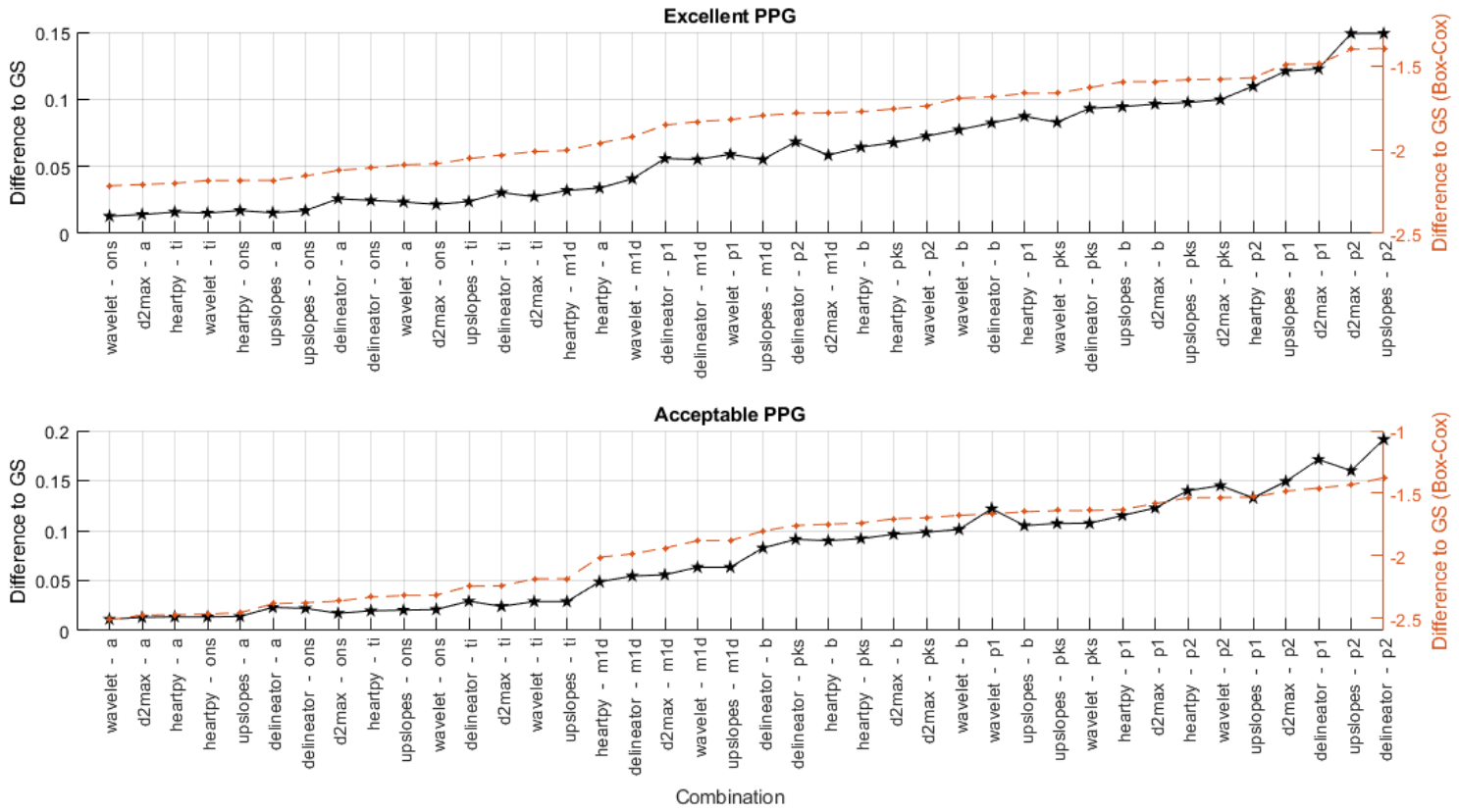

Figure 6.14: Mean value of the absolute differences between pNN50 measured from gold standard and extracted pulse rate variability (PRV), measured from excellent (top) and acceptable (bottom) quality photoplethysmographic signals. Left axis (black, continuous line): Difference to gold standard before Box-Cox transformations. Right axis (orange, dashed line): Difference to gold standard after Box-Cox transformation.

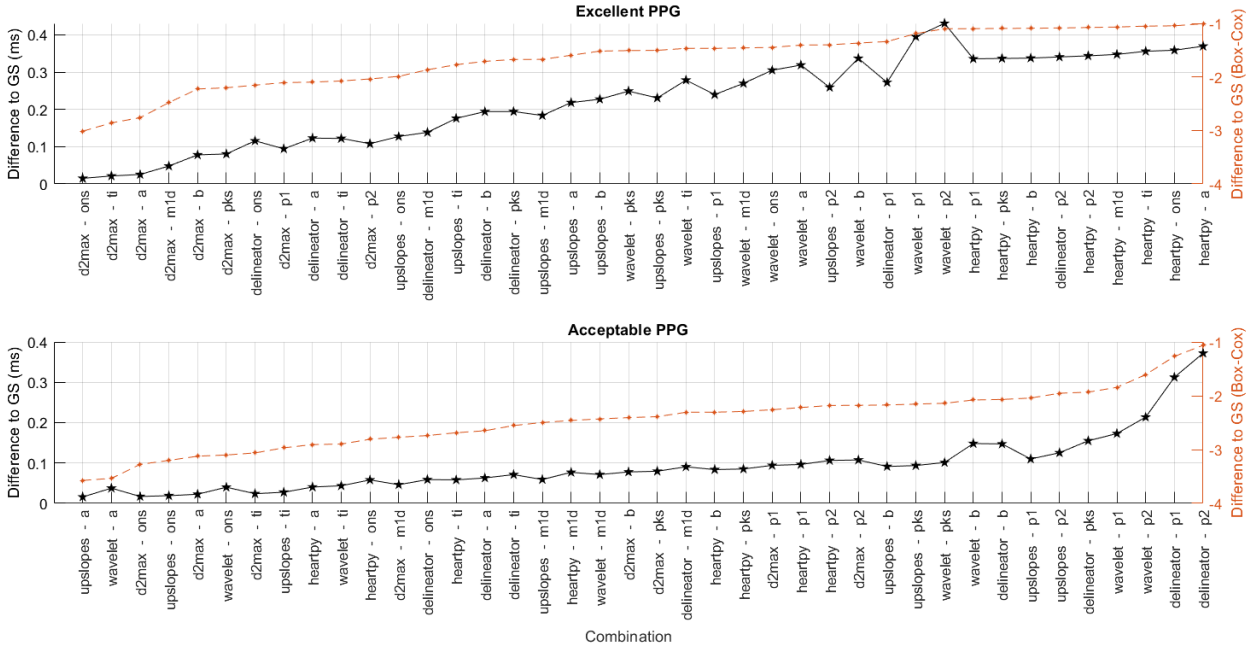

Figure 6.15: Mean value of the absolute differences between S measured from gold standard and extracted pulse rate variability (PRV), measured from excellent (top) and acceptable (bottom) quality photoplethysmographic signals. Left axis (black, continuous line): Difference to gold standard before Box-Cox transformations. Right axis (orange, dashed line): Difference to gold standard after Box-Cox transformation.

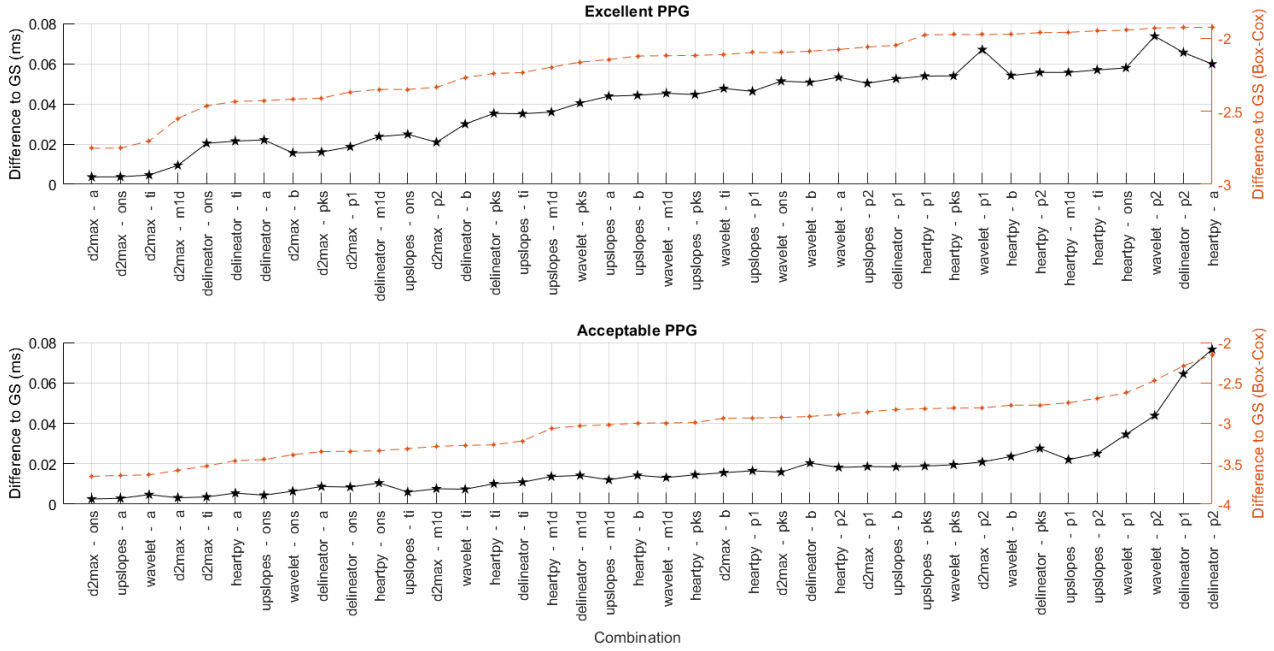

Figure 6.16: Mean value of the absolute differences between SD1 measured from gold standard and extracted pulse rate variability (PRV), measured from excellent (top) and acceptable (bottom) quality photoplethysmographic signals. Left axis (black, continuous line): Difference to gold standard before Box-Cox transformations. Right axis (orange, dashed line): Difference to gold standard after Box-Cox transformation.

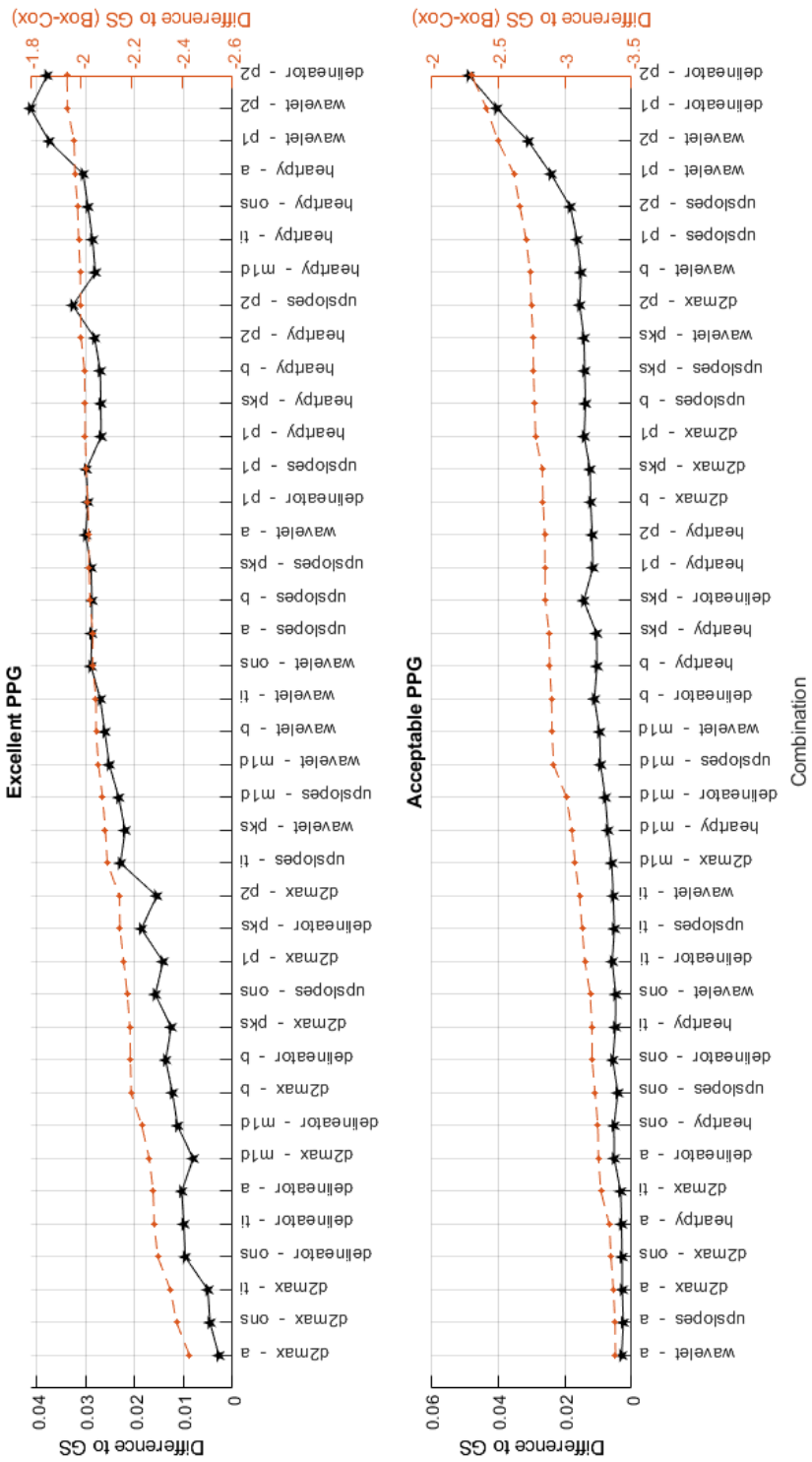

Figure 6.17: Mean value of the absolute differences between SD1/SD2 measured from gold standard and extracted pulse rate variability (PRV), measured from excellent (top) and acceptable (bottom) quality photoplethysmographic signals. Left axis (black, continuous line): Difference to gold standard before Box-Cox transformations. Right axis (orange, dashed line): Difference to gold standard after Box-Cox transformation.

In all cases, the minimum difference between indices obtained from gold standard and extracted PRV were obtained using D2Max, Upslopes or Wavelet algorithms, and using A and ONS fiducial points. It is also noticeable that there are differences in the best combination between excellent and acceptable PPG signals, with differences being lower in the acceptable quality signals only for SDNN analysis. Therefore, it is important to determine the algorithm and fiducial points to use in a given analysis considering also the quality of the signals used.

Table 6.7: Results of the post-hoc comparisons between the combination of algorithms and fiducial points with the five lowest differences to the gold standard for each time-domain index extracted from excellent and acceptable quality photoplethysmographic (PPG) signals. (-): Non-significant difference. (+): Significant differences.

Index	Excellent PPG						Acceptable PPG					
SDNN		d2max - a	d2max - ons	delineator - ons	d2max - ti	delineator - a		d2max - a	d2max - ons	delineator - ons	d2max - ti	delineator - a
	d2max - a	-	-	-	-	+	d2max - a	-	-	-	-	-
	d2max - ons	-	-	-	-	-	d2max - ons	-	-	-	-	-
	delineator - ons	-	-	-	-	-	delineator - ons	-	-	-	-	-
	d2max - ti	-	-	-	-	-	d2max - ti	-	-	-	-	-
	delineator - a	+	-	-	-	-	delineator - a	-	-	-	-	-
RMSSD		d2max - a	d2max - ons	d2max - ti	d2max - m1d	delineator - ons		d2max - a	d2max - ons	d2max - ti	d2max - m1d	delineator - ons
	d2max - a	-	-	-	+	+	d2max - a	-	-	-	+	+
	d2max - ons	-	-	-	+	+	d2max - ons	-	-	-	+	+
	d2max - ti	-	-	-	+	+	d2max - ti	-	-	-	+	-
	d2max - m1d	+	+	+	-	-	d2max - m1d	+	+	+	-	-
	delineator - ons	+	+	+	-	-	delineator - ons	+	+	-	-	-
pNN50		wavelet - ons	d2max - a	heartpy - ti	wavelet - ti	heartpy - ons		wavelet - ons	d2max - a	heartpy - ti	wavelet - ti	heartpy - ons
	wavelet - ons	-	-	-	-	-	wavelet - ons	-	+	-	+	+
	d2max - a	-	-	-	-	-	d2max - a	+	-	+	+	-
	heartpy - ti	-	-	-	-	-	heartpy - ti	-	+	-	+	+
	wavelet - ti	-	-	-	-	-	wavelet - ti	+	+	+	-	+
	heartpy - ons	-	-	-	-	-	heartpy - ons	+	-	+	+	-

Then, post-hoc comparisons were performed among the 5 combinations that showed the lowest differences, to determine whether there was a significant difference among them (p-value lower than 5%). These results are shown in Tables 6.7 and 6.8. For all indices, except for pNN50 obtained from acceptable PPG signals, the first three combinations with lowest differences do not show any statistical difference. For both excellent and acceptable PPG, D2max was the more frequent algorithm (15 out of 18 combinations), while Delineator for SDNN, and Wavelet and HeartPy for pNN50 also showed good performance. The only case in which D2max was not considered the best algorithm was for pNN50, in which Wavelet and HeartPy showed the best performance and did not have any statistically significant differences. When the fiducial points are considered, it can be seen that the A, ONS and TI points showed the best behaviour in all cases. There were statistically significant differences among these fiducial points only for pNN50 measured from acceptable PPG signals. However, the most frequency combination of algorithm and fiducial point that gave the lowest difference between gold standard and extracted PRV was D2max - A (8 out of 12 cases).

In summary, the algorithm with the best behaviour when compared to gold standard PRV was D2Max, while better results were obtained using the A point from the second derivative as fiducial point for extraction of interbeat intervals. In most applications, however, the TI and ONS points should give similarly good results.

6.3.2 Experiment 2: Sampling rate

Figure 6.18 summarises the time-domain and Poincaré plot indices extracted from the simulated data using different sampling rates. The red stars on top of the bars indicate statistically significant differences with the gold standard. In most cases, indices extracted from both acceptable and excellent quality simulated PPG signals showed lower values than those obtained from gold standard PRV. The standard deviation is similar among the groups and comparable in most cases as well. Importantly, the difference between gold standard and extracted PRV indices seem to remain stable for most of the sampling rates analysed, although differences become more noticeable for sampling rates below 128 Hz.

Most indices showed statistically significant differences to the gold standard when the sampling rate was 64 Hz, while above 256 Hz only SDNN showed statistically

Table 6.8: Results of the post-hoc comparisons between the combination of algorithms and fiducial points with the five lowest differences to the gold standard for each Poincaré-plot index extracted from excellent and acceptable quality photoplethysmographic (PPG) signals. (-): Non-significant difference. (+): Significant differences.

Index	Excellent PPG						Acceptable PPG					
S		d2max - ons	d2max - ti	d2max - a	d2max - m1d	d2max - b		d2max - ons	d2max - ti	d2max - a	d2max - m1d	d2max - b
	d2max - ons	-	-	-	+	+	d2max - ons	-	-	-	+	+
	d2max - ti	-	-	-	+	+	d2max - ti	-	-	-	-	+
	d2max - a	-	-	-	-	+	d2max - a	-	-	-	+	+
	d2max - m1d	+	+	-	-	-	d2max - m1d	+	-	+	-	+
	d2max - b	+	+	+	-	-	d2max - b	+	+	+	+	-
SD1		d2max - a	d2max - ons	d2max - ti	d2max - m1d	delineator - ons		d2max - a	d2max - ons	d2max - ti	d2max - m1d	delineator - ons
	d2max - a	-	-	-	+	+	d2max - a	-	-	-	+	+
	d2max - ons	-	-	-	+	+	d2max - ons	-	-	-	+	+
	d2max - ti	-	-	-	+	+	d2max - ti	-	-	-	+	-
	d2max - m1d	+	+	+	-	-	d2max - m1d	+	+	+	-	-
	delineator - ons	+	+	+	-	-	delineator - ons	+	+	-	-	-
SD1/SD2		d2max - a	d2max - ons	d2max - ti	delineator - ons	delineator - ti		d2max - a	d2max - ons	d2max - ti	delineator - ons	delineator - ti
	d2max - a	-	-	-	+	+	d2max - a	-	-	-	+	+
	d2max - ons	-	-	-	-	-	d2max - ons	-	-	-	-	+
	d2max - ti	-	-	-	-	-	d2max - ti	-	-	-	-	-
	delineator - ons	+	-	-	-	-	delineator - ons	+	-	-	-	-
	delineator - ti	+	-	-	-	-	delineator - ti	+	+	-	-	-

significant differences. The analyses performed in this experiment were based on the extraction of PRV information using inter-beat intervals detected with the D2Max algorithm, and the *a* point from the second derivative of PPG as fiducial point.

6.3.3 Experiment 3: Spectral analysis

Using 256 Hz as sampling rate for the simulated PPG signals, and D2Max and *a* fiducial point for the extraction of PRV trends, spectral analysis was performed to

these PRV trends using the different approaches described previously. From the obtained spectra, the difference between measured and gold standard frequency domain indices, as well as correlation indices between gold standard and measured spectra were obtained. As explained, a factorial analysis was performed for each independent spectral analysis method. This was done in order to evaluate the effects of interaction among the studied factors, i.e., type of interpolation used (A), the number of data points used for obtaining the spectrum (B), the sampling rate used for interpolation (C), and the order of the model (D). Tables 6.9 and 6.10 summarise the results obtained from these analyses.

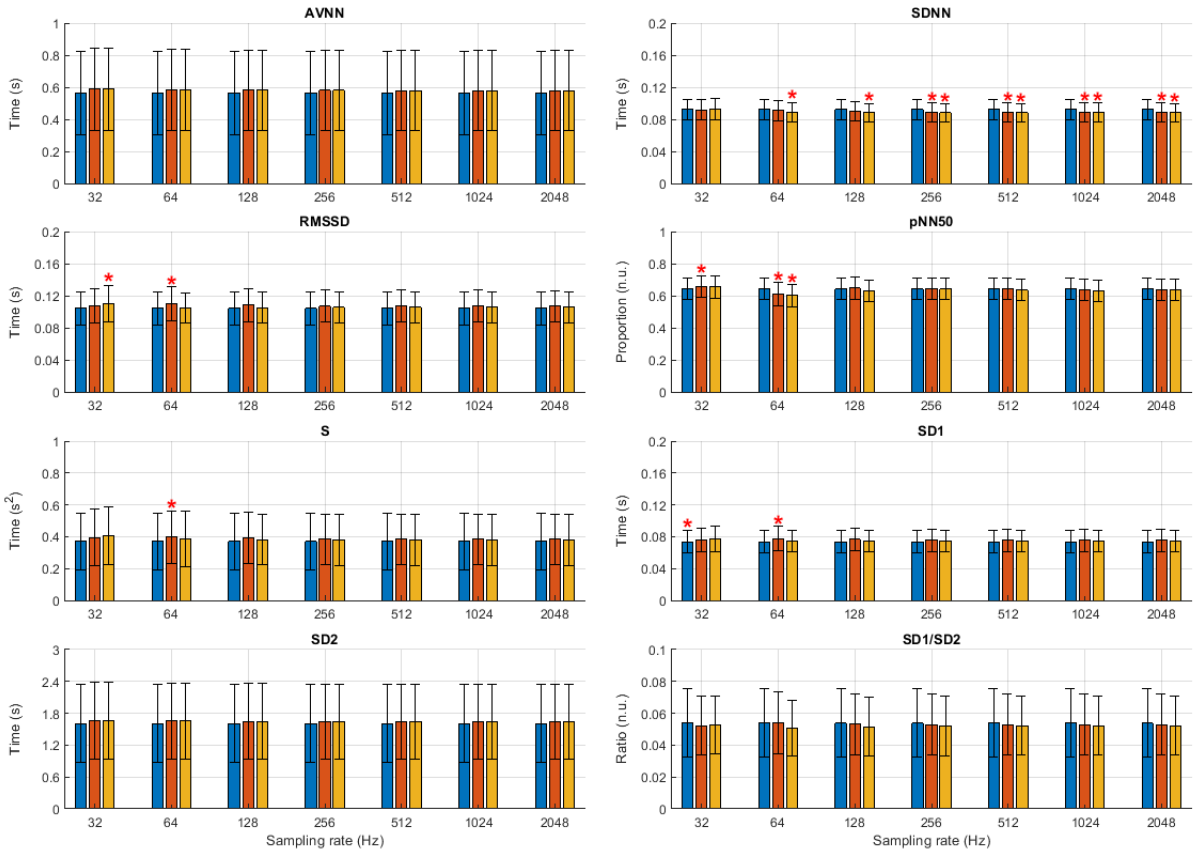

Figure 6.18: Mean and standard deviation of time-domain and Poincaré plot indices extracted from pulse rate variability (PRV), both from excellent and acceptable quality simulated photoplethysmographic (PPG) signals, with varying sampling rates. Blue bars: values obtained from gold standard PRV; orange bars: values obtained from PRV extracted from excellent quality PPG signals; yellow bars: values obtained from PRV extracted from acceptable quality PPG signals. Red stars indicate statistically significant difference to gold standard.

Table 6.9: Summary of results from factorial analyses performed to evaluate the effects of interactions among factors altered for spectral analysis of pulse rate variability obtained from excellent quality photoplethysmographic signals. A: Type of interpolation used; B: Number of data points used for obtaining the spectrum; C: Sampling rate used for interpolation; D: Order of the model. ⋆: Significant interaction or factor. -: Non-significant interaction or factor.

Algorithm	Interaction	Indices																
		VLF	LF	HF	TP	nLF	nHF	LF/HF	cLF_x	cLF_y	cHF_x	cHF_y	cTP_x	cTP_y	XC lags	XC max	XC Spearman	XC Pearson
FFT	A	-	-	⋆	⋆	⋆	⋆	⋆	-	-	-	⋆	-	⋆	⋆	⋆	-	-
	B	⋆	⋆	⋆	⋆	-	-	-	-	-	-	-	-	⋆	⋆	⋆	⋆	⋆
	C	⋆	⋆	⋆	⋆	-	-	-	-	-	-	-	-	⋆	⋆	⋆	⋆	⋆
	A × B	-	-	⋆	-	-	-	-	-	-	-	-	-	-	-	-	-	-
	A × C	-	-	-	-	-	-	-	-	-	-	-	-	-	-	-	-	-
	B × C	⋆	⋆	⋆	⋆	-	-	-	-	-	-	-	-	-	⋆	⋆	⋆	⋆
	A × B × C	-	-	-	⋆	-	-	-	-	-	-	-	-	-	⋆	-	-	-
PWELCH	A	-	-	⋆	-	⋆	⋆	⋆	-	-	-	⋆	-	-	⋆	⋆	⋆	-
	B	⋆	⋆	⋆	⋆	-	-	-	-	⋆	-	-	-	-	⋆	⋆	⋆	⋆
	C	⋆	⋆	⋆	⋆	-	-	-	-	-	-	-	-	-	⋆	⋆	⋆	⋆
	A × B	-	-	-	-	-	-	-	-	-	-	-	-	-	-	-	-	-
	A × C	-	-	-	-	-	-	-	-	-	-	-	-	-	-	-	-	-
	B × C	⋆	⋆	⋆	-	-	-	-	-	-	-	-	-	-	⋆	⋆	-	⋆
	A × B × C	-	-	⋆	-	-	-	-	-	-	-	-	-	-	⋆	-	⋆	-
PYULEAR	A	⋆	⋆	⋆	⋆	⋆	⋆	⋆	-	⋆	-	⋆	⋆	⋆	-	⋆	⋆	-
	B	⋆	⋆	⋆	⋆	⋆	⋆	⋆	⋆	⋆	⋆	⋆	⋆	⋆	⋆	⋆	⋆	⋆
	C	⋆	⋆	⋆	⋆	⋆	⋆	⋆	⋆	⋆	⋆	⋆	⋆	⋆	⋆	⋆	⋆	⋆
	D	⋆	⋆	⋆	⋆	⋆	⋆	⋆	⋆	⋆	⋆	⋆	⋆	⋆	⋆	⋆	⋆	⋆
	A × B	⋆	⋆	⋆	⋆	⋆	⋆	⋆	-	⋆	-	⋆	⋆	⋆	-	⋆	⋆	-
	A × C	⋆	⋆	⋆	⋆	⋆	⋆	⋆	-	⋆	-	⋆	⋆	⋆	-	⋆	-	-
	B × C	⋆	⋆	⋆	⋆	-	-	-	-	-	-	-	-	-	⋆	⋆	⋆	⋆
	A × D	⋆	⋆	⋆	⋆	⋆	⋆	⋆	-	⋆	-	⋆	⋆	⋆	-	⋆	-	-
	B × D	⋆	⋆	⋆	⋆	⋆	⋆	⋆	⋆	⋆	-	⋆	⋆	⋆	⋆	⋆	⋆	⋆
	C × D	⋆	⋆	⋆	⋆	⋆	⋆	⋆	⋆	⋆	-	⋆	⋆	⋆	⋆	⋆	⋆	⋆
	A × B × C	⋆	⋆	-	-	-	-	-	-	-	-	-	-	-	-	⋆	⋆	-
	A × B × D	⋆	⋆	⋆	⋆	⋆	⋆	⋆	-	⋆	-	⋆	⋆	⋆	-	⋆	-	-
	A × C × D	⋆	⋆	⋆	⋆	⋆	⋆	⋆	-	⋆	-	⋆	⋆	⋆	-	⋆	-	-
	B × C × D	⋆	⋆	⋆	⋆	-	-	-	-	-	-	-	-	-	⋆	⋆	⋆	⋆

Continued on next page

Table 6.9 – continued from previous page

Algorithm	Interaction	Indices																
		VLF	LF	HF	TP	nLF	nHF	LF/HF	cLF_x	cLF_y	cHF_x	cHF_y	cTP_x	cTP_y	XC lags	XC max	XC Spearman	XC Pearson
	A × B × C × D	-	-	-	-	-	-	-	-	-	-	-	-	-	-	-	-	-
PBURG	A	⋆	⋆	⋆	⋆	⋆	⋆	⋆	⋆	⋆	⋆	⋆	⋆	⋆	⋆	⋆	⋆	⋆
	B	⋆	⋆	⋆	⋆	⋆	⋆	⋆	⋆	⋆	⋆	⋆	⋆	⋆	⋆	⋆	⋆	⋆
	C	⋆	⋆	⋆	⋆	⋆	⋆	⋆	⋆	⋆	⋆	⋆	⋆	⋆	⋆	⋆	⋆	⋆
	D	⋆	⋆	⋆	⋆	⋆	⋆	⋆	⋆	⋆	⋆	⋆	⋆	⋆	⋆	⋆	⋆	⋆
	A × B	⋆	⋆	⋆	⋆	⋆	⋆	⋆	-	⋆	-	-	-	⋆	⋆	⋆	⋆	⋆
	A × C	⋆	⋆	⋆	⋆	⋆	⋆	⋆	⋆	-	-	-	⋆	⋆	⋆	⋆	⋆	⋆
	B × C	⋆	⋆	⋆	⋆	-	-	-	-	-	-	-	-	-	⋆	⋆	⋆	⋆
	A × D	⋆	-	⋆	⋆	⋆	⋆	⋆	-	⋆	-	⋆	⋆	-	⋆	⋆	-	⋆
	B × D	⋆	⋆	⋆	⋆	⋆	⋆	⋆	⋆	⋆	-	⋆	-	⋆	⋆	⋆	⋆	⋆
	C × D	⋆	⋆	⋆	⋆	⋆	⋆	⋆	⋆	⋆	-	⋆	⋆	⋆	⋆	⋆	⋆	⋆
	A × B × C	⋆	⋆	-	-	-	-	-	-	-	-	-	-	-	⋆	⋆	⋆	⋆
	A × B × D	⋆	-	-	-	-	⋆	⋆	-	-	-	-	-	⋆	⋆	-	-	⋆
	A × C × D	⋆	-	-	-	⋆	⋆	⋆	-	⋆	-	-	-	⋆	⋆	-	⋆	⋆
	B × C × D	⋆	⋆	⋆	⋆	-	-	-	-	-	-	-	-	-	⋆	⋆	⋆	⋆
	A × B × C × D	-	-	-	-	-	-	-	-	-	-	-	-	-	⋆	-	⋆	⋆
PCOV	A	⋆	⋆	⋆	⋆	⋆	⋆	⋆	⋆	⋆	⋆	-	⋆	⋆	⋆	⋆	⋆	⋆
	B	⋆	⋆	⋆	⋆	⋆	⋆	⋆	⋆	⋆	⋆	⋆	⋆	⋆	⋆	⋆	⋆	⋆
	C	⋆	⋆	⋆	⋆	⋆	⋆	⋆	⋆	⋆	⋆	⋆	⋆	⋆	⋆	⋆	⋆	⋆
	D	⋆	⋆	⋆	⋆	⋆	⋆	⋆	⋆	⋆	⋆	⋆	⋆	⋆	⋆	⋆	⋆	⋆
	A × B	⋆	⋆	⋆	⋆	⋆	⋆	⋆	-	⋆	-	-	-	⋆	⋆	⋆	⋆	⋆
	A × C	⋆	⋆	⋆	⋆	⋆	⋆	⋆	⋆	-	-	-	⋆	⋆	⋆	⋆	⋆	⋆
	B × C	⋆	⋆	⋆	⋆	-	-	-	-	-	-	-	-	-	⋆	⋆	⋆	⋆
	A × D	⋆	⋆	⋆	⋆	⋆	⋆	⋆	-	⋆	-	-	⋆	-	⋆	⋆	-	⋆
	B × D	⋆	⋆	⋆	⋆	⋆	⋆	⋆	⋆	⋆	-	⋆	⋆	⋆	⋆	⋆	⋆	⋆
	C × D	⋆	⋆	⋆	⋆	⋆	⋆	⋆	⋆	⋆	-	⋆	⋆	⋆	⋆	⋆	⋆	⋆
	A × B × C	⋆	⋆	-	-	-	-	-	-	-	-	-	-	-	⋆	⋆	⋆	⋆
	A × B × D	⋆	-	-	-	⋆	⋆	⋆	-	-	-	-	-	⋆	⋆	-	-	⋆
	A × C × D	⋆	-	-	-	⋆	⋆	⋆	-	⋆	-	-	-	⋆	⋆	-	⋆	⋆
	B × C × D	⋆	⋆	⋆	⋆	-	-	-	-	-	-	-	-	-	⋆	⋆	⋆	⋆
	A × B × C × D	-	-	-	-	-	-	-	-	-	-	-	-	-	⋆	-	⋆	⋆
	A	⋆	⋆	⋆	⋆	⋆	⋆	⋆	⋆	⋆	⋆	-	⋆	⋆	⋆	⋆	⋆	⋆

Continued on next page

Table 6.9 – continued from previous page

Algorithm	Interaction	Indices																
		VLF	LF	HF	TP	nLF	nHF	LF/HF	cLF_x	cLF_y	cHF_x	cHF_y	cTP_x	cTP_y	XC lags	XC max	XC Spearman	XC Pearson
PMCOV	B	⋆	⋆	⋆	⋆	⋆	⋆	⋆	⋆	⋆	⋆	⋆	⋆	⋆	⋆	⋆	⋆	⋆
	C	⋆	⋆	⋆	⋆	⋆	⋆	⋆	⋆	⋆	⋆	⋆	⋆	⋆	⋆	⋆	⋆	⋆
	D	⋆	⋆	⋆	⋆	⋆	⋆	⋆	⋆	⋆	⋆	⋆	⋆	⋆	⋆	⋆	⋆	⋆
	A × B	⋆	⋆	⋆	⋆	⋆	⋆	⋆	-	⋆	-	-	-	⋆	⋆	⋆	⋆	⋆
	A × C	⋆	⋆	⋆	⋆	⋆	⋆	⋆	⋆	-	-	-	⋆	⋆	⋆	⋆	⋆	⋆
	B × C	⋆	⋆	⋆	⋆	-	-	-	-	-	-	-	-	-	⋆	⋆	⋆	⋆
	A × D	⋆	-	⋆	⋆	⋆	⋆	⋆	-	⋆	-	-	⋆	-	⋆	⋆	-	⋆
	B × D	⋆	⋆	⋆	⋆	⋆	⋆	⋆	⋆	⋆	-	⋆	⋆	⋆	⋆	⋆	⋆	⋆
	C × D	⋆	⋆	⋆	⋆	⋆	⋆	⋆	⋆	⋆	-	⋆	⋆	⋆	⋆	⋆	⋆	⋆
	A × B × C	⋆	⋆	-	-	-	-	-	-	-	-	-	-	-	⋆	⋆	⋆	⋆
	A × B × D	⋆	-	-	-	-	⋆	⋆	-	-	-	-	-	⋆	⋆	⋆	-	-	⋆
	A × C × D	⋆	-	-	-	⋆	⋆	⋆	-	-	-	-	-	⋆	⋆	⋆	-	⋆	⋆
	B × C × D	⋆	⋆	⋆	⋆	-	-	-	-	-	-	-	-	-	⋆	⋆	⋆	⋆
	A × B × C × D	-	-	-	-	-	-	-	-	-	-	-	-	-	⋆	-	⋆	⋆
PMUSIC	A	⋆	⋆	⋆	⋆	⋆	⋆	⋆	⋆	⋆	-	⋆	⋆	⋆	⋆	⋆	⋆	⋆
	B	⋆	⋆	⋆	⋆	⋆	⋆	⋆	⋆	⋆	⋆	⋆	⋆	⋆	⋆	⋆	⋆	⋆
	C	⋆	⋆	⋆	⋆	⋆	⋆	⋆	⋆	⋆	⋆	⋆	⋆	⋆	⋆	⋆	⋆	⋆
	D	⋆	⋆	⋆	⋆	⋆	⋆	⋆	⋆	⋆	⋆	⋆	⋆	⋆	⋆	⋆	⋆	⋆
	A × B	⋆	⋆	⋆	⋆	⋆	⋆	⋆	-	⋆	-	⋆	⋆	⋆	⋆	⋆	⋆	⋆
	A × C	⋆	⋆	⋆	⋆	⋆	⋆	⋆	⋆	⋆	-	⋆	⋆	⋆	⋆	⋆	⋆	⋆
	B × C	⋆	⋆	⋆	⋆	-	⋆	⋆	-	-	-	⋆	-	⋆	⋆	⋆	⋆	⋆
	A × D	⋆	⋆	⋆	⋆	⋆	⋆	⋆	⋆	⋆	-	⋆	⋆	⋆	⋆	⋆	⋆	⋆
	B × D	⋆	⋆	⋆	⋆	⋆	⋆	⋆	⋆	⋆	-	⋆	⋆	⋆	⋆	⋆	⋆	⋆
	C × D	⋆	⋆	⋆	⋆	⋆	⋆	⋆	⋆	⋆	-	⋆	⋆	⋆	⋆	⋆	⋆	⋆
	A × B × C	-	⋆	-	-	-	-	-	-	-	-	-	-	-	-	-	⋆	⋆
	A × B × D	⋆	⋆	⋆	⋆	-	⋆	⋆	-	⋆	-	⋆	-	⋆	⋆	⋆	-	⋆
	A × C × D	⋆	⋆	⋆	⋆	-	⋆	⋆	-	-	-	⋆	⋆	⋆	-	⋆	-	-
	B × C × D	⋆	⋆	⋆	⋆	-	-	-	-	-	-	-	-	⋆	⋆	⋆	⋆	⋆
	A × B × C × D	-	-	-	-	-	-	-	-	-	-	-	-	-	⋆	-	⋆	⋆

It can be observed that the behaviour of indices extracted from excellent and acceptable quality PPG signals is, in general, very similar. Also, in all cases, except

for PWELCH and FFT, the features that showed a significant interaction among all factors were related to correlation between spectra. In the case of FFT and PWELCH, HF for excellent, and TP both for excellent and acceptable quality PPG signals showed significant interaction among the three factors (A × B × C). Also for these two methods, the number of data points used for spectral analysis and the sampling rate used for interpolation (B × C) were the factors with the largest amount of indices showing significant interaction. This shows the importance of choosing an appropriate frequency resolution for frequency-domain analysis of PRV when this is performed using classical methods.

Table 6.10: Summary of results from factorial analyses performed to evaluate the effects of interactions among factors altered for spectral analysis of pulse rate variability obtained from acceptable quality photoplethysmographic signals. A: Type of interpolation used; B: Number of data points used for obtaining the spectrum; C: Sampling rate used for interpolation; D: Order of the model. ⋆: Significant interaction or factor. -: Non-significant interaction or factor.

Algorithm	**Interaction**	**Indices**																
		VLF	LF	HF	TP	nLF	nHF	LF/HF	cLF_x	cLF_y	cHF_x	cHF_y	cTP_x	cTP_y	XC lags	XC max	XC Spearman	XC Pearson
FFT	A	-	-	⋆	⋆	⋆	⋆	⋆	-	-	-	⋆	-	-	⋆	⋆	-	-
	B	⋆	⋆	⋆	⋆	-	-	-	-	-	-	-	-	⋆	⋆	⋆	⋆	⋆
	C	⋆	⋆	⋆	⋆	-	-	-	-	-	-	-	-	⋆	⋆	⋆	⋆	⋆
	A × B	-	-	⋆	-	-	-	-	-	-	-	-	-	-	-	-	-	-
	A × C	-	-	-	-	-	-	-	-	-	-	-	-	-	-	-	-	-
	B × C	⋆	⋆	⋆	⋆	-	-	-	-	-	-	-	-	-	⋆	⋆	⋆	⋆
	A × B × C	-	-	-	⋆	-	-	-	-	-	-	-	-	-	⋆	-	-	-
PWELCH	A	-	-	⋆	-	⋆	⋆	⋆	-	-	-	⋆	-	-	⋆	⋆	⋆	-
	B	⋆	⋆	⋆	⋆	-	-	-	-	⋆	-	-	-	-	⋆	⋆	⋆	⋆
	C	⋆	⋆	⋆	⋆	-	-	-	-	-	-	-	-	-	⋆	⋆	⋆	⋆
	A × B	-	-	-	-	-	-	-	-	-	-	-	-	-	-	-	-	-
	A × C	-	-	-	-	-	-	-	-	-	-	-	-	-	-	-	-	-
	B × C	⋆	⋆	⋆	-	-	-	-	-	-	-	-	-	-	⋆	⋆	⋆	⋆
	A × B × C	-	-	-	-	-	-	-	-	-	-	-	-	-	⋆	-	⋆	-
PYULEAR	A	⋆	⋆	⋆	⋆	⋆	⋆	⋆	-	⋆	-	⋆	⋆	⋆	-	⋆	⋆	⋆
	B	⋆	⋆	⋆	⋆	⋆	⋆	⋆	⋆	⋆	⋆	⋆	⋆	⋆	⋆	⋆	⋆	⋆
	C	⋆	⋆	⋆	⋆	⋆	⋆	⋆	⋆	⋆	⋆	⋆	⋆	⋆	⋆	⋆	⋆	⋆
	D	⋆	⋆	⋆	⋆	⋆	-	⋆	-	⋆	⋆	⋆	⋆	⋆	⋆	⋆	⋆	⋆

Continued on next page

Table 6.10 – continued from previous page

Algorithm	Interaction	VLF	LF	HF	TP	nLF	nHF	LF/HF	cLF_x	cLF_y	cHF_x	cHF_y	cTP_x	cTP_y	XC lags	XC max	XC Spearman	XC Pearson
PYULEAR	A × B	⋆	⋆	⋆	⋆	⋆	⋆	⋆	-	⋆	-	⋆	⋆	⋆	-	⋆	⋆	⋆
	A × C	⋆	⋆	⋆	⋆	⋆	⋆	⋆	-	⋆	-	⋆	⋆	⋆	-	⋆	-	⋆
	B × C	⋆	⋆	⋆	⋆	-	-	-	-	-	-	-	-	-	⋆	⋆	⋆	⋆
	A × D	⋆	⋆	⋆	⋆	⋆	-	⋆	-	⋆	-	⋆	⋆	⋆	-	⋆	-	-
	B × D	⋆	⋆	⋆	⋆	⋆	-	⋆	-	⋆	-	⋆	⋆	⋆	⋆	⋆	⋆	⋆
	C × D	⋆	⋆	⋆	⋆	⋆	-	⋆	-	⋆	-	⋆	⋆	⋆	⋆	⋆	⋆	⋆
	A × B × C	⋆	⋆	-	-	-	-	-	-	-	-	-	-	-	-	⋆	⋆	⋆
	A × B × D	⋆	⋆	⋆	⋆	⋆	-	⋆	-	⋆	-	⋆	⋆	⋆	-	⋆	-	⋆
	A × C × D	⋆	⋆	⋆	⋆	⋆	-	⋆	-	⋆	-	⋆	⋆	⋆	-	⋆	-	⋆
	B × C × D	⋆	⋆	⋆	⋆	-	-	-	-	-	-	-	-	-	⋆	⋆	⋆	⋆
	A × B × C × D	-	-	-	-	-	-	-	-	-	-	-	-	-	-	-	-	⋆
PBURG	A	⋆	⋆	⋆	⋆	-	⋆	⋆	⋆	⋆	⋆	-	⋆	⋆	⋆	⋆	⋆	⋆
	B	⋆	⋆	⋆	⋆	⋆	⋆	⋆	⋆	⋆	⋆	⋆	⋆	⋆	⋆	⋆	⋆	⋆
	C	⋆	⋆	⋆	⋆	⋆	⋆	⋆	⋆	⋆	⋆	⋆	⋆	⋆	⋆	⋆	⋆	⋆
	D	⋆	⋆	⋆	⋆	⋆	⋆	⋆	⋆	⋆	⋆	⋆	⋆	⋆	⋆	⋆	⋆	⋆
	A × B	⋆	⋆	⋆	⋆	-	⋆	⋆	-	-	-	-	-	⋆	⋆	⋆	⋆	⋆
	A × C	⋆	⋆	⋆	⋆	-	⋆	⋆	⋆	-	-	-	⋆	⋆	⋆	⋆	⋆	⋆
	B × C	⋆	⋆	⋆	⋆	-	-	-	-	-	-	-	-	-	⋆	⋆	⋆	⋆
	A × D	⋆	-	⋆	⋆	-	⋆	⋆	-	⋆	-	-	⋆	-	⋆	⋆	-	⋆
	B × D	⋆	⋆	⋆	⋆	⋆	⋆	⋆	⋆	⋆	-	⋆	-	⋆	⋆	⋆	⋆	⋆
	C × D	⋆	⋆	⋆	⋆	⋆	⋆	⋆	⋆	⋆	-	⋆	⋆	⋆	⋆	⋆	⋆	⋆
	A × B × C	⋆	⋆	-	-	-	-	-	-	-	-	-	-	-	⋆	⋆	⋆	⋆
	A × B × D	⋆	-	-	-	-	⋆	⋆	-	-	-	-	-	⋆	⋆	-	-	⋆
	A × C × D	⋆	-	-	-	-	⋆	⋆	-	⋆	-	-	-	⋆	⋆	-	⋆	⋆
	B × C × D	⋆	⋆	⋆	⋆	-	-	-	-	-	-	-	-	-	⋆	⋆	⋆	⋆
	A × B × C × D	-	-	-	-	-	-	-	-	-	-	-	-	-	⋆	-	⋆	⋆
PCOV	A	⋆	⋆	⋆	⋆	⋆	⋆	⋆	⋆	⋆	⋆	-	⋆	⋆	⋆	⋆	⋆	⋆
	B	⋆	⋆	⋆	⋆	⋆	⋆	⋆	⋆	⋆	⋆	⋆	⋆	⋆	⋆	⋆	⋆	⋆
	C	⋆	⋆	⋆	⋆	⋆	⋆	⋆	⋆	⋆	⋆	⋆	⋆	⋆	⋆	⋆	⋆	⋆
	D	⋆	⋆	⋆	⋆	⋆	⋆	⋆	⋆	⋆	⋆	⋆	⋆	⋆	⋆	⋆	⋆	⋆
	A × B	⋆	⋆	⋆	⋆	⋆	⋆	⋆	-	-	-	-	-	⋆	⋆	⋆	⋆	⋆
	A × C	⋆	⋆	⋆	⋆	⋆	⋆	⋆	⋆	-	-	-	⋆	⋆	⋆	⋆	⋆	⋆

Continued on next page

Table 6.10 – continued from previous page

Algorithm	Interaction	Indices																
		VLF	LF	HF	TP	nLF	nHF	LF/HF	cLF_x	cLF_y	cHF_x	cHF_y	cTP_x	cTP_y	XC lags	XC max	XC Spearman	XC Pearson
PCOV	B × C	⋆	⋆	⋆	⋆	-	-	-	-	-	-	-	-	-	⋆	⋆	⋆	⋆
	A × D	⋆	⋆	⋆	⋆	⋆	⋆	⋆	-	⋆	-	-	⋆	-	⋆	⋆	-	⋆
	B × D	⋆	⋆	⋆	⋆	⋆	⋆	⋆	⋆	⋆	-	⋆	-	⋆	⋆	⋆	⋆	⋆
	C × D	⋆	⋆	⋆	⋆	⋆	⋆	⋆	⋆	⋆	-	⋆	⋆	⋆	⋆	⋆	⋆	⋆
	A × B × C	⋆	⋆	-	-	-	-	-	-	-	-	-	-	-	⋆	⋆	⋆	⋆
	A × B × D	⋆	-	-	-	-	⋆	⋆	-	-	-	-	-	⋆	⋆	-	-	⋆
	A × C × D	⋆	-	-	-	⋆	⋆	⋆	-	⋆	-	-	-	⋆	⋆	-	⋆	⋆
	B × C × D	⋆	⋆	⋆	⋆	-	-	-	-	-	-	-	-	-	⋆	⋆	⋆	⋆
	A × B × C × D	-	-	-	-	-	-	-	-	-	-	-	-	-	⋆	-	-	⋆
PMCOV	A	⋆	⋆	⋆	⋆	⋆	⋆	⋆	⋆	⋆	⋆	-	⋆	⋆	⋆	⋆	⋆	⋆
	B	⋆	⋆	⋆	⋆	⋆	⋆	⋆	⋆	⋆	⋆	⋆	⋆	⋆	⋆	⋆	⋆	⋆
	C	⋆	⋆	⋆	⋆	⋆	⋆	⋆	⋆	⋆	⋆	⋆	⋆	⋆	⋆	⋆	⋆	⋆
	D	⋆	⋆	⋆	⋆	⋆	⋆	⋆	⋆	⋆	⋆	⋆	⋆	⋆	⋆	⋆	⋆	⋆
	A × B	⋆	⋆	⋆	⋆	⋆	⋆	⋆	-	-	-	-	-	⋆	⋆	⋆	⋆	⋆
	A × C	⋆	⋆	⋆	⋆	⋆	⋆	⋆	⋆	-	-	-	⋆	⋆	⋆	⋆	⋆	⋆
	B × C	⋆	⋆	⋆	⋆	-	-	-	-	-	-	-	-	-	⋆	⋆	⋆	⋆
	A × D	⋆	⋆	⋆	⋆	⋆	⋆	⋆	-	⋆	-	-	⋆	-	⋆	⋆	-	⋆
	B × D	⋆	⋆	⋆	⋆	⋆	⋆	⋆	⋆	⋆	-	⋆	-	⋆	⋆	⋆	⋆	⋆
	C × D	⋆	⋆	⋆	⋆	⋆	⋆	⋆	⋆	⋆	-	⋆	⋆	⋆	⋆	⋆	⋆	⋆
	A × B × C	⋆	⋆	-	-	-	-	-	-	-	-	-	-	-	⋆	⋆	⋆	⋆
	A × B × D	⋆	-	-	-	-	⋆	⋆	-	-	-	-	-	⋆	⋆	-	-	⋆
	A × C × D	⋆	-	-	-	⋆	⋆	⋆	-	⋆	-	-	-	⋆	⋆	-	⋆	⋆
	B × C × D	⋆	⋆	⋆	⋆	-	-	-	-	-	-	-	-	-	⋆	⋆	⋆	⋆
	A × B × C × D	-	-	-	-	-	-	-	-	-	-	-	-	-	⋆	-	-	⋆
PMUSIC	A	⋆	⋆	-	⋆	⋆	⋆	⋆	⋆	⋆	-	⋆	⋆	⋆	⋆	⋆	-	⋆
	B	⋆	⋆	⋆	⋆	⋆	⋆	⋆	⋆	⋆	⋆	⋆	⋆	⋆	⋆	⋆	⋆	⋆
	C	⋆	⋆	⋆	⋆	⋆	⋆	⋆	⋆	⋆	⋆	⋆	⋆	⋆	⋆	⋆	⋆	⋆
	D	⋆	⋆	⋆	⋆	⋆	⋆	⋆	⋆	⋆	⋆	⋆	⋆	⋆	⋆	⋆	⋆	⋆
	A × B	⋆	⋆	-	⋆	⋆	⋆	⋆	⋆	⋆	-	⋆	⋆	⋆	⋆	⋆	-	⋆
	A × C	⋆	⋆	-	⋆	⋆	⋆	⋆	⋆	⋆	-	⋆	⋆	⋆	⋆	⋆	-	⋆
	B × C	⋆	⋆	⋆	⋆	-	⋆	⋆	-	-	-	⋆	-	⋆	⋆	⋆	⋆	⋆
	A × D	⋆	⋆	-	⋆	⋆	⋆	⋆	⋆	⋆	-	⋆	⋆	⋆	⋆	⋆	-	⋆

Continued on next page

Table 6.10 – continued from previous page

Algorithm	Interaction	VLF	LF	HF	TP	nLF	nHF	LF/HF	cLF_x	cLF_y	cHF_x	cHF_y	cTP_x	cTP_y	XC lags	XC max	XC Spearman	XC Pearson
PMUSIC	B × D	⋆	⋆	⋆	⋆	⋆	⋆	⋆	⋆	⋆	-	⋆	⋆	⋆	⋆	⋆	⋆	⋆
	C × D	⋆	⋆	⋆	⋆	⋆	⋆	⋆	⋆	⋆	-	⋆	⋆	⋆	⋆	⋆	⋆	⋆
	A × B × C	-	⋆	-	-	-	-	-	-	-	-	-	-	-	-	-	-	⋆
	A × B × D	⋆	⋆	-	⋆	-	⋆	⋆	-	⋆	-	⋆	⋆	⋆	⋆	⋆	-	⋆
	A × C × D	⋆	⋆	-	⋆	-	⋆	⋆	-	-	-	⋆	⋆	⋆	-	⋆	-	⋆
	B × C × D	⋆	⋆	⋆	⋆	-	-	-	-	-	-	-	-	⋆	⋆	⋆	⋆	⋆
	A × B × C × D	-	-	-	-	-	-	-	-	-	-	-	-	-	⋆	-	-	⋆

In the case of modern methods, the behaviour is not as clear, since each method showed different significant interactions. In the case of PYULEAR and PMUSIC, the interactions between the type of interpolation used, the number of data points and the order of the model (A × B × D), as well as the interactions between the type of interpolation, the sampling rate used and the order of the model (A × C × D) were significant in the majority of the indices, while for PBURG, PCOV and PMCOV the maximum level of significance for most of the indices was with two-factor interactions.

The best combination of factors that gave the lowest difference for the measurement of each of the PRV indices, as well as those that delivered maximal cross correlation to gold standard spectra were determined for each of the methods that allowed the selection of parameters, both for excellent and acceptable quality PPG signals (Tables 6.11 and 6.12, respectively). Once the best combinations were identified for each of the methods, these and the results obtained using the Lomb-Scargle periodogram were compared using a Kruskal-Wallis one-way analysis of variance for each index. Table 6.13 summarises these results. Figures 6.19 to 6.21 show the mean and standard deviation of the differences of frequency-domain indices obtained between gold standard and measured PRV trends, considering the best combinations of factors for each spectral analysis method, while Figure 6.22 summarise the correlation results after comparing gold standard and measured PRV spectra. The best spectral analysis should have minimal differences to gold standard results, while achieving maximal correlation results.

Table 6.11: Combinations of factors that delivered the lowest differences between indices or the maximal cross-correlation between gold-standard and measured spectra, from pulse rate variability extracted from excellent quality photoplethysmographic signals. A: Type of interpolation used; B: Number of data points used for obtaining the spectrum; C: Sampling rate used for interpolation; D: Order of the model.

Index	FFT	PWELCH	PYULEAR	PBURG	PCOV	PMCOV	PMUSIC
VLF	A: Spline	A: Spline	A: Spline	A: Spline	A: Spline	A: Spline	A: Spline
	B: 32768	B: 512	B: 512	B: 512	B: 512	B: 512	B: 512
	C: 256	C: 4	C: 4	C: 4	C: 4	C: 4	C: 4
			D: 50	D: 50	D: 50	D: 50	D: 50
LF	A: Linear	A: Linear	A: Linear	A: Linear	A: Linear	A: Linear	A: Linear
	B: 512	B: 8192	B: 512	B: 512	B: 512	B: 512	B: 512
	C: 4	C: 64	C: 4	C: 4	C: 4	C: 4	C: 4
			D: 50	D: 50	D: 50	D: 50	D: 25
HF	A: Spline	A: Spline	A: Spline	A: Spline	A: Spline	A: Spline	A: Spline
	B: 512	B: 2048	B: 512	B: 512	B: 512	B: 512	B: 512
	C: 4	C: 16	C: 4	C: 4	C: 4	C: 4	C: 4
			D: 50	D: 50	D: 50	D: 50	D: 40

Continued on next page

Table 6.11 – continued from previous page

Index	FFT	PWELCH	PYULEAR	PBURG	PCOV	PMCOV	PMUSIC
TP	A: Spline	A: Spline	A: Spline	A: Spline	A: Spline	A: Spline	A: Linear
	B: 32768	B: 2048	B: 512	B: 512	B: 512	B: 512	B: 512
	C: 256	C: 16	C: 4	C: 4	C: 4	C: 4	C: 4
			D: 50	D: 50	D: 50	D: 50	D: 40
nLF	A: Spline	A: Spline	A: Linear	A: Spline	A: Spline	A: Spline	A: Linear
	B: 512	B: 65536	B: 262144	B: 131072	B: 131072	B: 131072	B: 32768
	C: 4	C: 4	C: 256	C: 128	C: 128	C: 128	C: 32
			D: 5	D: 5	D: 5	D: 5	D: 5
nHF	A: Spline	A: Spline	A: Spline	A: Spline	A: Spline	A: Spline	A: Linear
	B: 512	B: 65536	B: 16384	B: 16384	B: 16384	B: 16384	B: 8192
	C: 4	C: 4	C: 128	C: 128	C: 128	C: 128	C: 64
			D: 45	D: 5	D: 5	D: 5	D: 5
LF/HF	A: Spline	A: Spline	A: Spline	A: Spline	A: Spline	A: Spline	A: Linear
	B: 4194304	B: 2097152	B: 4096	B: 131072	B: 131072	B: 131072	B: 2048
	C: 256	C: 128	C: 4	C: 128	C: 128	C: 128	C: 16
			D: 5	D: 5	D: 5	D: 5	D: 5

Continued on next page

Table 6.11 – continued from previous page

Index	FFT	PWELCH	PYULEAR	PBURG	PCOV	PMCOV	PMUSIC
cLF_x	A: Spline	A: Spline	A: Linear	A: Linear	A: Linear	A: Linear	A: Spline
	B: 32768	B: 8192	B: 32768	B: 32768	B: 32768	B: 32768	B: 32768
	C: 256	C: 8	C: 32	C: 32	C: 32	C: 32	C: 32
			D: 45	D: 40	D: 40	D: 40	D: 25
cLF_y	A: Linear	A: Linear	A: Linear	A: Linear	A: Linear	A: Linear	A: Linear
	B: 16384	B: 2097152	B: 131072	B: 262144	B: 262144	B: 262144	B: 4096
	C: 128	C: 128	C: 128	C: 256	C: 256	C: 256	C: 32
			D: 15	D: 5	D: 5	D: 5	D: 5
cHF_x	A: Spline	A: Spline	A: Linear	A: Spline	A: Spline	A: Spline	A: Spline
	B: 512	B: 1024	B: 16384	B: 16384	B: 32768	B: 32768	B: 32768
	C: 4	C: 8	C: 128	C: 128	C: 256	C: 256	C: 256
			D: 5	D: 5	D: 5	D: 5	D: 15
cHF_y	A: Spline	A: Spline	A: Spline	A: Linear	A: Spline	A: Spline	A: Linear
	B: 8192	B: 8192	B: 16384	B: 262144	B: 4096	B: 4096	B: 262144
	C: 8	C: 8	C: 16	C: 256	C: 32	C: 32	C: 256
			D: 5	D: 10	D: 10	D: 10	D: 10

Continued on next page

Table 6.11 – continued from previous page

Index	FFT	PWELCH	PYULEAR	PBURG	PCOV	PMCOV	PMUSIC
cTP_x	A: Linear	A: Linear	A: Spline	A: Spline	A: Spline	A: Spline	A: Linear
	B: 65536	B: 8192	B: 32768	B: 32768	B: 32768	B: 32768	B: 131072
	C: 4	C: 8	C: 32	C: 256	C: 256	C: 256	C: 128
			D: 10	D: 5	D: 5	D: 5	D: 15
cTP_y	A: Linear	A: Linear	A: Spline	A: Linear	A: Linear	A: Linear	A: Linear
	B: 2048	B: 16384	B: 2048	B: 2048	B: 2048	B: 8192	B: 524288
	C: 16	C: 128	C: 16	C: 16	C: 16	C: 64	C: 32
			D: 5	D: 15	D: 15	D: 50	D: 5
XC lags	A: Spline	A: Spline	A: Spline	A: Spline	A: Spline	A: Spline	A: Linear
	B: 4096	B: 16384	B: 2048	B: 1024	B: 2048	B: 1024	B: 262144
	C: 32	C: 128	C: 16	C: 8	C: 16	C: 8	C: 256
			D: 45	D: 20	D: 30	D: 20	D: 5
XC max	A: Spline	A: Spline	A: Linear	A: Linear	A: Linear	A: Linear	A: Linear
	B: 65536	B: 131072	B: 2097152	B: 2097152	B: 2097152	B: 2097152	B: 4194304
	C: 4	C: 8	C: 128	C: 128	C: 128	C: 128	C: 256
			D: 35	D: 25	D: 25	D: 25	D: 15

Continued on next page

Table 6.11 – continued from previous page

Index	FFT	PWELCH	PYULEAR	PBURG	PCOV	PMCOV	PMUSIC
XC Spearman	A: Linear	A: Linear	A: Linear	A: Linear	A: Linear	A: Linear	A: Spline
	B: 65536	B: 65536	B: 65536	B: 65536	B: 65536	B: 65536	B: 65536
	C: 4	C: 4	C: 4	C: 4	C: 4	C: 4	C: 4
			D: 40	D: 40	D: 35	D: 35	D: 15
XC Pearson	A: Linear	A: Linear	A: Linear	A: Linear	A: Linear	A: Linear	A: Linear
	B: 65536	B: 2097152	B: 65536	B: 65536	B: 65536	B: 65536	B: 65536
	C: 4	C: 128	C: 4	C: 4	C: 4	C: 4	C: 4
			D: 50	D: 50	D: 50	D: 50	D: 50

Table 6.12: Combinations of factors that delivered the lowest differences between indices or the maximal cross-correlation between gold-standard and measured spectra, from pulse rate variability extracted from acceptable quality photoplethysmographic signals. A: Type of interpolation used; B: Number of data points used for obtaining the spectrum; C: Sampling rate used for interpolation; D: Order of the model.

Index	FFT	PWELCH	PYULEAR	PBURG	PCOV	PMCOV	PMUSIC
VLF	A: Spline	A: Spline	A: Spline	A: Spline	A: Spline	A: Spline	A: Spline
	B: 32768	B: 4096	B: 512	B: 512	B: 512	B: 512	B: 512
	C: 256	C: 32	C: 4	C: 4	C: 4	C: 4	C: 4
			D: 50	D: 50	D: 50	D: 50	D: 50
LF	A: Linear	A: Linear	A: Linear	A: Linear	A: Linear	A: Linear	A: Spline
	B: 1024	B: 8192	B: 512	B: 512	B: 512	B: 512	B: 1024
	C: 8	C: 64	C: 4	C: 4	C: 4	C: 4	C: 8
			D: 50	D: 50	D: 50	D: 50	D: 50
HF	A: Spline	A: Spline	A: Spline	A: Spline	A: Spline	A: Spline	A: Spline
	B: 512	B: 2048	B: 512	B: 512	B: 512	B: 512	B: 512
	C: 4	C: 16	C: 4	C: 4	C: 4	C: 4	C: 4
			D: 50	D: 50	D: 50	D: 50	D: 45

Continued on next page

Table 6.12continued from previous page

Index	FFT	PWELCH	PYULEAR	PBURG	PCOV	PMCOV	PMUSIC
TP	A: Spline	A: Spline	A: Spline	A: Spline	A: Spline	A: Spline	A: Spline
	B: 32768	B: 2048	B: 512	B: 512	B: 512	B: 512	B: 512
	C: 256	C: 16	C: 4	C: 4	C: 4	C: 4	C: 4
			D: 50	D: 50	D: 50	D: 50	D: 40
nLF	A: Spline	A: Spline	A: Linear	A: Spline	A: Spline	A: Spline	A: Linear
	B: 512	B: 4096	B: 262144	B: 131072	B: 131072	B: 131072	B: 32768
	C: 4	C: 4	C: 256	C: 128	C: 128	C: 128	C: 32
			D: 5	D: 5	D: 5	D: 5	D: 5
nHF	A: Spline	A: Spline	A: Spline	A: Spline	A: Spline	A: Spline	A: Linear
	B: 512	B: 1048576	B: 8192	B: 16384	B: 16384	B: 16384	B: 1048576
	C: 4	C: 64	C: 64	C: 128	C: 128	C: 128	C: 64
			D: 40	D: 5	D: 5	D: 5	D: 5
LF/HF	A: Spline	A: Spline	A: Spline	A: Spline	A: Spline	A: Spline	A: Linear
	B: 262144	B: 2097152	B: 4096	B: 131072	B: 131072	B: 131072	B: 4096
	C: 256	C: 128	C: 4	C: 128	C: 128	C: 128	C: 32
			D: 5	D: 5	D: 5	D: 5	D: 5

Continued on next page

Table 6.12continued from previous page

Index	FFT	PWELCH	PYULEAR	PBURG	PCOV	PMCOV	PMUSIC
cLF_x	A: Spline	A: Spline	A: Linear	A: Linear	A: Linear	A: Linear	A: Spline
	B: 32768	B: 8192	B: 32768	B: 32768	B: 32768	B: 32768	B: 32768
	C: 256	C: 8	C: 32	C: 32	C: 32	C: 32	C: 32
			D: 45	D: 40	D: 40	D: 40	D: 25
cLF_y	A: Linear	A: Linear	A: Linear	A: Linear	A: Linear	A: Linear	A: Linear
	B: 4096	B: 131072	B: 262144	B: 262144	B: 262144	B: 262144	B: 4096
	C: 32	C: 8	C: 256	C: 256	C: 256	C: 256	C: 32
			D: 25	D: 5	D: 5	D: 5	D: 5
cHF_x	A: Spline	A: Spline	A: Linear	A: Spline	A: Spline	A: Spline	A: Spline
	B: 512	B: 1024	B: 16384	B: 16384	B: 32768	B: 32768	B: 32768
	C: 4	C: 8	C: 128	C: 128	C: 256	C: 256	C: 256
			D: 5	D: 5	D: 5	D: 5	D: 15
cHF_y	A: Spline	A: Spline	A: Spline	A: Spline	A: Spline	A: Spline	A: Linear
	B: 4096	B: 8192	B: 16384	B: 32768	B: 32768	B: 32768	B: 262144
	C: 4	C: 8	C: 16	C: 32	C: 32	C: 32	C: 256
			D: 5	D: 10	D: 10	D: 10	D: 10

Continued on next page

Table 6.12continued from previous page

Index	FFT	PWELCH	PYULEAR	PBURG	PCOV	PMCOV	PMUSIC
cTP_x	A: Linear	A: Linear	A: Linear	A: Spline	A: Spline	A: Spline	A: Linear
	B: 65536	B: 8192	B: 16384	B: 32768	B: 32768	B: 32768	B: 131072
	C: 4	C: 8	C: 16	C: 256	C: 256	C: 256	C: 128
			D: 5	D: 5	D: 5	D: 5	D: 15
cTP_y	A: Linear	A: Linear	A: Spline	A: Linear	A: Linear	A: Linear	A: Linear
	B: 512	B: 16384	B: 2048	B: 2048	B: 2048	B: 2048	B: 524288
	C: 4	C: 128	C: 16	C: 16	C: 16	C: 16	C: 32
			D: 5	D: 35	D: 35	D: 35	D: 5
XC lags	A: Spline	A: Spline	A: Linear	A: Linear	A: Linear	A: Spline	A: Linear
	B: 1024	B: 16384	B: 16384	B: 8192	B: 8192	B: 2048	B: 262144
	C: 8	C: 128	C: 128	C: 64	C: 64	C: 16	C: 256
			D: 20	D: 10	D: 10	D: 20	D: 5
XC max	A: Spline	A: Spline	A: Linear	A: Linear	A: Linear	A: Linear	A: Linear
	B: 65536	B: 131072	B: 2097152	B: 2097152	B: 2097152	B: 2097152	B: 4194304
	C: 4	C: 8	C: 128	C: 128	C: 128	C: 128	C: 256
			D: 25	D: 25	D: 25	D: 25	D: 15

Continued on next page

Table 6.12continued from previous page

Index	FFT	PWELCH	PYULEAR	PBURG	PCOV	PMCOV	PMUSIC
XC Spearman	A: Linear	A: Linear	A: Linear	A: Linear	A: Linear	A: Linear	A: Spline
	B: 65536	B: 65536	B: 65536	B: 65536	B: 65536	B: 65536	B: 131072
	C: 4	C: 4	C: 4	C: 4	C: 4	C: 4	C: 8
			D: 40	D: 35	D: 50	D: 35	D: 15
XC Pearson	A: Linear	A: Linear	A: Linear	A: Linear	A: Linear	A: Linear	A: Linear
	B: 65536	B: 131072	B: 65536	B: 65536	B: 65536	B: 65536	B: 65536
	C: 4	C: 8	C: 4	C: 4	C: 4	C: 4	C: 4
			D: 50	D: 50	D: 50	D: 50	D: 45

Table 6.13: Summary of results obtained from the Kruskal-Wallis one-way analysis of variance and post-hoc comparisons. ⋆: Significant differences. -: Non-significant differences.

PPG quality	Index	Best results	Significant differences							
			FFT	PWELCH	PYULEAR	PBURG	PCOV	PMCOV	PMUSIC	PLOMB
Excellent	VLF	PMUSIC	-	-	-	-	-	-		⋆
	LF	PWELCH	-		⋆	⋆	⋆	⋆	⋆	⋆
	HF	FFT		⋆	⋆	⋆	⋆	⋆	⋆	⋆
	TP	FFT		⋆	⋆	⋆	⋆	⋆	⋆	⋆
	nLF	PMUSIC	⋆	⋆	-	⋆	⋆	⋆		⋆
	nHF	PMUSIC	⋆	⋆	⋆	⋆	⋆	⋆		⋆
	LF/HF	PMUSIC	⋆	⋆	⋆	⋆	⋆	⋆		⋆
	cLF_x	PMUSIC	-	-	-	-	-	-		-
	cLF_y	PCOV	⋆	⋆	-	-		-	-	⋆
	cHF_x	PMUSIC	-	-	-	-	-	-		-
	cHF_y	PYULEAR	⋆	⋆		⋆	-	-	-	⋆
	cTP_x	PMUSIC	⋆	⋆	-	-	-	-		⋆
	cTP_y	PMUSIC	⋆	⋆	-	-	-	-		⋆
	XC lags	PMUSIC	⋆	⋆	⋆	⋆	⋆	⋆		⋆
	XC max	PLOMB	⋆	⋆	⋆	⋆	⋆	⋆	⋆	
	Spearman	PCOV	⋆	⋆	-	-		-	-	-
	Pearson	PWELCH	⋆		-	-	-	-	⋆	-
Acceptable	VLF	PMUSIC	-	-	-	-	-	-		⋆
	LF	PWELCH	-		⋆	⋆	⋆	⋆	⋆	⋆
	HF	FFT		⋆	⋆	⋆	⋆	⋆	⋆	⋆
	TP	FFT		⋆	⋆	⋆	⋆	⋆	⋆	⋆
	nLF	PMUSIC	⋆	⋆	-	⋆	⋆	⋆		⋆
	nHF	PMUSIC	⋆	⋆	⋆	⋆	⋆	⋆		⋆
	LF/HF	PMUSIC	⋆	⋆	⋆	⋆	⋆	⋆		⋆
	cLF_x	PMUSIC	-	-	-	-	-	-		-
	cLF_y	PBURG	⋆	⋆	-		-	-	-	⋆
	cHF_x	PBURG	-	-	-		-	-	-	-
	cHF_y	PYULEAR	⋆	-		-	-	-	-	⋆
	cTP_x	PMUSIC	⋆	⋆	-	-	-	-		⋆
	cTP_y	PMUSIC	⋆	⋆	-	⋆	⋆	⋆		⋆
	XC lags	PMUSIC	⋆	⋆	⋆	⋆	⋆	⋆		⋆
	XC max	PLOMB	⋆	⋆	⋆	⋆	⋆	⋆	⋆	
	Spearman	PCOV	⋆	⋆	-	-		-	-	-
	Pearson	PWELCH	⋆		-	-	-	-	⋆	-

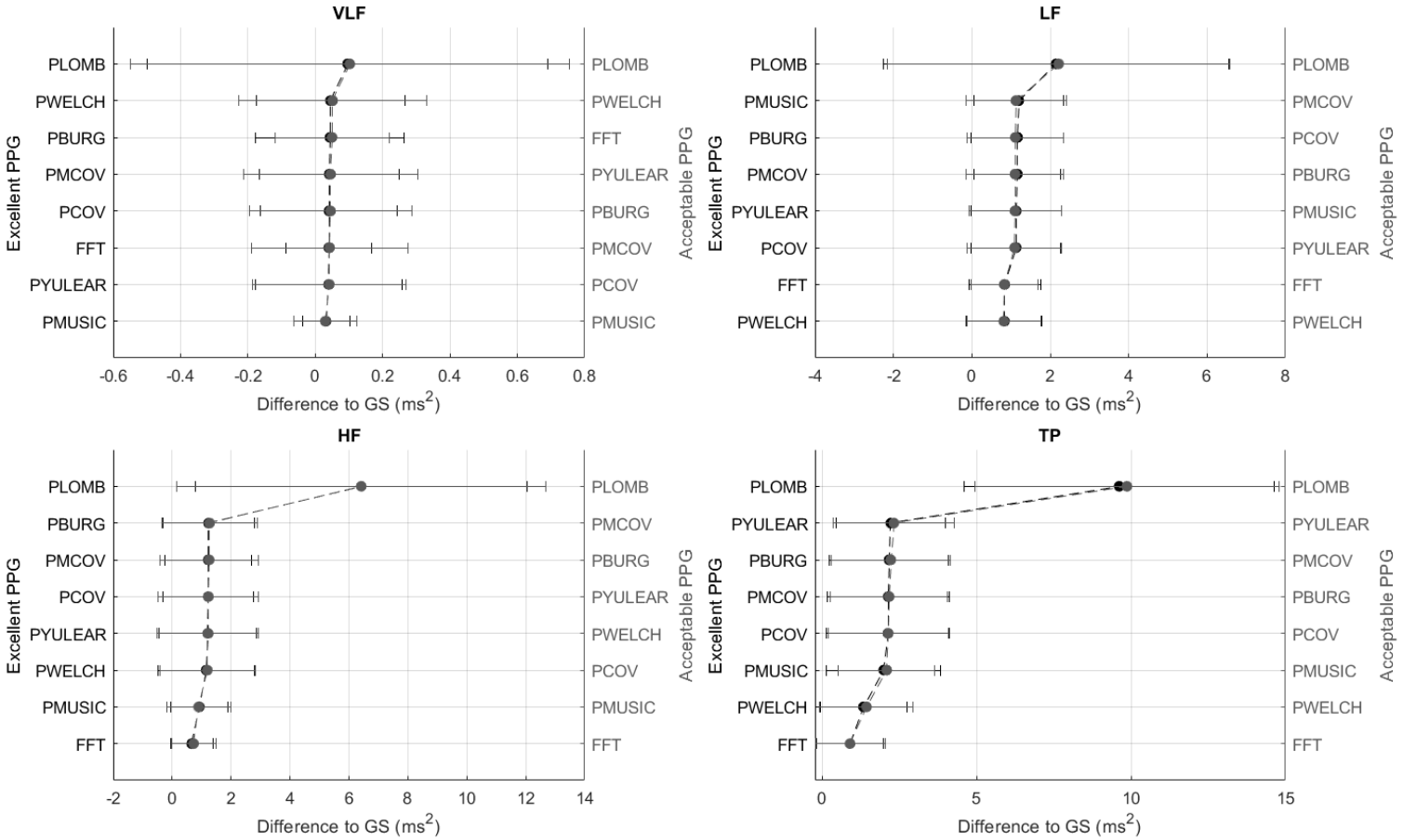

Figure 6.19: Mean and standard deviations of the differences obtained by comparing pulse rate variability absolute power frequency-domain indices obtained from extracted and gold standard trends. Differences are greater when Lomb-Scargle algorithm is used.

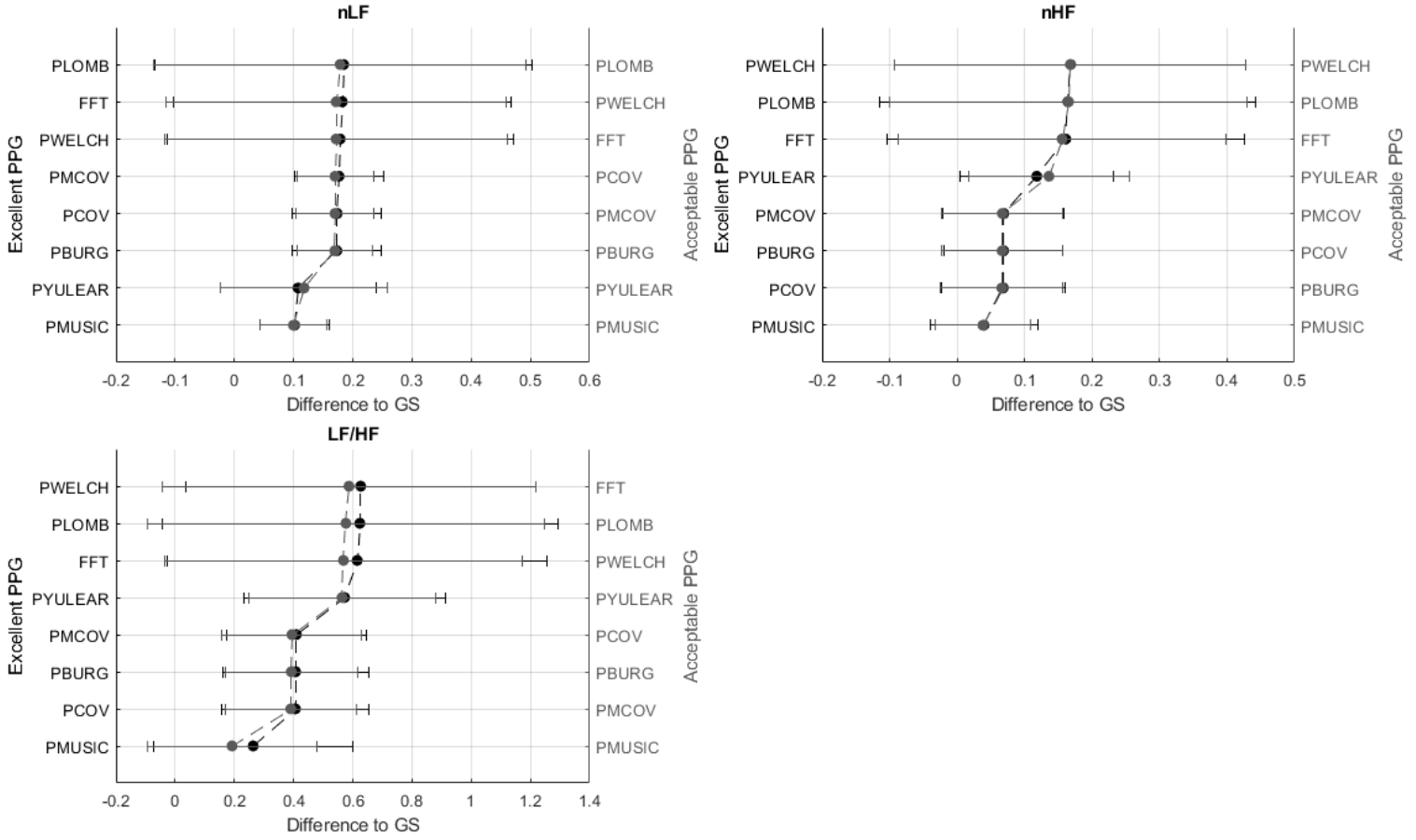

Figure 6.20: Mean and standard deviations of the differences obtained by comparing pulse rate variability relative power frequency-domain indices obtained from extracted and gold standard trends. Differences are greater when Lomb-Scargle or Welch algorithms are used.

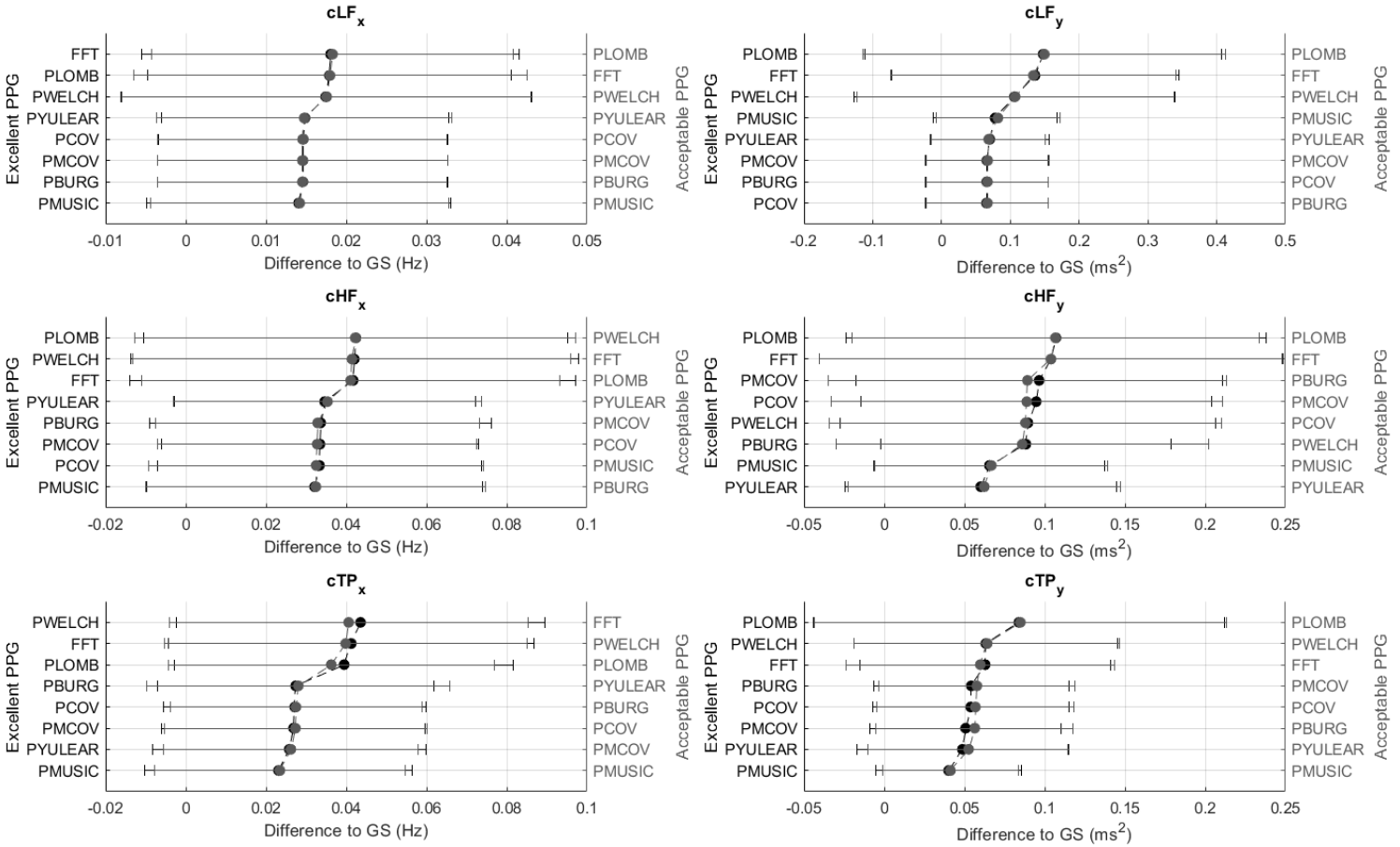

Figure 6.21: Mean and standard deviations of the differences obtained by comparing pulse rate variability centroid-related frequency-domain indices obtained from extracted and gold standard trends.Differences are greater mostly when Lomb-Scargle algorithm is used.

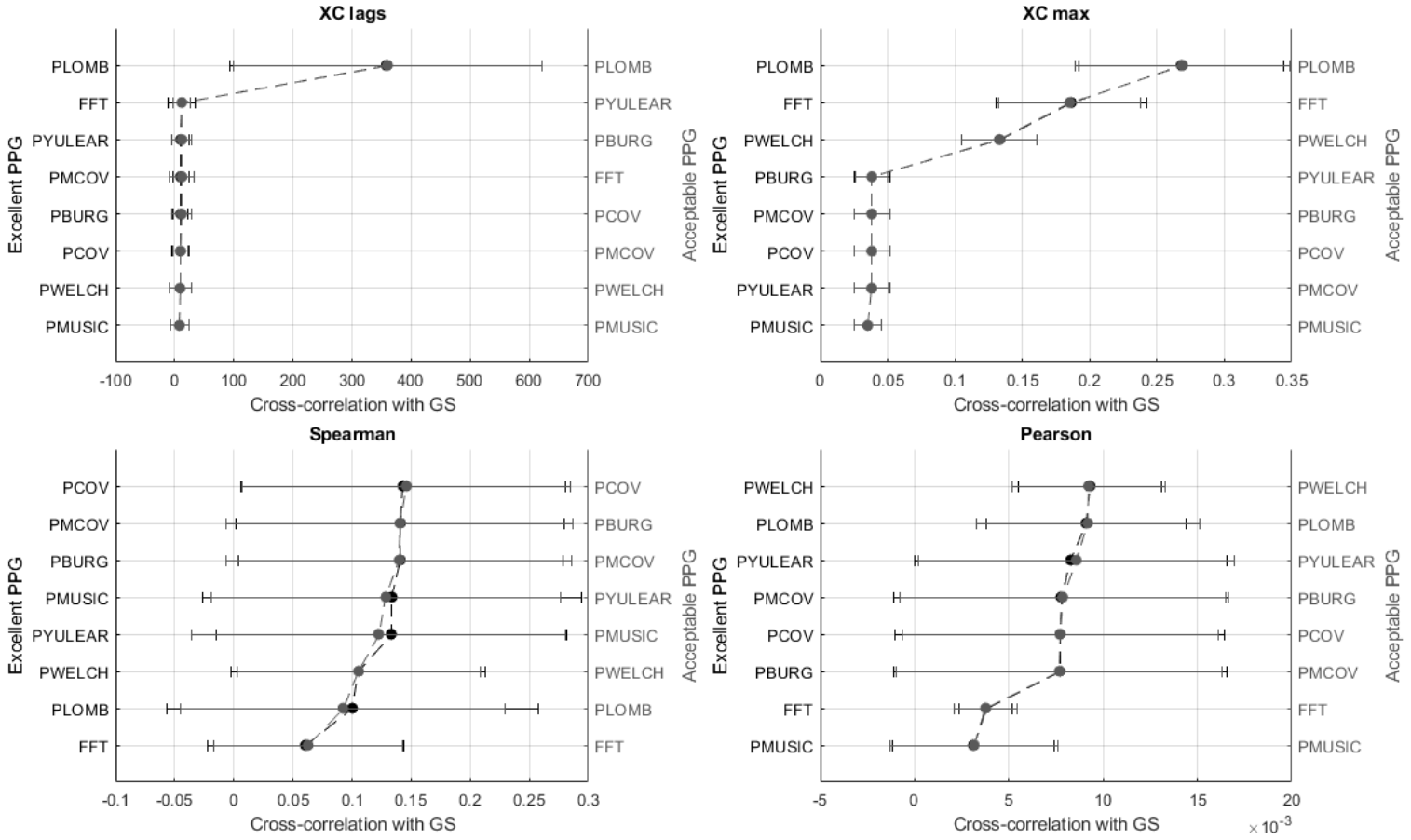

Figure 6.22: Mean and standard deviations of the correlation results obtained by comparing pulse rate variability spectra obtained from extracted and gold standard trends. Maximum correlations were obtained when Lomb-Scargle, FFT and Welch algorithms were used.

From these results, it can be observed that the classical method with better performance was FFT, while MUSIC showed the best performance among modern methods. Both for excellent and acceptable quality PPG signals, PMUSIC was the best performing method for 9 and 8 of 17 indices, respectively. In terms of classical methods, FFT showed better behaviour than PWELCH. Also, it was found that

Table 6.14: Best parameters found for spectral analysis using fast Fourier transform (FFT) for pulse rate variability (PRV) frequency-domain indices and for achieving maximal correlation between measured and gold standard spectra.

Index	**Excellent PPG**			**Acceptable PPG**		
	Inter-polation	nFFT (f_{res}, Hz)	fs_i (Hz)	Inter-polation	nFFT (f_{res}, Hz)	fs_i (Hz)
VLF	Spline	32768 (0.0078)	256	Spline	32768 (0.0078)	256
LF	Linear	512 (0.0078)	4	Linear	1024 (0.0078)	8
HF	Spline	512 (0.0078)	4	Spline	512 (0.0078)	4
TP	Spline	32768 (0.0078)	256	Spline	32768 (0.0078)	256
nLF	Spline	512 (0.0078)	4	Spline	512 (0.0078)	4
nHF	Spline	512 (0.0078)	4	Spline	512 (0.0078)	4
LF/HF	Spline	41944304 (0.000061)	256	Spline	262144 (0.00098)	256
cLF_x	Spline	32768 (0.0078)	256	Spline	32768 (0.0078)	256
cLF_y	Linear	16384 (0.0078)	128	Linear	4096 (0.0078)	32
cHF_x	Spline	512 (0.0078)	4	Spline	512 (0.0078)	4
cHF_y	Spline	8192 (0.00098)	8	Spline	4096 (0.00098)	4
cTP_x	Linear	65536 (0.000061)	4	Linear	65536 (0.000061)	4
cTP_y	Linear	2048 (0.0078)	16	Linear	512 (0.0078)	4
XC lags	Spline	4096 (0.0078)	32	Spline	1024 (0.0078)	8
XC max	Spline	65536 (0.000061)	4	Spline	65536 (0.000061)	4
Spearman	Linear	65536 (0.000061)	4	Linear	65536 (0.000061)	4
Pearson	Linear	65536 (0.000061)	4	Linear	65536 (0.000061)	4

the Lomb-Scargle periodogram did not show good reliability for the extraction of frequency-domain indices. Tables 6.14 and 6.15 summarise the parameters with best performance for the extraction of each index using FFT or PMUSIC, respectively. In summary, both for excellent and acceptable quality PPG signals, the FFT showed better performances when obtained after applying a cubic spline interpolation and resampling PRV trends to 4 Hz, while an optimal number of samples for measuring the spectrum is 512, which gives a resolution frequency of 0.0078 Hz. In the case of the MUSIC method, resampling PRV trends to 4 Hz using linear interpolation and using a fifth order model gave the best results both for excellent and acceptable quality signals. For excellent quality PPG signals, a resolution frequency of 0.0078 Hz was also found to perform the best, although for acceptable quality PPG signals a number of samples that gave best results increased to 32768, for a resolution frequency of 1.2207×10^{-4} Hz. Since FFT is less complex than PMUSIC, and there were not many significant differences between the best combinations of these two methods, applying FFT with the recommended parameters was found to be the best option for PRV spectral analysis.

6.3.4 Experiment 4: Duration of signal

One-hundred and ten excellent, and 110 acceptable quality PPG signals, with more than 30 min duration were simulated, using a sampling rate of 256 Hz. These PPG signals were then segmented into shorter PPG signals, with lengths ranging from 30 s to 20 min, in steps of 30 s. The interbeat intervals were then identified from each of the shorter PPG segments using D2Max and the a fiducial point, and time-domain, frequency-domain and Poincaré plot indices were assessed from these PRV trends. Spectral analysis was performed using FFT with 512 data points after interpolating the trends to 4 Hz with a cubic spline interpolation. The frequency resolution was then 0.0078 Hz.

Figure 6.23 shows the behaviour of PRV indices measured from excellent quality PPG signals with varying length. Statistical analyses showed non-significant differences among lengths for RMSSD, nHF, LF/HF, cHF_x, cHF_y, cTP_x, S, SD1 and SD1/SD2. The mean value of the differences for time-domain, non-centroid related frequency-domain and Poincaré plot indices tend to be smaller in PPG signals with duration longer than 120 s, as well as their standard deviations. The higher mean differences were observed in the extraction of non-centroid related frequency-domain

indices. In the case of centroid-related frequency-domain indices, the trend is opposite, with lower differences for y-coordinates with shorter signals, while values related to x-coordinates remain relatively stable regardless of the duration of the signals. As was observed in experiment 3, these indices seem to be less affected by technical aspects than y-coordinates of centroids.

Table 6.15: Best parameters found for spectral analysis using the multiple signal classification (PMUSIC) spectral analysis method for pulse rate variability (PRV) frequency-domain indices, and for achieving maximal correlation between measured and gold standard spectra.

Index	**Excellent PPG**				**Acceptable PPG**			
	Inter-polation	nFFT (f_{res}, Hz)	fs_i (Hz)	Order	Inter-polation	nFFT (f_{res}, Hz)	fs_i (Hz)	Order
VLF	Spline	512 (0.0078)	4	50	Spline	512 (0.0078)	4	50
LF	Linear	512 (0.0078)	4	25	Spline	1024 (0.0078)	8	50
HF	Spline	512 (0.0078)	4	40	Spline	512 (0.0078)	4	45
TP	Linear	512 (0.0078)	4	40	Spline	512 (0.0078)	4	40
nLF	Linear	32768 (0.00098)	32	5	Linear	32768 (0.00098)	32	5
nHF	Linear	8192 (0.0078)	64	5	Linear	1048576 (0.000061)	64	5
LF/HF	Linear	2048 (0.0078)	16	5	Linear	4096 (0.0078)	32	5
cLF_x	Spline	32768 (0.00098)	32	25	Spline	32768 (0.00098)	32	25
cLF_y	Linear	4096 (0.0078)	32	5	Linear	4096 (0.0078)	32	5
cHF_x	Spline	32768 (0.0078)	256	15	Spline	32768 (0.0078)	256	15
cHF_y	Linear	262144 (0.00098)	256	10	Linear	262144 (0.00098)	256	10
cTP_x	Linear	131072 (0.00098)	128	15	Linear	131072 (0.00098)	128	15
cTP_y	Linear	524288 (0.000061)	32	5	Linear	524288 (0.000061)	32	5
XC lags	Linear	262144 (0.00098)	256	5	Linear	262144 (0.00098)	256	5
XC max	Linear	4194304 (0.000061)	256	15	Linear	4194304 (0.000061)	256	15
Spearman	Spline	65536 (0.000061)	4	15	Spline	131072 (0.000061)	8	15
Pearson	Linear	65536 (0.000061)	4	50	Linear	65536 (0.000061)	4	45

In the case of acceptable quality PPG signals, Friedman rank sum tests showed non-significant differences among lengths for nHF, cLF_x, cHF_x, cHF_y, cTP_x and cTP_y. The behaviour of the mean values and standard deviations (Figure 6.24) is similar as that observed with excellent quality PPG signals: The differences become smaller and less variable with PPG signals longer than 120 s, and differences become stable with duration longer than 300 s. Again, differences are larger for non-centroid related frequency-domain indices, while the same behaviour can be observed in centroid-related indices.

Since the aim of this experiment was to determine how long PPG segments need to be for reliable estimation of PRV indices, the minimum length at which

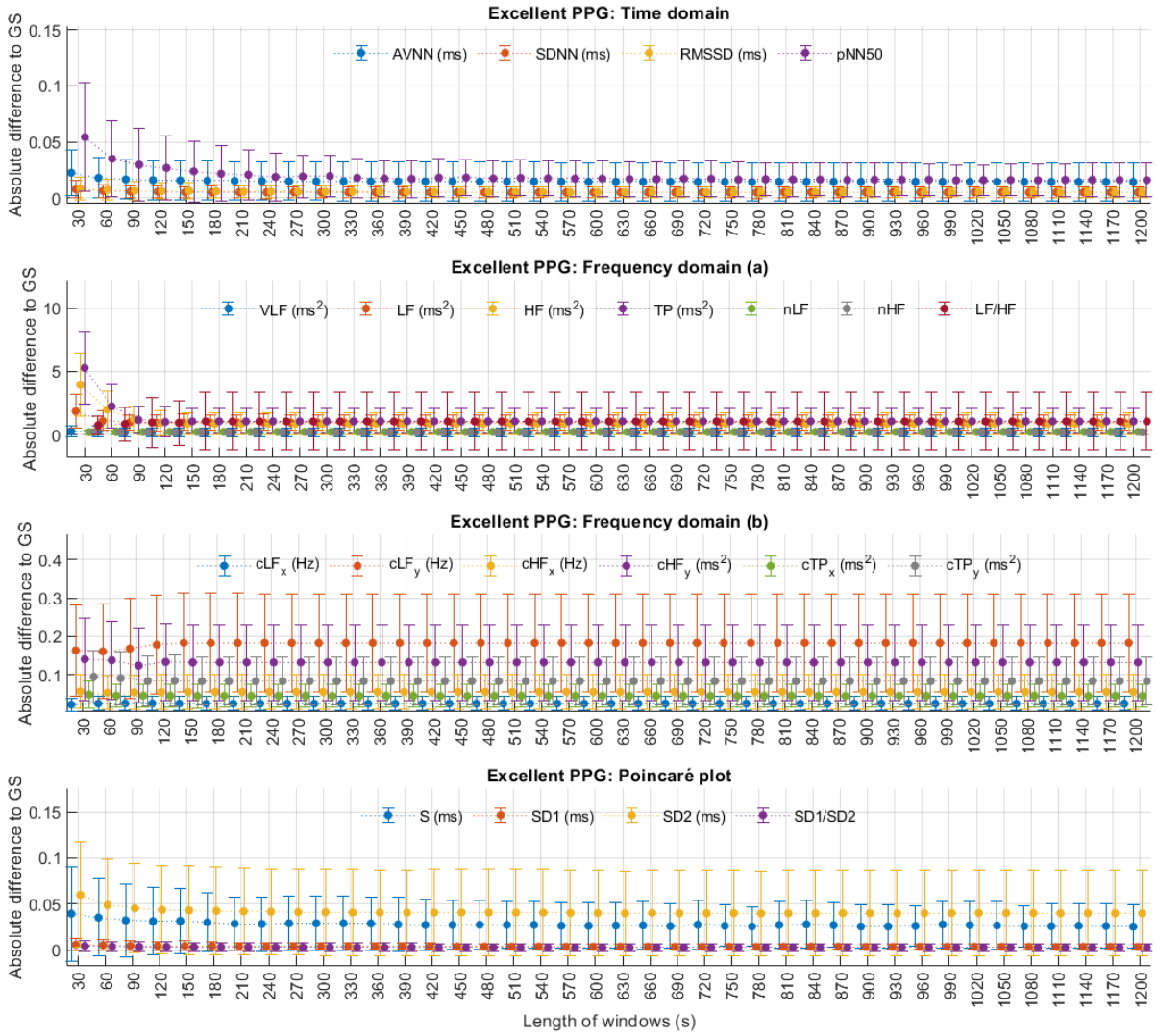

Figure 6.23: Mean and standard deviations of the differences between indices extracted from measured and gold standard pulse rate variability trends with varying lengths of excellent photoplethysmographic signals. Differences tended to stabilise with durations longer than 120 s.

no significant differences were observed for each index and each PPG signal quality were obtained from the post-hoc comparisons (Table 6.16). It was observed that pNN50, HF, and TP needed at least 90 s long PPG signals. Hence, PPG signals of at least this length should be considered for reliable PRV estimation.

6.3.5 Experiment 5: Outlier management

For this experiment, PPG signals were simulated using a sampling rate of 256 Hz and with a length of 300 s (5 min), given the current guidelines for HRV and PRV analysis (Task Force of the European Society of Cardiology and The North American Society of Pacing and Electrophysiology 1996) and that it is longer than what

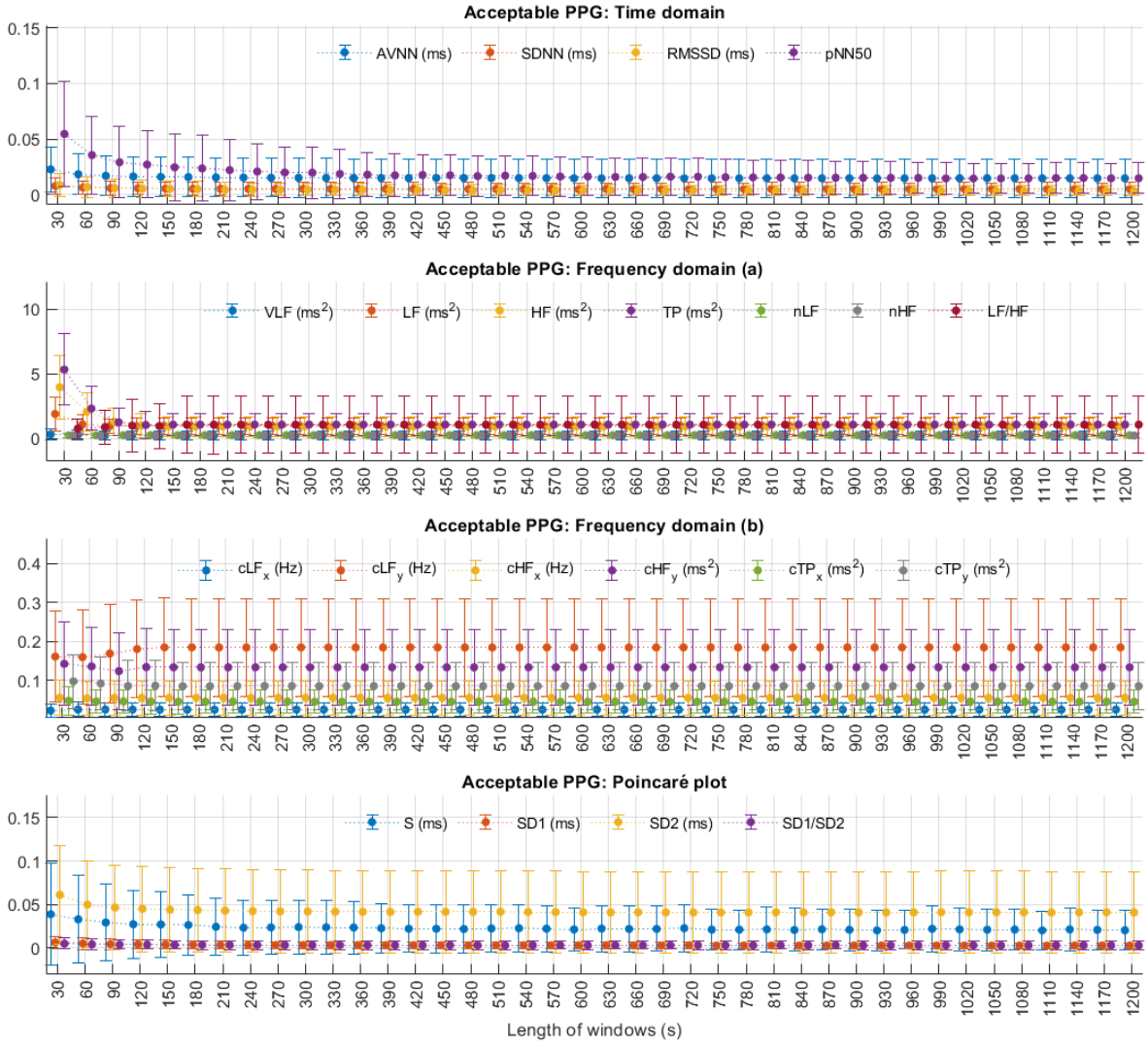

Figure 6.24: Mean and standard deviations of the differences between indices extracted from measured and gold standard pulse rate variability trends with varying lengths of acceptable photoplethysmographic signals. Differences tended to stabilise with durations longer than 120 s.

Table 6.16: Post-hoc comparisons results for differences between indices extracted from measured and gold standard pulse rate variability trends that showed statistically significant differences among photoplethysmographic signal duration, both with excellent and acceptable quality.

Index	Minimum length without significant differences (s)	
	Excellent PPG	**Acceptable PPG**
AVNN	60	60
SDNN	30	30
RMSSD	30	60
pNN50	90	90
VLF	30	30
LF	60	60
HF	90	90
TP	90	90
nLF	30	30
nHF	30	30
LF/HF	30	30
cLF_x	30	30
cLF_y	30	30
cHF_x	30	30
cHF_y	30	30
cTP_x	30	30
cTP_y	30	30
S	30	30
SD1	30	60
SD2	60	60
SD1/SD2	30	60

was found in the previous experiment. Using D2Max and the a points as fiducial points, PRV trends were obtained from the simulated PPG signals, and then outliers were detected and corrected as explained above. From these trends, time-domain, frequency-domain and Poincaré plot indices were extracted. As found in experiment 3, PRV trends were resampled to 4 Hz using a cubic spline interpolation and FFT with 512 data points was used for spectral analysis.

Factorial analyses with Box-Cox transform were performed to determine the effects of the different methods for identifying and managing outliers. It was found that there were significant differences due to the interaction of factors only for measuring pNN50, both with excellent and acceptable quality signals. The detection method was a significant factor for SDNN, RMSSD, SD1 and SD2 in both types of signals, while AVNN and SD1/SD2 showed significant differences due to the detection method only when measured in acceptable quality signals. The correction method did not show statistically significant differences for any index or any type

of signal. Table 6.17 summarises the combination of factors that gave the lowest difference to the gold standard for the estimated indices.

These best combination where then compared to PRV indices extracted from

Table 6.17: Combination of factors with the lowest difference to indices extracted from the gold standard.

Index	Excellent PPG		Acceptable PPG	
	A	**B**	**A**	**B**
AVNN †	Quartiles	Median	Quartiles	Median
SDNN ‡	GESD test	Next	Mean	Next
RMSSD ‡	Moving median	Next	Grubb's test	Next
pNN50 ⋆	Mean	Median $k = 5$	Mean	Median
LF	Moving median	Previous	Moving median	Previous
HF	Moving median	Median $k = 5$	Moving median	Piecewise Spline
TP	Moving median	Next	Moving median	Nearest
nLF	Moving median	Linear	Moving median	Linear
nHF	Moving median	Median $k = 5$	Mean	Linear
LF/HF	Moving median	Median $k = 5$	Moving median	Median $k = 5$
cLF_x	Mean	Clip	Moving median	Previous
cLF_y	Moving median	Linear	Moving median	Median $k = 5$
cHF_x	Moving median	Previous	Moving median	Previous
cHF_y	Moving median	Spline	Moving median	Linear
cTP_x	Moving median	Mean	Mean	Clip
cTP_y	Moving median	Nearest	Moving median	Clip
S	Moving median	Next	Moving median	Next
SD1 ‡	Moving median	Next	Grubb's test	Median
SD2 ‡	Quartiles	Linear	Quartiles	Median
SD1/SD2 †	Mean	Next	Grubb's test	Makima

A: Detection method
B: Correction method
‡ Significant difference due to A on both types of signals
† Significant difference due to A on acceptable signals
⋆ Significant difference due to the A × B on both types of signals

the original interbaet intervals without managing outliers. It was found that only RMSSD ($p < 0.001$) and SD1 ($p < 0.001$) showed significant differences when measured from excellent PPG signals, while S showed significant differences ($p < 0.001$) when measured from both types of signals. In all these cases, the mean difference between extracted and gold standard indices were lower when no outlier management strategy was applied, as shown in Table 6.18.

These results indicate that there is no need to apply any additional outlier management strategy besides those employed in the interbeat intervals detection algorithm for a reliable PRV estimation.

6.3.6 Experiment 6: Noise management

As explained in the previous section, 5-min PPG signals were simulated and all the possible combinations of noise were included to the simulated signals. These signals were simulated using a 256 Hz sampling rate. The contaminated signals were then filtered using different FIR and IIR filters, and varying cut-off frequencies. From the filtered signals, PRV trends were obtained applying the D2max algorithm, and using a points for the interbeat interval detection. No additional outlier management strategy was applied to these trends and time-domain, frequency-domain and Poincaré plot indices were obtained. Spectral analysis was performed after resampling the trends to 4 Hz using a cubic spline interpolation, and by applying the FFT with 512 data points.

Factorial analyses with Box-Cox transform were performed for each group of signals with a particular combination of noises, to evaluate the impact of the type of filter and cut-off frequencies on PRV analysis when contaminated PPG signals with each noise are analysed. Tables 6.19 and 6.20 summarise the results obtained from

Table 6.18: Average difference to gold standard for indices that showed significant differences between applying or not applying outlier management strategies

Index	**Excellent PPG**		**Acceptable PPG**	
	No management	**Best combination**	**No management**	**Best combination**
RMSSD	-0.0014 ± 0.0062	0.0045 ± 0.0064	-	-
S	-0.0100 ± 0.0408	0.0115 ± 0.0448	-0.0076 ± 0.0374	0.0135 ± 0.0410
SD1	$-9.78x10^{-4} \pm 0.0043$	0.0032 ± 0.0045	-	-

these factorial analyses, when using excellent and acceptable quality PPG signals, respectively.

Table 6.19: Summary of results from factorial analyses performed to evaluate the effects of interactions among factors altered for the filtering of excellent quality, noise contaminated photoplethysmographic signals and pulse rate variability analysis. A: Type of filter; B: Low cutoff frequency; C: High cutoff frequency. ⋆: Significant interaction or factor. - : Non-significant interaction or factor.

Noise	**Index**	**Interaction**						
		A	**B**	**C**	**A × B**	**A × C**	**B × C**	**A × B × C**
RES	AVNN	⋆	⋆	⋆	⋆	⋆	⋆	⋆
	SDNN	⋆	⋆	⋆	⋆	⋆	⋆	⋆
	RMSSD	⋆	⋆	⋆	⋆	⋆	⋆	⋆
	pNN50	⋆	⋆	⋆	⋆	⋆	⋆	⋆
	VLF	⋆	⋆	⋆	⋆	⋆	⋆	⋆
	LF	⋆	⋆	⋆	⋆	⋆	⋆	⋆
	HF	⋆	⋆	⋆	⋆	⋆	⋆	⋆
	TP	⋆	⋆	⋆	⋆	⋆	⋆	⋆
	nLF	⋆	-	-	⋆	⋆	⋆	⋆
	nHF	⋆	⋆	⋆	⋆	⋆	⋆	⋆
	LF/HF	⋆	⋆	⋆	⋆	⋆	⋆	⋆
	cLF_x	⋆	⋆	-	⋆	-	-	-
	cLF_y	⋆	⋆	⋆	⋆	⋆	-	-
	cHF_x	⋆	⋆	-	⋆	-	-	-
	cHF_y	⋆	⋆	⋆	⋆	⋆	⋆	⋆
	cTP_x	⋆	⋆	⋆	⋆	⋆	⋆	⋆
	cTP_y	⋆	⋆	⋆	⋆	⋆	⋆	⋆
	S	⋆	⋆	⋆	⋆	⋆	⋆	⋆
	SD1	⋆	⋆	⋆	⋆	⋆	⋆	⋆
	SD2	⋆	⋆	⋆	⋆	⋆	⋆	⋆
	SD1/SD2	⋆	⋆	⋆	⋆	⋆	⋆	⋆
BW	AVNN	⋆	⋆	⋆	⋆	⋆	⋆	⋆
	SDNN	⋆	⋆	⋆	⋆	⋆	⋆	⋆
	RMSSD	⋆	⋆	⋆	⋆	⋆	⋆	⋆
	pNN50	⋆	⋆	⋆	⋆	⋆	⋆	⋆

Continued on next page

Table 6.19 – continued from previous page

Noise	Index	Interaction						
		A	**B**	**C**	**A × B**	**A × C**	**B × C**	**A × B × C**
BW	VLF	⋆	⋆	⋆	⋆	⋆	⋆	⋆
	LF	⋆	⋆	⋆	⋆	⋆	⋆	⋆
	HF	⋆	⋆	⋆	⋆	⋆	⋆	⋆
	TP	⋆	⋆	⋆	⋆	⋆	⋆	⋆
	nLF	⋆	⋆	⋆	⋆	⋆	⋆	⋆
	nHF	⋆	⋆	⋆	⋆	⋆	⋆	⋆
	LF/HF	⋆	⋆	⋆	⋆	⋆	⋆	⋆
	cLF_x	⋆	⋆	-	⋆	-	-	-
	cLF_y	⋆	⋆	⋆	⋆	⋆	⋆	⋆
	cHF_x	⋆	-	-	⋆	-	-	-
	cHF_y	⋆	⋆	⋆	⋆	⋆	⋆	⋆
	cTP_x	⋆	⋆	⋆	⋆	⋆	⋆	⋆
	cTP_y	⋆	⋆	⋆	⋆	⋆	⋆	⋆
	S	⋆	⋆	⋆	⋆	⋆	⋆	⋆
	SD1	⋆	⋆	⋆	⋆	⋆	⋆	⋆
	SD2	⋆	⋆	⋆	⋆	⋆	⋆	⋆
	SD1/SD2	⋆	⋆	⋆	⋆	⋆	⋆	⋆
EM	AVNN	⋆	⋆	⋆	⋆	⋆	⋆	⋆
	SDNN	⋆	⋆	⋆	⋆	⋆	⋆	⋆
	RMSSD	⋆	⋆	⋆	⋆	⋆	⋆	⋆
	pNN50	⋆	⋆	⋆	⋆	⋆	⋆	⋆
	VLF	⋆	⋆	⋆	⋆	⋆	⋆	⋆
	LF	⋆	⋆	⋆	⋆	⋆	⋆	⋆
	HF	⋆	⋆	⋆	⋆	⋆	⋆	⋆
	TP	⋆	⋆	⋆	⋆	⋆	⋆	⋆
	nLF	⋆	-	-	⋆	⋆	-	⋆
	nHF	⋆	⋆	⋆	⋆	⋆	⋆	⋆
	LF/HF	⋆	⋆	⋆	⋆	⋆	⋆	⋆
	cLF_x	⋆	⋆	-	⋆	-	-	-
	cLF_y	⋆	⋆	⋆	⋆	⋆	-	-

Continued on next page

Table 6.19 – continued from previous page

Noise	Index	Interaction						
		A	**B**	**C**	**A × B**	**A × C**	**B × C**	**A × B × C**
EM	cHF_x	⋆	⋆	-	⋆	-	-	-
	cHF_y	⋆	⋆	⋆	⋆	⋆	⋆	⋆
	cTP_x	⋆	⋆	⋆	⋆	⋆	⋆	⋆
	cTP_y	⋆	⋆	⋆	⋆	⋆	⋆	⋆
	S	⋆	⋆	⋆	⋆	⋆	⋆	⋆
	SD1	⋆	⋆	⋆	⋆	⋆	⋆	⋆
	SD2	⋆	⋆	⋆	⋆	⋆	⋆	⋆
	SD1/SD2	⋆	⋆	⋆	⋆	⋆	⋆	⋆
MA	AVNN	⋆	⋆	⋆	⋆	⋆	⋆	⋆
	SDNN	⋆	⋆	⋆	⋆	⋆	⋆	⋆
	RMSSD	⋆	⋆	⋆	⋆	⋆	⋆	⋆
	pNN50	⋆	⋆	⋆	⋆	⋆	⋆	⋆
	VLF	⋆	⋆	⋆	⋆	⋆	⋆	⋆
	LF	⋆	⋆	⋆	⋆	⋆	⋆	⋆
	HF	⋆	⋆	⋆	⋆	⋆	⋆	⋆
	TP	⋆	⋆	⋆	⋆	⋆	⋆	⋆
	nLF	⋆	⋆	-	⋆	⋆	⋆	⋆
	nHF	⋆	⋆	⋆	⋆	⋆	⋆	⋆
	LF/HF	⋆	⋆	⋆	⋆	⋆	⋆	⋆
	cLF_x	⋆	⋆	-	⋆	-	-	-
	cLF_y	⋆	⋆	⋆	⋆	⋆	-	-
	cHF_x	⋆	⋆	-	⋆	-	-	-
	cHF_y	⋆	⋆	⋆	⋆	⋆	⋆	⋆
	cTP_x	⋆	⋆	⋆	⋆	⋆	⋆	⋆
	cTP_y	⋆	⋆	⋆	⋆	⋆	⋆	⋆
	S	⋆	⋆	⋆	⋆	⋆	⋆	⋆
	SD1	⋆	⋆	⋆	⋆	⋆	⋆	⋆
	SD2	⋆	⋆	⋆	⋆	⋆	⋆	⋆
	SD1/SD2	⋆	⋆	⋆	⋆	⋆	⋆	⋆
	AVNN	⋆	⋆	⋆	⋆	⋆	⋆	⋆

Continued on next page

Table 6.19 – continued from previous page

Noise	Index	Interaction						
		A	**B**	**C**	**A × B**	**A × C**	**B × C**	**A × B × C**
RES + BW	SDNN	⋆	⋆	⋆	⋆	⋆	⋆	⋆
	RMSSD	⋆	⋆	⋆	⋆	⋆	⋆	⋆
	pNN50	⋆	⋆	⋆	⋆	⋆	⋆	⋆
	VLF	⋆	⋆	⋆	⋆	⋆	⋆	⋆
	LF	⋆	⋆	⋆	⋆	⋆	⋆	⋆
	HF	⋆	⋆	⋆	⋆	⋆	⋆	⋆
	TP	⋆	⋆	⋆	⋆	⋆	⋆	⋆
	nLF	⋆	⋆	⋆	⋆	⋆	⋆	⋆
	nHF	⋆	⋆	⋆	⋆	⋆	⋆	⋆
	LF/HF	⋆	⋆	⋆	⋆	⋆	⋆	⋆
	cLF_x	⋆	⋆	-	⋆	-	-	-
	cLF_y	⋆	⋆	⋆	⋆	⋆	⋆	⋆
	cHF_x	⋆	-	-	⋆	-	-	-
	cHF_y	⋆	⋆	⋆	⋆	⋆	⋆	⋆
	cTP_x	⋆	⋆	⋆	⋆	⋆	⋆	⋆
	cTP_y	⋆	⋆	⋆	⋆	⋆	⋆	⋆
	S	⋆	⋆	⋆	⋆	⋆	⋆	⋆
	SD1	⋆	⋆	⋆	⋆	⋆	⋆	⋆
	SD2	⋆	⋆	⋆	⋆	⋆	⋆	⋆
	SD1/SD2	⋆	⋆	⋆	⋆	⋆	⋆	⋆
RES + EM	AVNN	⋆	⋆	⋆	⋆	⋆	⋆	⋆
	SDNN	⋆	⋆	⋆	⋆	⋆	⋆	⋆
	RMSSD	⋆	⋆	⋆	⋆	⋆	⋆	⋆
	pNN50	⋆	⋆	⋆	⋆	⋆	⋆	⋆
	VLF	⋆	⋆	⋆	⋆	⋆	⋆	⋆
	LF	⋆	⋆	⋆	⋆	⋆	⋆	⋆
	HF	⋆	⋆	⋆	⋆	⋆	⋆	⋆
	TP	⋆	⋆	⋆	⋆	⋆	⋆	⋆
	nLF	⋆	-	-	⋆	⋆	-	⋆
	nHF	⋆	⋆	⋆	⋆	⋆	⋆	⋆

Continued on next page

Table 6.19 – continued from previous page

Noise	Index	Interaction						
		A	**B**	**C**	**A × B**	**A × C**	**B × C**	**A × B × C**
RES + EM	LF/HF	⋆	⋆	⋆	⋆	⋆	⋆	⋆
	cLF_x	⋆	⋆	-	⋆	-	-	-
	cLF_y	⋆	⋆	⋆	⋆	⋆	-	-
	cHF_x	⋆	⋆	-	⋆	-	-	-
	cHF_y	⋆	⋆	⋆	⋆	⋆	⋆	⋆
	cTP_x	⋆	⋆	⋆	⋆	⋆	⋆	⋆
	cTP_y	⋆	⋆	⋆	⋆	⋆	⋆	⋆
	S	⋆	⋆	⋆	⋆	⋆	⋆	⋆
	SD1	⋆	⋆	⋆	⋆	⋆	⋆	⋆
	SD2	⋆	⋆	⋆	⋆	⋆	⋆	⋆
	SD1/SD2	⋆	⋆	⋆	⋆	⋆	⋆	⋆
RES + MA	AVNN	⋆	⋆	⋆	⋆	⋆	⋆	⋆
	SDNN	⋆	⋆	⋆	⋆	⋆	⋆	⋆
	RMSSD	⋆	⋆	⋆	⋆	⋆	⋆	⋆
	pNN50	⋆	⋆	⋆	⋆	⋆	⋆	⋆
	VLF	⋆	⋆	⋆	⋆	⋆	⋆	⋆
	LF	⋆	⋆	⋆	⋆	⋆	⋆	⋆
	HF	⋆	⋆	⋆	⋆	⋆	⋆	⋆
	TP	⋆	⋆	⋆	⋆	⋆	⋆	⋆
	nLF	⋆	⋆	-	⋆	⋆	⋆	⋆
	nHF	⋆	⋆	⋆	⋆	⋆	⋆	⋆
	LF/HF	⋆	⋆	⋆	⋆	⋆	⋆	⋆
	cLF_x	⋆	⋆	-	⋆	-	-	-
	cLF_y	⋆	⋆	⋆	⋆	⋆	-	-
	cHF_x	⋆	⋆	-	⋆	-	-	-
	cHF_y	⋆	⋆	⋆	⋆	⋆	⋆	⋆
	cTP_x	⋆	⋆	⋆	⋆	⋆	⋆	⋆
	cTP_y	⋆	⋆	⋆	⋆	⋆	⋆	⋆
	S	⋆	⋆	⋆	⋆	⋆	⋆	⋆
	SD1	⋆	⋆	⋆	⋆	⋆	⋆	⋆

Continued on next page

Table 6.19 – continued from previous page

Noise	Index	Interaction						
		A	**B**	**C**	**A × B**	**A × C**	**B × C**	**A × B × C**
RES + MA	SD2	⋆	⋆	⋆	⋆	⋆	⋆	⋆
	SD1/SD2	⋆	⋆	⋆	⋆	⋆	⋆	⋆
BW + EM	AVNN	⋆	⋆	⋆	⋆	⋆	⋆	⋆
	SDNN	⋆	⋆	⋆	⋆	⋆	⋆	⋆
	RMSSD	⋆	⋆	⋆	⋆	⋆	⋆	⋆
	pNN50	⋆	⋆	⋆	⋆	⋆	⋆	⋆
	VLF	⋆	⋆	⋆	⋆	⋆	⋆	⋆
	LF	⋆	⋆	⋆	⋆	⋆	⋆	⋆
	HF	⋆	⋆	⋆	⋆	⋆	⋆	⋆
	TP	⋆	⋆	⋆	⋆	⋆	⋆	⋆
	nLF	⋆	⋆	⋆	⋆	⋆	⋆	⋆
	nHF	⋆	⋆	⋆	⋆	⋆	⋆	⋆
	LF/HF	⋆	⋆	⋆	⋆	⋆	⋆	⋆
	cLF_x	⋆	⋆	-	⋆	-	-	⋆
	cLF_y	⋆	⋆	⋆	⋆	⋆	⋆	⋆
	cHF_x	⋆	-	-	⋆	-	-	-
	cHF_y	⋆	⋆	⋆	⋆	⋆	⋆	⋆
	cTP_x	⋆	⋆	⋆	⋆	⋆	⋆	⋆
	cTP_y	⋆	⋆	⋆	⋆	⋆	⋆	⋆
	S	⋆	⋆	⋆	⋆	⋆	⋆	⋆
	SD1	⋆	⋆	⋆	⋆	⋆	⋆	⋆
	SD2	⋆	⋆	⋆	⋆	⋆	⋆	⋆
	SD1/SD2	⋆	⋆	⋆	⋆	⋆	⋆	⋆
BW + MA	AVNN	⋆	⋆	⋆	⋆	⋆	⋆	⋆
	SDNN	⋆	⋆	⋆	⋆	⋆	⋆	⋆
	RMSSD	⋆	⋆	⋆	⋆	⋆	⋆	⋆
	pNN50	⋆	⋆	⋆	⋆	⋆	⋆	⋆
	VLF	⋆	⋆	⋆	⋆	⋆	⋆	⋆
	LF	⋆	⋆	⋆	⋆	⋆	⋆	⋆
	HF	⋆	⋆	⋆	⋆	⋆	⋆	⋆

Continued on next page

Table 6.19 – continued from previous page

Noise	Index	Interaction						
		A	**B**	**C**	**A × B**	**A × C**	**B × C**	**A × B × C**
BW + MA	TP	⋆	⋆	⋆	⋆	⋆	⋆	⋆
	nLF	⋆	⋆	⋆	⋆	⋆	⋆	⋆
	nHF	⋆	⋆	⋆	⋆	⋆	⋆	⋆
	LF/HF	⋆	⋆	⋆	⋆	⋆	⋆	⋆
	cLF_x	⋆	⋆	-	⋆	-	-	-
	cLF_y	⋆	⋆	⋆	⋆	⋆	⋆	⋆
	cHF_x	⋆	⋆	-	⋆	-	-	⋆
	cHF_y	⋆	⋆	⋆	⋆	⋆	⋆	⋆
	cTP_x	⋆	⋆	⋆	⋆	⋆	⋆	⋆
	cTP_y	⋆	⋆	⋆	⋆	⋆	⋆	⋆
	S	⋆	⋆	⋆	⋆	⋆	⋆	⋆
	SD1	⋆	⋆	⋆	⋆	⋆	⋆	⋆
	SD2	⋆	⋆	⋆	⋆	⋆	⋆	⋆
	SD1/SD2	⋆	⋆	⋆	⋆	⋆	⋆	⋆
EM + MA	AVNN	⋆	⋆	⋆	⋆	⋆	⋆	⋆
	SDNN	⋆	⋆	⋆	⋆	⋆	⋆	⋆
	RMSSD	⋆	⋆	⋆	⋆	⋆	⋆	⋆
	pNN50	⋆	⋆	⋆	⋆	⋆	⋆	⋆
	VLF	⋆	⋆	⋆	⋆	⋆	⋆	⋆
	LF	⋆	⋆	⋆	⋆	⋆	⋆	⋆
	HF	⋆	⋆	⋆	⋆	⋆	⋆	⋆
	TP	⋆	⋆	⋆	⋆	⋆	⋆	⋆
	nLF	⋆	⋆	-	⋆	⋆	⋆	⋆
	nHF	⋆	⋆	⋆	⋆	⋆	⋆	⋆
	LF/HF	⋆	⋆	⋆	⋆	⋆	⋆	⋆
	cLF_x	⋆	⋆	-	⋆	-	-	-
	cLF_y	⋆	⋆	⋆	⋆	⋆	-	-
	cHF_x	⋆	⋆	-	⋆	-	-	-
	cHF_y	⋆	⋆	⋆	⋆	⋆	⋆	⋆
	cTP_x	⋆	⋆	⋆	⋆	⋆	⋆	⋆

Continued on next page

Table 6.19 – continued from previous page

Noise	Index	Interaction						
		A	**B**	**C**	**A × B**	**A × C**	**B × C**	**A × B × C**
EM + MA	cTP_y	⋆	⋆	⋆	⋆	⋆	⋆	⋆
	S	⋆	⋆	⋆	⋆	⋆	⋆	⋆
	SD1	⋆	⋆	⋆	⋆	⋆	⋆	⋆
	SD2	⋆	⋆	⋆	⋆	⋆	⋆	⋆
	SD1/SD2	⋆	⋆	⋆	⋆	⋆	⋆	⋆
RES + BW + EM	AVNN	⋆	⋆	⋆	⋆	⋆	⋆	⋆
	SDNN	⋆	⋆	⋆	⋆	⋆	⋆	⋆
	RMSSD	⋆	⋆	⋆	⋆	⋆	⋆	⋆
	pNN50	⋆	⋆	⋆	⋆	⋆	⋆	⋆
	VLF	⋆	⋆	⋆	⋆	⋆	⋆	⋆
	LF	⋆	⋆	⋆	⋆	⋆	⋆	⋆
	HF	⋆	⋆	⋆	⋆	⋆	⋆	⋆
	TP	⋆	⋆	⋆	⋆	⋆	⋆	⋆
	nLF	⋆	⋆	⋆	⋆	⋆	⋆	⋆
	nHF	⋆	⋆	⋆	⋆	⋆	⋆	⋆
	LF/HF	⋆	⋆	⋆	⋆	⋆	⋆	⋆
	cLF_x	⋆	⋆	-	⋆	-	-	-
	cLF_y	⋆	⋆	⋆	⋆	⋆	⋆	⋆
	cHF_x	⋆	-	-	⋆	-	-	-
	cHF_y	⋆	⋆	⋆	⋆	⋆	⋆	⋆
	cTP_x	⋆	⋆	⋆	⋆	⋆	⋆	⋆
	cTP_y	⋆	⋆	⋆	⋆	⋆	⋆	⋆
	S	⋆	⋆	⋆	⋆	⋆	⋆	⋆
	SD1	⋆	⋆	⋆	⋆	⋆	⋆	⋆
	SD2	⋆	⋆	⋆	⋆	⋆	⋆	⋆
	SD1/SD2	⋆	⋆	⋆	⋆	⋆	⋆	⋆
RES + BW + MA	AVNN	⋆	⋆	⋆	⋆	⋆	⋆	⋆
	SDNN	⋆	⋆	⋆	⋆	⋆	⋆	⋆
	RMSSD	⋆	⋆	⋆	⋆	⋆	⋆	⋆
	pNN50	⋆	⋆	⋆	⋆	⋆	⋆	⋆

Continued on next page

Table 6.19 – continued from previous page

Noise	Index	Interaction						
		A	**B**	**C**	**A × B**	**A × C**	**B × C**	**A × B × C**
RES + BW + MA	VLF	⋆	⋆	⋆	⋆	⋆	⋆	⋆
	LF	⋆	⋆	⋆	⋆	⋆	⋆	⋆
	HF	⋆	⋆	⋆	⋆	⋆	⋆	⋆
	TP	⋆	⋆	⋆	⋆	⋆	⋆	⋆
	nLF	⋆	⋆	⋆	⋆	⋆	⋆	⋆
	nHF	⋆	⋆	⋆	⋆	⋆	⋆	⋆
	LF/HF	⋆	⋆	⋆	⋆	⋆	⋆	⋆
	cLF_x	⋆	⋆	-	⋆	-	-	-
	cLF_y	⋆	⋆	⋆	⋆	⋆	⋆	⋆
	cHF_x	⋆	⋆	-	⋆	-	-	⋆
	cHF_y	⋆	⋆	⋆	⋆	⋆	⋆	⋆
	cTP_x	⋆	⋆	⋆	⋆	⋆	⋆	⋆
	cTP_y	⋆	⋆	-	⋆	⋆	⋆	⋆
	S	⋆	⋆	⋆	⋆	⋆	⋆	⋆
	SD1	⋆	⋆	⋆	⋆	⋆	⋆	⋆
	SD2	⋆	⋆	⋆	⋆	⋆	⋆	⋆
	SD1/SD2	⋆	⋆	⋆	⋆	⋆	⋆	⋆
RES + EM + MA	AVNN	⋆	⋆	⋆	⋆	⋆	⋆	⋆
	SDNN	⋆	⋆	⋆	⋆	⋆	⋆	⋆
	RMSSD	⋆	⋆	⋆	⋆	⋆	⋆	⋆
	pNN50	⋆	⋆	⋆	⋆	⋆	⋆	⋆
	VLF	⋆	⋆	⋆	⋆	⋆	⋆	⋆
	LF	⋆	⋆	⋆	⋆	⋆	⋆	⋆
	HF	⋆	⋆	⋆	⋆	⋆	⋆	⋆
	TP	⋆	⋆	⋆	⋆	⋆	⋆	⋆
	nLF	⋆	⋆	-	⋆	⋆	⋆	⋆
	nHF	⋆	⋆	⋆	⋆	⋆	⋆	⋆
	LF/HF	⋆	⋆	⋆	⋆	⋆	⋆	⋆
	cLF_x	⋆	⋆	-	⋆	-	-	-
	cLF_y	⋆	⋆	⋆	⋆	⋆	-	⋆

Continued on next page

Table 6.19 – continued from previous page

Noise	Index	Interaction						
		A	**B**	**C**	**A × B**	**A × C**	**B × C**	**A × B × C**
RES + EM + MA	cHF_x	⋆	⋆	-	⋆	-	-	-
	cHF_y	⋆	⋆	⋆	⋆	⋆	⋆	⋆
	cTP_x	⋆	⋆	⋆	⋆	⋆	⋆	⋆
	cTP_y	⋆	⋆	⋆	⋆	⋆	⋆	⋆
	S	⋆	⋆	⋆	⋆	⋆	⋆	⋆
	SD1	⋆	⋆	⋆	⋆	⋆	⋆	⋆
	SD2	⋆	⋆	⋆	⋆	⋆	⋆	⋆
	SD1/SD2	⋆	⋆	⋆	⋆	⋆	⋆	⋆
BW + EM + MA	AVNN	⋆	⋆	⋆	⋆	⋆	⋆	⋆
	SDNN	⋆	⋆	⋆	⋆	⋆	⋆	⋆
	RMSSD	⋆	⋆	⋆	⋆	⋆	⋆	⋆
	pNN50	⋆	⋆	⋆	⋆	⋆	⋆	⋆
	VLF	⋆	⋆	⋆	⋆	⋆	⋆	⋆
	LF	⋆	⋆	⋆	⋆	⋆	⋆	⋆
	HF	⋆	⋆	⋆	⋆	⋆	⋆	⋆
	TP	⋆	⋆	⋆	⋆	⋆	⋆	⋆
	nLF	⋆	⋆	⋆	⋆	⋆	⋆	⋆
	nHF	⋆	⋆	⋆	⋆	⋆	⋆	⋆
	LF/HF	⋆	⋆	⋆	⋆	⋆	⋆	⋆
	cLF_x	⋆	⋆	⋆	⋆	-	-	⋆
	cLF_y	⋆	⋆	⋆	⋆	⋆	⋆	⋆
	cHF_x	⋆	⋆	-	⋆	-	-	⋆
	cHF_y	⋆	⋆	⋆	⋆	⋆	⋆	⋆
	cTP_x	⋆	⋆	⋆	⋆	⋆	⋆	⋆
	cTP_y	⋆	⋆	⋆	⋆	⋆	⋆	⋆
	S	⋆	⋆	⋆	⋆	⋆	⋆	⋆
	SD1	⋆	⋆	⋆	⋆	⋆	⋆	⋆
	SD2	⋆	⋆	⋆	⋆	⋆	⋆	⋆
	SD1/SD2	⋆	⋆	⋆	⋆	⋆	⋆	⋆
	AVNN	⋆	⋆	⋆	⋆	⋆	⋆	⋆

Continued on next page

Table 6.19 – continued from previous page

Noise	Index	Interaction						
		A	**B**	**C**	**A × B**	**A × C**	**B × C**	**A × B × C**
RES + BW + EM + MA	SDNN	⋆	⋆	⋆	⋆	⋆	⋆	⋆
	RMSSD	⋆	⋆	⋆	⋆	⋆	⋆	⋆
	pNN50	⋆	⋆	⋆	⋆	⋆	⋆	⋆
	VLF	⋆	⋆	⋆	⋆	⋆	⋆	⋆
	LF	⋆	⋆	⋆	⋆	⋆	⋆	⋆
	HF	⋆	⋆	⋆	⋆	⋆	⋆	⋆
	TP	⋆	⋆	⋆	⋆	⋆	⋆	⋆
	nLF	⋆	⋆	⋆	⋆	⋆	⋆	⋆
	nHF	⋆	⋆	⋆	⋆	⋆	⋆	⋆
	LF/HF	⋆	⋆	⋆	⋆	⋆	⋆	⋆
	cLF_x	⋆	⋆	-	⋆	-	-	-
	cLF_y	⋆	⋆	⋆	⋆	⋆	⋆	⋆
	cHF_x	⋆	⋆	-	⋆	-	-	⋆
	cHF_y	⋆	⋆	⋆	⋆	⋆	⋆	⋆
	cTP_x	⋆	⋆	⋆	⋆	⋆	⋆	⋆
	cTP_y	⋆	⋆	-	⋆	⋆	⋆	⋆
	S	⋆	⋆	⋆	⋆	⋆	⋆	⋆
	SD1	⋆	⋆	⋆	⋆	⋆	⋆	⋆
	SD2	⋆	⋆	⋆	⋆	⋆	⋆	⋆
	SD1/SD2	⋆	⋆	⋆	⋆	⋆	⋆	⋆

Table 6.20: Summary of results from factorial analyses performed to evaluate the effects of interactions among factors altered for the filtering of acceptable quality, noise contaminated photoplethysmographic signals and pulse rate variability analysis. A: Type of filter; B: Low cutoff frequency; C: High cutoff frequency. ⋆: Significant interaction or factor. - : Non-significant interaction or factor.

Noise	Index	Interaction						
		A	**B**	**C**	**A × B**	**A × C**	**B × C**	**A × B × C**
RES	AVNN	⋆	⋆	⋆	⋆	⋆	⋆	⋆
	SDNN	⋆	⋆	⋆	⋆	⋆	⋆	⋆
	RMSSD	⋆	⋆	⋆	⋆	⋆	⋆	⋆

Continued on next page

Table 6.20 – continued from previous page

Noise	Index	Interaction						
		A	**B**	**C**	**A × B**	**A × C**	**B × C**	**A × B × C**
RES	pNN50	⋆	⋆	⋆	⋆	⋆	⋆	⋆
	VLF	⋆	⋆	⋆	⋆	⋆	⋆	⋆
	LF	⋆	⋆	⋆	⋆	⋆	⋆	⋆
	HF	⋆	⋆	⋆	⋆	⋆	⋆	⋆
	TP	⋆	⋆	⋆	⋆	⋆	⋆	⋆
	nLF	⋆	-	-	⋆	⋆	-	-
	nHF	⋆	⋆	⋆	⋆	⋆	⋆	⋆
	LF/HF	⋆	⋆	⋆	⋆	⋆	⋆	⋆
	cLF_x	⋆	⋆	-	⋆	-	-	-
	cLF_y	⋆	⋆	⋆	⋆	⋆	-	-
	cHF_x	⋆	-	-	⋆	-	-	-
	cHF_y	⋆	⋆	⋆	⋆	⋆	⋆	⋆
	cTP_x	⋆	⋆	⋆	⋆	⋆	⋆	⋆
	cTP_y	⋆	⋆	⋆	⋆	⋆	⋆	⋆
	S	⋆	⋆	⋆	⋆	⋆	⋆	⋆
	SD1	⋆	⋆	⋆	⋆	⋆	⋆	⋆
	SD2	⋆	⋆	⋆	⋆	⋆	⋆	⋆
	SD1/SD2	⋆	⋆	⋆	⋆	⋆	⋆	⋆
BW	AVNN	⋆	⋆	⋆	⋆	⋆	⋆	⋆
	SDNN	⋆	⋆	⋆	⋆	⋆	⋆	⋆
	RMSSD	⋆	⋆	⋆	⋆	⋆	⋆	⋆
	pNN50	⋆	⋆	⋆	⋆	⋆	⋆	⋆
	VLF	⋆	⋆	⋆	⋆	⋆	⋆	⋆
	LF	⋆	⋆	⋆	⋆	⋆	⋆	⋆
	HF	⋆	⋆	⋆	⋆	⋆	⋆	⋆
	TP	⋆	⋆	⋆	⋆	⋆	⋆	⋆
	nLF	⋆	⋆	⋆	⋆	⋆	⋆	⋆
	nHF	⋆	⋆	⋆	⋆	⋆	⋆	⋆
	LF/HF	⋆	⋆	⋆	⋆	⋆	⋆	⋆
	cLF_x	⋆	⋆	-	⋆	-	-	⋆

Continued on next page

Table 6.20 – continued from previous page

Noise	Index	Interaction						
		A	**B**	**C**	**A × B**	**A × C**	**B × C**	**A × B × C**
BW	cLF_y	⋆	⋆	⋆	⋆	⋆	-	-
	cHF_x	⋆	⋆	-	⋆	-	-	-
	cHF_y	⋆	⋆	⋆	⋆	⋆	⋆	⋆
	cTP_x	⋆	⋆	⋆	⋆	⋆	⋆	⋆
	cTP_y	⋆	⋆	⋆	⋆	⋆	⋆	⋆
	S	⋆	⋆	⋆	⋆	⋆	⋆	⋆
	SD1	⋆	⋆	⋆	⋆	⋆	⋆	⋆
	SD2	⋆	⋆	⋆	⋆	⋆	⋆	⋆
	SD1/SD2	⋆	⋆	⋆	⋆	⋆	⋆	⋆
EM	AVNN	⋆	⋆	⋆	⋆	⋆	⋆	⋆
	SDNN	⋆	⋆	⋆	⋆	⋆	⋆	⋆
	RMSSD	⋆	⋆	⋆	⋆	⋆	⋆	⋆
	pNN50	⋆	⋆	⋆	⋆	⋆	⋆	⋆
	VLF	⋆	⋆	⋆	⋆	⋆	-	⋆
	LF	⋆	⋆	⋆	⋆	⋆	⋆	⋆
	HF	⋆	⋆	⋆	⋆	⋆	⋆	⋆
	TP	⋆	⋆	⋆	⋆	⋆	⋆	⋆
	nLF	⋆	⋆	-	⋆	⋆	⋆	⋆
	nHF	⋆	⋆	⋆	⋆	⋆	⋆	⋆
	LF/HF	⋆	⋆	⋆	⋆	⋆	⋆	⋆
	cLF_x	⋆	⋆	-	⋆	-	-	-
	cLF_y	⋆	⋆	⋆	⋆	⋆	-	-
	cHF_x	⋆	-	-	⋆	-	-	-
	cHF_y	⋆	⋆	⋆	⋆	⋆	⋆	⋆
	cTP_x	⋆	⋆	⋆	⋆	⋆	⋆	⋆
	cTP_y	⋆	⋆	⋆	⋆	⋆	⋆	⋆
	S	⋆	⋆	⋆	⋆	⋆	⋆	⋆
	SD1	⋆	⋆	⋆	⋆	⋆	⋆	⋆
	SD2	⋆	⋆	⋆	⋆	⋆	⋆	⋆
	SD1/SD2	⋆	⋆	⋆	⋆	⋆	⋆	⋆

Continued on next page

Table 6.20 – continued from previous page

Noise	Index	Interaction						
		A	**B**	**C**	**A × B**	**A × C**	**B × C**	**A × B × C**
MA	AVNN	⋆	⋆	⋆	⋆	⋆	⋆	⋆
	SDNN	⋆	⋆	⋆	⋆	⋆	⋆	⋆
	RMSSD	⋆	⋆	⋆	⋆	⋆	⋆	⋆
	pNN50	⋆	⋆	⋆	⋆	⋆	⋆	⋆
	VLF	⋆	⋆	⋆	⋆	⋆	-	⋆
	LF	⋆	⋆	⋆	⋆	⋆	⋆	⋆
	HF	⋆	⋆	⋆	⋆	⋆	⋆	⋆
	TP	⋆	⋆	⋆	⋆	⋆	⋆	⋆
	nLF	⋆	⋆	-	⋆	⋆	⋆	⋆
	nHF	⋆	⋆	⋆	⋆	⋆	⋆	⋆
	LF/HF	⋆	⋆	⋆	⋆	⋆	⋆	⋆
	cLF_x	⋆	⋆	-	⋆	-	-	-
	cLF_y	⋆	⋆	⋆	⋆	⋆	-	-
	cHF_x	⋆	⋆	-	⋆	-	-	-
	cHF_y	⋆	⋆	⋆	⋆	⋆	⋆	⋆
	cTP_x	⋆	⋆	⋆	⋆	⋆	⋆	⋆
	cTP_y	⋆	⋆	⋆	⋆	⋆	⋆	⋆
	S	⋆	⋆	⋆	⋆	⋆	⋆	⋆
	SD1	⋆	⋆	⋆	⋆	⋆	⋆	⋆
	SD2	⋆	⋆	⋆	⋆	⋆	⋆	⋆
	SD1/SD2	⋆	⋆	⋆	⋆	⋆	⋆	⋆
RES + BW	AVNN	⋆	⋆	⋆	⋆	⋆	⋆	⋆
	SDNN	⋆	⋆	⋆	⋆	⋆	⋆	⋆
	RMSSD	⋆	⋆	⋆	⋆	⋆	⋆	⋆
	pNN50	⋆	⋆	⋆	⋆	⋆	⋆	⋆
	VLF	⋆	⋆	⋆	⋆	⋆	⋆	⋆
	LF	⋆	⋆	⋆	⋆	⋆	⋆	⋆
	HF	⋆	⋆	⋆	⋆	⋆	⋆	⋆
	TP	⋆	⋆	⋆	⋆	⋆	⋆	⋆
	nLF	⋆	⋆	⋆	⋆	⋆	⋆	⋆

Continued on next page

Table 6.20 – continued from previous page

Noise	Index	Interaction						
		A	**B**	**C**	**A × B**	**A × C**	**B × C**	**A × B × C**
RES + BW	nHF	⋆	⋆	⋆	⋆	⋆	⋆	⋆
	LF/HF	⋆	⋆	⋆	⋆	⋆	⋆	⋆
	cLF_x	⋆	⋆	-	⋆	-	-	-
	cLF_y	⋆	⋆	⋆	⋆	⋆	-	⋆
	cHF_x	⋆	⋆	-	⋆	-	-	-
	cHF_y	⋆	⋆	⋆	⋆	⋆	⋆	⋆
	cTP_x	⋆	⋆	⋆	⋆	⋆	⋆	⋆
	cTP_y	⋆	⋆	⋆	⋆	⋆	⋆	⋆
	S	⋆	⋆	⋆	⋆	⋆	⋆	⋆
	SD1	⋆	⋆	⋆	⋆	⋆	⋆	⋆
	SD2	⋆	⋆	⋆	⋆	⋆	⋆	⋆
	SD1/SD2	⋆	⋆	⋆	⋆	⋆	⋆	⋆
RES + EM	AVNN	⋆	⋆	⋆	⋆	⋆	⋆	⋆
	SDNN	⋆	⋆	⋆	⋆	⋆	⋆	⋆
	RMSSD	⋆	⋆	⋆	⋆	⋆	⋆	⋆
	pNN50	⋆	⋆	⋆	⋆	⋆	⋆	⋆
	VLF	⋆	⋆	⋆	⋆	⋆	⋆	⋆
	LF	⋆	⋆	⋆	⋆	⋆	⋆	⋆
	HF	⋆	⋆	⋆	⋆	⋆	⋆	⋆
	TP	⋆	⋆	⋆	⋆	⋆	⋆	⋆
	nLF	⋆	-	-	⋆	⋆	-	-
	nHF	⋆	⋆	⋆	⋆	⋆	⋆	⋆
	LF/HF	⋆	⋆	⋆	⋆	⋆	⋆	⋆
	cLF_x	⋆	⋆	-	⋆	-	-	-
	cLF_y	⋆	⋆	⋆	⋆	⋆	-	-
	cHF_x	⋆	-	-	⋆	-	-	-
	cHF_y	⋆	⋆	⋆	⋆	⋆	⋆	⋆
	cTP_x	⋆	⋆	⋆	⋆	⋆	⋆	⋆
	cTP_y	⋆	⋆	⋆	⋆	⋆	⋆	⋆
	S	⋆	⋆	⋆	⋆	⋆	⋆	⋆

Continued on next page

Table 6.20 – continued from previous page

Noise	Index	Interaction						
		A	**B**	**C**	**A × B**	**A × C**	**B × C**	**A × B × C**
RES + EM	SD1	⋆	⋆	⋆	⋆	⋆	⋆	⋆
	SD2	⋆	⋆	⋆	⋆	⋆	⋆	⋆
	SD1/SD2	⋆	⋆	⋆	⋆	⋆	⋆	⋆
RES + MA	AVNN	⋆	⋆	⋆	⋆	⋆	⋆	⋆
	SDNN	⋆	⋆	⋆	⋆	⋆	⋆	⋆
	RMSSD	⋆	⋆	⋆	⋆	⋆	⋆	⋆
	pNN50	⋆	⋆	⋆	⋆	⋆	⋆	⋆
	VLF	⋆	⋆	⋆	⋆	⋆	⋆	⋆
	LF	⋆	⋆	⋆	⋆	⋆	⋆	⋆
	HF	⋆	⋆	⋆	⋆	⋆	⋆	⋆
	TP	⋆	⋆	⋆	⋆	⋆	⋆	⋆
	nLF	⋆	⋆	-	⋆	⋆	⋆	⋆
	nHF	⋆	⋆	⋆	⋆	⋆	⋆	⋆
	LF/HF	⋆	⋆	⋆	⋆	⋆	⋆	⋆
	cLF_x	-	⋆	-	⋆	-	-	-
	cLF_y	⋆	⋆	⋆	⋆	⋆	-	-
	cHF_x	⋆	⋆	-	-	-	-	-
	cHF_y	⋆	⋆	⋆	⋆	⋆	⋆	⋆
	cTP_x	⋆	⋆	⋆	⋆	⋆	⋆	⋆
	cTP_y	⋆	⋆	⋆	⋆	⋆	⋆	⋆
	S	⋆	⋆	⋆	⋆	⋆	⋆	⋆
	SD1	⋆	⋆	⋆	⋆	⋆	⋆	⋆
	SD2	⋆	⋆	⋆	⋆	⋆	⋆	⋆
	SD1/SD2	⋆	⋆	⋆	⋆	⋆	⋆	⋆
BW + EM	AVNN	⋆	⋆	⋆	⋆	⋆	⋆	⋆
	SDNN	⋆	⋆	⋆	⋆	⋆	⋆	⋆
	RMSSD	⋆	⋆	⋆	⋆	⋆	⋆	⋆
	pNN50	⋆	⋆	⋆	⋆	⋆	⋆	⋆
	VLF	⋆	⋆	⋆	⋆	⋆	⋆	⋆
	LF	⋆	⋆	⋆	⋆	⋆	⋆	⋆

Continued on next page

Table 6.20 – continued from previous page

Noise	Index	Interaction						
		A	**B**	**C**	**A × B**	**A × C**	**B × C**	**A × B × C**
BW + EM	HF	⋆	⋆	⋆	⋆	⋆	⋆	⋆
	TP	⋆	⋆	⋆	⋆	⋆	⋆	⋆
	nLF	⋆	⋆	⋆	⋆	⋆	⋆	⋆
	nHF	⋆	⋆	⋆	⋆	⋆	⋆	⋆
	LF/HF	⋆	⋆	⋆	⋆	⋆	⋆	⋆
	cLF_x	⋆	⋆	⋆	⋆	-	-	⋆
	cLF_y	⋆	⋆	⋆	⋆	⋆	-	-
	cHF_x	⋆	⋆	-	⋆	-	-	-
	cHF_y	⋆	⋆	⋆	⋆	⋆	⋆	⋆
	cTP_x	⋆	⋆	⋆	⋆	⋆	⋆	⋆
	cTP_y	⋆	⋆	⋆	⋆	⋆	⋆	⋆
	S	⋆	⋆	⋆	⋆	⋆	⋆	⋆
	SD1	⋆	⋆	⋆	⋆	⋆	⋆	⋆
	SD2	⋆	⋆	⋆	⋆	⋆	⋆	⋆
	SD1/SD2	⋆	⋆	⋆	⋆	⋆	⋆	⋆
BW + MA	AVNN	⋆	⋆	⋆	⋆	⋆	⋆	⋆
	SDNN	⋆	⋆	⋆	⋆	⋆	⋆	⋆
	RMSSD	⋆	⋆	⋆	⋆	⋆	⋆	⋆
	pNN50	⋆	⋆	⋆	⋆	⋆	⋆	⋆
	VLF	⋆	⋆	⋆	⋆	⋆	⋆	⋆
	LF	⋆	⋆	⋆	⋆	⋆	⋆	⋆
	HF	⋆	⋆	⋆	⋆	⋆	⋆	⋆
	TP	⋆	⋆	⋆	⋆	⋆	⋆	⋆
	nLF	⋆	⋆	⋆	⋆	⋆	⋆	⋆
	nHF	⋆	⋆	⋆	⋆	⋆	⋆	⋆
	LF/HF	⋆	⋆	⋆	⋆	⋆	⋆	⋆
	cLF_x	⋆	⋆	-	⋆	-	-	⋆
	cLF_y	⋆	⋆	⋆	⋆	⋆	-	⋆
	cHF_x	⋆	⋆	-	⋆	-	-	-
	cHF_y	⋆	⋆	⋆	⋆	⋆	⋆	⋆

Continued on next page

Table 6.20 – continued from previous page

Noise	Index	Interaction						
		A	**B**	**C**	**A × B**	**A × C**	**B × C**	**A × B × C**
BW + MA	cTP_x	⋆	⋆	⋆	⋆	⋆	⋆	⋆
	cTP_y	⋆	⋆	⋆	⋆	⋆	⋆	⋆
	S	⋆	⋆	⋆	⋆	⋆	⋆	⋆
	SD1	⋆	⋆	⋆	⋆	⋆	⋆	⋆
	SD2	⋆	⋆	⋆	⋆	⋆	⋆	⋆
	SD1/SD2	⋆	⋆	⋆	⋆	⋆	⋆	⋆
EM + MA	AVNN	⋆	⋆	⋆	⋆	⋆	⋆	⋆
	SDNN	⋆	⋆	⋆	⋆	⋆	⋆	⋆
	RMSSD	⋆	⋆	⋆	⋆	⋆	⋆	⋆
	pNN50	⋆	⋆	⋆	⋆	⋆	⋆	⋆
	VLF	⋆	⋆	⋆	⋆	⋆	-	⋆
	LF	⋆	⋆	⋆	⋆	⋆	⋆	⋆
	HF	⋆	⋆	⋆	⋆	⋆	⋆	⋆
	TP	⋆	⋆	⋆	⋆	⋆	⋆	⋆
	nLF	⋆	⋆	-	⋆	⋆	⋆	⋆
	nHF	⋆	⋆	⋆	⋆	⋆	⋆	⋆
	LF/HF	⋆	⋆	⋆	⋆	⋆	⋆	⋆
	cLF_x	⋆	⋆	⋆	⋆	-	-	-
	cLF_y	⋆	⋆	⋆	⋆	⋆	-	-
	cHF_x	⋆	⋆	-	⋆	-	-	-
	cHF_y	⋆	⋆	⋆	⋆	⋆	⋆	⋆
	cTP_x	⋆	⋆	⋆	⋆	⋆	⋆	⋆
	cTP_y	⋆	⋆	⋆	⋆	⋆	⋆	⋆
	S	⋆	⋆	⋆	⋆	⋆	⋆	⋆
	SD1	⋆	⋆	⋆	⋆	⋆	⋆	⋆
	SD2	⋆	⋆	⋆	⋆	⋆	⋆	⋆
	SD1/SD2	⋆	⋆	⋆	⋆	⋆	⋆	⋆
RES + BW + EM	AVNN	⋆	⋆	⋆	⋆	⋆	⋆	⋆
	SDNN	⋆	⋆	⋆	⋆	⋆	⋆	⋆
	RMSSD	⋆	⋆	⋆	⋆	⋆	⋆	⋆

Continued on next page

Table 6.20 – continued from previous page

Noise	Index	Interaction						
		A	**B**	**C**	**A × B**	**A × C**	**B × C**	**A × B × C**
RES + BW + EM	pNN50	⋆	⋆	⋆	⋆	⋆	⋆	⋆
	VLF	⋆	⋆	⋆	⋆	⋆	⋆	⋆
	LF	⋆	⋆	⋆	⋆	⋆	⋆	⋆
	HF	⋆	⋆	⋆	⋆	⋆	⋆	⋆
	TP	⋆	⋆	⋆	⋆	⋆	⋆	⋆
	nLF	⋆	⋆	⋆	⋆	⋆	⋆	⋆
	nHF	⋆	⋆	⋆	⋆	⋆	⋆	⋆
	LF/HF	⋆	⋆	⋆	⋆	⋆	⋆	⋆
	cLF_x	⋆	⋆	-	⋆	-	-	-
	cLF_y	⋆	⋆	⋆	⋆	⋆	-	⋆
	cHF_x	⋆	⋆	-	⋆	-	-	-
	cHF_y	⋆	⋆	⋆	⋆	⋆	⋆	⋆
	cTP_x	⋆	⋆	⋆	⋆	⋆	⋆	⋆
	cTP_y	⋆	⋆	⋆	⋆	⋆	⋆	⋆
	S	⋆	⋆	⋆	⋆	⋆	⋆	⋆
	SD1	⋆	⋆	⋆	⋆	⋆	⋆	⋆
	SD2	⋆	⋆	⋆	⋆	⋆	⋆	⋆
	SD1/SD2	⋆	⋆	⋆	⋆	⋆	⋆	⋆
RES + BW + MA	AVNN	⋆	⋆	⋆	⋆	⋆	⋆	⋆
	SDNN	⋆	⋆	⋆	⋆	⋆	⋆	⋆
	RMSSD	⋆	⋆	⋆	⋆	⋆	⋆	⋆
	pNN50	⋆	⋆	⋆	⋆	⋆	⋆	⋆
	VLF	⋆	⋆	⋆	⋆	⋆	⋆	⋆
	LF	⋆	⋆	⋆	⋆	⋆	⋆	⋆
	HF	⋆	⋆	⋆	⋆	⋆	⋆	⋆
	TP	⋆	⋆	⋆	⋆	⋆	⋆	⋆
	nLF	⋆	⋆	⋆	⋆	⋆	⋆	⋆
	nHF	⋆	⋆	⋆	⋆	⋆	⋆	⋆
	LF/HF	⋆	⋆	⋆	⋆	⋆	⋆	⋆
	cLF_x	⋆	⋆	-	⋆	-	-	⋆

Continued on next page

Table 6.20 – continued from previous page

Noise	Index	Interaction						
		A	**B**	**C**	**A × B**	**A × C**	**B × C**	**A × B × C**
RES + BW + MA	cLF_y	⋆	⋆	⋆	⋆	⋆	-	⋆
	cHF_x	⋆	⋆	-	⋆	-	-	-
	cHF_y	⋆	⋆	⋆	⋆	⋆	⋆	⋆
	cTP_x	⋆	⋆	⋆	⋆	⋆	⋆	⋆
	cTP_y	⋆	⋆	⋆	⋆	⋆	⋆	⋆
	S	⋆	⋆	⋆	⋆	⋆	⋆	⋆
	SD1	⋆	⋆	⋆	⋆	⋆	⋆	⋆
	SD2	⋆	⋆	⋆	⋆	⋆	⋆	⋆
	SD1/SD2	⋆	⋆	⋆	⋆	⋆	⋆	⋆
RES + EM + MA	AVNN	⋆	⋆	⋆	⋆	⋆	⋆	⋆
	SDNN	⋆	⋆	⋆	⋆	⋆	⋆	⋆
	RMSSD	⋆	⋆	⋆	⋆	⋆	⋆	⋆
	pNN50	⋆	⋆	⋆	⋆	⋆	⋆	⋆
	VLF	⋆	⋆	⋆	⋆	⋆	⋆	⋆
	LF	⋆	⋆	⋆	⋆	⋆	⋆	⋆
	HF	⋆	⋆	⋆	⋆	⋆	⋆	⋆
	TP	⋆	⋆	⋆	⋆	⋆	⋆	⋆
	nLF	⋆	⋆	-	⋆	⋆	⋆	⋆
	nHF	⋆	⋆	⋆	⋆	⋆	⋆	⋆
	LF/HF	⋆	⋆	⋆	⋆	⋆	⋆	⋆
	cLF_x	-	⋆	-	⋆	-	-	-
	cLF_y	⋆	⋆	⋆	⋆	⋆	-	-
	cHF_x	⋆	⋆	-	⋆	-	-	-
	cHF_y	⋆	⋆	⋆	⋆	⋆	⋆	⋆
	cTP_x	⋆	⋆	⋆	⋆	⋆	⋆	⋆
	cTP_y	⋆	⋆	⋆	⋆	⋆	⋆	⋆
	S	⋆	⋆	⋆	⋆	⋆	⋆	⋆
	SD1	⋆	⋆	⋆	⋆	⋆	⋆	⋆
	SD2	⋆	⋆	⋆	⋆	⋆	⋆	⋆
	SD1/SD2	⋆	⋆	⋆	⋆	⋆	⋆	⋆

Continued on next page

Table 6.20 – continued from previous page

Noise	Index	Interaction						
		A	**B**	**C**	**A × B**	**A × C**	**B × C**	**A × B × C**
BW + EM + MA	AVNN	⋆	⋆	⋆	⋆	⋆	⋆	⋆
	SDNN	⋆	⋆	⋆	⋆	⋆	⋆	⋆
	RMSSD	⋆	⋆	⋆	⋆	⋆	⋆	⋆
	pNN50	⋆	⋆	⋆	⋆	⋆	⋆	⋆
	VLF	⋆	⋆	⋆	⋆	⋆	⋆	⋆
	LF	⋆	⋆	⋆	⋆	⋆	⋆	⋆
	HF	⋆	⋆	⋆	⋆	⋆	⋆	⋆
	TP	⋆	⋆	⋆	⋆	⋆	⋆	⋆
	nLF	⋆	⋆	⋆	⋆	⋆	⋆	⋆
	nHF	⋆	⋆	⋆	⋆	⋆	⋆	⋆
	LF/HF	⋆	⋆	⋆	⋆	⋆	⋆	⋆
	cLF_x	⋆	⋆	-	⋆	⋆	-	⋆
	cLF_y	⋆	⋆	⋆	⋆	⋆	-	⋆
	cHF_x	⋆	⋆	-	⋆	-	-	-
	cHF_y	⋆	⋆	⋆	⋆	⋆	⋆	⋆
	cTP_x	⋆	⋆	⋆	⋆	⋆	⋆	⋆
	cTP_y	⋆	⋆	⋆	⋆	⋆	⋆	⋆
	S	⋆	⋆	⋆	⋆	⋆	⋆	⋆
	SD1	⋆	⋆	⋆	⋆	⋆	⋆	⋆
	SD2	⋆	⋆	⋆	⋆	⋆	⋆	⋆
	SD1/SD2	⋆	⋆	⋆	⋆	⋆	⋆	⋆
RES + BW + EM + MA	AVNN	⋆	⋆	⋆	⋆	⋆	⋆	⋆
	SDNN	⋆	⋆	⋆	⋆	⋆	⋆	⋆
	RMSSD	⋆	⋆	⋆	⋆	⋆	⋆	⋆
	pNN50	⋆	⋆	⋆	⋆	⋆	⋆	⋆
	VLF	⋆	⋆	⋆	⋆	⋆	⋆	⋆
	LF	⋆	⋆	⋆	⋆	⋆	⋆	⋆
	HF	⋆	⋆	⋆	⋆	⋆	⋆	⋆
	TP	⋆	⋆	⋆	⋆	⋆	⋆	⋆
	nLF	⋆	⋆	⋆	⋆	⋆	⋆	⋆

Continued on next page

Table 6.20 – continued from previous page

Noise	Index	Interaction						
		A	**B**	**C**	**A × B**	**A × C**	**B × C**	**A × B × C**
RES + BW + EM + MA	nHF	⋆	⋆	⋆	⋆	⋆	⋆	⋆
	LF/HF	⋆	⋆	⋆	⋆	⋆	⋆	⋆
	cLF_x	⋆	⋆	-	⋆	⋆	-	-
	cLF_y	⋆	⋆	⋆	⋆	⋆	-	⋆
	cHF_x	⋆	⋆	-	⋆	-	-	-
	cHF_y	⋆	⋆	⋆	⋆	⋆	⋆	⋆
	cTP_x	⋆	⋆	⋆	⋆	⋆	⋆	⋆
	cTP_y	⋆	⋆	⋆	⋆	⋆	⋆	⋆
	S	⋆	⋆	⋆	⋆	⋆	⋆	⋆
	SD1	⋆	⋆	⋆	⋆	⋆	⋆	⋆
	SD2	⋆	⋆	⋆	⋆	⋆	⋆	⋆
	SD1/SD2	⋆	⋆	⋆	⋆	⋆	⋆	⋆

From these results, it can be seen that the three factors, i.e., the type of filter and its cut-off frequencies, have a significant effect in most PRV indices, as well as their interactions, when excellent and acceptable quality PPG signals are used, and these are contaminated with different kind of noises. In line with what was found in previous experiments, the x-coordinates of centroid-related indices tend to be less affected by the interaction of factors.

As was done in previous experiments, the combinations of factors that gave the lowest difference to gold standard indices were determined. These differences found using the best combination of factors for each type of noise and each index are shown in Figures 6.25 and 6.26. These figures show the absolute difference between PRV indices obtained from measured and gold standard PRV trends. The pNN50 index is not shown given the extremely large differences shown in the measurement of this index, probably due to the presence of outliers in the detection of IBIs from contaminated PPG signals. Therefore, care should be taken when this particular index is measured from PRV extracted from noisy PPG signals regardless of the filtering strategy used. Interestingly, pNN50 was more affected when extracted from noise-contaminated excellent quality PPG signals.

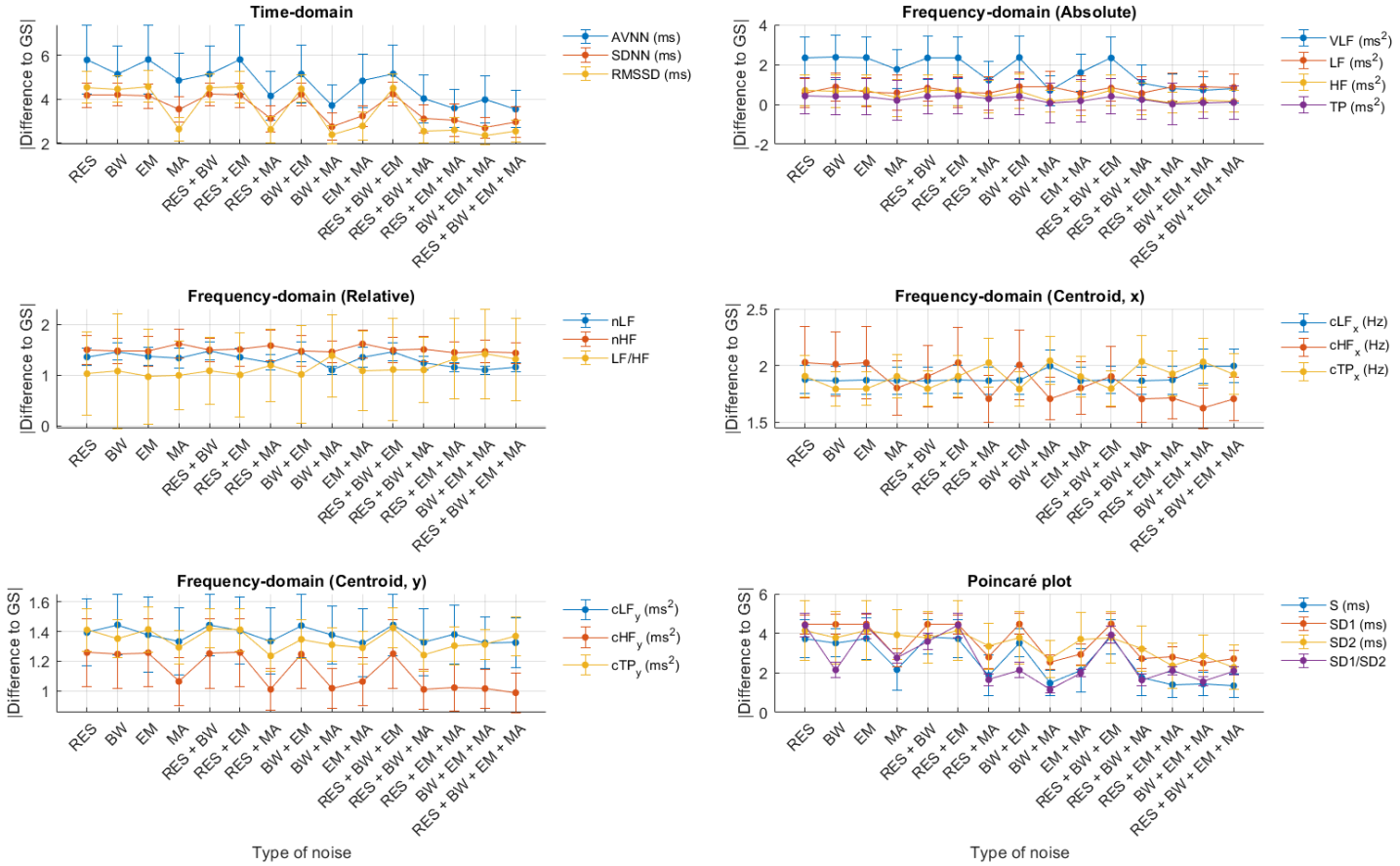

Figure 6.25: Mean and standard deviation of absolute differences between pulse rate variability (PRV) indices extracted from excellent quality photoplethysmographic (PPG) signals contaminated with different noises and filtered using the best combination of factors obtained, against indices obtained from gold standard PRV trends. RES: Respiratory noise. BW: Baseline wandering. EM: Electromagnetic noise. MA: Movement artifact.

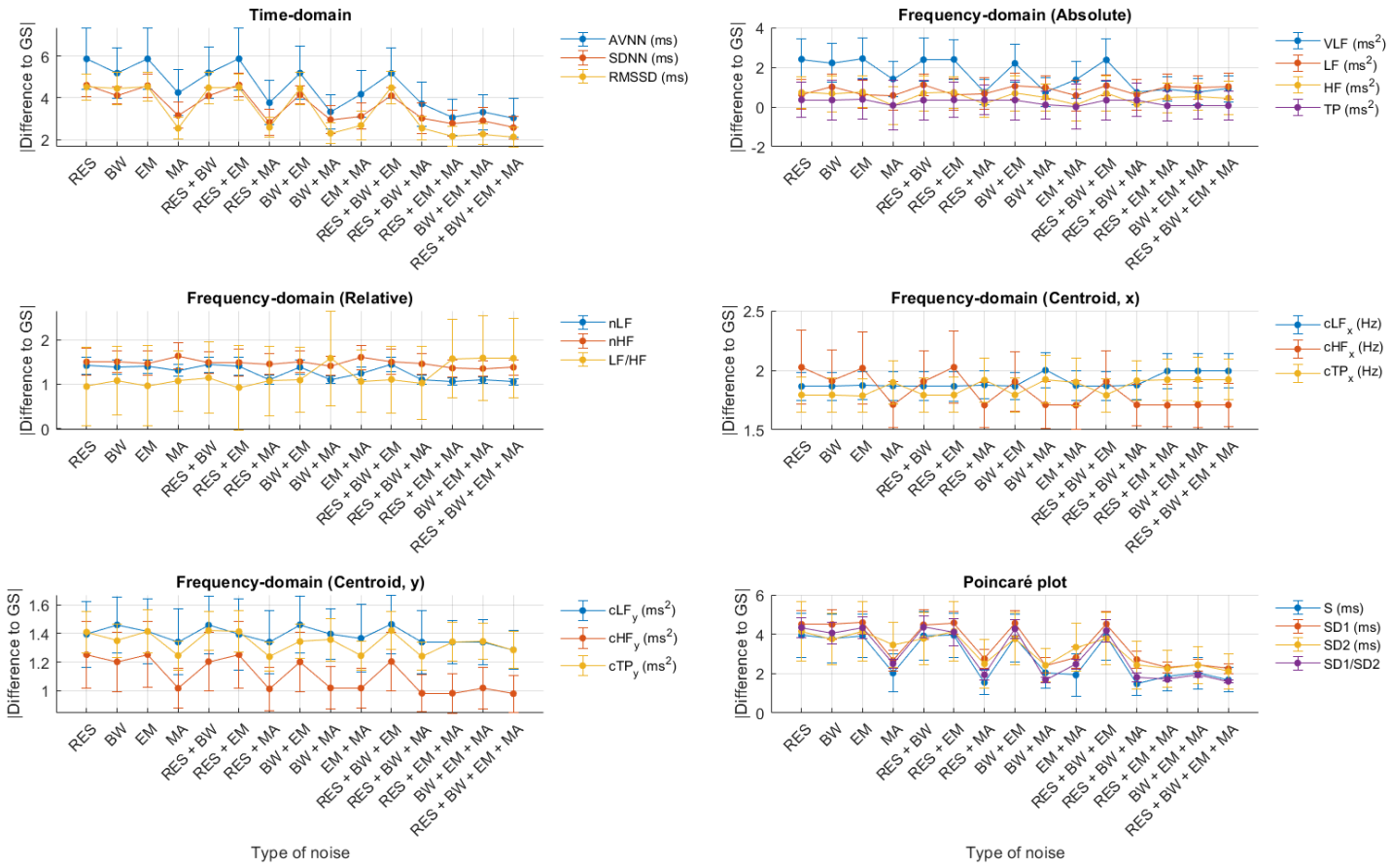

Figure 6.26: Mean and standard deviation of absolute differences between pulse rate variability (PRV) indices extracted from acceptable quality photoplethysmographic (PPG) signals contaminated with different noises and filtered using the best combination of factors obtained, against indices obtained from gold standard PRV trends. RES: Respiratory noise. BW: Baseline wandering. EM: Electromagnetic noise. MA: Movement artifact.

Table 6.21: Best combination of factors for filtering excellent quality photoplethysmographic signals with different types of noise. FIR: Finite impulse response filters. IIR: Infinite impulse response filters. RES: Respiratory noise. BW: Baseline wandering. EM: Electromagnetic noise. MA: Movement artifact. fc_{low}: Low cut-off frequency. fc_{high}: High cut-off frequency.

Noise	Type of filter	fc_{low} (Hz)	fc_{high} (Hz)
RES	IIR Elliptic	0	20
BW	IIR Elliptic	0	12
EM	IIR Elliptic	0	20
MA	IIR Elliptic	0.2	20
RES + BW	IIR Elliptic	0	20
RES + EM	IIR Elliptic	0.2	20
RES + MA	FIR Equiripple	1	8
BW + EM	IIR Elliptic	0	20
BW + MA	FIR Parks-McClellan	2	12
EM + MA	IIR Elliptic	0.1	20
RES + BW + EM	IIR Elliptic	0.1	20
RES + BW + MA	FIR Equiripple	1	8
RES + EM + MA	FIR Equiripple	0.1	12
BW + EM + MA	FIR Equiripple	0.1	12
RES + BW + EM + MA	FIR Equiripple	0.1	12

In the case of the other PRV indices obtained from noise contaminated, excellent quality PPG signals, frequency-domain indices showed a relatively stable difference to gold standard, regardless of the type of noise. VLF was the index that showed the larger differences to gold standard. Time-domain and Poincaré plot indices did show changes in the differences due to the noise present in the signal. Interestingly, the more complex the noise, the lower differences were obtained after filtering the PPG signal with optimal parameters. For these indices, AVNN was the most affected one. A similar behaviour can be observed when PRV is obtained from noise-contaminated, acceptable quality PPG signals.

The most common parameters that gave the lowest differences for each of the types of noise are shown in Tables 6.21 and 6.22, for excellent and acceptable quality PPG signals respectively. It was observed that the extraction of PRV from excellent and acceptable quality PPG signals contaminated with different types of noise tends to be more reliable if the PPG signals are filtered using elliptic IIR filters, or equiripple or Parks-McClellan FIR filters. There were differences in these results due to the different quality of signals, but these three types of filters showed the lowest differences to gold standard indices. Again, it should be remarked that pNN50 showed an unreliable behaviour, and care should be taken when measuring this index from PRV extracted from noise-contaminated PPG signals.

Table 6.22: Best combination of factors for filtering acceptable quality photoplethysmographic signals with different types of noise. FIR: Finite impulse response filters. IIR: Infinite impulse response filters. RES: Respiratory noise. BW: Baseline wandering. EM: Electromagnetic noise. MA: Movement artifact. fc_{low}: Low cut-off frequency. fc_{high}: High cut-off frequency.

Noise	Type of filter	fc_{low} (Hz)	fc_{high} (Hz)
RES	IIR Elliptic	0	20
BW	FIR Parks-McClellan	0	20
EM	IIR Elliptic	0	20
MA	IIR Elliptic	0.1	20
RES + BW	IIR Elliptic	0	12
RES + EM	IIR Elliptic	0	20
RES + MA	FIR Parks-McClellan	0	10
BW + EM	FIR Parks-McClellan	0	20
BW + MA	FIR Parks-McClellan	0	12
EM + MA	FIR Parks-McClellan	0.1	20
RES + BW + EM	IIR Elliptic	0	20
RES + BW + MA	FIR Parks-McClellan	0	10
RES + EM + MA	FIR Equiripple	0	8
BW + EM + MA	FIR Parks-McClellan	0.5	15
RES + BW + EM + MA	FIR Equiripple	0.5	8

For excellent quality PPG signals and most of the types of noises studied in this experiment, lower low cut-off frequencies gave better results. In the case of high cut-off frequencies, most results showed better performance when 20 Hz was used as high cut-off frequency. Only when movement artifact and respiratory noise, or when movement artifact, respiratory noise and baseline wandering where present in the signal, the high cut-off frequency with better performance was found to be 8 Hz. This could be a result of the frequency content of the movement artifact.

When acceptable quality signals were analysed, the lower low cut-off frequency used, the better results were obtained, with most filters acting as low pass filters. For high cut-off frequencies, a similar pattern was observed as in excellent quality PPG signals.

6.4 Discussion

PPG-based PRV has been proposed as an alternative to evaluate cardiovascular autonomic activity, instead of HRV acquired from ECG signals. However, the relationship between these two variables is not entirely understood, and there is evidence of both physiological and technical aspects that may affect PRV differently to HRV (Schäfer & Vagedes 2013). Moreover, although guidelines have been proposed for

the extraction and analysis of HRV information from ECG signals (Task Force of the European Society of Cardiology and The North American Society of Pacing and Electrophysiology 1996), there is not a standard procedure for the analysis of PRV information from pulse wave signals, specifically from PPG. In this chapter, the aim was to evaluate how certain technical aspects affect the assessment of frequently used time-domain, frequency-domain and Poincaré plot indices from PRV. For this, a model for simulating PPG signals with varying PRV information was proposed, and six experiments were performed for evaluating the effects of these technical aspects on PRV assessment.

6.4.1 Signal simulation

Simulation of PPG signals opens the door for the development and assessment of novel algorithms and techniques that aid in a more efficient and reliable analysis of the PPG (Tang, Chen, Ward & Elgendi 2020, Tang, Chen, Allen, Alian, Menon, Ward & Elgendi 2020). This is due to the capability of simulating a large number of signals with varying features, such as sampling rate, mean heart rate or the quality of the signal. Moreover, it allows for the analysis of signals in a controlled environment, in which no physiological or environmental factors can affect the information obtained from the PPG.

Different mathematical models have been proposed in the literature for the simulation of PPG signals. As in the model used for this study, Tang et al. (Tang, Chen, Ward & Elgendi 2020, Tang, Chen, Allen, Alian, Menon, Ward & Elgendi 2020) and Martín-Martínez et al. (2013) proposed simulating PPG signals based on the summation of two independent Gaussian functions, whereas other models have used more Gaussian functions for the simulation and parameter estimation of PPG signals (Rubins 2008, Wang et al. 2013, Sološenko et al. 2017). The selection of the 2 Gaussian models for this study was based on the simplicity for modelling a single pulse with a given duration. Moreover, the quality of the simulated signal in the proposed model can be varied by changing the ratio of amplitudes of the Gaussian functions, which allow for the simulation of PPG signals with varying morphology, which could more reliably simulate signals acquired from different body sites, such as the earlobe or the neck (Charlton et al. 2019), or with varying vascular conditions, such as ageing (Allen & Murray 2003). Being able to simulate PPG signals with varying morphology could also allow for other studies, such as the development of

signal quality indices for PPG signals measured from different body sites (Nardelli et al. 2020).

Since the main aim of this study was to evaluate the effects of some technical aspects on PRV information extracted from PPG, the duration of the pulses for the simulated PPG signals were determined using a sinusoidal wave with randomly selected features, i.e., random amplitude, frequency content and offset. Each of these features were related to specific PRV indices: The amplitude relates to the standard deviation of the inter-beat intervals, SDNN; the frequency content was determined to belong in the frequency bands of interest for short-term PRV analysis (i.e. low- and high-frequency bands, LF and HF); and the offset relates to the average duration of the inter-beat intervals, AVNN. Therefore, these parameters were generated in specific ranges that could be observed in human beings.

By comparing the results obtained after processing the simulated signals to known features from the simulated PRV information, it was possible to evaluate the effects of some of these technical aspects on PRV, specifically the algorithms and fiducial points used to detect cardiac cycles and the sampling rate used to acquire PPG signals, in the absence of other confounding factors, such as movement or respiration. Although these aspects may alter the technical aspects of PRV analysis, they also have a physiological effect that may confound results of similar studies when PRV is obtained from real PPG signals and compared to ECG-derived HRV. Hence, although similar studies can be found in the literature, the validation of these factors in these studies is based on the comparison between PRV- and HRV-related indices, with HRV extracted from ECG signals considered as the gold standard. As has been mentioned, although PRV and HRV have a similar origin and HR and PR can be used as surrogates (Schäfer & Vagedes 2013), HRV and PRV are not always the same, and by comparing indices extracted from these two techniques, a bias could be introduced in the results. Hence, using simulated PPG signals with known PRV information allows for an unbiased assessment of technical aspects related to the acquisition and processing of PPG signals for the analysis of PRV information.

6.4.2 Experiment 1: Interbeat interval detection algorithms and fiducial points

The first experiment performed in this study aimed to determine the effects of changing the inter-beat intervals detection algorithm and the fiducial points used for the

extraction of PRV from PPG signals.

In general, it was observed that D2Max outperformed the other evaluated algorithms, especially when onset-related fiducial points were used, i.e., the A point from the second derivative of the PPG, the valley (ONS), and the intersection point of the tangent lines (TI) of the PPG. On the other hand, the combination of HeartPy and A points, for excellent PPG quality, and Delineator and P2 points, for acceptable PPG quality, were the algorithms and fiducial points that showed the worst performance for extracting PRV indices. In line with previous studies that have shown that PPG can be used to reliably estimate HR (Schäfer & Vagedes 2013), AVNN and SD2, which has been shown to reflect the same processes from the PRV (Khandoker et al. 2013), did not show a significant effect when the fiducial points were modified. Therefore, these indices could be extracted reliably from PRV traces derived using any of these fiducial points.

Although the combination of algorithms and fiducial points selected could affect the extracted indices, it is important to notice that most of the best performing combinations did not show statistically significant differences among them, opening a variety of options for the extraction of PRV from PPG signals, which could depend on several factors for the selection of the best combination for a given application, such as the computing power available, the indices of interest and the expected signal quality. Other algorithms and fiducial points have been proposed in the literature, and could give different results. However, it is evident that fiducial points related to the onset of the pulse tend to perform better, as do algorithms that are based on the identification for these points for the segmentation of inter-beat intervals from the PPG signal.

Similar studies can be found in the literature, in which authors compared PRV indices extracted from PPG using different fiducial points for the estimation of inter-beat intervals. Posada-Quintero, H.F., Delisle-Rodríguez, D., Cuadra-Sanz, M.B., & Fernández de la Vara-Prieto, R.R. (2013) and Hemon & Phillips (2016) found a better performance when PRV was extracted from TI points, while Pinheiro et al. (2016) concluded that using the time instants corresponding to 50%, 80% and the maximum peak amplitude of the PPG waveform resulted in less errors for measuring PRV. Although the results obtained by the latter authors do not correspond to those obtained in this experiment, they also concluded that the selection of the best fiducial point to use depended on the context, which is in line with the differences observed

between PRV extracted from excellent and acceptable quality PPG signals. This same conclusion has been achieved by Peralta et al. (2019), who found that there are differences in the performance of PRV extracted from several fiducial points when signals are obtained from the finger and the forehead, and they concluded that there is a need to define the fiducial points with best performance under different circumstances. In their results, they found that the middle amplitude point of the PPG signal, M1D and TI points have the best accuracy for PRV analysis. In these studies, however, the comparison was made between HRV and PRV indices, and the number of signals used in each study were limited.

Regarding the analysis of the best performing algorithms for PRV analysis, studies reported in the literature are much more scarce. In 2020, Argüello Prada & Paredes Higinio analysed the differences between a modified version of Upslopes and detecting cardiac cycles by identifying the maximum of the first derivative of the PPG signal, to determine PRV from PPG signals with sudden decreases in the signal amplitude (Argüello Prada & Paredes Higinio 2020). They found that the modified version of their algorithm, which they called MMPD, had better performance for detecting the sudden amplitude changes in PPG signals, while also gave better results in terms of PRV, although the differences were relatively small except for pNN50. In a similar analysis, Koch et al. evaluated the performance of their algorithm for PRV analysis (Koch et al. 2020). They applied their algorithm, which is based on the detection of systolic peaks from the PPG using artificial neural networks, for the extraction of PRV indices from PPG signals included in two publicly available databases, and found that it performed better when compared to two reference algorithms, i.e., an automatic multiscale-based peak detection and a decision tree-based peak detection, especially when noisy PPG signals were involved. However, in both cases, the details about how the reference algorithms were applied is not included.

In the case of the algorithms used in the present study, their performance has been evaluated according to their sensitivity (Sen), positive predictivity ($P+$) and root-mean-square error (RMSE) for the detection of cardiac cycles. Li et al. found a Sen of 99.43%, a $P+$ of 99.45% and an average error rate of 1.14% for Delineator when applied to arterial blood pressure waveforms (Li et al. 2010); Conn & Borkholder reported $Sen = 99.29\%$ and $P+ = 99.23\%$, with a temporal accuracy of 3.8 ± 2.6 ms when their algorithm, Wavelet, was applied to PPG signals ac-

quired from 13 subjects while exercising on a bike (Conn & Borkholder 2013); van Gent et al. reported RMSE for HeartPy when comparing the developed algorithm against the annotations from a PPG dataset with 20.7 h of recordings, and found that, when compared against other algorithms available in the literature (i.e., the Pan-Tompkins and HRVAS ECGViewer algorithms), HeartPy had lower errors for peak location (0.89 ms), RMSE for peak-to-peak intervals (29.64), RMSE for beats per minute (3.77) and RMSE for SDSD (167.77) (van Gent et al. 2019); Elgendi et al. reported $Sen = 99.84\%$ and $P+ = 99.89\%$ for D2max, when signals obtained from 40 healthy subjects under challenging conditions, and claim that D2max have comparable performance to other algorithms even if it showed lower accuracy (Elgendi et al. 2013); while Prada & Maldonado reported $Se = 99.75\%$, $P+ = 98.02\%$ and a Failure Detection Rate of 0.02% for Upslopes, concluding that their algorithm performed better than a benchmark algorithm and two previous versions of their own algorithm, when tested using two pediatric PPG recordings (Prada & Maldonado 2018). The only case in which an index from PRV was assessed for any of these algorithms was for HeartPy, and all of these algorithms were evaluated under different circumstances and databases. To the best of the knowledge of the author of this thesis, there have not been any studies that aimed to find the best combination of algorithms and fiducial points for the extraction of PRV information from PPG signals.

6.4.3 Experiment 2: Sampling rate

Using lower sampling rates for the extraction of PRV from PPG signals is highly desirable, especially for the continuous measurement of PRV indices in real-time scenarios using wearable devices or video-based PPG signals. From the second experiment performed in this study, it can be observed that, in most cases, the higher the sampling rate, the better performance for the extraction of PRV information. However, for most indices, the sampling frequency can be lowered to around 128 Hz, compared to the sampling rate suggested for HRV analysis (above 1 kHz (Task Force of the European Society of Cardiology and The North American Society of Pacing and Electrophysiology 1996)). Moreover, for applications in which obtaining the instant heart rate is the aim, having sampling rates as low as 32 Hz does not significantly affect the results. Hence, the selection of sampling rate depends on the intended application, but can be around 8 times lower than that suggested for HRV

analysis from ECG, which could save resources especially in real-time scenarios.

The results obtained for SDNN show an unexpected behaviour, in which increasing sampling rate affects the results obtained, showing a significant difference between the gold standard and the extracted PRV. More studies should aim to understand this behaviour, but it could be related to the way PRV information is being simulated in the model applied in this study.

Previous studies have aimed to understand how using lower sampling rates may affect PRV-related indices. Choi & Shin (2017) found that a sampling rate as low as 25 Hz was appropriate for the extraction of several PRV indices, while Ahn & Kim (2020) suggested that the sampling rate of PPG signals should not be lowered than 500 Hz for PRV analysis, after they compared HRV and PRV tachograms using cross-correlation. Also, Béres & Hejjel (2021) found that, as has been observed in this study, the sampling rate needed depends on the indices of interest, with a sampling rate as low as 5 Hz for the estimation of AVNN, and a sampling interval of at least 20 ms for the estimation of SDNN and RMSSD without interpolation of the PPG signal. In line with this study, the results obtained suggest that the sampling rate should be higher than 64 Hz for obtaining reliable results. As before, these previous studies were performed comparing HRV and PRV indices from smaller databases, unlike the results obtained in this experiment, in which PRV was compared to a known value and from a larger database, where the sample size was statistically determined. Therefore, there might be differences among the results and the conclusions that can relate to these two factors.

It is important to mention that reducing the sampling rate below the suggested values does not imply that PRV analysis cannot be performed. If PPG is acquired using low sampling rates, interpolation can be used to increase the performance for PRV measurement, as suggested by Béres, Holczer and Hejjel (Béres et al. 2019, Béres & Hejjel 2021), while other alternatives have been suggested, such as the parabola approximation method (Baek et al. 2017, Béres & Hejjel 2021), curve fitting (Panganiban, F.C. & de Leon, F.A. 2019), or other interval compensation methods (Watanabe et al. 2020).

6.4.4 Experiment 3: Spectral analysis

Frequency-domain indices are probably the most used HRV and PRV features since their relationship with specific processes related to autonomic regulation have been

shown in the literature (Task Force of the European Society of Cardiology and The North American Society of Pacing and Electrophysiology 1996, Billman 2013, Shaffer & Ginsberg 2017). However, at least for PRV analysis, there is no consensus regarding how frequency spectra should be derived from PRV time-domain trends, and very few research have been done concerning this issue.

As is mentioned in the guidelines for HRV analysis, the power spectral density (PSD) from HRV can be obtained using non-parametric (classical, such as FFT) and parametric (modern) methods (Task Force of the European Society of Cardiology and The North American Society of Pacing and Electrophysiology 1996). However, there are multiple algorithms and parameters that can be modified in order to calculate this PSD both from HRV and PRV trends, and research is scarce related to the optimisation of these parameters and their suitability to obtain frequency-domain indices from PRV. Li et al. (2019) provide a useful summary of the different methodologies used for spectral analysis from HRV trends. In the case of PRV, Akar et al. (2013) applied several pre-processing techniques for the extraction of PRV indices from PPG signals, and compared the spectra obtained using the periodogram, Welch's and Burg's algorithms. Although qualitative, their results showed differences in the extracted spectra due to the methods used for its extraction. Chen et al. (2018) evaluated the differences between frequency-domain indices extracted from PRV trends re-sampled using different sampling rates, concluding that, from data obtained from wearable devices, better results were obtained using a 1 Hz re-sampling rate for interpolating pulse rate information and extracting frequency-related information. And other studies have suggested the extraction of frequency-related indices using novel time-frequency techniques, such as empirical mode decomposition (Abeysekera & Jaisankar 2015, Chuang et al. 2015).

In the experiment performed in this study, the aim was to determine the best parameters for the extraction of spectral information from PRV trends. It was found that the morphology of the spectra, assessed by measuring cross-correlation indices between spectra obtained from gold standard and measured PRV trends, is affected, in most cases, by all the factors considered for obtaining the PSD and their interaction. However, PRV indices did not show this behaviour. In the case of classical spectral analysis, indices were mostly affected by the number of data points and the sampling rate used for interpolation before extracting PSD. Both these factors are related to the frequency resolution of the obtained spectra, which was shown to

be a critical factor for the assessment of frequency-related information regardless of the algorithm used for obtaining the spectra. The comparison of the behaviour of indices extracted using different modern methods is less straightforward, indicating the variability among the mathematical foundations for each of these algorithms. In the case of Yule-Walker and MUSIC algorithms, three-way interactions including the type of interpolation used and the order of the model showed significant behaviour, while for the remaining methods two-way interactions showed the most significant results.

It is noticeable that, in the case of centroid-related indices, there were more significant interactions for indices related to the y-coordinate, particularly for the centroid of the high-frequency band. This could be indicating that the different methods for assessing PRV frequency-content tend to be relatively stable for the distribution of the frequency-content, but there are differences in terms of the amplitude of the spectra. Hence, additional care should be taken when amplitude-related indices are of interest. Also of interest is the fact that Lomb-Scargle algorithm did not show a better performance than the other methods studied. This algorithm is based on probability distributions and does not require a periodically-sampled signal (Clifford 2006). However, its lower performance might be related precisely to the unpredictability of PRV trends and the largely variable parameters used for the simulation of PRV information.

In general, it was found that MUSIC and FFT had the best behaviour both for excellent and acceptable quality PPG signals. In the case of MUSIC, the best behaviour was found when PRV trends were resampled to 4 Hz using linear interpolation and when a fifth-order model was used, both for excellent and acceptable quality PPG signals, with frequency resolution of 0.0078 and 0.000122 Hz respectively. In the case of FFT, the best results regardless of quality of the signal were obtained after applying a cubic spline interpolation to obtain a 4-Hz PRV trend, and calculating the spectrum with 512 data points, for a frequency resolution of 0.0078 Hz. Given the simplicity of FFT, the computational load it has and the easiness to perform it in any platform, including embedded systems, it is recommended to obtain spectral information from PRV trends using this algorithm and these combination of parameters.

It is important to remark that the gold standard measurements were extracted using FFT, hence a bias could be present due to this. Nonetheless, the fact that the

MUSIC algorithm also showed a good performance, and that Welch's periodogram showed comparable results to FFT, indicate that the results obtained are reliable. Future studies should aim to verify these results using real data, or using simulated data by considering as gold standard not the measured indices but the frequency of sinusoidal components used for the generation of PRV trends.

6.4.5 Experiment 4: Duration of signal

Similarly as with sampling rate and given the growing interest in acquiring and analysing PPG signals using everyday devices, such as smartwatches, or smartbands or video-based PPG signals from smartphones, as well as using PRV for the extraction of physiological information in a continuous manner, there is interest in understanding how short can the analysis window be to obtain reliable PRV information. In the case of HRV, the standard is to use windows as short as 5 min (Task Force of the European Society of Cardiology and The North American Society of Pacing and Electrophysiology 1996), although shorter segments of ECG signals have been proposed for ultra-short HRV analysis (Pecchia et al. 2018). The results of this experiment suggest that PPG signals as short as 120 s, for obtaining time-domain, frequency-domain and Poincaré plot indices, give sufficiently reliable results, and that the differences to gold standard indices stabilise using PPG signals longer than 300 s.

It has usually been accepted that frequency-domain indices are more affected by the duration of the PPG signals used for PRV analysis than time-domain and non-linear indices, although further validation and analysis of ultra-short-term indices extracted both from HRV and PRV are needed (Shaffer & Ginsberg 2017). From the results obtained in this study, it can be concluded that the differences between indices obtained from longer duration gold standard trends and PRV indices measured from ultra-short term signals of at least 120 s duration are comparable, and that these differences become stable when measured from signals longer than 5 min. However, these results should be considered with care given the simulated nature of the signals used, and the fact that physiological processes are not considered in this study. The effects of using ultra-short signals for PRV analysis could be larger in diseased subjects or while executing different experimental protocols that may alter PRV behaviour, and care should be taken given the effects of outliers in ultra-short-term recordings (Shaffer & Ginsberg 2017).

As should have been expected, indices related to long-term changes in PRV, i.e. AVNN, LF- and TP-related indices, and SD2, are more affected by the duration of the signal, mostly showing larger differences to gold standard as shorter segments are employed. This could be explained by the nature of these indices, which are related to long-term changes in PRV, and as explained by Shaffer & Ginsberg (2017) most of these indices are not comparable between long-term and short-term analysis results.

Previous studies have reported on the validity of ultra-short-term measurements for HRV or PRV. Baek et al. (2015) obtained 5-min PPG signals from 467 healthy volunteers with a wide range of ages, and partitioned them into 270, 240, 210, 180, 150, 120, 90, 60, 30, 20 and 10 s segments. PRV indices were extracted from these short segments as well as the 5-min original signals, which were used as gold standard, and compared using correlation analysis, Kruskal-Wallis tests and Bland-Altman analysis. They found that the minimum duration of PPG segments varied according to group age and index, with a minimal duration of 10 s for AVNN; 20 s for HF; 30 s for RMSSD; 60 s for pNN50; 90 s for LF, nLF, nHF, and LF/HF; 240 s for SDNN; and 270 s for VLF. Most of these results are in line with those found in the current experiment, and the differences could be explained by the fact that these authors used shorter segments as gold standard than what was used in this experiment, and the effects of physiological factors that are not considered using simulated data. Regardless, these authors suggest the reliability of obtaining most PRV indices from ultra-short PPG signals. Similarly, Finžgar & Podržaj (2020) investigated the feasibility of assessing ultra-short-term PRV from video PPG, and compared their results to most of previous studies using video-based PPG and ultra-short recordings. Although their results suggest that SDNN, RMSSD and pNN50 could be reliably extracted from ultra-short PPG segments (10 s, 30 s and 60 s), their gold standard was indices extracted from 60 s segments, which should not be considered as accepted yet. Hence, validity of their results is under question and further analyses should be performed in the area of video-based PRV analysis. Nonetheless, other studies have suggested the validity of using 60 s segments for PRV analysis in healthy, fit subjects (Holmes et al. 2020).

Recently, similar studies have been reported for ECG-derived ultra-short-term HRV analysis. Kim et al. (2021) showed that ultra-short-term HRV could be assessed under static conditions with ECG signals with duration between 30 and 240 s, while under dynamic conditions longer segments are needed, even with unreliable

results for some indices regardless of the duration of the segments for ultra-short-term analysis. Gallardo et al. (2022) extracted LF/HF and SD1/SD2 from HRV trends with varying lengths, and concluded that signals with duration of 180 s and 120 s, respectively, should be considered as the minimum reliable duration for ultra-short-term HRV analysis. Finally, Canino et al. (2022) evaluated the feasibility of using 120 s ECG signals for the extraction of ultra-short-term HRV indices under different physiological conditions and data pre-processing techniques, and found that indices carry information related to different physiological states, although were not strongly predictors of aerobic fitness in healthy men, and found that most indices are robust to artifact correction procedures.

According to the results found in this experiment, PPG segments should be longer than 90 s for reliable estimation of PRV indices, which is in line with the results reported in the previously mentioned studies. Nonetheless, further studies with real data both from healthy and unhealthy populations are needed to understand the differences among ultra-short-, short- and long-term PRV indices, and how and when could shorter segments of PPG signals be used for reliable estimation of PRV.

6.4.6 Experiment 5: Outlier management

In this experiment, the aim was to determine the best way to manage outliers and ectopic beats from PRV traces, by investigating the effects of different detection and correction strategies. The obtained results showed that most of the extracted indices were not affected by the selection of outlier management strategies, and even not controlling for outliers showed good results when compared against the gold standard. This means that with good quality signals there is no need to manage outliers before extracting PRV indices. This is especially true for the assessment of frequency domain indices, which did not show any difference among outlier management strategies. These results are both for excellent and acceptable PPG signals, suggesting that PRV analysis might be performed without managing outliers when the signal has a good signal-to-noise ratio and when the signal is measured from different sites of the body.

However, the algorithm used for the detection of interbeat intervals in this experiment did correct for possibly wrongly detected cycles. Hence, these results indicate that there is no need to further correct outliers in PRV trends after applying the steps already considered in the interbeat interval detection algorithm, which include

the correction or deletion of longer or shorter than expected IBIs.

6.4.7 Experiment 6: Noise management

The final analysis performed in this study aimed to evaluate the effects of pre-processing filters on PRV analysis extracted from PPG signals contaminated with different types of noise. The application of filters in the PPG signal is essential to improve the signal-to-noise ratio (SNR) of the signal, which tends to be low due to the multiple artifacts that may affect the signal (Allen 2007, Mejía-Mejía, Allen, Budidha, El-Hajj, Kyriacou & Charlton 2021). However, these filters may generate changes in the PPG waveform that could affect the identification of fiducial points from the signal and, hence, affect the reliability of the PRV information. Moreover, the filters could induce time-shifts in the detection of fiducial points that could determine the reliability of the PRV information extracted from the signal (Liu, H., Allen, J., Ghufran Khalid, S., Fei Chen, F. & Zheng, D. 2021).

The capability of simulating several types of noise with different parameters is one of the main contributions of the proposed framework and, considering the susceptibility of PPG signals to noise, having a simulation framework that includes different types and magnitude of noises could help in the development and testing of robust algorithms for PPG signal processing, not only for PRV analysis. Further types of noise could be modelled and included in the framework, but the currently used types of noise were considered due to its effect on PPG signals. In this study, each combination of noises was treated independently, since in most cases it is possible to identify the noise present in real PPG signals, and the filtering strategies to each of types of noise can significantly vary. In line with this, it was observed that, regardless of the combination of noise present in the PPG signal, the filter applied and its cut-off frequencies had a significant effect on most PRV indices. Again, the x-coordinates of centroid-related indices showed a more robust performance than y-coordinates, indicating once more the robustness of these indices above those related with the magnitude of frequency bands.

It is important to discuss the particular behaviour of pNN50. This index showed important differences against gold standard indices, regardless of the noise and the filters applied. Hence, care should be taken when this index is analysed from PRV trends extracted from noise-contaminated signals, given it is largely affected by outliers in the trends. For the other indices, a similar behaviour between excellent

and acceptable quality, noise-contaminated PPG signals was observed. Interestingly, for time-domain and Poincaré plot indices the differences to gold standard tended to become smaller as the noise combination became more complex. For frequency-domain indices, the differences tended to remain stable, especially for relative and x-coordinate related indices. Time-domain and Poincaré plot indices showed larger differences to gold standard than frequency-domain indices, from which VLF was the index that showed larger differences. This could be explained by the fact that PRV was extracted from short 5-min PPG signals, contaminated with noise, which could have an important effect on the frequency spectra and the near DC components of the signal. Nonetheless, it was observed that, applying the best performance filtering strategies, the differences to gold standard can be considered acceptable.

In general, it was observed that PRV indices tend to show better reliability when PPG signals are filtered using elliptic IIR filters or equiripple or Parks-McClellan FIR filters. In terms of cut-off frequencies, lower low cut-off frequencies tended to give better results, except for those excellent quality PPG signals contaminated with a combination of baseline wandering, movement artifact and respiratory noise, which needed higher low cut-off frequencies, most likely due to the frequency content of the respiratory and baseline wandering noises. For higher cut-off frequencies, both with excellent and acceptable quality PPG signals, the most common high cut-off frequency was 20 Hz, which was the maximum considered cut-off frequency. This could be an indication of the more important role played by the lower cut-off frequency of the filter to remove the types of noises included in this study. Moreover, higher cut-off frequencies affect less the morphology of the anacrotic phase of the pulse, probably allowing a more precise detection of the fiducial point used in this study. These results are in line with the results obtained in a similar study performed with data obtained from healthy, resting subjects and by comparing PRV to HRV information (Mejía-Mejía, May & Kyriacou 2021).

Other studies have aimed to understand the effects of digital filtering on PRV. Akar et al. (2013) concluded that using a Butterworth filter and a nonlinear weighted Myriad filter did not have a significant difference on PRV analysis. Kim & Ahn (2019) evaluated the effects of Butterworth and elliptic filters for the assessment of PRV from PPG signals, and concluded that there were no significant differences between HRV and PRV time series, although small differences were observed in some extracted indices. The results found in this study indicate differences in the type of

filter and its parameters used given the different types of noise involved in the signal, which is a factor that has not been taken into account in previous studies and could explain, to some extent, the differences in results. Nonetheless, the present study involves a large data set and multiple different factors that were not included in these previous studies. Further studies should aim to validate the obtained results in real data with different but controlled types of noise.

6.4.8 Limitations of the study

This study has some limitations. Firstly, simulated PPG signals with simulated PRV information were used in this study. This was done for two main purposes. It is simpler to obtain larger number of samples using simulated data, which gives statistical validity to the experiment. The sample size for each of the experiments in this study was estimated to be the optimal value in order to observe differences of 2% in the measurement of the indices, compared to the gold standard. Also, by simulating PRV information it was possible to obtain a gold standard that was not HRV information obtained from the ECG. As mentioned, physiological aspects may explain part of the differences between HRV and PRV, hence comparing them in order to establish methodologies and strategies for obtaining PRV information is not ideal. Regardless of the benefits, using simulated PPG signals may not represent the entire variation of the PPG morphology, and the results from these experiments need to be validated using real (in vivo based) PPG data. The simulation of PRV information may also affect the results obtained. However, PRV was simulated using physiologically feasible values, which may introduce larger variability of the PRV but also simulate PRV information that could be obtained from most of the healthy population. Future studies could optimise the PRV model to have a better reflection of real PRV information.

Secondly, the experiments were done in a sequential manner, which means that the results from one of the experiments were used in the subsequent ones. This was done to have a controlled way to modify the parameters, but the combination of factors, especially the effect of noise in previous experiments, needs to be considered in future studies. Finally, the agreement between indices was not assessed. Future studies should investigate not only the significance of the difference but also determine how the indices agree using techniques such as Bland-Altman analysis.

6.5 Summary

The relationship between PRV and HRV is not straightforward, both due to physiological differences and to effects caused by technical aspects on the extraction of PRV information from pulsatile signals such as the PPG. The latter has not been thoroughly studied and there is no consensus regarding the methodologies for the extraction of PRV. In this chapter, a first approach for determining the best combination of factors for the extraction of PRV information from simulated PPG signals was presented.

It was found that PRV information can be extracted from PPG signals with a duration longer than 120 s and sampling rates above 128 Hz. This signals should be filtered using lower low cut-off frequencies and elliptic IIR or equiripple or Parks-McClellan FIR filters, depending on the type of noise present in the signal. Then, PRV trends obtained using D2max and the a-point for the detection of cardiac cycles and the measurement of interbeat intervals resulted in the best results, with other algorithms such as Delineator showing a similar performance when coupled with onset-related fiducial points. Also, it was found that there is no need to further manage outliers and that FFT and MUSIC are the best methods for spectral analysis, each of them with specific parameters.

In the next chapter, and considering most of these technical aspects that gave the best results for the extraction of PRV from PPG signals, the effect of cold exposure on the relationship between PPG-derived PRV and ECG-derived HRV is analysed, as a first approach to understand the effect of physiological changes on the relationship between these two variables.

Chapter 7

Investigation of pulse rate variability and heart rate variability in conditions of whole-body cold exposure

7.1 Aims and objectives

Besides the effects of technical aspects on PRV and its relationship to HRV, it has been hypothesised that factors such as stress (Giardino et al. 2002), respiratory patterns (Jan et al. 2019), exercise (Lin et al. 2014), orthostatic changes (Pernice et al. 2018), and ambient temperature (Shin 2016) may have different effects on PRV when compared to HRV, affecting their relationship. However, the origin of these differences is still not clear, and may be related to changes in haemodynamics, blood pressure or pulse transit time (PTT) (Charlot et al. 2009, Gil, Orini, Bailón, Vergara, Mainardi & Laguna 2010, Chen et al. 2015). Since haemodynamics are largely controlled by the ANS (Fox 2016), PRV might be affected by changes in this regulation in response to external stimuli, such as colder temperature.

There are changes in the autonomic response that are generated by cold exposure. When the body is exposed to cold the sympathetic nervous system is activated, which increases vasoconstriction, involuntary contraction of muscles, heart rate, cardiac output and blood pressure. These responses help maintain homeothermy by modifying cardiovascular dynamics (Budidha & Kyriacou 2019). The strength of

the sympathetic vasoconstriction, however, varies between core and peripheral locations. This was verified by Budidha & Kyriacou (2019), who aimed to differentiate the autonomic response between peripheral and core tissue by measuring the frequency response of PPG signals obtained from the finger, the toe, the ear lobe and the ear canal. They found that the autonomic response was altered in peripheral vasculature, whereas core vasculature was not as disturbed by cold exposure, implying that the sympathetic response in core circulation is maintained during cold exposure in order to keep homeostasis in the life-sustaining organs, such as the brain and the heart.

To investigate the dependency of PRV on external factors such as the acquisition site and the temperature, a whole-body cold exposure study was performed on healthy volunteers. PRV and HRV information was extracted from simultaneously obtained PPG and ECG signals, respectively. Red (660 nm) PPG signals were recorded from the earlobe, the ear canal, the finger and the toe. It was hypothesised that (1) PRV information from PPG signals obtained from the earlobe and ear canal might not be affected by cold exposure as that of the finger and the toe; and (2) the agreement between HRV and PRV is altered by whole body cold exposure. The results obtained from this study are important for understanding the possible differences between HRV and PRV, and might lead to further research that aims to better understand PRV and its clinical applications.

7.2 Methods and materials

7.2.1 Experimental protocol

Twenty healthy volunteers (11 male and 9 female, 30.3 $\pm$ 10.4 years old) were recruited to take part in this study. Subjects with any cardiovascular, pulmonary, or metabolic conditions were excluded. All subjects were normotensive, normothermic, did not take any medication at the time of the study, and were not diagnosed with Raynaud's disease. The study protocol was approved by Senate Research Ethics Committee at City, University of London, and all subjects gave informed consent before taking part in the study. Subjects were asked to refrain from ingesting beverages with caffeine and alcohol, not to exercise or smoke at least 2 hours before the test, and they were instructed to wear only one layer of clothes during the data acquisition period, in order to maximise the effect of the stimulus on the body. Data

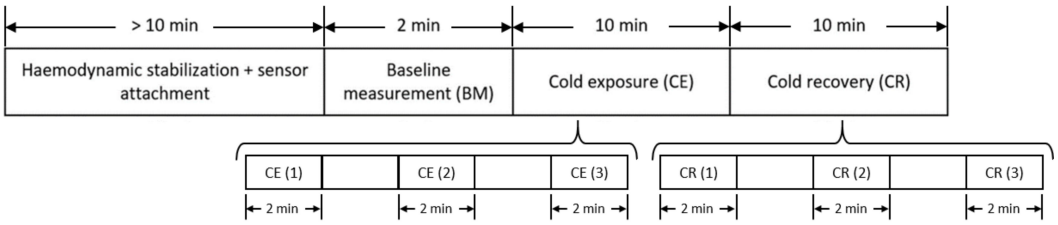

Figure 7.1: Measurement protocol for the whole-body cold exposure study.

from all subjects was collected between 10:00 a.m. and 6:00 p.m., under controlled conditions of temperature and humidity. This data was collected as part of a previous study performed at the Research Centre for Biomedical Engineering, at City, University of London (Abay 2016).

The measurement protocol is shown in Figure 7.1. Upon arrival, subjects were seated in a room maintained at 24 ± 1 °C for at least 10 minutes, to ensure haemodynamic stabilization. After this period, the sensors for acquiring the signals were attached to the subjects. The measurement started with a 2-min baseline measurement (BM) stage, in which two minutes of signals were recorded from the subjects while the room temperature was 24 ± 1 °C. The volunteers were then moved to an adjacent, temperature-controlled room, maintained at 10 ± 1 °C (Cold Exposure, CE). This temperature was selected because it reflects a more realistic change in ambient temperature, which can be sustained for longer periods of time by healthy adults, and generates changes in haemodynamics (King et al. 2013). Subjects remained in this room and signals were recorded for 10 minutes before returning to the original room at 24 ± 1 °C, for additional 10 minutes of signals recording (Cold Recovery, CR). During each phase of the measurement protocol, subjects were seated in a comfortable *swivel chair*, with both hands located on the arm rest.

After each of the recording on the different stages, the measurement was paused and the subject was transferred to the room for recording the next stage. The recording was resumed as soon as the subject was moved, in order to record the shock response of the autonomic activity on the periphery.

7.2.2 Signal acquisition and processing

7.2.2.1 Signal acquisition

Disposable electrodes were placed on the left and right shoulders, and on the right hip (reference electrode) for obtaining lead I ECG signals, while PPG signals from

the left index finger (F), toe (T), ear canal (EC) and earlobe (EL) were obtained from each subject during the three stages of the study. Both red and infrared light were used for acquiring PPG signals, but only those signals related to red light were used for subsequent analysis. The signal acquisition was paused during the transitions between the two rooms in order to avoid movement artefacts.

All PPG and ECG measurements were acquired using a research PPG acquisition system (*ZenPPG*) developed in the Research Centre for Biomedical Engineering, at City, University of London (Budidha 2016). All signals were acquired at a sampling rate of 1 kHz.

7.2.2.2 PPG and ECG signal processing

PPG signals were down-sampled to 100 Hz to restrict the bandwidth of the signals and remove any unwanted noise. Afterwards, they were detrended, and the first and last 10 seconds of each stage of the protocol were removed, to eliminate any non-stationarities of the signal. Signals were then filtered using a fourth-order bandpass Butterworth filter, with cut-off frequencies of 0.1 and 2 Hz. These cut-off frequencies were selected to attenuate any unwanted noise and strengthen the pulsatile component of the PPG signal.

Interbeat intervals were detected applying the algorithm Delineator described in Chapter 6 and based on the work by Li et al. (2010). Then, different fiducial

Table 7.1: Signal quality indices (SQI) extracted from finger, toe, ear canal and ear lobe PPG signals.

Signal quality index (SQI)	Description
Template (SQI_T)	Correspondence of each pulse to a template derived from the whole signal
Skewness (SQI_S)	Skewness of each pulse of the PPG waveform
Kurtosis (SQI_K)	Kurtosis of each pulse of the PPG waveform
Ratio of frequencies (SQI_R)	Ratio of the frequency contents of each pulse
Signal to noise ratio (SQI_{SNR})	Signal to noise ratio of each pulse
Zero crossing rate (SQI_{ZC})	Zero-crossing rate of each pulse
Entropy (SQI_E)	Entropy of the signal in each cardiac cycle
Centroid (SQI_C)	Location of the centroid of each pulse, considered as the point in which the 50% of the pulse is concentrated
Area under the curve (SQI_{AUC})	Area under the curve concentrated at the centroid of each pulse
Gaussian filters (SQI_G)	Level of correspondence of each pulse to a series of Gaussian filters

points such as systolic peaks (PKS), onsets of the pulse (ONS), maximum slope point (SLO), and the intersection point between tangent lines from the onset and the maximum slope point were obtained from each PPG signal (TI). Once detected, signal quality indices (SQI) described in the literature (Li & Clifford 2012, Karlen et al. 2012, Elgendi 2016, Calle Uribe 2018), were applied to identify the quality of the pulses segmented by each fiducial point in each PPG signal during each test stage, and those that better segmented the pulses of each PPG signal were selected and used for measuring PRV. Table 7.1 summarise the extracted SQI.

Using a k-means algorithm, the cardiac cycles were classified as bad and good quality. This was done assuming that during the first stage of the test the quality of the signal was maximal, and the cluster with most of the cardiac cycles of this stage was considered as the good quality (GQ) group. Hence, the cycles classified in this group during the other two stages (CE and CR) were considered as good quality pulses. The proportion between GQ pulses and the total number of pulses was measured for each fiducial point during each stage and from each body location. Then, the fiducial point that showed the highest proportion of GQ pulses in each case were selected for further analysis. This was performed to diminish the effect of noise in the measurement of PRV, and in an attempt to automatically determine the better fiducial point for each condition, as proposed in (Pinheiro et al. 2016).

ECG signals were also down-sampled to 100 Hz and R peaks were detected using an algorithm based on the algorithms described in Pan & Tompkins (1985) and Hamilton & Tompkins (1986). These processing steps were performed using the 2019a version of MATLAB® (Mathworks, USA). Figure 7.2 shows a segment of PPG and ECG signals and the extracted fiducial points from each of these signals.

7.2.2.3 HRV and PRV analysis

Using the time-difference between consecutive selected fiducial points from PPG (IBIs trends) and the R peaks obtained from the ECG (RR intervals trends), HRV and PRV were extracted, respectively. IBIs and RRIs that were 50% above or below the median value of the trend were corrected. Time- and frequency-domain indices, as well as Poincaré plot-derived indices, were obtained from the corrected trends.

The standard deviation of normal-to-normal intervals (SDNN), the root mean square of successive interval differences (RMSSD) and the percentage of successive intervals that differ by more than 50 ms (pNN50). For frequency-domain analysis,

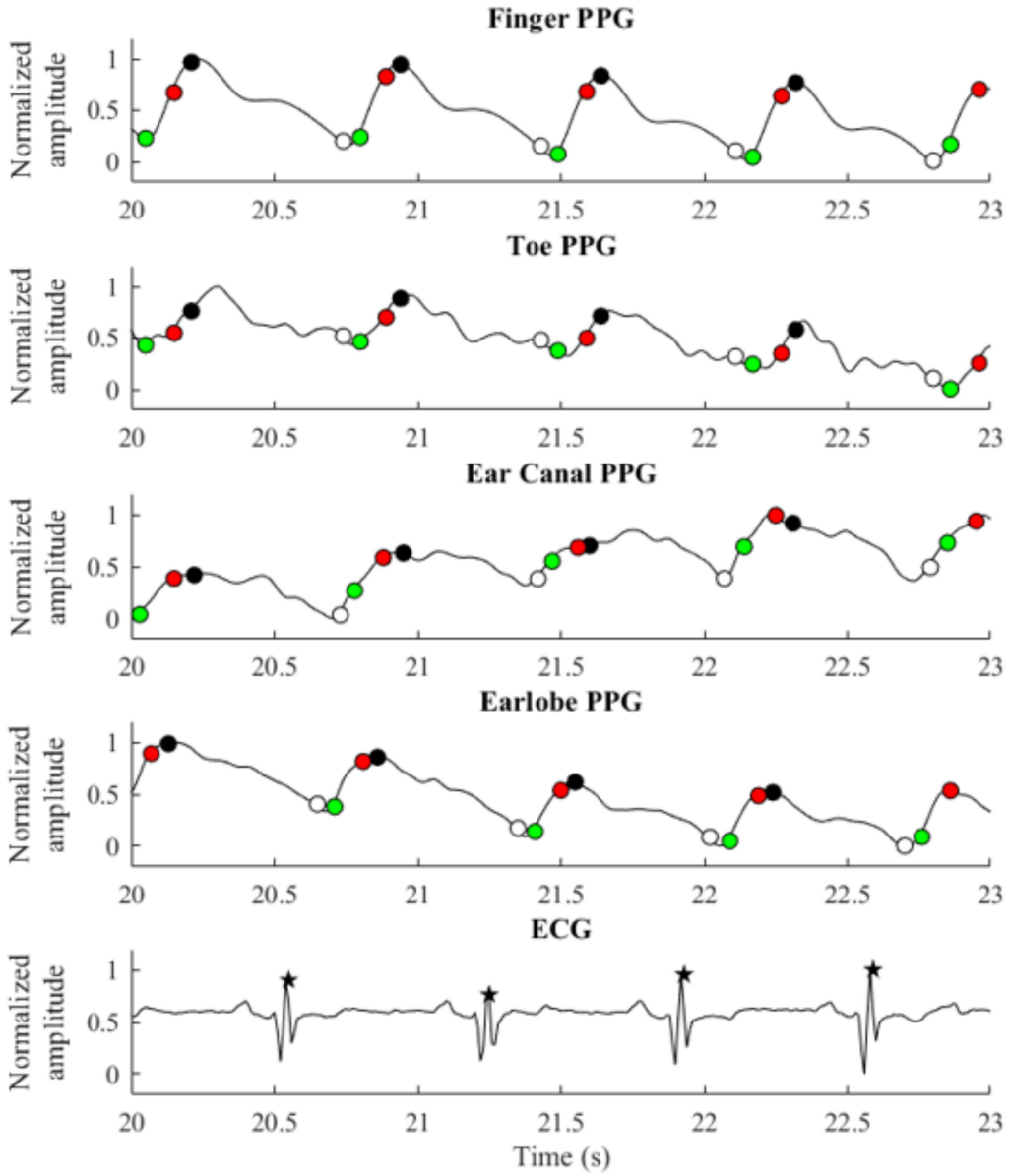

Figure 7.2: Example of photoplethysmographic (PPG) and electrocardiographic (ECG) signals used for the extraction of pulse rate variability and heart rate variability, respectively. From top to bottom, the PPG signals correspond to the signals obtained from the finger, the toe, the ear canal and the earlobe. The black stars show the R peaks detected from the ECG signal, while the white, black, red and green circles show the detected onsets, peaks, maximum slope points and tangent intersection points, respectively.

trends were interpolated using cubic-spline interpolation and a sampling rate of 4 Hz, and the power spectra were obtained using fast Fourier transform (FFT). The absolute and relative powers of the low-frequency (0.04 - 0.15 Hz, LF and nLF) and high-frequency (0.15 - 0.4 Hz, HF and nHF) bands, as well as the total power of the spectrum (0.04 - 0.4 Hz, TP) and the ratio of the low-frequency and high-frequency powers (LF/HF) were measured. Finally, the standard deviation of data located

perpendicular (SD1) and along (SD2) the line of identity of the Poincaré plot and their ratio (SD1/SD2) were obtained.

7.2.3 Statistical analysis

As explained above, the aim of this study was to compare the behaviour of core and peripheral PRV during cold exposure, and to evaluate if and how PRV differed to HRV during mild whole body cold exposure. Hence, two hypotheses were proposed: (1) PRV from core vasculature (ear canal and earlobe) is less affected by cold exposure than PRV from the periphery (finger and toe); and (2) PRV from core vasculature is more similar to HRV than PRV from peripheral tissue, especially during cold exposure.

To evaluate the first hypothesis, PRV indices obtained during the middle 2-min segments of each stage of the test were compared using repeated-measures analysis of variance (ANOVA), with sphericity corrections. Multiple comparisons with pairwise t-tests and Bonferroni corrections were performed in case the ANOVA showed a statistically significant difference during at least one stage. Also, the first (minutes 0 to 2), middle (minutes 4 to 6) and last (minutes 8 to 10) segments of cold exposure and cold recovery stages were compared to baseline measurement, to evaluate the behaviour of PRV and HRV indices when the ambient temperature was changing and during stabilization in each stage. Although the guidelines recommend the use of 5-min segments for HRV and PRV analysis, it was shown in previous chapter that 120 s windows show reliable values for all analysed indices in this study. This allowed for a comparison of condition within stages in order to understand the progression of the conditions with cold exposure or cold recovery. Moreover, since baseline measurements were only 2 min duration, the signals obtained on the rest of the stages were also segmented to maintain consistency among stages.

The second hypothesis was evaluated using Bland-Altman analysis, to assess the agreement between PRV and HRV indices during the first two minutes of each stage of the test. A Bland-Altman ratio (BAR) was defined as the ratio of half the range of limits of agreement (LoA, 7.1) to the average of the pairwise measurement means, as proposed by Peng et al. (2015) (7.2). Agreement between HRV and PRV indices was considered good (BAR $\leq$ 10%), moderate (10% $\leq$ BAR $\leq$ 20%) or insufficient (BAR $\geq$ 20%). Also, the behaviour of the indices extracted from PRV and HRV during each stage of the test was evaluated using a Friedman rank sum test with

post hoc analyses performed using Nemenyi's test, as post-hoc pairwise multiple comparison test appropriate after the Friedman rank sum test (RDocumentation 2022). Finally, the level of linear relationship between the indices, was assessed using Pearson or Spearman correlation analysis, for normally and non-normally distributed data respectively. Normality of data was determined using a Shapiro-Wilk test and a significance level of 5% (p-value < 0.05) was considered significant for all analyses.

$$LoA = \overline{(x)} \pm 1.96\sigma_x, x = HRV - PRV \tag{7.1}$$

$$BAR = \left| \frac{1.96(\sigma_x)}{\overline{(HRV + PRV)}} \right|, x = HRV - PRV \tag{7.2}$$

Statistical analyses were done in RStudio (version 1.4.1717), while figures were developed using MATLAB (version 2019a).

7.3 Results

7.3.1 Selection of fiducial points

After applying the proposed algorithm for selecting the best fiducial point in each condition, it was observed that the lower proportion of good quality cardiac cycles was obtained in the finger and toe, i.e. the peripheral tissue. The most accurate results were obtained when cardiac cycles were segmented using the intersection of tangent lines (TI) and the location of the maximum slope (SLO) as fiducial points. The lowest performance was achieved when the systolic peaks (PKS) were used, except for the finger PPG in which the performance of the peak detection algorithm was better than most of the others. The behaviour of the extracted indices from these fiducial points and from HRV is shown in Figure 7.3.

7.3.2 Changes in PRV and HRV during cold exposure

Results from the repeated-measures ANOVA and its related multiple comparisons for time-domain and Poincaré plot indices are shown in Table 7.2, while Table 7.3 shows the results obtained from absolute frequency-domain indices. Relative frequency domain indices, i.e., nLF, nHF and LF/HF, did not show any statistically significant differences among stages.

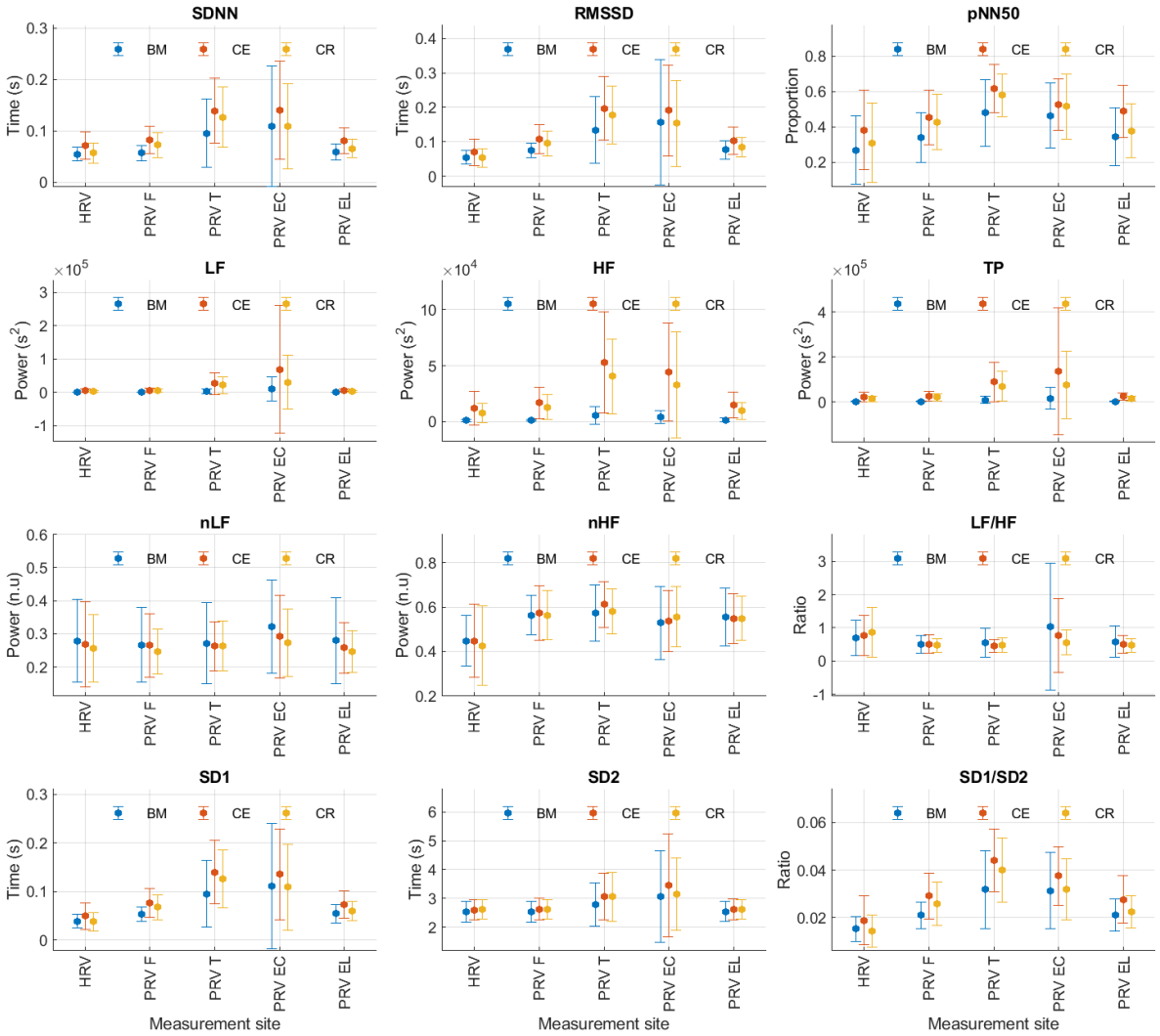

Figure 7.3: Behaviour (mean value and standard deviation) of heart rate variability (HRV) and pulse rate variability (PRV) indices extracted during the whole duration of basal measurement (BM, blue), cold exposure (CE, orange) and cold recovery (CR, yellow) stages. PRV indices were extracted from photoplethysmograms acquired from the finger (F), toe (T), ear canal (EC) and earlobe (EL). HRV was obtained from electrocardiograms.

7.3.2.1 Time-domain indices

SDNN showed statistically significant differences between baseline measurement and cold exposure when measured from any location, except for the ear canal, while RMSSD and pNN50 did not show statistically significant differences between these stages when measured from the finger and the ear canal. All indices behaved similarly when cold exposure and cold recovery were compared, except for pNN50 measured from the earlobe. Ear canal was the only location from which none of the indices measured show any statistically-significant differences among stages.

Table 7.2: P-values obtained from the repeated-measures ANOVA and its post hoc analyses, when applied to time-domain and Poincaré plot-derived indices of PRV and HRV. Values in red indicate statistical significance (p-value < 0.05). Sphericity corrections using Greenhouse-Geisser correction were applied when Mauchly's test showed statistically significant results, and p-values shown are after these corrections. BM: baseline measurement; CE: cold exposure; CR: cold recovery.

Index	Source	ANOVA	Post hoc comparisons		
			BM vs CE	CE vs CR	BM vs CR
SDNN (s)	HRV	<0.001	0.005	0.086	0.025
	Finger PRV	0.007	0.039	1.000	0.024
	Toe PRV	<0.001	<0.001	0.295	0.003
	Ear canal PRV	0.118	-	-	-
	Earlobe PRV	0.006	0.021	0.199	0.310
RMSSD (s)	HRV	0.001	0.004	0.174	0.004
	Finger PRV	0.015	0.066	1.000	0.053
	Toe PRV	<0.001	<0.001	0.208	0.007
	Ear canal PRV	0.250	-	-	-
	Earlobe PRV	0.009	0.022	0.331	0.265
pNN50	HRV	<0.001	<0.001	0.068	0.062
	Finger PRV	0.006	0.123	0.633	0.018
	Toe PRV	<0.001	0.002	0.639	0.011
	Ear canal PRV	0.168	-	-	-
	Earlobe PRV	<0.001	<0.001	0.002	0.774
SD1 (s)	HRV	0.001	0.004	0.170	0.005
	Finger PRV	0.015	0.067	1.000	0.053
	Toe PRV	<0.001	<0.001	0.206	0.007
	Ear canal PRV	0.250	-	-	-
	Earlobe PRV	0.009	0.023	0.330	0.266
SD2 (s)	HRV	0.001	0.017	1.000	0.003
	Finger PRV	0.004	0.029	1.000	0.012
	Toe PRV	0.002	0.003	1.000	0.013
	Ear canal PRV	0.076	-	-	-
	Earlobe PRV	0.001	0.036	1.000	<0.001
SD1/SD2	HRV	0.001	0.005	0.131	0.015
	Finger PRV	0.025	0.097	1.000	0.083
	Toe PRV	0.002	0.004	0.261	0.046
	Ear canal PRV	0.044	0.178	0.060	1.000
	Earlobe PRV	0.021	0.047	0.192	0.724

7.3.2.2 Frequency-domain indices

Relative-power indices, i.e. nLF, nHF and LF/HF, did not show any difference among stages. Regarding absolute-power indices (LF, HF and TP), and similar to what was observed from time-domain indices, the ear canal-derived PRV indices did not show any differences among stages. HRV-derived LF and HF did not show differences among stages, and finger HF did not show differences in the post hoc

Table 7.3: P-values obtained from the repeated-measures ANOVA and its post hoc analyses, when applied to frequency-domain indices of PRV and HRV. Values in red indicate statistical significance (p-value < 0.05). Sphericity corrections using Greenhouse-Geisser correction were applied when Mauchly's test showed statistically significant results, and p-values shown are after these corrections. Normalised frequency-domain indices did not show statistical differences between stages from any of the signals. BM: baseline measurement; CE: cold exposure; CR: cold recovery.

Index	Source	ANOVA	Post hoc comparisons		
			BM vs CE	CE vs CR	BM vs CR
LF (s^2)	HRV	0.057	-	-	-
	Finger PRV	0.008	0.028	0.162	0.077
	Toe PRV	0.009	0.010	1.000	0.083
	Ear canal PRV	0.622	-	-	-
	Earlobe PRV	0.004	0.016	0.352	0.122
HF (s^2)	HRV	0.024	0.070	0.134	0.059
	Finger PRV	0.016	0.058	1.000	0.057
	Toe PRV	<0.001	<0.001	0.236	0.013
	Ear canal PRV	0.057	-	-	-
	Earlobe PRV	0.008	0.018	0.458	0.016
TP (s^2)	HRV	0.031	0.085	0.230	0.061
	Finger PRV	0.013	0.047	1.000	0.052
	Toe PRV	<0.001	<0.001	0.546	0.007
	Ear canal PRV	0.581	-	-	-
	Earlobe PRV	0.002	0.015	0.459	0.037

analyses. LF, HF and TP did not differ between cold exposure and cold recovery when measured from any of the locations.

7.3.2.3 Non-linear indices

Ear canal-derived indices did not differ among stages from any of the Poincaré plot-derived indices. Similarly, SD1 and SD1/SD2 did not show differences among stages when measured from the finger. Most differences were obtained when baseline measurement and cold exposure where compared, while no differences were shown when cold exposure and cold recovery were compared.

7.3.3 Behaviour of PRV and HRV indices

Figure 7.4 illustrates the behaviour of the extracted indices when 2-min segments of each stage were compared. Most indices showed a similar behaviour when measured from PRV and HRV, but with a notorious overestimation of most indices when measured from PRV. LF/HF was the only index that was underestimated when measured from PRV, while nLF was the index with the least overestimation when measured

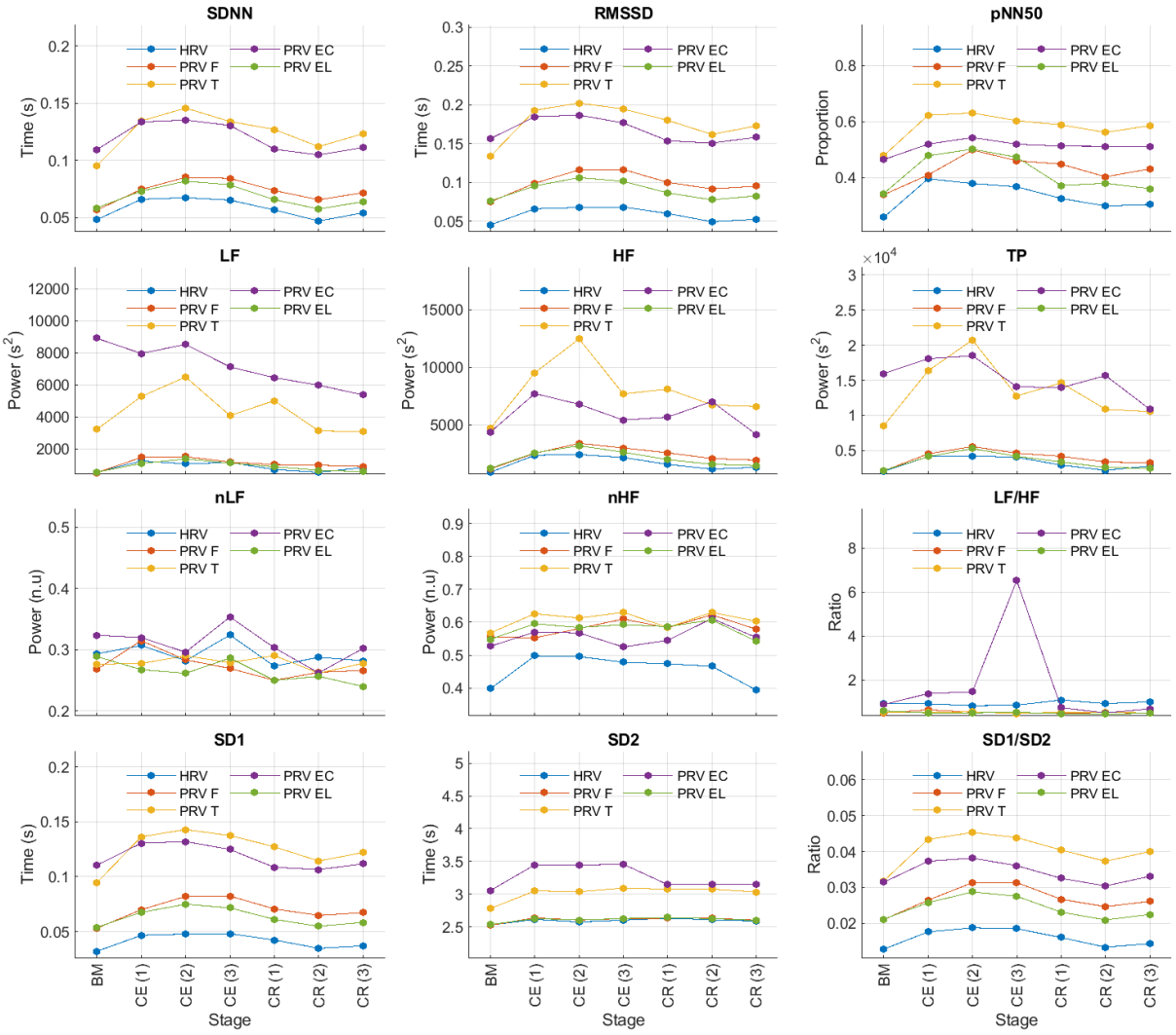

Figure 7.4: Behaviour of indices measured from HRV (blue line) and PRV from the finger (orange line), toe (yellow line), ear canal (purple line) and earlobe (green line). BM: Baseline measurement; CE (1): Cold exposure between the start of the stage and the second minute of this stage; CE (2): Cold exposure between the 4th and 6th minutes of this stage; CE (3): Cold exposure between the 8th and 10th minutes of this stage; CR (1): Cold recovery between the start of the stage and the second minute of this stage; CE (2): Cold recovery between the 4th and 6th minutes of this stage; CE (3): Cold recovery between the 8th and 10th minutes of this stage.

from PRV. The ear canal showed the higher differences in the trends between PRV and HRV. Time-domain and non-linear indices showed that values tended to increase after baseline measurement, and then, during cold recovery, indices tended to recover to the values obtained during baseline. Frequency-domain indices did not show this behaviour, probably due to the short segments used for analysis.

When indices measured from the different segments were compared using a repeated-measures ANOVA (Table 7.4), ear canal was found to be the only location with non-statistically significant differences among each 2-min segments. Most

differences observed were among baseline measurements and the segments obtained during cold exposure, and among cold exposure and cold recovery segments. On the other hand, baseline measurement and cold recovery were statistically similar, except for SD1, SD2 and RMSSD. Regarding frequency-domain indices, nLF and LF/HF failed to show any difference among stages, probably due to the short time segments used for this analysis.

Table 7.4: Results from repeated-measures ANOVA for the comparison among indices extracted from 2-min segments of data, during basal measurement, cold exposure and cold recovery. BM: Baseline measurement; CE (1): Cold exposure between the start of the stage and the second minute of this stage; CE (2): Cold exposure between the 4th and 6th minutes of this stage; CE (3): Cold exposure between the 8th and 10th minutes of this stage; CR (1): Cold recovery between the start of the stage and the second minute of this stage; CE (2): Cold recovery between the 4th and 6th minutes of this stage; CE (3): Cold recovery between the 8th and 10th minutes of this stage. ⋆: Significant differences. -: Non-significant differences.

Index	**Source**	**ANOVA**	**Post hoc comparisons**																					
			BM vs CE (1)	**BM vs CE (2)**	**BM vs CE (3)**	**BM vs CR (1)**	**BM vs CR (2)**	**BM vs CR (3)**	**CE (1) vs CE (2)**	**CE (1) vs CE (3)**	**CE (1) vs CR (1)**	**CE (1) vs CR (2)**	**CE (1) vs CR (3)**	**CE (2) vs CE (3)**	**CE (2) vs CR (1)**	**CE (2) vs CR (2)**	**CE (2) vs CR (3)**	**CE (3) vs CR (1)**	**CE (3) vs CR (2)**	**CE (3) vs CR (3)**	**CR (1) vs CR (2)**	**CR (1) vs CR (3)**	**CR (2) vs CR (3)**
SDNN	HRV	< 0.001	⋆	⋆	⋆	-	-	-	-	-	-	⋆	-	-	-	⋆	⋆	-	⋆	-	⋆	-	-
	Finger PRV	< 0.001	⋆	⋆	⋆	-	-	-	-	-	-	⋆	-	-	-	⋆	⋆	-	⋆	-	⋆	-	-
	Toe PRV	< 0.001	⋆	⋆	⋆	-	-	-	-	-	-	⋆	-	-	-	⋆	⋆	-	⋆	-	⋆	-	-
	Ear canal PRV	0.086	⋆	⋆	⋆	-	-	-	-	-	-	⋆	-	-	-	⋆	⋆	-	⋆	-	⋆	-	-
	Earlobe PRV	< 0.001	⋆	⋆	⋆	-	-	-	-	-	-	⋆	-	-	-	⋆	⋆	-	⋆	-	⋆	-	-
RMSSD	HRV	< 0.001	⋆	⋆	⋆	⋆	-	-	-	-	-	⋆	⋆	-	-	-	-	-	⋆	⋆	-	-	-
	Finger PRV	< 0.001	⋆	⋆	⋆	⋆	-	-	-	-	-	⋆	⋆	-	-	-	-	-	⋆	⋆	-	-	-
	Toe PRV	< 0.001	⋆	⋆	⋆	⋆	-	-	-	-	-	⋆	⋆	-	-	-	-	-	⋆	⋆	-	-	-

Continued on next page

Table 7.4 – continued from previous page

Index	Source	ANOVA	Post hoc comparisons																				
			BM vs CE (1)	BM vs CE (2)	BM vs CE (3)	BM vs CR (1)	BM vs CR (2)	BM vs CR (3)	CE (1) vs CE (2)	CE (1) vs CE (3)	CE (1) vs CR (1)	CE (1) vs CR (2)	CE (1) vs CR (3)	CE (2) vs CE (3)	CE (2) vs CR (1)	CE (2) vs CR (2)	CE (2) vs CR (3)	CE (3) vs CR (1)	CE (3) vs CR (2)	CE (3) vs CR (3)	CR (1) vs CR (2)	CR (1) vs CR (3)	CR (2) vs CR (3)
	Ear canal PRV	0.219	⋆	⋆	⋆	⋆	-	-	-	-	-	⋆	⋆	-	-	-	-	-	⋆	⋆	-	-	-
	Earlobe PRV	< 0.001	⋆	⋆	⋆	⋆	-	-	-	-	-	⋆	⋆	-	-	-	-	-	⋆	⋆	-	-	-
pNN50	HRV	< 0.001	⋆	⋆	⋆	-	-	-	-	-	-	-	⋆	-	-	-	-	-	-	-	-	-	-
	Finger PRV	< 0.001	⋆	⋆	⋆	-	-	-	-	-	-	-	⋆	-	-	-	-	-	-	-	-	-	-
	Toe PRV	< 0.001	⋆	⋆	⋆	-	-	-	-	-	-	-	⋆	-	-	-	-	-	-	-	-	-	-
	Ear canal PRV	0.260	⋆	⋆	⋆	-	-	-	-	-	-	-	⋆	-	-	-	-	-	-	-	-	-	-
	Earlobe PRV	< 0.001	⋆	⋆	⋆	-	-	-	-	-	-	-	⋆	-	-	-	-	-	-	-	-	-	-
LF	HRV	0.024	-	⋆	-	-	-	-	-	-	-	-	-	-	-	-	-	-	⋆	-	-	-	-
	Finger PRV	0.009	-	⋆	-	-	-	-	-	-	-	-	-	-	-	-	-	-	⋆	-	-	-	-
	Toe PRV	0.039	-	⋆	-	-	-	-	-	-	-	-	-	-	-	-	-	-	⋆	-	-	-	-
	Ear canal PRV	0.478	-	⋆	-	-	-	-	-	-	-	-	-	-	-	-	-	-	⋆	-	-	-	-

Continued on next page

Table 7.4 – continued from previous page

Index	Source	ANOVA	Post hoc comparisons																				
			BM vs CE (1)	BM vs CE (2)	BM vs CE (3)	BM vs CR (1)	BM vs CR (2)	BM vs CR (3)	CE (1) vs CE (2)	CE (1) vs CE (3)	CE (1) vs CR (1)	CE (1) vs CR (2)	CE (1) vs CR (3)	CE (2) vs CE (3)	CE (2) vs CR (1)	CE (2) vs CR (2)	CE (2) vs CR (3)	CE (3) vs CR (1)	CE (3) vs CR (2)	CE (3) vs CR (3)	CR (1) vs CR (2)	CR (1) vs CR (3)	CR (2) vs CR (3)
	Earlobe PRV	< 0.001	-	⋆	-	-	-	-	-	-	-	-	-	-	-	-	-	-	⋆	-	-	-	-
HF	HRV	0.003	-	-	⋆	-	-	-	-	-	-	-	-	-	-	⋆	⋆	-	⋆	⋆	-	-	-
	Finger PRV	0.001	-	-	⋆	-	-	-	-	-	-	-	-	-	-	⋆	⋆	-	⋆	⋆	-	-	-
	Toe PRV	0.029	-	-	⋆	-	-	-	-	-	-	-	-	-	-	⋆	⋆	-	⋆	⋆	-	-	-
	Ear canal PRV	0.387	-	-	⋆	-	-	-	-	-	-	-	-	-	-	⋆	⋆	-	⋆	⋆	-	-	-
	Earlobe PRV	< 0.001	-	-	⋆	-	-	-	-	-	-	-	-	-	-	⋆	⋆	-	⋆	⋆	-	-	-
TP	HRV	0.002	-	⋆	⋆	-	-	-	-	-	-	-	-	-	-	⋆	⋆	-	⋆	-	-	-	-
	Finger PRV	0.001	-	⋆	⋆	-	-	-	-	-	-	-	-	-	-	⋆	⋆	-	⋆	-	-	-	-
	Toe PRV	0.017	-	⋆	⋆	-	-	-	-	-	-	-	-	-	-	⋆	⋆	-	⋆	-	-	-	-
	Ear canal PRV	0.432	-	⋆	⋆	-	-	-	-	-	-	-	-	-	-	⋆	⋆	-	⋆	-	-	-	-
	Earlobe PRV	< 0.001	-	⋆	⋆	-	-	-	-	-	-	-	-	-	-	⋆	⋆	-	⋆	-	-	-	-

Continued on next page

Table 7.4 – continued from previous page

Index	Source	ANOVA	Post hoc comparisons																				
			BM vs CE (1)	BM vs CE (2)	BM vs CE (3)	BM vs CR (1)	BM vs CR (2)	BM vs CR (3)	CE (1) vs CE (2)	CE (1) vs CE (3)	CE (1) vs CR (1)	CE (1) vs CR (2)	CE (1) vs CR (3)	CE (2) vs CE (3)	CE (2) vs CR (1)	CE (2) vs CR (2)	CE (2) vs CR (3)	CE (3) vs CR (1)	CE (3) vs CR (2)	CE (3) vs CR (3)	CR (1) vs CR (2)	CR (1) vs CR (3)	CR (2) vs CR (3)
nLF	HRV	0.821	-	-	-	-	-	-	-	-	-	-	-	-	-	-	-	-	-	-	-	-	-
	Finger PRV	0.359	-	-	-	-	-	-	-	-	-	-	-	-	-	-	-	-	-	-	-	-	-
	Toe PRV	0.915	-	-	-	-	-	-	-	-	-	-	-	-	-	-	-	-	-	-	-	-	-
	Ear canal PRV	0.062	-	-	-	-	-	-	-	-	-	-	-	-	-	-	-	-	-	-	-	-	-
	Earlobe PRV	0.348	-	-	-	-	-	-	-	-	-	-	-	-	-	-	-	-	-	-	-	-	-
nHF	HRV	0.020	-	-	-	-	-	-	-	-	-	-	-	-	-	-	⋆	-	-	-	-	-	-
	Finger PRV	0.204	-	-	-	-	-	-	-	-	-	-	-	-	-	-	⋆	-	-	-	-	-	-
	Toe PRV	0.390	-	-	-	-	-	-	-	-	-	-	-	-	-	-	⋆	-	-	-	-	-	-
	Ear canal PRV	0.243	-	-	-	-	-	-	-	-	-	-	-	-	-	-	⋆	-	-	-	-	-	-
	Earlobe PRV	0.336	-	-	-	-	-	-	-	-	-	-	-	-	-	-	⋆	-	-	-	-	-	-
LF/HF	HRV	0.845	-	-	-	-	-	-	-	-	-	-	-	-	-	-	-	-	-	-	-	-	-

Continued on next page

Table 7.4 – continued from previous page

Index	Source	ANOVA	Post hoc comparisons																				
			BM vs CE (1)	BM vs CE (2)	BM vs CE (3)	BM vs CR (1)	BM vs CR (2)	BM vs CR (3)	CE (1) vs CE (2)	CE (1) vs CE (3)	CE (1) vs CR (1)	CE (1) vs CR (2)	CE (1) vs CR (3)	CE (2) vs CE (3)	CE (2) vs CR (1)	CE (2) vs CR (2)	CE (2) vs CR (3)	CE (3) vs CR (1)	CE (3) vs CR (2)	CE (3) vs CR (3)	CR (1) vs CR (2)	CR (1) vs CR (3)	CR (2) vs CR (3)
	Finger PRV	0.450	-	-	-	-	-	-	-	-	-	-	-	-	-	-	-	-	-	-	-	-	-
	Toe PRV	0.883	-	-	-	-	-	-	-	-	-	-	-	-	-	-	-	-	-	-	-	-	-
	Ear canal PRV	0.320	-	-	-	-	-	-	-	-	-	-	-	-	-	-	-	-	-	-	-	-	-
	Earlobe PRV	0.524	-	-	-	-	-	-	-	-	-	-	-	-	-	-	-	-	-	-	-	-	-
SD1	HRV	< 0.001	⋆	⋆	⋆	⋆	-	-	-	-	-	⋆	⋆	-	-	-	-	-	⋆	⋆	-	-	-
	Finger PRV	< 0.001	⋆	⋆	⋆	⋆	-	-	-	-	-	⋆	⋆	-	-	-	-	-	⋆	⋆	-	-	-
	Toe PRV	0.001	⋆	⋆	⋆	⋆	-	-	-	-	-	⋆	⋆	-	-	-	-	-	⋆	⋆	-	-	-
	Ear canal PRV	0.219	⋆	⋆	⋆	⋆	-	-	-	-	-	⋆	⋆	-	-	-	-	-	⋆	⋆	-	-	-
	Earlobe PRV	< 0.001	⋆	⋆	⋆	⋆	-	-	-	-	-	⋆	⋆	-	-	-	-	-	⋆	⋆	-	-	-
SD2	HRV	0.056	-	-	-	⋆	-	-	-	-	-	-	-	-	-	-	-	-	-	-	-	-	-
	Finger PRV	0.029	-	-	-	⋆	-	-	-	-	-	-	-	-	-	-	-	-	-	-	-	-	-

Continued on next page

Table 7.4 – continued from previous page

Index	Source	ANOVA	Post hoc comparisons																				
			BM vs CE (1)	BM vs CE (2)	BM vs CE (3)	BM vs CR (1)	BM vs CR (2)	BM vs CR (3)	CE (1) vs CE (2)	CE (1) vs CE (3)	CE (1) vs CR (1)	CE (1) vs CR (2)	CE (1) vs CR (3)	CE (2) vs CE (3)	CE (2) vs CR (1)	CE (2) vs CR (2)	CE (2) vs CR (3)	CE (3) vs CR (1)	CE (3) vs CR (2)	CE (3) vs CR (3)	CR (1) vs CR (2)	CR (1) vs CR (3)	CR (2) vs CR (3)
	Toe PRV	0.002	-	-	-	⋆	-	-	-	-	-	-	-	-	-	-	-	-	-	-	-	-	-
	Ear canal PRV	0.050	-	-	-	⋆	-	-	-	-	-	-	-	-	-	-	-	-	-	-	-	-	-
	Earlobe PRV	0.032	-	-	-	⋆	-	-	-	-	-	-	-	-	-	-	-	-	-	-	-	-	-
SD1/SD2	HRV	< 0.001	⋆	⋆	⋆	-	-	-	-	-	-	⋆	-	-	-	-	-	-	⋆	⋆	-	-	-
	Finger PRV	< 0.001	⋆	⋆	⋆	-	-	-	-	-	-	⋆	-	-	-	-	-	-	⋆	⋆	-	-	-
	Toe PRV	< 0.001	⋆	⋆	⋆	-	-	-	-	-	-	⋆	-	-	-	-	-	-	⋆	⋆	-	-	-
	Ear canal PRV	0.053	⋆	⋆	⋆	-	-	-	-	-	-	⋆	-	-	-	-	-	-	⋆	⋆	-	-	-
	Earlobe PRV	< 0.001	⋆	⋆	⋆	-	-	-	-	-	-	⋆	-	-	-	-	-	-	⋆	⋆	-	-	-

7.3.4 Agreement between PRV and HRV

7.3.4.1 Friedman rank sum tests

Results for the Friedman rank sum tests and its post hoc comparisons are presented in Table 7.5. Since the aim was to evaluate the relationship between HRV and PRV, only multiple comparisons between HRV and PRV are shown.

During baseline measurement, nLF and LF/HF did not show differences between HRV and PRV, while LF, TP and SD2 failed to show differences from post hoc analysis. Most of the other indices showed differences between HRV and toe PRV, and between HRV and ear canal PRV, while RMSSD, nHF, SD1 and SD1/SD2 showed differences when PRV was measured from any location. Similar behaviour was observed for nLF and LF/HF during cold exposure. However, all other indices showed differences from post hoc analyses, mainly between HRV and toe PRV, and HRV and ear canal PRV. None of the indices showed differences from all locations, but RMSSD, SD1, and SD1/SD2 showed statistically significant differences when measured from the earlobe. Finally, during cold recovery, the same results were obtained for nLF and LF/HF. In this stage, also nHF failed to show any difference among locations, and post hoc analyses from SD2 did not show any differences between HRV and any of the PRV data. All differences observed were between HRV and toe PRV, and between HRV and ear canal PRV.

7.3.4.2 Correlation analysis

During baseline measurement, non-significant correlation were observed from RMSSD, nLF, LF/HF, SD1 and SD1/SD2 when these indices were measured from toe and ear canal PRV. nHF did not show significant correlations when measured from any location, and SDNN and LF had non-significant correlations when measured from the ear canal. pNN50, HF, TP and SD2 showed statistically significant correlations when measured from all locations.

The correlation between HRV and PRV during cold exposure showed that non-significant correlations were obtained from SDNN, RMSSD, LF, TP and SD1, when measured from the toe and the ear canal; from HF, nHF and SD1/SD2, when measured from the toe; from nLF, when measured from the earlobe; and from LF/HF, when measured from the toe and the earlobe. Significant correlations from all locations were only observed from pNN50 and SD2. Similarly, during cold recovery,

Table 7.5: P-values obtained from the Friedman rank sum test and the multiple comparison tests performed between HRV and PRV from each location (F: Finger; T: Toe; EC: Ear canal; EL: Earlobe), during each stage (BM: baseline measurement; CE: cold exposure; CR: cold recovery) and with each index. Values in red indicate statistically significant differences (p-value < 0.05).

Stage	Index	Friedman test	PRV vs HRV (Nemenyi's Test)			
			F	T	EC	EL
BM	SDNN (s)	<0.001	0.028	0.001	<0.001	0.067
	RMSSD (s)	<0.001	0.001	<0.001	<0.001	0.005
	pNN50	<0.001	0.488	<0.001	<0.001	0.429
	LF (s^2)	<0.001	1.000	1.000	0.610	1.000
	HF (s^2)	<0.001	0.270	0.007	0.002	0.488
	TP (s^2)	<0.001	0.940	0.302	0.143	0.992
	nLF (n.u.)	0.527	-	-	-	-
	nHF (n.u.)	<0.001	0.013	0.001	0.007	0.016
	LF/HF	0.107	-	-	-	-
	SD1 (s)	<0.001	0.001	<0.001	<0.001	0.005
	SD2 (s)	<0.001	0.954	0.650	0.372	1.000
	SD1/SD2	<0.001	0.001	<0.001	<0.001	0.007
CE	SDNN (s)	<0.001	0.988	<0.001	<0.001	0.529
	RMSSD (s)	<0.001	0.302	<0.001	<0.001	0.028
	pNN50	<0.001	1.000	<0.001	0.061	0.429
	LF (s^2)	<0.001	0.988	0.092	0.019	1.000
	HF (s^2)	<0.001	0.954	<0.001	<0.001	0.569
	TP (s^2)	<0.001	0.999	<0.001	<0.001	0.923
	nLF (n.u.)	0.558	-	-	-	-
	nHF (n.u.)	0.026	0.997	0.107	0.650	0.213
	LF/HF	0.431	-	-	-	-
	SD1 (s)	<0.001	0.302	<0.001	<0.001	0.028
	SD2 (s)	<0.001	0.988	0.005	0.014	0.960
	SD1/SD2	<0.001	0.270	<0.001	<0.001	0.013
CR	SDNN (s)	<0.001	0.372	<0.001	<0.001	0.336
	RMSSD (s)	<0.001	0.164	<0.001	<0.001	0.092
	pNN50	<0.001	0.762	0.001	0.003	1.000
	LF (s^2)	<0.001	0.992	0.001	0.040	0.975
	HF (s^2)	<0.001	0.610	<0.001	<0.001	0.448
	TP (s^2)	<0.001	0.940	<0.001	0.008	0.855
	nLF (n.u.)	0.387	-	-	-	-
	nHF (n.u.)	0.160	-	-	-	-
	LF/HF	0.390	-	-	-	-
	SD1 (s)	<0.001	0.164	<0.001	<0.001	0.092
	SD2 (s)	0.001	1.000	0.143	0.187	0.827
	SD1/SD2	<0.001	0.057	<0.001	<0.001	0.107

pNN50 and SD2 showed significant correlations from all locations. However, non-significant correlations were obtained from SDNN, RMSSD, nLF, nHF, LF/HF, SD1, and SD1/SD2, when measured from the toe; from LF and TP, when measured from the toe and the ear canal; and from HF, when measured from the ear canal. The

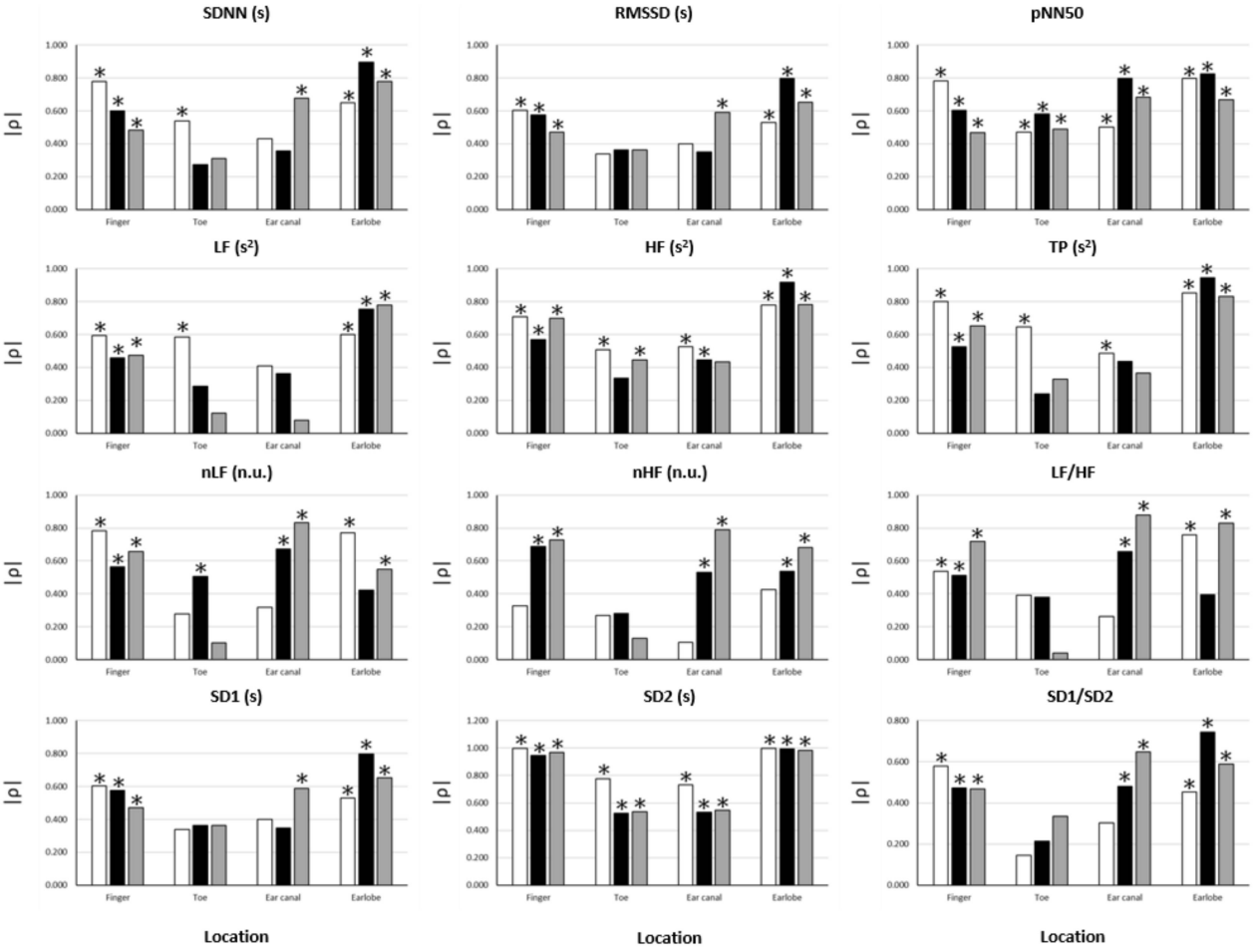

Figure 7.5: Correlation coefficients (ρ) between HRV and PRV from each location during each stage (BM: baseline measurement, white bars; CE: cold exposure, black bars; CR: cold recovery, grey bars) and with each index. Stars over bars indicate statistically significant correlations (p-value < 0.05).

results from the correlation analyses between HRV and PRV are shown in Figure 7.5.

7.3.4.3 Bland-Altman analysis

Since a high correlation does not necessarily indicate a strong agreement (Bland & Altman 1986), Bland-Altman analysis was performed to assess the agreement between PRV and HRV. Bland-Altman ratios (BAR's) are presented in Figure 7.6. Agreement between HRV and PRV measured from the earlobe was the highest and most stable during the three stages, while ear canal PRV showed the worst agreement in most of the indices during the three stages.

From time-domain indices, pNN50 showed a relatively stable, moderate agreement when measured from all locations except for the finger. SDNN and RMSSD

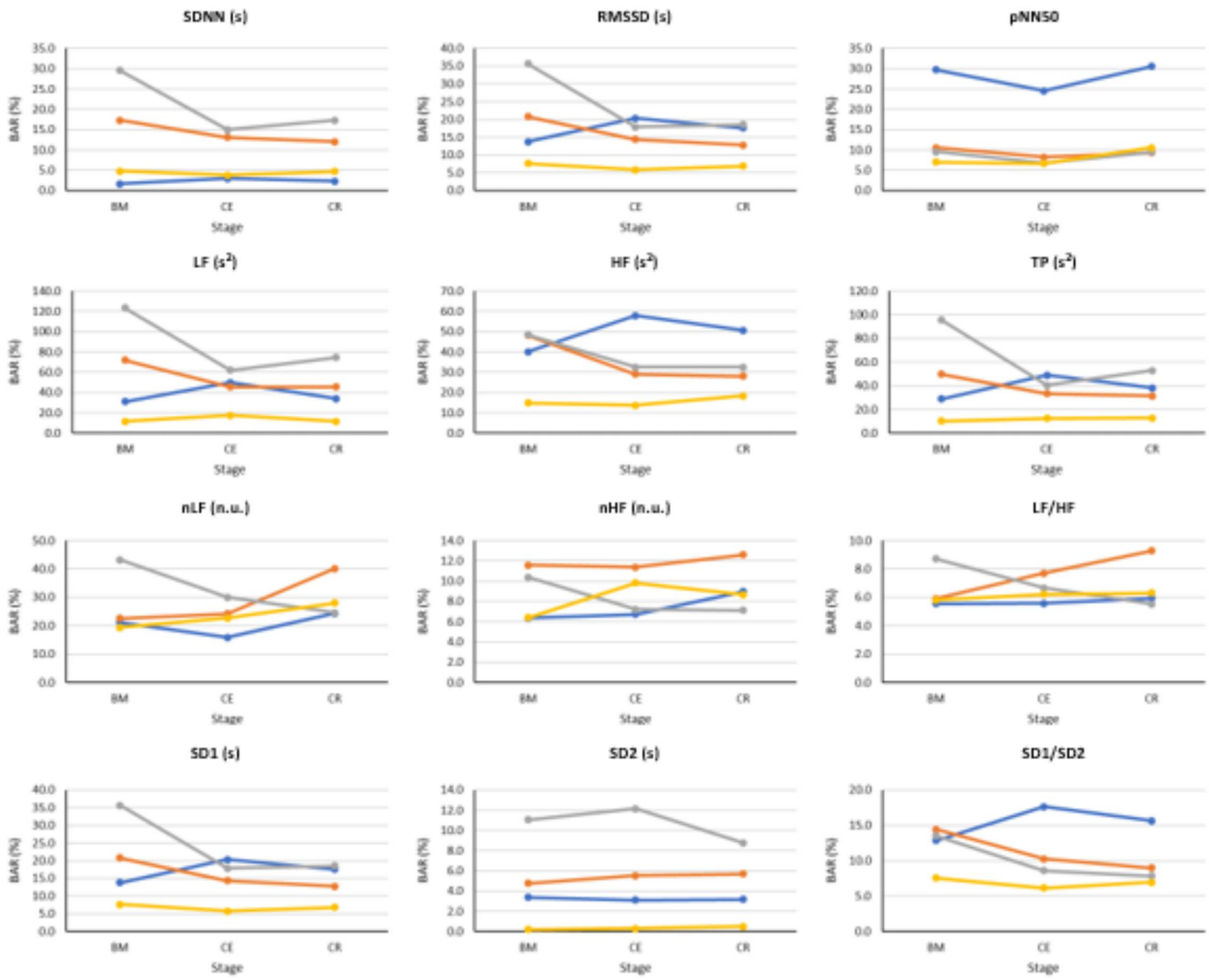

Figure 7.6: Bland-Altman ratios (BAR's) between HRV and PRV from each location (finger: blue line; toe: orange line; ear canal: grey line; earlobe: yellow line), during each stage (BM: baseline measurement; CE: cold exposure; CR: cold recovery) and with each index. Agreements were considered as good (BAR $\leq$ 10%), moderate (10% $\leq$ BAR $\leq$ 20%) or insufficient (BAR $\geq$ 20%).

had the lowest agreement when measured from the ear canal and the toe.

Frequency-domain indices obtained using absolute powers (i.e. LF, HF and TP) showed the worst agreement, reaching BAR's of up to 120%. Once again, earlobe showed the best agreement during the three stages. Relative-power indices had a different behaviour: nHF had good agreement from most locations and stages, and moderate agreement was obtained when PRV was measured from the toe; and LF/HF showed a good agreement from every location and during all stages, and only toe-derived measurements showed a diminished agreement during cold exposure.

From Poincaré plot indices, SD2 showed good agreement in every location except for the ear canal; the earlobe, finger and toe measurements showed a good and stable

agreement. SD1 showed a bad agreement from the ear canal, especially during the baseline measurement.

Bland-Altman plots (Figures 7.7 to 7.18) showed something similar. Cold exposure affected agreement in most of the cases, but the measurement was not necessarily recovered during cold recovery. SDNN, nHF and TP from the earlobe and the ear canal tended to recover the agreement faster during cold recovery, than that measured from the finger. However, most of the indices (i.e. nHF, LF/HF, SD1, SD2, and SD1/SD2) showed that agreement was diminished during cold exposure, but did not recover during the first two minutes of measurement during cold recovery. From these plots, it can be seen that all indices showed an overestimation of the measurement when obtained from PRV, except for LF/HF that tends to be underestimated. Over- and underestimation tend to be larger during cold exposure stage, and toe-derived PRV indices were strongly affected by under- and overestimation.

7.4 Discussion

The main aims of this study were to evaluate if PRV showed any difference between body locations during and after whole-body cold exposure, and if HRV and PRV differed during these thermal changes. The obtained results provide strong evidence for the primary hypotheses regarding the differences between HRV and PRV. Results indicate that cold exposure may affect PRV in different ways when obtained from peripheral and core vasculature, and that PRV may contain different information that is not available in HRV. Although HRV and PRV showed a similar trend during the whole-body cold exposure test, it was evident that PRV overestimated the indices obtained from HRV, usually in a larger scale during the cold exposure. Also, HRV and PRV should not be regarded as the same when different temperature conditions are studied, and PRV may contain different information not available from HRV, although further studies are needed to better understand the contribution of sympathetic activity to PRV measurements.

7.4.1 Effects of cold exposure in peripheral and core vasculature

The sympathetic control of the ANS over cutaneous blood vessels is thought to act differently over peripheral and core vasculature during cold exposure, probably caused by modifications of cutaneous blood flow to changes in temperature, which

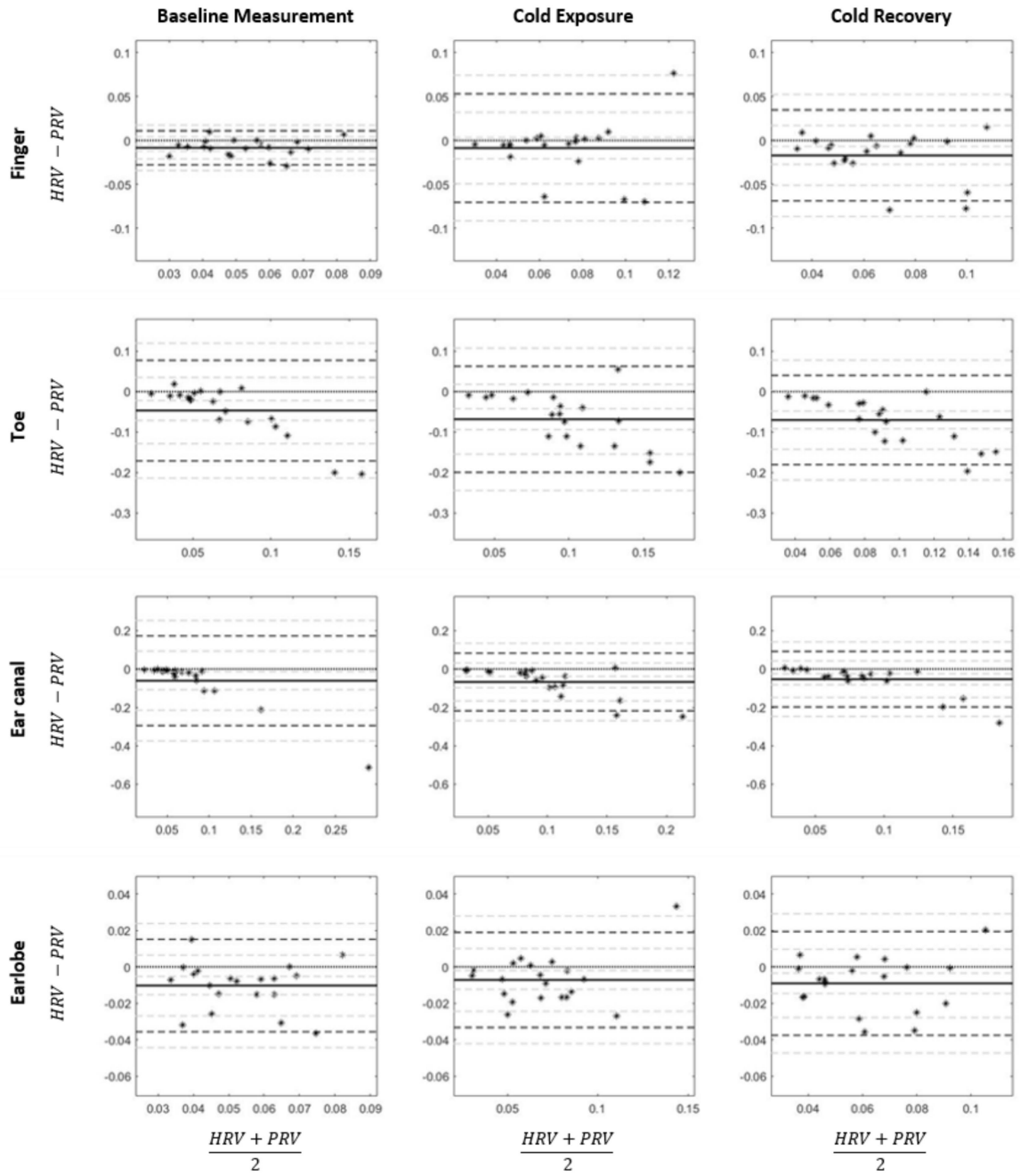

Figure 7.7: Bland-Altman analysis for the assessment of agreement between SDNN indices extracted from HRV and PRV, measured during the three stages of the study. Differences and averages are shown in seconds. From left to right: Basal measurement, cold exposure and cold recovery. From top to bottom, SDNN was obtained from the finger, the toe, the earlobe and the ear canal. Continuous line: Mean value of the difference. Dashed lines: Limits of agreement. Dotted lines: Confidence intervals. Black line: Zero difference.

are intended to maintain thermoregulation and homeostasis (Fox 2016). The sympathetic nervous system generates vasoconstriction in the cutaneous vessels when the temperature is low, producing a decrease in the cutaneous blood flow, which reduces the rate at which the body losses heat, and the amount of blood that is

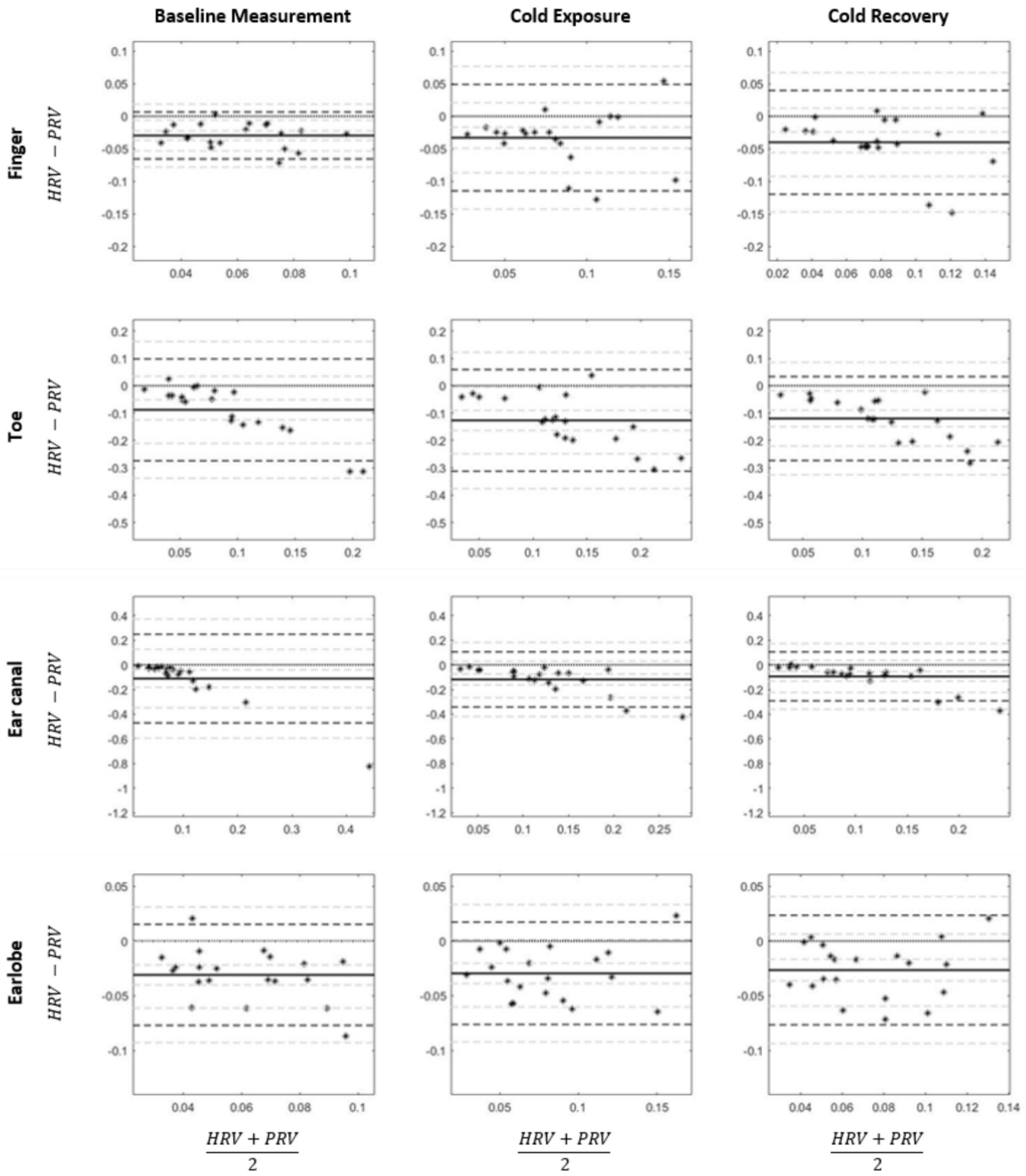

Figure 7.8: Bland-Altman analysis for the assessment of agreement between RMSSD indices extracted from HRV and PRV, measured during the three stages of the study. Differences and averages are shown in seconds. From left to right: Basal measurement, cold exposure and cold recovery. From top to bottom, RMSSD was obtained from the finger, the toe, the earlobe and the ear canal. Continuous line: Mean value of the difference. Dashed lines: Limits of agreement. Dotted lines: Confidence intervals. Black line: Zero difference.

travelling to peripheral tissues such as the fingertips, the palms of the hands, the toes, and the nose, among others.

Different authors have reported distinct responses in core and peripheral vasculature response to cardiovascular changes (Budidha & Kyriacou 2019, Alian et al.

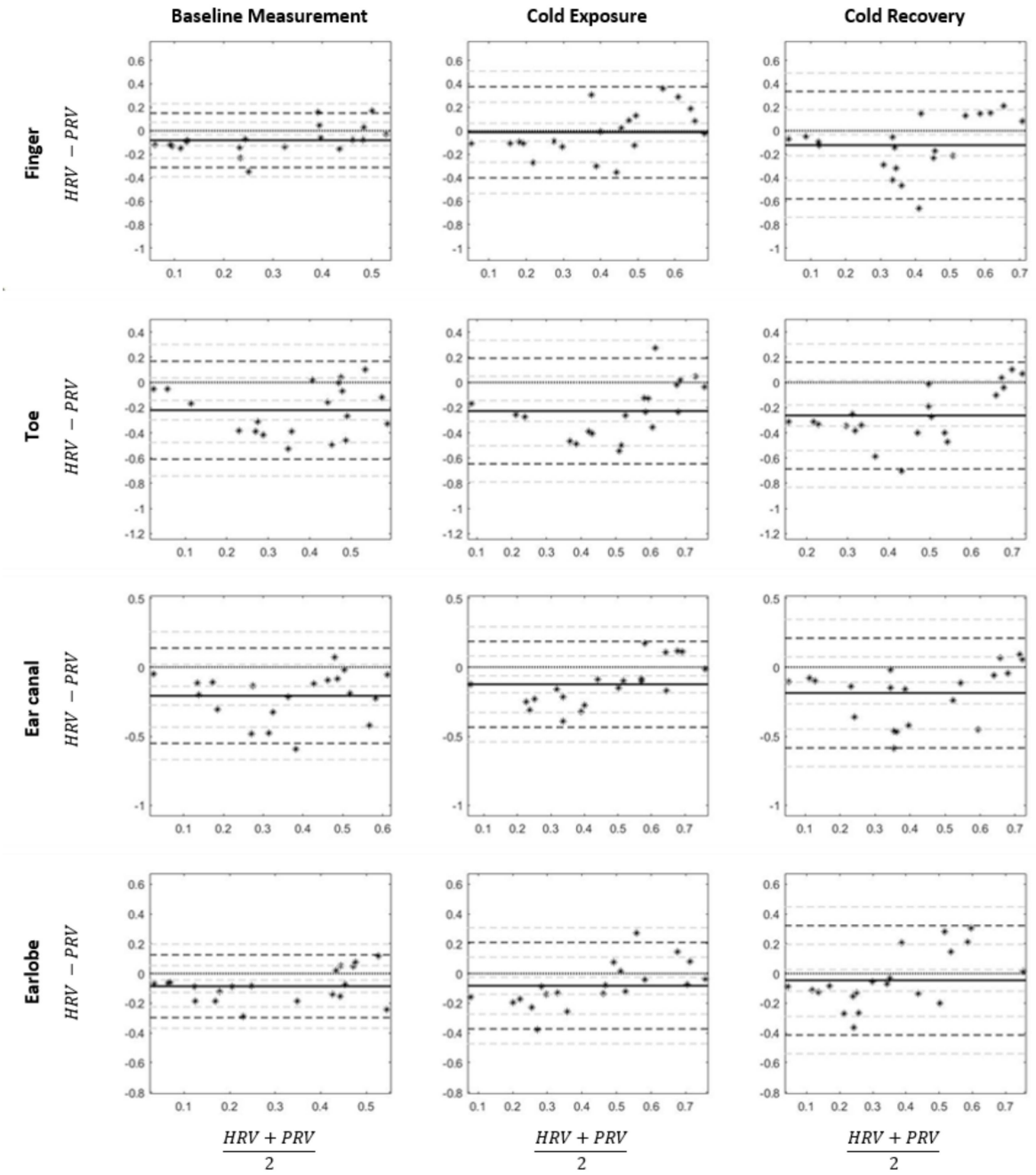

Figure 7.9: Bland-Altman analysis for the assessment of agreement between pNN50 indices extracted from HRV and PRV, measured during the three stages of the study. From left to right: Basal measurement, cold exposure and cold recovery. From top to bottom, pNN50 was obtained from the finger, the toe, the earlobe and the ear canal. Continuous line: Mean value of the difference. Dashed lines: Limits of agreement. Dotted lines: Confidence intervals. Black line: Zero difference.

2011*a*,*b*). The former showed that PPG amplitude was differently affected by whole-body cold exposure when PPG was measured from the finger (peripheral tissue) and the earlobe and ear canal (core tissue), and concluded that ANS regulation is highly affected in peripheral tissue, whereas core vasculature remains almost untouched,

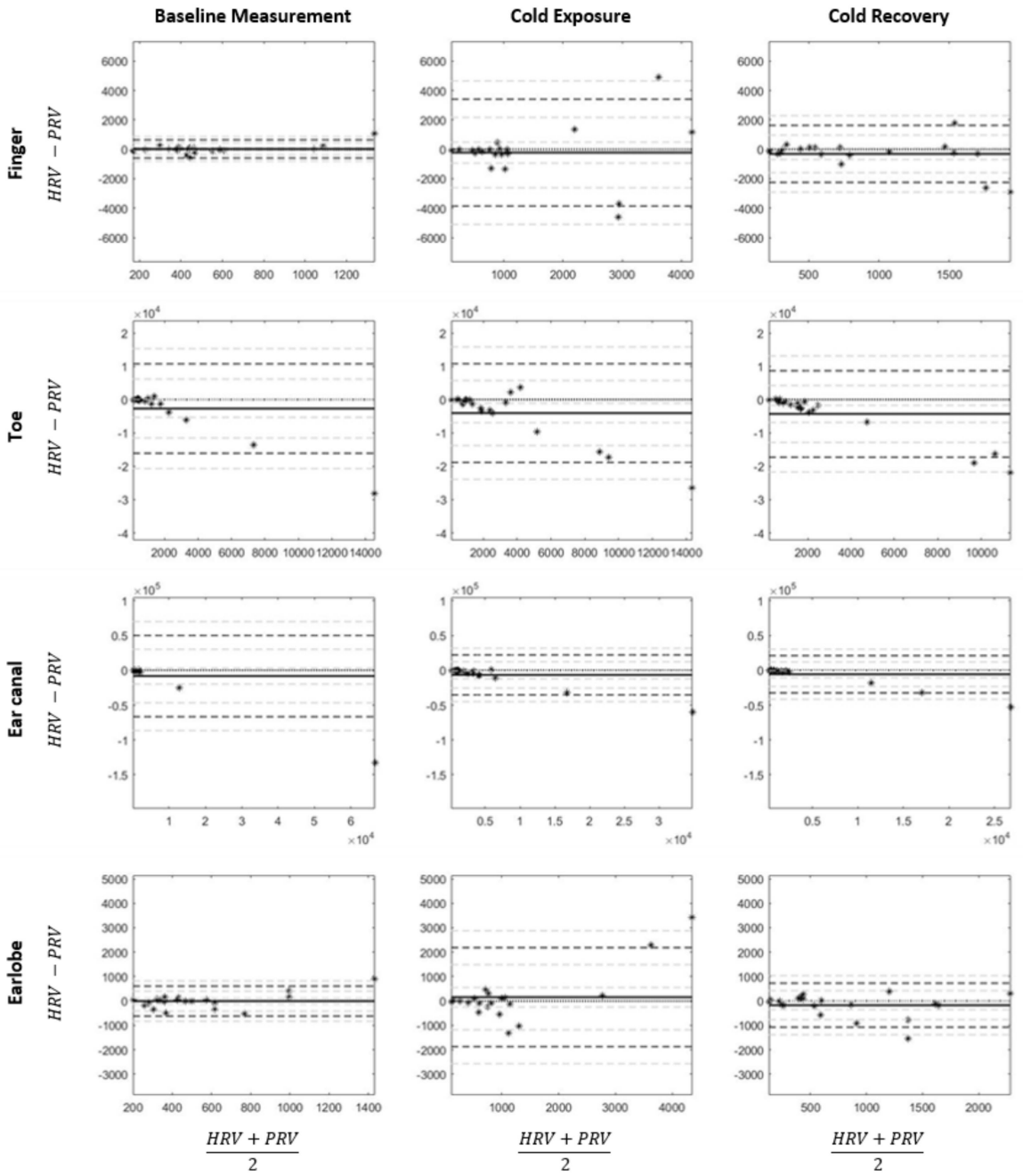

Figure 7.10: Bland-Altman analysis for the assessment of agreement between LF indices extracted from HRV and PRV, measured during the three stages of the study. Differences and averages are shown in squared seconds (s^2). From left to right: Basal measurement, cold exposure and cold recovery. From top to bottom, LF was obtained from the finger, the toe, the earlobe and the ear canal. Continuous line: Mean value of the difference. Dashed lines: Limits of agreement. Dotted lines: Confidence intervals. Black line: Zero difference.

indicating a prevalence of the body to maintain the conditions in vital organs at the expense of peripheral circulation (Budidha & Kyriacou 2019). Alian et. al. demonstrated that, when low-body negative pressure (LBNP) was used as a model of haemorrhage, both time- (Alian et al. 2011*a*) and frequency-domain parameters

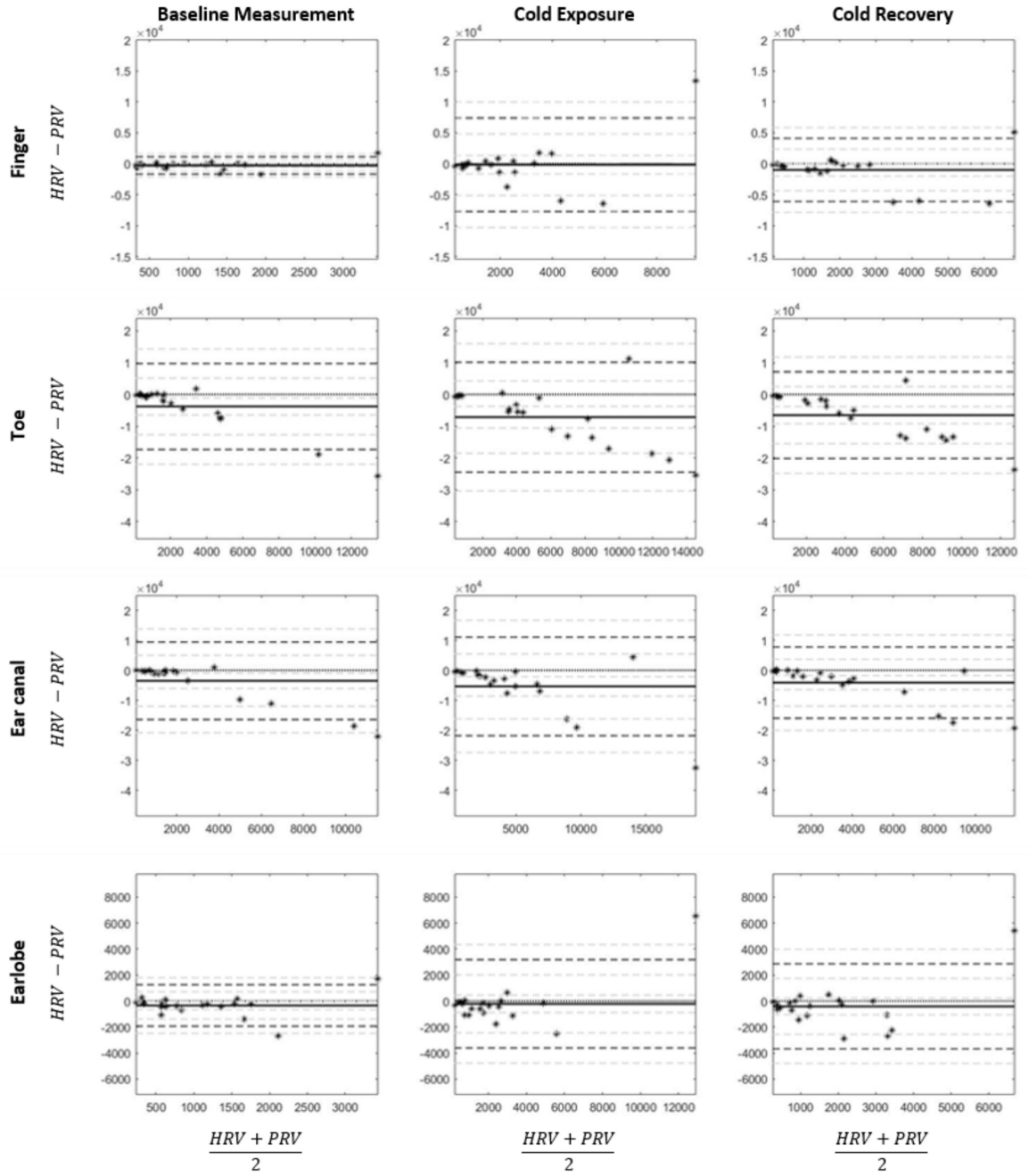

Figure 7.11: Bland-Altman analysis for the assessment of agreement between HF indices extracted from HRV and PRV, measured during the three stages of the study. Differences and averages are shown in squared seconds (s^2). From left to right: Basal measurement, cold exposure and cold recovery. From top to bottom, HF was obtained from the finger, the toe, the earlobe and the ear canal. Continuous line: Mean value of the difference. Dashed lines: Limits of agreement. Dotted lines: Confidence intervals. Black line: Zero difference.

(Alian et al. 2011*b*) measured from the variability of PPG amplitude from the earlobe (core vasculature) and the finger (peripheral vasculature) showed different behaviour after LBNP, and that peripheral vasculature showed larger changes that were not significant from core tissue, probably due to greater changes in vasoconstriction in

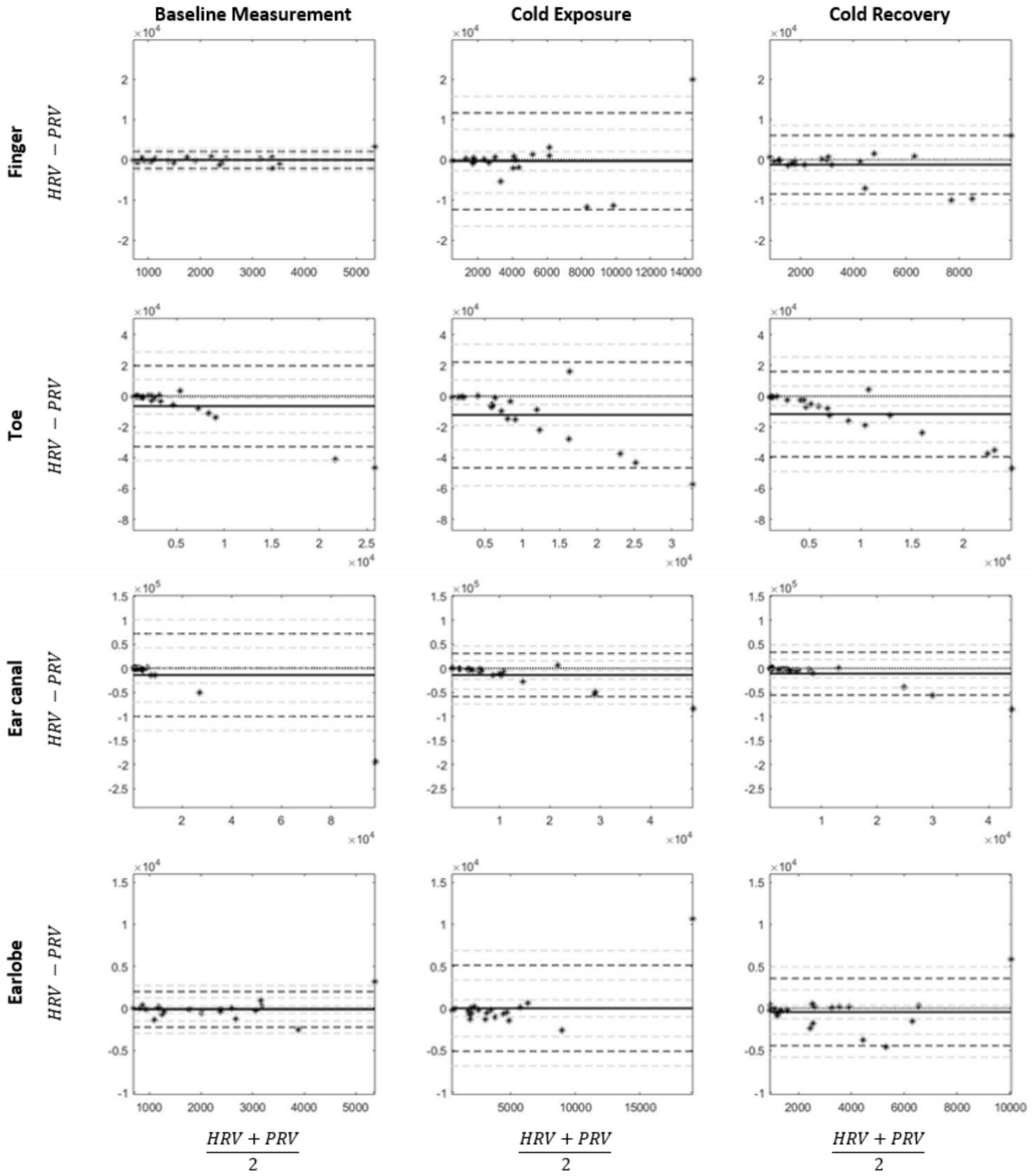

Figure 7.12: Bland-Altman analysis for the assessment of agreement between TP indices extracted from HRV and PRV, measured during the three stages of the study. Differences and averages are shown in squared seconds (s^2). From left to right: Basal measurement, cold exposure and cold recovery. From top to bottom, TP was obtained from the finger, the toe, the earlobe and the ear canal. Continuous line: Mean value of the difference. Dashed lines: Limits of agreement. Dotted lines: Confidence intervals. Black line: Zero difference.

peripheral tissue controlled by sympathetic activity.

In this study, it was observed that most PRV- and HRV-derived indices increased during cold exposure when measured from any of the locations. However, certain differences were observed. Remarkably, the ear canal indices did not show

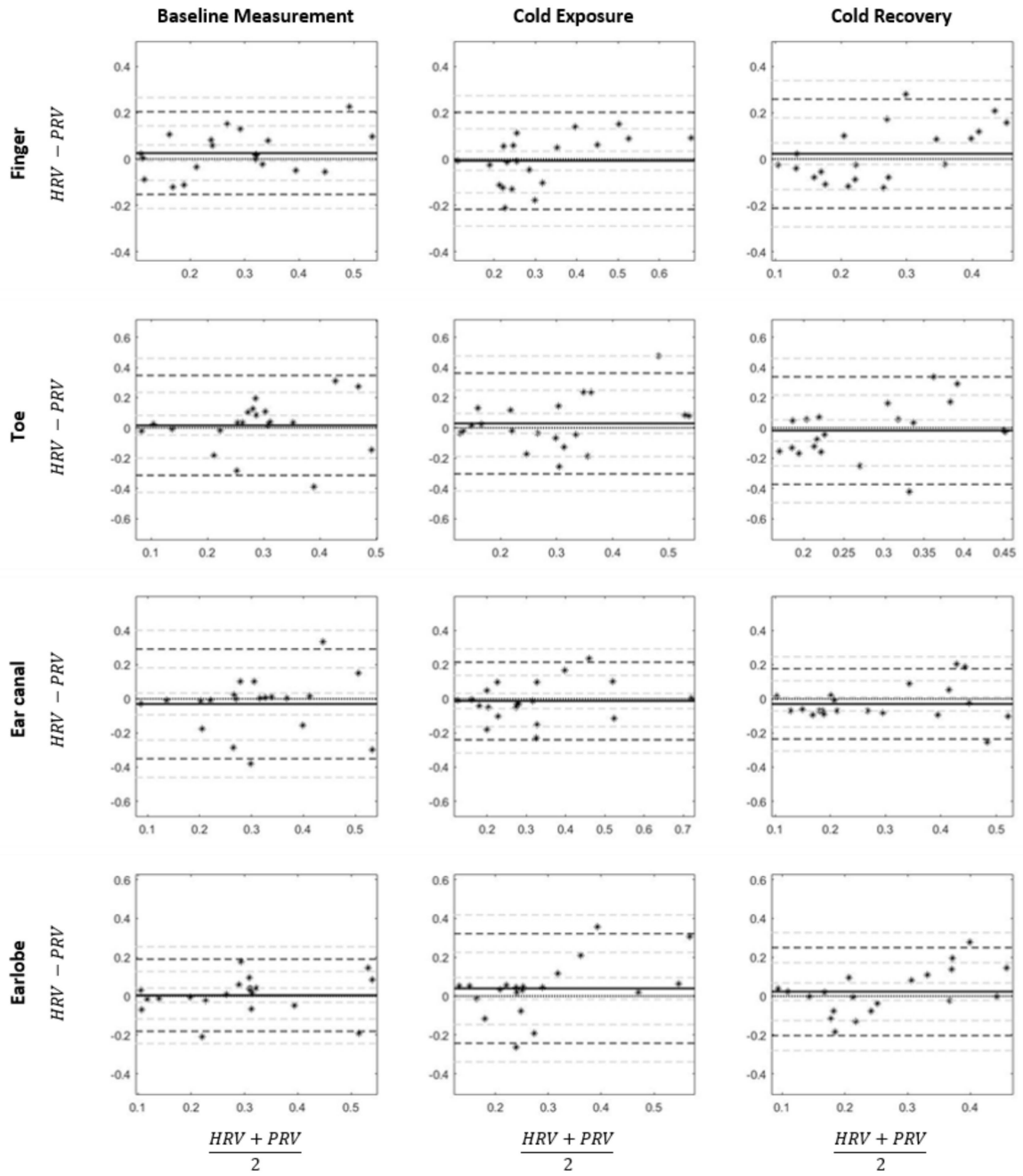

Figure 7.13: Bland-Altman analysis for the assessment of agreement between nLF indices extracted from HRV and PRV, measured during the three stages of the study. From left to right: Basal measurement, cold exposure and cold recovery. From top to bottom, nLF was obtained from the finger, the toe, the earlobe and the ear canal. Continuous line: Mean value of the difference. Dashed lines: Limits of agreement. Dotted lines: Confidence intervals. Black line: Zero difference.

a statistically significant difference due to cold exposure when any of the indices were compared among stages, while most of the other locations showed differences between baseline measurement and cold exposure, as well as between baseline measurement and cold recovery. This behaviour observed from the ear canal could be a

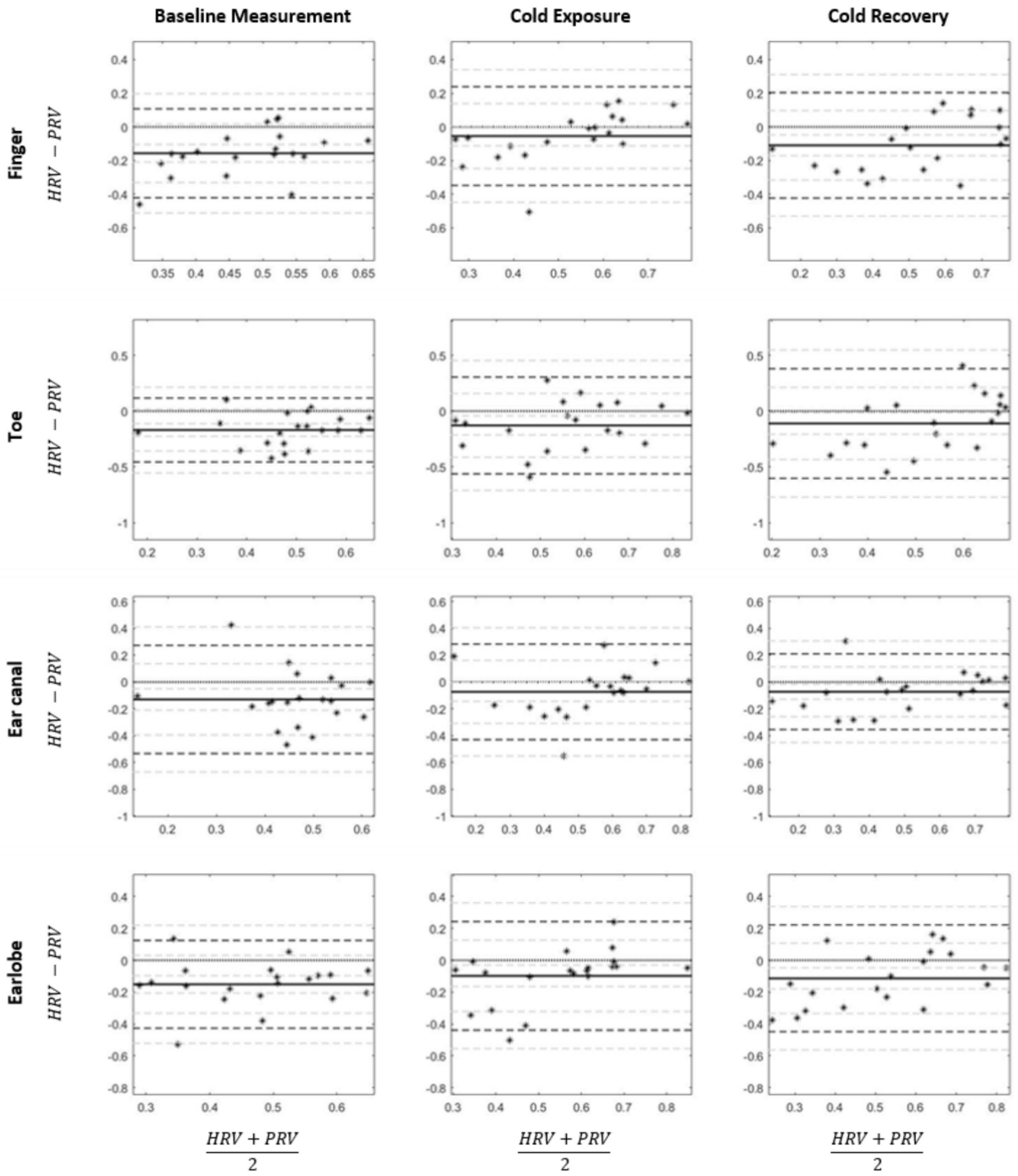

Figure 7.14: Bland-Altman analysis for the assessment of agreement between nHF indices extracted from HRV and PRV, measured during the three stages of the study. From left to right: Basal measurement, cold exposure and cold recovery. From top to bottom, nHF was obtained from the finger, the toe, the earlobe and the ear canal. Continuous line: Mean value of the difference. Dashed lines: Limits of agreement. Dotted lines: Confidence intervals. Black line: Zero difference.

hint of the differences on vascular regulation that is performed by the ANS when the body is exposed to temperature differences (Fox 2016). Interestingly, HRV failed to show any difference among stages when LF, HF and TP were measured, while most of the PRV-derived indices showed differences between baseline measurement and

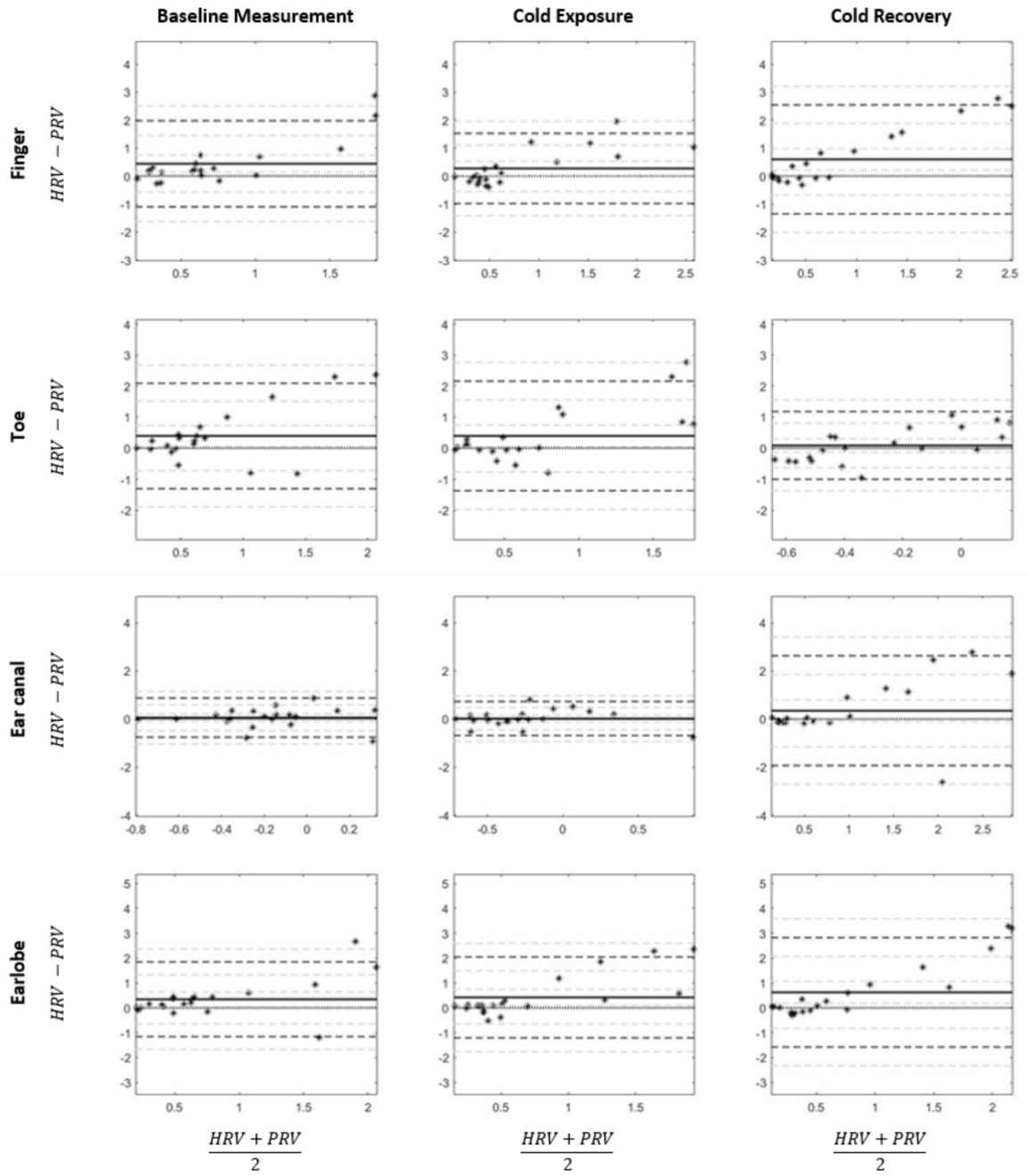

Figure 7.15: Bland-Altman analysis for the assessment of agreement between LF/HF indices extracted from HRV and PRV, measured during the three stages of the study. From left to right: Basal measurement, cold exposure and cold recovery. From top to bottom, LF/HF was obtained from the finger, the toe, the earlobe and the ear canal. Continuous line: Mean value of the difference. Dashed lines: Limits of agreement. Dotted lines: Confidence intervals. Black line: Zero difference.

the subsequent stages. Nonetheless, these results need to be considered with care due to the short segments used for analysis, that may affect the results obtained from frequency-domain analysis (Task Force of the European Society of Cardiology and The North American Society of Pacing and Electrophysiology 1996).

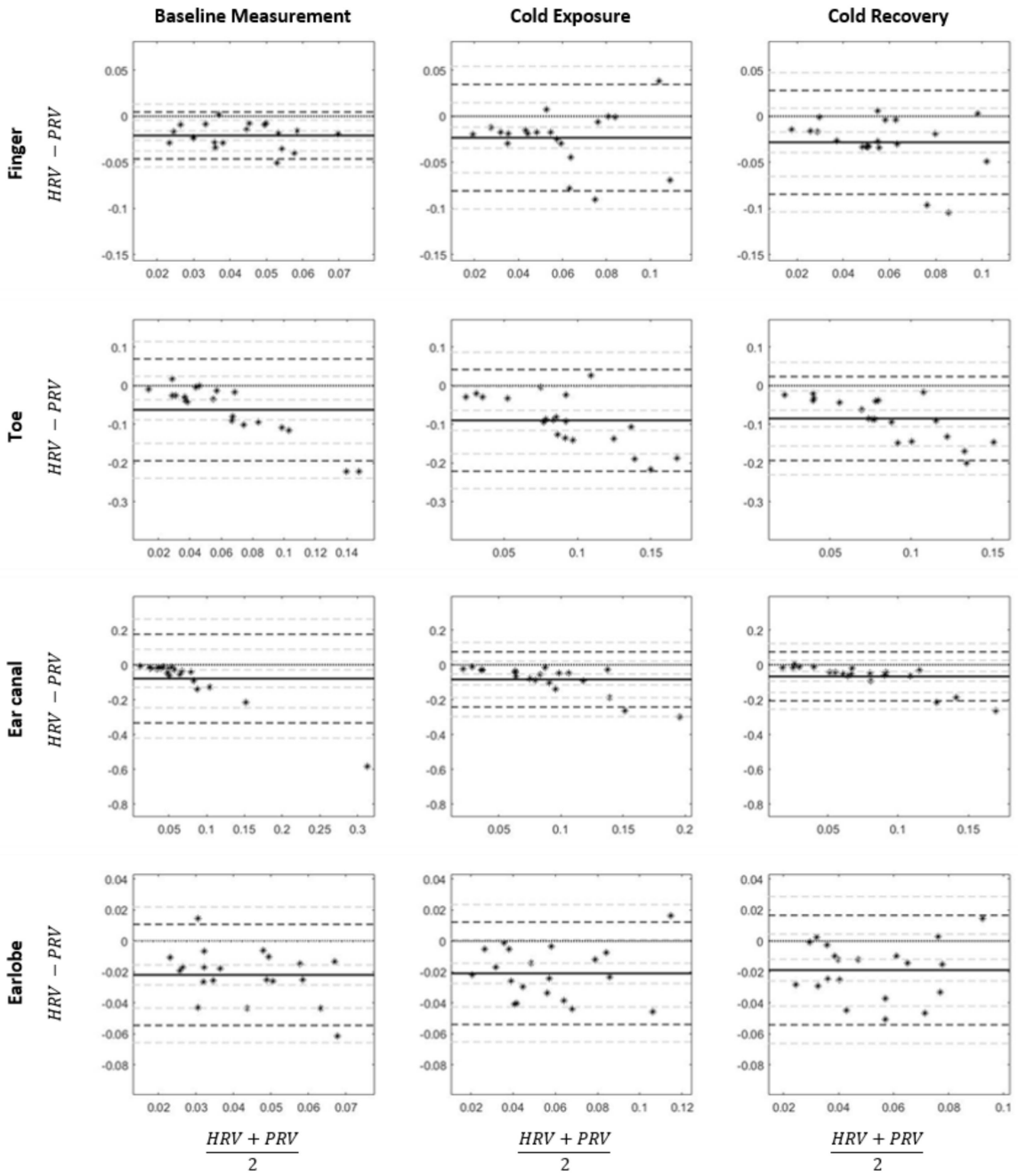

Figure 7.16: Bland-Altman analysis for the assessment of agreement between SD1 indices extracted from HRV and PRV, measured during the three stages of the study. Differences and averages are shown in seconds. From left to right: Basal measurement, cold exposure and cold recovery. From top to bottom, SD1 was obtained from the finger, the toe, the earlobe and the ear canal. Continuous line: Mean value of the difference. Dashed lines: Limits of agreement. Dotted lines: Confidence intervals. Black line: Zero difference.

Although the same trend was observed between data obtained from HRV and most PRV locations during the test, it is remarkable how over- and underestimation are a constant factor in PRV analysis. Moreover, it tended to increase during cold exposure, and was higher when PRV was measured from the toe and the ear canal.

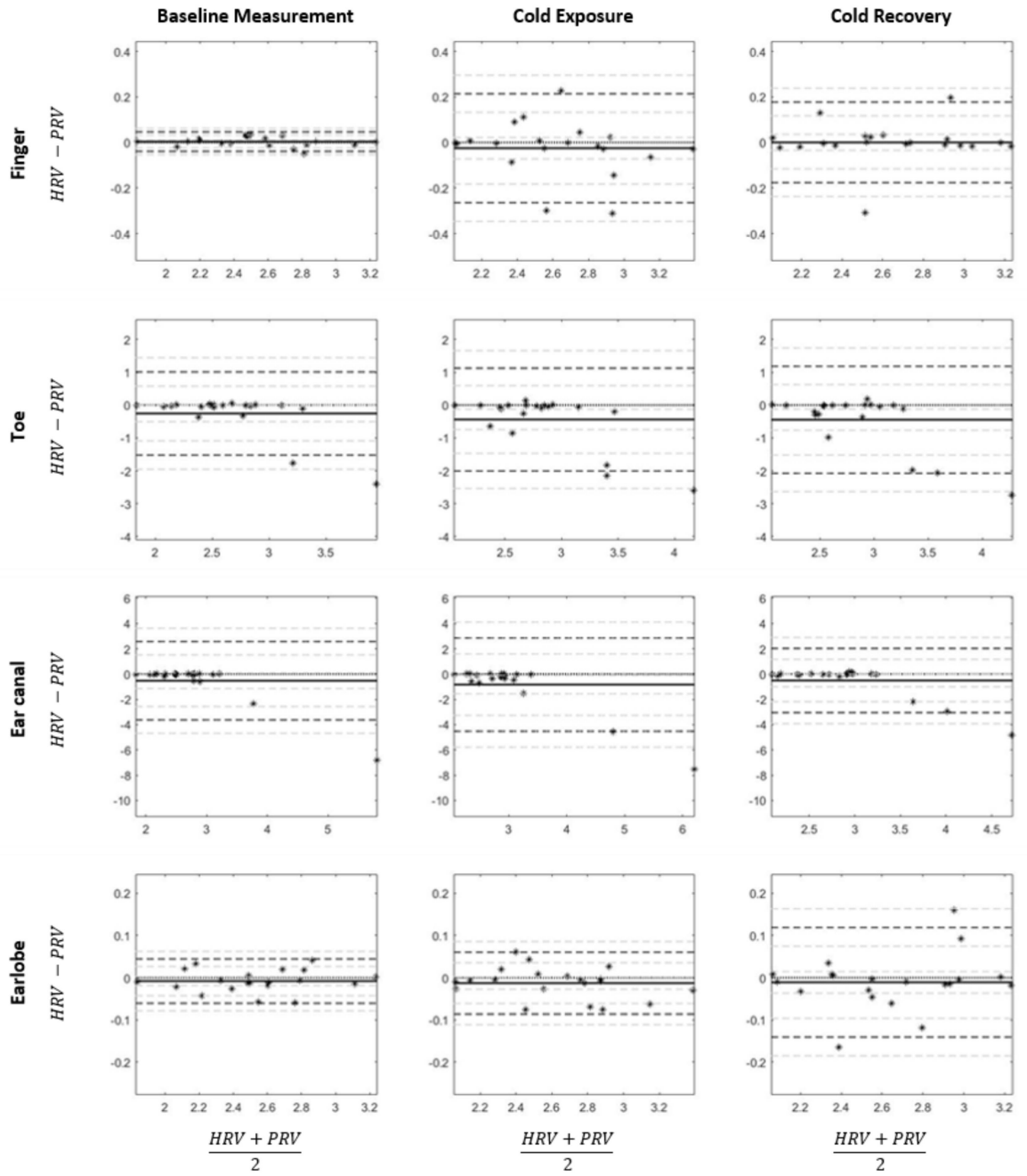

Figure 7.17: Bland-Altman analysis for the assessment of agreement between SD2 indices extracted from HRV and PRV, measured during the three stages of the study. Differences and averages are shown in seconds. From left to right: Basal measurement, cold exposure and cold recovery. From top to bottom, SD2 was obtained from the finger, the toe, the earlobe and the ear canal. Continuous line: Mean value of the difference. Dashed lines: Limits of agreement. Dotted lines: Confidence intervals. Black line: Zero difference.

These two locations could be considered as the most peripheral and the most core vasculature of the four locations used in this study, respectively, and it should be further analysed how this differences may be influenced by ANS activity in these sites. It is also interesting to observe how the values measured during baseline

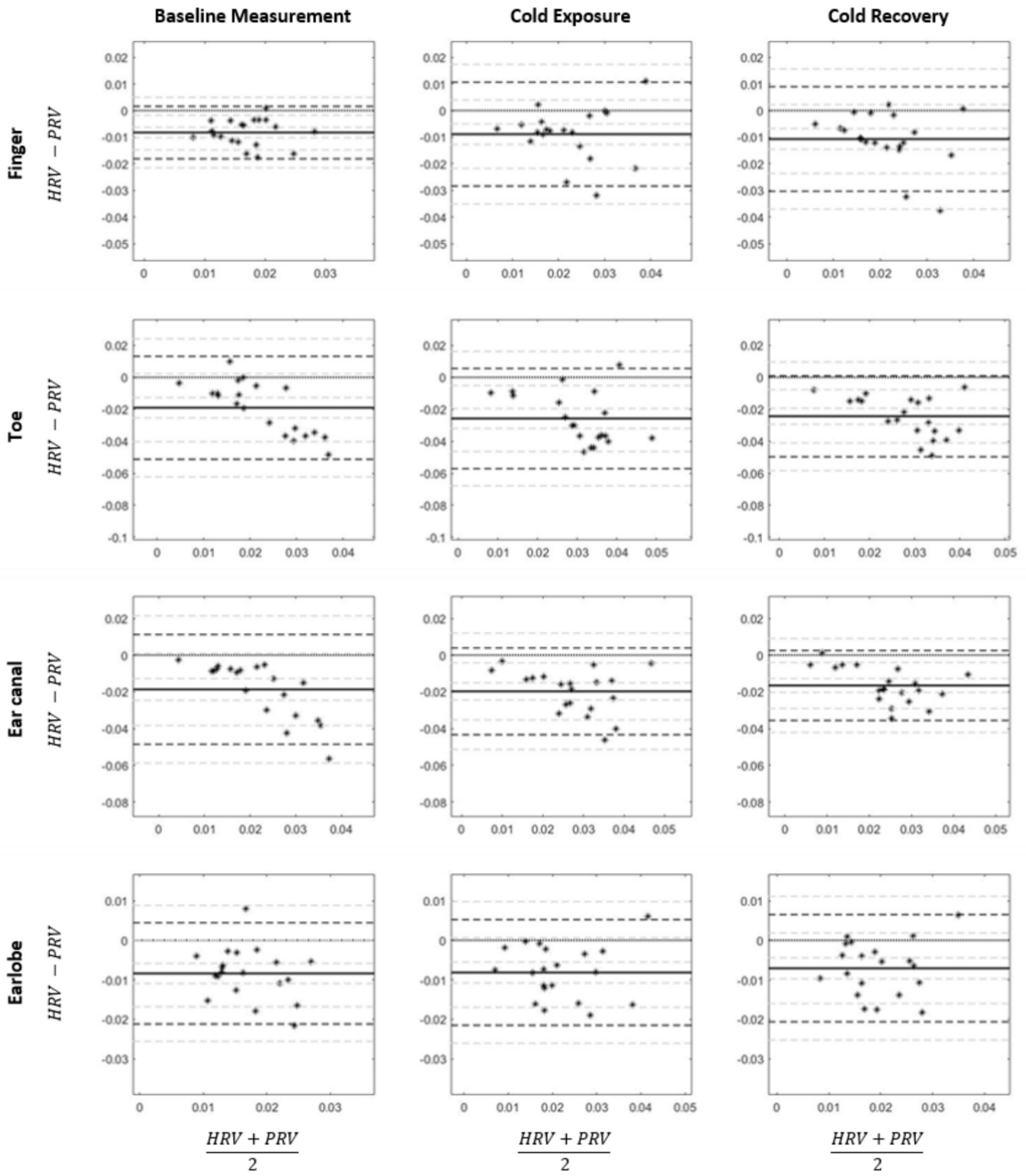

Figure 7.18: Bland-Altman analysis for the assessment of agreement between SD1/SD2 indices extracted from HRV and PRV, measured during the three stages of the study. From left to right: Basal measurement, cold exposure and cold recovery. From top to bottom, SD1/SD2 was obtained from the finger, the toe, the earlobe and the ear canal. Continuous line: Mean value of the difference. Dashed lines: Limits of agreement. Dotted lines: Confidence intervals. Black line: Zero difference.

were achieved from almost all locations after 10 minutes of recovery from the cold recovery, but how they were affected almost immediately at the beginning of the cold exposure. This could be considered as an example of the behaviour of ANS regulation performed over the cardiovascular system during thermal changes.

It is important to remark that only the fiducial points that proved to detect cardiac cycles in a strongly reliable way were used for each subject and each PPG signal, and PRV data was obtained after important pre-processing stages applied to the PPG signals in order to improve their signal-to-noise ratio. Hence, these results can be considered as a strong indication of the differences between PRV and HRV when cardiovascular conditions are modified.

7.4.2 Relationship between PRV and HRV during whole-body cold exposure

It was hypothesised that cold exposure affected the relationship between HRV and PRV, implying that PRV may not be a suitable surrogate of HRV under conditions that alter the vasculature and that it may contain different information due to cardiovascular changes.

From the Friedman rank sum test, it was observed that there were statistically significant differences between HRV and PRV, when the latter was measured from different body sites. However, the relationship between PRV and HRV changed during each stage, and from each location. Interestingly, and in line with the results obtained from the other analyses, toe and ear canal PRV consistently showed statistically significant differences to HRV. Also, frequency-domain indices, especially nLF and LF/HF, were not found different between HRV and PRV. This was probably due to the short time of analysis.

In general, the finger and the earlobe were the locations in which less differences were observed, and during all stages the earlobe proved to be the body site in which the relationship between HRV and PRV was less affected by the changes in temperature. Especially during the baseline measurement, it was observed that HRV and PRV differed especially when RMSSD, nHF, SD1 and SD1/SD2 parameters were measured. All these parameters, except for SD1/SD2, reflect the short-term HRV and PRV. Hence, PRV and HRV tend to differ more in short-term indices. In this same line, some indices showed no difference among locations. These parameters, which include LF, TP, nLF, LF/HF, and SD2, are expected to be a measurement of long-term variability (Khandoker et al. 2013). Hence, the lack of differences may be explained by the short measurement and due to the changes that are induced with short exposure to cold temperatures, that may not be reflected in long-term variability changes.

SD1, RMSSD and HF reflect parasympathetic activity in HRV (Shaffer & Ginsberg 2017), which usually leads to diminished heart rate and lowered force of atrial contraction, among other effects (Drew & Sinoway 2012). In vessels, most of the ANS activity is controlled by the sympathetic nervous system, which is in charge of vasoconstriction and vasodilation in response to environmental changes (Lombard & Cowley 2012). In this study, it was observed that a diminished temperature induced a higher similarity between these indices from HRV and PRV in different body sites, which might be explained by a lower parasympathetic activity and an increased sympathetic activity. It is not clear how sympathetic and parasympathetic changes may be affecting PRV-derived indices, and it might be possible that PRV may be affected by these changes in a different manner when compared to HRV, which is mainly a reflection of vagal activity (Laborde et al. 2017), and that sympathetic changes in vascular autonomic activity are observable from PRV indices. SD1/SD2, on the other hand, is supposed to be an index of short-term and long-term changes of ANS activity (Khandoker et al. 2013). Hence, a change in either parasympathetic or sympathetic activity should be reflected in this index, as was observed in the results obtained in this study.

However, further studies are needed to better understand and characterize PRV changes, and to evaluate how sympathetic changes may be affecting PRV-extracted indices. This could be done by using blockade techniques for assessing the contribution of each branch of the ANS to PRV indices, or by comparing PRV results to more specific measurements such as microneurography. To the knowledge of the authors, the only blockade study that has been performed to evaluate changes in PRV was done by Pellegrino et al. (2014). They showed that cardiovagal blockade induced an overestimation of HF measured from PRV; cardiac sympathetic blockade implied a moderate to high agreement between HRV and PRV in time- and frequency-domain indices; and dual blockade implied a poor accuracy and precision for normalized measures and LF/HF indices. Also, non-linear indices obtained from HRV and PRV were largely affected by both sympathetic and parasympathetic blockade. Hence, PRV and HRV can be supposed to act differently under different ANS conditions.

The correlation analysis was performed to further compare HRV and PRV. The main result was the stronger correlations observed from the earlobe and the finger, in all indices, compared to those measured from the ear canal and the toe. SD2 showed an interesting behaviour: Significant correlations tended to show a lower correlation

coefficient when PRV was measured from all locations during cold exposure; during baseline measurement and cold recovery, the correlation is slightly higher, indicating that the correlation of SD2 from HRV and PRV was more affected during the induced hypothermia response. Several studies have used correlation analysis to assess the relationship between HRV and PRV, some of them finding results similar to those reported in this paper. When PRV and HRV correlation was assessed in subjects at rest, earlobe and finger PRV have a good correlation to HRV indices (Shi et al. 2008, Lu et al. 2009, Bulte et al. 2011, Okkesim et al. 2016); however, certain changes in cardiovascular conditions have been found to alter the correlation between HRV and PRV, including changes due to mental stress (Giardino et al. 2002), changes in the position of the subjects (Lu et al. 2008, Gil, Orini, Bailón, Vergara, Mainardi & Laguna 2010), and changes in cardiovascular dynamics (Charlot et al. 2009).

Finally, from the Bland-Altman analysis, SD2 and pNN50, to a lower extent, showed the better agreement between HRV and PRV in all stages and from all body sites. This is in line with the results obtained from the correlation analysis and the Friedman's test results. However, LF/HF showed a good agreement as well, which is not reflected in the other analyses. This could be due to the short recordings which highly affect frequency-domain indices. Interestingly, some of the Bland-Altman plots derived from HRV and PRV data showed a behaviour similar to what was hypothesised: The agreement is affected during cold exposure in all locations, but during cold recovery, the agreement tends to recover. Although Shin (2016) does not explain the location from which PPG signals were obtained, these results are in line with those shown by in his study, in which differences in the relationship between PRV and HRV were observed when ambient temperature increased.

Frequency-domain indices reflecting absolute powers, i.e. LF, HF and TP, showed higher values of BARs than any other indices, reaching BARs above 100%. This might be an indication of the effect of short-term recordings on these indices, but further analyses should be performed to better understand how these indices may relate when extracted from PRV and HRV. Also, the toe and ear canal measurements were the ones that showed the higher differences between HRV and PRV, in all three stages. It is hard to conclude regarding the origin of these differences. Regarding the toe measurements, although the quality of the signals was the lowest, it is plausible that the higher differences were due to the measurement site: PRV has been shown to be affected by pulse transit time (PTT) variability (Gil, Orini,

Bailón, Vergara, Mainardi & Laguna 2010), and the distance between the heart and the toe is larger than the others, implying a longer time for the pulse wave to arrive to the site of measurement and increasing the chances of cardiovascular changes that may affect PTT variability. And regarding the ear canal, these differences in agreement might be explained by the hypothesis that core vasculature is less affected by environmental changes than the other locations. Although HRV is measured directly from the heart, it could be considered as a measurement of the summation of the changes in ANS activity in the cardiovascular system as a whole, whereas the ear canal might be a reflection of more localised changes. Nevertheless, the measurement on this body site is relatively new (Budidha 2016), and further analyses should be performed.

It must be considered as well the effects that lower temperatures may have on the photoplethysmographic signal, and how it is affected differently by these changes to the electrocardiogram. Khan et al. (2015) demonstrated that the quality of PPG signals acquired from colder fingers is much lower than those obtained at normal temperature conditions, while higher temperatures allow for an improvement in the quality of the signal and consequently of the oxygenation measurements obtained from it. Pilt et al. (2013) and Pi et al. (2022) also reported important differences in the PPG signal quality due to changes in temperature, which make it harder to reliable extract physiological information from the signal. Although cold also induces changes in the morphology of the ECG (Raiko et al. 2021), it's quality, especially for HRV assessment is less affected than the PPG. Hence, this may have had an impact on the results obtained.

7.4.3 Limitations of the study

One of the main limitations for the analysis of PRV under the exposed circumstances is the fact that PPG signals are highly affected by changes in vasculature derived from cold exposure. This represents an increased difficulty for obtaining high quality PPG signals and, therefore, for extracting reliable fiducial points from the signals. To overcome this difficulty, different signal quality indices were extracted from PPG cardiac cycles delimited by several fiducial points, i.e., systolic peaks, diastolic onsets, maximum slope points, and the point of intersection between tangent lines from the diastolic onset and the maximum slope point. It was found that the best quality of cardiac cycles was when cycles were delimited by the intersection point between

the tangent lines, whereas the worst quality was obtained from the cardiac cycles delimited by systolic peaks. These results are in line with those obtained by Peng et al. (2015) and Hemon & Phillips (2016). However, the fiducial point selected for each case was different, according to the results of each signal, as recommended in the literature (Pinheiro et al. 2016). With this methodology, the probabilities of having a low-quality PRV time-series was reduced. Also, the IBIs and RRIs were manually corrected, to avoid outliers and mistakes that could affect the results.

It is important to consider as well that the sample size of this study was relatively small, and composed mainly of young and healthy subjects, that do not represent the population as a whole. Finally, a note should be made on the short segments of signals used for the analyses performed in this study, which might affect the results, especially those obtained from frequency-domain parameters. These short recordings were selected in order to be able to compare the three stages, and to observe the differences along time. Although longer recordings are recommended, several studies have shown that short recordings of less than 10 minutes can be used reliably for the analysis of time-domain and nonlinear indices from HRV and PRV (Shaffer & Ginsberg 2017).

7.5 Summary

Cardiovascular responses to cold exposure have been shown to differ among different body locations, and it has been suggested that this is due to autonomic activity and that it can be assessed using PPG signals (Budidha & Kyriacou 2019). In this study, a whole-body exposure protocol was performed to evaluate the effect of temperature changes in PRV acquired from several body places, and its relationship with HRV.

From the obtained results, it can be concluded that PRV and HRV should not be regarded as equal under all circumstances, and that hypothermia affects PRV in a different manner, not only when compared to HRV but also when compared among different body sites. PRV generally overestimates HRV indices, especially under cold exposure. Moreover, there seems to be a tendency to maintain the autonomic balance more properly in core vasculature.

Although further investigation is needed, the results shown in this chapter serve as an indication of the effects of changes in vessel characteristics that can be observed in PRV, but are not reflected in HRV, and are promising for future research,

which may aim to understand the contribution of parasympathetic and sympathetic activity in the measurement of these indices from PRV. Nonetheless, further research that aims to clarify the contribution of sympathetic and parasympathetic activity on PRV, by using methodological considerations such as using blockade studies, are needed to better understand the results obtained in this study.

In the next chapter of this thesis, other crucial cardiovascular variable, i.e. blood pressure, and its effect on PRV and its relationship with HRV is analysed, with the objective of further understanding how PRV could be used for the assessment of different cardiovascular changes.

Chapter 8

Relationship between pulse rate variability and heart rate variability under different blood pressure states in critically-ill subjects

8.1 Aims and objectives

As mentioned in previous chapters, some studies have shown that PRV is a promising technique for identifying several physiological conditions, and that it is highly correlated with HRV. However, these results have mainly been observed in healthy or resting subjects in the supine position and several researchers have argued that PRV is not necessarily a good surrogate for HRV, probably due to physiological factors, such as changes in pulse transit time (PTT) (Schäfer & Vagedes 2013). As explained by Constant et al. (1999) and Gil, Orini, Bailón, Vergara, Mainardi & Laguna (2010), PTT plays an important role in the differences that are seen between PRV and HRV.

PTT is the time it takes for the pulse wave to travel from the heart to the peripheral tissue where it is being measured, and it has been shown to be related to blood pressure (BP) (i Caros 2011). BP refers to the force that the heart uses to pump blood through the circulatory system and is one of the main measurements

used to understand the behaviour of the cardiovascular system (National Health Service 2019*b*). Its associated abnormalities, especially hypertension (i.e., high blood pressure), are associated with fatal cardiovascular diseases (Mousavi et al. 2019). As explained by Karmali et al. (2017), HRV has been found to aid in the diagnosis and increase the prognostic value of predisposing conditions for critical illness, including hypertension, and some HRV parameters have been found to be abnormal even in the early stages of this particular condition.

Because of the relationship between PTT and BP, and the effects of PTT on PRV measurements (Constant et al. 1999, Gil, Orini, Bailón, Vergara, Mainardi & Laguna 2010), the aim of this study was to evaluate the relationship between HRV and PRV measured from ECG and PPG signals, respectively, obtained from critically ill patients with hypotension, hypertension, or normotension. It was hypothesised that HRV and PRV would not exhibit the same behaviour and that their relationship would be affected by the BP state. To evaluate these hypotheses, signals obtained from the public MIMIC-III database from Physionet were analysed, and PRV and HRV indices were extracted and compared to assess the relationship between HRV and PRV.

8.2 Methods and materials

8.2.1 Signal selection

A subset of 500 records was obtained from the MIMIC-III Waveform Database (Johnson et al. 2016, Goldberger et al. 2000). Each record in the subset contained the ECG, PPG, and invasive arterial BP (ABP) signals, which were obtained at a 125 Hz sampling rate, from critically ill subjects in adult intensive care units. As the MIMIC-III is a publicly available database, ethical approval was not required for this study.

These records were filtered to reject poor-quality signals and signals with length of less than 5 min. First, signals with a duration of less than 5 min were discarded. Then, a signal quality index (SQI) algorithm similar to that described in Chapter 7 was employed to detect good- and poor-quality ABP signals. A block diagram of this algorithm is shown in Figure 8.1. It begins with the detection of the onsets from each ABP signal, applying the Delineator algorithm (Li et al. 2010), and obtaining the cardiac cycles. Then, the quality of each cardiac cycle was assessed using SQIs

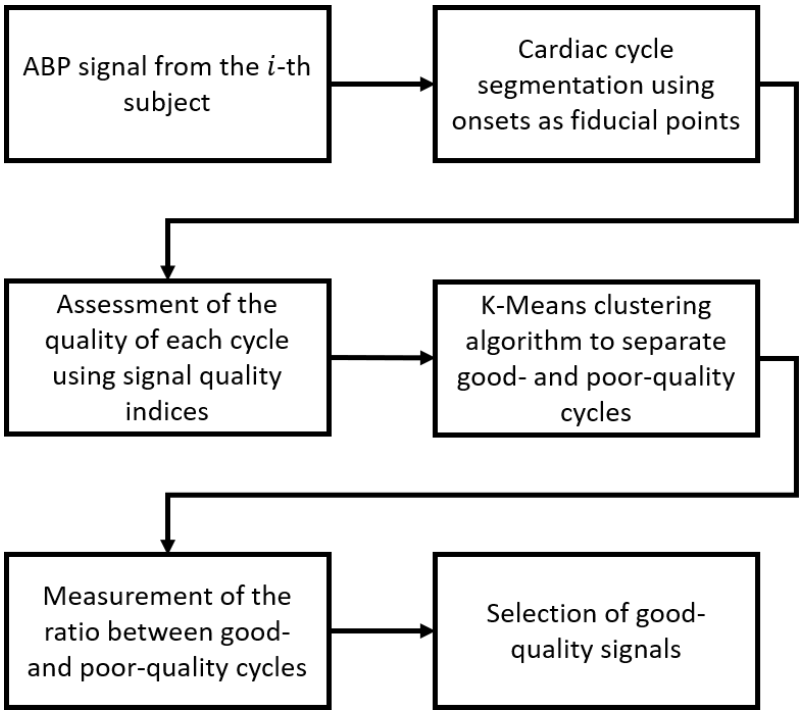

Figure 8.1: Signal quality assessment algorithm. The arterial blood pressure (ABP) signals are segmented into cardiac cycles and signal quality indices are extracted for each cardiac cycle. Then, these indices are used as features to group the cycles in two clusters, using a k-Means algorithm. Then, signals are classified as good or poor-quality cycles using the ratio between the number of points grouped in each cluster.

proposed in the literature (Li & Clifford 2012, Elgendi 2016, Karlen et al. 2012). A K-Means clustering algorithm was employed to automatically group good-quality (GQ) and poor-quality (PQ) cardiac cycles in two clusters, with the SQIs used as features. Because it was expected that most of the cycles would be of good quality, the larger cluster was considered the good-quality cluster. Then, the ratio (R_{GQ}) between the number of cycles grouped as "good-quality cycles" and the total number of cycles was obtained as in (8.1). The records with a R_{GQ} greater than or equal to 80% were considered good-quality signals, and the remaining records were discarded.

$$R_{GQ} = (100\%)\frac{n_{GQ}}{n_{GQ} + n_{PQ}} \tag{8.1}$$

8.2.2 Signal processing

MATLAB® (version 2020a) was used for signal processing and figure generation. ECG, PPG, and ABP signals from selected recordings were segmented into 5-min-long portions, with a stride of 10 s between consecutive segments.

8.2.2.1 Arterial blood pressure signals

After segmentation, 5-min-long ABP signals were filtered using a 12 Hz, fourth order, lowpass Butterworth filter. Peaks and onsets were detected, corrected, and interpolated using a cubic spline to obtain systolic blood pressure (SBP) and diastolic blood pressure (DBP) trends. From the SBP and DBP information, events of hypertension (SBP greater than 140 mmHg or DBP greater than 90 mmHg) and hypotension (SBP lower than 90 mmHg or DBP lower than 60 mmHg) were identified. Then, each 5 min segment was labelled as hypertension, normotension, or hypotension according to the most frequent label in each 5 min segment. An example of these trends and labels is shown in Figure 8.2.

8.2.2.2 Heart rate variability

After segmentation, R peaks were detected from ECG signals using the algorithm proposed by Pan & Tompkins (1985). HRV was measured as the time difference, in milliseconds, between consecutive R peaks. For the frequency-domain analysis, the uneven HRV series was interpolated using a cubic spline interpolation and a

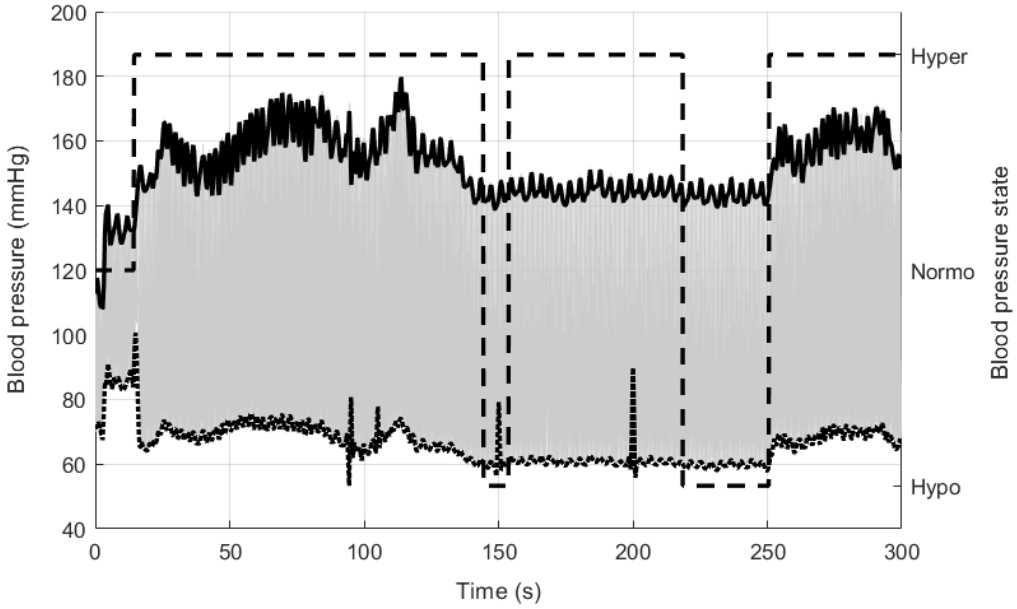

Figure 8.2: Example of the analysis of a 5 -min arterial blood pressure (ABP, gray line) signal, with the trends for systolic (SBP, continuous line) and diastolic (DBP, dotted line) blood pressure, as well as the determination of blood pressure state (BP State, dashed line). Each 5-min segment is classified as hypotension (hypo), normotension (normo) or hypertension (hyper) according to the most frequent state during the 300 seconds.

sampling rate of 4 Hz, and the power spectrum was obtained using the Fast Fourier Transform (FFT). Outliers in both the original and interpolated time series were defined as values higher or lower than the mean value plus or minus 1.96 times the standard deviation of the series. These outliers were then replaced with the mean value of the five previous values in the time series. Figure 8.3 (a) illustrates this process.

8.2.2.3 Pulse rate variability

After segmentation, the onset of each cardiac cycle from the 5-min-long PPG signals was obtained as the intersection point of the tangent lines arising from the maximum slope point and the valley of the waveform. This fiducial point was selected because of its robustness for PRV analysis, as shown in previous work published by Hemon & Phillips (2016) and Posada-Quintero, H.F., Delisle-Rodríguez, D., Cuadra-Sanz, M.B., & Fernández de la Vara-Prieto, R.R. (2013) and on the results obtained in

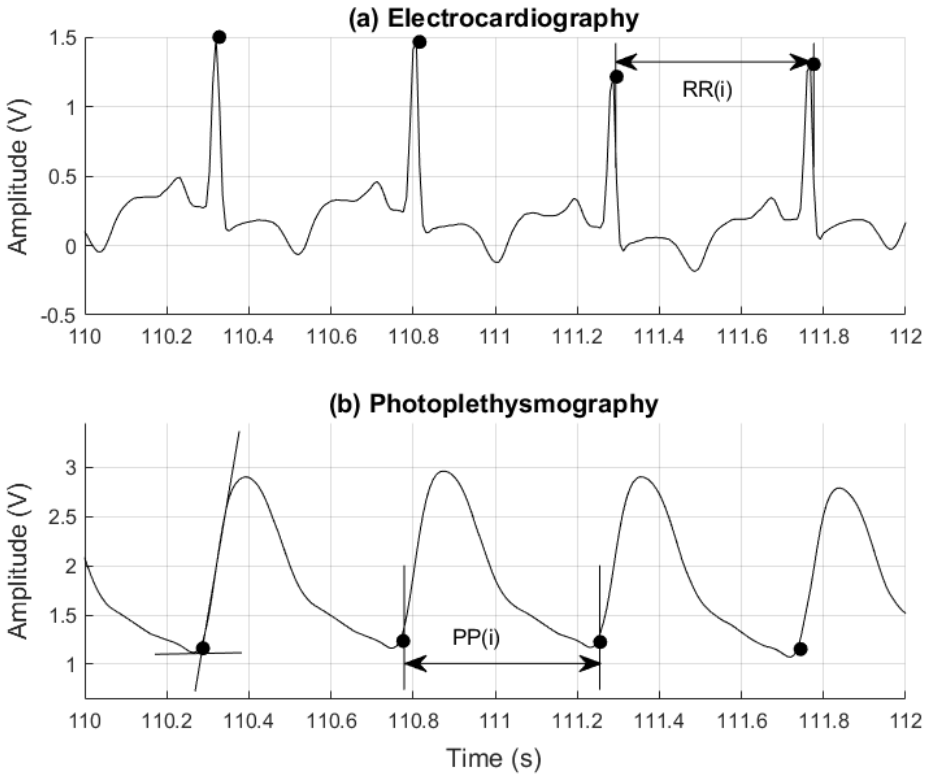

Figure 8.3: Example of (a) an electrocardiographic (ECG) and (b) a photoplethysmographic (PPG) signal. R peaks (black circles on the ECG signal) were detected from ECG signals to measure heart rate variability (HRV) as the time interval between consecutive R peaks (RR intervals). Onsets (black circles on the PPG signal) were detected from PPG signals to measure pulse rate variability (PRV) as the time interval between consecutive onsets (PP intervals).

Chapter 6. PRV was measured as the time difference, in milliseconds, between consecutive onsets from the PPG signal, as shown in Figure 8.3 (b). Similar to the method used for HRV trends, PRV was interpolated using a 4 Hz sampling rate and a cubic spline interpolation, and outliers were detected and corrected. Again, FFT was used to obtain the power spectrum.

8.2.2.4 Pulse rate and heart rate variability indices

Time- and frequency-domain, as well as non-linear indices extracted from Poincaré plot, entropy, phase, and detrended-fluctuation analyses were obtained. A short description of these indices is presented in Table 8.1. In addition to the classical indices extracted from time-domain, frequency-domain and Poincaré plot analysis, additional indices were obtained. From the spectral analysis, spectral analysis (SpEn) was extracted as a measure of the level of entropy in the frequency representation of HRV and PRV trends, while x- and y-coordinates from the centroids of each band of interest, i.e. LF, HF and TP, were obtained as an additional characterisation of these bands.

SpEn was computed as shown in (8.2), where N is the total number of points available in the frequency spectrum and $P(i)$ corresponds to the probability distribution of the power spectrum, calculated as in (8.3), where PS represents the power spectrum.

$$SpEn = \frac{\sum_{i=1}^{N} P(i) \log_2 P(i)}{\log_2 N} \tag{8.2}$$

$$P = \frac{PS}{\sum_i PS(i)} \tag{8.3}$$

The x- and y-coordinates of the centroid or centre of mass of the low- and high-frequency bands and the total spectrum were calculated as shown in (8.4) and (8.5), in which B refers to each of the bands (LF, HF or TP), f_1 is the lower frequency of each band, f_2 is the higher frequency of each band, P is the power of the frequency spectrum and f is the frequency value related to each power in the frequency spectrum.

$$cB_x = \frac{\sum_{i=f_1}^{f_2} f(i)P(i)}{\sum_{i=f_1}^{f_2} (P(i))} \tag{8.4}$$

$$cB_y = \frac{\sum_{i=f_1}^{f_2} \frac{1}{2} P(i)^2}{\sum_{i=f_1}^{f_2} (P(i))} \tag{8.5}$$

From the Poincaré plot representation of PRV and HRV trends, a novel index was proposed for the assessment of the compaction of these plots, as described in (8.6), where N refers to the number of points in the Poincaré plot, $\mathbf{X}_i$ refers to the i-th point, and $\mathbf{U}$ refers to the mean value of the ellipse. This index was inspired from measures of performance in clustering analysis, and determines the Euclidean distance between the points that form the ellipse and the mean value of the ellipse, assessing how close the points are. Further validation of this index is needed, but less compact ellipses are expected to be related to less varying PRV and HRV trends.

$$COM = \frac{\sum_{i=1}^{N} \|\mathbf{X}_i - \mathbf{U}\|}{N - 1} \tag{8.6}$$

Additional non-linear measures based on entropy, phase and detrended fluctuation analysis were extracted. Entropy-related indices were the basic-scale entropy (BSE), sign-series entropy (SSE), approximate entropy (ApEn), sample entropy (SampEn) and multi-scale entropy (MSE) with SampEn as base function. All these indices have been extracted previously from PRV or HRV trends to characterise their behaviour under specific conditions (Shaffer & Ginsberg 2017, Chou, Zhang, Feng, Lu, Lu & Xu 2017, Chou, Zhang & Yang 2017).

The basic scale entropy (BSE) was measured as proposed by Chou, Zhang, Feng, Lu, Lu & Xu (2017), using temporal sequence vectors of length $m = 2$ and a scaling factor of $\alpha = 0.2$. The measurement of BSE was done as follows: (1) A series of vectors of size m, denoted as temporal sequence vectors (TSV), are constructed from the PRV time series and the basic scales (BS) of these vectors was measured, as shown in (8.7); (2) TSVs are classified and symbolized according to their mean values and a scale BS, with a scale factor α; (3) the probability of each beat mode is computed and $BSE(m)$ is calculated as shown in (8.8), where π denotes the different possible sequences to be obtained.

$$BS(i) = \frac{\sum_{j=1}^{m-1} (IBI(i+j) - IBI(i+j-1))^2}{m-1} \tag{8.7}$$

$$BSE(m) = -\sum_{pi} p(\pi) \log_2 p(\pi) \tag{8.8}$$

Table 8.1: Indices extracted from pulse rate variability (PRV) and heart rate variability (HRV).

Indices		**Description, units of measurement**
Time domain	AVNN [1,2]	Average value of the normal-to-normal beats (NN), s
	SDNN [1,2]	Standard deviation of the NN, s
	RMSSD [1,2]	Root mean squared value of successive differences of NN, s
	NN50 [1,2]	Number of interval differences of successive NN intervals greater than 50 ms
	pNN50 [1,2]	Proportion of NN50 divided by the total number of NN intervals
Frequency domain	VLF [1,2]	Power of the power spectrum of interpolated PRV/HRV in the band between 0.0033 and 0.04 Hz, s^2
	LF [1,2]	Power of the power spectrum of interpolated PRV/HRV in the band between 0.04 and 0.15 Hz, s^2
	HF [1,2]	Power of the power spectrum of interpolated PRV/HRV in the band between 0.15 and 0.40 Hz, s^2
	TP [1,2]	Power of the power spectrum of interpolated PRV/HRV in the band between 0.0033 and 0.40 Hz, s^2
	nLF [1,2]	Normalized power of the LF band
	nHF [1,2]	Normalized power of the HF band
	LF/HF [1,2]	Ratio of the LF and HF bands
	$cLF_{x,y}$	X and Y coordinates of the centroid of the LF band, Hz
	$cHF_{x,y}$	X and Y coordinates of the centroid of the HF band, Hz
	$cTP_{x,y}$	X and Y coordinate of the centroid of the TP band, Hz

Continued on next page

Table 8.1 – continued from previous page

Indices		Description, units of measurement
	SpEn [3]	Spectral entropy of the power spectrum
Poincaré plot	S [4]	Area of the ellipse formed in the Poincaré plot, s^2
	SD1 [4]	Dispersion of the Poincaré plot points perpendicular to the line of identity, s
	SD2 [4]	Dispersion of the Poincaré plot points along the line of identity, s
	SD1/SD2 [4]	Ratio between SD1 and SD2
	COM	Normalized summation of the distances between each point of the Poincaré plot and its centroid
Entropy analysis	BSE [5]	Basic scale entropy of PRV/HRV trends
	SSE [6,7]	Sign-series entropy of PRV/HRV trends
	ApEn [3]	Approximate entropy of PRV/HRV trends
	SampEn [3]	Sample entropy of PRV/HRV trends
	MSE [3]	Multiscale entropy of PRV/HRV trends
Phase analysis	D2 [3]	Correlation dimension of PRV/HRV trends
	LYA [3]	Lyapunov exponent of PRV/HRV trends
Detrended fluctuation analysis	A1, A2 [8]	Short- and long-range scaling exponents, α_1 and α_2

[1] Task Force Guidelines (1996); [2] Shaffer & Ginsberg (2017); [3] Semmlow & Griffel (2014); [4] Khandoker et al. (2013);

[5] Chou, Zhang, Feng, Lu, Lu & Xu (2017); [6] Bian et al. (2009); [7] Chou, Zhang & Yang (2017); [8] Golińska (2012)

The sign-series entropy (SSE) of PRV was assessed as explained by Bian et al. (2009), using a number of modes of $m = 2$. In the case of SSE, the first step was to represent the inter-beat intervals according to their direction. Then, vectors of size m were created to analyse the changing rule of the signal, according to the representation obtained in the previous step. Then, the probability of each mode of variation was computed and the SSE is calculated using (8.9).

$$SSE(m) = -\sum_{j=1}^{M} p(j) \log_2 p(j) \tag{8.9}$$

Similarly, detrended-fluctuation analysis was used to obtain the short- (α_1) and long-range (α_2) scaling exponents of these trends, as has also been done previously (Shaffer & Ginsberg 2017), while phase analysis, i.e. Lyapunov exponents and correlation dimension analysis, have also been performed to further understand the non-linear behaviour of PRV and HRV trends, using analysis techniques explained by Semmlow & Griffel (2014). The main drawback from the extraction of these non-linear indices is the lack of standardisation for its assessment, and the difficulty in finding physiological explanations for their behaviour. Future studies, both in HRV and PRV, should aim to better determine the usefulness and interpretation of these indices.

8.2.3 Statistical analysis

All statistical analyses were performed in MATLAB® and R (version 3.6.1). A significance level of 5% (p-value < 0.05) was considered significant for all analyses, and the normality of data was assessed using a Lilliefors test. The aim of this study was to assess the differences between HRV and PRV indices extracted from critically ill subjects during hypo-, normo-, and hypertensive events. Hence, the level of the linear relationship between PRV and HRV indices was evaluated using Spearman correlation coefficients. The differences between HRV and PRV were also evaluated using Friedman rank sum tests, and the differences among BP states were assessed using Kruskal-Wallis tests, with pairwise Wilcoxon tests with Bonferroni correction as post hoc analyses. Moreover, because a good correlation does not imply good agreement, the agreement between HRV and PRV during each of the BP states was assessed using Bland-Altman analysis.

Table 8.2: Mean ± standard deviation of indices measured from pulse rate variability (PRV) and heart rate variability (HRV) under each blood pressure state. $*$ Values multiplied by 1×10^{-3}. $**$ Values divided by 1×10^{6}. $***$ Values divided by 1×10^{9}.

Indices	**Hypotension**		**Normotension**		**Hypertension**	
	PRV	**HRV**	**PRV**	**HRV**	**PRV**	**HRV**
AVNN $*$	826.4 ± 104.5	826.0 ± 104.5	755.7 ± 136.6	755.4 ± 136.5	836.9 ± 93.9	836.5 ± 93.7
SDNN $*$	10.8 ± 7.12	9.49 ± 7.12	14.4 ± 10.6	12.9 ± 10.5	16.3 ± 12.5	15.0 ± 12.7
RMSSD $*$	11.8 ± 5.48	8.66 ± 4.33	14.7 ± 8.12	10.5 ± 6.23	15.6 ± 8.84	11.9 ± 7.64
NN50	2.58 ± 9.18	1.37 ± 6.97	4.88 ± 12.7	2.03 ± 9.21	6.13 ± 13.5	2.93 ± 8.03
pNN50 $*$	6.25 ± 21.0	3.00 ± 14.1	12.7 ± 34.0	5.27 ± 24.9	16.9 ± 38.6	8.21 ± 23.2
VLF $***$	1.31 ± 3.11	1.30 ± 3.20	1.54 ± 3.10	1.60 ± 3.18	4.21 ± 9.14	4.29 ± 9.44
LF $***$	0.75 ± 1.30	0.68 ± 1.15	1.05 ± 2.10	0.98 ± 2.01	2.06 ± 4.13	1.97 ± 4.31
HF $***$	1.44 ± 3.09	1.09 ± 2.75	1.69 ± 2.89	1.23 ± 3.06	2.15 ± 3.99	1.69 ± 3.93
TP $***$	3.50 ± 5.81	3.07 ± 5.31	4.28 ± 7.43	3.82 ± 7.46	8.41 ± 15.1	7.95 ± 15.4
LF/HF	0.71 ± 0.39	0.95 ± 0.51	0.93 ± 0.82	1.55 ± 1.36	0.97 ± 0.74	1.26 ± 0.92
nLF	0.26 ± 0.10	0.28 ± 0.11	0.24 ± 0.10	0.26 ± 0.11	0.27 ± 0.11	0.28 ± 0.11
nHF	0.43 ± 0.17	0.36 ± 0.17	0.42 ± 0.22	0.34 ± 0.24	0.36 ± 0.17	0.30 ± 0.16
cLF_x	0.09 ± 0.01	0.09 ± 0.01	0.08 ± 0.01	0.08 ± 0.01	0.09 ± 0.01	0.08 ± 0.01
cHF_x	0.27 ± 0.01	0.27 ± 0.01	0.28 ± 0.02	0.27 ± 0.02	0.28 ± 0.02	0.27 ± 0.02

Continued on next page

Table 8.2 – continued from previous page

Indices	Hypotension		Normotension		Hypertension	
	PRV	**HRV**	**PRV**	**HRV**	**PRV**	**HRV**
cTP_x	0.15 ± 0.05	0.13 ± 0.05	0.14 ± 0.05	0.12 ± 0.06	0.13 ± 0.05	0.11 ± 0.05
cLF_y **	6.84 ± 11.8	6.26 ± 9.84	10.9 ± 22.3	10.4 ± 21.5	24.0 ± 69.5	24.6 ± 81.1
cHF_y **	8.15 ± 22.9	6.78 ± 23.0	15.4 ± 24.8	10.3 ± 19.5	9.23 ± 16.3	7.39 ± 16.6
cTP_y **	48.3 ± 201.7	50.5 ± 204.4	35.1 ± 61.7	36.1 ± 66.1	105.6 ± 273.1	110.2 ± 279.0
SpEn	24.5 ± 1.65	24.2 ± 1.95	23.9 ± 1.29	23.2 ± 1.60	23.8 ± 1.91	23.4 ± 2.14
S	0.06 ± 0.03	0.05 ± 0.02	0.07 ± 0.05	0.05 ± 0.04	0.08 ± 0.05	0.06 ± 0.04
SD1 *	8.32 ± 3.87	6.12 ± 3.06	10.4 ± 5.74	7.43 ± 4.41	11.1 ± 6.25	8.39 ± 5.40
SD2	2.34 ± 0.30	2.34 ± 0.30	2.14 ± 0.39	2.14 ± 0.30	2.37 ± 0.27	2.37 ± 0.27
SD1/SD2 *	3.65 ± 2.00	2.70 ± 1.71	4.86 ± 2.51	3.48 ± 1.90	4.73 ± 2.71	3.59 ± 2.31
COM *	0.34 ± 0.60	0.28 ± 0.58	0.64 ± 1.21	0.55 ± 1.14	0.84 ± 1.61	0.76 ± 1.59
BSE	5.65 ± 0.29	5.29 ± 0.45	5.68 ± 0.23	5.31 ± 0.40	5.71 ± 0.23	5.45 ± 0.36
SSE	2.69 ± 0.17	2.78 ± 0.12	2.66 ± 0.21	2.80 ± 0.14	2.63 ± 0.18	2.75 ± 0.15
ApEn	0.43 ± 0.13	0.40 ± 0.17	0.42 ± 0.12	0.36 ± 0.16	0.42 ± 0.13	0.38 ± 0.16
SampEn	0.45 ± 0.20	0.43 ± 0.25	0.40 ± 0.16	0.34 ± 0.19	0.42 ± 0.20	0.39 ± 0.23
MSE	4.99 ± 1.95	4.47 ± 2.16	4.63 ± 1.93	4.20 ± 1.88	4.86 ± 1.92	4.48 ± 1.98

Continued on next page

Table 8.2 – continued from previous page

Indices	Hypotension		Normotension		Hypertension	
	PRV	**HRV**	**PRV**	**HRV**	**PRV**	**HRV**
D2	-0.54 ± 33.2	-0.98 ± 19.6	-1.12 ± 31.7	-0.34 ± 8.56	-1.19 ± 33.2	-1.31 ± 20.1
LYA	3.27 ± 1.10	3.03 ± 1.04	3.52 ± 1.18	3.13 ± 1.08	3.54 ± 1.12	3.34 ± 1.14
A1	0.67 ± 0.39	0.77 ± 0.65	0.68 ± 0.18	0.80 ± 0.25	0.74 ± 0.21	0.84 ± 0.25
A2	0.87 ± 0.25	0.91 ± 0.27	0.90 ± 0.24	0.94 ± 0.23	0.88 ± 0.23	0.91 ± 0.24

From the Bland-Altman plots, the bias and difference between limits of agreement (LoAs) were obtained, and the ratio of agreement (BAR), as described in Chapter 7, was measured using (7.1) and (7.2). Agreement values were categorised as good (BAR $\leq$ 10%), moderate (10% $<$ BAR $\leq$ 20%), or insufficient (BAR $>$ 20%).

8.3 Results

8.3.1 Signal selection and segmentation

The dataset was filtered according to the length of the recordings and the quality of the ABP signals for each patient. In total, 230 records with poor-quality ABP signals and a short duration were discarded. The signals from the remaining 270 records were used in the subsequent analysis. From these signals, 4937 5 min segments were extracted, of which 54% were labelled as hypertensive, 25% were labelled as hypotensive, and the remaining 22% were labelled as normotensive events. Table 8.2 summarises the behaviour of PRV and HRV indices extracted from signals labelled as hypotension, normotension, and hypertension.

8.3.2 Correlation between PRV and HRV indices

The results from the analysis of the correlation between PRV and HRV indices are summarised in Figure 8.4. Most of the indices showed a good correlation between HRV and PRV during all three BP states, although some of the indices tended to show a lower correlation during normotension. Interestingly, the entropy- and phase derived indices had lower correlations. In addition, lower correlation coefficients were observed for indices associated with short-term changes, such as RMSSD, SD1, HF, and A1.

8.3.3 Comparison between HRV and PRV using the Friedman rank sum test

Because most of the data obtained from the different indices were non-normally distributed and did not comply with the assumption of homogeneity of variances, Friedman rank sum tests were used as a non-parametric alternative to repeated measures ANOVA. The results from these tests for the comparison between HRV

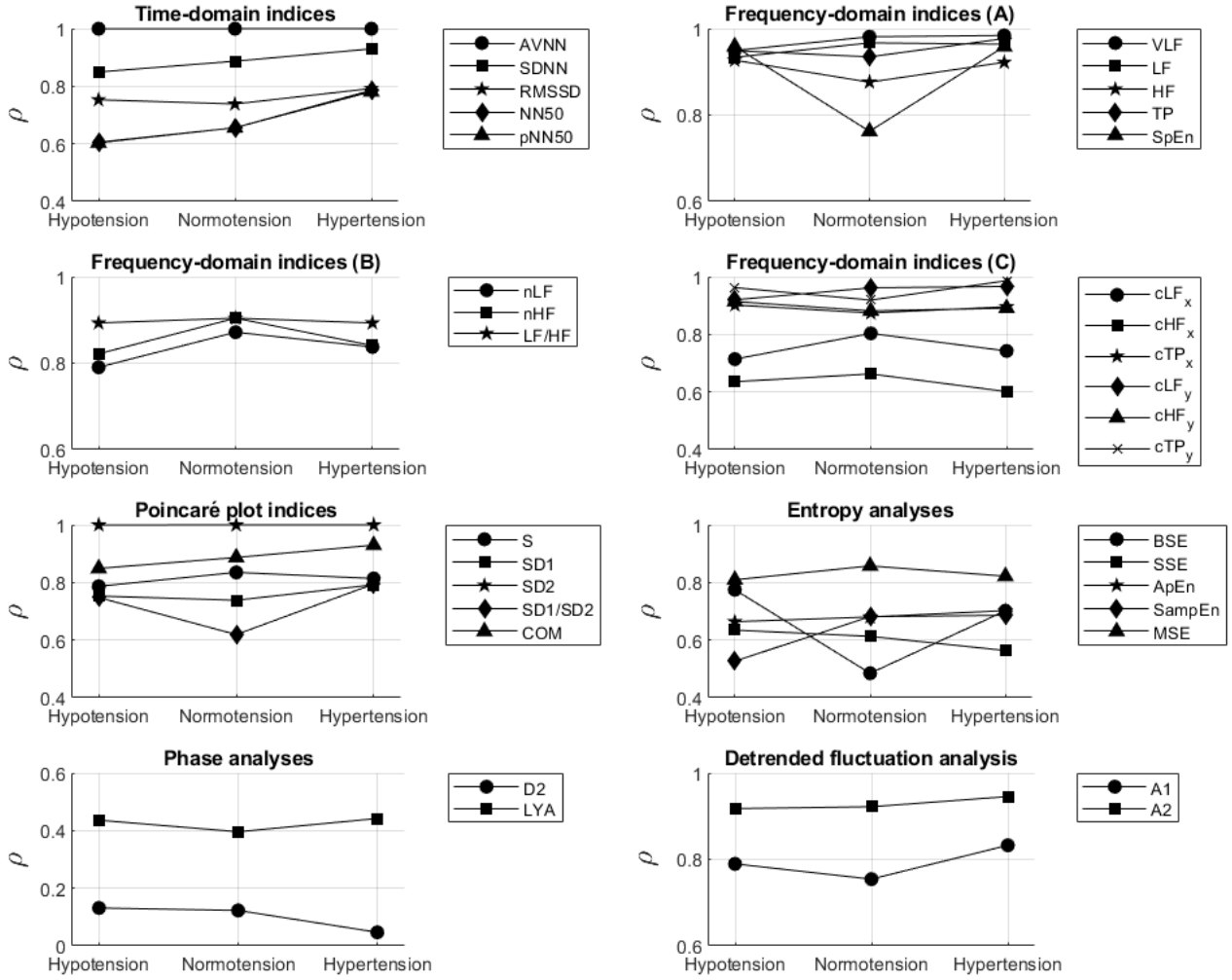

Figure 8.4: Spearman correlation coefficients (ρ) between indices obtained from pulse rate variability and heart rate variability in each blood pressure state. Most indices showed good correlation regardless of blood pressure state, although some, such as SpEn and BSE, showed lower correlations during normotension.

and PRV are shown in Table 8.3. For most indices, there were significant differences (p-value < 0.001) between HRV and PRV, regardless of the BP state. Only VLF and cTPy showed non-significant differences between the two measurement sources during normotension.

8.3.4 Comparison between blood pressure states using Kruskal-Wallis tests

Kruskal-Wallis tests, a non-parametric alternative to one-way ANOVA, were used to compare indices among BP states when measured using PRV or HRV. Pairwise

Table 8.3: Friedman rank sum tests results for the comparison between pulse rate variability and heart rate variability in the different blood pressure states.

Indices	**Friedman rank sum test p-values**		
	Hypotension	**Normotension**	**Hypertension**
AVNN	9.48×10^{-14} ⋆	6.24×10^{-10} ⋆	1.53×10^{-21} ⋆
SDNN	3.32×10^{-72} ⋆	2.01×10^{-50} ⋆	9.98×10^{-169} ⋆
RMSSD	1.21×10^{-181} ⋆	1.40×10^{-158} ⋆	0.00 ⋆
NN50	7.25×10^{-22} ⋆	2.30×10^{-50} ⋆	1.01×10^{-134} ⋆
pNN50	1.23×10^{-22} ⋆	5.56×10^{-52} ⋆	8.87×10^{-137} ⋆
VLF	2.48×10^{-3} †	4.83×10^{-1}	2.42×10^{-9} ⋆
LF	3.78×10^{-34} ⋆	3.27×10^{-46} ⋆	8.82×10^{-89} ⋆
HF	7.96×10^{-180} ⋆	4.73×10^{-160} ⋆	0.00 ⋆
TP	1.86×10^{-79} ⋆	7.94×10^{-73} ⋆	1.00×10^{-159} ⋆
nLF	4.39×10^{-17} ⋆	6.89×10^{-19} ⋆	5.16×10^{-16} ⋆
nHF	1.12×10^{-136} ⋆	1.07×10^{-151} ⋆	3.10×10^{-236} ⋆
LF/HF	3.62×10^{-109} ⋆	1.31×10^{-129} ⋆	4.12×10^{-189} ⋆
cLF_x	3.05×10^{-14} ⋆	6.61×10^{-24} ⋆	2.49×10^{-66} ⋆
cHF_x	4.05×10^{-22} ⋆	1.44×10^{-30} ⋆	6.27×10^{-66} ⋆
cTP_x	5.12×10^{-134} ⋆	8.87×10^{-163} ⋆	4.34×10^{-250} ⋆
cLF_y	1.17×10^{-19} ⋆	8.72×10^{-24} ⋆	3.47×10^{-34} ⋆
cHF_y	1.13×10^{-142} ⋆	7.43×10^{-136} ⋆	1.33×10^{-242} ⋆
cTP_y	1.40×10^{-7} ⋆	4.31×10^{-1}	1.61×10^{-9} ⋆
SpEn	5.09×10^{-56} ⋆	1.32×10^{-90} ⋆	1.74×10^{-172} ⋆
S	4.08×10^{-183} ⋆	5.69×10^{-161} ⋆	0.00 ⋆
SD1	1.21×10^{-181} ⋆	1.40×10^{-158} ⋆	0.00 ⋆
SD2	8.76×10^{-14} ⋆	5.67×10^{-10} ⋆	1.42×10^{-21} ⋆
SD1/SD2	1.69×10^{-179} ⋆	3.20×10^{-156} ⋆	0.00 ⋆
COM	2.75×10^{-73} ⋆	2.70×10^{-50} ⋆	1.56×10^{-169} ⋆
BSE	1.35×10^{-262} ⋆	1.58×10^{-230} ⋆	0.00 ⋆
SSE	2.22×10^{-77} ⋆	7.27×10^{-114} ⋆	1.34×10^{-251} ⋆
ApEn	2.58×10^{-21} ⋆	8.74×10^{-57} ⋆	4.37×10^{-83} ⋆
SampEn	2.44×10^{-19} ⋆	8.46×10^{-56} ⋆	4.03×10^{-88} ⋆
MSE	3.63×10^{-30} ⋆	2.21×10^{-29} ⋆	9.07×10^{-30} ⋆
D2	1.09×10^{-11} ⋆	3.28×10^{-22} ⋆	1.00×10^{-14} ⋆
LYA	1.18×10^{-12} ⋆	7.83×10^{-18} ⋆	5.71×10^{-16} ⋆
A1	1.71×10^{-102} ⋆	1.04×10^{-101} ⋆	8.73×10^{-215} ⋆
A2	5.62×10^{-25} ⋆	2.89×10^{-29} ⋆	1.45×10^{-34} ⋆

‡: p-value less than 5.00×10^{-2}; †: p-value less than 5.00×10^{-3}; ⋆: p-value less than 5.00×10^{-4}.

Wilcoxon tests were used as post hoc analyses when the Kruskal-Wallis results indicated significant differences. The results are shown in Table 8.4 and Table 8.5. There were statistically significant differences among BP states from all indices, except for cHF_x measured using HRV. The pairwise comparisons revealed that most of the indices showed differences among the three stages, especially when measured using PRV.

Table 8.4: Kruskal-Wallis and post-hoc multiple comparisons p-values for the comparison among blood pressure states from indices measured from pulse rate variability.

Indices	**KW**[a]	**Multiple comparisons**		
		PW1[b]	**PW2**[c]	**PW3**[d]
AVNN	2.1×10^{-60} ⋆	7.5×10^{-36} ⋆	6.3×10^{-1}	3.8×10^{-59} ⋆
SDNN	9.8×10^{-57} ⋆	1.0×10^{-25} ⋆	1.8×10^{-55} ⋆	1.9×10^{-4} ⋆
RMSSD	1.1×10^{-53} ⋆	2.8×10^{-20} ⋆	1.4×10^{-55} ⋆	1.6×10^{-3} †
NN50	8.5×10^{-43} ⋆	1.7×10^{-6} ⋆	6.6×10^{-41} ⋆	8.7×10^{-12} ⋆
pNN50	1.5×10^{-43} ⋆	1.3×10^{-6} ⋆	1.4×10^{-41} ⋆	5.6×10^{-12} ⋆
VLF	2.7×10^{-70} ⋆	1.5×10^{-14} ⋆	7.6×10^{-64} ⋆	3.5×10^{-21} ⋆
LF	5.1×10^{-75} ⋆	2.5×10^{-4} ⋆	1.1×10^{-66} ⋆	2.1×10^{-30} ⋆
HF	9.2×10^{-32} ⋆	1.6×10^{-8} ⋆	1.3×10^{-33} ⋆	2.8×10^{-4} ⋆
TP	1.3×10^{-62} ⋆	2.5×10^{-11} ⋆	1.6×10^{-57} ⋆	2.9×10^{-19} ⋆
nLF	4.7×10^{-5} ⋆	2.7×10^{-4} ⋆	7.4×10^{-1}	2.3×10^{-4} ⋆
nHF	4.2×10^{-29} ⋆	6.1×10^{-3} ‡	1.9×10^{-29} †	1.5×10^{-8} †
LF/HF	4.8×10^{-20} ⋆	6.2×10^{-1}	5.0×10^{-19} ⋆	2.8×10^{-8} ⋆
cLF_x	8.8×10^{-12} ⋆	5.5×10^{-12} ⋆	2.1×10^{-4} ⋆	1.8×10^{-5} ⋆
cHF_x	1.6×10^{-7} ⋆	3.5×10^{-5} ⋆	4.6×10^{-7} ⋆	6.9×10^{-1}
cTP_x	2.0×10^{-21} ⋆	1.2×10^{-2} ‡	3.1×10^{-21} ⋆	7.8×10^{-7} ⋆
cLF_y	3.2×10^{-73} ⋆	1.3×10^{-6} ⋆	4.4×10^{-67} ⋆	3.1×10^{-26} ⋆
cHF_y	1.3×10^{-40} ⋆	3.0×10^{-29} ⋆	3.8×10^{-31} ⋆	1.6×10^{-6} ⋆
cTP_y	1.1×10^{-56} ⋆	2.5×10^{-43} ⋆	2.5×10^{-48} ⋆	2.3×10^{-1}
SpEn	2.5×10^{-40} ⋆	4.2×10^{-39} ⋆	5.8×10^{-28} ⋆	8.3×10^{-3} ‡
S	1.3×10^{-49} ⋆	2.3×10^{-6} ⋆	8.6×10^{-51} ⋆	6.8×10^{-12} ⋆
SD1	1.1×10^{-53} ⋆	2.8×10^{-20} ⋆	1.4×10^{-55} ⋆	1.6×10^{-3} †
SD2	2.0×10^{-60} ⋆	7.9×10^{-36} ⋆	6.2×10^{-1}	3.6×10^{-59} ⋆
SD1/SD2	1.2×10^{-64} ⋆	4.9×10^{-53} ⋆	2.8×10^{-51} ⋆	2.3×10^{-2} ‡
COM	1.1×10^{-56} ⋆	8.8×10^{-26} ⋆	2.1×10^{-55} ⋆	2.0×10^{-4} ⋆
BSE	1.4×10^{-7} ⋆	9.5×10^{-1}	2.5×10^{-6} ⋆	1.7×10^{-4} ⋆
SSE	7.1×10^{-24} ⋆	4.4×10^{-2} ‡	2.2×10^{-23} ⋆	3.0×10^{-8} ⋆
ApEn	1.1×10^{-6} ⋆	1.2×10^{-5} ⋆	9.5×10^{-6} ⋆	1.0
SampEn	8.2×10^{-10} ⋆	9.2×10^{-11} ⋆	1.4×10^{-5} ⋆	2.8×10^{-2} ‡
MSE	1.1×10^{-5} ⋆	6.0×10^{-6} ⋆	1.2×10^{-2} ‡	1.5×10^{-2} ‡
D2	5.7×10^{-3} ‡	4.0×10^{-1}	3.5×10^{-3} †	7.0×10^{-1}
LYA	2.9×10^{-14} ⋆	6.9×10^{-8} ⋆	2.3×10^{-14} ⋆	1.0
A1	1.3×10^{-37} ⋆	3.7×10^{-2} ‡	3.8×10^{-33} ⋆	1.7×10^{-16} ⋆
A2	2.4×10^{-2} ‡	1.8×10^{-2} ‡	3.9×10^{-1}	2.8×10^{-1}

[a] Kruskal-Wallis test results. [b] Pairwise comparisons (PW) between hypotension and normotension. [c] PW between hypotension and hypertension. [d] PW between normotension and hypertension.
‡: p-value less than 5.00×10^{-2}; †: p-value less than 5.00×10^{-3}; ⋆: p-value less than 5.00×10^{-4}.

8.3.5 Bland-Altman analysis to assess agreement

Because neither correlation analyses nor ANOVA could be used to evaluate the agreement between HRV and PRV measurements, Bland-Altman analyses were performed

Table 8.5: Kruskal-Wallis and post-hoc multiple comparisons p-values for the comparison among blood pressure states from indices measured from heart rate variability.

Indices	**KW**[a]	**Multiple comparisons**		
		PW1[b]	**PW2**[c]	**PW3**[d]
AVNN	3.8×10^{-61} ⋆	3.5×10^{-36} ⋆	6.4×10^{-1}	6.1×10^{-60} ⋆
SDNN	4.0×10^{-53} ⋆	4.8×10^{-26} ⋆	6.1×10^{-51} ⋆	3.2×10^{-4} ⋆
RMSSD	2.6×10^{-63} ⋆	4.0×10^{-15} ⋆	2.2×10^{-63} ⋆	1.3×10^{-11} ⋆
NN50	5.8×10^{-46} ⋆	5.3×10^{-2}	2.9×10^{-36} ⋆	8.0×10^{-21} ⋆
pNN50	5.7×10^{-46} ⋆	5.1×10^{-2}	2.5×10^{-36} ⋆	9.4×10^{-21} ⋆
VLF	4.2×10^{-68} ⋆	3.8×10^{-19} ⋆	3.1×10^{-63} ⋆	4.2×10^{-16} ⋆
LF	3.0×10^{-64} ⋆	2.2×10^{-4} ⋆	1.7×10^{-57} ⋆	1.6×10^{-25} ⋆
HF	3.8×10^{-30} ⋆	1.1×10^{-1}	1.8×10^{-26} ⋆	1.2×10^{-13} ⋆
TP	5.6×10^{-57} ⋆	5.0×10^{-9} ⋆	1.3×10^{-51} ⋆	2.8×10^{-19} ⋆
nLF	7.1×10^{-7} ⋆	1.2×10^{-6} ⋆	2.4×10^{-3} †	4.4×10^{-3} †
nHF	1.4×10^{-20} ⋆	3.9×10^{-9} ⋆	3.1×10^{-22} ⋆	1.0
LF/HF	1.5×10^{-17} ⋆	3.3×10^{-11} ⋆	2.0×10^{-16} ⋆	2.7×10^{-1}
cLF_x	7.6×10^{-17} ⋆	6.9×10^{-15} ⋆	5.8×10^{-11} ⋆	7.9×10^{-4} †
cHF_x	5.5×10^{-1}	-	-	-
cTP_x	3.2×10^{-17} ⋆	2.4×10^{-8} ⋆	4.1×10^{-18} ⋆	1.0
cLF_y	1.3×10^{-65} ⋆	8.3×10^{-7} ⋆	5.9×10^{-61} ⋆	2.5×10^{-22} ⋆
cHF_y	8.9×10^{-20} ⋆	8.2×10^{-8} ⋆	1.1×10^{-21} ⋆	8.9×10^{-1}
cTP_y	2.0×10^{-55} ⋆	1.2×10^{-46} ⋆	2.9×10^{-45} ⋆	3.7×10^{-1}
SpEn	9.8×10^{-48} ⋆	1.4×10^{-48} ⋆	3.9×10^{-25} ⋆	6.5×10^{-10} ⋆
S	5.7×10^{-59} ⋆	6.3×10^{-2}	2.4×10^{-50} ⋆	2.4×10^{-27} ⋆
SD1	2.6×10^{-63} ⋆	4.0×10^{-15} ⋆	2.2×10^{-63} ⋆	1.3×10^{-11} ⋆
SD2	3.7×10^{-61} ⋆	3.8×10^{-36} ⋆	6.3×10^{-1}	5.9×10^{-60} ⋆
SD1/SD2	3.1×10^{-71} ⋆	6.4×10^{-61} ⋆	2.1×10^{-56} ⋆	4.7×10^{-1}
COM	2.7×10^{-53} ⋆	2.7×10^{-26} ⋆	4.6×10^{-51} ⋆	3.6×10^{-4} ⋆
BSE	8.6×10^{-34} ⋆	1.0	6.3×10^{-24} ⋆	1.0×10^{-21} ⋆
SSE	1.9×10^{-23} ⋆	9.7×10^{-4} †	3.7×10^{-10} ⋆	1.9×10^{-20} ⋆
ApEn	4.2×10^{-10} ⋆	1.9×10^{-10} ⋆	7.1×10^{-6} ⋆	1.5×10^{-2} ‡
SampEn	4.7×10^{-16} ⋆	3.4×10^{-17} ⋆	1.7×10^{-7} ⋆	6.6×10^{-5} ⋆
MSE	1.5×10^{-4} ⋆	1.2×10^{-3} †	1.0	2.3×10^{-4} ⋆
D2	1.2×10^{-7} ⋆	4.2×10^{-2} ‡	2.8×10^{-3} †	5.5×10^{-7} ⋆
LYA	3.3×10^{-24} ⋆	3.3×10^{-3} †	1.4×10^{-22} ⋆	7.8×10^{-9} ⋆
A1	4.8×10^{-30} ⋆	3.0×10^{-6} ⋆	7.0×10^{-32} ⋆	3.2×10^{-5} ⋆
A2	2.4×10^{-2} ‡	1.1×10^{-1}	1.0	2.3×10^{-2} ‡

[a] Kruskal-Wallis test results. [b] Pairwise comparisons (PW) between hypotension and normotension. [c] PW between hypotension and hypertension. [d] PW between normotension and hypertension.
‡: p-value less than 5.00×10^{-2}; †: p-value less than 5.00×10^{-3}; ⋆: p-value less than 5.00×10^{-4}.

for each extracted index. Bias and limits of agreement (LoAs) were measured, and the results are summarised in Figure 8.5 and Figure 8.6.

As shown in Figure 8.5, most of the indices were overestimated when measured from PRV. Some others were underestimated, such as nLF, nHF, LF/HF, SSE, D2,

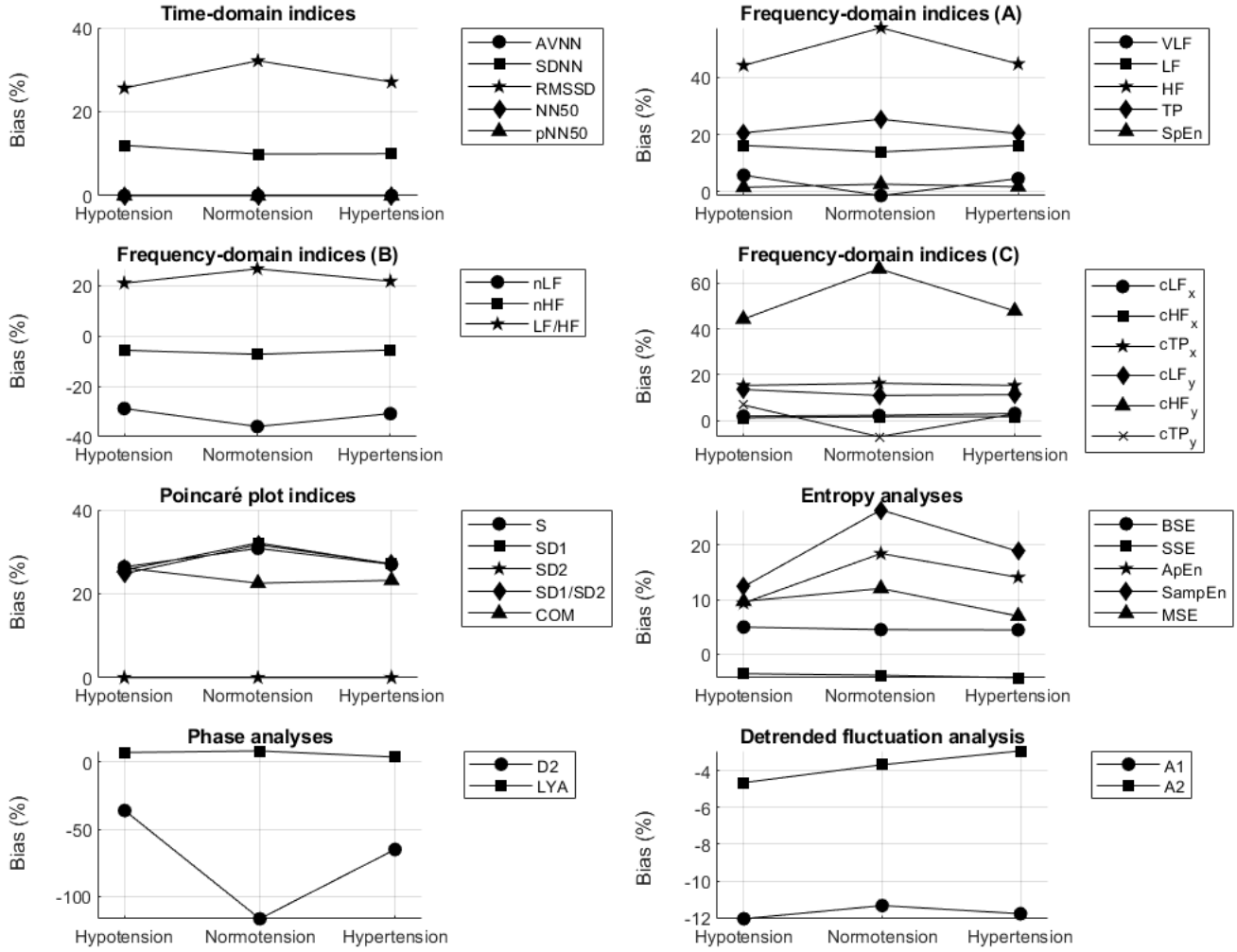

Figure 8.5: Bias between indices obtained from pulse rate variability and heart rate variability in each blood pressure state. Pulse rate variability tends to overestimate most indices, while the differences between these variables is more notorious during normotension.

A1, and A2. Indices associated with short-term changes were especially overestimated when measured from PRV. Although a general conclusion is difficult to be achieved, for most of the indices the bias differed according to the blood pressure state. Interestingly, most indices showed a larger absolute bias during normotension. A similar trend was observed in the differences between the upper and lower LoAs, with large differences especially in indices associated with short-term changes. The largest differences were observed for D2, SampEn, and most of the frequency-domain indices. NN50 and pNN50 showed a bias and difference between LoAs of zero, which shows very good agreement between HRV and PRV.

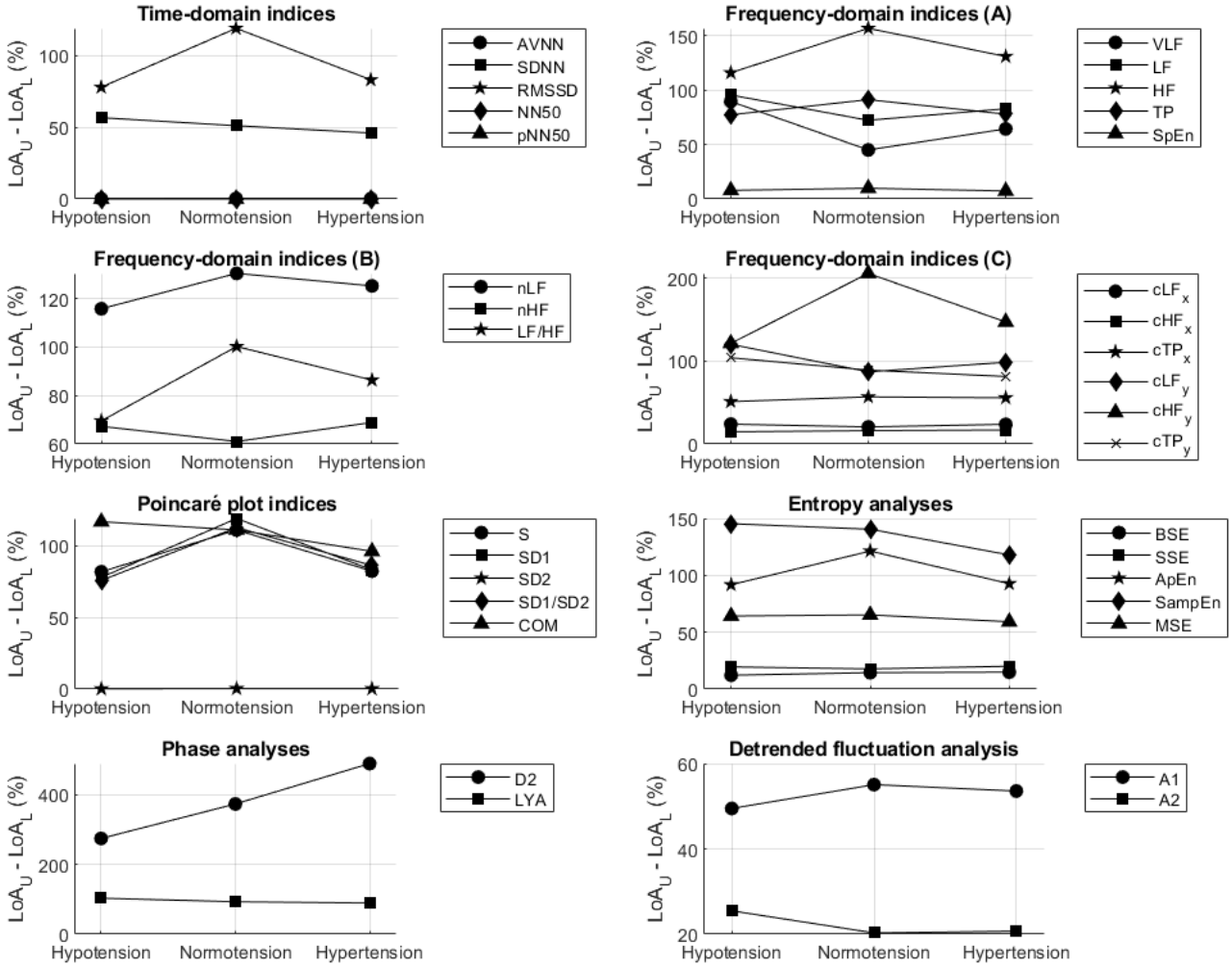

Figure 8.6: Differences between upper (LoA_U) and lower (LoA_L) limits of agreement obtained from Bland-Altman analysis comparing indices measured from pulse rate variability and heart rate variability in each blood pressure state. Most indices related to short-term changes showed insufficient agreement, and the state of agreement was generally not affected by blood pressure.

The BAR results are shown in Table 8.6. For NN50 and pNN50, the bias and difference between LoAs were equal to zero for all conditions, and thus, the ratio was not measured because the agreement was total. The agreement tended to remain as good, moderate, or insufficient regardless of the blood pressure state. Most of the indices that showed insufficient agreement are associated with short-term changes.

Table 8.6: Ratio of agreement (BAR, %) derived from Bland-Altman analysis

Indices	Hypotension	Normotension	Hypertension
AVNN	3.92×10^{-1} ↑	5.01×10^{-1} ↑	4.43×10^{-1} ↑
SDNN	2.64×10^{3} ↓	1.81×10^{3} ↓	1.57×10^{3} ↓
RMSSD	5.12×10^{3} ↓	5.31×10^{3} ↓	4.29×10^{3} ↓
NN50	0.00 ↑	0.00 ↑	0.00 ↑
pNN50	0.00 ↑	0.00 ↑	0.00 ↑
VLF	2.27×10^{-7} ↑	5.01×10^{-8} ↑	7.81×10^{-8} ↑
LF	6.29×10^{-7} ↑	4.99×10^{-7} ↑	3.71×10^{-7} ↑
HF	1.36×10^{-6} ↑	1.33×10^{-6} ↑	9.33×10^{-7} ↑
TP	2.23×10^{-7} ↑	2.27×10^{-7} ↑	1.16×10^{-7} ↑
nLF	7.41×10^{1} ↓	6.44×10^{1} ↓	6.65×10^{1} ↓
nHF	4.47×10^{1} ↓	6.03×10^{1} ↓	4.53×10^{1} ↓
LF/HF	1.05×10^{2} ↓	1.37×10^{2} ↓	1.26×10^{2} ↓
cLF_x	3.07×10^{1} ↓	3.96×10^{1} ↓	5.81×10^{1} ↓
cHF_x	3.49 ↑	7.39 ↑	7.86 ↑
cTP_x	2.14×10^{2} ↓	2.41×10^{2} ↓	2.40×10^{2} ↓
cLF_y	6.08×10^{-5} ↑	4.00×10^{-5} ↑	2.63×10^{-5} ↑
cHF_y	3.36×10^{-4} ↑	2.45×10^{-4} ↑	2.43×10^{-4} ↑
cTP_y	1.70×10^{-5} ↑	8.54×10^{-6} ↑	2.83×10^{-6} ↑
SpEn	7.04×10^{-2} ↑	1.72×10^{-1} ↑	8.91×10^{-2} ↑
S	1.00×10^{3} ↓	1.01×10^{3} ↓	8.08×10^{2} ↓
SD1	7.24×10^{3} ↓	7.51×10^{3} ↓	6.07×10^{3} ↓
SD2	1.39×10^{-1} ↑	1.77×10^{-1} ↑	1.56×10^{-1} ↑
SD1/SD2	1.66×10^{4} ↓	1.61×10^{4} ↓	1.46×10^{4} ↓
COM	3.36×10^{5} ↓	2.27×10^{5} ↓	1.66×10^{5} ↓
BSE	1.58 ↑	1.41 ↑	1.37 ↑
SSE	2.90 ↑	3.12 ↑	3.49 ↑
ApEn	4.09×10^{1} ↓	9.03×10^{1} ↓	6.70×10^{1} ↓
SampEn	5.28×10^{1} ↓	1.39×10^{2} ↓	8.97×10^{1} ↓
MSE	3.80 ↑	5.14 ↑	2.71 ↑
D2	3.33×10^{2} ↓	1.17×10^{3} ↓	9.49×10^{2} ↓
LYA	4.15 ↑	4.58 ↑	1.85 ↑
A1	3.58×10^{1} ↓	3.17×10^{1} ↓	3.10×10^{1} ↓
A2	1.13×10^{1} ↔	9.12 ↑	7.47 ↑

Good agreement (↑): BAR $< 10\%$; moderate agreeement (↔): $10\% \leq$ BAR $< 20\%$; insufficient agreement (↓): BAR $\geq 20\%$.

8.4 Discussion

HRV has been proposed as a useful, non-invasive, indirect measurement of the cardiac autonomic nervous system. It has been used for several decades as an indicator of parasympathetic and sympathetic activity (Clifford 2006), and it has been studied as a biomarker for a broad range of diseases. However, it has been found that the measurement of HRV in real-life scenarios can be impaired by several conditions,

especially because of the cumbersome instrumentation needed for the acquisition of the ECG signals, which has, to some extent, precluded the usefulness and acceptance of HRV as a tool for clinicians to diagnose and monitor diseases, and for larger public health applications (Karmali et al. 2017). Hence, several researchers have started to investigate the possibility of replacing HRV information with a very similar signal, PRV, which is based on pulse waves that are easier to obtain and more ubiquitous, such as PPG signals (Georgiou et al. 2018, Kyriacou 2021). Nonetheless, and as was largely discussed in Chapter 5, the promise of PRV as a valid surrogate for HRV has been questioned, and some studies have concluded that, although they are very similar, PRV and HRV are not exactly the same and that PRV may not be a suitable surrogate for HRV, especially when measured in disease states and in older subjects (Schäfer & Vagedes 2013).

Various explanations for the differences between HRV and PRV have been given. Some authors argue that the differences are mainly due to processing issues, such as the identification of fiducial points from the PPG signal (Hemon & Phillips 2016, Pinheiro et al. 2016), the sampling rate used for the acquisition of the signals (Béres et al. 2019, Béres & Hejjel 2021), and the processing techniques used for the analysis of PRV (Akar et al. 2013). A profound analysis regarding the effects of these technical aspects on PRV is presented in Chapter 6. However, other authors have suggested that, although these factors may affect PRV, physiological issues may have a more profound effect on the differences between these two signals (Schäfer & Vagedes 2013, Yuda, Shibata, Ogata, Ueda, Yambe, Yoshizawa & Hayano 2020). The relationship between HRV and PRV may be affected by not only PTT but also other factors, such as external forces on the arterial vessels (Trajkovic et al. 2011), the presence of pathologies, including cardiovascular disorders (Parasnis et al. 2015, Shi et al. 2009), and the body location at which PRV is being measured (Heathers 2013, Yuda, Yamamoto, Yoshida & Hayano 2020). An important contributor to these differences is respiratory activity, which affects vasoconstriction and modulates aortic and left-ventricular pressure, altering the time of opening of the aortic valve during the cardiac cycle (Khoo & Chalacheva 2019). Nonetheless, several processes take part in the information transmission from the pure electrical ECG and the R waves to the mechanical PPG pulse wave, as is explained in (Yuda, Shibata, Ogata, Ueda, Yambe, Yoshizawa & Hayano 2020). These factors may also explain in part the differences observed between HRV and PRV, especially under non-resting

conditions and in non-healthy, older subjects. Hence, PRV should not be considered a surrogate of HRV, but should be treated as an independent biomarker instead, which may contain additional information not available in HRV (Yuda, Shibata, Ogata, Ueda, Yambe, Yoshizawa & Hayano 2020).

Thus, because of the differences observed in previous studies between HRV and PRV, the aim of this study was to assess the relationship between these two signals in critically ill subjects hospitalised in intensive care units. Because these subjects exhibited changes in blood pressure, PRV and HRV were also compared when the subjects experienced normotension or hyper- and hypotensive events.

8.4.1 Selection of signals using Signal Quality Indices

Good quality ABP signals were selected for the reliable labelling and extraction of blood pressure information. This was done merging several signal quality indices (SQI's) proposed in the literature for the assessment of signal quality in pulse waves. These indices are capable of identifying low-quality segments of a pulse wave by themselves according to different criteria, but merging them and establishing proper thresholds to identify the good and poor quality signals is not an easy task (Orphanidou 2018). Therefore, the use of machine learning techniques has been applied in different studies for automatically setting these thresholds and grouping the data, with varying success (Li & Clifford 2012, Pereira et al. 2020). The methodology proposed in this study, which employs a largely used clustering algorithm, the k-Means, has one important advantage: It does not require prior labels regarding the quality of the signal, and is very simple to apply. Nonetheless, as is usual with this clustering technique, it depends on the presence of outliers, on the initialisation parameters of the algorithm, and on the embedded structure of the data. Therefore, its applicability and suitability should be evaluated for each application. Future studies should aim to validate and optimise this algorithm for multiple applications, and to evaluate the behaviour of other clustering algorithms for the identification of poor-quality PPG signals.

8.4.2 Linear correlation between PRV and HRV

Among the time-domain indices, an almost perfect correlation was observed between HRV and PRV for AVNN, regardless of BP state. For SDNN, NN50, and pNN50, higher correlations were observed as BP increased, but pNN50 had the lowest corre-

lation of the time-domain indices in all BP states. RMSSD, which reflects short-term changes in HRV and PRV (Shaffer & Ginsberg 2017), had a lower correlation, with a correlation coefficient below 0.8, during normotension.

The frequency-domain indices exhibited different trends. Absolute indices (VLF, LF, HF, and TP) and the ratio between LF and HF (LF/HF) had stable and high correlations. For normalised indices, on the other hand, there were differences according to the BP state, with better correlations during normotension. Spectral entropy (SpEn) exhibited a behaviour similar to that observed for RMSSD. Indices related to the centroid of the frequency bands in the y-coordinate were relatively stable, while the x-coordinate of the centroids featured the worst correlations, especially for the x-coordinate of the HF band centroid.

The correlations for the non-linear indices were, in general, worse than those for the time- and frequency-domain indices. This was especially true for the phase-related indices, the correlation dimension and the Lyapunov exponent. Among the Poincaré plot indices, SD2 had a nearly perfect correlation between HRV and PRV, while SD1/SD2 and SD1 exhibited behaviors similar to that of RMSSD. The correlations for the entropy-related indices were also relatively poor. The correlation for the BSE values was strongly affected by normotension, and although SampEn, ApEn, and SSE were stable regardless of the BP state, their correlation coefficients were low. Finally, A1 and A2 from the detrended fluctuation analysis behaved similarly to SD1 and SD2, respectively, probably because of the differences between the short- and long-term changes in HRV and PRV.

8.4.3 Comparison between PRV and HRV under each BP state

The Friedman rank sum test results indicated that there were differences between PRV and HRV in all BP states for all indices, except for the measurements of VLF and cTP_y, which showed non-significant differences between HRV and PRV during normotension. These two indices need to be considered with care because they are probably a reflection of long-term changes, especially VLF, and require recordings longer than 5 min. In general, these results indicate that PRV and HRV are not the same, regardless of the BP state.

In addition, it was also determined if there were individual differences in PRV and HRV among BP states. The Kruskal-Wallis test results revealed that, in general, both HRV and PRV were different among hypotension, normotension, and hyper-

tension states. The only index for which there was not a statistically significant difference was cHF_x when measured from HRV. Based on the post hoc comparisons, it was concluded that PRV showed more differences than HRV. Again, as was observed for the correlations, these differences were especially observed in the nonlinear indices and in indices reflecting short-term changes, such as RMSSD, SD1, SpEn, and A1. Interestingly, most of the differences were observed when normotension was compared to either of the two other BP states.

8.4.4 Agreement between PRV and HRV

Three measurements were obtained from the Bland-Altman analysis to evaluate the agreement between HRV and PRV: the bias, difference between limits of agreement, and BAR.

For the time-domain indices, SDNN and RMSSD were overestimated when using PRV, whereas AVNN, NN50, and pNN50 had a bias close to zero. The absolute-power frequency-domain indices were also overestimated when using PRV, especially HF, LF/HF, and TP. On the contrary, the relative power indices were usually underestimated. The y-coordinate of the centroid of the HF band was also largely overestimated when using PRV. This same trend was observed for all Poincaré-plot indices, as well as for SampEn and ApEn, whereas SSE, D2, and both A1 and A2 were underestimated. The degrees of over- and underestimation tended to be larger during normotension. This same trend was observed for the limits of agreement: larger differences were observed during normotension and when some short-term indices, such as RMSSD, HF, cHF_y, SD1, and A1, were measured.

The obtained BARs indicated good agreement for AVNN, VLF, LF, HF, TP cHF_x, cLF_y, cHF_y, cTP_y, SpEn, SD2, BSE, SSE, MSE, LYA, and A2. Insufficient agreement was observed for SDNN, RMSSD, nLF, nHF, LF/HF, cLF_x, cTP_x, S, SD1, SD1/SD2, COM, ApEn, SampEn, D2, and A1. Most short-term indices showed an extremely large BAR, which indicates a very poor agreement between HRV and PRV for the measurement of these indices in critically ill patients regardless of the blood pressure state. There was no indication that blood pressure changes caused significant changes in the agreement.

8.4.5 Limitations of the study

This study has several limitations. First, the signals used were obtained from an available database from Physionet. Thus, several variables were not controlled for, and although all subjects were hospitalised in an intensive care unit, their diagnosis was unknown, which may have affected the results. Another limitation involves the segmentation of the data into 5-min-long segments, which may have been too short for the extraction of some indices, especially frequency-domain indices. However, this length was considered necessary to obtain as many segments as possible during each BP state and still ensure sufficient data for the PRV and HRV analysis, and was a good trade-off considering the results obtained from the analyses shown in Chapter 6. Moreover, an overlap of 10 s was used to separate the segments, which might have been too short to reflect BP changes. Again, this was done to produce a larger database. Another limitation of the study involves the classification of segments in each BP state, specifically determining exactly which state was predominant in each segment, especially in subjects who exhibited two or more BP states during the entire recording. A larger number of available segments might have helped to mitigate this effect, and outliers for each PRV and HRV index were corrected. It is important to mention that MIMIC-III database lacks synchronicity (Liang et al. 2019), which could bias the results obtained in this study. Finally, it is also worth noting that some of the extracted indices were not optimised, especially the non-linear indices such as Poincaré-plot indices, BSE, SSE, phase indices, and DFA-related indices. Using an optimisation procedure for these indices might lead to different results than those obtained in this study, as can be seen in (Shi et al. 2009).

8.5 Summary

The aim of this study was to assess the differences between HRV and PRV in critically ill subjects with different blood pressure values. For this aim, the correlation, comparison, and agreement between HRV and PRV were investigated. The results indicated that PRV and HRV were not the same regardless of the blood pressure state of the subjects, especially when nonlinear indices and indices associated with short-term changes were analysed, which agrees with the results obtained by other researchers (Gil, Orini, Bailón, Vergara, Mainardi & Laguna 2010, Shi et al. 2009, Bolea et al. 2017) and those described in Chapter 7. Interestingly, the differences

tended to be larger during normotension. Moreover, PRV tends to over- or underestimate HRV regardless of blood pressure state. Although both signals behaved similarly in most cases, the Kruskal-Wallis results indicate that PRV seems to be more sensitive to changes in blood pressure. This could be considered as an indication that PRV contains additional information not available in HRV, which might help increase the applicability of the technique in clinical scenarios. Moreover, the widespread use of PPG in wearable devices is generating a lot of research with PRV, which is aiming to apply this more practical technique, in comparison with HRV, for the diagnosis and monitoring of several physiological phenomena related to disease (i.e., cardiovascular disease, mental health). This, in turn, shows the applicability and potential of PRV for public health studies and, hence, for screening subjects that may need later further analyses in the clinical setting, with more specialised tools.

Future studies are needed to clarify the origin of the differences between HRV and PRV. Moreover, and as was done with classical time-domain, frequency-domain and Poincaré plot indices in Chapter 6, it is critical that non-linear indices are standardised and their physiological explanation determined for them to be adopted in PRV studies, given their increased sensitivity to scenarios such as the one presented in this study. This would enhance the quality of the research in this field, allowing the comparability among results obtained in different studies using these indices, and possibly increasing the applicability of PRV in clinical settings and its capability to diagnose and screen for disease.

In the next chapter the capability of PRV to identify BP states and estimate BP values using machine learning algorithms is evaluated. This could aid in the non-invasive, continuous measurement of blood pressure using PPG signals.

Chapter 9

Pulse rate variability for the classification and estimation of blood pressure states using machine learning algorithms

9.1 Aims and objectives

As mentioned in previous chapters, blood pressure (BP), the force with which the blood is pumped around the circulatory system (National Health Service 2019*b*), is one of the main vital signs measured in clinical and non-clinical environments (El-Hajj & Kyriacou 2020, 2021). Ideal BP values are considered to be between 90/60 and 120/80 mmHg, for diastolic (DBP) and systolic BP (SBP) respectively, whereas sustained high BP, also called hypertension, and sustained low BP, known as hypotension, are considered to be BP measurements higher than 140/90 mmHg and lower than 90/60 mmHg (National Health Service 2019*b*). Both hypertension and hypotension are abnormal conditions that may affect the blood flow to tissues and, hence, regular BP monitoring is essential for the detection, prevention and treatment of related diseases (El-Hajj & Kyriacou 2020). Specifically with hypertension, although it usually does not have noticeable symptoms, it increases the risk of various serious disorders, such as heart attacks and strokes (Chan et al. 2019). Since most patients are asymptomatic at the early stages of hypertension, it is usually detected only after substantial vascular damage has occurred and when more serious diseases

appear, not only in the cardiovascular system but in other vital organs (El-Hajj & Kyriacou 2020, Beevers & Robertson 2007, Welykholowa et al. 2020).

The measurement of BP has been traditionally performed using invasive, direct methods based on catheters, or non-invasive indirect techniques based on the inflation of a cuff (El-Hajj & Kyriacou 2020). However, both techniques pose several challenges and limitations. The invasive alternative can only be performed during surgery or in patients in intensive care units and carries with an increased risk of infection (El-Hajj & Kyriacou 2020). On the other hand, although the cuff-based methods can be applied in any environment, it does not allow for continuous measurements due to the inflation and deflation of the cuff, and having repetitive measures in short periods can be cumbersome and impractical for certain applications, such as in sleep studies (Mukkamala et al. 2015, Radha et al. 2019).

In the last few decades, increased attention has been given to non-invasive, continuous and cuff-less alternatives for the estimation of BP (Chan et al. 2019, Welykholowa et al. 2020, Hosanee et al. 2020). Most of these novel techniques are based on the analysis of physiological signals, especially PPG (El-Hajj & Kyriacou 2020, Hosanee et al. 2020, Elgendi et al. 2019). Some proposed strategies for the estimation of BP using PPG are based on machine learning (ML) algorithms and the extraction of PPG features that may reflect BP-related changes in PPG signals (El-Hajj & Kyriacou 2020, 2021). With the increasing availability of data and the development of powerful ML techniques, BP estimation based on this kind of analysis seems like a promising alternative for the ubiquitous, continuous measurement of BP values, as well as for the identification of hypertensive and hypotensive events in a real-time manner.

Blood pressure is primarily regulated by the sympathoadrenal system on a beat-to-beat basis (Fox 2016) and PPG-based PRV might contain information related to BP that allows for the identification of hypertension and hypotension using ML techniques. Moreover, the appearance of essential hypertension (i.e. high BP without underlying conditions) has been related with autonomic dysfunction (Carthy 2014). Therefore, and after the results obtained in the previous chapter, where differences were observed between PRV measured under different blood pressure states, the aim of this study was to evaluate the applicability of PRV for the identification of hypertensive, normotensive and hypotensive events, and to assess the capability of PRV-based ML algorithms for the estimation of BP values. This was done initially

with data obtained from critically ill patients available at MIMIC-III, but was also applied in a small sample of healthy volunteers as a proof of concept.

9.2 Methods and materials

9.2.1 Critically-ill patients

9.2.1.1 Signal selection

The same set of data used in Chapter 8 was considered for this study. This consists of 270 records extracted from MIMIC-III (Johnson et al. 2016, Goldberger et al. 2000), with simultaneously acquired PPG and ABP signals from critically-ill patients using a sampling rate of 125 Hz. ABP signals were obtained invasively from one of the radial arteries, while PPG signals were measured as the uncalibrated raw output of a probe located in the fingertip.

9.2.1.2 Signal processing

MATLAB® (version 2020a) was used for signal processing and figure generation. PPG and ABP signals were segmented into 5-min (PPG5 and ABP5) and 1-min (PPG1 and ABP1) segments, with a stride of 10 s between consecutive segments in both cases. These lengths were selected in order to evaluate the behaviour of PRV in short segments of time, i.e. 1-min segments, which would better characterise instantaneous changes in physiological parameters and lead to lower delays in the identification of BP states; and to compare these results to those obtained using the standard duration of signals for HRV and PRV analysis, i.e. 5-min segments.

After segmentation, ABP5 and ABP1 segments were filtered using a 12 Hz, fourth-order, lowpass Butterworth filter. As was done for the analysis in Chapter 8, the peak and onset of each cycle in the filtered segments were detected using Delineator (Li et al. 2010) and used for estimating the SBP and diastolic blood pressure (DBP) values. Then, each cycle was classified as a hypertension event (SBP greater than 140 mmHg or DBP greater than 90 mmHg), a hypotension event (SBP lower than 90 mmHg or DBP lower than 60 mmHg) or a normotension event. An example of these classification is shown in Figure 9.1. Then, the whole 5-min or 1-min segment was labelled as hypertension, normotension or hypotension according to the most frequent event in the segment.

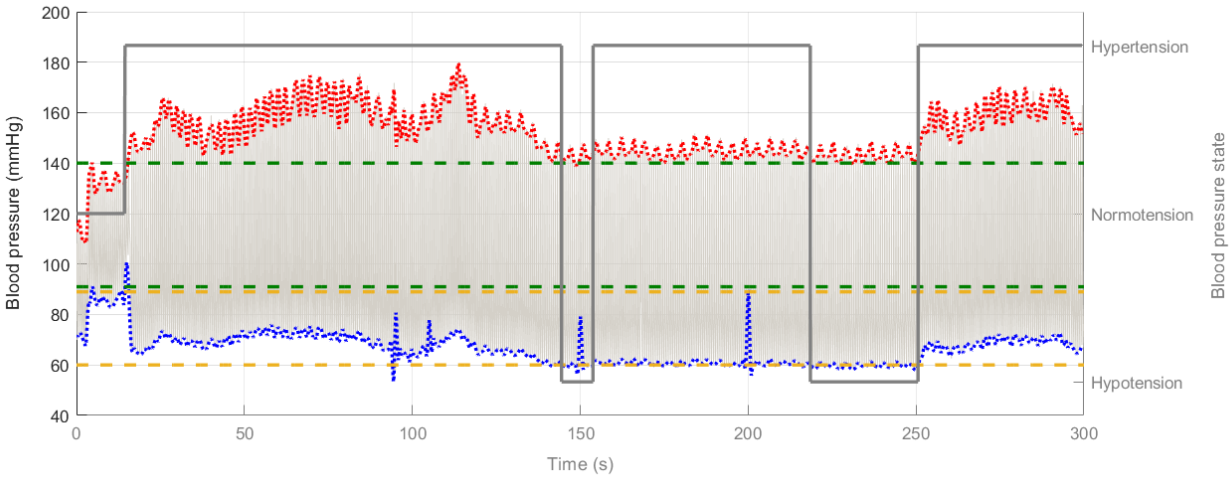

Figure 9.1: Example of the analysis of a 5-min arterial blood pressure signal (light gray line), with the trends for systolic (red, dotted line) and diastolic (blue, dotted line) blood pressure, as well as the determination of the instantaneous blood pressure state (dark gray line). Each cycle was classified as hypertensive, normotensive or hypotensive according to the thresholds for hypertension (green, discontinuous lines) and hypotension (yellow discontinuous lines), and the most common state in the segment. For instance, this 5-min segment was labelled as hypertension since this was the most common state for the individuals pulses.

The mean SBP, DBP and mean arterial pressure (MAP, calculated as shown in 9.1) values for each ABP5 and ABP1 segment were also extracted for regression analyses.

$$MAP = \frac{1}{3}SBP + \frac{2}{3}DBP \tag{9.1}$$

Similarly, the cardiac cycles were detected from PPG5 and PPG1 signals using the same algorithm, and the intersection point of the tangent lines arising from the maximum slope point and the valley of the waveform was used as fiducial point to determine the time location of each cardiac cycle. PRV was measured as the time difference, in milliseconds, between consecutive onsets from the PPG signal, as shown in Figure 9.2. For the frequency-domain analysis, the unevenly sampled PRV series were interpolated using a cubic spline interpolation and a sampling rate of 4 Hz, and the power spectrum was obtained using the Fast Fourier Transform (FFT). Outliers in both the original and interpolated time series were defined as values higher or lower than the mean value plus or minus 1.96 times the standard deviation of the series. These outliers were detected and replaced with the mean value of the five previous values in the time series.

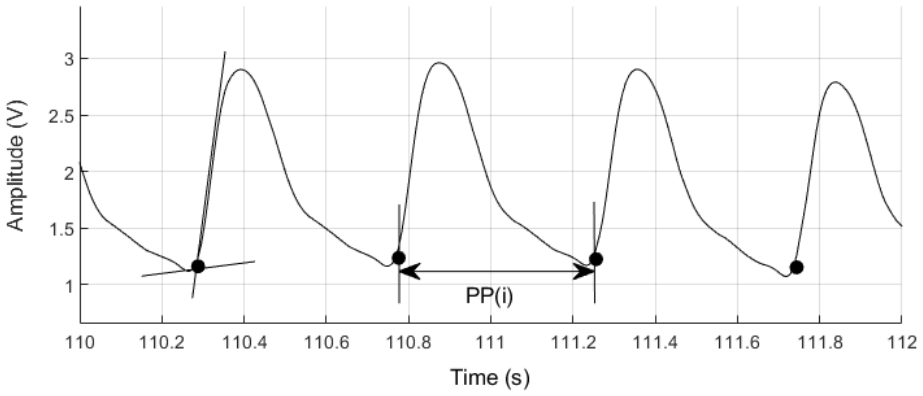

Figure 9.2: Example of a photoplethysmography (PPG) signal. Onsets (black circles) were detected from PPG signals to measure pulse rate variability (PRV) as the time interval between consecutive onsets (PP intervals).

9.2.1.3 Feature extraction

The time-domain, frequency-domain and non-linear indices analysed in Chapter 8 were obtained from PRV data from each 5 min and 1 min segment. These indices were considered as features for the identification of blood pressure states and the estimation of blood pressure values. Some non-linear indices were extracted solely from 5-min segments due to the lack of changes in shorter periods of time.

Alongside the already extracted indices, the auto-mutual information function (AMIF) was obtained from PRV trends as explained in (Semmlow & Griffel 2014). This function was then characterised using the lag at which the AMIF reached a value of $\frac{1}{e}$ (LagT); the value of the first local maximum of the function (PD); and the lag of this first local maximum (LagPD). The AMIF function describes the relationship between a signal (x) and its delayed version (x'), and its a measurement related to the long-term memory of a signal (Semmlow & Griffel 2014). The AMIF can be estimated as shown in (9.2), where $p(x, x')$ is the probability of events in the original and delayed signals to occur simultaneously, and $p(x)$ and $p(x')$ are the probabilities of obtaining a particular value from the signal and its delayed version, respectively.

$$AMIF = \sum p(x, x') \log_2 \frac{p(x, x')}{p(x)p(x')} \tag{9.2}$$

Also, the embedded dimension (EMB DIM) was computed for the extraction of LYA and to be used as a feature. It was computed using a nearest neighbours

algorithm, as suggested by Semmlow & Griffel (2014).

9.2.1.4 Classification of blood pressure states

Extracted features were used for the classification of blood pressure states applying machine learning (ML) algorithms. These algorithms were used in a multi-class scenario, in which the aim was to classify each segment in three classes: hypotension, normotension, and hypertension. In order to compare the performance in each scenario, all processes explained here were applied to the features extracted from 5-min and 1-min segments. In both cases, the dataset obtained was initially balanced in order to randomly include the same amount of samples for each of the three classes.

A feature selection framework was applied to determine the combination of features that better discriminate among classes. Three receiver operating characteristic (ROC) curves were obtained for each feature, one for each class against the other two classes, the ROC curve for the bi-class problem of hypotension against all other classes, normotension against all other classes, and hypertension against all other classes. Then, the mean area under the ROC curve ($\mathrm{AUC_k}$) was measured as a first separability criterion for each feature. Then, the multi-class Fisher Discriminant Ratio ($\mathrm{FDR_k}$) was obtained from each feature applying (9.3), where M is the number of classes; μ_i and μ_j are the mean values of the k-th feature when measured from the observations of class i and j, respectively; and σ_i and σ_j are the standard deviations of the k-th feature when measured from the observations of class i and j, respectively.

$$FDR_k = \sum_{i}^{M} \sum_{j \neq i}^{M} \frac{(\mu_i - \mu_j)^2}{\sigma_i^2 + \sigma_j^2} \tag{9.3}$$

Features were filtered using the scheme suggested in (Theodoridis & Koutroumbas 2009). A single separability criterion $\mathrm{C_k}$ was obtained for each feature as the mean value of $\mathrm{AUC_k}$ and $\mathrm{FDR_k}$. Then, the features were sorted in descending order and a subset of the features was initialised with the feature with higher $\mathrm{C_k}$, x_{i1}. To select the next feature to be included in the subset, x_{i2}, the Pearson correlation coefficients $\rho_{i_1 j}$ between x_{i1} and the remaining features were computed, and S(j) was computed as the difference between 0.8 times $\mathrm{C_k}$ and 0.2 times $|\rho_{i_1 j}|, j \neq i_1$. x_{i2} was selected as the feature for which S(j) was maximum.

This procedure was repeated until all features were included in the subset, but using the difference between C_j and the mean value of the correlation coefficients of the j-th feature with respect to the n features already included in the subset, as shown in (9.4). Once all features were included in the subset, those with S(j) lower than the median value of all resulting S were discarded.

$$S(j) = 0.8C_j - \frac{0.2}{n}\sum_{r=1}^{n-1}|\rho_{i_r j}| \tag{9.4}$$

After this filtering process, a sequential forward selection (SFS) scheme with k-fold cross-validation ($k = 10$) was applied to identify the best combination of features for each machine learning algorithm applied. This resulted in the combination of ranked features which delivered the maximum F1 score in the classification using each of the tested machine learning algorithms, described in the next section.

Several machine learning algorithms were applied for the multi-class classification of hypertensive, hypotensive and normotensive events (Table 9.1). These algorithms were applied using all filtered and forward-selected features. The performance of these algorithms was assessed applying a 10-fold cross-validation methodology and computing the confusion matrices for each fold. From the confusion matrices, the true positives (TP-2), true negatives (TN), false positives (FP) and false negatives (FN) where obtained for each class, as shown in Figure 9.3. These values were used for computing the accuracy (ACC), sensitivity (TPR), specificity (TNR), positive predictive values (PPV) and F1 scores (F1) for hypertension, hypotension and normotension classification, as shown in (9.5) to (9.9). Then, the mean and standard deviations of the performance in the 10 folds was measured.

Table 9.1: Machine learning algorithms applied for the classification of blood pressure states.

Algorithm	Parameters
k Nearest Neighbors (k-NN)	$k = 3, 5, 7, 9$.
Artificial Neural Networks (NN)	Feed forward networks with one n layer, with n n neurons, $n = 2, 3, ..., 20$.
Support Vector Machines (SVM)	Support vector machines with linear (S1), radial-basis (scale $\sigma = 0.5, 1, 1.5, 2$, S2-S5) and polynomial (order $n = 3, 4, 5$, S6-S8) kernels, both using a One-vs-All (OvA) and One-vs-One (OvO) scheme.

$$ACC = \frac{TP-2+TN}{TP-2+TN+FP+FN} \tag{9.5}$$

$$TPR = \frac{TP-2}{TP-2+FN} \tag{9.6}$$

$$TNR = \frac{TN}{TN+FP} \tag{9.7}$$

$$PPV = \frac{TP-2}{TP-2+FP} \tag{9.8}$$

$$F1 = \frac{2TP}{2TP+FP+FN} \tag{9.9}$$

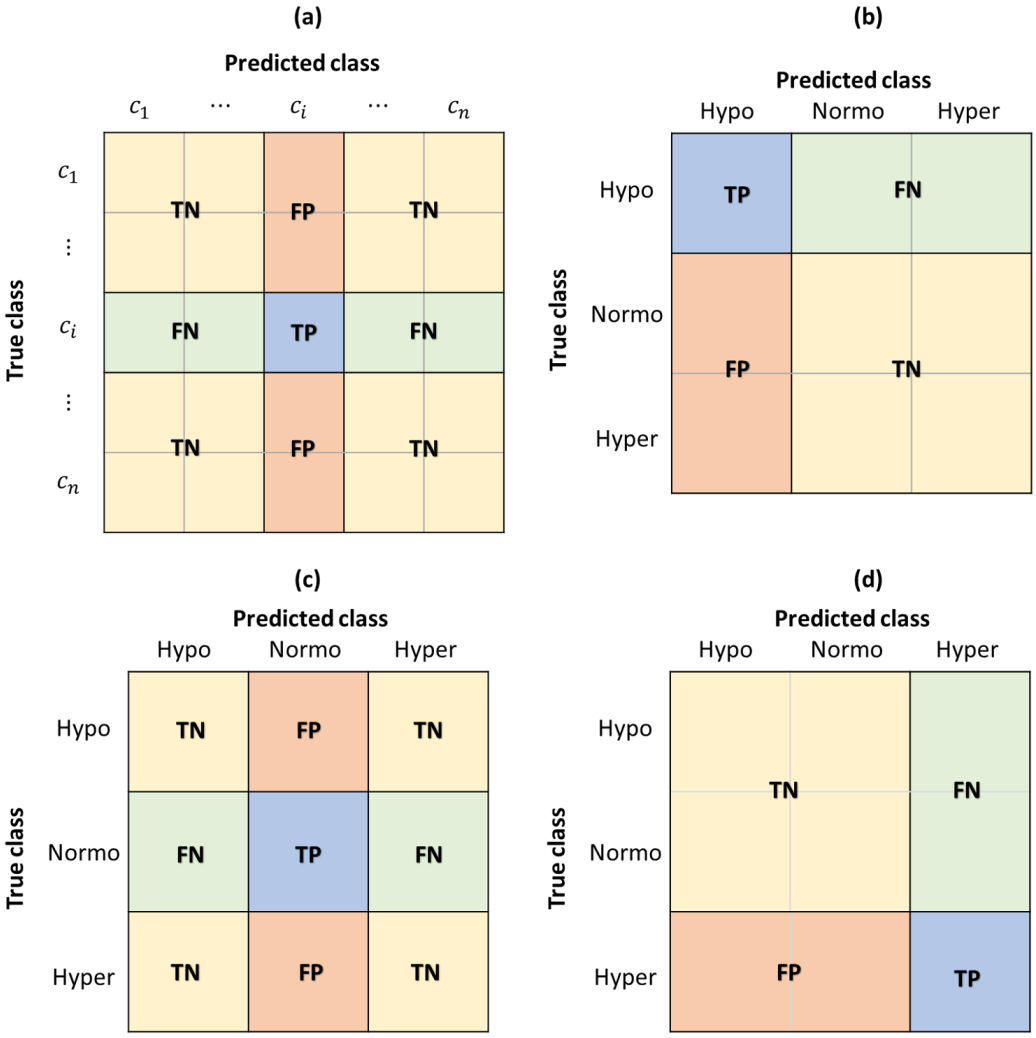

Figure 9.3: Definition of true positives (TP-2), true negatives (TN), false positives (FP) and false negatives (FN) from (a) the confusion matrix for the i-th class of a multi-class problems; (b) the confusion matrix of this study for the hypotension class; (c) the confusion matrix of this study for the normotension class; (d) the confusion matrix of this study for the hypertension class.

9.2.1.5 Estimation of blood pressure values

The extracted features were also used to estimate the mean value of SBP, DBP and MAP in each 5-min and 1-min segment. This was done using all extracted features and the best features selected after the filtering steps as previously explained. The combinations of features that provided the best performance regression algorithms were also obtained using a forward selection scheme, using the mean absolute error (MAE) as the optimisation function (9.10).

$$MAE = \frac{\sum_{i=1}^{n} |BP_{real} - BP_{estimated}|}{n} \tag{9.10}$$

Regressive support vector machines (rSVM) and function fitting neural networks (fNN), using the Levenberg-Marquardt training function and one hidden layer, were applied for the estimation of blood pressure values. As in the classification scheme, a 10-fold cross-validation technique was applied to avoid over fitting of the model. rSVM's were applied using a linear kernel, radial-basis kernels with varying scale, and polynomial kernels with varying orders; and fNN's were optimised by increasing the number of neurons in the hidden layer from 5 to 20.

The results from the regression algorithms were analysed using the mean and standard deviations of MAE with each algorithm. The best performance algorithm was then applied to the whole data set to assess the accuracy of the model. Wilcoxon rank sum tests were applied to compare the real values of SBP, DBP and MAP with the estimated values obtained from the selected model, and the agreement between real and estimated values was assessed using Bland-Altman analysis. These analyses were performed after detecting and correcting outliers.

9.2.2 Healthy volunteers

9.2.2.1 Signal acquisition

PPG and continuous, non-invasive ABP signals were simultaneously acquired from 20 healthy volunteers (12 men, 34 ± 5 years old; 8 women, 32 ± 4 years old). Subjects with cardiovascular, pulmonary, or metabolic diseases were excluded from this study. All subjects were seated on a comfortable chair, with their hands approximately at heart level. Infrared PPG signals were acquired from the index finger of each subject, using a custom-made, research-grade PPG acquisition system, BioBlocks^{TM} (*Pleth*

AILytics Ltd, United Kingdom). ABP signals were simultaneously acquired using a CNAP Monitor (*CN Systems, Austria*) with the sensor located on the middle and ring fingers of the same hand as the PPG probe. The CNAP monitor is based on the Vascular Unloading Technique and utilises a dual finger probe for a beat-to-beat measurement of ABP (*CNAP Blood Pressure* 2021). Both PPG and BP signals were digitised and acquired using a Data Acquisition Card (*National Instruments, United States*) and a Virtual Instrument developed in LabVIEW$^{\text{TM}}$ (*National Instruments, United States*). Signals were acquired for approximately 15 minutes with a sampling rate of 1 kHz, and stored for offline processing, which was performed in MATLAB R2019b (*Mathworks, United States*).

9.2.2.2 Arterial blood pressure analysis

Arterial blood pressure (ABP) signals were segmented into 5-minute segments with the stride length of 10 seconds. Once segmented, each ABP signal portion was filtered using a 50th-order moving-average filter and calibrated using (9.11), where X_{Volts} is the measured signal, in Volts, and X_{mmHg} is the calibrated pressure signal in pressure units (mmHg). This calibration equation was determined as suggested for the CNAP Monitor.

$$X_{mmHg} = 50 + 100\frac{X_{Volts} - 0.0703}{0.1683 - 0.0703} \tag{9.11}$$

Peaks and onsets were detected from the calibrated pressure signals using the Delineator algorithm (Li et al. 2010). Then, these points were interpolated using a cubic spline interpolation, to obtain an estimated trend for the systolic (SBP) and diastolic blood pressures (DBP). The mean values of these three trends were then obtained for each ABP segment.

9.2.2.3 Pulse rate variability analysis

Similar to ABP signals, PPG signals were segmented into 5-min and 1-min segments with a 10-second stride between consecutive segments. The segmented PPG signals were then filtered using a second order Butterworth band pass filter, with cut-off frequencies of 0.5 and 12 Hz. Inter-beat intervals (IBIs) were extracted from the PPG segments applying the D2Max algorithm (Elgendi et al. 2013). From the extracted IBIs, PRV trends were obtained from the duration of IBIs for the

subsequent extraction of PRV-related features. Outliers from these trends were detected as those IBIs with duration lower than the average duration of IBIs minus 1.96 times their standard deviation, or with duration higher than the average plus 1.96 time their standard deviation. An interpolated trend was also obtained for the assessment of frequency-related information, using a cubic spline interpolation with sampling rate of 4 Hz.

The features extracted from the signals obtained from critically-ill patients were also extracted from this data.

9.2.2.4 Estimation of blood pressure values

In the case of healthy subjects, only the estimation of blood pressure values was considered, given the smaller sample and low numbers of hypertensive and hypotensive events. A process similar to that performed with critically-ill patients was followed, were regressive support vector machines were trained and their performance evaluated for the estimation of SBP, DBP and MAP.

Regressive SVMs were trained using a 10-fold cross-validation strategy after randomising the features extracted from 5-min and 1-min segments. In the case of models trained using all and filtered features, linear, radial-basis ($\sigma \in [0.5, 1.0, 1.5, 2.0]$) and polynomial (order $n \in [2, 3, 4, 5]$) Kernel functions were considered; only radial-basis Kernel functions were used when sequentially forward selected features were considered. Filtered and SFS features were those chosen in the analysis performed with signals from MIMIC-III. As with data obtained from hospitalised subjects, the average and standard deviation of MAEs were computed to evaluate the performance of these models, and the agreement between target and estimated BP values was assessed using Bland-Altman analyses and the values estimated using the best performing algorithms for the estimation of SBP, DBP and MAP.

9.3 Results

9.3.1 Critically-ill patients

A total of 4937 5-min segments were extracted and merged, of which 54% were labelled as hypertensive, 25% as hypotensive, and the remaining 22% as normotensive events. Similarly, 11417 1-min segments were obtained and merged. From these,

51% corresponded to hypertensive events, 31% to normotensive events, and 18% were labelled as hypotensive. These data sets were used for the regression tasks.

The data set in the classification task was balanced by randomly selecting equal number of segments for each class. This was applied to both the 5-min and 1-min segment data sets. Hence, for the 5-min segments, randomly-selected hypertensive and hypotensive segments were discarded to obtain 1080 samples for each class, whereas for 1-min segments, some normotensive and hypertensive events were not included in the final data set so a total of 2049 segments were considered for each sample. A total of 3240 5-min segments and 6147 1-min segments were included for further analyses.

9.3.1.1 Feature extraction

Tables 9.2 to 9.4 summarise the features extracted from 5-min and 1-min segments, respectively, of PRV under each BP state. Appendix A includes figures comparing the behaviour of PRV indices compared to blood pressure values.

Table 9.2: Time-domain and Poincaré plot indices extracted from 5-min and 1-min segments of pulse rate variability. Values are shown as Mean ± Standard Deviation.

Features, units	Length of segments	Hypotension	Normotension	Hypertension
AVNN, s	5-min	0.826 ± 0.104	0.756 ± 0.137	0.837 ± 0.094
	1-min	0.827 ± 0.098	0.775 ± 0.133	0.835 ± 0.092
SDNN, s	5-min	0.011 ± 0.007	0.014 ± 0.011	0.016 ± 0.012
	1-min	0.049 ± 0.032	0.041 ± 0.029	0.053 ± 0.037
RMSSD, s	5-min	0.012 ± 0.005	0.015 ± 0.008	0.016 ± 0.009
	1-min	0.066 ± 0.040	0.055 ± 0.038	0.069 ± 0.043
NN50	5-min	2.580 ± 9.182	4.879 ± 12.732	6.129 ± 13.496
	1-min	9.473 ± 9.510	7.672 ± 8.012	9.519 ± 8.241
pNN50	5-min	0.006 ± 0.021	0.013 ± 0.034	0.017 ± 0.039
	1-min	0.135 ± 0.125	0.108 ± 0.118	0.141 ± 0.123
S, s^2	5-min	0.061 ± 0.027	0.072 ± 0.045	0.082 ± 0.048
	1-min	0.353 ± 0.230	0.281 ± 0.217	0.372 ± 0.249
SD1, s	5-min	0.008 ± 0.004	0.010 ± 0.006	0.011 ± 0.006
	1-min	0.047 ± 0.028	0.039 ± 0.027	0.049 ± 0.030
SD2, s	5-min	2.337 ± 0.295	2.138 ± 0.386	2.367 ± 0.265
	1-min	2.340 ± 0.279	2.194 ± 0.375	2.363 ± 0.260
SD1/SD2	5-min	0.004 ± 0.002	0.005 ± 0.003	0.005 ± 0.003
	1-min	0.020 ± 0.011	0.017 ± 0.011	0.020 ± 0.012
COM	5-min	0.000 ± 0.001	0.001 ± 0.001	0.001 ± 0.002
	1-min	0.007 ± 0.011	0.005 ± 0.009	0.008 ± 0.016

Table 9.3: Frequency-domain indices extracted from 5-min and 1-min segments of pulse rate variability. Values are shown as Mean ± Standard Deviation.

Features, units	Length of segments	Hypotension	Normotension	Hypertension
VLF, s^2	5-min	1.309 ± 3.112	1.544 ± 3.099	4.208 ± 9.140
($\times 10^8$)	1-min	2.097 ± 9.329	1.383 ± 6.101	3.484 ± 18.230
LF, s^2	5-min	0.751 ± 1.297	1.045 ± 2.097	2.056 ± 4.128
($\times 10^8$)				
	1-min	6.239 ± 20.470	4.632 ± 18.681	8.910 ± 33.490
HF, s^2	5-min	1.444 ± 3.085	1.687 ± 2.889	2.147 ± 3.985
($\times 10^8$)				
	1-min	9.818 ± 17.896	7.447 ± 15.194	11.031 ± 20.958
TP, s^2	5-min	3.504 ± 5.811	4.277 ± 7.431	8.411 ± 15.108
($\times 10^8$)				
	1-min	18.154 ± 42.404	13.462 ± 36.295	23.425 ± 63.988
LF/HF	5-min	0.705 ± 0.388	0.931 ± 0.824	0.974 ± 0.742
	1-min	0.499 ± 0.515	0.599 ± 0.708	0.668 ± 0.897
nLF	5-min	0.259 ± 0.101	0.242 ± 0.097	0.266 ± 0.114
	1-min	0.269 ± 0.096	0.273 ± 0.116	0.275 ± 0.118
nHF	5-min	0.432 ± 0.169	0.419 ± 0.221	0.363 ± 0.171
	1-min	0.643 ± 0.135	0.617 ± 0.175	0.607 ± 0.191
cLF_x, Hz	5-min	0.087 ± 0.008	0.084 ± 0.009	0.086 ± 0.009
	1-min	0.094 ± 0.010	0.092 ± 0.011	0.093 ± 0.012
cHF_x, Hz	5-min	0.273 ± 0.013	0.276 ± 0.021	0.275 ± 0.016
	1-min	0.273 ± 0.016	0.275 ± 0.019	0.275 ± 0.020
cTP_x, Hz	5-min	0.146 ± 0.046	0.141 ± 0.052	0.130 ± 0.049
	1-min	0.204 ± 0.033	0.197 ± 0.042	0.197 ± 0.049
cLF_y, s^2	5-min	0.684 ± 1.177	1.087 ± 2.226	2.399 ± 6.954
($\times 10^6$)	1-min	3.843 ± 12.577	2.716 ± 9.698	5.726 ± 22.975
cHF_y, s^2	5-min	0.815 ± 2.288	1.541 ± 2.485	0.923 ± 1.633
($\times 10^6$)	1-min	3.087 ± 5.292	2.322 ± 4.622	3.540 ± 7.142
cTP_y, s^2	5-min	4.825 ± 20.172	3.514 ± 6.168	10.562 ± 27.309
($\times 10^6$)	1-min	4.199 ± 12.652	2.958 ± 9.023	6.397 ± 25.340
SpEn	5-min	24.537 ± 1.645	23.862 ± 1.292	23.806 ± 1.909
	1-min	22.089 ± 0.580	22.298 ± 0.636	21.981 ± 0.572

9.3.1.2 Five-minute segments

Figure 9.4 (a) shows the results from the filtering of the features according to the separability criterion S, which includes the AUC and FDR values of each feature, as well as the cross-correlation coefficient among features. Nineteen out of the original 37 features were selected, whereas the remaining features were discarded from further analyses. The selected features were then used for the identification of the best combination of features for each machine learning algorithm. The results of the SFS scheme are shown in Tables 9.5 and 9.6.

Table 9.4: Entropy, phase and detrended-fluctuation analysis indices extracted from 5-min and 1-min segments of pulse rate variability. Values are shown as Mean ± Standard Deviation.

Features	**Length of segments**	**Hypotension**	**Normotension**	**Hypertension**
BSE	5-min	5.654 ± 0.288	5.684 ± 0.231	5.709 ± 0.232
	1-min	4.788 ± 0.321	4.914 ± 0.259	4.886 ± 0.275
SSE	5-min	2.693 ± 0.169	2.663 ± 0.205	2.631 ± 0.175
	1-min	2.597 ± 0.242	2.547 ± 0.258	2.505 ± 0.252
ApEn	5-min	0.433 ± 0.131	0.417 ± 0.120	0.417 ± 0.126
	1-min	0.294 ± 0.168	0.331 ± 0.194	0.295 ± 0.149
SampEn	5-min	0.454 ± 0.203	0.403 ± 0.164	0.424 ± 0.199
	1-min	0.245 ± 0.196	0.295 ± 0.235	0.244 ± 0.170
MSE	5-min	4.985 ± 1.952	4.625 ± 1.932	4.858 ± 1.923
	1-min	6.154 ± 1.626	6.118 ± 1.753	6.068 ± 1.595
LagT	5-min	1.122 ± 1.093	1.007 ± 0.086	1.067 ± 0.446
PD	5-min	0.092 ± 0.080	0.088 ± 0.024	0.097 ± 0.039
LagPD	5-min	153.950 ± 42.452	164.540 ± 59.024	154.471 ± 36.301
D2	5-min	-0.541 ± 33.236	-1.120 ± 31.724	-1.189 ± 33.201
	1-min	-1.272 ± 23.880	-0.039 ± 23.496	0.039 ± 19.490
LYA	5-min	3.271 ± 1.101	3.524 ± 1.182	3.536 ± 1.117
	1-min	3.787 ± 0.879	3.710 ± 0.797	3.977 ± 0.822
EMB. DIM	5-min	0.951 ± 0.133	0.962 ± 0.131	0.963 ± 0.108
	1-min	0.976 ± 0.033	0.972 ± 0.041	0.976 ± 0.033
A1	5-min	0.665 ± 0.386	0.676 ± 0.180	0.740 ± 0.209
	1-min	0.768 ± 0.406	0.748 ± 0.339	0.757 ± 0.395
A2	5-min	0.865 ± 0.252	0.897 ± 0.239	0.878 ± 0.231
	1-min	0.561 ± 0.252	0.600 ± 0.281	0.610 ± 0.304

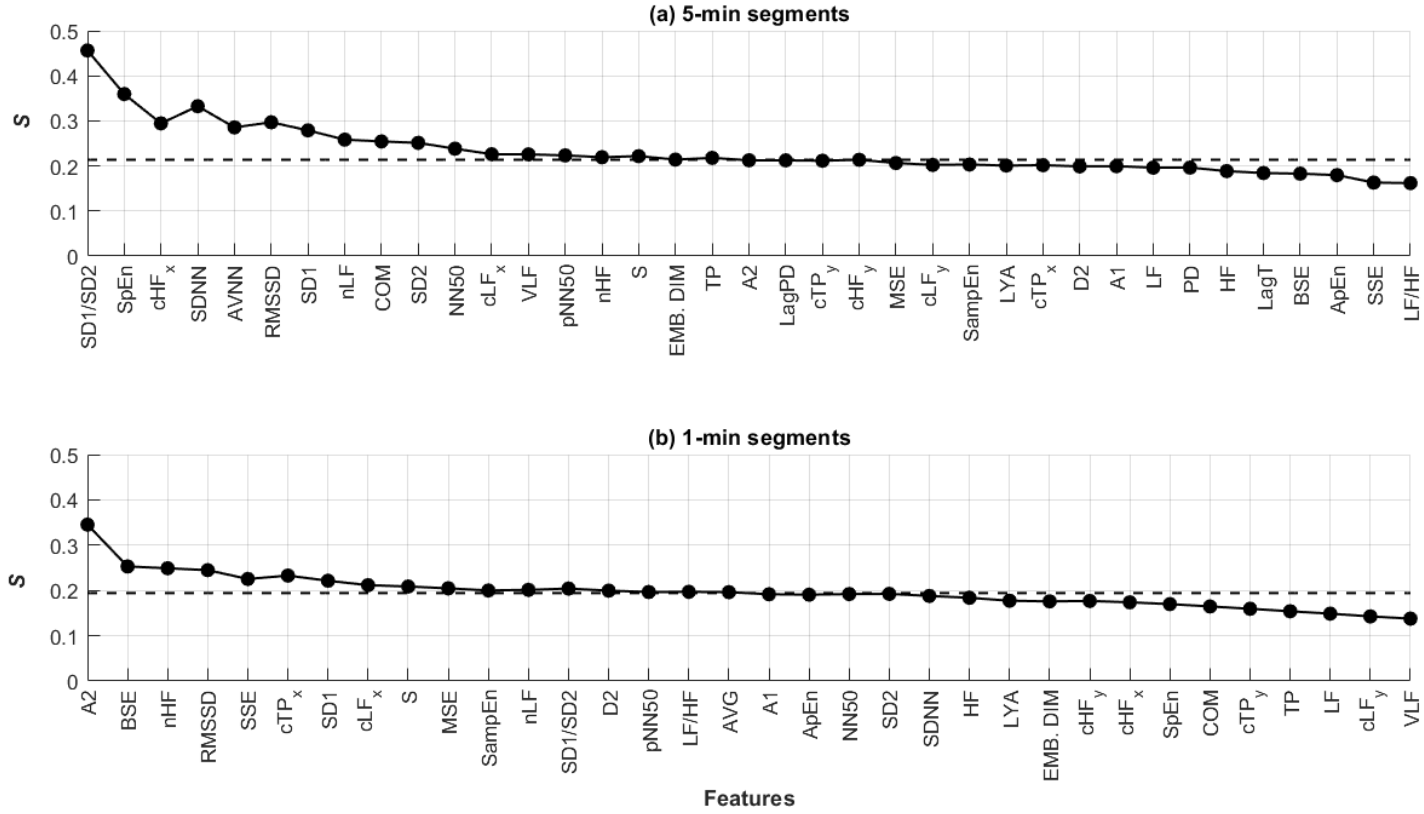

Figure 9.4: Filtering of features obtained from (a) 5-min and (b) 1-min segments of pulse rate variability. Features with separability criterion $S(j)$ lower than the median value of S's (dashed lines) were discarded.

Table 9.5: Results of the sequential forward selection scheme to identify the best combination of features for each machine learning algorithm using 5 min segments. Bullets indicate the features selected as part of the best combination for each algorithm.

	Algorithm																			
Features	k-NN [a]				Support Vector Machine															
					One vs All									One vs One						
						RBF [c]				Poly [d]				RBF				Poly		
	k = 3	k = 5	k = 7	k = 9	Linear [a]	$\sigma = 0.5$	$\sigma = 1.0$	$\sigma = 1.5$	$\sigma = 2.0$	n = 3	n = 4	n = 5	Linear	$\sigma = 0.5$	$\sigma = 1.0$	$\sigma = 1.5$	$\sigma = 2.0$	n = 3	n = 4	n = 5
SD1/SD2	-	-	-	-	●	-	-	●	-	-	●	-	●	-	●	-	-	-	-	●
SpEn	-	-	-	-	●	-	-	-	-	-	-	●	●	-	-	●	●	●	●	●
cHF_x	-	-	-	-	-	-	-	-	-	●	●	-	-	-	-	-	-	●	-	-
SDNN	●	-	-	-	-	-	-	-	●	-	-	-	-	-	-	-	-	-	-	-
AVNN	●	●	●	-	●	●	-	●	●	●	●	●	●	-	-	-	●	-	-	●
RMSSD	-	-	-	-	-	-	-	●	-	-	-	-	-	●	●	●	●	-	●	-
SD1	-	-	-	-	-	-	-	-	-	●	-	-	-	-	-	-	●	-	-	-
nLF	-	-	-	-	●	-	-	-	-	●	●	-	-	-	-	-	-	-	-	-
COM	●	●	●	-	-	-	-	-	-	-	-	-	-	-	-	-	-	-	-	-
SD2	●	-	●	●	-	-	●	-	●	-	-	-	●	-	-	-	-	●	-	-
NN50	-	●	-	-	-	-	-	-	-	-	-	-	●	-	-	-	-	●	-	-
cLF_x	-	-	-	-	-	-	-	-	-	●	-	-	-	-	-	-	-	-	-	-
VLF	-	●	-	●	-	-	-	-	-	-	-	-	-	-	-	-	-	-	-	-
pNN50	-	-	-	-	-	-	-	-	-	-	-	-	●	-	●	-	-	-	-	-
nHF	-	-	-	-	●	-	-	-	-	-	-	-	-	-	-	-	-	-	-	-
S	●	-	-	-	-	●	●	-	-	-	-	●	●	●	●	●	-	-	●	-
EMB. DIM	-	-	-	-	-	-	-	-	-	-	-	-	-	-	-	-	-	-	-	-
TP	●	●	-	-	-	-	-	-	-	-	-	-	-	-	-	-	-	-	-	-
cHF_y	●	●	-	-	-	-	-	-	-	-	-	-	-	-	-	●	-	-	-	-

[a] k-NN: k-Nearest neighbors. k: Number of nearest neighbors.
[b] Linear: Support vector machine with linear kernel function.
[c] RBF: Support vector machine with radial-basis kernel function. σ: Scale of the function.
[d] Poly: Support vector machine with polynomial kernel function. n: Order of the polynomial.

The results from the classification of each blood pressure state using all, filtered and forward selected features are shown in Figures 9.5 to 9.9.

Table 9.6: Results of the sequential forward selection scheme to identify the best combination of features for each feed forward neural network using 5 min segments. Bullets indicate the features selected as part of the best combination for each algorithm.

Features	**Hidden neurons**																		
	2	3	4	5	6	7	8	9	10	11	12	13	14	15	16	17	18	19	20
SD1/SD2	●	-	-	-	-	-	-	-	-	-	-	-	-	-	-	●	●	-	-
SpEn	-	-	-	●	●	-	-	-	●	●	-	●	●	-	-	-	-	●	-
cHF_x	-	●	●	-	-	-	●	-	●	-	-	-	-	-	-	-	-	-	●
SDNN	-	-	-	-	-	-	-	-	-	-	-	-	-	-	-	-	-	-	-
AVNN	-	-	●	-	●	●	●	●	●	-	-	-	-	-	●	-	●	●	-
RMSSD	-	●	-	-	●	-	-	-	-	●	●	-	●	-	-	-	-	-	-
SD1	-	-	-	-	-	-	●	-	-	-	-	-	-	-	-	-	-	-	●
nLF	-	●	-	-	-	-	-	-	-	-	-	-	-	-	-	-	●	-	-
COM	-	-	-	-	-	-	-	-	-	-	-	-	-	-	-	-	-	-	-
SD2	-	●	-	●	-	-	-	-	-	●	●	●	●	●	-	●	-	-	●
NN50	-	-	-	-	-	-	-	-	-	-	-	-	-	-	-	-	-	-	-
cLF_x	-	-	●	-	-	-	-	-	-	-	-	-	-	-	-	-	-	-	-
VLF	-	-	-	-	-	-	-	●	-	-	-	-	-	-	-	-	-	-	-
pNN50	-	-	-	-	-	-	-	-	-	-	-	-	-	-	-	-	-	-	-
nHF	-	-	-	●	-	-	-	-	●	-	-	-	-	-	-	-	-	-	-
S	-	-	●	●	●	●	-	●	●	-	-	●	●	●	●	-	-	●	-
EMB. DIM	-	-	-	-	-	-	-	-	-	-	-	-	-	-	-	-	●	-	-
TP	-	-	-	-	-	-	-	-	-	-	-	-	-	-	-	-	-	-	-
cHF_y	-	●	-	-	-	-	-	-	●	-	-	-	-	-	-	-	-	-	-

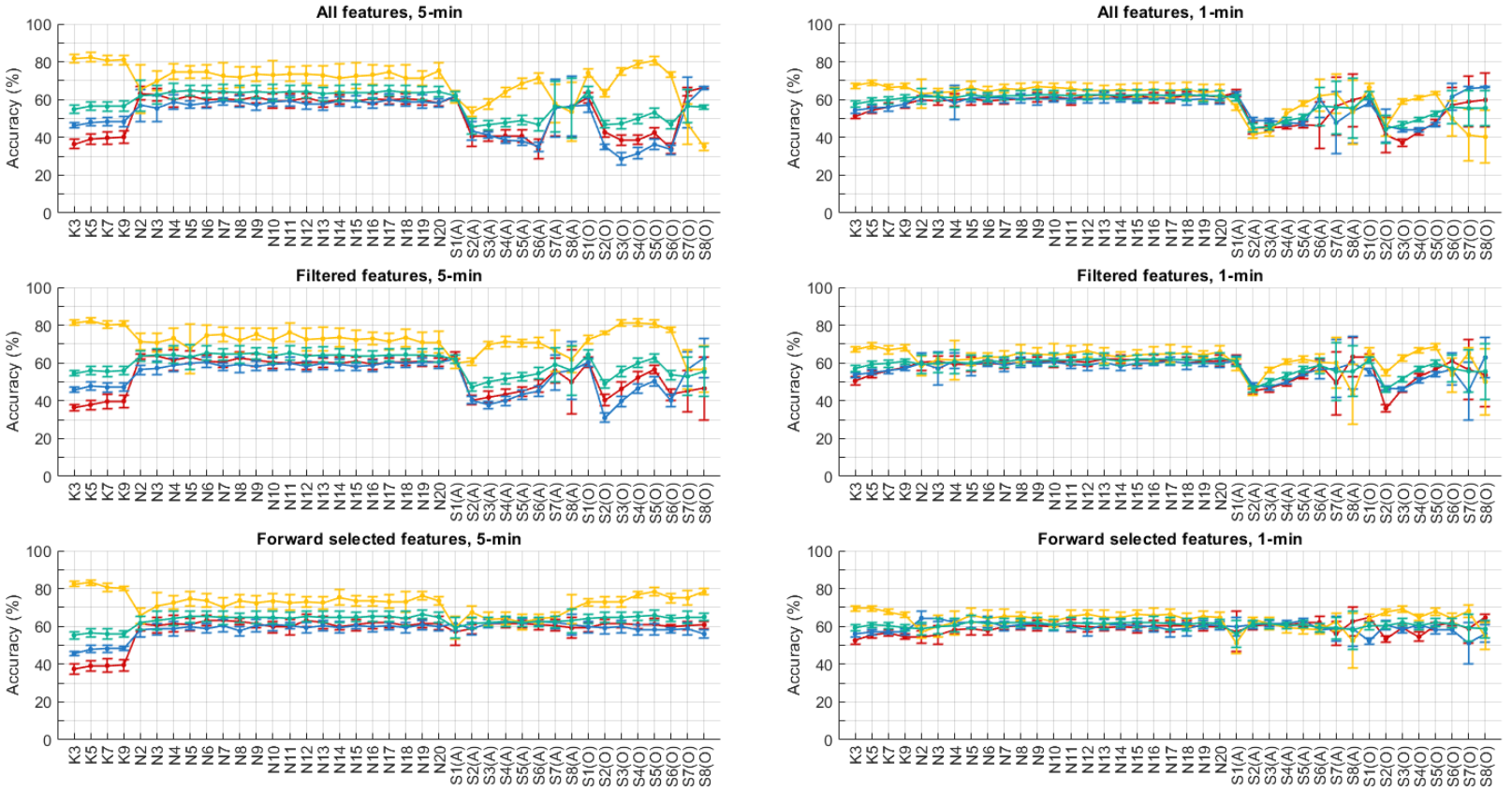

Figure 9.5: Accuracy (mean ± standard deviation) of the machine learning algorithms for the classification of hypotension (red lines), normotension (blue lines) and hypertension (yellow lines), as well as the average performance for all three classes (green lines), using all, filtered (ranked) and forward-selected features extracted from 5-min (left column) and 1-min (right column) segments. Results are presented as the average performance and its standard deviation after a 10-fold cross-validation. KX: k-NN algorithms with X nearest neighbors; NX: Feed-forward networks with X n neurons; SX(Y): Support vector machines with X kernel functions using a one-vs-all (Y = A) or one-vs-one scheme (Y = O). Accuracy tends to be higher for hypertension classification, especially with 5 min segments and using support vector machines.

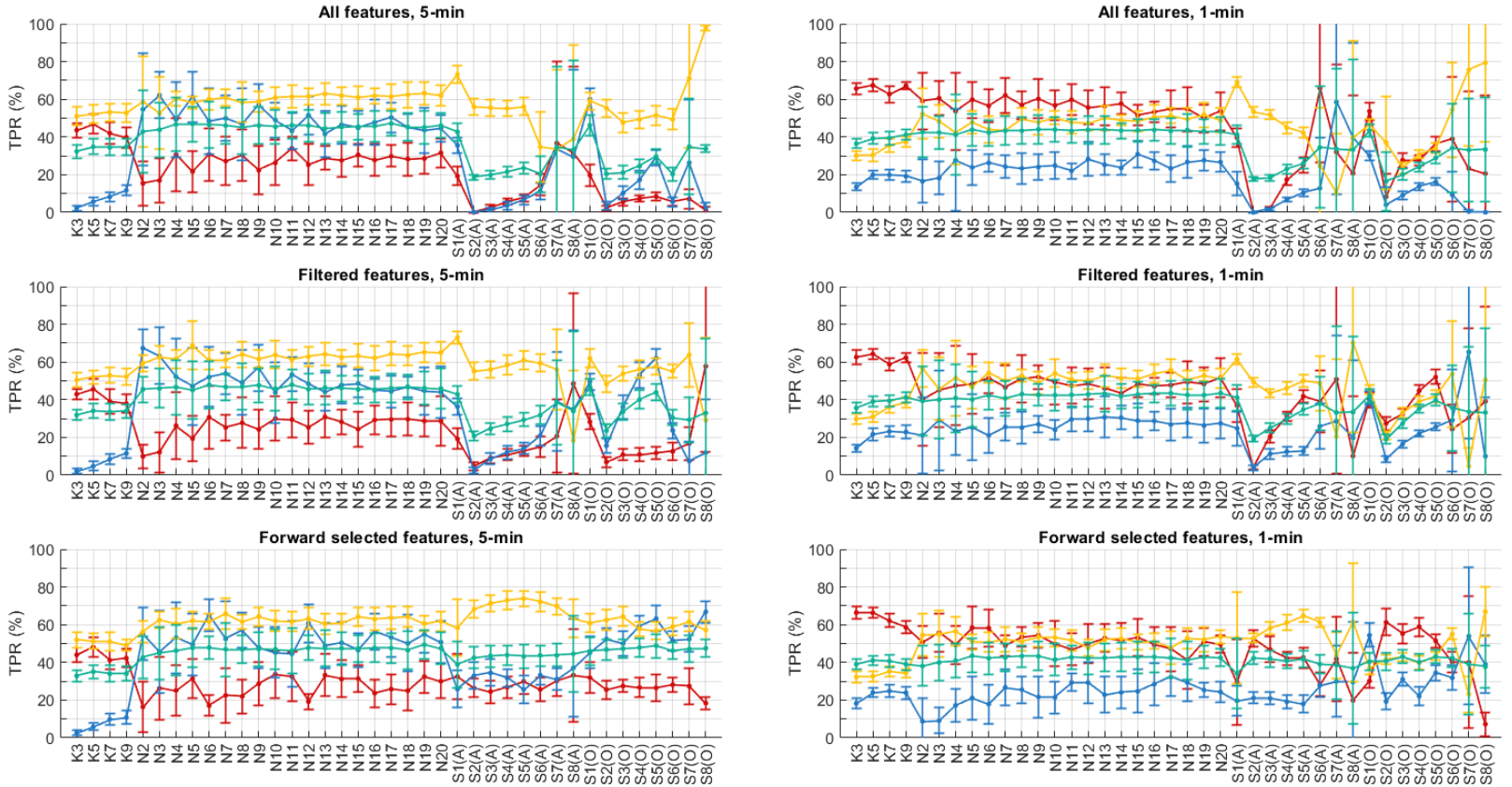

Figure 9.6: True Positive Rate (TPR, mean ± standard deviation) of the machine learning algorithms for the classification of hypotension (red lines), normotension (blue lines) and hypertension (yellow lines), as well as the average performance for all three classes (green lines), using all, filtered (ranked) and forward-selected features extracted from 5-min (left column) and 1-min (right column) segments. Results are presented as the average performance and its standard deviation after a 10-fold cross-validation. KX: k-NN algorithms with X nearest neighbors; NX: Feed-forward networks with X n neurons; SX(Y): Support vector machines with X kernel functions using a one-vs-all (Y = A) or one-vs-one scheme (Y = O). TPR tends to be higher for hypertension classification, and is higher using all features extracted from 1-min segments and one-vs-one SVM.

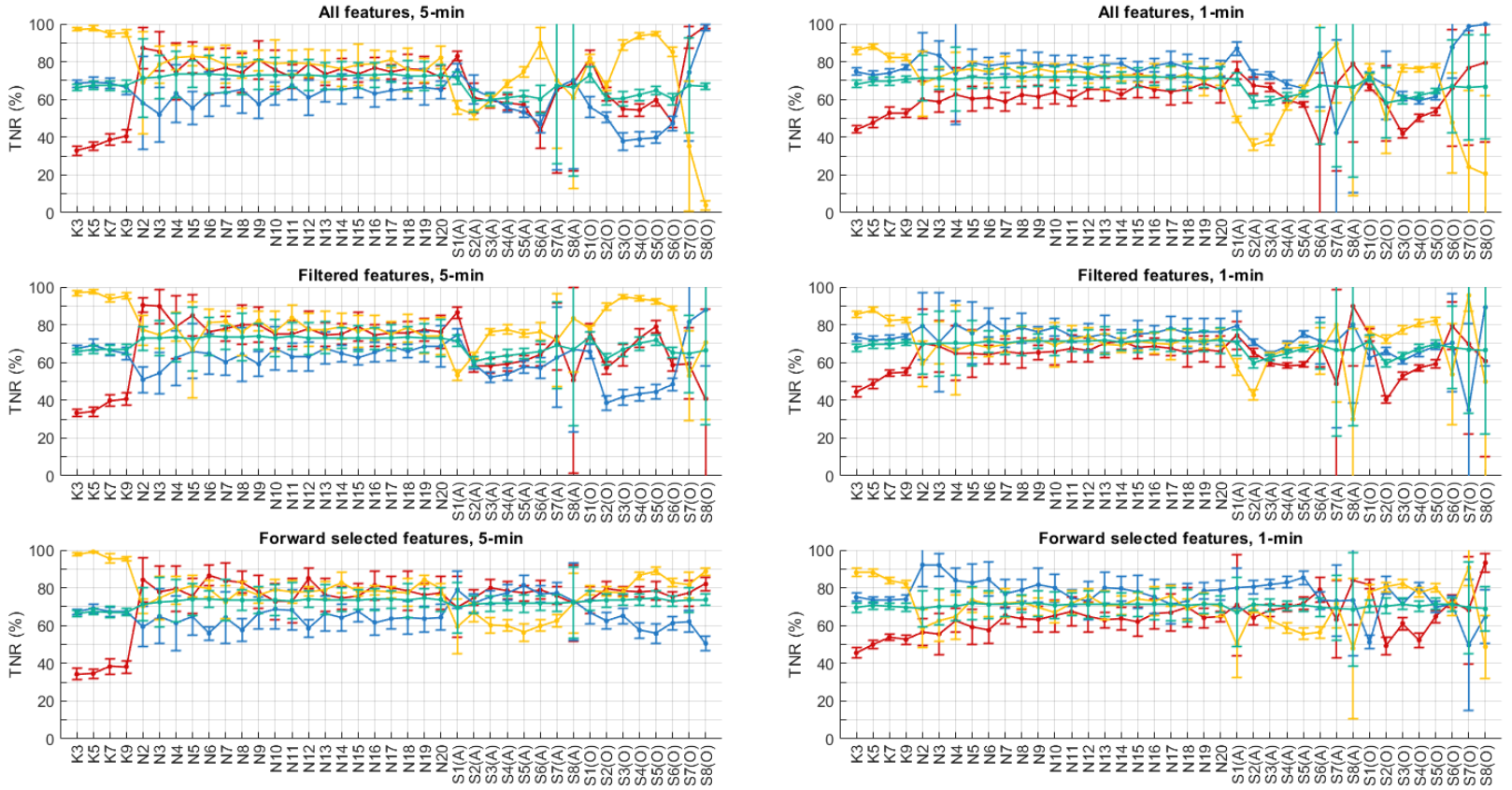

Figure 9.7: True Negative Rate (TNR, mean ± standard deviation) of the machine learning algorithms for the classification of hypotension (red lines), normotension (blue lines) and hypertension (yellow lines), as well as the average performance for all three classes (green lines), using all, filtered (ranked) and forward-selected features extracted from 5-min (left column) and 1-min (right column) segments. Results are presented as the average performance and its standard deviation after a 10-fold cross-validation. KX: k-NN algorithms with X nearest neighbors; NX: Feed-forward networks with X n neurons; SX(Y): Support vector machines with X kernel functions using a one-vs-all (Y = A) or one-vs-one scheme (Y = O). TNR is higher than other performance metrics, which could indicate a good capacity to detect false cases for all classification models.

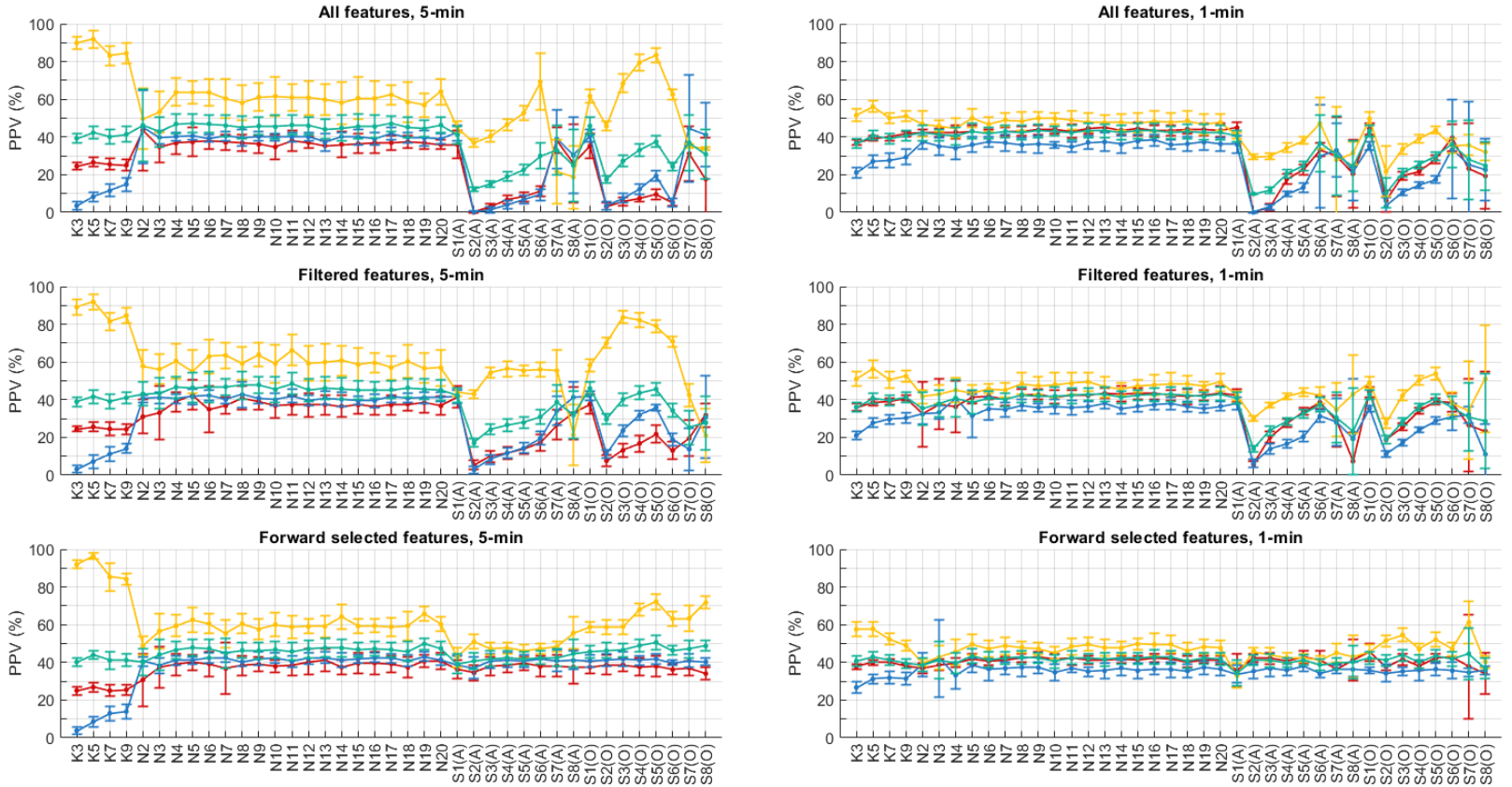

Figure 9.8: Positive Predictive Value (PPV, mean ± standard deviation) of the machine learning algorithms for the classification of hypotension (red lines), normotension (blue lines) and hypertension (yellow lines), as well as the average performance for all three classes (green lines), using all, filtered (ranked) and forward-selected features extracted from 5-min (left column) and 1-min (right column) segments. Results are presented as the average performance and its standard deviation after a 10-fold cross-validation. KX: k-NN algorithms with X nearest neighbors; NX: Feed-forward networks with X n neurons; SX(Y): Support vector machines with X kernel functions using a one-vs-all (Y = A) or one-vs-one scheme (Y = O). PPV tends to be higher for hypertension classification with support vector machines.

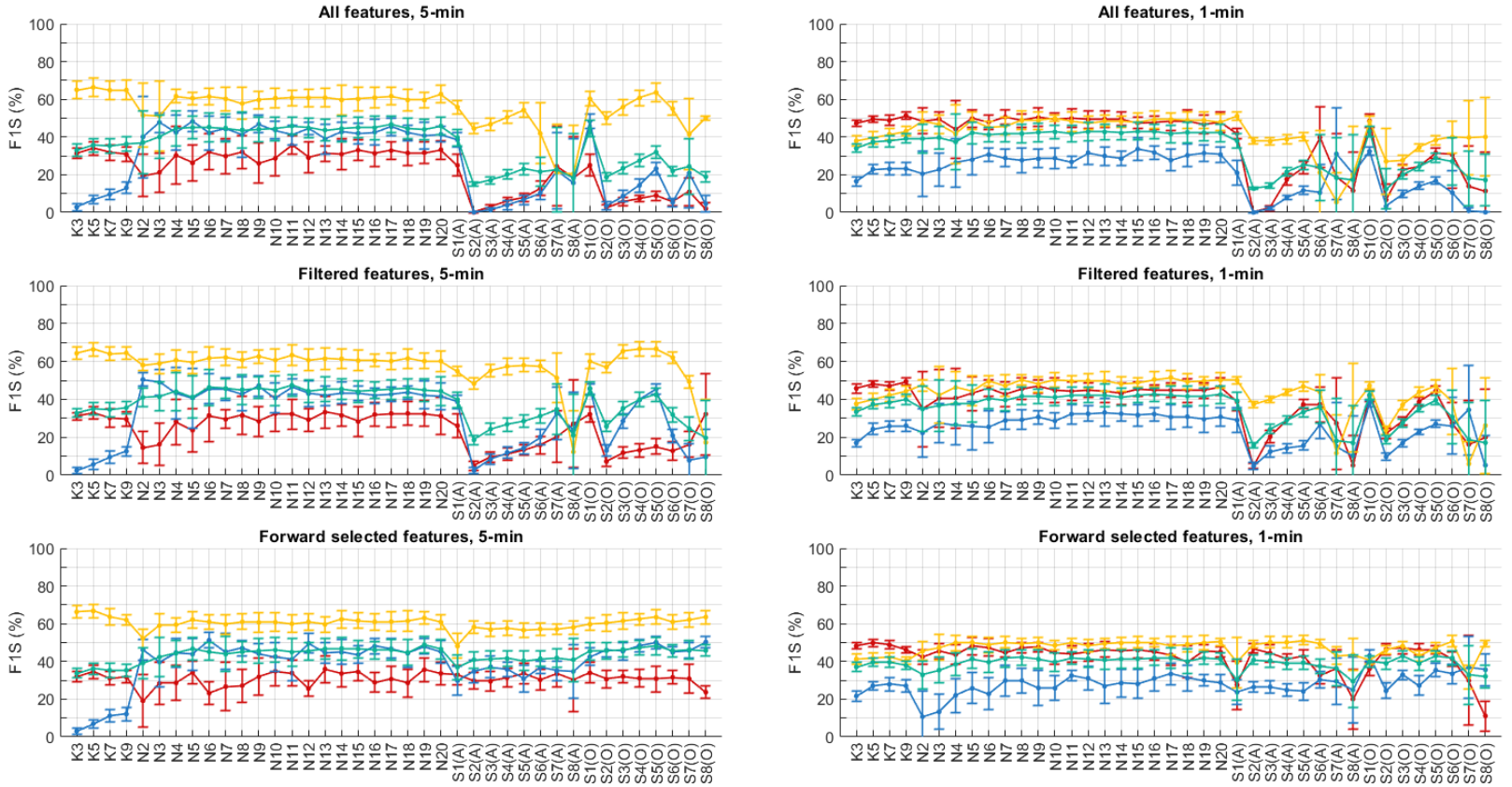

Figure 9.9: F1 Score (F1S, mean ± standard deviation) of the machine learning algorithms for the classification of hypotension (red lines), normotension (blue lines) and hypertension (yellow lines), as well as the average performance for all three classes (green lines), using all, filtered (ranked) and forward-selected features extracted from 5-min (left column) and 1-min (right column) segments. Results are presented as the average performance and its standard deviation after a 10-fold cross-validation. KX: k-NN algorithms with X nearest neighbors; NX: Feed-forward networks with X n neurons; SX(Y): Support vector machines with X kernel functions using a one-vs-all (Y = A) or one-vs-one scheme (Y = O). F1 Scores tend to be higher for when using 5 min segments, and performance is better for hypertension classification.

The results from the regression analyses using each of the fNN's and rSVM's models and all and filtered features are shown in Figure 9.10. Since the best results were obtained using radial-basis functions, these algorithms were optimised and the best combination of features for these models were obtained (Table 9.7).

Using 5-min segments, the algorithm with lower MAE's was the RBF SVM with a scale of 0.5, with less than 5 mmHg mean MAE for each blood pressure value. Hence, this model was applied and agreement between estimated and real values was assessed using Bland-Altman analysis (Figure 9.11). The mean difference between real and estimated values was -0.034, 0.020 and -0.051 mmHg for MAP, SBP and DBP values, respectively. From these analyses, it can be observed that the difference between real and estimated values has a directly proportional behaviour, i.e. as the mean value increases, so does the difference between the real and estimated values. Wilcoxon rank sum tests resulted in p-values of 0.313, 0.697 and 0.140 for MAP, SBP and DBP, respectively, indicating a similar behaviour of the estimated values when compared to real values obtained from invasive ABP signals.

9.3.1.3 One-minute segments

The same process as described above was performed using the features extracted from 1-min segments of PRV. Figure 9.4 (b) shows the filtering process of the features, which resulted in 17 out of 34 features rejected, and Tables 9.8 and 9.9 show the results obtained after the SFS scheme. The results from the classification using

Table 9.7: Mean absolute errors ± standard deviation of the estimation of blood pressure values measured using regressive support vector machines (rSVM's) with radial-basis functions after obtaining the best combinations of features using sequential forward selection, extracted from 5-min and 1-min segments of pulse rate variability.

Length of segments	**Kernel scale (σ)**	**Mean absolute error (mmHg)**		
		MAP [a]	**SBP** [b]	**DBP** [c]
5-min	0.5	2.55 ± 0.78	4.74 ± 2.33	1.78 ± 0.14
	1.0	2.59 ± 0.77	4.95 ± 2.37	1.86 ± 0.13
	1.5	2.90 ± 0.79	5.50 ± 2.37	2.08 ± 0.18
	2.0	3.35 ± 0.79	6.35 ± 2.34	2.39 ± 0.18
1-min	0.5	6.08 ± 0.14	10.93 ± 0.21	4.88 ± 0.11
	1.0	6.24 ± 0.07	11.39 ± 0.24	4.90 ± 0.14
	1.5	6.32 ± 0.09	11.58 ± 0.16	5.02 ± 0.13
	2.0	6.48 ± 0.09	11.91 ± 0.19	5.13 ± 0.12

[a] MAP: Mean arterial pressure.
[b] SBP: Systolic blood pressure.
[c] DBP: Diastolic blood pressure.

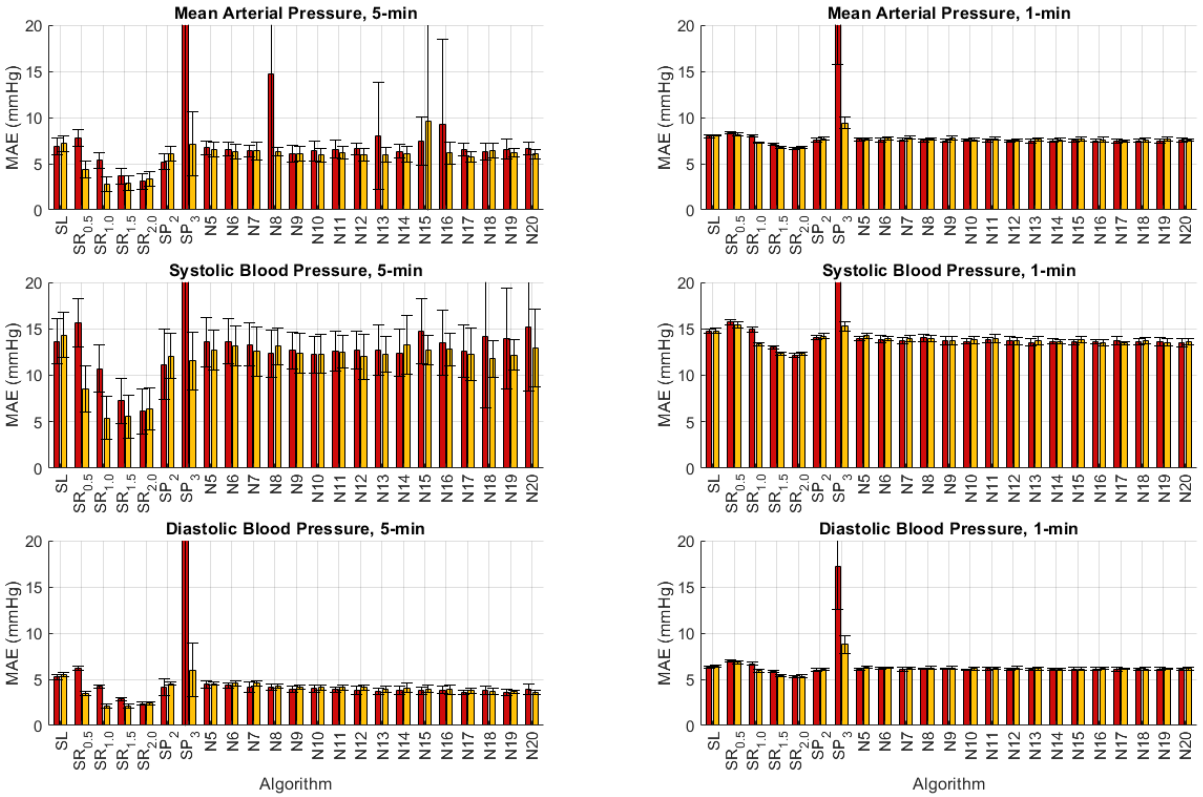

Figure 9.10: Results of the estimation of blood pressure values measured using regressive support vector machines (rSVM's) and fitting neural networks (fNN's). Mean absolute errors and standard deviations were measured from models obtained using all (red bars) and filtered features (yellow bars) extracted from 5-min (left column) and 1-min (right column) segments of pulse rate variability. SX_n: Support vector machine with linear kernel (X = L), radial-basis kernel (R) with varying scale n, or polynomial kernel (P) with varying polynomial order n. NX: Neural network with X n neurons.

all, filtered and forward-selected features are shown in Figure 9.5 to 9.9.

Confusion matrices for classification algorithms using 5-min and 1-min segments and the analysed algorithms using all, filtered and forward-selected features are shown in Appendix B.

Regression analysis was also performed and results using all and filtered features are shown in Figure 9.10. Table 9.7 contains the results obtained after regression analysis using the best combination of features obtained from radial-basis rSVM's, which showed the lowest MAE's using all and filtered features. As was done with the models obtained using 5-min PRV segments, Bland-Altman analysis was performed to assess agreement between real and estimated values, results of which are shown in Figure 9.12. MAP, SBP and DBP showed biases of 0.311, 0.265 and 0.377 mmHg, respectively. Once again, there is a directly proportional behaviour in the difference between real and estimated values. Wilcoxon rank sum tests indicated that both real

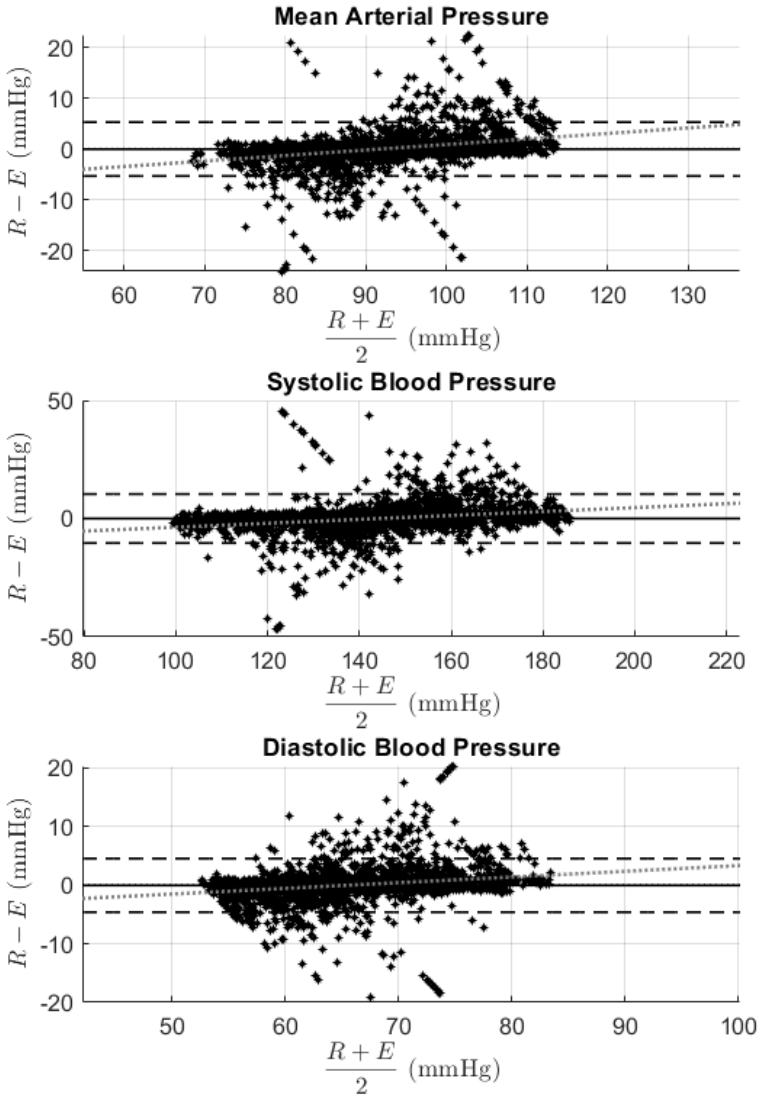

Figure 9.11: Bland-Altman plots for the assessment of agreement between real (R) and estimated (E) values of mean arterial pressure (MAP), systolic blood pressure (SBP) and diastolic blood pressure (DBP). Estimated values were obtained using support vector machines with radial-basis kernel function, and using the best combination of features measured from 5-min pulse rate variability segments. Dashed lines: Limits of agreement. Solid line: Bias. In all cases, agreement between predicted and target values was good, indicated by low biases and limits of agreement, although a better agreement was observed for estimation of MAP and DBP.

and estimated values come from comparable distributions, with p-values of 0.986, 0.600 and 0.400 for MAP, SBP and DBP, respectively.

Table 9.8: Results of the sequential forward selection scheme to identify the best combination of features for each machine learning algorithm using 1 min segments. Bullets indicate the features selected as part of the best combination for each algorithm.

	Algorithm																			
Features	k-NN [a]				Support Vector Machine															
					One vs All									One vs One						
						RBF [c]				Poly [d]				RBF				Poly		
	k = 3	k = 5	k = 7	k = 9	Linear [a]	$\sigma = 0.5$	$\sigma = 1.0$	$\sigma = 1.5$	$\sigma = 2.0$	n = 3	n = 4	n = 5	Linear	$\sigma = 0.5$	$\sigma = 1.0$	$\sigma = 1.5$	$\sigma = 2.0$	n = 3	n = 4	n = 5
A2	-	-	-	-	-	-	-	-	-	-	-	●	●	-	-	-	-	-	●	●
BSE	-	-	-	-	-	-	-	-	-	●	●	-	-	-	-	-	-	-	-	-
nHF	-	-	-	-	-	-	-	-	●	-	●	-	-	-	-	-	-	-	-	-
RMSSD	-	-	●	-	-	-	-	-	●	●	-	-	●	-	-	-	-	-	-	-
SSE	-	-	-	-	-	-	-	-	●	●	●	●	-	-	-	●	●	-	-	-
cTP_x	-	-	-	-	●	-	-	-	-	-	-	-	-	-	-	-	-	-	-	-
SD1	-	-	-	-	-	-	●	-	-	●	-	-	-	-	-	-	-	●	-	-
cLF_x	-	-	-	-	-	-	-	-	-	-	-	-	●	-	-	-	-	●	-	-
S	●	●	-	●	-	-	●	-	-	●	-	-	-	●	●	●	-	-	●	-
MSE	-	-	-	-	-	-	-	-	-	●	-	-	●	-	-	-	-	-	-	-
SampEn	●	●	-	●	-	-	●	●	-	●	-	-	-	●	●	-	-	-	-	-
nLF	-	-	-	-	-	-	-	-	-	-	-	-	-	-	-	-	-	-	-	-
SD1/SD2	-	●	-	●	-	●	●	-	-	-	●	-	●	-	-	-	●	-	-	-
D2	-	-	-	-	-	-	-	-	-	-	-	-	●	-	-	-	-	-	-	-
pNN50	●	●	●	●	-	-	●	-	-	-	●	●	●	-	●	●	●	-	●	●
LF/HF	-	-	-	-	-	-	-	-	-	-	-	-	●	-	-	-	-	-	-	-
AVNN	●	●	●	●	-	●	●	●	●	●	●	●	-	●	●	●	●	●	●	●

[a] k-NN: k-Nearest neighbors. k: Number of nearest neighbors.
[b] Linear: Support vector machine with linear kernel function.
[c] RBF: Support vector machine with radial-basis kernel function. σ: Scale of the function.
[d] Poly: Support vector machine with polynomial kernel function. n: Order of the polynomial.

9.3.2 Healthy volunteers

9.3.2.1 Feature extraction

Table 9.10 summarises the features extracted from 5-min and 1-min segments. A total of 1280 samples were obtained from 5-min segments, while 1760 1-min segments were considered.

9.3.2.2 Estimation of blood pressure values

Results from the regression analyses using rSVM's models and all, filtered and SFS features extracted from 5-min segments are shown in Table 9.11, while those obtained

Table 9.9: Results of the sequential forward selection scheme to identify the best combination of features for each feed forward neural network using 1 min segments. Bullets indicate the features selected as part of the best combination for each algorithm.

Features	**Hidden neurons**																		
	2	3	4	5	6	7	8	9	10	11	12	13	14	15	16	17	18	19	20
A2	-	-	-	●	●	-	-	-	-	-	-	-	-	-	-	-	-	-	-
BSE	-	-	-	●	-	-	-	-	-	-	-	-	-	-	-	-	-	-	-
nHF	-	-	-	-	-	-	-	-	-	-	-	-	-	-	-	-	-	-	-
RMSSD	●	-	-	-	-	-	-	●	-	-	-	-	-	-	-	-	-	-	-
SSE	-	-	-	●	●	-	-	●	-	-	-	-	-	-	-	-	-	●	-
cTP_x	-	-	-	-	●	-	-	-	-	-	-	-	-	-	-	-	-	-	-
SD1	-	-	-	-	●	-	-	-	-	-	-	-	-	-	-	-	-	●	-
cLF_x	-	●	-	-	-	-	-	-	-	-	-	-	-	-	-	-	-	-	-
S	-	-	-	-	●	-	-	-	-	-	-	-	-	-	-	-	-	-	-
MSE	-	-	-	-	-	-	-	●	-	-	-	-	-	-	-	-	-	-	-
SampEn	●	-	-	-	-	-	-	-	-	-	-	-	-	-	-	-	-	-	-
nLF	-	-	-	-	-	-	-	-	-	-	-	-	-	-	-	-	-	-	-
SD1/SD2	-	-	-	-	-	-	-	-	-	-	-	-	-	-	-	-	-	-	-
D2	-	-	-	-	-	-	-	-	-	-	-	-	-	-	-	-	-	-	-
pNN50	-	-	●	-	-	-	-	-	-	-	-	-	-	-	-	-	-	-	-
LF/HF	-	-	-	-	-	-	-	-	-	-	-	-	-	-	-	-	-	-	-
AVNN	-	●	●	●	●	●	●	●	●	●	●	●	●	●	●	●	●	●	●

from 1-min segments are shown in Table 9.12. It can be seen that, with features obtained from both 5-min and 1-min PRV trends, the best performance was achieved when using SFS features and a RBF Kernel function with a scale of 2. In the case of 5-min segments, the mean absolute errors were 1.22 ± 0.09 mmHg, 1.54 ± 0.17 mmHg, and 1.07 ± 0.06 mmHg for the estimation of MAP, SBP and DBP, respectively. MAE's of 4.68 ± 0.49 mmHg, 6.86 ± 0.72 mmHg and 4.06 ± 0.44 mmHg for the estimation of MAP, SBP and SBP respectively, were obtained when using SFS features extracted from 1 min PPG signals.

Bland-Altman analyses were performed to assess the agreement between the estimated values using the best performing algorithms for each case and the target BP values. Bland-Altman plots are shown in Figures 9.13 and 9.14, for 5-min and 1-min segments respectively, alongside a scatter plot comparing the estimated (dots) and target (crosses) values. It can be observed that the agreement tends to be satisfactory when 5-min segments are considered, with limits of agreement around 3 mmHg, 5 mmHg and 2 mmHg for MAP, SBP and DBP respectively, and with a small positive bias. On the contrary, limits of agreement for 1 min segments are larger, with near 20 mmHg, 30 mmHg and 10 mmHg for MAP, SBP and DBP.

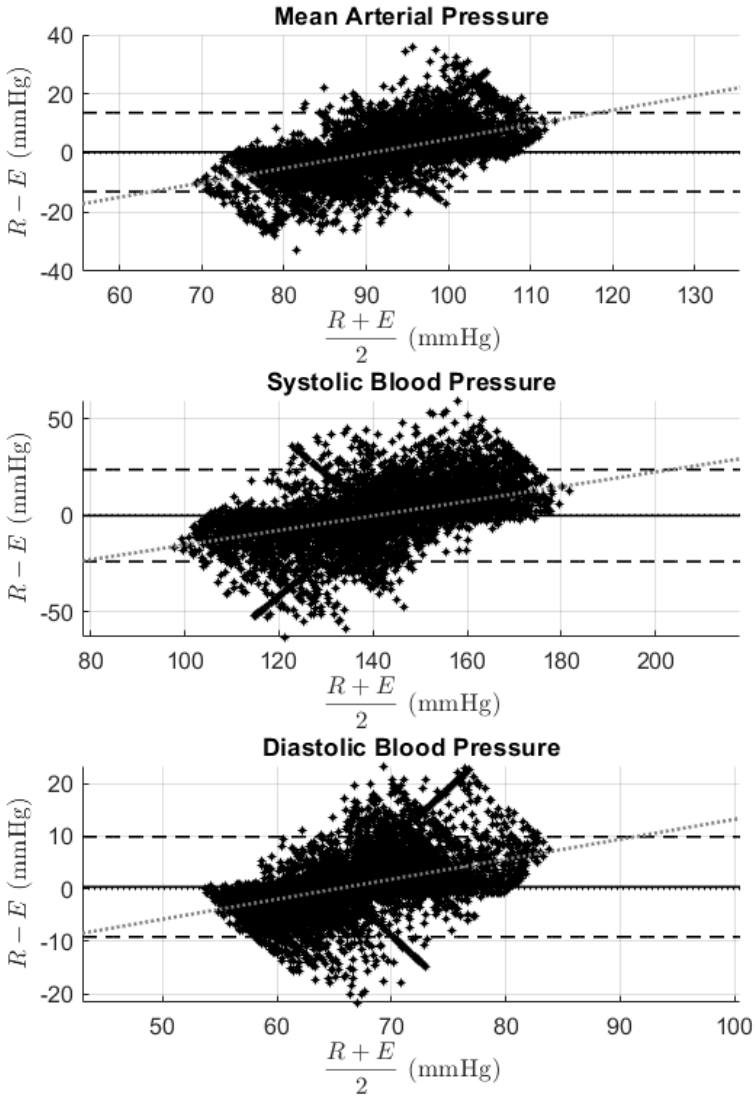

Figure 9.12: Bland-Altman plots for the assessment of agreement between real (R) and estimated (E) values of mean arterial pressure (MAP), systolic blood pressure (SBP) and diastolic blood pressure (DBP). Estimated values were obtained using support vector machines with radial-basis kernel function, and using the best combination of features measured from 1-min pulse rate variability segments. Dashed lines: Limits of agreement. Solid line: Bias. The agreement was better for MAP and DBP, indicated by tighter limits of agreement.

However, this is probably explained by the larger amount and magnitude of outliers. Both with 5-min and 1-min data, there are increased errors as the mean value of the target and predicted values get higher, implying that, as BP increases, the proposed model tends to have lower performance. This might be due to the fact that the vast majority of segments considered were normotensive and the homogeneity of the sample used in this study. From the scatter plots, nonetheless, it can be observed that the predicted values follow a similar trend to that of the target values, both

Table 9.10: Pulse rate variability indices extracted from 5-min and 1-min segments. Values are shown as mean ± standard deviation.

Features, units		Length of segments	
		5 min	1 min
Time-domain	AVNN, s	0.861 ± 0.141	0.860 ± 0.141
	SDNN, s	0.038 ± 0.017	0.035 ± 0.018
	RMSSD, s	0.032 ± 0.016	0.031 ± 0.016
	NN50	43.002 ± 40.111	7.757 ± 7.922
	pNN50	0.137 ± 0.141	0.133 ± 0.148
Frequency-domain	VLF, s^2 ($\times 10^8$)	13.244 ± 11.431	1.420 ± 2.473
	LF, s^2 ($\times 10^8$)	15.469 ± 15.580	2.957 ± 3.606
	HF, s^2 ($\times 10^8$)	11.584 ± 8.939	2.248 ± 2.059
	TP, s^2 ($\times 10^8$)	40.297 ± 31.144	6.625 ± 6.738
	LF/HF	1.850 ± 1.664	1.864 ± 2.205
	nLF	0.351 ± 0.134	0.414 ± 0.172
	nHF	0.298 ± 0.151	0.387 ± 0.204
	cLF$_x$, Hz	0.084 ± 0.011	0.085 ± 0.013
	cHF$_x$, Hz	0.248 ± 0.029	0.250 ± 0.031
	cTP$_x$, Hz	0.109 ± 0.034	0.136 ± 0.044
	cLF$_y$, s^2 ($\times 10^6$)	15.773 ± 17.869	2.545 ± 3.305
	cHF$_y$, s^2 ($\times 10^6$)	8.938 ± 7.746	1.442 ± 1.419
	cTP$_y$, s^2 ($\times 10^6$)	23.478 ± 18.602	2.974 ± 3.591
	SpEn	20.802 ± 0.812	21.788 ± 1.241
Poincaré plot	S, s^2	0.181 ± 0.110	0.177 ± 0.113
	SD1, s	0.022 ± 0.011	0.022 ± 0.012
	SD2, s	2.435 ± 0.399	2.432 ± 0.400
	SD1/SD2	0.009 ± 0.004	0.009 ± 0.004
	COM	0.003 ± 0.003	0.003 ± 0.003
Detrended fluctuation analysis (DFA)	A1	0.995 ± 0.228	1.085 ± 0.319
	A2	0.790 ± 0.156	0.804 ± 0.275
Entropy analysis	BSE	5.113 ± 0.359	4.510 ± 0.353
	SSE	2.083 ± 0.102	2.045 ± 0.131
	ApEn	0.385 ± 0.066	0.309 ± 0.066
	SampEn	0.359 ± 0.076	0.446 ± 0.150
	MSE	5.561 ± 1.249	2.467 ± 0.979
Phase analysis	LagT	1.003 ± 0.056	1.000 ± 0.000
	PD	0.103 ± 0.019	0.309 ± 0.060
	LagPD	161.064 ± 33.189	30.386 ± 6.754
	D2	2.325 ± 32.153	0.482 ± 25.139
	LYA	4.335 ± 0.973	4.035 ± 0.625
	EMBDIM	0.993 ± 0.074	0.987 ± 0.023

[a] Detrended fluctuation analysis

with data obtained from 5-min and 1-min segments. Again, the differences become larger as the target blood pressure becomes larger.

Table 9.11: Mean absolute errors ± standard deviation of the estimation of blood pressure values measured using regressive support vector machines (rSVM's) with linear, radial-basis (RBF, different scales σ) and polynomial (different orders n) Kernel functions, with all, filtered and sequentially forward selected (SFS) features, extracted from 5-min pulse rate variability segments.

Features	**Kernel function**	**Mean absolute error (mmHg)**		
		MAP [a]	**SBP** [b]	**DBP** [c]
All	Linear	9.32 ± 0.99	13.10 ± 1.75	7.62 ± 0.65
	RBF ($\sigma = 0.5$)	12.75 ± 0.62	16.98 ± 1.60	11.01 ± 0.52
	RBF ($\sigma = 1.0$)	8.76 ± 0.54	12.58 ± 1.54	7.40 ± 0.37
	RBF ($\sigma = 1.5$)	4.78 ± 0.34	6.82 ± 0.87	4.07 ± 0.30
	RBF ($\sigma = 2.0$)	3.12 ± 0.22	4.25 ± 0.50	2.72 ± 0.22
	Polynomial ($n = 2$)	2.77 ± 0.23	4.43 ± 0.36	2.17 ± 0.18
	Polynomial ($n = 3$)	2.73 ± 0.28	4.34 ± 0.52	2.21 ± 0.25
	Polynomial ($n = 4$)	11.43 ± 13.54	5.71 ± 1.63	15.30 ± 7.02
Filtered	Linear	10.34 ± 1.39	14.23 ± 2.22	8.76 ± 1.02
	RBF ($\sigma = 0.5$)	5.26 ± 0.57	7.65 ± 1.01	4.44 ± 0.44
	RBF ($\sigma = 1.0$)	2.33 ± 0.22	2.95 ± 0.37	2.05 ± 0.22
	RBF ($\sigma = 1.5$)	1.65 ± 0.15	2.05 ± 0.23	1.46 ± 0.16
	RBF ($\sigma = 2.0$)	1.48 ± 0.16	1.90 ± 0.27	1.29 ± 0.15
	Polynomial ($n = 2$)	4.11 ± 0.55	6.36 ± 0.98	3.14 ± 0.37
	Polynomial ($n = 3$)	2.11 ± 0.29	3.10 ± 0.49	1.70 ± 0.20
	Polynomial ($n = 4$)	2.72 ± 0.74	4.52 ± 1.41	2.25 ± 0.90
SFS	RBF ($\sigma = 0.5$)	2.48 ± 0.32	2.52 ± 0.44	1.66 ± 0.16
	RBF ($\sigma = 1.0$)	1.49 ± 0.12	1.83 ± 0.22	1.33 ± 0.12
	RBF ($\sigma = 1.5$)	1.28 ± 0.11	1.57 ± 0.20	1.14 ± 0.07
	RBF ($\sigma = 2.0$)	1.22 ± 0.09	1.54 ± 0.17	1.07 ± 0.06

[a] MAP: Mean arterial pressure.
[b] SBP: Systolic blood pressure.
[c] DBP: Diastolic blood pressure.

9.4 Discussion

In this proof-of-concept study, PRV was used for the identification of BP states and the estimation of BP values in critically ill patients and healthy volunteers. BP is one of the main vital signs, and identifying trends that may lead to hypertensive or hypotensive events, as well as estimating reliable BP values in a continuous manner could aid in the prevention, monitoring and treatment of cardiovascular changes and disorders related to hypertension or hypotension (El-Hajj & Kyriacou 2020). Hence, the results presented in this paper show the applicability of PRV as a tool for assessing BP changes using only PPG signals.

Although the classification results are not satisfactory for identifying all the classes, the proposed methodology showed a relatively good performance for the identification of hypertension events, which might be of particular interest due to

Table 9.12: Mean absolute errors ± standard deviation of the estimation of blood pressure values measured using regressive support vector machines (rSVM's) with linear, radial-basis (RBF, different scales σ) and polynomial (different orders n) Kernel functions, with all, filtered and sequentially forward selected (SFS) features, extracted from 1-min pulse rate variability segments.

Features	**Kernel function**	**Mean absolute error (mmHg)**		
		MAP [a]	**SBP** [b]	**DBP** [c]
All	Linear	11.11 ± 0.82	15.07 ± 1.24	9.59 ± 0.58
	RBF ($\sigma = 0.5$)	13.07 ± 0.73	17.24 ± 1.10	11.40 ± 0.65
	RBF ($\sigma = 1.0$)	12.93 ± 0.73	17.10 ± 1.09	12.28 ± 0.65
	RBF ($\sigma = 1.5$)	11.31 ± 0.68	15.21 ± 1.02	9.84 ± 0.58
	RBF ($\sigma = 2.0$)	8.58 ± 0.57	11.98 ± 0.98	7.43 ± 0.43
	Polynomial ($n = 2$)	8.14 ± 0.64	11.41 ± 1.31	6.95 ± 0.40
	Polynomial ($n = 3$)	15.60 ± 1.78	25.50 ± 3.85	12.30 ± 1.33
	Polynomial ($n = 4$)	21.12 ± 7.35	28.35 ± 7.40	43.26 ± 39.21
Filtered	Linear	11.49 ± 0.74	15.43 ± 1.46	10.11 ± 0.59
	RBF ($\sigma = 0.5$)	11.65 ± 0.79	15.76 ± 1.63	10.08 ± 0.53
	RBF ($\sigma = 1.0$)	7.12 ± 0.49	10.11 ± 1.02	6.12 ± 0.39
	RBF ($\sigma = 1.5$)	5.25 ± 0.37	7.42 ± 0.70	4.61 ± 0.31
	RBF ($\sigma = 2.0$)	4.91 ± 0.41	7.10 ± 0.71	4.29 ± 0.32
	Polynomial ($n = 2$)	7.76 ± 0.47	11.30 ± 0.95	6.52 ± 0.34
	Polynomial ($n = 3$)	8.81 ± 1.44	12.07 ± 1.47	7.55 ± 1.42
	Polynomial ($n = 4$)	39.95 ± 40.68	56.33 ± 44.07	28.75 ± 18.64
SFS	RBF ($\sigma = 0.5$)	6.83 ± 0.77	8.04 ± 1.07	4.39 ± 0.51
	RBF ($\sigma = 1.0$)	5.19 ± 0.62	7.48 ± 0.96	4.31 ± 0.50
	RBF ($\sigma = 1.5$)	4.91 ± 0.54	6.92 ± 0.83	4.19 ± 0.47
	RBF ($\sigma = 2.0$)	4.68 ± 0.49	6.86 ± 0.72	4.06 ± 0.44

[a] MAP: Mean arterial pressure.
[b] SBP: Systolic blood pressure.
[c] DBP: Diastolic blood pressure.

the relationship of hypertension and the appearance or worsening of cardiovascular diseases. Also, the results from the task of estimating blood pressure values shows promise as a potential tool for the non-invasive, continuous blood pressure estimation using PPG-based devices. Moreover, using more powerful machine learning models and additional non-linear features, as well as optimising some of the indices extracted in this study and improving the ABP data labelling process, could improve classification results, in order to reach better performance for identification of all classes.

9.4.1 Classification of blood pressure states

The results obtained from the classification of hyper-, normo- and hypotensive events show that PRV may aid in the identification of these trends, although the perfor-

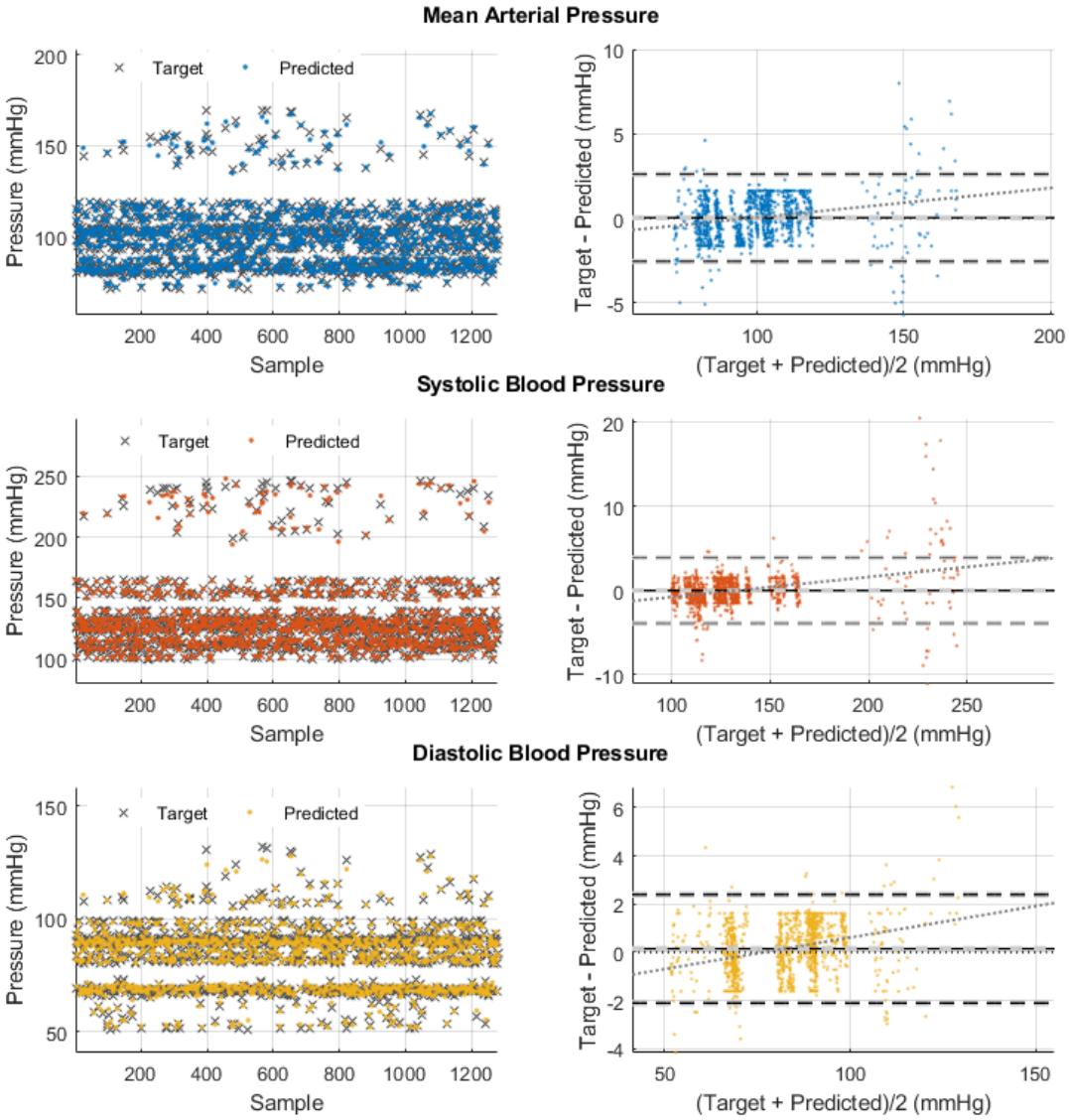

Figure 9.13: Bland-Altman plots for the assessment of agreement between real (R) and estimated (E) values of mean arterial pressure (MAP), systolic blood pressure (SBP) and diastolic blood pressure (DBP) from healthy subjects. Estimated values were obtained using support vector machines with radial-basis kernel function, and using the best combination of features measured from 5-min pulse rate variability segments. Dashed lines: Limits of agreement. Solid line: Bias. Dotted lines: Linear model. Left column: Scatter plot of estimated and target values. Right column: Bland-Altman plots. Bland-Altman plots show good agreement, indicated by low biases and limits of agreement, and a tendency to increase the error as the mean value of the estimated and target values increase. It can also be observed that most predicted values follow the behaviour of targets.

mance metrics were lower than 80% in most cases. Similar studies have reported encouraging results related to the identification of BP states using PRV. Lan et al. (2018) used PRV information for identifying hypertensive and normotensive subjects and compared the capability of some PRV indices for classifying the subjects,

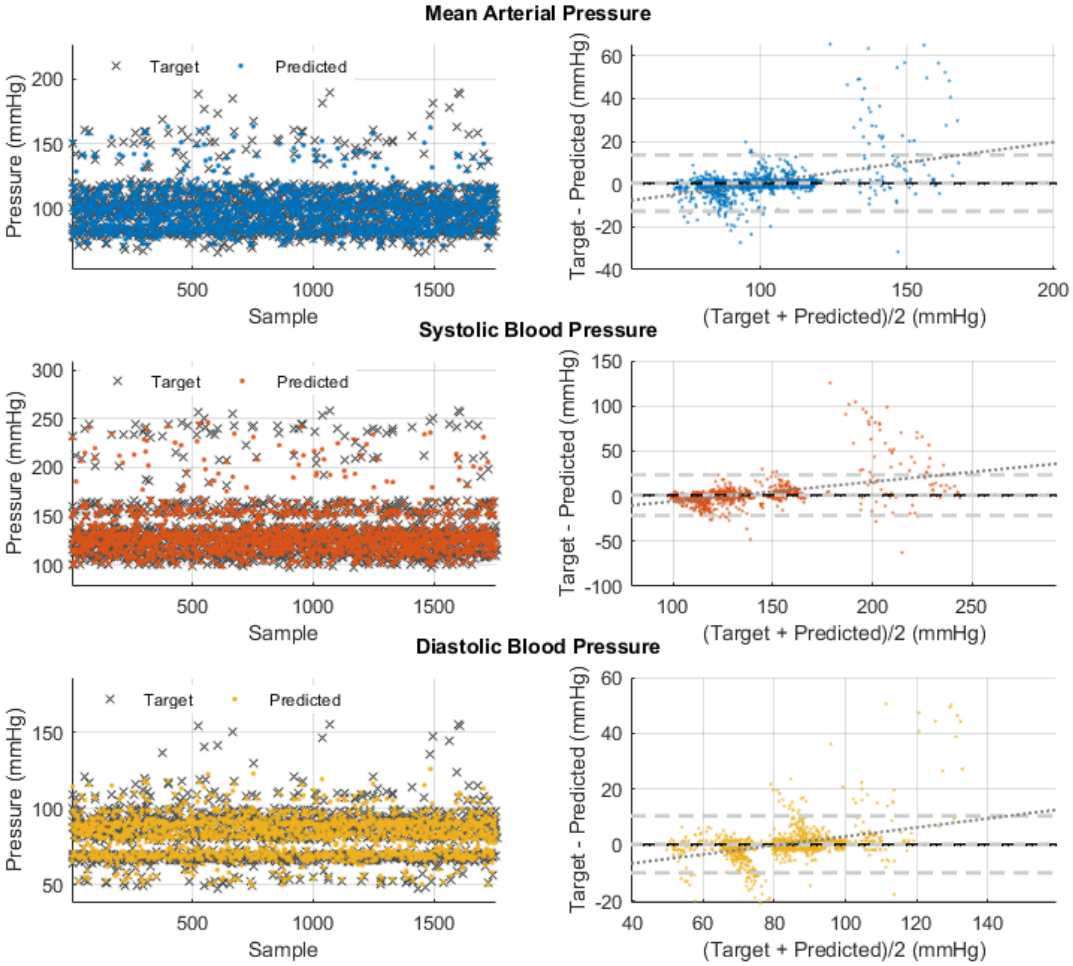

Figure 9.14: Bland-Altman plots for the assessment of agreement between real (R) and estimated (E) values of mean arterial pressure (MAP), systolic blood pressure (SBP) and diastolic blood pressure (DBP) from healthy subjects. Estimated values were obtained using support vector machines with radial-basis kernel function, and using the best combination of features measured from 1-min pulse rate variability segments. Dashed lines: Limits of agreement. Solid line: Bias. Dotted lines: Linear model. Left column: Scatter plot of estimated and target values. Right column: Bland-Altman plots. Bland-Altman plots show good agreement, although limits of agreement are larger than those obtained with 5 min segments. Most predicted values follow the behaviour of targets, especially during normotension.

with SDNN, AVNN, and nHF having the best performance. Bolea et al. (2017) used PRV- and PTT-based features to predict hypotension after spinal anaesthesia during caesarean labor, and reported a sensitivity of 76%, specificity of 70%, and accuracy of 72%. These two studies illustrate the capability of PRV to identify hyper- and hypotensive events, such as is presented in this study. Moreover, other studies have aimed to classify hypertensive events from the MIMIC database using only PPG information. Nath et al. (2018) reported an overall accuracy of 90.8% for classifying normotension, stage 1 and 2 of pre-hypertension, and hypertension; Liang et al.

(2018) obtained F-scores of 80.52%, 92.55% and 82.95% for classifying normotension against pre-hypertension, normotension against hypertension, and pre-hypertension against hypertension, respectively; and Xiaoxiao et al. (2020) reached F-scores of 88.03%, 70.94% and 84.88% for the same classification tasks as the previous study. The last two studies used deep learning models for the identification of blood pressure states. To the knowledge of the author of this thesis, no studies have aimed to classify hypotension events from the MIMIC database.

It was observed that the ML algorithms tested in this study showed better specificity and accuracy than sensitivity and precision. This means that the algorithms were more powerful when classifying those events that did not belong to each of the classes (i.e., true negatives). This was especially true for hypotensive and normotensive events. On the other hand, the identification of hypertensive events outperformed the other two classes. This is important because of the effect hypertension has in blood flow and cardiovascular mechanics. As has been mentioned, hypertension has several physiological effects, such as the thickening of large and medium arteries, the appearance of coronary artery atheroma and long-term cardiac function impairment with left ventricular systolic dysfunction; micro aneurysms that appear in small arteries within the brain that may result in intracerebral hemorrhage and cerebral infarction, the thickening and appearance of emboli in the retinal artery, and extensive and progressive fibrinoid necrosis of glomerular arterioles and consequent renal impairment (Beevers & Robertson 2007). Therefore, identifying hypertensive events is crucial for monitoring cardiovascular health. In the case of the classification of hypertension events, the proposed methodology showed a maximum F1-score of 66.78% $\pm$ 3.65% and a maximum accuracy of 83.08% $\pm$ 1.48%, obtained with forward selected features and a k-NN model.

For the 5-min PRV segments, the k-NN algorithms showed a very stable performance, with no evident changes due to the number of nearest neighbours. These algorithms showed a relatively high PPV, as well as a high TNR, for the identification of hypertensive events, and this behaviour was not highly affected by the features used (all, filtered, or SFS). Nonetheless, hypo- and normotensive segments were not well identified using k-NN algorithms. NNs and SVMs had similar behavior, but with relatively better performance for identifying normotension. As with k-NNs, hypotensive events were difficult to identify using only PRV-based features.

SVMs were highly affected by the features used. It can be observed that the

identification of normotension and hypotension is highly improved by using the best combination of features in each case, although the performance of the identification of hypertension is slightly diminished. In this case, the SVMs with RBF kernels showed the best average performance, with mean ACC around 70%; mean TPR, mean PPV and mean F1 around 50%; and mean TNR around 75%. From these results, it can be concluded that PRV may aid in the classification of blood pressure states, although using additional information, probably available also in PPG signals, may improve the performance of the algorithms.

Interestingly, by diminishing the window size to 1-min the performance of the classifiers for identifying hypotension and normotension was improved. However, the mean performance was better using 5-min segments. This might be explained by the fact that a 1-min window for PRV analysis is not enough for reflecting changes due to the nature of PRV and the dynamics of autonomic activity. Again, using SFS features improved the mean performance, especially on SVMs. This difference in performance between 5-min and 1-min segments for identifying hypo- and normotension might be explained by the way the segments are labelled; for example, when using 1-min segments it is more likely that small changes are identified and correctly labelled in each class. However, the analysis of HRV and PRV is recommended to be done using windows of at least 5-min due to the slow-changing nature of these variables (Task Force of the European Society of Cardiology and The North American Society of Pacing and Electrophysiology 1996, Shaffer & Ginsberg 2017) and making it possible that the changes are not as evident in 1-min segments, which might explain the better average performance of the classification using 5-min segments. Both for the classification and estimation of BP, having shorter segments of PPG for the extraction of PRV features might be desirable, to allow for smaller delays in estimating the states or the values. However, this variable should be optimised in future studies, to achieve a balance between good performance and duration of segments.

9.4.2 Estimation of blood pressure values

Although identifying BP states could aid in the monitoring of BP, estimating BP values using only PPG signals could enhance the prevention and treatment of disorders related to BP changes. From the obtained results using signals from critically-ill subjects, especially those obtained using 5-min segments, and signals acquired from

healthy volunteers, it can be observed that using only PRV-derived features and ML algorithms, it is possible to obtain good estimates of mean, systolic and diastolic arterial blood pressures using the proposed methodology.

The application of machine learning algorithms for the extraction of BP values from the PPG is currently widely studied, and several authors have proposed different methods for the estimation of blood pressure values from signals obtained from the MIMIC database. Table 9.10 summarises some of these results found in the literature and compares them to the results obtained in this study. It can be observed that using PRV-based features and regression SVMs, a comparable and acceptable performance was obtained.

As stated by El-Hajj & Kyriacou (2020), the American National Standards of the Association for the Advancement of Medical Instrumentation (AAMI) established that a non-invasive technique is reliable for the estimation of BP values if the mean difference and standard deviation does not exceed 5 ± 8 mmHg when compared to a reference BP evaluated on no less than 85 patients. The obtained results from critically-ill patients showed that, using 5-min segments with an overlap of 10 s, it is possible to have reliable measures of MAP, SBP and DBP using radial-basis SVM's with scales of 0.5 and 1, using only PRV-based features. The minimum average errors obtained were 2.55 ± 0.78, 4.74 ± 2.33 and 1.78 ± 0.14 mmHg for MAP, SBP and DBP, respectively. The results obtained using 1-min segments

Table 9.13: Comparison of the obtained results to results found in the literature. SBP: Systolic blood pressure. DBP: Diastolic blood pressure. MAP: Mean arterial pressure.

Study	**Mean Absolute Error (mmHg)**		
	SBP	**DBP**	**MAP**
Slapničar et al. (2018)	4.47	2.02	-
Slapničar et al. (2019)	9.43	6.88	-
Leitner et al. (2019)	3.43	1.73	-
Athaya and Choi (2021)	3.68 ± 4.42	1.97 ± 2.92	2.17 ± 3.06
Aguirre et al. (2021)	14.39 ± 0.42	6.57 ± 0.20	8.89 ± 0.10
This study (critically-ill subjects, 5-min)	4.74 ± 2.33	1.78 ± 0.14	2.55 ± 0.78
This study (critically-ill subjects, 1-min)	10.93 ± 0.21	4.88 ± 0.11	6.08 ± 0.14
This study (healthy subjects, 5-min)	1.22 ± 0.09	1.54 ± 0.17	1.07 ± 0.06
This study (healthy subjects, 1-min)	4.68 ± 0.49	6.86 ± 0.72	4.06 ± 0.44

from critically-ill patients did not show enough reliability according to the AAMI standards, with minimum average errors of 6.08 ± 0.14, 10.93 ± 0.21 and 4.88 ± 0.11 mmHg for MAP, SBP and DBP respectively. This can be also explained by the slow-changing nature of PRV, which does not reflect changes in a reliable manner in windows shorter than 5-min. Although the sample size in the healthy subjects experiments was small and hence the results are not necessarily generalisable, this same behaviour is observed, where results obtained using 5-min segments showed better performance than those obtained using 1-min segments. All MAE's become smaller and achieve AAMI's standards except for the estimation of SBP using 1-min segments when healthy subjects' signals were analysed, with errors below 2 mmHg for the estimation of all three BP values when using PRV features selected from 5-min PPG signals. Adding additional PPG-based features to the 1-min PRV features may also result in better performance with shorter signal windows. It is important to notice as well that SBP tends to have higher errors than MAP and DBP in both critically-ill and healthy subjects. This could be related to the autonomic regulation of systolic and diastolic pressures, or to the variability of these values. Further analysis is needed to better understand these differences.

Other studies have aimed to use PRV to estimate BP values. Gaurav et al. (2016) extracted PRV- and PPG-based features from PPG signals obtained from the MIMIC II database (Saeed et al. 2011) and applied artificial neural networks to estimate systolic and diastolic blood pressure, with mean absolute errors of 4.47 and 3.21 mmHg. Fong et al. (2019) obtained PPG signals using a multi-sensor system located at the wrist, and extracted PRV, PPG and PTT features in order to estimate BP values using support vector machines. They obtained a mean absolute error of 7.29 ± 5.3 mmHg for SBP, and 5.01 ± 4.1 mmHg for DBP.

The results obtained in the present study, using ML algorithms based only on PRV features, are comparable to what has been reported in these studies. Moreover, Bland-Altman analysis from results obtained from critically-ill subjects indicate a small bias between estimated and real values, with limits of agreement around ± 5 mmHg for MAP and DBP, and around ± 10 mmHg for SBP; and Wilcoxon rank sum tests showed that estimated and real values did not have statistically significant differences. It is important to remark that these results, including the Bland-Altman plots, were obtained using data from all segments, not for individual subjects, which probably improves the performance of the algorithms. Nonetheless, and as a proof-

of-concept study, these results show that PRV might be used for the estimation of BP, although SBP tends to show higher errors than MAP and DBP.

9.4.3 Limitations of the study

This study has some limitations that need to be highlighted. First, the critically-ill patients signals were obtained from an available database from Physionet. Thus, several variables were not controlled for, and although all subjects were hospitalised in an intensive care unit, their diagnosis was unknown, which may have affected the results. In the case of the signals obtained from healthy volunteers, these were acquired from a small, relatively homogeneous sample and under controlled circumstances, which decreases the sources of error and makes these results less generalisable.

Another limitation involves the stride of 10 s used to separate the segments, which might have been too short to reflect BP changes. This was done to produce a larger database, but the performance might be improved using a different overlap. Also, although the segments were randomised, the introduction of just 10 s of stride could imply the use of very similar segments in the training and testing dataset and hence increase the risk of overtraining. In the classification task, another limitation of the study involves the classification of segments in each BP state, specifically determining exactly which state was predominant in each segment, especially in subjects who exhibited two or more BP states during the entire recording. Although outliers for each PRV index were corrected, a larger number of available segments might have helped to mitigate this effect. Also, the balancing of the dataset could have affected the results. Future studies should aim to alleviate the class imbalance problem using more robust strategies, such as applying gradient boosting techniques.

Finally, it is also worth noting that some of the extracted indices were not optimised, especially the non-linear indices. Using an optimisation procedure for these indices might lead to different results from those obtained in this study. Moreover, additional non-linear indices, such as slope entropy and state space correlation entropy, could prove useful for this application and might yield different results. It might be worth evaluating the behaviour of such indices in future studies; however, there is no standard for the extraction of this type of features for PRV analysis, which make it hard to select which non-linear features to use for a given application. The extraction of different non-linear indices could lead to different and possibly better results.

9.5 Summary

The aim of this study was to evaluate the applicability of PRV-derived features for the classification and estimation of BP values using ML algorithms, using data obtained from critically ill patients and healthy subjects. The results obtained show promise for the use of PRV for both tasks, although several aspects should be further optimised in order to increase performance, especially for the classification of BP states. Specifically, the identification of hypertensive events in critically ill subjects using the proposed methodology shows promise and could be a useful tool for a continuous, non-invasive monitoring of cardiovascular diseases that may arise due to the presence of hypertensive events.

Also, this study shows that using only PRV-based features, BP can be reliably estimated. This is a promising result, since PRV features are easily computed from PPG signals, which can be continuously obtained in real-life scenarios, including intensive care units. In future studies, the applicability of these technique should be evaluated in less homogeneous samples and in daily-life scenarios. Moreover, additional PRV-based features, as well as other machine learning algorithms, should be evaluated for increasing the performance of the classification of blood pressure states using only PRV information, which could lead to a non-invasive, non-intrusive, continuous, and low-complexity system for the identification of blood pressure using wearable devices. Future studies should aim to evaluate how applying more complex techniques for the extraction of features from PPG and PRV can increase the performance of the models for the classification and estimation of blood pressure, and to optimise the duration of the segments and their overlap for delivering better and more instantaneous results.

From this chapter and the results found in Chapters 7 and 8, it can be concluded that PRV does not always behave exactly the same as HRV, that haemodynamic changes alter the relationship of these two variables, and that PRV could be used to assess certain haemodynamic variables, such as blood pressure. However, the origin of PRV and its differences to HRV are still not clarified. In the next chapter, the results from an in-vitro study performed to evaluate PRV and its relationship with some haemodynamic variables in the absence of HRV are presented and discussed.

Chapter 10

In-vitro Study to Assess Pulse Rate Variability in the Absence of Heart Rate Variability

10.1 Aims and objectives

It has been concluded from previous studies that PRV could be used for assessing cardiovascular variables such as blood pressure (Chapter 9), and that, although HRV and PRV show similar trends under haemodynamic changes, they should not be considered to be the same, since the former tends to over- or underestimate some of these indices and to a different extent depending on the cardiovascular state (Chapters 7 and 8). However, it is difficult to understand the origin of these differences in data obtained from in-vivo studies, since both HRV and PRV relate to the changes in the duration of cardiac cycles, but are measured using signals with different origins (Schäfer & Vagedes 2013).

In an attempt to understand the differences between HRV and PRV, Constant et al. (1999) evaluated how PRV changed in children with pacemakers set to a fixed heart rate. They observed that PRV was present even in the absence of HRV and concluded that the differences between PRV and HRV arise from respiratory patterns and Pulse Transit Time (PTT). In 2014, Pellegrino et al. aimed to understand the relationship between PRV and HRV in rabbits during ventricular pacing, to drive HRV to zero, and cardiac autonomic blockade, using atropine (cardiovagal blockade), metoprolol (sympathetic blockade) and both drugs (dual blockade)

to understand the autonomic substrates of HRV and PRV. Their results showed that: (a) PRV remained non-negligible even during ventricular pacing, when HRV was almost completely eliminated, and HRV and PRV behaviour was not related in this scenario; (b) time-domain indices showed strong correlations between HRV and PRV during cardiac autonomic blockade; (c) LF and HF indices showed a relatively good agreement between HRV and PRV during cardiac autonomic blockade, but with a consistent overestimation of HF and TP values, while normalised indices and LF/HF showed very poor accuracy and precision, especially during atropine and dual blockade and most likely because of the intrinsic PRV when HRV is decreased; and (d) non-linear measures, especially those based on entropy analysis, showed poor agreement and low correlation between HRV and PRV during any of the conditions of autonomic blockade. Although they did not obtain PRV from human PPG signals, but from an invasive arterial pressure sensor placed into the abdominal aorta of rabbits, their results showed that PRV contains different information that may explain its differences to HRV; and they hypothesized that these differences must come from changes in pre-ejection time, i.e., the time after ventricular depolarization and before opening of the aortic valve and which is a function of contractility, preload and afterload, or in PTT, which changes due to pulse pressure and arterial elasticity.

It can be difficult to perform studies to understand the effects of specific parameters on PRV changes and its relationship with HRV in healthy volunteers. Hence, in this chapter, the development of an in-vitro setup for the simulation of the upper body circulatory system is proposed, from which PPG signals can be acquired while blood pressure and flow are modified by changing the stroke rate of a commercial pump that replicates the activity of the heart, but without the effects of autonomic modulation, i.e., in the absence of HRV. Moreover, given the limitations of this in-vitro setup, the effects of respiration are also not present. This allows for the investigation of the effects of changing only cardiovascular parameters on PRV assessed from the obtained PPG signals. It was hypothesised that PRV indices would be present even in the absence of HRV changes, and that they are affected both by blood pressure and blood flow changes.

10.2 Materials and methods

10.2.1 In-vitro setup

An in-vitro setup was built for the simulation of the upper-body circulatory system, which includes the heart, the arteries and the venous return, as well as the simulation of tissue for the acquisition of optical signals from this setup, including the use of artificial blood and the simulation of skin layers in the points of PPG measurement.

10.2.1.1 Upper body circulatory rig

Figure 10.1 shows a diagram of the designed rig that simulates the upper-body circulatory system. This consists of a commercial pulsatile pump (PD-1100, BDC Laboratories, United States) that replicates heart activity; silicon tubes with varying diameters and wall thicknesses that simulate arterial segments and venous return; and a tank that mimics the venous blood reservoir. Table 10.1 summarises the characteristics of arterial and venous segments replicated in this setup, which were selected according to average human vessel sizes reported in the literature (Dotter et al. 1950, Poonam et al. 2013, Chakravarthi et al. 2014, Nasr 2012).

10.2.1.2 Radial and deep-palmar arch phantoms

Since the aim of this study was to acquire and analyse PRV information obtained from PPG signals from this in-vitro model, two independent phantoms were used to simulate the points of measurement of these PPG signals. The inclusion of the

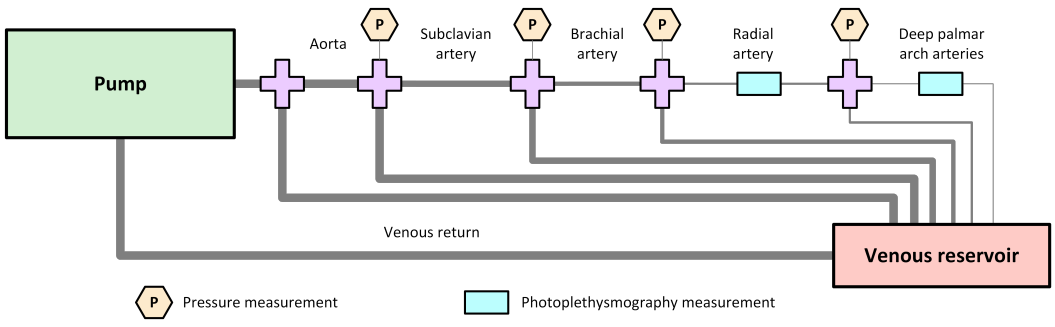

Figure 10.1: Diagram of designed rig for the simulation of upper-body circulatory system, which consists of a commercial pump that replicates heart activity; aorta, subclavian, brachial, radial and deep-palmar arch arterial segments; a venous reservoir; and a single vein replicating the venous return. Pressure sensors are placed to measure the pressure of the fluid flowing through the system, and silicon, custom-made phantoms are used for the placement of photoplethysmography (PPG) sensors.

Table 10.1: Characteristics of arterial and venous segments replicated on the in-vitro setup.

Vessel segment	Length (mm)	Inside diameter (mm)
Aorta	120	20
Subclavian artery	80	10
Brachial artery	200	4
Radial artery	220	2.3
Deep palmar arch arteries	250	1.6
Venous system	220	2.3

phantoms allows a better positioning of PPG sensors and a more accurate replication of tissue surrounding the arteries.

Figure 10.2 illustrates the design of the built phantoms. In both cases, the phantoms consist of a clear, hollow cuboid with length of $L = 60mm$, width of $15mm$, height of $H = 5mm$, and wall thickness of $T = 1.5mm$. These cuboids were 3D printed using clear resin (Formlabs, Somerville, MA, USA) and filled with clear polydimethylsiloxane (PDMS) with 3% catalyst, which has been shown to replicate mechanical properties of skin (Nomoni et al. 2020), and a single custom-made tube was passed through each of the phantoms, to replicate the radial and deep-palmar arch arteries. In the case of the radial artery, this was located closer to the edge of the phantom, since the radial artery is relatively superficial in the wrist. Hence, $x_1 < x_2$ for the radial phantom. On the contrary, and since the deep palmar arch phantom is replicating a finger, the vessel passing through this phantom was located aproximately in the vertical center of the cuboid, with $x_1 = x_2$. In both cases, the inner diameters d_r and d_p have the values selected and shown in Table 10.1. The vessels used for the simulation of these arterial segments were custom-made following the methodology proposed by Nomoni et. al. (Nomoni et al. 2019, 2020).

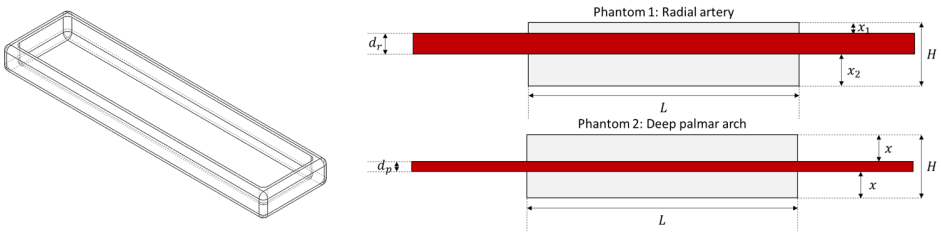

Figure 10.2: Design of phantoms for replicating tissue and positioning photoplethysmographic sensors

10.2.1.3 Artificial blood

In order to be able to acquire PPG signals from this in-vitro system, it was necessary to produce a fluid that simulates some of the optical properties of blood. This was done using deioinized water, Indian ink, phosphate-buffered saline (PBS) and a cyan die (Epson 102 cyan ink, Epson, Japan). The amount of each of these components were determined according to the volume of Indian ink, V_{ind}. The volume of deionized water, V_{H_2O} used was determined as shown in (10.1), while the amount of PBS, m_{PBS}, and the volume of cyan ink, V_{cyan}, were determined according to (10.2) and (10.3), respectively. This recipe was based on the work presented by Akl et al. (2012).

$$V_{H_2O} = \frac{100V_{ind}}{0.226} \tag{10.1}$$

$$m_{PBS} = 98.9V_{H_2O} \tag{10.2}$$

$$V_{cyan} = \frac{4.17V_{H_2O}}{100} \tag{10.3}$$

The optical spectrum of this fluid were verified using a UV/VIS/NIR spectrophotometer (Lambda 1050, PerkinElmer, United States), with which the absorbance of the fluid at different wavelengths was assessed. This artificial blood was expected to have a green/blue colour which would increase the absorbance in red and infrared regions of light.

10.2.1.4 Pressure and photoplethysmography measurements

As illustrated in Figure 10.1, several pressure measurements were obtained in the system. Pressure sensors (PRESS-S-000, PendoTECH, United States) were connected to the tubing via plastic Luer connectors. The readings of these pressure sensors were acquired using a data acquisition card (NI cDAQ-9178, National Instruments, United States) connected to a computer in which a LabVIEW^{TM} (National Instruments, United States) Virtual Instrument (VI) was running.

Simultaneously, two modified commercial neonatal PPG probes (Solaris Medical Technology Inc., United States) were placed on the developed phantoms and connected to a ZenPPG, a dual-wavelength, dual-channel research PPG acquisition and

processing system developed in the Research Centre for Biomedical Engineering at City, University of London (Rybynok et al. 2012, Budidha et al. 2018). The PPG signals were also acquired using a data acquisition card (NI USB-6162, National Instruments, United States) and the same LabVIEW^{TM} VI. In this VI, signals were acquired, visualised and stored for offline processing, and was also used to set the currents going through the red and infrared LEDs in the commercial PPG probes to a value around 30 mA.

10.2.1.5 Setup validation

Cardiac output (CO) has a direct relationship with stroke rate (SR) and stroke volume (SV), as shown in (10.4). As explained by Kumar et al. (2019), SV refers to the volume of blood ejected from the ventricle with each heartbeat and depends on the difference between end-diastolic (EDV) and end-systolic volumes (ESV), and is decreased as heart rate increases due to shortening of diastolic filling time.

$$CO = Q = SR \times SV \tag{10.4}$$

Moreover, blood pressure (BP) can be described as the ratio between CO and the compliance (C) of the system (10.5). Hence, BP can be described in terms of SR and SV, and is expected to increase if CO increases.

$$BP = \frac{CO}{C} = \frac{SR \times SV}{C} \tag{10.5}$$

Therefore, the behaviour of the in-vitro setup was assessed by changing stroke rate (SR) and target flow (TF) of the pump, which changes SV. Modifying these two variables, changes in cardiac output (CO) can be controlled and the measured pressure should be modified. SR was changed from 60 beats per minute (bpm) to 180 bpm in steps of 30 bpm, while TF was changed from 1 L/min to 5 L/min, in steps of 0.5 L/min. The mean pressure at each measuring location was assessed to evaluate the changes in BP as SR and TF are modified, while HR was measured from both pressure and PPG signals. Finally, SV values were assessed by extracting the maximum value of the pattern used to drive the pump. The pattern used was the built-in pattern recommended by the pump manufacturer.

10.2.2 In-vitro experiment

Since the main aim of this study was to determine the relationship between PRV and haemodynamic changes in the absence of HRV, a experiment was carried out to evaluate the effects of changing stroke rate and target flow on PRV indices.

10.2.2.1 Experimental protocol

A experimental protocol was established to evaluate the effects of changing stroke rate and target flow on PRV indices. Stroke rates were changed from 60 to 180 bpm with 30 bpm steps, while target flow was increased from 1 to 5 L/min, in steps of 0.5 L/min. This results in a total of 45 combinations. Target flow was kept stable until data with all stroke rates was acquired, and then target flow was increased. 10-min of data was acquired from each combination of factors, and this was repeated two times.

As was mentioned previously, a LabVIEW^{TM} VI was employed to acquire PPG and pressure signals. A sampling rate of 2 kHz was used for acquiring data. Pressure measurements were taken from the aortic, subclavian, brachial, radial and deep palmar arch (DPA) arterial segments, while PPG signals were obtained from the phantoms located at the radial and DPA vessels.

Before acquiring the data, the baseline values of pressure measurements without any pumping activity were acquired to obtain the offset of each of the pressure sensors, which were then used to convert this data from voltage units to pressure units (mmHg), considering a sensitivity of 3.85 psi/mV for the pressure sensors.

10.2.2.2 Data processing

The acquired signals were processed offline using MATLAB® (version 2020a). Initially, pressure signals were converted from voltage to millimeters of mercury (mmHg), as explained above. Then, both PPG and pressure signals were resampled to 256 Hz using linear interpolation, and filtered using a second order, low pass Butterworth filter, with cutoff frequency of 20 Hz.

Only red PPG signals were used for further analysis in this study. These were segmented into 5 min portions, with a stride of 30 seconds between consecutive segments. Then, interbeat intervals (IBIs) were identified using D2Max (Elgendi et al. 2013) and, as was done in previous studies, IBIs were corrected according to

their length. The *a* fiducial point was used to extract PRV trends from the portioned signals and time-domain (AVNN, SDNN, RMSSD, NN50 and pNN50), frequency-domain (VLF, LF, HF, TP, LF/HF, nLF, nHF, cLF_x, cLF_y, cHF_x, cHF_y, cTP_x, cTP_y and SpEn), Poincaré plot (S, SD1, SD2, SD1/SD2 and COM), detrended fluctuation analysis (A1 and A2) and entropy indices (BSE, SSE, ApEn, SampEn and MSE) were extracted from these PRV trends.

Pressure signals were also segmented into 5 min intervals with a 30 s stride. Peaks and valleys were detected from these signals, and the mean systolic (SBP) and diastolic (DBP) pressure per each 5 min segment and each measurement location were determined as the mean amplitude of the peaks and onsets, respectively. Mean pressure (MAP) was calculated as shown in (10.6).

$$MAP = \frac{1}{3}SBP + \frac{2}{3}DBP \tag{10.6}$$

10.2.2.3 Statistical analysis

Figures were generated using MATLAB® (version 2020a) and statistical analyses were performed using RStudio (version 1.4.1717). Two independent analyses were performed to evaluate the effects of changing haemodynamics on PRV indices. Firstly, linear regression was used to evaluate the linear relationship between pressures measured from each location, and PRV indices. This was done to assess if a linear model could explain the relationship between BP and PRV. Secondly, a factorial analysis was performed to assess if changing SR and TF had an effect on PRV indices. This was done to evaluate if these changes had a significant impact on PRV, even in the absence of HRV. Since data did not follow a normal distribution, as was verified with the Lilliefors test, Box-Cox transformations were applied by finding the optimal lambda for each index. In all cases, a level of significance of 5% was considered.

10.3 Results

10.3.1 In-vitro setup

Figure 10.3 shows the constructed rig to simulate part of the upper-body circulatory system. As explained, this system includes a commercial pulsatile pump that replicates the heart activity. This pump can follow different patterns for generating

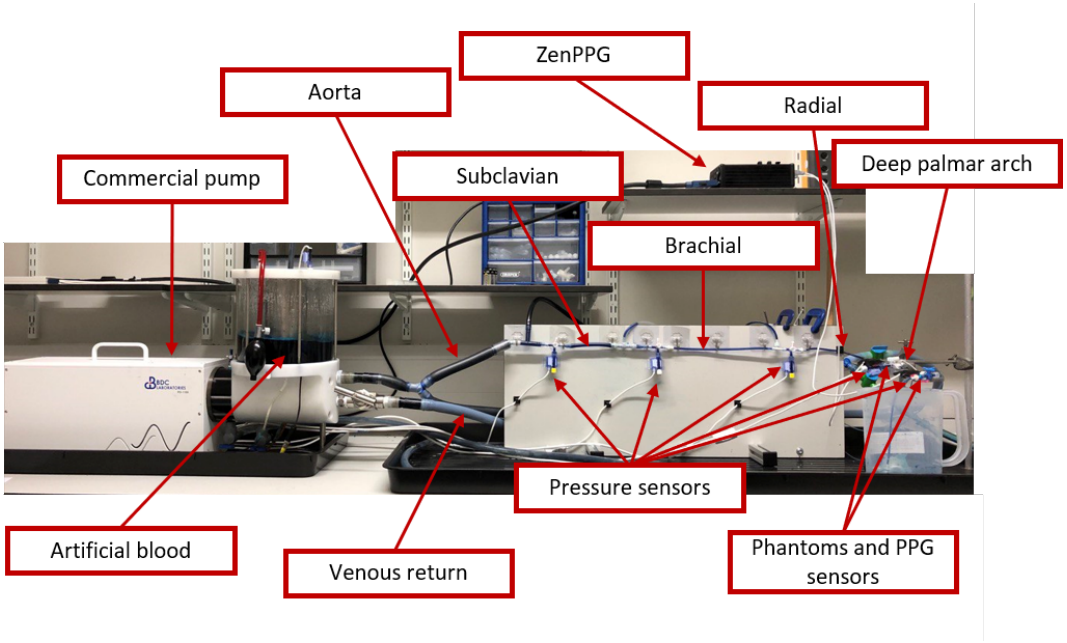

Figure 10.3: Constructed rig for the in-vitro experiment. This consists of a commercial pump that replicates heart activity, tubing that mimics arteries and veins from the upper-body circulatory system, and a fluid that have similar optical properties as blood. Pressure sensors and photoplethysmographic (PPG) probes were used to measure the pressure in the tubes and the optical pulsatile signals from two developed phantoms, that model the skin. PPG signals are acquired and processed using a custom-made system (ZenPPG) while pressure information is acquired directly from a data acquisition card.

each cardiac cycle. In this study, the built-in pattern was used, which changes the stroke volume according to the SR and TF (Figure 10.4). Greater stroke volumes can be obtained by decreasing SR and increasing TF.

In order to acquire optical signals such as the PPG, it was necessary to develop a fluid that replicates the optical behaviour of blood, which is referred as artificial blood in Figure 10.3. Figure 10.5 shows the absorbance spectra obtained when the developed fluid was tested using the spectrophotometer. It can be observed that the artificial blood has a peak absorbance at around 610 nm, replicating part of the optical behaviour of real blood. Since the maximum absorbance was observed at this wavelength, the subsequent analysis with PPG signals and PRV information were performed using only this wavelength.

A validation of this setup was performed, to assess if the measured pressure is affected by changes in SR and TF, and if the correct SR can be measured from the optical signals acquired. Figure 10.6 exemplifies the signals acquired from the rig using a SR of 60 bpm and a TF of 3 L/min, while Figures 10.7 and 10.8 show the behaviour of pressure measurements and pulse rate measurement, respectively,

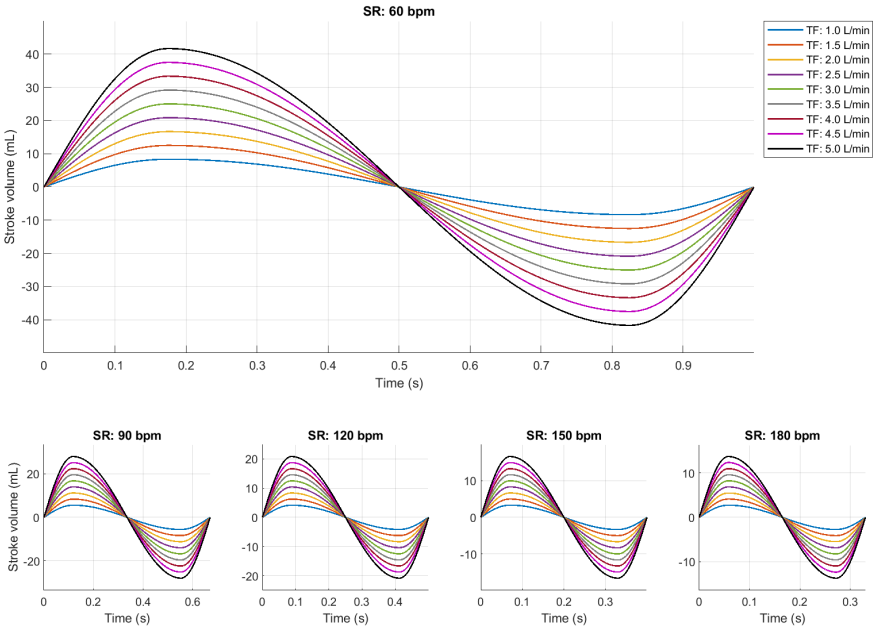

Figure 10.4: Pattern used for controlling the pumping activity of the pulsatile pump. The ejected volume is larger as target flow increases, while it becomes smaller as stroke rate increases.

as SR and TF are modified. As can be observed, the measured pressure signals feature good quality and follow the expected behaviour, i.e. the pressure increases as target flow increases within a same stroke rate, while it decreases when stroke rate is increased. Also, it can be observed that the pressure measured in the aorta is

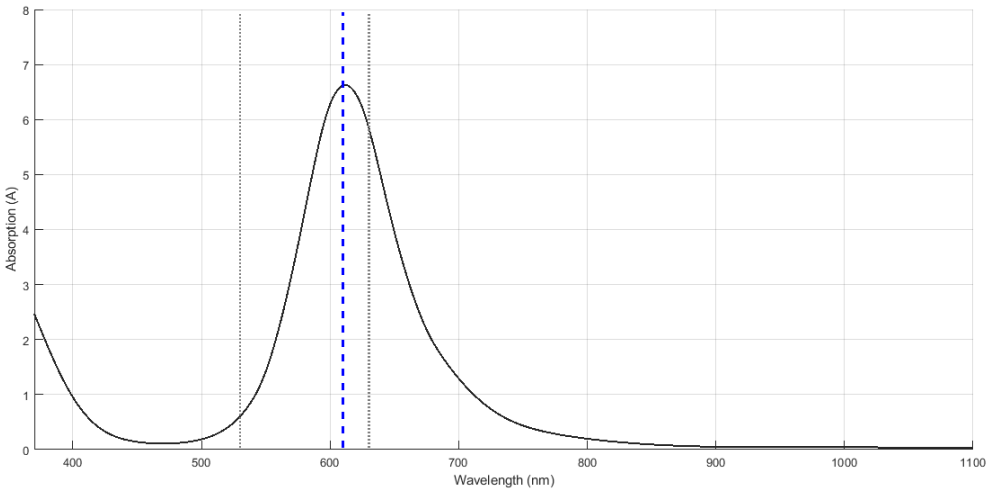

Figure 10.5: Spectrum obtained from the spectrophotometer and the artificial blood. The maximum absorbance was obtained with a wavelength of 610 nm.

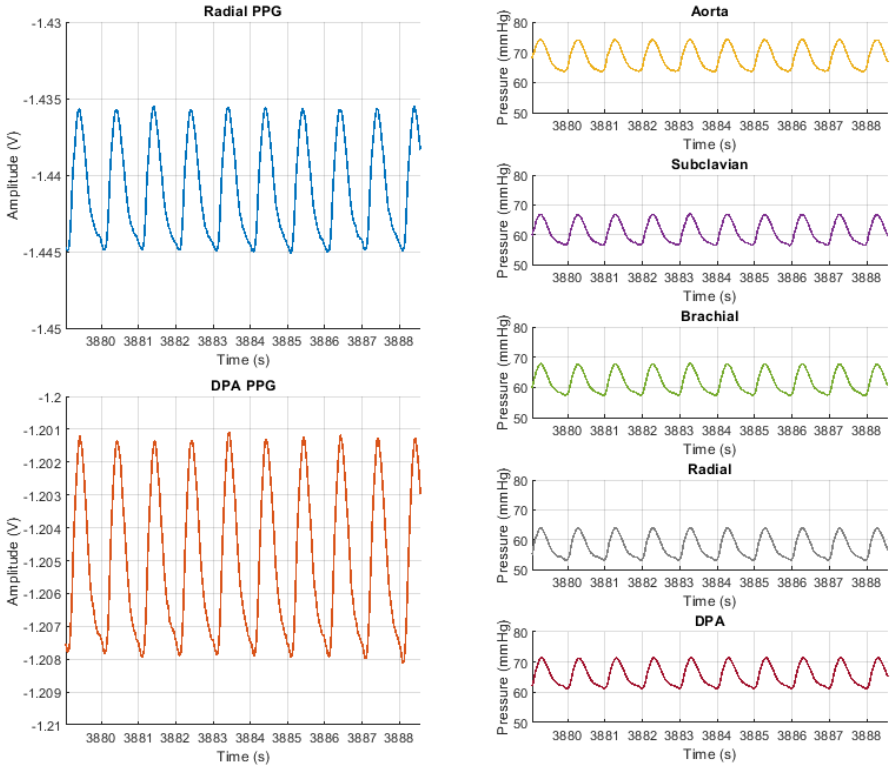

Figure 10.6: Pressure and photoplethysmographic (PPG) signals acquired from the constructed rig when stroke rate was set to 60 beats per minute and target flow was set to 3 L/min. DPA: Deep palmar arch.

greater than the rest of the locations, and becomes lower in the subclavian segment. Then, it starts increasing slightly due to the smaller area and increased resistance in the subsequent arterial segments. From the PPG signals, it can be observed that the pulse rate can be reliable extracted from the signals, although the measurement becomes less reliable with lower stroke volumes, i.e. higher stroke rates and lower target flows.

10.3.2 Pressure and Pulse Rate Variability measurements

Figures 10.9 and 10.10 exemplify the PPG and pressure signals measured under different stroke rates and target flows, respectively. It can be observed that the quality of the PPG signals decreases as the stroke volume decreases, while the pressure values are also diminished. From these signals, the mean pressure value and PRV indices were extracted.

Figure 10.11 summarises the behaviour of systolic, diastolic and mean pressure

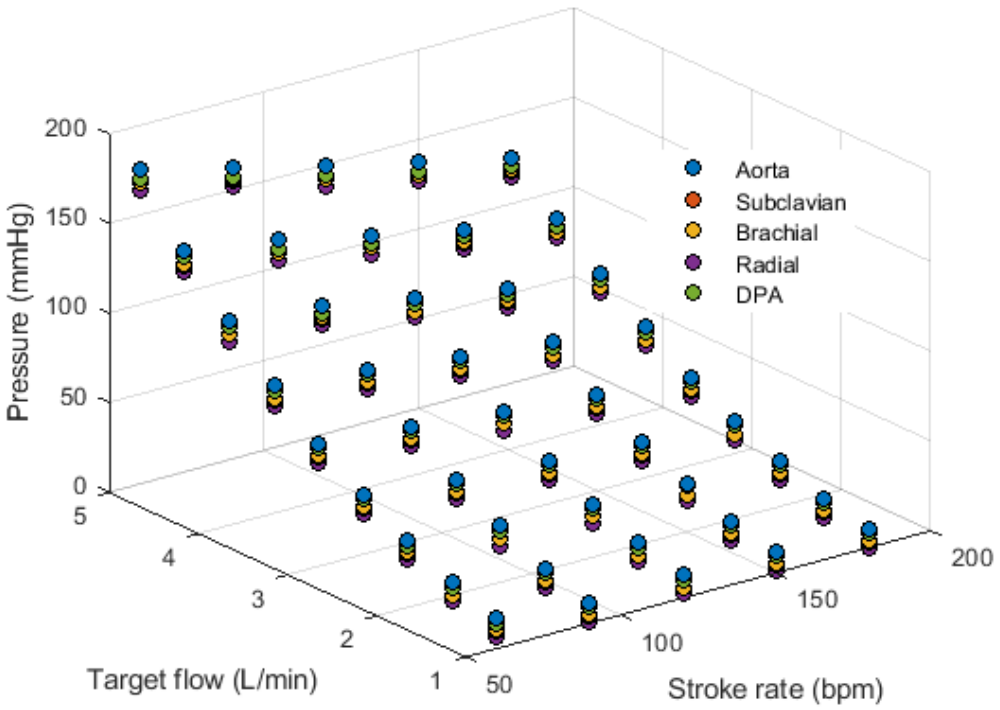

Figure 10.7: Behaviour of mean pressure measured from the aorta, subclavian, brachial, radial and deep palmar arch (DPA) locations while changing stroke rate and target flow. The measured pressure increases as target flow increases within the same stroke rate. At lower target flows and greater stroke rates, pressure values decrease.

measurements extracted from each of the acquired pressure signals during the experiment, while Figures 10.12 to 10.19 show the mean and standard deviation of

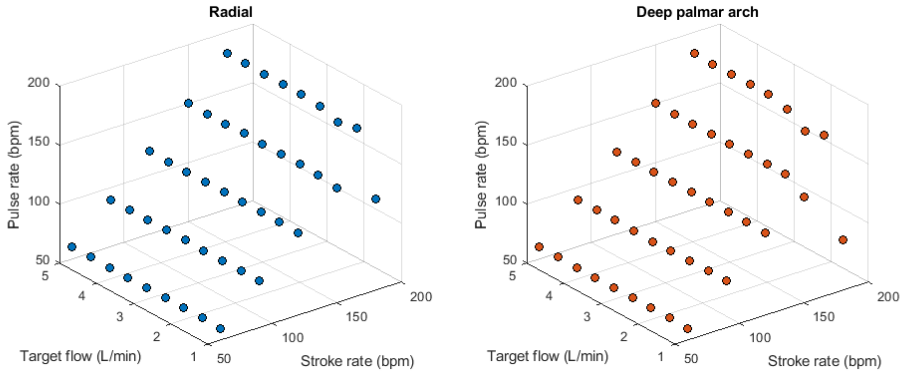

Figure 10.8: Behaviour of pulse rate measured from the radial (left) and deep palmar arch (right) phantoms using photoplethysmographic sensors while changing stroke rate and target flow. As stroke rate increases, the measured pulse rate increases as well. With greater stroke rates and lower target flows, i.e., lower pulse pressure, the quality of the signals obtained from the deep palmar arch phantom is lowered, increasing the errors in the measurement of pulse rate.

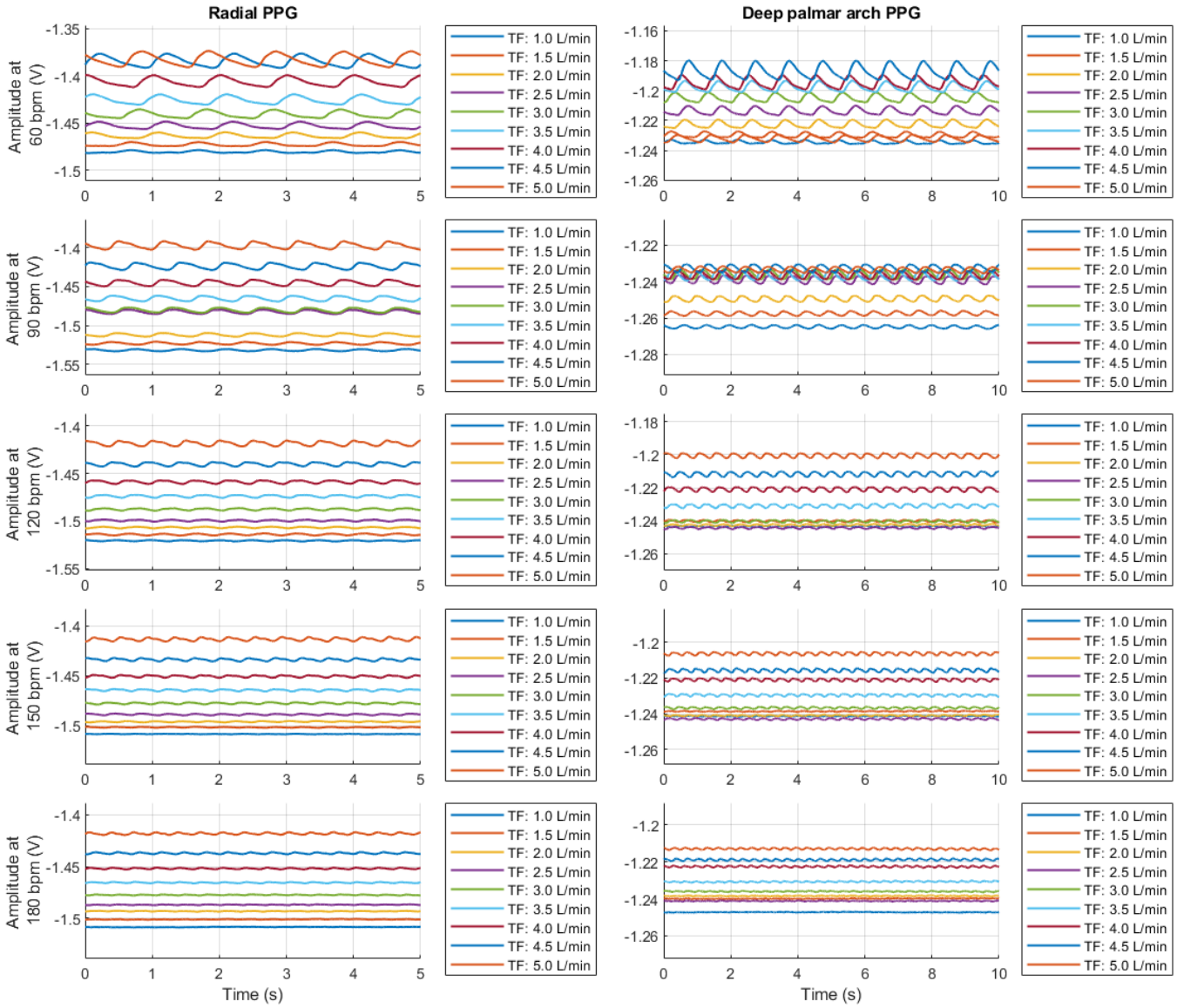

Figure 10.9: Example of photoplethysmographic (PPG) signals acquired from the constructed rig under different stroke rates and target flows. The amplitude of the signals become larger as the target flow increases and the stroke rate decreases, and when measured from the radial PPG phantom.

PRV indices extracted from each of the PPG signals during each combination of SR and TF.

10.3.3 Linear regression between PRV and arterial blood pressure

Linear regression and correlation analyses were done to evaluate if there is a linear relationship between PRV indices and any of the measured pressure values, i.e., systolic blood pressure (SBP), diastolic blood pressure (DBP) and mean pressure (MAP), from any of the measurement locations. The Spearman correlation coef-

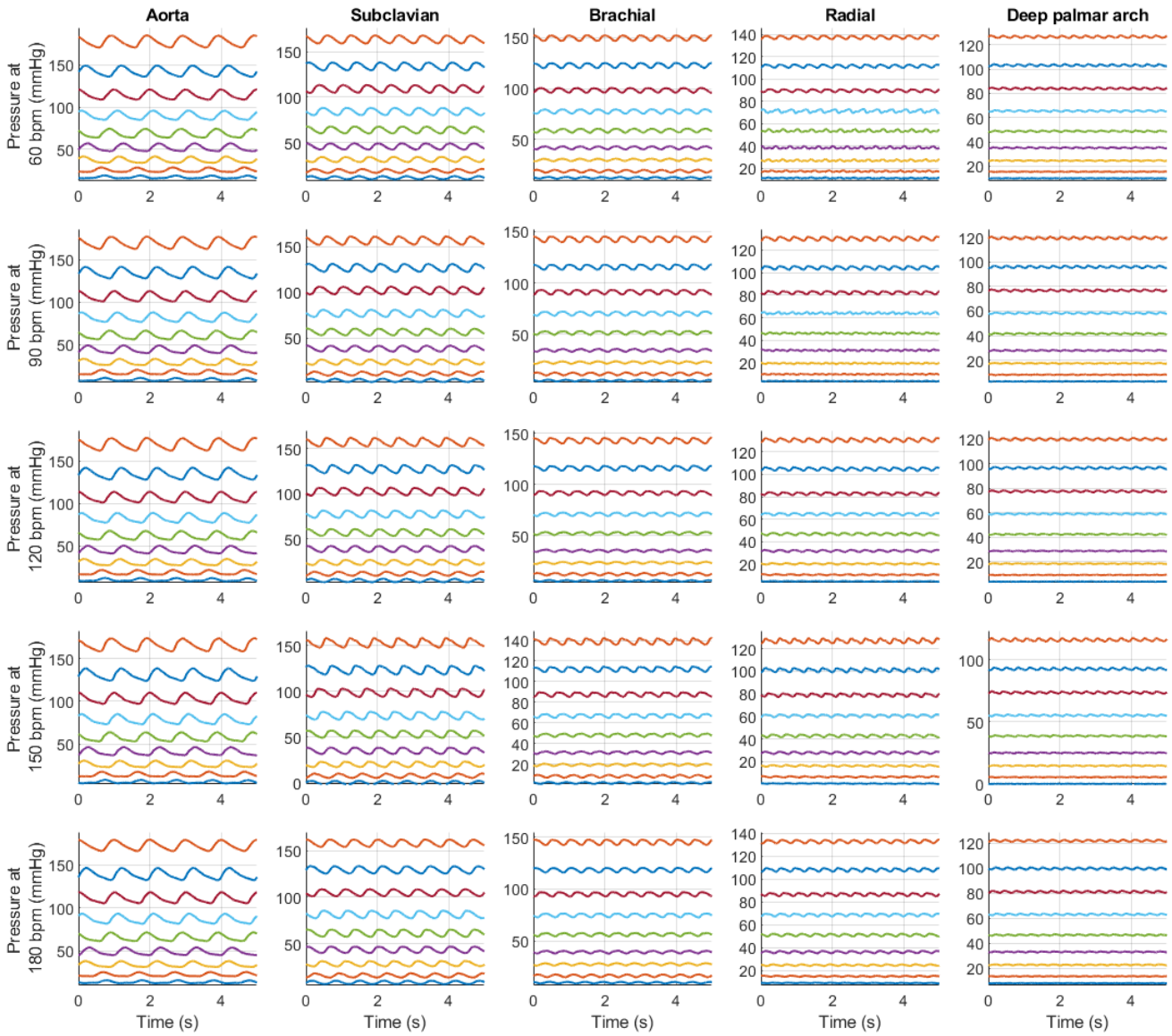

Figure 10.10: Example of pressure signals acquired from the constructed rig under different stroke rates and target flows. The amplitude of the signals become smaller as the pulse travels further away from the pump, and as the target flow decreases and the stroke rate increases.

ficient (ρ) was extracted for each case (Figure 10.20) and a linear model between pressure values and PRV indices was fitted after applying Box-Cox transformations to the data. From these models, the adjusted coefficient of determination (R^2, the greater the better), and the Akaike's Information Criteria (AIC, the lower the better) and Bayesian Information Criteria (BIC, the lower the better) were extracted. Figures 10.21 to 10.23 show the behaviour of these indices. It can be observed that a linear model does not properly reflect changes in PRV indices. However, from the cross-correlation results, some of the indices showed a relatively high inverse relationship (ρ closer to -1), and higher correlation between indices extracted from the

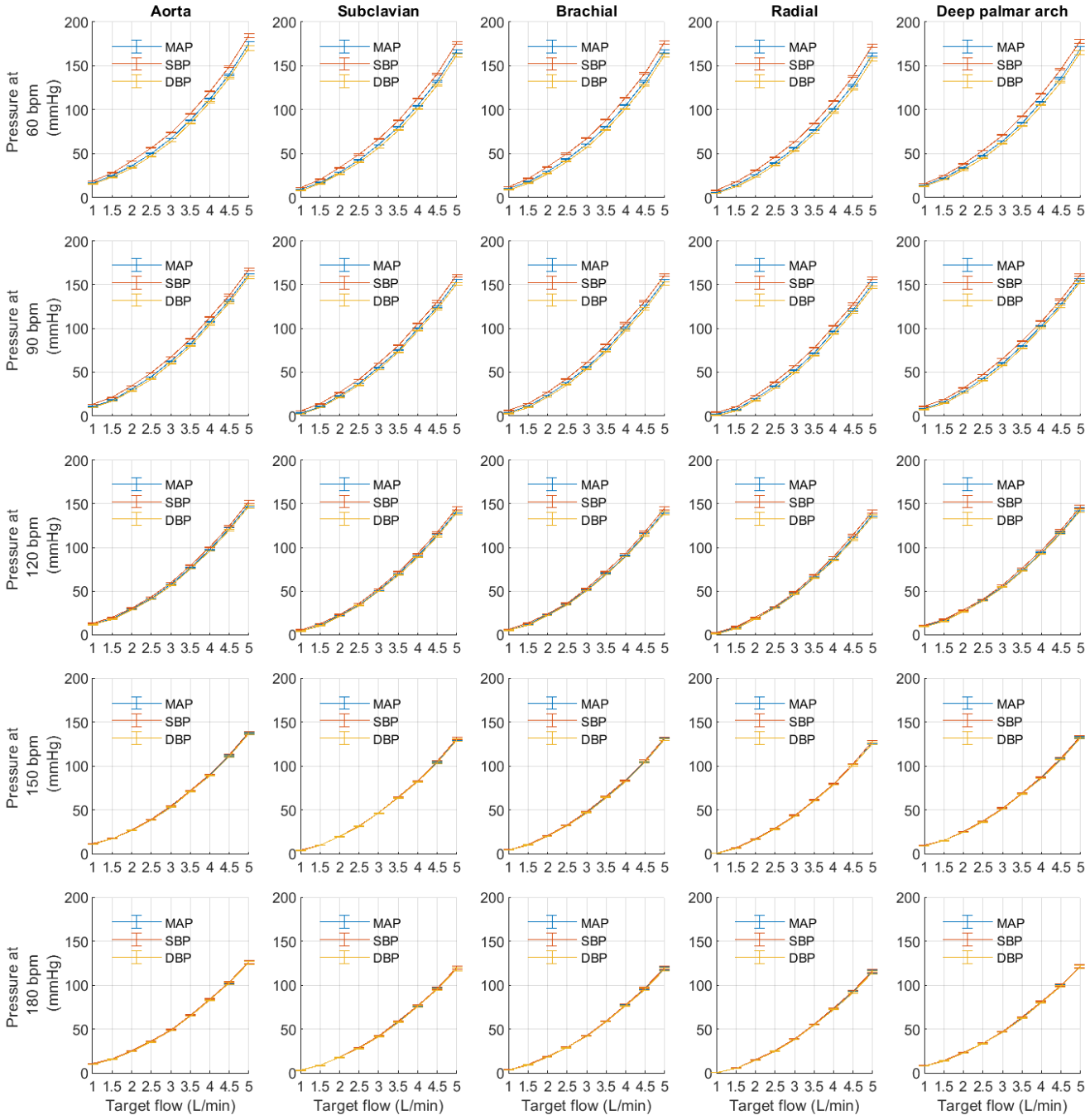

Figure 10.11: Mean and standard deviation of pressure measurements acquired under different stroke rates (SR) and target flows (TF) conditions. MAP: Mean arterial pressure. SBP: Systolic blood pressure. DBP: Diastolic blood pressure. Pressure measurements are higher with lower stroke rates and higher target flows, while the difference between SBP, DBP and MAP become unsignificant as stroke rates increase.

radial PPG and pressure values. Moreover, the three different pressure values have a similar tendency. The R^2 values show a similar trend, in which relationship seems to be stronger between radial-related PRV indices and pressure measurements. It is also worth noting that the behaviour of the linear regression results was very similar

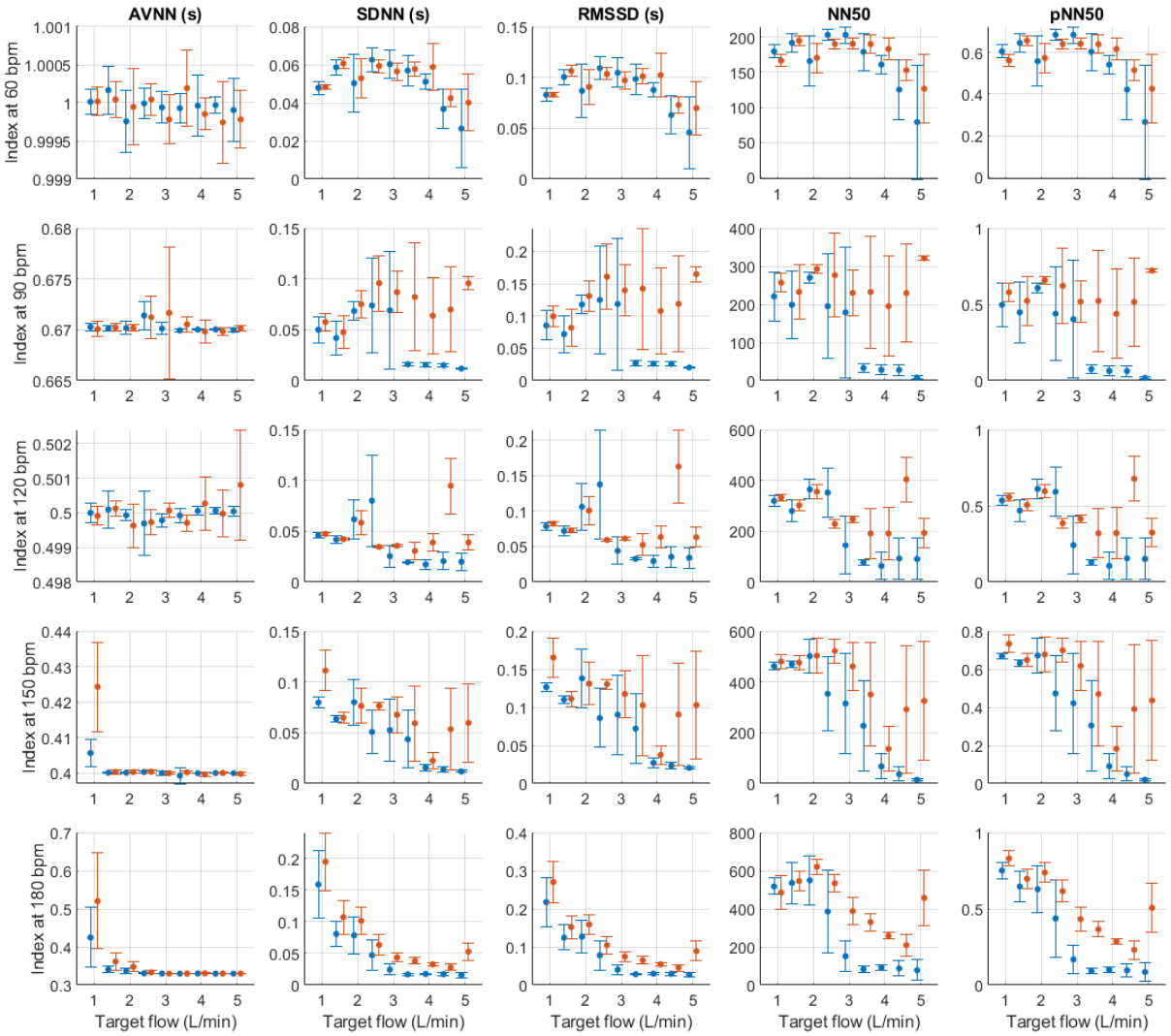

Figure 10.12: Mean and standard deviation of time-domain indices extracted from pulse rate variability under different stroke rates (SR) and target flows (TF) conditions, and measured from the radial (blue) and deep palmar arch (orange) phantoms. Most indices show larger variability when measured from the deep palmar arch phantom, while some indices show clear differences due to changes in stroke rate and target flow.

regardless of the location of measurement of pressure information.

10.3.4 Relationship between PRV and cardiac output changes

Factorial analyses were performed to understand the relationship between each of the extracted indices and SR and TF changes. Figures 10.24 and 10.25 summarise the effect estimates and significance for each of the factors and their combination when PRV indices were extracted from the radial and DPA phantoms, respectively. All interactions showed statistically significant differences, meaning that changing SR and TF has a statistically significant effect on all PRV indices.

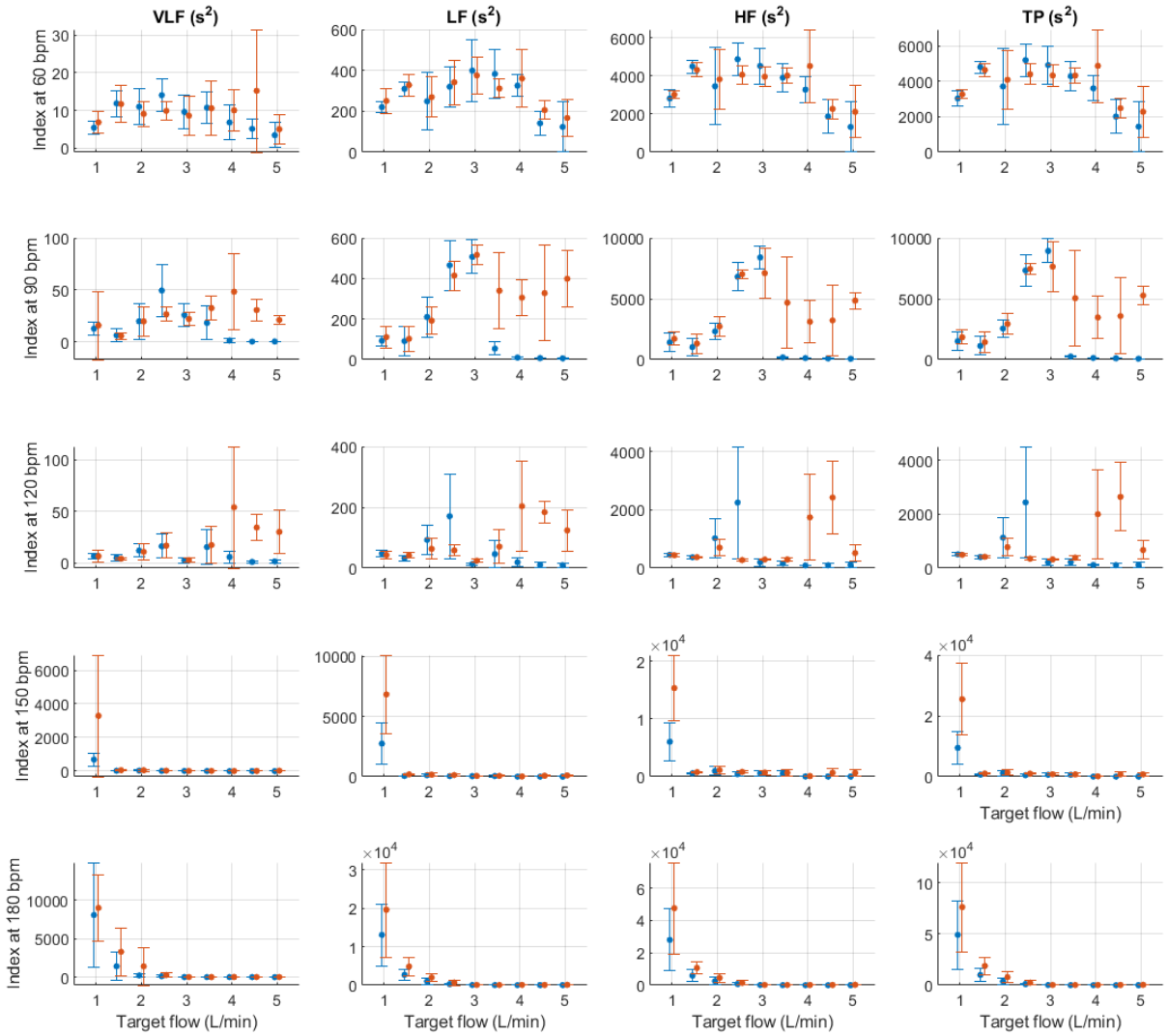

Figure 10.13: Mean and standard deviation of absolute frequency-domain indices extracted from pulse rate variability under different stroke rates (SR) and target flows (TF) conditions, and measured from the radial (blue) and deep palmar arch (orange) phantoms. Most indices show larger variability when measured from the deep palmar arch phantom.

When measured from the radial phantom, some of the indices were clearly more affected by SR, such as AVNN, NN50 and SD2, in which the estimate for the effect of SR is clearly larger than the estimate for the effect of TF and the interaction. Similarly, some indices had larger estimates for TF, such as SDNN, RMSSD, COM, absolute frequency domain indices, and y-coordinate centroid-related indices. A1 is the only index measured from this location that has a larger effect estimate for the interaction between the two factors.

In the case of indices extracted from the DPA phantom, this behaviour changes. SD2, AVNN and NN50 continue to have a remarkable larger effect estimate with changes in SR, while the interactions become stronger in this case, with most indices

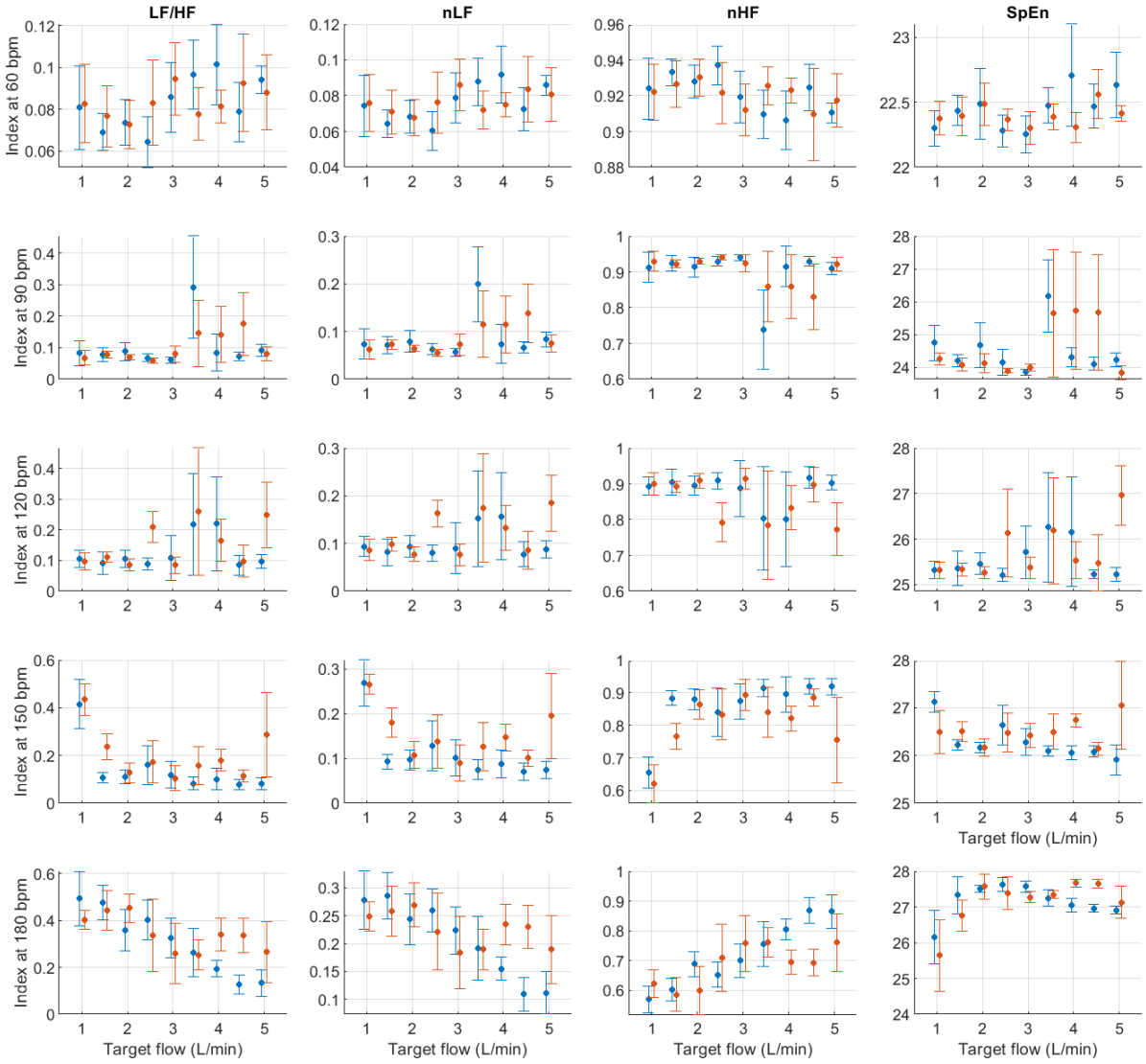

Figure 10.14: Mean and standard deviation of relative frequency-domain indices extracted from pulse rate variability under different stroke rates (SR) and target flows (TF) conditions, and measured from the radial (blue) and deep palmar arch (orange) phantoms. Most indices show larger variability when measured from the deep palmar arch phantom. There are notable differences due to target flow within each stroke rate level.

showing larger effects for these than for the independent factors.

Figures 10.26 to 10.29 show the post hoc analyses for each of the independent factors. Target flow changes induce statistically significant differences especially on time domain, Poincaré plot, DFA and entropy-related indices, both for radial and DPA measured PRV, while relative and centroid-related frequency-domain indices were more affected by TF changes when extracted from signals obtained from the radial phantom. The effects of changing SR showed a very similar behaviour regardless of the point of measurement, with significant differences observed among most levels, especially again on time-domain and non-linear indices.

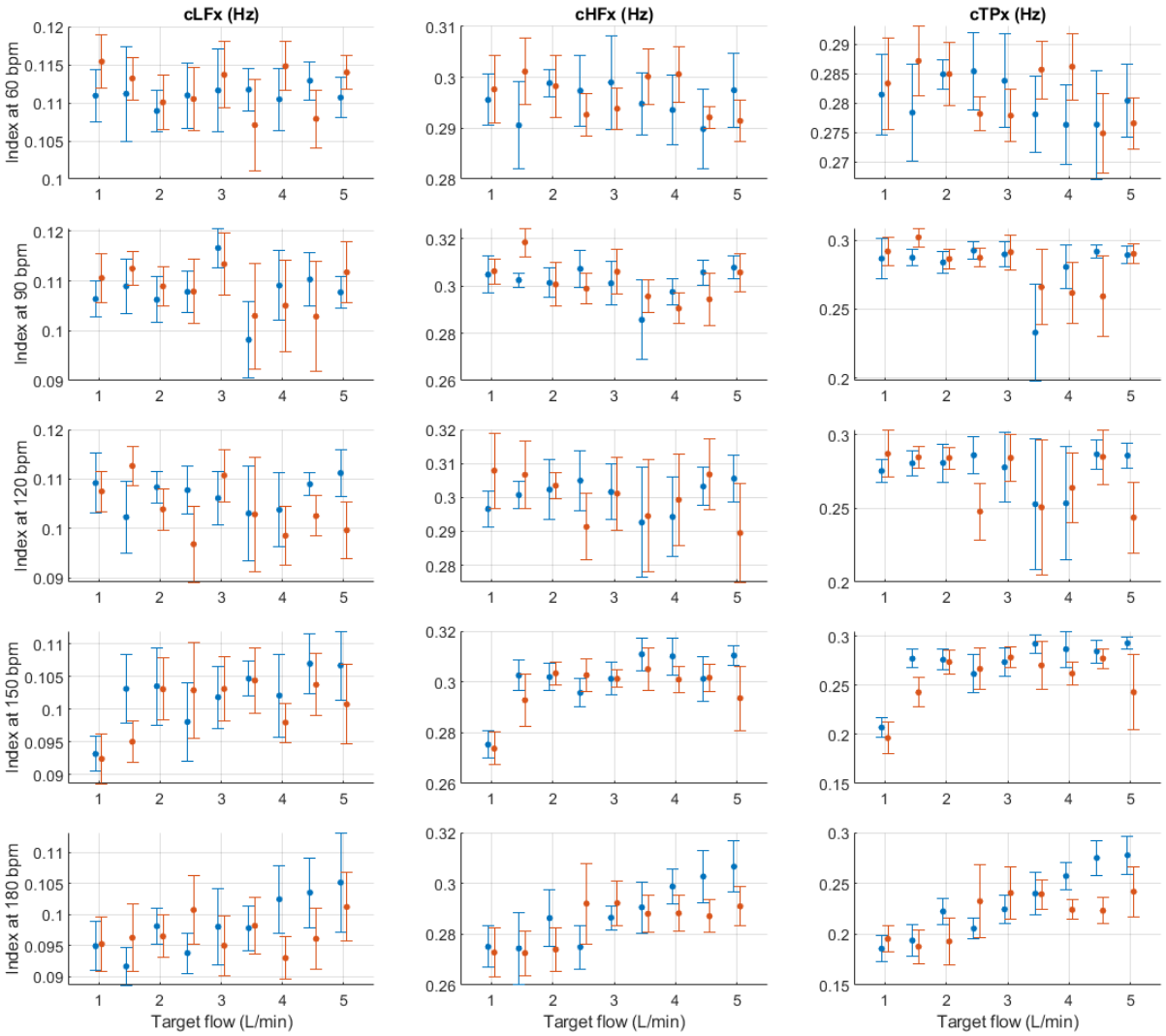

Figure 10.15: Mean and standard deviation of the x-coordinates of the centroid-related indices extracted from pulse rate variability under different stroke rates (SR) and target flows (TF) conditions, and measured from the radial (blue) and deep palmar arch (orange) phantoms. Most indices show larger variability when measured from the deep palmar arch phantom, although this variability is lower than other type of indices.

Figures 10.30 and 10.31 show the results for the post-hoc analyses of the interactions. Both for radial and DPA PRV indices the results follow the same trend. Time-domain, centroid-related frequency-domain and non-linear indices are largely affected by the changes in target flow and stroke rate, while absolute and relative frequency-domain indices showed less significant differences among possible combinations. There were more significant differences as SR and TF increased.

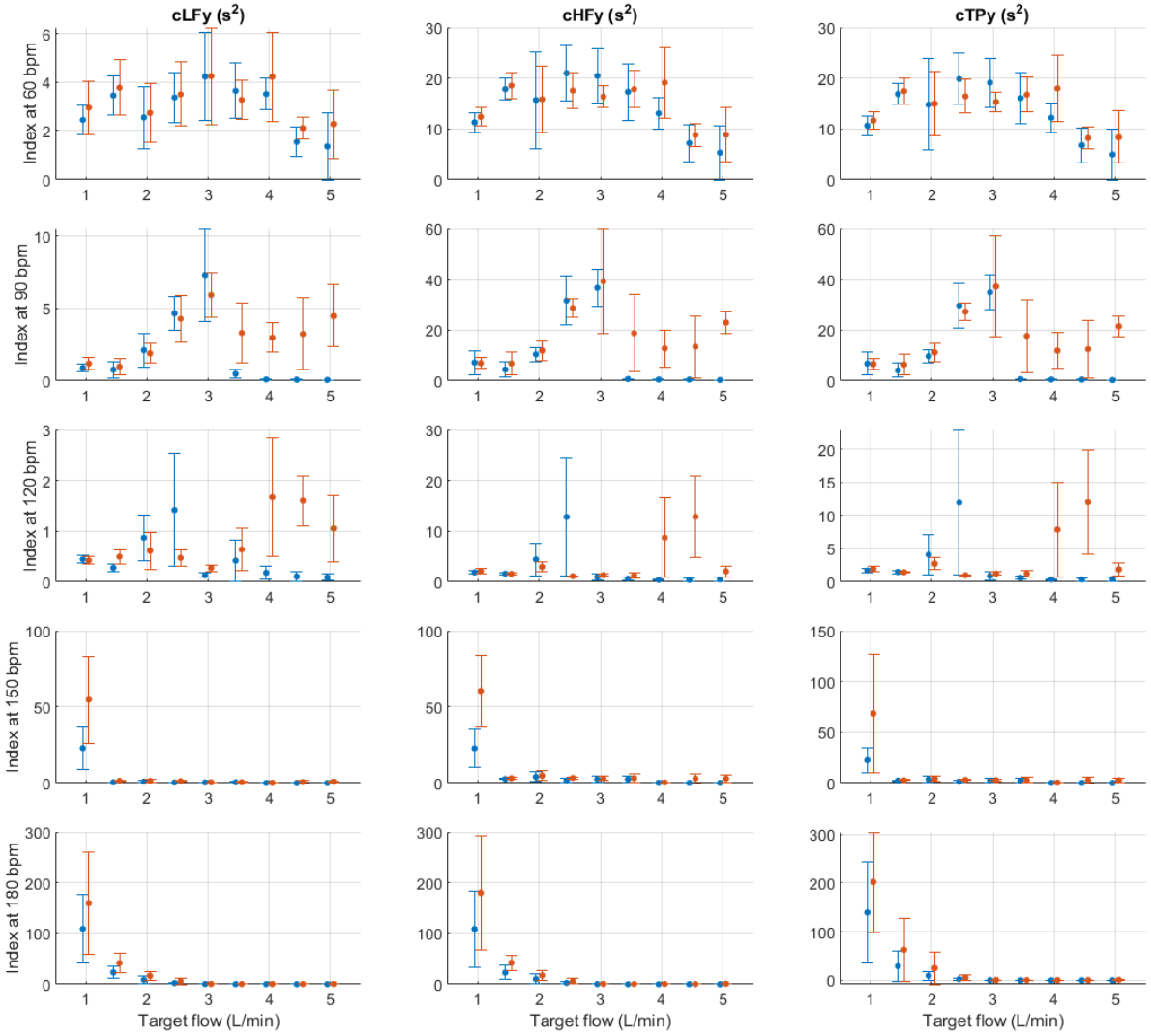

Figure 10.16: Mean and standard deviation of the y-coordinates of the centroid-related indices extracted from pulse rate variability under different stroke rates (SR) and target flows (TF) conditions, and measured from the radial (blue) and deep palmar arch (orange) phantoms. Most indices show larger variability when measured from the deep palmar arch phantom. There is notorious differences in the behaviour of the indices due to stroke rate.

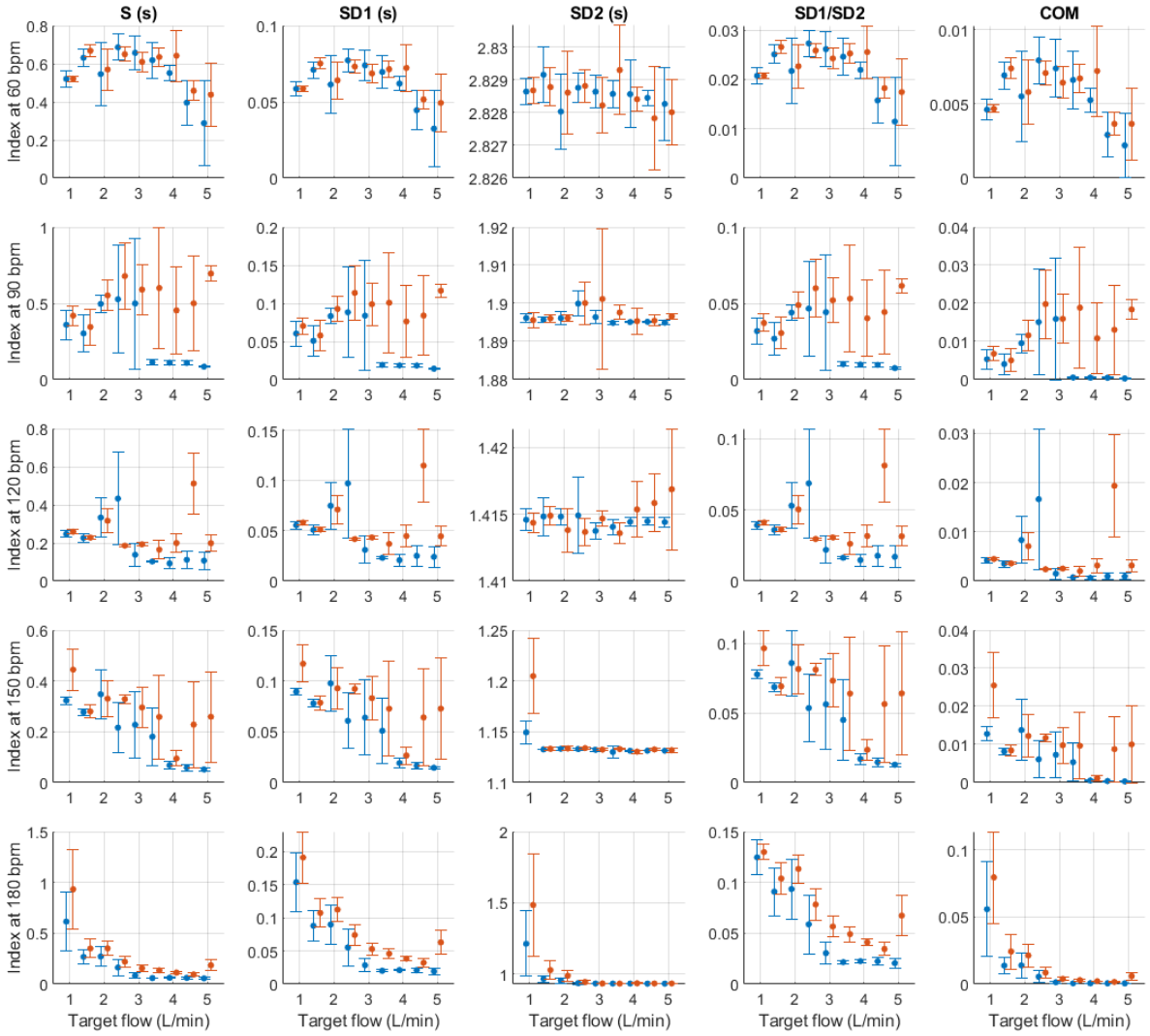

Figure 10.17: Mean and standard deviation of Poincaré plot indices extracted from pulse rate variability under different stroke rates (SR) and target flows (TF) conditions, and measured from the radial (blue) and deep palmar arch (orange) phantoms. Most indices show larger variability when measured from the deep palmar arch phantom. As the stroke rate increases, indices become lower with increasing target flow.

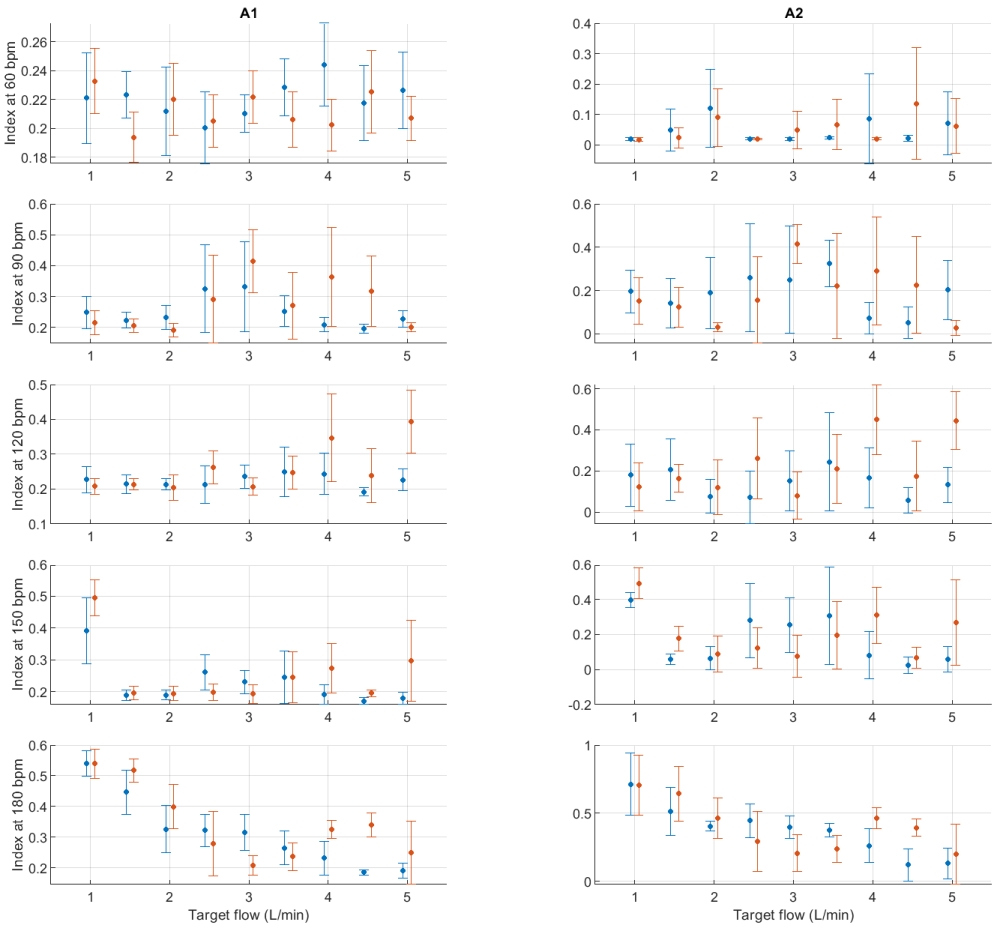

Figure 10.18: Mean and standard deviation of detrended fluctuation analysis indices extracted from pulse rate variability under different stroke rates (SR) and target flows (TF) conditions, and measured from the radial (blue) and deep palmar arch (orange) phantoms. The variability of these indices measured from either phantom is similar.

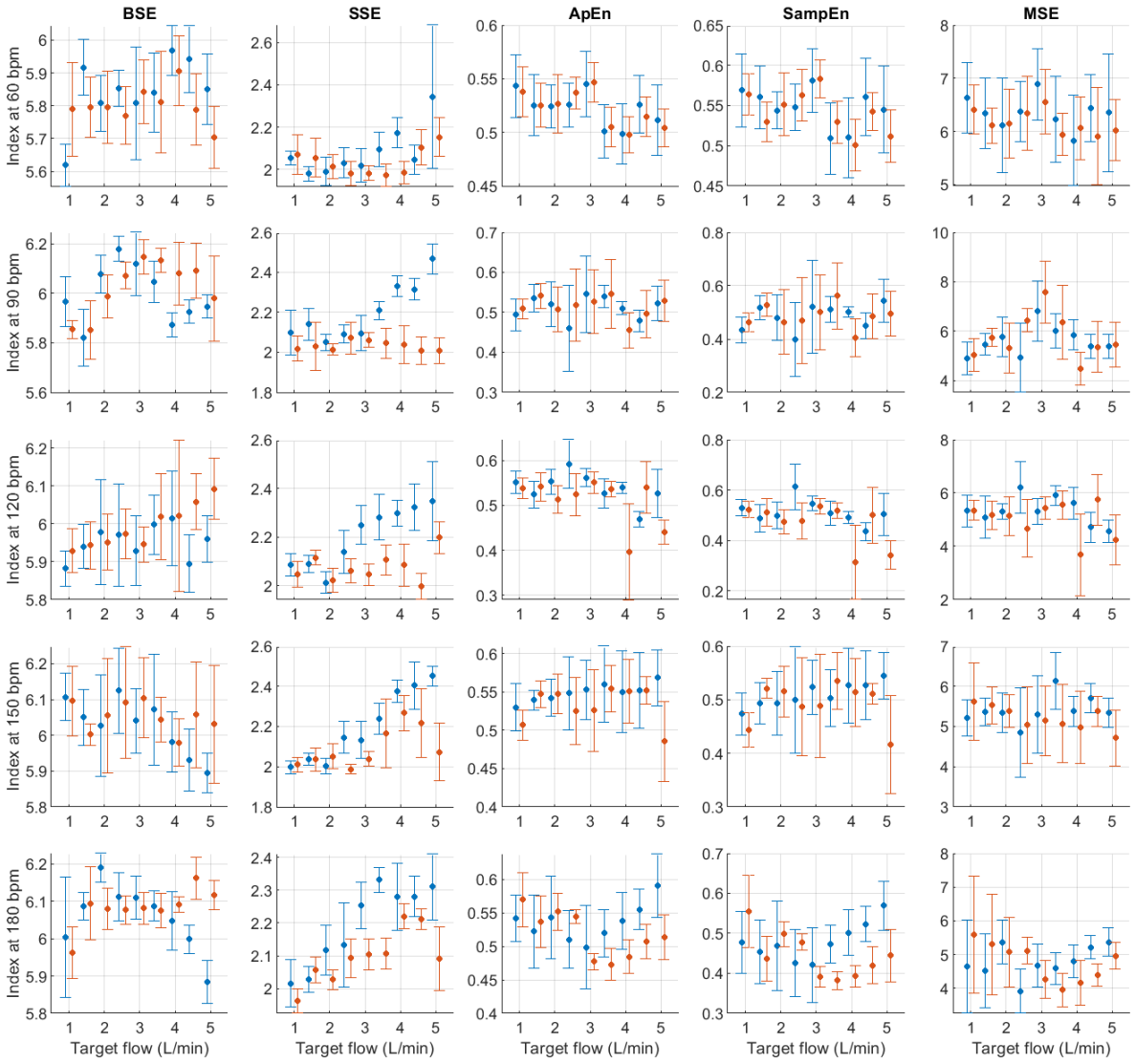

Figure 10.19: Mean and standard deviation of entropy-related indices extracted from pulse rate variability under different stroke rates (SR) and target flows (TF) conditions, and measured from the radial (blue) and deep palmar arch (orange) phantoms. Most indices show larger variability when measured from the deep palmar arch phantom. Some indices show increasing values as target flow increases within the same stroke rate.

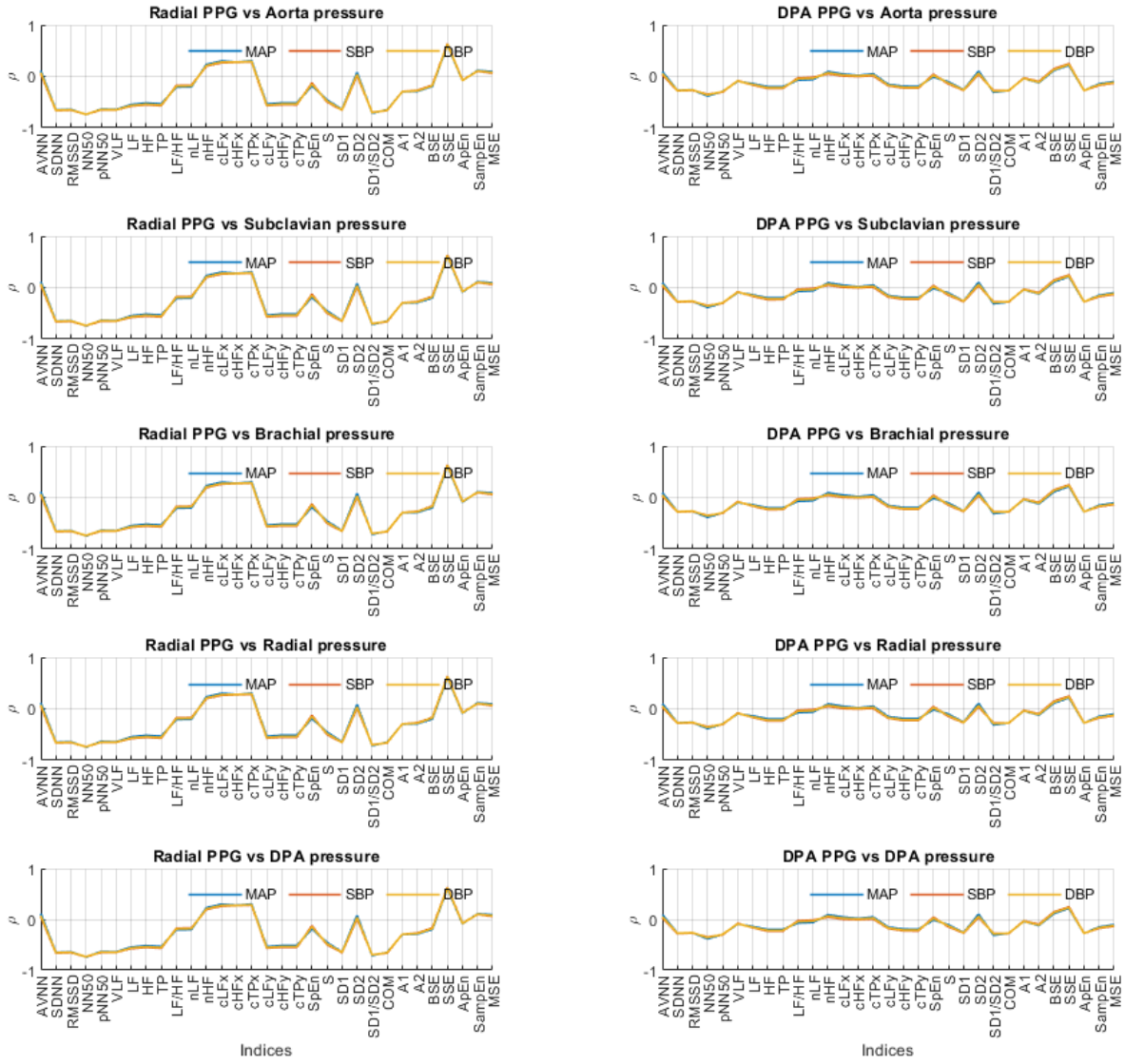

Figure 10.20: Cross-correlation coefficients (ρ) between systolic, diastolic and mean pressure signals measured from the aorta, subclavian, brachial, radial and deep palmar arch (DPA), and pulse rate variability indices extracted from photoplethysmographic signals acquired from the radial (left column) and DPA (right column) phantoms. Some of the indices showed a relatively high inverse relationship (ρ closer to -1), and there was higher correlation between indices extracted from the radial PPG and pressure values. The three pressure measures have a similar tendency.

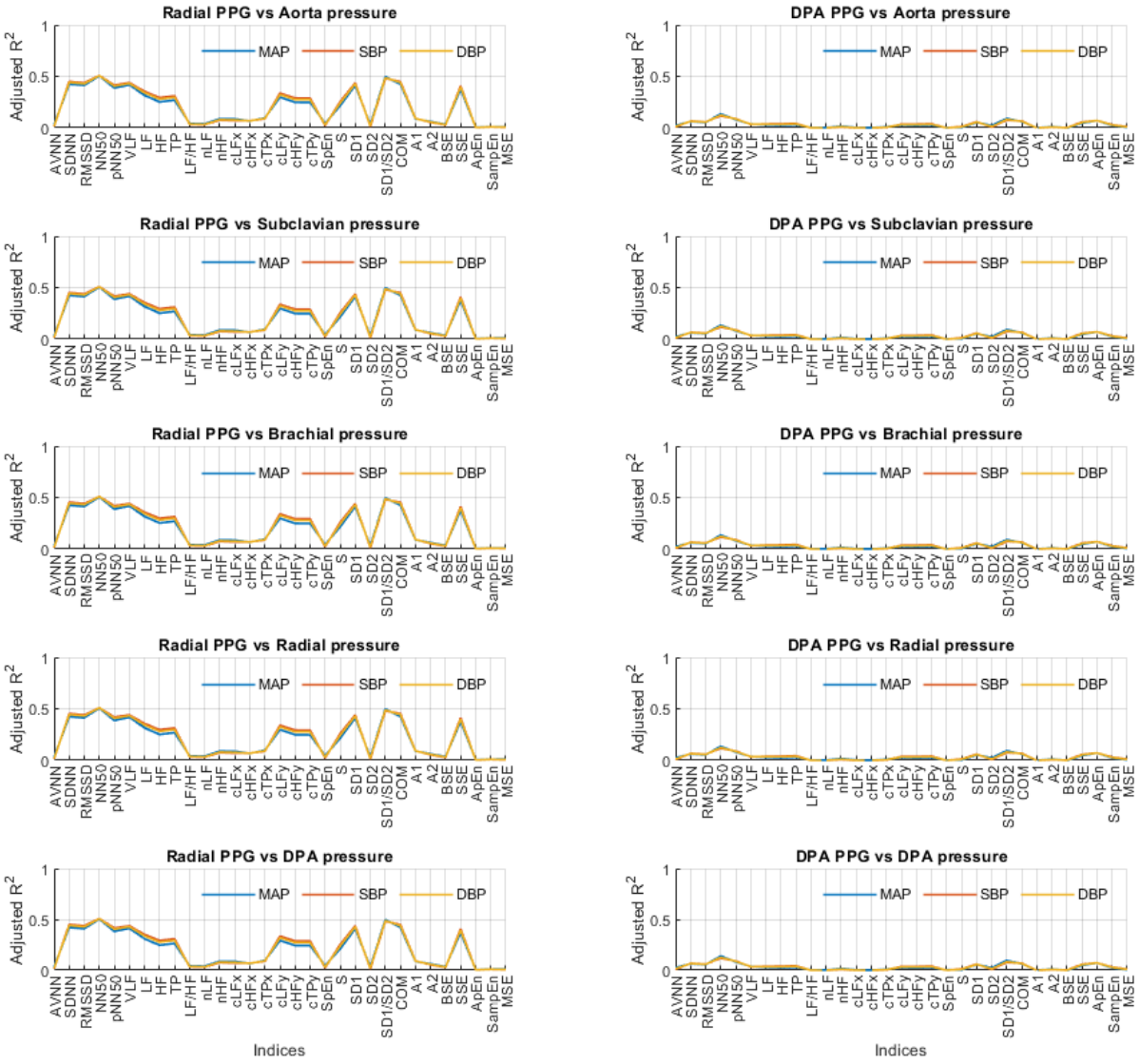

Figure 10.21: Adjusted coefficient of determination (R^2) for linear models between systolic, diastolic and mean pressure values measured from the aorta, subclavian, brachial, radial and deep palmar arch (DPA), and pulse rate variability indices obtained from red photoplethysmographic signals acquired from the radial and DPA phantoms. The relationship between pressure measures and pulse rate variability indices seems to be stronger when radial-related indices are considered. The behaviour of the linear regression results was very similar regardless of the location of measurement of pressure information.

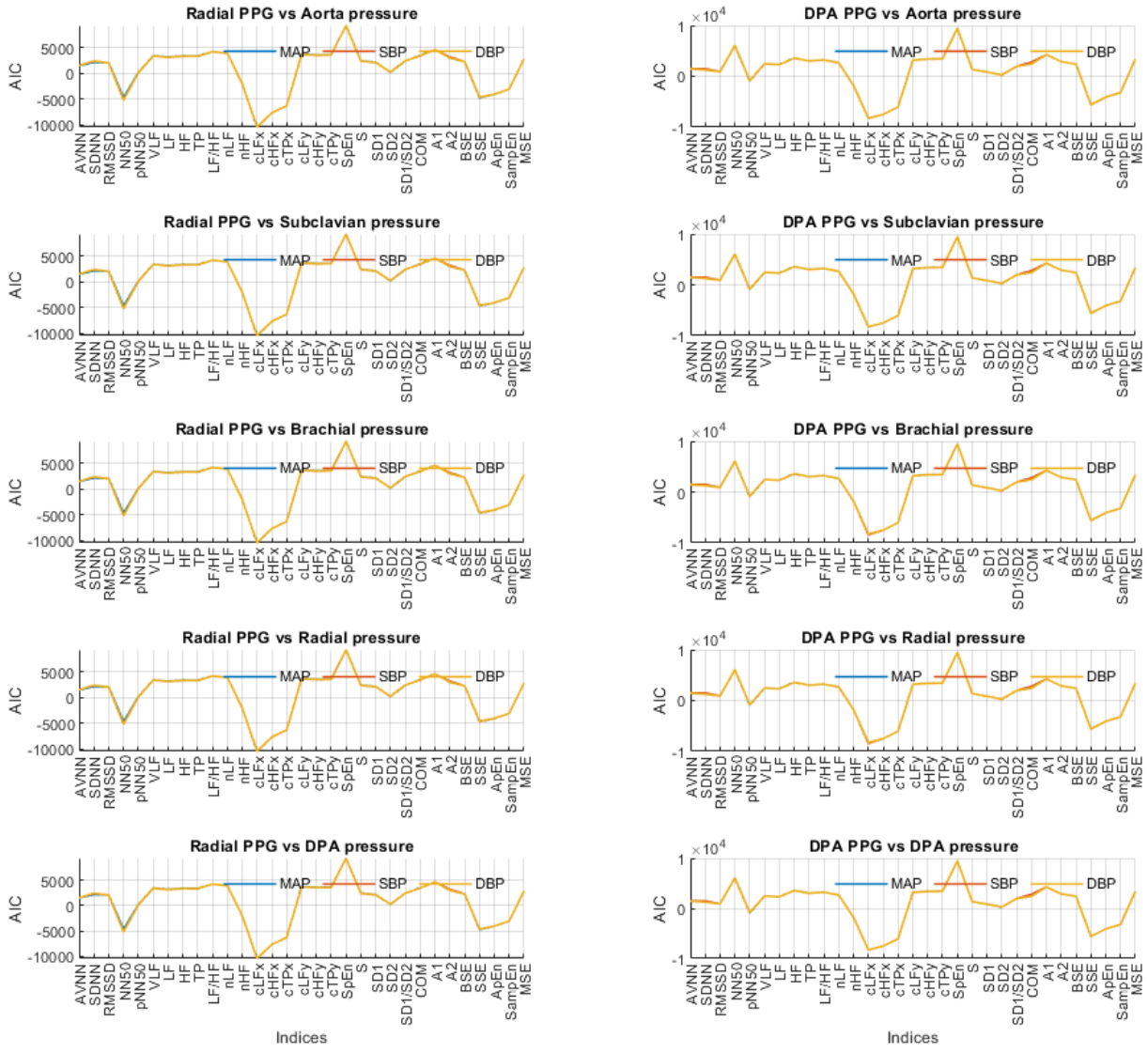

Figure 10.22: Akaike's Information Criteria (AIC) for linear models between systolic, diastolic and mean pressure values measured from the aorta, subclavian, brachial, radial and deep palmar arch (DPA), and pulse rate variability indices obtained from red photoplethysmographic signals acquired from the radial and DPA phantoms. A lower AIC implies a better fit of the linear model. Better results were observed with the x-coordinates of centroid-related indices.

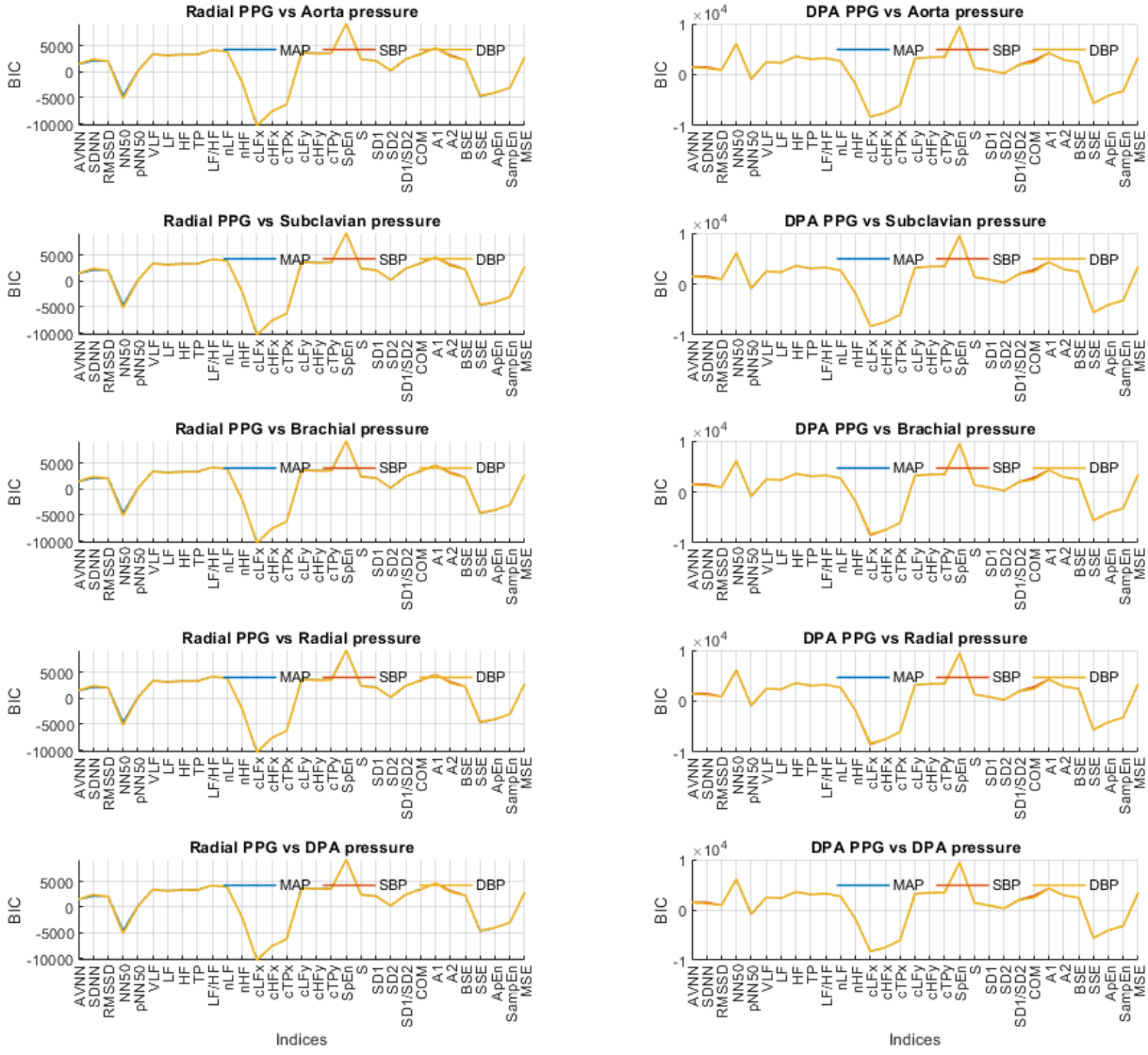

Figure 10.23: Bayesian Information Criteria (BIC) for linear models between systolic, diastolic and mean pressure values measured from the aorta, subclavian, brachial, radial and deep palmar arch (DPA), and pulse rate variability indices obtained from red photoplethysmographic signals acquired from the radial and DPA phantoms. A lower BIC implies a better fit of the linear model. Better results were observed with the x-coordinates of centroid-related indices.

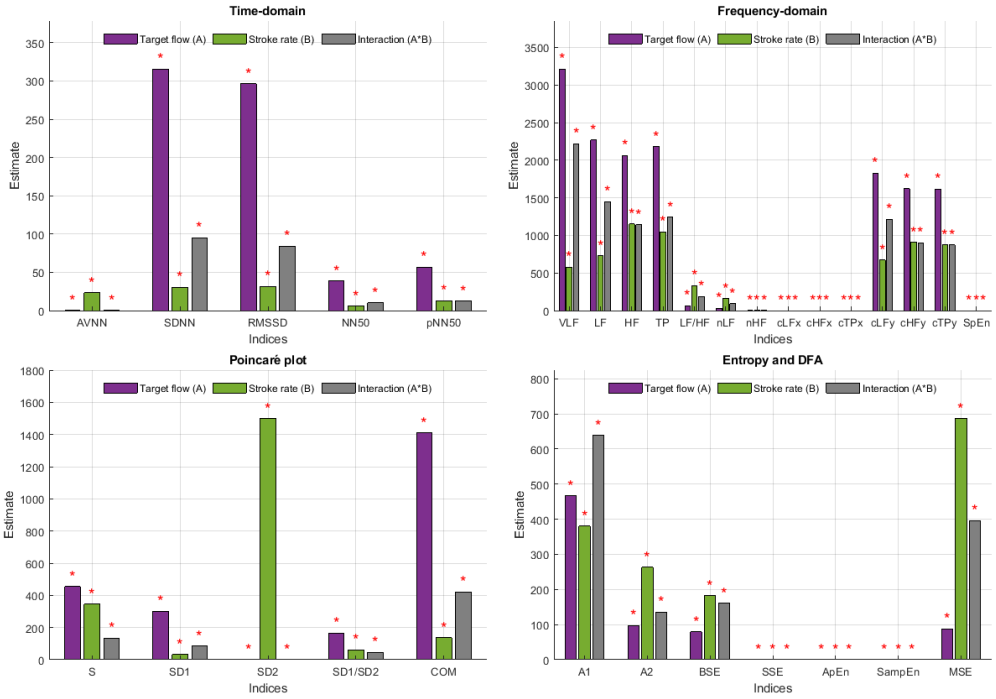

Figure 10.24: Effect estimates for stroke rate (SR), target flow (TF) and their interaction on each of the indices extracted from pulse rate variability (PRV) measured from the radial phantom. Red stars on top of the bars indicate statistically significant effects. All indices showed statistically significant effects from each factor and their interaction.

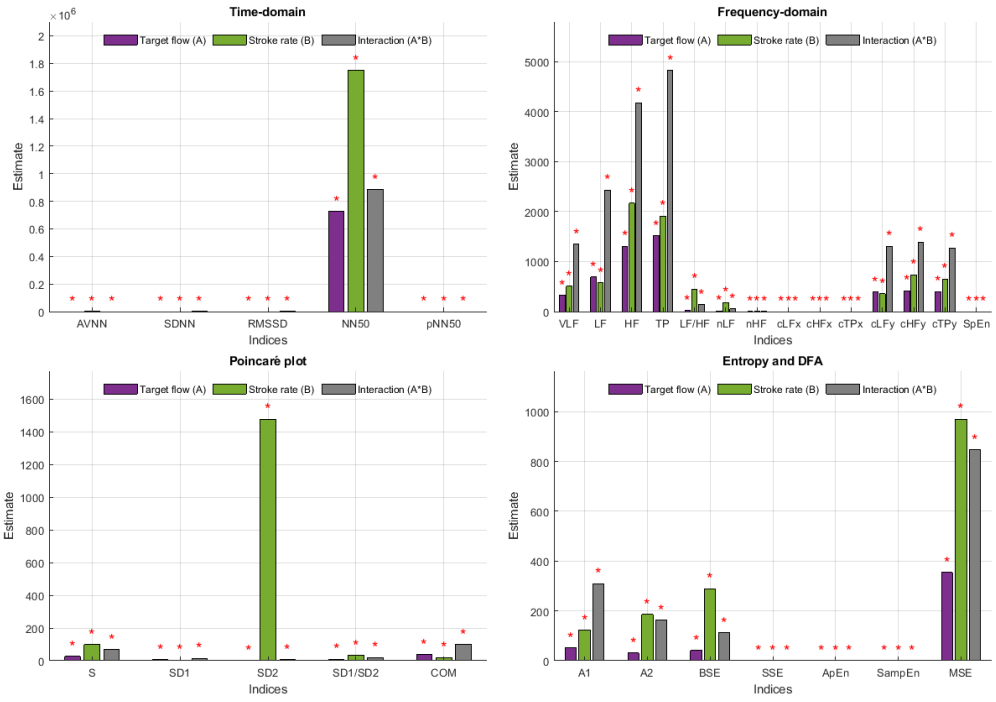

Figure 10.25: Effect estimates for stroke rate (SR), target flow (TF) and their interaction on each of the indices extracted from pulse rate variability (PRV) measured from the deep palmar arch phantom. Red stars on top of the bars indicate statistically significant effects. All indices showed statistically significant effects from each factor and their interaction.

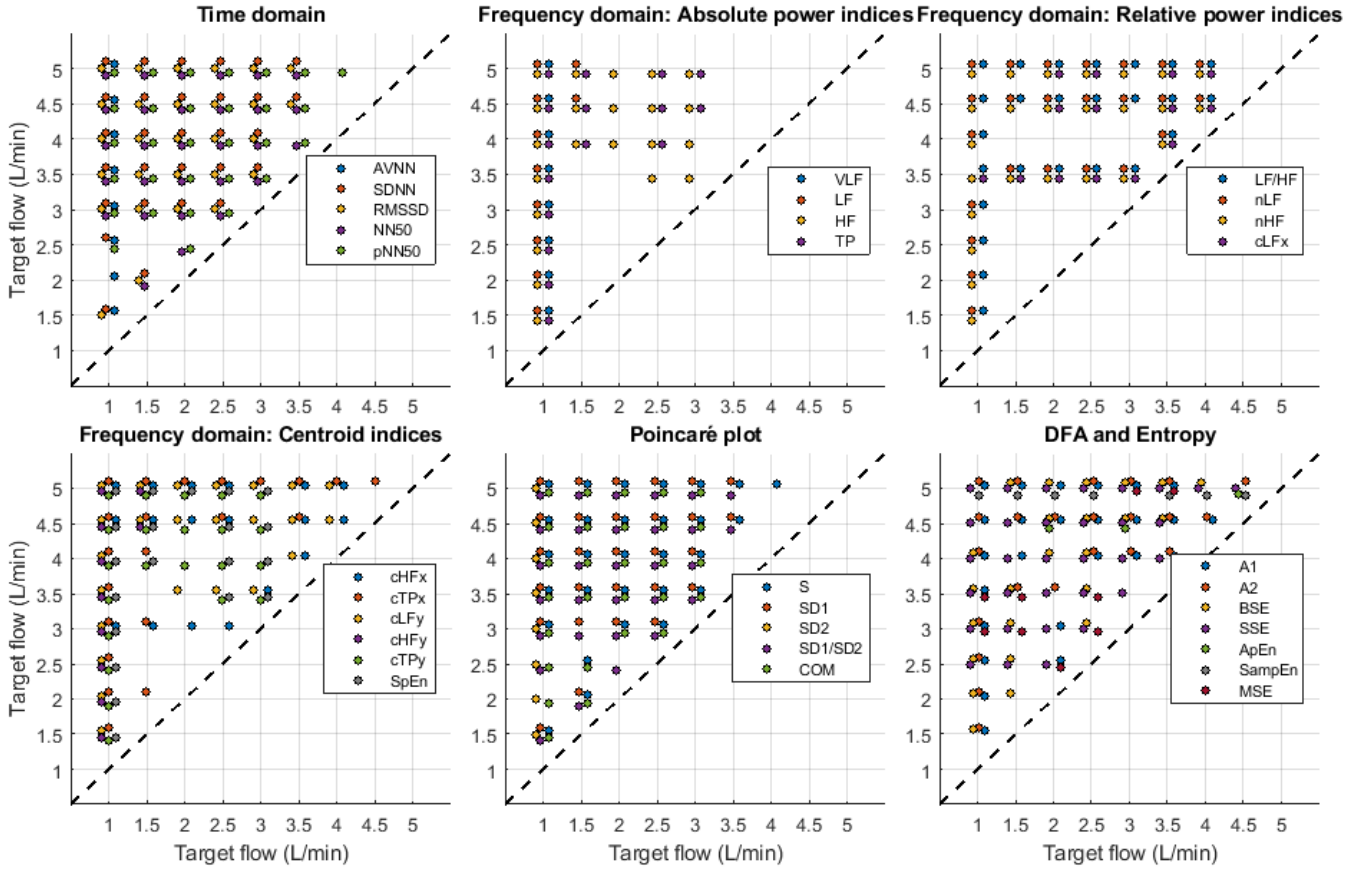

Figure 10.26: Post-hoc comparisons for target flow (TF) levels when pulse rate variability indices are measured from the radial phantom. The appearance of a circle indicates a significant difference between the corresponding levels for each of the indices. There were more statistically significant differences for time domain, Poincaré plot, DFA and entropy-related indices, while relative and centroid-related frequency-domain indices were less affected by TF changes.

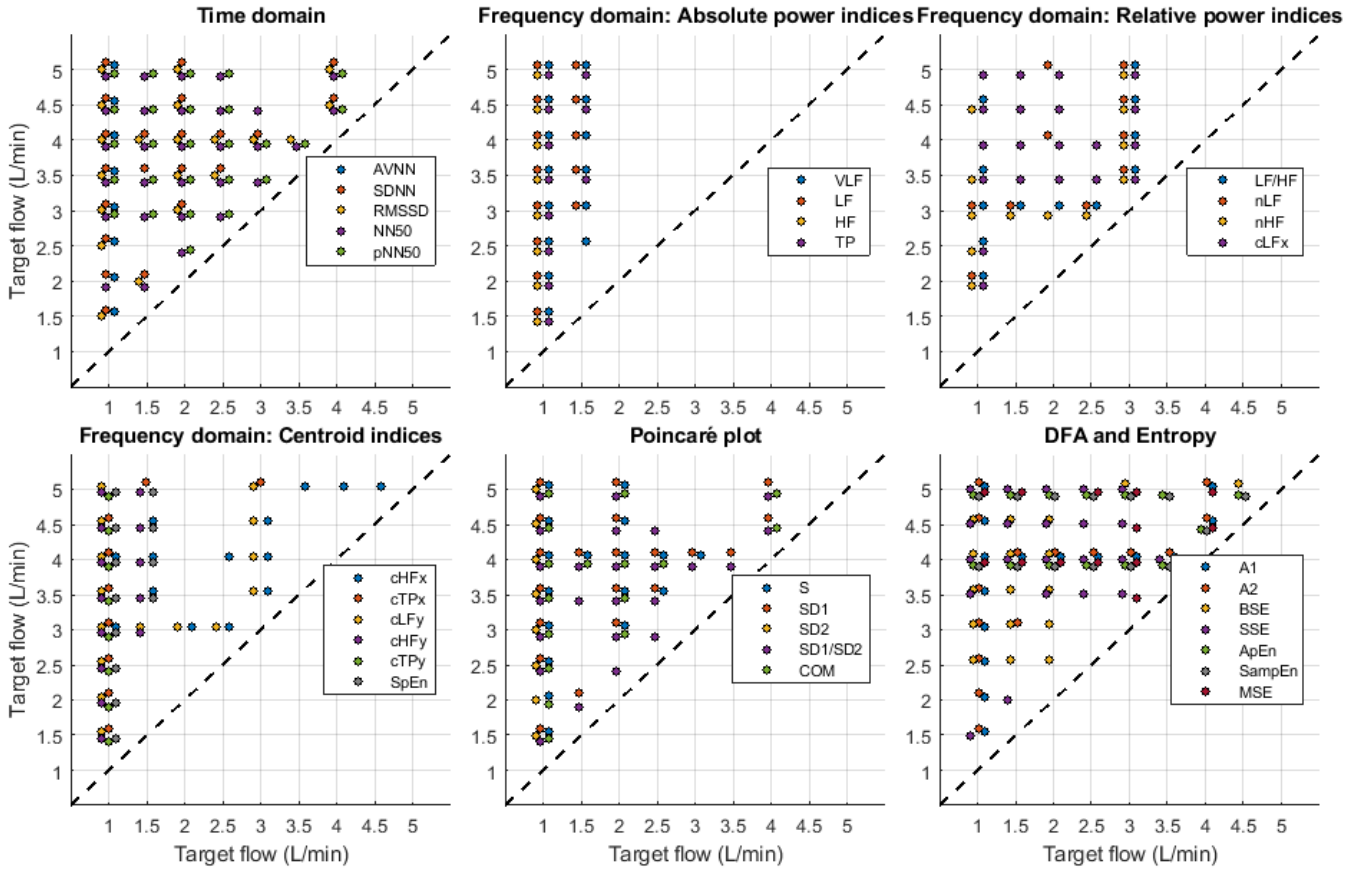

Figure 10.27: Post-hoc comparisons for target flow (TF) levels when pulse rate variability indices are measured from the deep palmar arch phantom. The appearance of a circle indicates a significant difference between the corresponding levels for each of the indices. Absolute, relative and centroid-related frequency-domain indices were less affected by TF changes as TF increased.

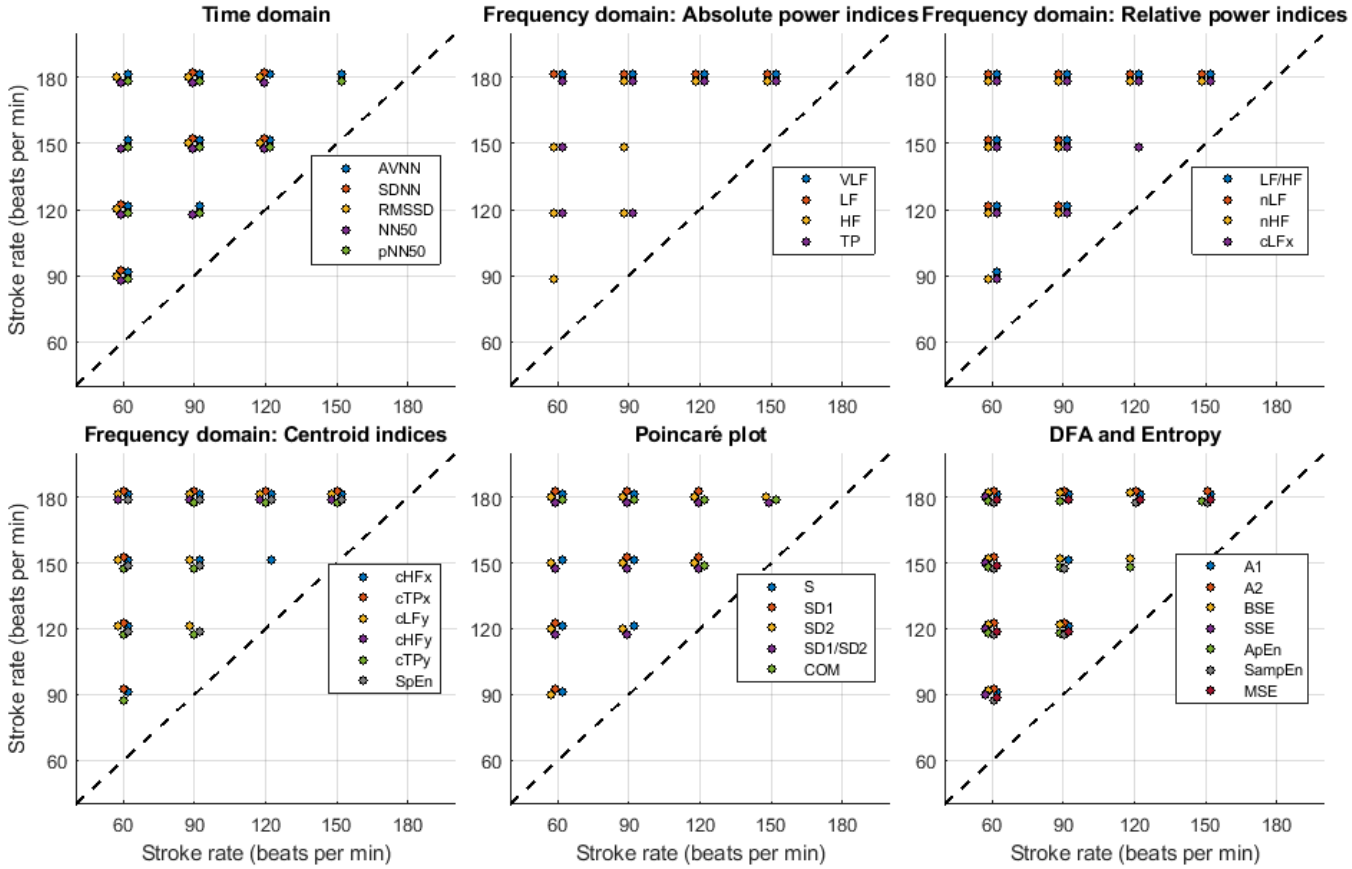

Figure 10.28: Post-hoc comparisons for stroke rate (SR) levels when pulse rate variability indices are measured from the radial phantom. The appearance of a circle indicates a significant difference between the corresponding levels for each of the indices. Most significant differences were observed as stroke rate increased.

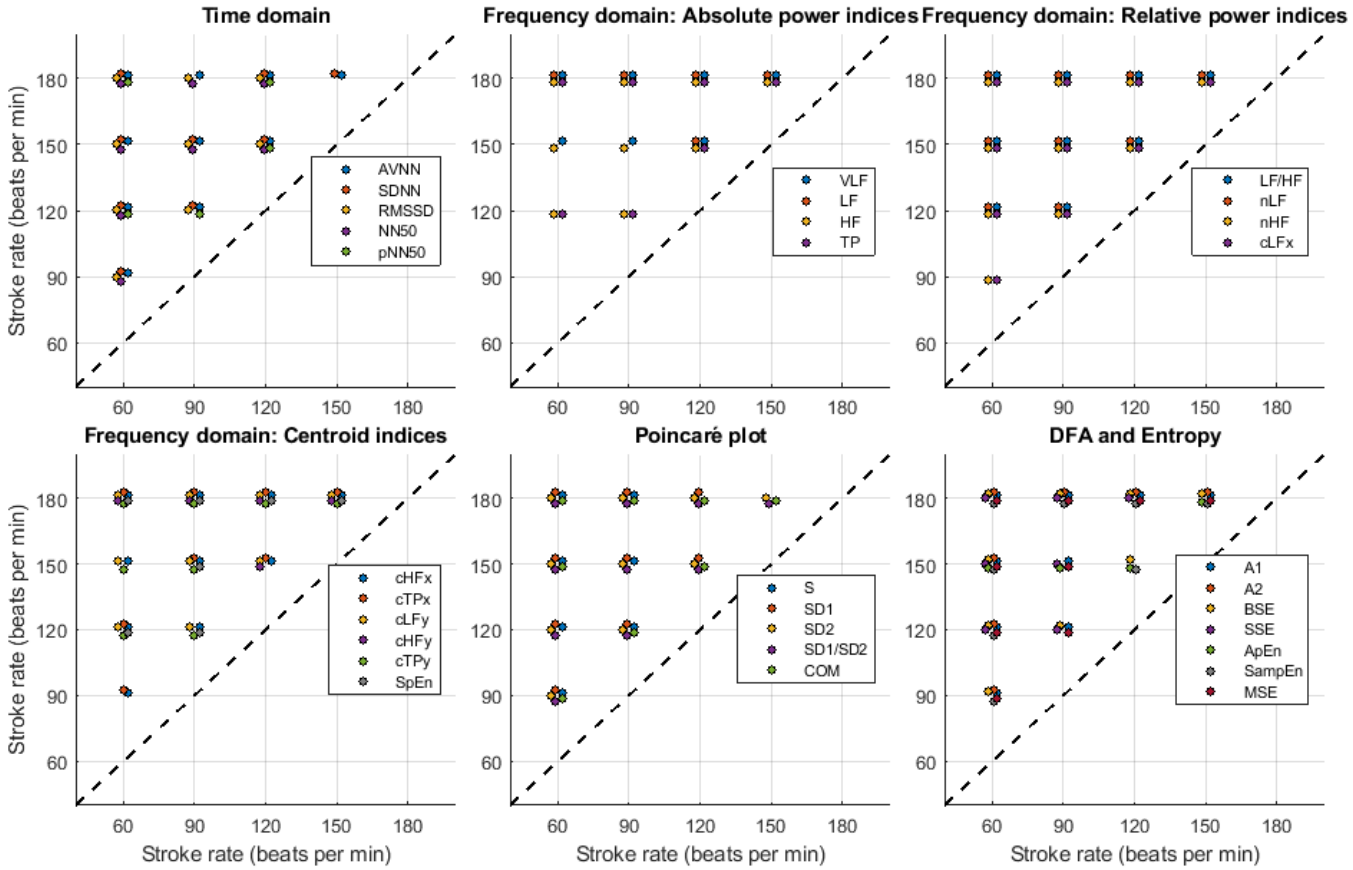

Figure 10.29: Post-hoc comparisons for stroke rate (SR) levels when pulse rate variability indices are measured from the deep palmar arch phantom. The appearance of a circle indicates a significant difference between the corresponding levels for each of the indices. Most significant differences were observed as stroke rate increased.

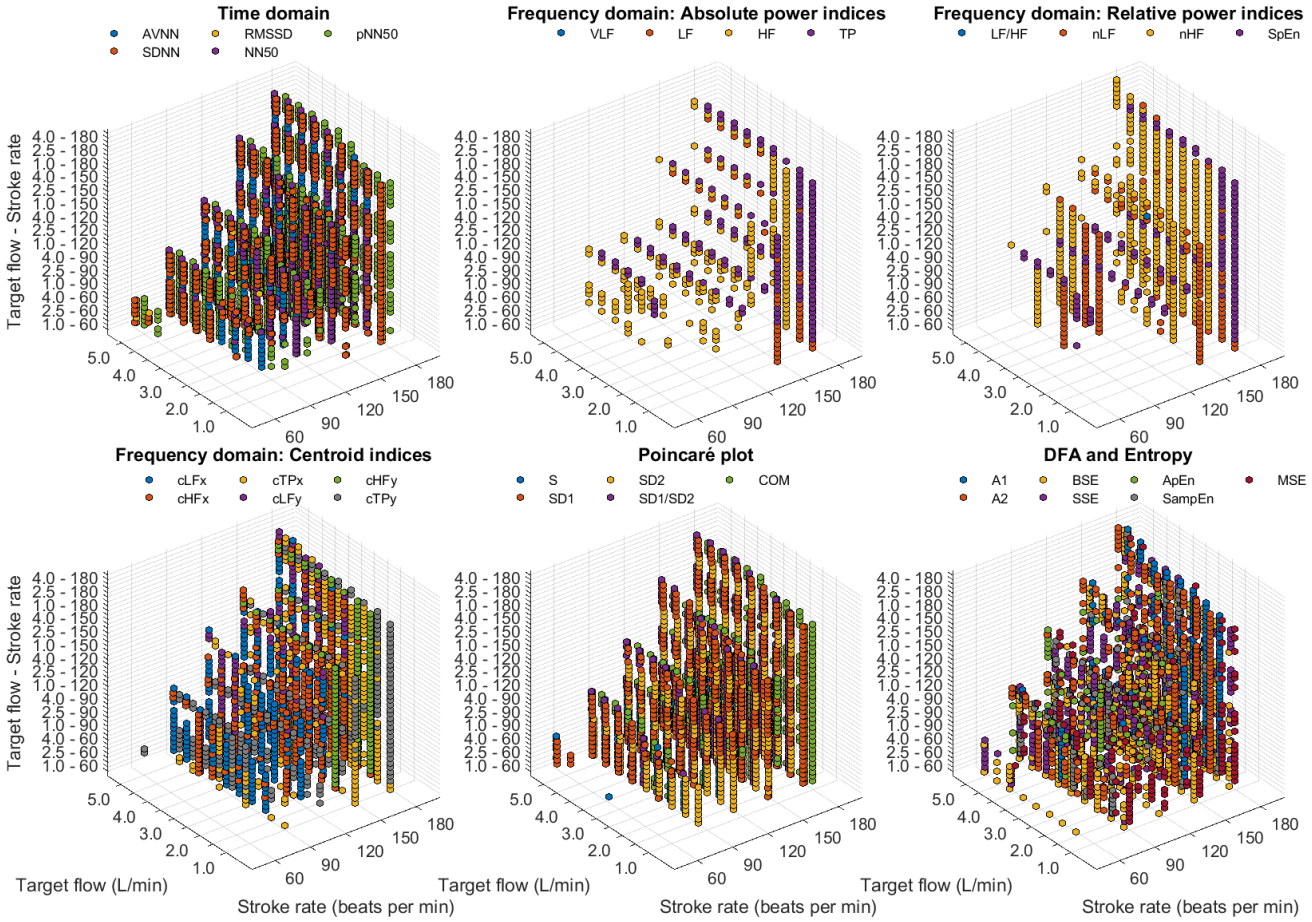

Figure 10.30: Post-hoc comparisons for the interaction between stroke rate (SR) and target flow (TF) when pulse rate variability indices are measured from the radial phantom. The appearance of a circle indicates a significant difference between the corresponding levels for each of the indices. Time-domain, centroid-related frequency-domain and non-linear indices are largely affected by the changes in target flow and stroke rate. There were more significant differences as SR and TF increased.

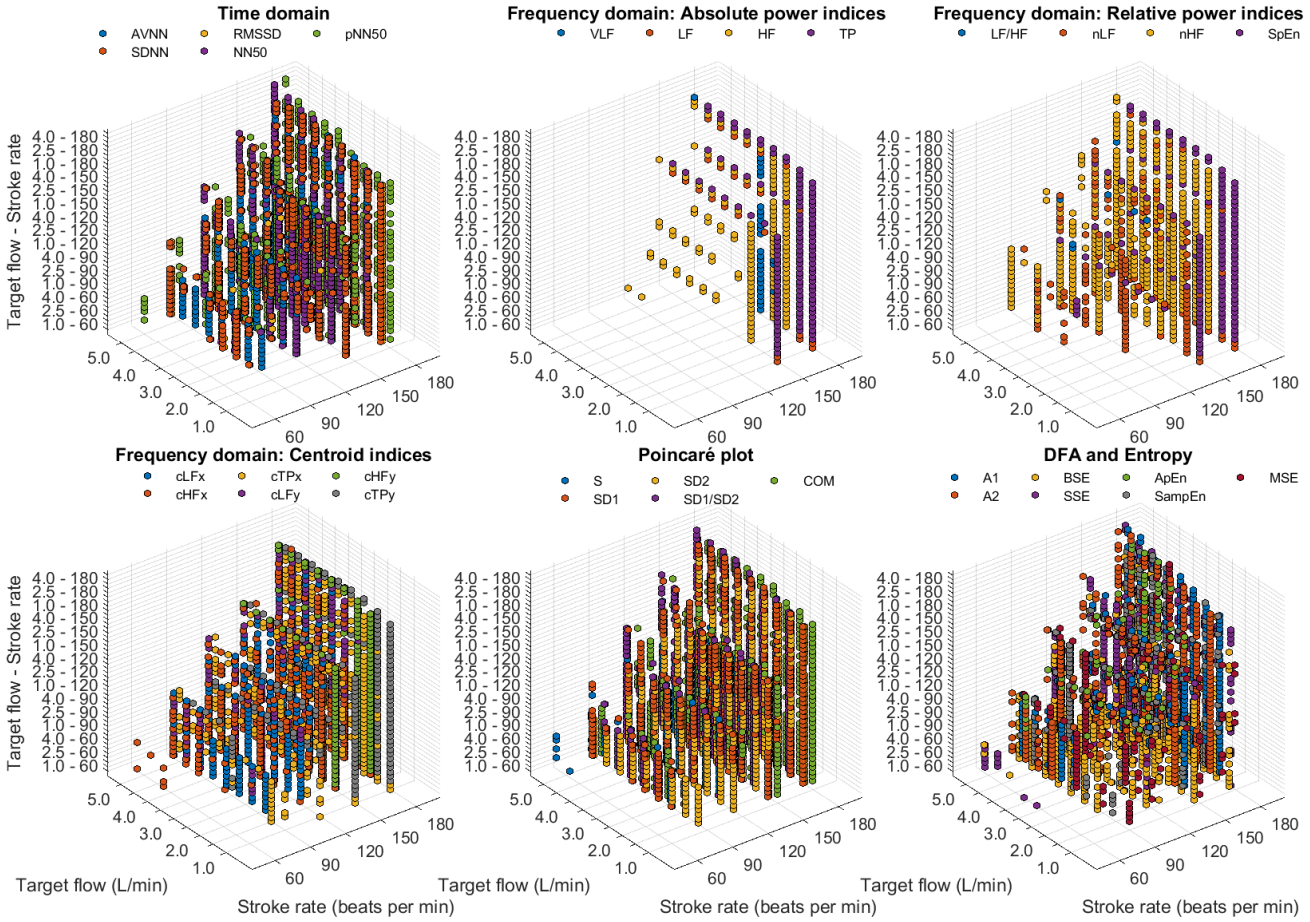

Figure 10.31: Post-hoc comparisons for the interaction between stroke rate (SR) and target flow (TF) when pulse rate variability indices are measured from the deep palmar arch phantom. The appearance of a circle indicates a significant difference between the corresponding levels for each of the indices. Absolute and relative frequency-domain indices showed less significant differences among possible combinations. There were more significant differences as SR and TF increased.

10.4 Discussion

As has been seen in previous studies and in the previous chapters of this thesis, PRV has been shown to be different to HRV (Schäfer & Vagedes 2013, Yuda, Shibata, Ogata, Ueda, Yambe, Yoshizawa & Hayano 2020), even in circumstances in which HRV is reduced or absent (Constant et al. 1999, Pellegrino et al. 2014). However, the origin of these differences are not entirely clear, and could be related to respiratory modulation or to cardiovascular changes, such as changes in PTT (Constant et al. 1999, Pellegrino et al. 2014).

Understanding how much cardiovascular changes, specifically changes in haemodynamics, explain the differences between HRV and PRV is difficult in in-vivo studies. Hence, in this study, the use of an in-vitro setup was proposed to evaluate if, in the absence of HRV in this simplified model, changes in cardiac output generated by changes in stroke rate and stroke volume could affect PRV indices. Moreover, it was evaluated if there exists a linear relationship between PRV indices and blood pressure measurements.

10.4.1 In-vitro setup

An in-vitro model was built following anatomical characteristics of the upper-limb circulatory system. This section of the body was chosen since PRV is usually measured from the finger or the wrist, and because blood pressure is usually assessed on the arm, both invasively and non-invasively. Although it is not possible to completely mimic the anatomy and physiology of the circulatory system in an in-vitro model, the length of the arterial segments, the diameter of the vessels and the behaviour of the pulsatile pump were designed and selected to have them as similar as possible to the average human being. Also, the artificial blood used was shown to have an optical response partly similar to the optical spectrum of blood. Hence, optical signals can be acquired using the proposed artificial blood recipe, with better performance for red wavelengths, where the absorbance peak is maximum.

The behaviour of the system was validated by measuring pressure signals at each arterial segment, PPG signals at the radial and deep palmar arch segments, and by altering stroke rate, target flow, and hence stroke volume. It was observed that the system behaved as expected. From the PPG signals it was possible to determine stroke rate reliably, although the signals became noisier as the stroke

volume was decreased, lowering signal-to-noise ratio in these signals and making it harder to properly determine stroke rate. From the pressure signals, the expected performance was observed: As stroke volume increased, pressure increased in all measurement sites. Also, there were differences in the magnitudes of the pressure signals that were expected given the differences in resistance to flow given by the different vessel diameters.

As explained by Nomoni et al. (2020) and May et al. (2021), using this kind of setups have become increasingly useful in the study of PPG signals and light-tissue interaction, since it allows for a dynamic simulation of the circulatory system as well as the investigation of several processes that are difficult to investigate in in-vivo studies due to the large amount of uncontrolled variables. Moreover, using these in-vitro setups allows for the investigation of extreme conditions that can be difficult or unethical to simulate in in-vivo circumstances, such as the complete absence of autonomic regulation. To the best of the knowledge of the author of this thesis, this is the first study that aims to investigate PRV in an in-vitro model in the absence of HRV or any other physiological processes, such as respiration.

10.4.2 Behaviour of pressure measurements and PRV indices with haemodynamic changes

Pressure values were measured from each arterial segment of the rig. From these signals, mean arterial pressure (MAP), and systolic (SBP) and diastolic blood pressure (DBP) values were extracted. Pressure measurements behaved as expected, with increased pressures as stroke volume increased. Hence, with increased target flows at a given stroke rate, the blood pressure increased. But when stroke rate is increased, blood pressure decreases since the volume of blood per stroke is lowered. The measurements obtained are relatively robust, as shown by the small standard deviations, even when pressures are near zero. Also, and as expected, the difference between MAP, SBP and DBP become larger as pressure increases, since the amplitude of the signal acquired is also increased.

The behaviour of PRV indices extracted from PPG signals acquired from both phantoms is also worth analysing. In general, it can be seen that indices extracted from the DPA phantom tend to have larger variabilities, probably due to the lower quality of the signal obtained from this location, which makes it harder to accurately determine cardiac cycles.

Specifically, from time-domain indices, it can be observed that the measurement of AVNN is generally stable except for the cases in which the amplitude of the signal is too small, such as when SR is 150 and 180 bpm and TF is lower than 2 L/min. SDNN and RMSSD had a very similar behaviour, with relatively lower values as TF increases. A similar although not as clear behaviour can be observed from NN50 and pNN50.

In absolute-power frequency-domain indices, the results obtained when SR was 150 and 180 bpm had an important outlier when TF was 1 L/min. Again, this is likely due to the lower quality of the signals at this stroke volumes. LF, HF and TP showed a similar behaviour, with increased values as TF increased to 3 L/min and then decreased values as TF was increased to 5 L/min. Interestingly, it can be observed that there is an important difference in magnitudes between VLF, LF and HF, with larger magnitudes in the HF band. This is in line with the results reported by Constant et al. (1999), who concluded that this frequency band was more affected by cardiovascular factors such as PTT, even when HRV was dramatically reduced. This can also be observed from nLF and nHF, with most nHF values close to 0.9. However, the trend of increasing and decreasing values as TF increases is not visible in these two indices. However, as SR increased, LF/HF and nLF tended to decrease with increases in TF, while nHF showed the opposite behaviour. SpEn did not show a clear trend with changes in TF, but did show a continuous increase as SR surged.

Centroid-related indices showed similar results when y-coordinates were analysed. Again, there is an important outlier as stroke rate increased and target flow was kept low, but the inverted parabolic behaviour observed when SR is lower is also present in these indices. However, x-coordinates were less affected by changes, meaning that the power of the band tends to be around the same frequencies regardless of stroke volume changes, while the amplitude of the band does vary with haemodynamic changes. This is in line with what was observed in the studies presented in previous chapters of this thesis.

As has been explained in previous chapters, SD1 is expected to behave as RMSSD. This can be seen in the results obtained from Poincaré plot indices, where the behaviour is exactly the same. S, SD1/SD2 and COM also have the same trend with varying magnitudes. And SD2 has a similar behaviour as AVNN, which is also expected from the literature (Khandoker et al. 2013).

Finally, from the remaining non-linear indices, it can be seen that magnitudes

tend to remain relatively stable regardless of changes in stroke rate. A trend is hard to determine from DFA-related indices, while from entropy-related indices, the most visible trend can be observed from SSE, where it increases with rising TF. BSE, ApEn, SampEn and MSE did not show such clear patterns of behaviour.

10.4.3 Linear regression between PRV and arterial blood pressure

Linear regression analyses between pressure measurements and PRV indices were performed to evaluate if the relationship between these variables could be explained using a linear model. Three main conclusions can be derived from these results: (a) The models behaved similarly regardless of the location of measurement of the pressure; (b) the models did not show a difference between MAP, SBP and DBP; and (c) the linear relationship tends to be stronger when PRV indices are extracted from the radial phantom.

From the Spearman correlation analysis it was found that stronger correlations, reflected in correlation coefficients closer to $\pm$ 1, were observed with SDNN, RMSSD, NN50, pNN50, VLF, SD1, SD1/SD2 and SSE measured from the radial phantom. AVNN and SD2 showed the correlation coefficients closer to zero, hence these indices are not expected to be linearly related with blood pressure. These two indices reflect changes in instantaneous heart rate, which has been shown to be robust when measured from PPG signals (Schäfer & Vagedes 2013). With the results found in this study, it can be concluded that these measurements should not be linearly affected by blood pressure changes, and have a robust performance regardless of changes in stroke rate and target flow. Similar results were observed from the adjusted coefficients of determination, R^2. The indices that showed better R^2 were SDNN, RMSSD, NN50, pNN50, VLF, SD1, SD1/SD2 and SSE, but values were below 0.5 for all indices, indicating that a linear model is not the best fit for modelling the relationship between blood pressure and PRV indices. Since there are several non-linear processes that affect HRV and PRV in in-vivo circumstances (Shaffer & Ginsberg 2017), it is possible that fitting higher-order models to this data increases the R^2 values.

Both Akaike's and Bayesian Information Criteria were extracted as well, as a relative assessment of the linear model fit for each of the indices and each of the pressure measurements. Both show similar results, with lower values for x-coordinates of centroids, SSE, ApEn and SampEn. Hence, these models were classified as the

better fit. Interestingly, NN50 showed lower values when measured from the radial phantom, while when it was measured from the DPA phantom it did not show low values of AIC or BIC. This could be due to effects of noise in the measurement of this variable and hence in the linear models.

In conclusion, from these analyses it can be seen that some PRV indices tend to have a strong cross-correlation with pressure measurements, although these do not behave linearly. Also, it is worth noting again that there is no difference due to the magnitude of the pressure (which changes with location of measurement) or due to the type of pressure that is being analysed.

10.4.4 Relationship between PRV and cardiac output changes

The main aim of this study was to assess if PRV indices were affected by stroke rate and target flow changes, in the absence of HRV and autonomic regulation. From the factorial analyses, it was observed that all indices measured from both phantoms had statistically significant effects due to the interaction of factors and due to the factors individually.

From the radial phantom, and similarly to what was observed from the behaviour of PRV indices, AVNN and SD2 had an important effect due to SR. MSE showed also larger estimates due to the effect of SR on its magnitude. In addition to these indices, NN50, S, SD1/SD2, A2 and BSE also showed larger estimates due to the effect of SR than TF or the interaction when measured from the DPA phantom. This might be due to the increased number of outliers and the lower quality of the signal. In concordance too with the qualitative observations of the behaviour of the indices, SDNN, RMSSD, pNN50, absolute-power and y-coordinates of centroid related frequency domain indices, S, SD1, SD1/SD2 and COM showed that TF has the larger effect estimate when measured from the radial phantom. When measured from the DPA phantom, and again most likely due to the quality of the signal, the greater effect estimates were found on the interaction of both factors.

Regardless of the differences between phantoms and signal qualities obtained, it is remarkable that all indices showed a statistically significant effect due to these haemodynamic changes, meaning that even in the absence of HRV and autonomic regulation, changing stroke rate and target flow affect PRV indices. Given the greater susceptibility of DPA-related indices to noise, the remaining discussion is focused solely on data obtained from the radial phantom.

Post hoc analyses were performed to evaluate the origin of these differences. Only focusing on target flow changes, most differences occurred when comparing lower flows to TF values greater than 2.5 L/min and for time-domain, centroid related frequency-domain, and non-linear indices. For absolute and relative power indices, the majority of the differences were observed when comparing TF = 1 L/min to the rest of the conditions. Changes on stroke rate had a significant effect on most indices, especially when SR was increased to 180 bpm. The indices that showed the lower amount of significant comparisons among levels were VLF, LF and COM. Moreover, the interactions showed significant differences in most possible combinations of factors, showing that both SR and TF play an important role in PRV and its regulation even in the absence of HRV.

These results corroborate those reported by Constant et al. (1999) and Pellegrino et al. (2014), who concluded that PRV is modulated by other aspects different to HRV. Although from these results it is evident that in this in-vitro setup PRV was present and affected by stroke volume changes, further studies should be performed to better understand the origins of the changes in PRV and to try to replicate these results in an in-vivo model. Moreover, these results alongside the development of the in-vitro model could allow for a better understanding of PRV in a controlled manner and its relationship with cardiovascular diseases.

10.4.5 Limitations of the study

The main limitation of this study is the restrictions imposed by the in-vitro model. As has been already mentioned, it is not possible to completely simulate the behaviour of the cardiovascular system and the autonomic nervous system in an in-vitro model, limiting the physiological phenomena and anatomical features to be studied (May et al. 2021). However, having this controlled scenario allowed for understanding how PRV alone would react to haemodynamic changes, and was considered a good first step in the route to better understand the interaction of PRV and cardiovascular changes. Also, lower quality of signals with decrease stroke volumes may have affected the results obtained, especially when PPG signals were measured from the DPA phantom. However, the best performing algorithm and fiducial point selected on Chapter 6 were used in an attempt to make the results more robust and it was observed that only very extreme conditions were difficult to analyse. Finally, only a linear model was used to relate PRV indices and blood pressure values.

Future studies should aim to apply higher-order models to better understand the relationship between these variables.

10.5 Summary

PRV has been shown to be affected by additional aspects different to HRV (Constant et al. 1999, Pellegrino et al. 2014, Gil, Orini, Bailón, Vergara, Mainardi & Laguna 2010) but it is difficult to isolate PRV from these other variables in order to understand how it could be affected by changes such as increases or decreases on blood flow and blood pressure. An in-vitro model was designed and implemented in this study, in which the upper-circulatory system was simulated and from which pressure and PPG signals could be measured. In the absence of HRV and autonomic regulation, PRV indices were extracted from PPG signals measured from this in-vitro system, alongside pressure signals. It was observed that PRV was affected due to changes in stroke rate and target flow, and that some of these PRV indices are related with pressure measurements.

Although there is a need to validate these results in in-vivo studies, it can be concluded that PRV acts differently due to changes in cardiovascular parameters regardless of the presence of HRV. Nonetheless, it should be expected that HRV plays an important role in the modulation of PRV, making it difficult to observe these changes in data obtained from healthy or diseased subjects. Future studies could aim to utilise both HRV and PRV to dilucidate the effects of cardiovascular changes on PRV after subtracting HRV information.

Moreover, future studies should aim to better understand the origin of these differences between HRV and PRV under the light of cardiovascular changes. Also, it could be beneficial to implement autonomic regulation in the in-vitro setup, in order to improve the physiological simulation of the cardiovascular system and to analyse the differences between HRV and PRV under different cardiovascular parameters.

Chapter 11

Discussion, Conclusions and Future Work

HRV has been largely explored in the last 40 years due to its simplicity and non-invasive nature to evaluate changes in the cardiac ANS and related diseases (Xhyheri et al. 2012). The rate at which the heart pumps blood to the circulatory system is determined by the sinus node in the heart, which is controlled by the sympathetic and parasympathetic branches of the ANS (Rangayyan 2002). Hence, changes in heart rate indirectly reflect the behaviour of the cardiac control exercised by this system. Its analysis has been used in the understanding and perhaps detection and diagnosis of various cardiovascular diseases amongst other pathophysiological phenomena. For example, HRV has been studied and used for the diagnosis and assessment of acute myocardial infarction (Task Force of the European Society of Cardiology and The North American Society of Pacing and Electrophysiology 1996, Takase 2010, Karmali et al. 2017), diabetes (Takase 2010, Xhyheri et al. 2012), hypertension (Takase 2010), and atherosclerosis (Xhyheri et al. 2012), among others.

Some researchers have tried to implement HRV measurements using physiological signals different from the ECG. A commonly used alternative to ECG for the assessment of HRV is PPG, as a non-invasive, non-intrusive, simple and low-cost technique for the acquisition of pulse waves (Allen 2007, Kyriacou 2021). HRV information derived from these pulse waves has been denoted as PRV, indicating that the information is not based on heart rate but on pulse rate changes over time. PRV has been derived for the analysis of autonomic changes under different conditions, such as the presence of mental or somatic diseases, during sleep, or for evaluating

the effects of pharmacological drugs.

PRV seems like a logical alternative to HRV since PPG signals carry a lot of valuable information regarding cardiovascular parameters, and is very easy to acquire in a long-term manner and in real-life scenarios. However, several technical and physiological factors may affect PPG and probably alter PRV. In this thesis, two main work packages were executed to (1) identify which selection of some technical factors allow for better extraction of PRV data from PPG signals, and (2) explore how cardiovascular changes affect PRV.

11.1 Standardisation of pulse rate variability extraction from PPG signals

PRV has been shown to be affected by technical aspects selected for its extraction from PPG signals, such as sampling rate, the selection of fiducial points used to extract cardiac cycles, and the filtering of PPG signals before detecting these fiducial points. One important aspect that has been studied is the effect of the fiducial points used for determining each cardiac cycle. This issue is not remarkable when discussing HRV: R peaks are easily identified in most ECG traces, and due to its magnitude, physical origin, and frequency content, they are ideal marks for segmenting cardiac cycles and deriving HRV data. PPG, on the other hand, is a smooth signal, with slow changes and relatively constant frequency content. Identifying the fiducial point of the pulse wave may present an interesting challenge and an important pitfall for PRV. As mentioned by Pinheiro et al. (2016), the best fiducial point to be used in the analysis of PRV depends on the physiological conditions of each subject and on the analysis to be performed, making it crucial to select the fiducial point to use appropriately.

The way PPG signals are acquired and processed for measuring PRV is also important. PPG, being an optical technique, is based on the interaction between tissue and light (Kyriacou 2021). The wavelength at which the tissue is illuminated affect the depth at which light penetrates, with longer wavelengths reaching deeper tissue (Ash et al. 2017). It is still not clear if this could imply a difference in PRV measured from several wavelengths, although PRV has been measured indistinctly using red, infrared, green and even orange light. Another important aspect is the

sampling frequency used for measuring PRV, as well as the pre-processing of PPG and frequency domain analysis techniques that could affect PRV results. Hence, it is important to establish guidelines for standardising PRV estimation, which would allow comparing results from similar studies without having to consider processing and acquisition differences, which may affect the conclusions reached.

In this thesis, a first approach to establish these guidelines was performed. It was found that, with simulated signals with excellent and acceptable quality, the sampling rate needed for reliable estimation of PRV from PPG signals was at least 256 Hz, and the duration should be at least 120 s. Also, the D2Max algorithm along with the a fiducial point delivered the best estimation of PRV trends, as well as using FFT for spectral analysis with cubic-spline interpolation and a 4 Hz sampling rate. Finally, it was found that using Elliptic IIR filters to pre-process the PPG signal tended to deliver the best results.

It is worth remarking that these results were obtained using simulated signals, with varying PRV content. As has been explained, this was done in order to increase the sample size available and, at the same time, obtain a gold standard different to HRV, since PRV should not be considered exactly the same as HRV and hence should not be coerced to exactly replicate HRV data. Nonetheless, the use of simulated signals implies that many of the physiological and technical aspects that may affect the PPG waveform, such as changes in amplitude, the presence and absence of dicrotic notches, or even the inversion of the signal, have not been considered in this study. Also, most of the results were obtained using signals that were not contaminated with any noise, in an attempt to identify those parameters that allowed for a better extraction of PRV indices from PPG signals under ideal conditions. Therefore, more studies are needed to continue determining how noise affects the parameters established in this thesis. However, although more studies are needed, this is one of the first studies aiming to establish these guidelines considering a gold standard different to HRV, and provides a first framework to understand how using different technical aspects for PRV assessment may affect the results under different conditions. Although this studies have concerned mainly on PRV analysis from PPG signals, establishing guidelines for many PPG-related applications is becoming crucial for the advancement of the technique.

Future studies should aim to validate and further standardise PRV assessment from PPG using both simulated and real data, including also evaluating the effects

of other technical aspects, such as body site, wavelength and type of sensor used for the acquisition of PPG signals.

11.2 Relationship between cardiovascular changes and pulse rate variability

As was concluded by Schäfer & Vagedes (2013), PRV is different from HRV not only due to errors in the fiducial points or due to the processing and acquisition methods applied, but also due to the nature of PPG and ECG signals and the physiological factors that affect each of these. PPG, being of a mechanical nature, can be affected by other factors different to those that affect HRV. The most renowned differential factor is PTT, the time that the blood takes to travel from the heart to the peripheral site where the pulse wave is being measured (i Caros 2011). As demonstrated by Constant et al. (1999) and Gil, Orini, Bailón, Vergara, Mainardi & Laguna (2010), PTT has an important role in explaining the differences between HRV and PRV, especially in short-term parameters, such as HF and RMSSD. Therefore, the location of the sensor used for acquiring PPG could affect the relationship between PRV and HRV, and thus it is possible to hypothesize that PRV measured from different body sites may yield different information regarding the vascular path that the blood had to travel. Moreover, Lu et al. (2009) indicated that three factors (electromechanical coupling in the cardiomyocyte, pre-ejection period, and PTT) are subject to variations independent from heart rate and may be influenced by cardiovascular and ANS diseases, which could affect the relationship between HRV and PRV in diseased subjects. Gil, Orini, Bailón, Vergara, Mainardi & Laguna (2010) also pointed out the effects of aging and blood pressure on PRV, suggesting that differences between PRV and HRV could be also due to vascular aging. Trajkovic et al. (2011) concluded that not only PTT may affect PRV, but also other factors such as external forces on the arterial vessels, pathologies, movement artefacts and methodological issues. Heathers (2013) indicated that PRV from different body locations could allow to differentiate local and systemic vasoconstrictive responses. Parasnis et al. (2015), after evaluating non-linear parameters in cardiovascular patients both from HRV and PRV; concluded by raising a question: Could cardiovascular disorders be responsible for altering the behaviour of PRV differently to that of HRV? And as Vasconcellos et al. (2015) pointed out, there is not a profound explanation yet for

the physiological or technical aspects that may affect the relationship between HRV and PPG-derived PRV, nor there is a clear hypothesis regarding the relationship between PRV and cardiovascular diseases, or the enhanced capability of PRV to detect cardiovascular changes over HRV.

Although not all these questions were answered in this thesis, from the studies carried out two main conclusions were reached: (1) PRV is affected by cardiovascular changes in a different manner to HRV and is present even in the absence of autonomic regulation and HRV; and (2) PRV is a potential tool capable of aiding in the diagnosis and monitoring of cardiovascular variables, such as blood pressure and blood flow.

From the results obtained from the whole-body cold exposure study, it was evident that cold exposure affects PRV in different ways when obtained from peripheral and core vasculature, and that it contains different information that is not available in HRV. Although HRV and PRV showed a similar trend during the whole-body cold exposure test, it was evident that PRV overestimated the indices obtained from HRV, usually in a larger scale during the cold exposure. Also, HRV and PRV should not be regarded as the same when different temperature conditions are studied, and PRV may contain different information not available from HRV. Further studies are needed to better understand the contribution of sympathetic activity to PRV measurements as well as to characterize the effects of vasoconstriction of PRV indices. Also, future studies could aim to evaluate the capability of PRV to detect and monitor disorders related to arterial stiffening and vasoconstriction.

Similarly, PRV was shown to be affected differently to HRV with changes in blood pressure and was successfully used for the estimation of blood pressure values, both with data obtained from critically-ill subjects and from healthy volunteers. As has been reported in the literature, short-term related indices such as SDNN, RMSSD and HF were more affected by blood pressure states in PRV, and although PRV and HRV had similar trends again, it was found that PRV overestimated these indices. Future studies trying to understand the relationship between HRV and PRV should aim to better understand the contribution of SNS activity on PRV measurements. Moreover, it could be worth analysing how the differences between HRV and PRV change with this kind of changes, since the way PRV and HRV differ could be an indication of changes in peripheral and central ANS. For instance, Figure 11.1 shows the behaviour of AVNN and SDNN indices extracted from both HRV and PRV signals from different subjects at different blood pressure values. It can be seen that,

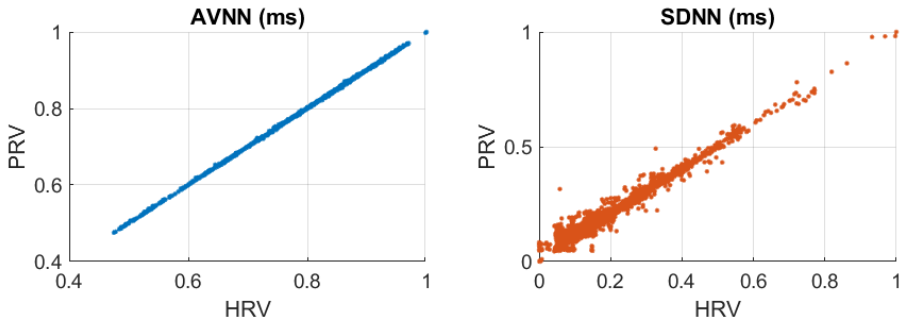

Figure 11.1: Comparison between AVNN and SDNN indices extracted from pulse rate variability (PRV) and heart rate variability (HRV) from subjects with different blood pressure values.

while AVNN extracted from HRV is almost perfectly linearly related to this index extracted from PRV, this is not the case for SDNN. Some of the differences could be due to technical factors, but it could be interesting to relate these differences to changes in blood pressure and evaluate the capability of these differences in the assessment of cardiovascular changes.

As has been mentioned previously, an additional contribution of this thesis was that it was shown that PRV is a potential tool capable of aiding in the monitoring and diagnosis of cardiovascular diseases. This was done by showing that PRV indices were capable of estimating BP values in a proof-of-concept study, and that there are differences in PRV due to haemodynamics changes even in the absence of HRV. Although the classification results were not satisfactory for identifying blood pressure states, PRV was shown to be able to classify hypertensive events in a relatively good manner, as well as to estimate blood pressure values with low errors. Future studies should aim to validate these results in larger datasets and to dilucidate the physiological explanation of the relationship between PRV indices and hyper- and hypotension.

Finally, in a first attempt to better understand how PRV may relate with haemodynamic changes, an in-vitro model was built to evaluate PRV in the absence of HRV and autonomic regulation. It was found that PRV was present and showed differences due to changes in blood flow and blood pressure. Although the relationship between PRV indices and blood pressure was not linear, it was evident that stroke volume changes have an effect on PRV indices, especially those related with short-term variability. This was observed in a setup without any other confounding variable, which suggests that PRV might contain information regarding

these changes, and is a potential tool for the non-invasive, continuous detection of these changes. Future studies should aim to validate these results in data obtained from healthy and diseased subjects. Furthermore, the availability of the in-vitro model opens the door for the generation of PPG signals with varying haemodynamic conditions, which could aid in the development of techniques that apply PRV information for the assessment, diagnoses and monitoring of cardiovascular diseases, and for carrying out other research related with PPG and cardiovascular changes, with or without the extraction of PRV.

11.3 Conclusion

Pulse rate variability has been used in recent decades for multiple applications as a surrogate of heart rate variability. It has been applied for the monitoring of mental health disorders, such as depression, anxiety and stress; for the assessment of sleep quality and obstructive sleep apnea; for the diagnosis, monitoring and assessment of respiratory and somatic disorders; and for the evaluation of cardiovascular health, using it for the evaluation of conditions such as peripheral arterial disease, atrial fibrillation, diabetes and blood pressure changes. Nonetheless, pulse rate variability is far from being fully understood, and there is still no consensus about the different physiological phenomena that may be affecting it, and how it relates to its precursor, i.e., heart rate variability.

In this thesis two main contributions were made. First, an initial approach to establish guidelines for the assessment of pulse rate variability from photoplethysmographic signals was proposed. This is one of the first attempts to standardise the technique, which is essential to reach its full potential and to allow for the comparison of different studies and to establish methodologies that can allow for the validation of the technique. Although this was done using simulated data and it still needs to be validated using data obtained from healthy subjects, the results obtained show that the effect of technical aspect on pulse rate variability assessment can be controlled and diminished by using appropriate processing and extraction strategies.

Secondly, it was shown that pulse rate variability is affected by cardiovascular changes, such as blood pressure changes and vasoconstriction, that this is true even in the absence of heart rate variability, and that its relationship with heart rate

variability is not straightforward and it may contain additional information to heart rate variability. More research is needed to fully explain these differences between pulse and heart rate variability, and to better link the physiology to the different indices that are extracted from pulse rate variability, especially for the non-linear indices, but it was found that pulse rate variability is a potential tool for the assessment of cardiovascular changes and that it has applications in the monitoring and assessment of several diseases, not only in clinical setting but also in everyday scenarios, making it a useful technique for public health.

Appendix A

Behaviour of Pulse Rate Variability indices against Blood Pressure

Figures A1 to A9 show the behaviour of pulse rate variability indices when compared against blood pressure values.

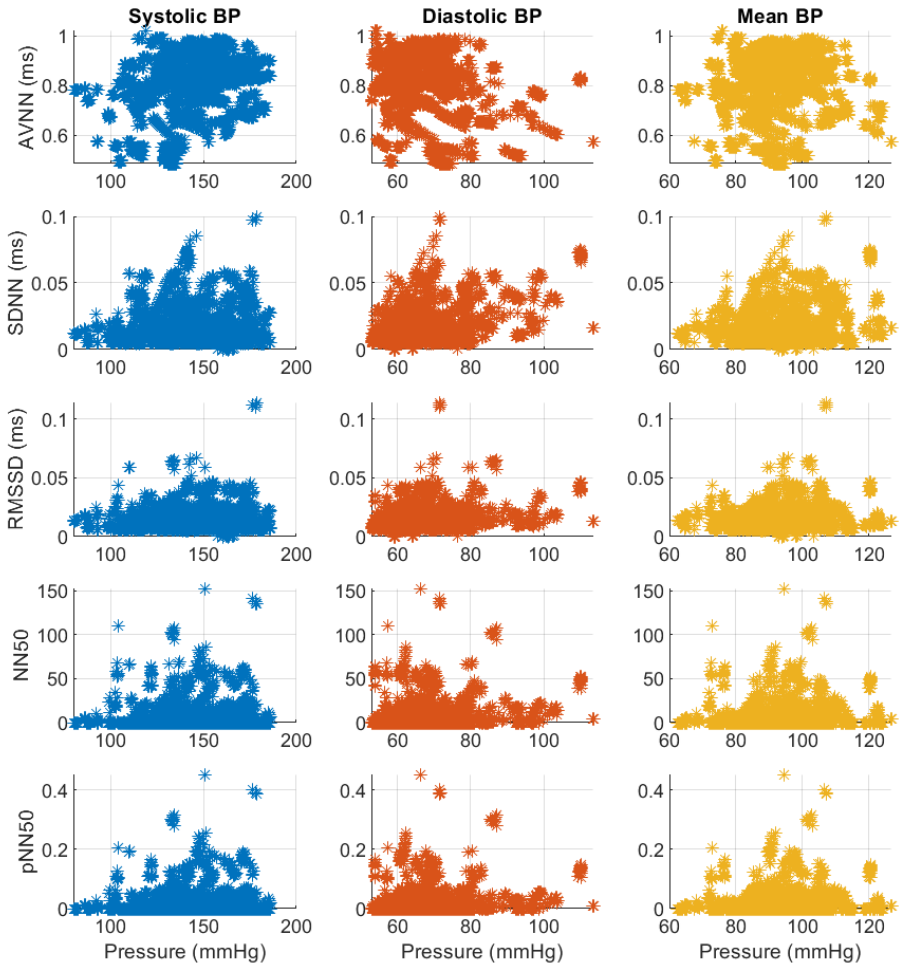

Figure A1: Behaviour of time domain indices extracted from pulse rate variability, compared to systolic blood pressure (BP, left column), diastolic BP (centre column) and mean arterial BP (right column).

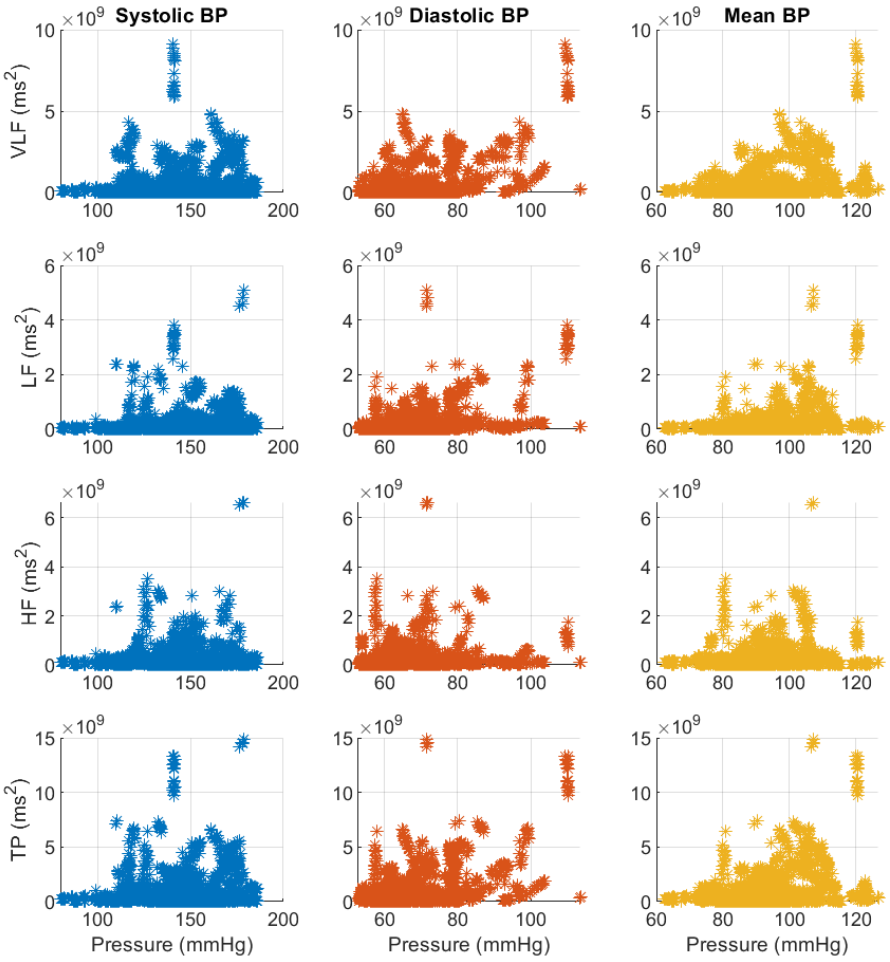

Figure A2: Behaviour of absolute frequency domain indices extracted from pulse rate variability, compared to systolic blood pressure (BP, left column), diastolic BP (centre column) and mean arterial BP (right column).

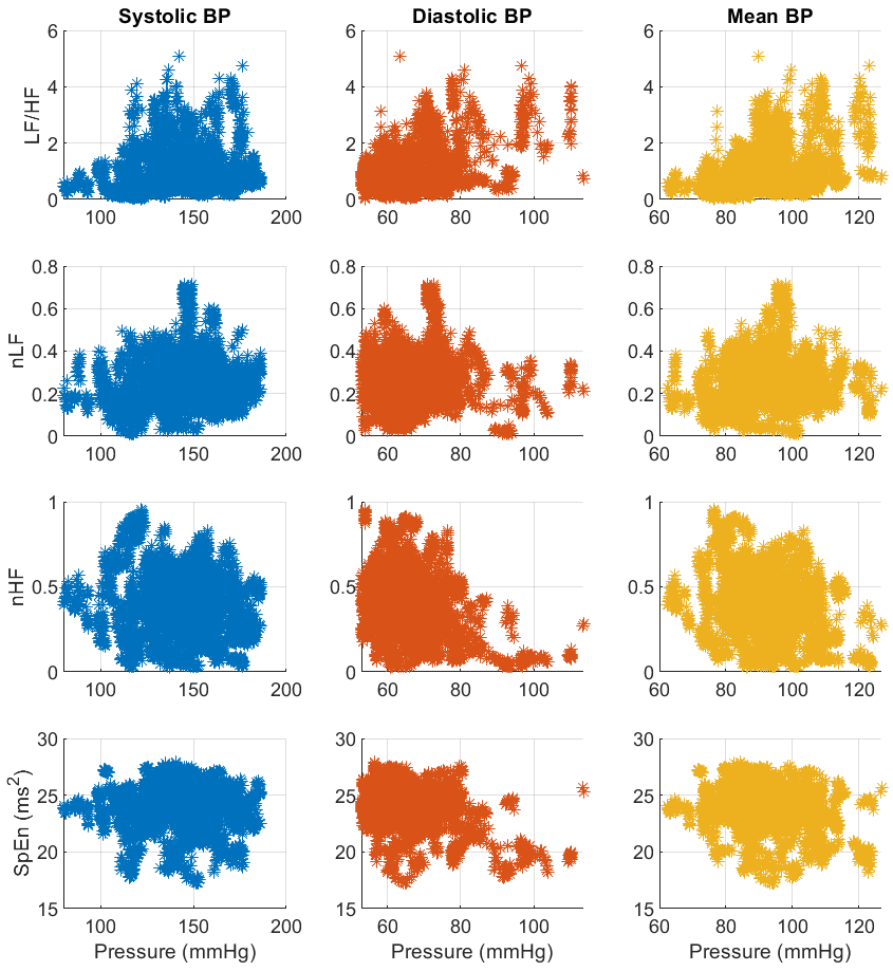

Figure A3: Behaviour of relative frequency domain indices extracted from pulse rate variability, compared to systolic blood pressure (BP, left column), diastolic BP (centre column) and mean arterial BP (right column).

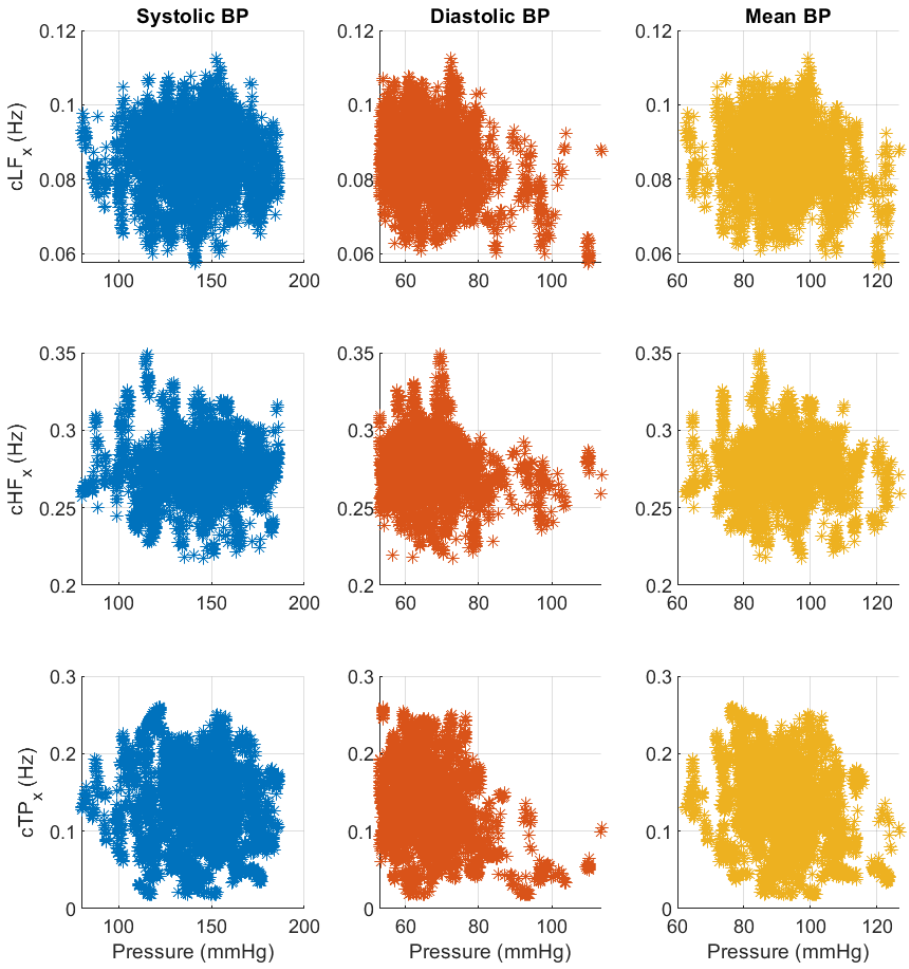

Figure A4: Behaviour of the x-coordinate of centroid-related frequency domain indices extracted from pulse rate variability, compared to systolic blood pressure (BP, left column), diastolic BP (centre column) and mean arterial BP (right column).

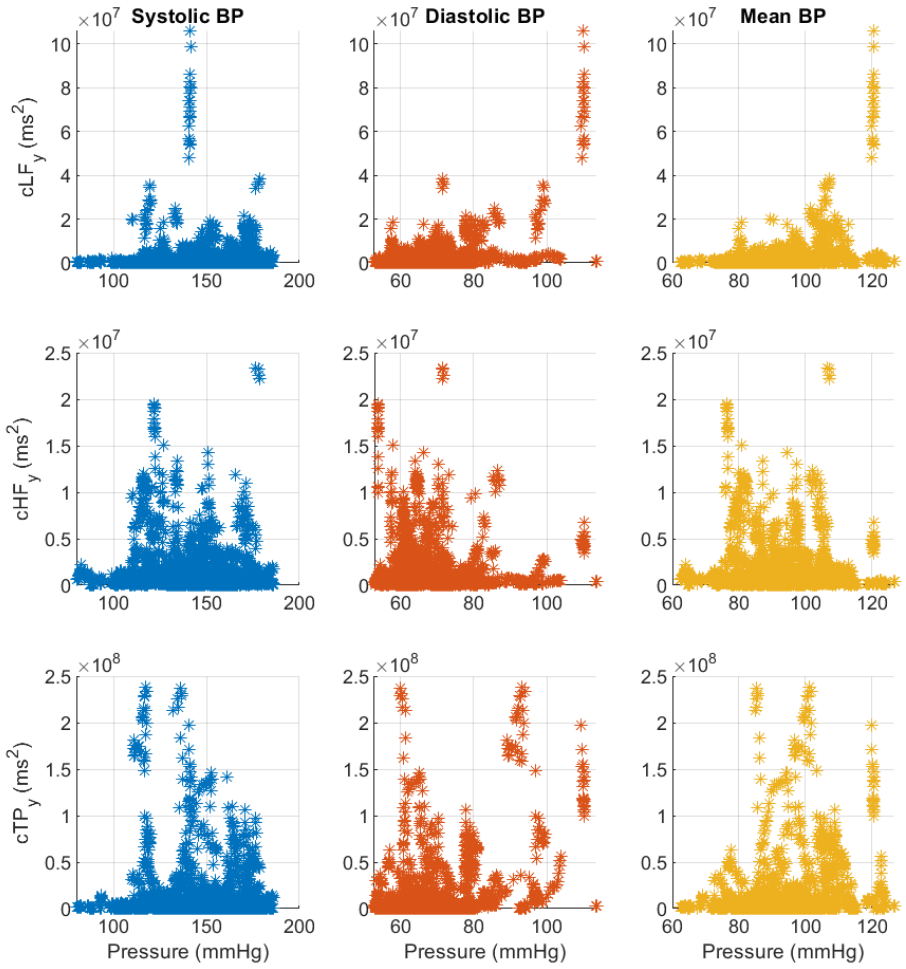

Figure A5: Behaviour of the y-coordinate of centroid-related frequency domain indices extracted from pulse rate variability, compared to systolic blood pressure (BP, left column), diastolic BP (centre column) and mean arterial BP (right column).

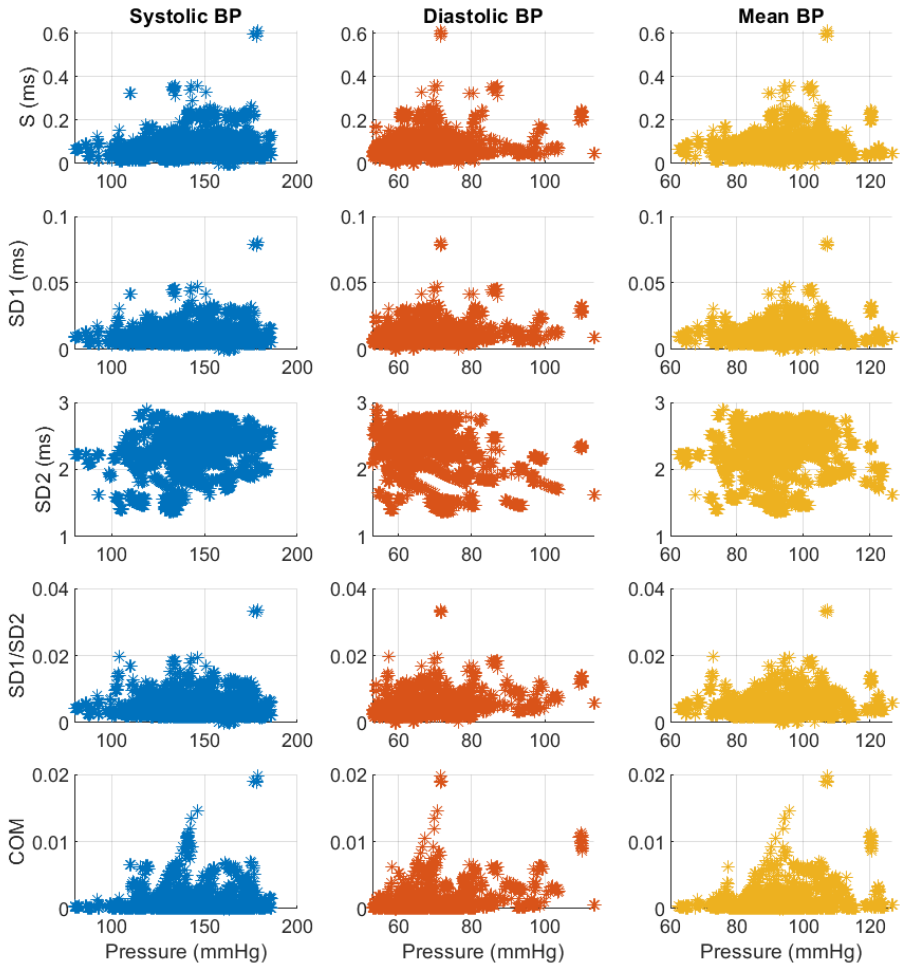

Figure A6: Behaviour of Poincaré plot indices extracted from pulse rate variability, compared to systolic blood pressure (BP, left column), diastolic BP (centre column) and mean arterial BP (right column).

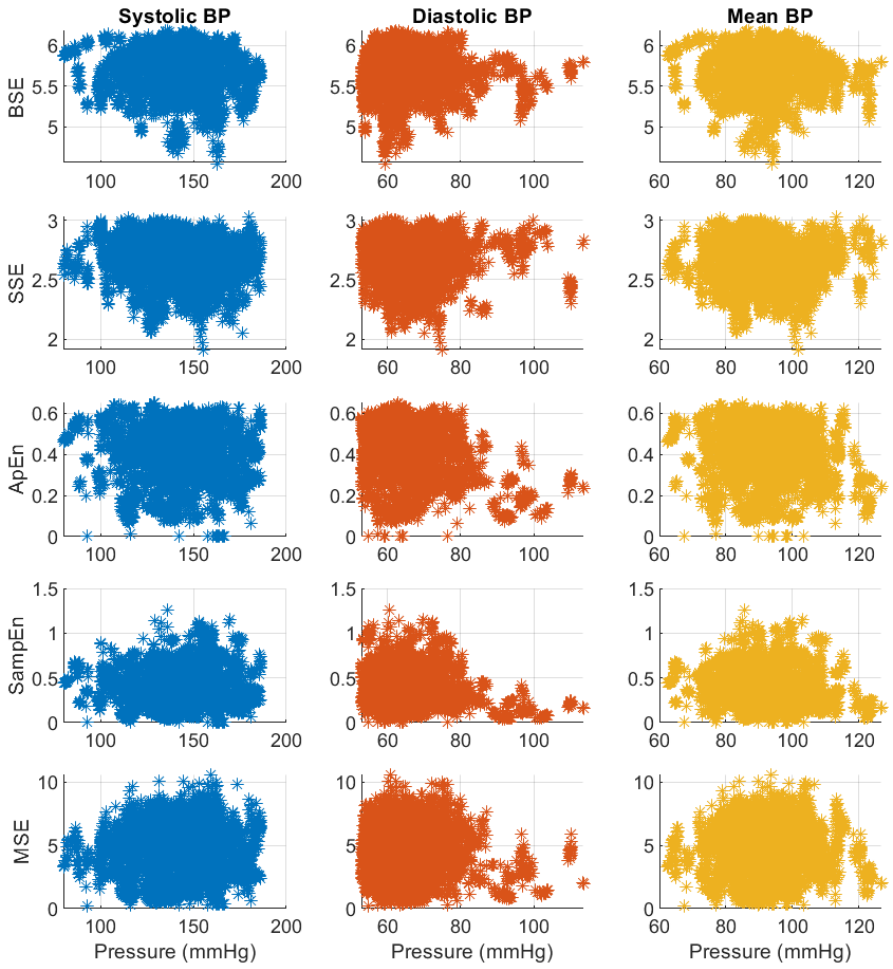

Figure A7: Behaviour of entropy-related indices extracted from pulse rate variability, compared to systolic blood pressure (BP, left column), diastolic BP (centre column) and mean arterial BP (right column).

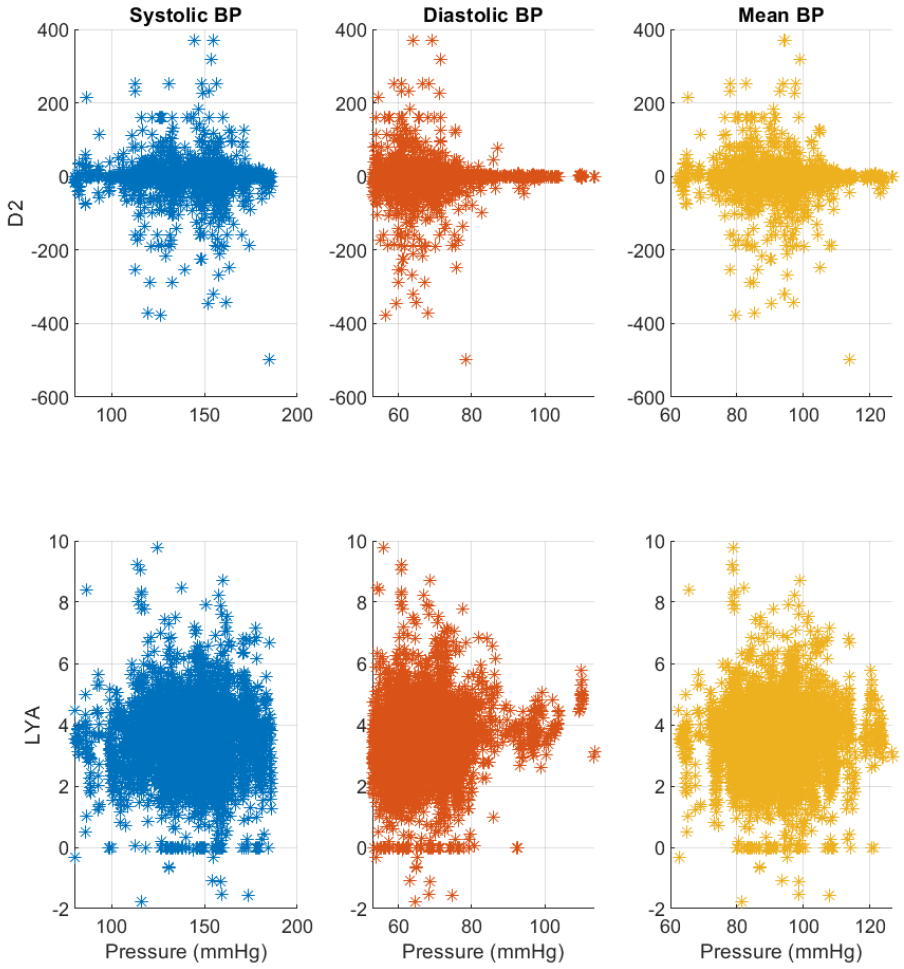

Figure A8: Behaviour of phase-related indices extracted from pulse rate variability, compared to systolic blood pressure (BP, left column), diastolic BP (centre column) and mean arterial BP (right column).

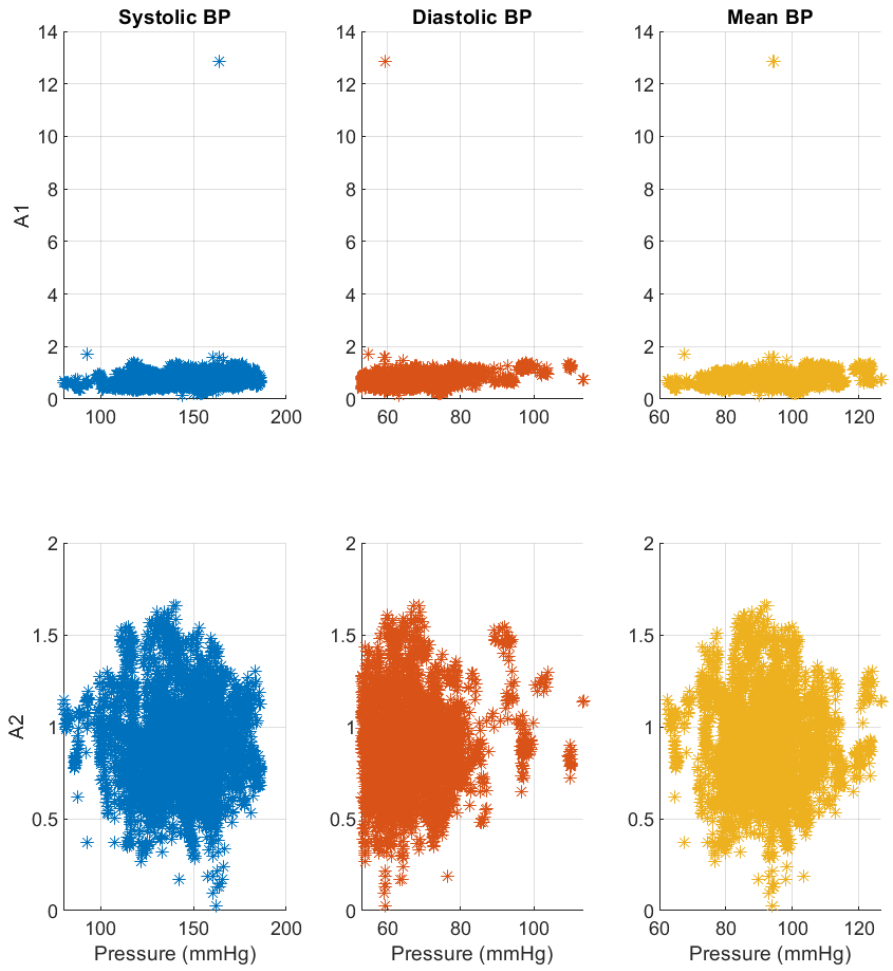

Figure A9: Behaviour of detrended fluctuation analysis related indices extracted from pulse rate variability, compared to systolic blood pressure (BP, left column), diastolic BP (centre column) and mean arterial BP (right column).

Appendix B

Confusion matrices

Tables A1 to A33 show the confusion matrices obtained with each of the algorithms developed in this study. These matrices were calculated as shown previously, but are presented as the percentage of samples classified as each condition, and as the mean ± standard deviation after the 10-fold cross-validation.

Table A1: Confusion matrices obtained for the k-Nearest Neighbors algorithms evaluated using all features extracted from 5- and 1-min segments. Values are presented as the mean percentage ± the standard deviation, obtained after the 10-fold cross-validation. Hypo: hypotension. Normo: normotension. Hyper: hypertension.

k	**True class**	**Predicted class**					
		5-min segments			**1-min segments**		
		Hypo	Normo	Hyper	Hypo	Normo	Hyper
3	Hypo	14.54 ± 1.25	17.47 ± 1.19	1.33 ± 0.36	21.91 ± 0.98	8.54 ± 0.90	2.88 ± 0.69
	Normo	32.01 ± 0.82	0.77 ± 0.49	0.56 ± 0.46	22.24 ± 0.63	4.51 ± 0.67	6.59 ± 0.71
	Hyper	12.72 ± 1.69	3.61 ± 0.76	17.01 ± 1.67	15.05 ± 1.12	8.25 ± 0.78	10.04 ± 0.81
5	Hypo	15.62 ± 1.70	16.67 ± 1.43	1.05 ± 0.62	22.45 ± 1.05	8.64 ± 0.90	2.25 ± 0.58
	Normo	30.99 ± 0.76	1.88 ± 0.67	0.46 ± 0.55	21.00 ± 0.84	6.64 ± 0.74	5.69 ± 0.69
	Hyper	12.16 ± 1.37	3.83 ± 1.08	17.35 ± 1.66	13.89 ± 1.31	9.29 ± 0.83	10.15 ± 1.10
7	Hypo	14.01 ± 1.95	17.38 ± 1.62	1.94 ± 0.68	20.90 ± 1.44	8.18 ± 1.08	4.25 ± 0.76
	Normo	28.95 ± 1.28	2.75 ± 0.85	1.64 ± 0.70	19.12 ± 0.90	6.62 ± 0.95	7.60 ± 0.91
	Hyper	11.91 ± 1.18	3.70 ± 1.10	17.72 ± 1.58	12.30 ± 1.47	9.19 ± 0.83	11.84 ± 1.26
9	Hypo	13.27 ± 1.81	17.90 ± 1.64	2.16 ± 0.76	22.40 ± 0.67	6.83 ± 0.74	4.10 ± 0.51
	Normo	28.36 ± 1.07	3.89 ± 0.88	1.08 ± 0.76	19.16 ± 1.07	6.39 ± 1.01	7.78 ± 0.98
	Hyper	11.33 ± 1.65	4.41 ± 1.56	17.59 ± 1.64	12.36 ± 1.03	8.56 ± 0.77	12.41 ± 0.93

Table A2: Confusion matrices obtained for the neural networks evaluated using all features extracted from 5- and 1-min segments. Values are presented as the mean percentage ± the standard deviation, obtained after the 10-fold cross-validation. Hypo: hypotension. Normo: normotension. Hyper: hypertension. N: number of neurons in the hidden layer.

N	**True class**	**Predicted class**					
		5-min segments			**1-min segments**		
		Hypo	Normo	Hyper	Hypo	Normo	Hyper
2	Hypo	5.12 ± 3.92	17.28 ± 9.43	10.93 ± 9.09	19.68 ± 5.00	4.60 ± 2.99	9.04 ± 5.85
	Normo	5.40 ± 4.71	18.21 ± 9.88	9.72 ± 9.11	15.76 ± 4.09	5.50 ± 3.82	12.07 ± 5.54
	Hyper	3.09 ± 2.58	10.74 ± 8.01	19.51 ± 8.01	10.90 ± 2.73	5.03 ± 3.65	17.41 ± 4.45
3	Hypo	5.65 ± 3.96	19.81 ± 4.81	7.87 ± 3.59	20.21 ± 3.03	5.68 ± 2.69	7.45 ± 1.42
	Normo	6.20 ± 3.77	20.71 ± 4.11	6.42 ± 3.19	15.80 ± 2.32	6.07 ± 2.87	11.47 ± 2.09
	Hyper	3.61 ± 3.37	12.22 ± 5.79	17.50 ± 6.38	11.81 ± 1.68	5.43 ± 2.71	16.09 ± 2.96
4	Hypo	10.22 ± 6.50	16.39 ± 6.67	6.73 ± 2.78	17.90 ± 6.87	8.86 ± 8.89	6.57 ± 2.76
	Normo	11.73 ± 6.86	16.42 ± 6.66	5.19 ± 1.71	14.20 ± 5.43	9.22 ± 9.03	9.91 ± 4.06
	Hyper	5.15 ± 3.28	8.12 ± 3.56	20.06 ± 1.28	10.69 ± 4.08	8.56 ± 9.21	14.09 ± 5.62
5	Hypo	7.22 ± 3.69	19.66 ± 4.56	6.45 ± 2.33	19.93 ± 3.19	7.29 ± 2.61	6.12 ± 1.64
	Normo	8.09 ± 3.95	20.40 ± 4.49	4.85 ± 1.53	15.49 ± 3.14	7.95 ± 3.07	9.89 ± 1.71
	Hyper	3.83 ± 1.64	10.15 ± 1.52	19.35 ± 1.12	10.93 ± 1.64	6.47 ± 2.22	15.93 ± 2.08
6	Hypo	10.25 ± 4.69	16.20 ± 5.48	6.88 ± 2.60	18.82 ± 2.91	7.16 ± 2.10	7.35 ± 1.93
	Normo	12.16 ± 5.58	16.17 ± 5.80	5.00 ± 1.63	14.95 ± 2.37	8.75 ± 1.50	9.63 ± 2.27
	Hyper	4.78 ± 2.79	8.52 ± 2.68	20.03 ± 1.82	11.08 ± 1.54	7.57 ± 1.96	14.69 ± 2.36

Table A3: Confusion matrices obtained for the neural networks evaluated using all features extracted from 5- and 1-min segments. Values are presented as the mean percentage ± the standard deviation, obtained after the 10-fold cross-validation. Hypo: hypotension. Normo: normotension. Hyper: hypertension. N: number of neurons in the hidden layer.

N	**True class**	**Predicted class**					
		5-min segments			**1-min segments**		
		Hypo	Normo	Hyper	Hypo	Normo	Hyper
7	Hypo	9.07 ± 4.24	16.14 ± 3.58	8.12 ± 4.16	20.68 ± 3.01	6.44 ± 2.36	6.21 ± 1.24
	Normo	10.49 ± 4.93	16.64 ± 4.04	6.20 ± 2.64	16.19 ± 2.36	8.09 ± 1.98	9.06 ± 2.45
	Hyper	4.94 ± 2.29	8.09 ± 1.89	20.31 ± 1.40	11.26 ± 1.18	7.53 ± 2.02	14.54 ± 2.67
8	Hypo	10.15 ± 4.55	15.25 ± 5.67	7.93 ± 2.07	18.99 ± 2.44	7.50 ± 2.23	6.85 ± 1.60
	Normo	11.33 ± 4.31	15.56 ± 6.31	6.45 ± 3.01	14.66 ± 1.84	7.79 ± 2.71	10.88 ± 1.65
	Hyper	5.86 ± 3.02	7.99 ± 3.25	19.48 ± 3.62	10.48 ± 1.82	6.33 ± 2.64	16.53 ± 2.01
9	Hypo	7.47 ± 4.26	18.61 ± 3.38	7.25 ± 2.25	20.07 ± 3.48	7.01 ± 2.61	6.25 ± 1.27
	Normo	8.73 ± 4.52	19.04 ± 3.63	5.56 ± 1.65	15.63 ± 2.30	8.02 ± 2.20	9.68 ± 1.32
	Hyper	4.01 ± 2.45	9.72 ± 2.46	19.60 ± 1.88	10.09 ± 1.64	7.31 ± 2.24	15.94 ± 2.16
10	Hypo	8.77 ± 4.02	16.73 ± 3.13	7.84 ± 4.17	18.94 ± 2.71	7.74 ± 1.97	6.65 ± 1.80
	Normo	10.93 ± 4.54	16.33 ± 3.08	6.08 ± 4.14	14.61 ± 2.50	8.28 ± 2.45	10.44 ± 1.65
	Hyper	5.28 ± 2.61	7.75 ± 1.37	20.31 ± 1.83	9.52 ± 1.81	7.08 ± 1.98	16.74 ± 1.23
11	Hypo	11.33 ± 2.08	14.57 ± 3.28	7.44 ± 2.13	19.93 ± 2.79	6.74 ± 1.57	6.67 ± 1.86
	Normo	12.87 ± 2.84	14.41 ± 3.18	6.05 ± 2.32	16.07 ± 1.59	7.35 ± 1.38	9.91 ± 1.04
	Hyper	5.80 ± 1.90	7.10 ± 2.92	20.43 ± 1.98	10.28 ± 1.53	7.14 ± 1.62	15.91 ± 1.97

Table A4: Confusion matrices obtained for the neural networks evaluated using all features extracted from 5- and 1-min segments. Values are presented as the mean percentage ± the standard deviation, obtained after the 10-fold cross-validation. Hypo: hypotension. Normo: normotension. Hyper: hypertension. N: number of neurons in the hidden layer.

N	**True class**	**Predicted class**					
		5-min segments			**1-min segments**		
		Hypo	Normo	Hyper	Hypo	Normo	Hyper
12	Hypo	8.43 ± 3.66	16.94 ± 4.06	7.96 ± 2.82	18.54 ± 3.01	7.53 ± 2.26	7.26 ± 2.18
	Normo	10.25 ± 3.74	17.16 ± 3.38	5.93 ± 2.30	13.70 ± 2.65	9.44 ± 2.97	10.20 ± 1.82
	Hyper	3.83 ± 1.55	8.98 ± 2.47	20.52 ± 1.47	9.27 ± 1.30	8.26 ± 1.88	15.80 ± 1.22
13	Hypo	9.60 ± 2.10	15.77 ± 3.86	7.96 ± 3.20	18.79 ± 3.40	6.88 ± 1.50	7.66 ± 2.25
	Normo	12.59 ± 3.00	13.89 ± 4.11	6.85 ± 2.94	13.81 ± 2.84	8.43 ± 1.78	11.10 ± 2.32
	Hyper	5.09 ± 1.19	7.28 ± 1.55	20.96 ± 1.94	9.31 ± 1.56	7.30 ± 2.24	16.72 ± 2.17
14	Hypo	9.20 ± 2.91	15.25 ± 4.69	8.89 ± 3.30	19.25 ± 1.90	6.91 ± 1.19	7.17 ± 1.63
	Normo	10.99 ± 2.75	15.49 ± 3.40	6.85 ± 3.25	14.77 ± 1.47	7.86 ± 1.26	10.70 ± 1.33
	Hyper	4.88 ± 1.59	7.84 ± 1.03	20.62 ± 1.58	10.07 ± 1.28	7.01 ± 1.08	16.25 ± 0.94
15	Hypo	10.15 ± 1.98	15.25 ± 3.21	7.93 ± 4.08	17.15 ± 1.82	8.43 ± 1.95	7.76 ± 1.71
	Normo	11.91 ± 1.57	14.94 ± 2.95	6.48 ± 3.56	12.88 ± 2.16	10.28 ± 2.36	10.17 ± 1.16
	Hyper	5.80 ± 1.55	7.19 ± 1.04	20.34 ± 2.03	8.90 ± 2.36	8.35 ± 1.87	16.09 ± 1.85
16	Hypo	9.26 ± 2.86	16.36 ± 3.70	7.72 ± 2.35	17.77 ± 1.90	7.66 ± 1.03	7.91 ± 1.85
	Normo	11.05 ± 2.45	15.93 ± 4.07	6.36 ± 2.90	13.80 ± 2.03	9.11 ± 1.49	10.43 ± 2.69
	Hyper	4.51 ± 1.37	8.21 ± 1.61	20.62 ± 1.36	9.52 ± 1.18	6.95 ± 1.68	16.87 ± 2.16

Table A5: Confusion matrices obtained for the neural networks evaluated using all features extracted from 5- and 1-min segments. Values are presented as the mean percentage ± the standard deviation, obtained after the 10-fold cross-validation. Hypo: hypotension. Normo: normotension. Hyper: hypertension. N: number of neurons in the hidden layer.

N	**True class**	**Predicted class**					
		5-min segments			**1-min segments**		
		Hypo	Normo	Hyper	Hypo	Normo	Hyper
17	Hypo	9.94 ± 1.90	16.39 ± 2.41	7.01 ± 1.57	18.29 ± 3.22	6.93 ± 2.22	8.12 ± 2.24
	Normo	11.05 ± 2.34	16.79 ± 2.60	5.49 ± 1.70	14.61 ± 2.84	7.78 ± 2.41	10.95 ± 2.15
	Hyper	5.90 ± 1.10	6.98 ± 1.59	20.46 ± 2.17	9.32 ± 2.07	6.90 ± 2.13	17.11 ± 1.44
18	Hypo	9.44 ± 2.93	15.12 ± 3.22	8.77 ± 3.92	18.23 ± 3.94	7.86 ± 2.89	7.24 ± 2.50
	Normo	10.96 ± 3.77	15.06 ± 2.37	7.31 ± 3.88	13.89 ± 3.10	8.92 ± 2.89	10.53 ± 2.30
	Hyper	4.81 ± 1.40	7.72 ± 1.45	20.80 ± 2.25	9.17 ± 1.99	7.68 ± 2.33	16.48 ± 1.93
19	Hypo	9.51 ± 2.61	15.09 ± 4.42	8.73 ± 2.54	16.61 ± 2.45	8.18 ± 1.61	8.54 ± 3.01
	Normo	11.11 ± 3.57	14.54 ± 3.99	7.69 ± 2.05	12.48 ± 1.42	9.22 ± 1.86	11.63 ± 2.37
	Hyper	5.09 ± 1.33	7.16 ± 2.54	21.08 ± 1.98	8.54 ± 0.81	7.52 ± 2.42	17.28 ± 2.20
20	Hypo	10.52 ± 2.52	15.96 ± 1.56	6.85 ± 2.05	17.91 ± 3.35	7.82 ± 1.76	7.60 ± 2.60
	Normo	13.36 ± 2.91	14.88 ± 2.39	5.09 ± 2.38	14.02 ± 2.82	8.91 ± 1.70	10.40 ± 1.62
	Hyper	5.37 ± 1.32	7.31 ± 1.91	20.65 ± 1.77	9.27 ± 2.17	7.83 ± 1.24	16.23 ± 2.17

Table A6: Confusion matrices obtained for the one-vs-all linear support vector machine evaluated using all features extracted from 5- and 1-min segments. Values are presented as the mean percentage ± the standard deviation, obtained after the 10-fold cross-validation. Hypo: hypotension. Normo: normotension. Hyper: hypertension.

True class	**Predicted class**					
	5-min segments			**1-min segments**		
	Hypo	Normo	Hyper	Hypo	Normo	Hyper
Hypo	6.42 ± 1.61	11.20 ± 1.89	15.71 ± 2.18	13.21 ± 1.66	5.01 ± 1.33	15.11 ± 0.98
Normo	7.53 ± 1.25	11.85 ± 1.41	13.95 ± 1.15	9.70 ± 1.89	5.06 ± 2.12	18.58 ± 0.69
Hyper	3.83 ± 0.72	5.12 ± 1.34	24.38 ± 1.52	6.67 ± 1.37	3.66 ± 1.26	23.00 ± 0.96

Table A7: Confusion matrices obtained for the one-vs-all radial basis support vector machines evaluated using all features extracted from 5- and 1-min segments. Values are presented as the mean percentage ± the standard deviation, obtained after the 10-fold cross-validation. Hypo: hypotension. Normo: normotension. Hyper: hypertension. σ: Scale of kernel.

σ	**True class**	**Predicted class**					
		5-min segments			**1-min segments**		
		Hypo	Normo	Hyper	Hypo	Normo	Hyper
0.5	Hypo	0.00 ± 0.00	17.16 ± 1.17	16.17 ± 1.17	0.00 ± 0.00	11.99 ± 1.14	21.34 ± 1.17
	Normo	17.50 ± 1.16	0.03 ± 0.10	15.80 ± 1.14	11.99 ± 1.27	0.00 ± 0.00	21.34 ± 1.28
	Hyper	8.67 ± 4.37	5.99 ± 4.28	18.67 ± 1.37	9.78 ± 1.74	5.78 ± 1.79	17.78 ± 0.94
1.0	Hypo	0.90 ± 0.40	19.29 ± 1.18	13.15 ± 1.42	0.63 ± 0.45	12.20 ± 1.16	20.50 ± 1.18
	Normo	18.80 ± 1.61	0.37 ± 0.38	14.17 ± 1.61	12.38 ± 1.13	0.55 ± 0.26	20.40 ± 1.24
	Hyper	8.27 ± 1.50	6.54 ± 1.11	18.52 ± 1.47	10.10 ± 1.04	5.99 ± 0.45	17.24 ± 0.85
1.5	Hypo	1.94 ± 0.58	21.39 ± 0.97	10.00 ± 0.89	5.81 ± 1.04	13.57 ± 0.94	13.96 ± 0.95
	Normo	20.99 ± 1.59	1.23 ± 0.76	11.11 ± 1.46	16.17 ± 1.17	2.28 ± 0.31	14.89 ± 1.13
	Hyper	6.79 ± 1.55	8.15 ± 1.45	18.40 ± 1.37	10.64 ± 1.24	7.71 ± 0.66	14.98 ± 1.01
2.0	Hypo	2.56 ± 0.68	22.93 ± 1.11	7.84 ± 0.90	8.38 ± 1.35	14.17 ± 0.63	10.79 ± 1.01
	Normo	22.10 ± 2.11	2.25 ± 0.84	8.98 ± 1.60	17.70 ± 0.92	3.47 ± 0.66	12.17 ± 1.01
	Hyper	6.42 ± 1.57	8.21 ± 1.60	18.70 ± 1.56	10.77 ± 1.22	8.46 ± 0.81	14.10 ± 0.92

Table A8: Confusion matrices obtained for the one-vs-all polynomial support vector machines evaluated using all features extracted from 5- and 1-min segments. Values are presented as the mean percentage ± the standard deviation, obtained after the 10-fold cross-validation. Hypo: hypotension. Normo: normotension. Hyper: hypertension. n: Order of the polynomial kernel.

n	**True class**	**Predicted class**					
		5-min segments			**1-min segments**		
		Hypo	Normo	Hyper	Hypo	Normo	Hyper
3	Hypo	4.91 ± 1.91	25.15 ± 1.63	3.27 ± 2.67	21.97 ± 13.17	5.50 ± 9.66	5.87 ± 8.79
	Normo	26.05 ± 1.83	3.77 ± 1.46	3.52 ± 3.02	22.13 ± 12.09	4.28 ± 8.87	6.93 ± 9.17
	Hyper	11.60 ± 4.71	10.15 ± 1.85	11.57 ± 6.14	20.15 ± 13.10	4.96 ± 9.12	8.23 ± 10.20
4	Hypo	12.25 ± 14.49	11.45 ± 14.13	9.63 ± 11.86	10.70 ± 15.48	19.13 ± 16.37	3.50 ± 10.49
	Normo	11.88 ± 14.21	11.17 ± 14.12	10.28 ± 12.07	10.33 ± 15.41	19.51 ± 16.38	3.50 ± 10.49
	Hyper	11.39 ± 15.11	10.80 ± 15.10	11.14 ± 14.10	10.62 ± 15.43	19.30 ± 16.41	3.41 ± 10.51
5	Hypo	10.43 ± 15.26	9.91 ± 15.39	12.99 ± 15.80	6.92 ± 13.78	13.14 ± 16.77	13.27 ± 17.03
	Normo	10.40 ± 15.48	9.81 ± 15.45	13.12 ± 16.15	6.95 ± 13.80	13.13 ± 16.85	13.26 ± 17.01
	Hyper	10.37 ± 15.78	10.00 ± 15.82	12.96 ± 16.61	7.05 ± 13.80	13.03 ± 16.69	13.26 ± 17.08

Table A9: Confusion matrices obtained for the one-vs-one linear support vector machine evaluated using all features extracted from 5- and 1-min segments. Values are presented as the mean percentage ± the standard deviation, obtained after the 10-fold cross-validation. Hypo: hypotension. Normo: normotension. Hyper: hypertension.

True class	**Predicted class**					
	5-min segments			**1-min segments**		
	Hypo	Normo	Hyper	Hypo	Normo	Hyper
Hypo	6.57 ± 1.91	19.88 ± 2.71	6.88 ± 1.43	17.88 ± 1.55	9.44 ± 1.02	6.02 ± 1.19
Normo	7.99 ± 1.78	20.00 ± 1.92	5.34 ± 0.80	13.52 ± 1.30	10.01 ± 0.80	9.81 ± 1.07
Hyper	4.17 ± 1.32	9.48 ± 1.86	19.69 ± 1.56	8.85 ± 0.85	8.92 ± 1.00	15.57 ± 0.88

Table A10: Confusion matrices obtained for the one-vs-one radial-basis support vector machines evaluated using all features extracted from 5- and 1-min segments. Values are presented as the mean percentage ± the standard deviation, obtained after the 10-fold cross-validation. Hypo: hypotension. Normo: normotension. Hyper: hypertension. σ: Scale of kernel.

σ	**True class**	**Predicted class**					
		5-min segments			**1-min segments**		
		Hypo	Normo	Hyper	Hypo	Normo	Hyper
0.5	Hypo	0.77 ± 0.44	21.82 ± 0.64	10.74 ± 0.82	2.77 ± 4.15	14.02 ± 4.98	16.54 ± 6.13
	Normo	20.96 ± 1.16	1.23 ± 0.76	11.14 ± 1.42	14.92 ± 5.82	1.35 ± 3.14	17.06 ± 6.17
	Hyper	3.83 ± 1.61	11.08 ± 1.77	18.43 ± 1.50	13.18 ± 7.83	7.83 ± 7.17	12.33 ± 8.24
1.0	Hypo	1.85 ± 0.63	28.21 ± 1.26	3.27 ± 1.19	9.24 ± 1.30	16.85 ± 1.22	7.24 ± 0.80
	Normo	25.74 ± 1.59	3.40 ± 1.19	4.20 ± 1.14	21.96 ± 1.08	3.03 ± 0.67	8.35 ± 0.93
	Hyper	4.26 ± 1.31	13.21 ± 2.58	15.86 ± 1.77	16.76 ± 0.92	8.72 ± 0.74	7.86 ± 0.96
1.5	Hypo	2.44 ± 0.61	28.49 ± 1.08	2.41 ± 0.74	9.19 ± 0.96	17.10 ± 0.78	7.04 ± 0.49
	Normo	25.74 ± 1.26	5.74 ± 1.59	1.85 ± 0.93	19.90 ± 0.98	4.60 ± 0.66	8.83 ± 0.95
	Hyper	4.66 ± 1.41	12.25 ± 2.27	16.42 ± 1.61	13.10 ± 0.88	9.99 ± 0.70	10.25 ± 0.78
2.0	Hypo	2.81 ± 0.72	28.36 ± 0.85	2.16 ± 0.56	12.07 ± 1.28	15.36 ± 1.03	5.91 ± 0.82
	Normo	22.44 ± 1.47	9.66 ± 1.37	1.23 ± 0.70	19.15 ± 0.92	5.40 ± 0.65	8.78 ± 0.87
	Hyper	4.44 ± 0.95	11.73 ± 1.83	17.16 ± 1.72	11.78 ± 1.06	10.15 ± 0.57	11.40 ± 0.96

Table A11: Confusion matrices obtained for the one-vs-one polynomial support vector machines evaluated using all features extracted from 5- and 1-min segments. Values are presented as the mean percentage ± the standard deviation, obtained after the 10-fold cross-validation. Hypo: hypotension. Normo: normotension. Hyper: hypertension. n: Order of the polynomial kernel.

n	**True class**	**Predicted class**					
		5-min segments			**1-min segments**		
		Hypo	Normo	Hyper	Hypo	Normo	Hyper
3	Hypo	1.94 ± 0.68	26.60 ± 1.25	4.78 ± 1.07	12.98 ± 11.03	4.12 ± 5.69	16.24 ± 9.08
	Normo	26.33 ± 1.33	1.88 ± 0.83	5.12 ± 1.46	11.63 ± 10.47	3.11 ± 4.01	18.60 ± 8.73
	Hyper	8.30 ± 1.48	8.58 ± 1.66	16.45 ± 1.86	11.04 ± 10.09	4.13 ± 5.39	18.16 ± 8.40
4	Hypo	2.38 ± 1.75	8.92 ± 11.88	22.04 ± 11.58	7.76 ± 13.73	0.37 ± 0.72	25.20 ± 13.51
	Normo	3.40 ± 2.71	8.80 ± 11.16	21.14 ± 11.33	7.84 ± 13.63	0.16 ± 0.36	25.33 ± 13.56
	Hyper	1.39 ± 1.04	8.21 ± 12.30	23.73 ± 12.39	7.70 ± 13.55	0.44 ± 0.77	25.20 ± 13.36
5	Hypo	0.37 ± 0.60	0.99 ± 1.04	31.98 ± 1.06	6.88 ± 13.84	0.03 ± 0.10	26.42 ± 13.80
	Normo	0.40 ± 0.48	0.86 ± 0.88	32.07 ± 0.79	6.88 ± 13.92	0.02 ± 0.05	26.43 ± 13.89
	Hyper	0.40 ± 0.36	0.34 ± 0.37	32.59 ± 0.49	6.85 ± 13.89	0.02 ± 0.05	26.47 ± 13.91

Table A12: Confusion matrices obtained for the k-Nearest Neighbors algorithms evaluated using ranked features extracted from 5- and 1-min segments. Values are presented as the mean percentage ± the standard deviation, obtained after the 10-fold cross-validation. Hypo: hypotension. Normo: normotension. Hyper: hypertension.

k	**True class**	**Predicted class**					
		5-min segments			**1-min segments**		
		Hypo	Normo	Hyper	Hypo	Normo	Hyper
3	Hypo	14.32 ± 0.92	17.59 ± 0.74	1.42 ± 0.64	20.87 ± 1.22	9.31 ± 0.87	3.16 ± 0.83
	Normo	31.94 ± 0.70	0.71 ± 0.46	0.68 ± 0.46	22.17 ± 1.00	4.75 ± 0.59	6.41 ± 1.04
	Hyper	12.53 ± 1.17	3.98 ± 1.01	16.82 ± 1.25	14.87 ± 1.16	8.52 ± 0.86	9.94 ± 0.92
5	Hypo	15.19 ± 1.82	16.98 ± 1.71	1.17 ± 0.77	21.42 ± 0.87	9.48 ± 0.71	2.42 ± 0.88
	Normo	31.39 ± 0.90	1.57 ± 0.82	0.37 ± 0.28	20.51 ± 0.95	7.22 ± 1.08	5.60 ± 0.80
	Hyper	12.56 ± 1.43	3.46 ± 1.00	17.31 ± 1.19	13.73 ± 1.31	9.29 ± 0.93	10.31 ± 0.91
7	Hypo	13.06 ± 2.14	18.06 ± 2.36	2.22 ± 0.77	19.59 ± 1.08	9.05 ± 0.86	4.70 ± 0.95
	Normo	28.70 ± 1.02	2.81 ± 0.94	1.82 ± 0.62	18.51 ± 1.02	7.71 ± 0.96	7.11 ± 0.95
	Hyper	11.39 ± 1.52	4.32 ± 1.03	17.62 ± 1.39	11.92 ± 0.92	9.34 ± 0.73	12.07 ± 1.09
9	Hypo	12.65 ± 1.63	18.55 ± 1.69	2.13 ± 0.82	20.77 ± 0.80	8.43 ± 0.91	4.13 ± 0.71
	Normo	28.43 ± 0.91	3.83 ± 0.79	1.08 ± 0.55	18.32 ± 1.30	7.61 ± 1.15	7.40 ± 0.64
	Hyper	11.11 ± 1.90	4.81 ± 1.60	17.41 ± 1.39	11.63 ± 0.57	8.95 ± 0.67	12.75 ± 0.91

Table A13: Confusion matrices obtained for the neural networks evaluated using ranked features extracted from 5- and 1-min segments. Values are presented as the mean percentage ± the standard deviation, obtained after the 10-fold cross-validation. Hypo: hypotension. Normo: normotension. Hyper: hypertension. N: number of neurons in the hidden layer.

N	**True class**	**Predicted class**					
		5-min segments			**1-min segments**		
		Hypo	Normo	Hyper	Hypo	Normo	Hyper
2	Hypo	3.30 ± 2.10	21.57 ± 3.57	8.46 ± 3.07	13.39 ± 8.22	7.45 ± 6.61	12.49 ± 3.88
	Normo	4.10 ± 2.04	22.44 ± 3.37	6.79 ± 2.61	11.68 ± 6.91	7.06 ± 6.74	14.59 ± 4.51
	Hyper	2.35 ± 0.99	11.20 ± 1.78	19.78 ± 1.42	8.13 ± 5.01	6.33 ± 5.47	18.87 ± 3.33
3	Hypo	4.04 ± 3.50	20.09 ± 4.63	9.20 ± 2.38	15.03 ± 6.49	9.81 ± 8.82	8.49 ± 3.67
	Normo	4.66 ± 3.87	21.05 ± 5.00	7.62 ± 2.97	12.45 ± 5.22	9.69 ± 8.79	11.19 ± 4.27
	Hyper	2.16 ± 2.31	10.31 ± 2.99	20.86 ± 1.93	8.48 ± 3.98	9.56 ± 8.72	15.29 ± 5.56
4	Hypo	8.73 ± 5.97	16.82 ± 6.20	7.78 ± 2.99	15.84 ± 7.10	7.38 ± 4.90	10.11 ± 8.37
	Normo	9.66 ± 7.33	17.38 ± 6.78	6.30 ± 2.51	13.22 ± 5.42	7.82 ± 4.32	12.29 ± 7.60
	Hyper	4.51 ± 3.86	8.30 ± 3.66	20.52 ± 1.65	10.17 ± 4.75	6.00 ± 3.51	17.16 ± 6.63
5	Hypo	6.45 ± 4.04	15.12 ± 6.03	11.76 ± 8.17	16.14 ± 5.22	8.10 ± 5.67	9.09 ± 2.30
	Normo	7.16 ± 4.85	15.68 ± 6.89	10.49 ± 8.75	13.88 ± 4.69	8.43 ± 5.79	11.03 ± 2.74
	Hyper	2.90 ± 2.55	7.50 ± 3.86	22.93 ± 4.35	9.58 ± 3.78	8.23 ± 5.52	15.52 ± 3.76
6	Hypo	10.22 ± 5.56	15.99 ± 4.97	7.13 ± 2.69	17.15 ± 2.75	6.85 ± 3.00	9.34 ± 1.85
	Normo	10.62 ± 5.56	17.31 ± 5.28	5.40 ± 2.32	14.25 ± 2.06	7.03 ± 3.05	12.06 ± 1.64
	Hyper	5.40 ± 2.88	7.56 ± 2.77	20.37 ± 1.68	9.53 ± 1.63	5.76 ± 2.49	18.04 ± 1.83

Table A14: Confusion matrices obtained for the neural networks evaluated using ranked features extracted from 5- and 1-min segments. Values are presented as the mean percentage ± the standard deviation, obtained after the 10-fold cross-validation. Hypo: hypotension. Normo: normotension. Hyper: hypertension. N: number of neurons in the hidden layer.

N	**True class**	**Predicted class**					
		5-min segments			**1-min segments**		
		Hypo	Normo	Hyper	Hypo	Normo	Hyper
7	Hypo	8.43 ± 2.27	17.81 ± 3.39	7.10 ± 1.94	15.50 ± 3.82	8.96 ± 2.81	8.87 ± 1.68
	Normo	10.46 ± 3.36	17.93 ± 3.66	4.94 ± 1.86	13.45 ± 2.67	8.52 ± 2.46	11.35 ± 1.62
	Hyper	4.20 ± 1.17	8.77 ± 1.77	20.37 ± 1.36	9.26 ± 2.05	7.39 ± 2.84	16.69 ± 3.11
8	Hypo	9.26 ± 4.41	15.77 ± 6.80	8.30 ± 4.51	17.00 ± 4.14	8.05 ± 3.17	8.28 ± 2.73
	Normo	9.35 ± 4.77	16.36 ± 5.69	7.62 ± 4.04	14.07 ± 3.26	8.39 ± 2.76	10.87 ± 2.46
	Hyper	4.01 ± 2.21	7.99 ± 3.09	21.33 ± 2.33	9.29 ± 2.21	6.49 ± 2.28	17.55 ± 1.07
9	Hypo	8.09 ± 3.40	18.49 ± 3.47	6.76 ± 1.64	17.33 ± 2.03	8.31 ± 1.41	7.70 ± 1.90
	Normo	9.26 ± 4.11	18.95 ± 4.05	5.12 ± 2.25	13.78 ± 1.46	9.00 ± 1.52	10.56 ± 1.86
	Hyper	4.04 ± 2.10	8.73 ± 1.36	20.56 ± 1.60	9.37 ± 1.55	7.68 ± 0.91	16.28 ± 2.00
10	Hypo	10.00 ± 3.97	14.78 ± 5.49	8.55 ± 3.17	16.40 ± 4.00	7.92 ± 2.34	9.01 ± 4.19
	Normo	11.48 ± 3.82	14.60 ± 5.38	7.25 ± 4.27	13.86 ± 2.95	8.02 ± 1.66	11.45 ± 3.61
	Hyper	5.06 ± 1.86	7.01 ± 2.57	21.27 ± 2.44	9.05 ± 1.97	6.30 ± 1.11	17.99 ± 2.45
11	Hypo	9.81 ± 3.08	17.28 ± 3.41	6.23 ± 2.12	15.81 ± 3.25	9.29 ± 1.39	8.23 ± 2.40
	Normo	10.93 ± 2.69	17.78 ± 3.02	4.63 ± 2.36	13.42 ± 3.06	9.86 ± 2.20	10.05 ± 2.48
	Hyper	5.49 ± 2.09	7.44 ± 1.95	20.40 ± 1.80	8.23 ± 1.82	8.18 ± 1.64	16.92 ± 1.16

Table A15: Confusion matrices obtained for the neural networks evaluated using ranked features extracted from 5- and 1-min segments. Values are presented as the mean percentage ± the standard deviation, obtained after the 10-fold cross-validation. Hypo: hypotension. Normo: normotension. Hyper: hypertension. N: number of neurons in the hidden layer.

N	**True class**	**Predicted class**					
		5-min segments			**1-min segments**		
		Hypo	Normo	Hyper	Hypo	Normo	Hyper
12	Hypo	8.46 ± 2.93	16.39 ± 4.13	8.49 ± 3.16	16.15 ± 2.75	9.65 ± 2.84	7.53 ± 1.65
	Normo	10.56 ± 4.52	16.14 ± 3.67	6.64 ± 2.77	13.65 ± 2.93	9.97 ± 2.23	9.71 ± 1.47
	Hyper	4.20 ± 1.87	8.18 ± 1.60	20.96 ± 1.67	8.59 ± 1.71	7.99 ± 2.03	16.76 ± 1.46
13	Hypo	10.31 ± 3.68	14.75 ± 4.12	8.27 ± 3.54	15.32 ± 3.65	9.03 ± 3.53	8.98 ± 1.86
	Normo	11.64 ± 2.62	14.72 ± 3.32	6.98 ± 3.37	11.91 ± 3.38	10.25 ± 3.66	11.18 ± 1.78
	Hyper	5.19 ± 1.76	6.76 ± 2.34	21.39 ± 2.00	8.09 ± 1.86	7.65 ± 3.27	17.60 ± 2.02
14	Hypo	9.41 ± 2.22	16.02 ± 2.40	7.90 ± 2.19	14.46 ± 2.74	9.94 ± 2.49	8.93 ± 1.76
	Normo	11.42 ± 2.33	15.93 ± 3.31	5.99 ± 2.74	11.57 ± 1.96	10.15 ± 2.11	11.62 ± 1.18
	Hyper	5.09 ± 1.54	7.44 ± 1.32	20.80 ± 1.31	7.52 ± 1.44	8.69 ± 1.80	17.13 ± 1.80
15	Hypo	8.12 ± 3.04	16.88 ± 1.94	8.33 ± 2.63	16.12 ± 2.31	8.69 ± 2.63	8.52 ± 1.76
	Normo	9.85 ± 4.02	16.20 ± 2.38	7.28 ± 3.20	13.03 ± 2.34	9.63 ± 3.04	10.67 ± 1.93
	Hyper	4.20 ± 1.50	8.02 ± 1.70	21.11 ± 2.06	8.30 ± 1.98	8.04 ± 2.82	17.00 ± 1.43
16	Hypo	9.75 ± 2.48	15.83 ± 2.34	7.75 ± 1.80	15.71 ± 1.52	9.09 ± 1.71	8.52 ± 1.87
	Normo	11.64 ± 2.43	14.97 ± 2.10	6.73 ± 3.01	12.48 ± 1.61	9.58 ± 1.63	11.27 ± 2.13
	Hyper	5.46 ± 1.67	7.16 ± 1.62	20.71 ± 2.20	8.33 ± 1.70	7.08 ± 1.23	17.93 ± 1.64

Table A16: Confusion matrices obtained for the neural networks evaluated using ranked features extracted from 5- and 1-min segments. Values are presented as the mean percentage ± the standard deviation, obtained after the 10-fold cross-validation. Hypo: hypotension. Normo: normotension. Hyper: hypertension. N: number of neurons in the hidden layer.

N	**True class**	**Predicted class**					
		5-min segments			**1-min segments**		
		Hypo	Normo	Hyper	Hypo	Normo	Hyper
17	Hypo	9.85 ± 2.93	14.26 ± 3.98	9.23 ± 2.59	15.91 ± 2.15	8.53 ± 2.73	8.90 ± 2.59
	Normo	11.11 ± 2.71	14.81 ± 2.81	7.41 ± 2.25	12.98 ± 2.03	8.93 ± 2.80	11.42 ± 2.79
	Hyper	5.28 ± 1.51	6.57 ± 1.82	21.48 ± 2.11	8.59 ± 1.07	6.17 ± 1.87	18.58 ± 1.86
18	Hypo	9.88 ± 2.94	15.59 ± 1.53	7.87 ± 2.69	16.45 ± 3.72	8.93 ± 2.73	7.95 ± 1.60
	Normo	11.11 ± 2.66	15.62 ± 1.79	6.60 ± 2.45	13.96 ± 3.13	9.24 ± 2.63	10.13 ± 1.89
	Hyper	5.12 ± 1.51	7.07 ± 1.44	21.14 ± 1.70	9.17 ± 2.29	7.34 ± 2.79	16.82 ± 1.63
19	Hypo	9.57 ± 2.75	14.04 ± 3.99	9.72 ± 2.83	16.09 ± 3.03	8.54 ± 2.55	8.70 ± 1.58
	Normo	10.68 ± 2.71	14.91 ± 4.19	7.75 ± 3.59	13.39 ± 3.06	8.75 ± 2.99	11.19 ± 0.43
	Hyper	4.57 ± 1.54	7.04 ± 1.79	21.73 ± 1.71	8.56 ± 1.46	7.16 ± 2.16	17.62 ± 0.89
20	Hypo	9.57 ± 4.29	14.48 ± 4.90	9.29 ± 2.96	17.26 ± 3.43	8.48 ± 2.27	7.60 ± 1.97
	Normo	10.62 ± 4.08	14.66 ± 4.50	8.06 ± 3.71	13.96 ± 3.41	9.14 ± 2.63	10.23 ± 1.55
	Hyper	5.25 ± 2.10	6.42 ± 2.58	21.67 ± 1.96	8.77 ± 2.44	7.47 ± 2.79	17.10 ± 1.78

Table A17: Confusion matrices obtained for the one-vs-all linear support vector machine evaluated using ranked features extracted from 5- and 1-min segments. Values are presented as the mean percentage ± the standard deviation, obtained after the 10-fold cross-validation. Hypo: hypotension. Normo: normotension. Hyper: hypertension.

True class	**Predicted class**					
	5-min segments			**1-min segments**		
	Hypo	Normo	Hyper	Hypo	Normo	Hyper
Hypo	6.42 ± 1.79	10.93 ± 1.50	15.99 ± 1.72	12.30 ± 2.97	8.09 ± 3.34	12.95 ± 1.42
Normo	6.08 ± 1.72	12.10 ± 1.47	15.15 ± 0.95	9.94 ± 2.93	8.26 ± 3.00	15.13 ± 1.75
Hyper	2.90 ± 0.96	6.08 ± 1.57	24.35 ± 1.09	7.17 ± 2.35	5.68 ± 2.04	20.48 ± 0.89

Table A18: Confusion matrices obtained for the one-vs-all radial basis support vector machines evaluated using ranked features extracted from 5- and 1-min segments. Values are presented as the mean percentage ± the standard deviation, obtained after the 10-fold cross-validation. Hypo: hypotension. Normo: normotension. Hyper: hypertension. σ: Scale of kernel.

σ	**True class**	**Predicted class**					
		5-min segments			**1-min segments**		
		Hypo	Normo	Hyper	Hypo	Normo	Hyper
0.5	Hypo	1.54 ± 0.70	20.00 ± 0.94	11.79 ± 1.27	1.40 ± 0.37	12.67 ± 1.05	19.26 ± 1.10
	Normo	19.97 ± 1.13	0.77 ± 0.51	12.59 ± 1.12	13.13 ± 1.16	1.32 ± 0.48	18.89 ± 1.24
	Hyper	7.81 ± 1.71	7.13 ± 1.15	18.40 ± 1.46	10.04 ± 1.00	6.85 ± 0.71	16.45 ± 0.80
1.0	Hypo	3.06 ± 0.88	22.99 ± 0.98	7.28 ± 0.88	6.82 ± 1.12	14.71 ± 0.71	11.81 ± 1.09
	Normo	22.04 ± 1.48	2.87 ± 0.97	8.43 ± 1.28	16.67 ± 0.99	3.77 ± 0.88	12.88 ± 1.06
	Hyper	5.83 ± 1.41	8.83 ± 1.77	18.67 ± 1.40	10.18 ± 0.73	8.67 ± 0.61	14.48 ± 0.67
1.5	Hypo	3.61 ± 1.05	22.56 ± 1.17	7.16 ± 0.77	10.43 ± 0.86	13.14 ± 0.95	9.76 ± 1.17
	Normo	21.42 ± 1.88	4.07 ± 1.17	7.84 ± 1.67	17.39 ± 0.88	4.16 ± 0.77	11.78 ± 1.23
	Hyper	5.68 ± 1.56	8.18 ± 1.84	19.48 ± 1.69	10.30 ± 0.70	7.65 ± 0.96	15.39 ± 1.04
2.0	Hypo	4.26 ± 0.93	20.62 ± 1.39	8.46 ± 1.13	13.94 ± 1.08	10.26 ± 1.00	9.13 ± 1.02
	Normo	20.65 ± 1.67	4.72 ± 1.04	7.96 ± 1.31	16.97 ± 0.64	4.21 ± 0.73	12.15 ± 0.93
	Hyper	5.46 ± 1.56	7.53 ± 1.56	20.34 ± 1.58	10.46 ± 0.97	6.18 ± 0.79	16.69 ± 1.08

Table A19: Confusion matrices obtained for the one-vs-all polynomial support vector machines evaluated using ranked features extracted from 5- and 1-min segments. Values are presented as the mean percentage ± the standard deviation, obtained after the 10-fold cross-validation. Hypo: hypotension. Normo: normotension. Hyper: hypertension. n: Order of the polynomial kernel.

n	**True class**	**Predicted class**					
		5-min segments			**1-min segments**		
		Hypo	Normo	Hyper	Hypo	Normo	Hyper
3	Hypo	5.03 ± 1.79	20.99 ± 2.55	7.31 ± 1.42	13.02 ± 5.42	10.64 ± 5.10	9.68 ± 3.61
	Normo	17.96 ± 2.75	6.98 ± 1.70	8.40 ± 2.05	11.71 ± 4.46	8.64 ± 3.97	12.98 ± 4.76
	Hyper	5.96 ± 1.51	7.56 ± 1.53	19.81 ± 1.52	8.79 ± 3.51	8.31 ± 4.06	16.23 ± 4.84
4	Hypo	6.88 ± 6.50	15.93 ± 10.25	10.52 ± 9.04	16.93 ± 16.70	9.62 ± 15.28	6.78 ± 13.66
	Normo	11.91 ± 7.58	13.06 ± 8.76	8.36 ± 7.62	17.22 ± 16.72	9.51 ± 15.19	6.60 ± 13.54
	Hyper	5.68 ± 4.45	8.98 ± 8.08	18.67 ± 7.17	16.95 ± 16.68	9.57 ± 15.30	6.81 ± 13.60
5	Hypo	16.17 ± 15.96	11.54 ± 14.35	5.62 ± 9.67	3.37 ± 10.53	6.63 ± 13.82	23.33 ± 15.95
	Normo	16.27 ± 15.89	11.64 ± 14.04	5.43 ± 9.35	3.40 ± 10.46	6.60 ± 13.79	23.33 ± 15.95
	Hyper	16.60 ± 16.86	10.59 ± 14.94	6.14 ± 12.26	3.35 ± 10.54	6.60 ± 13.79	23.38 ± 15.88

Table A20: Confusion matrices obtained for the one-vs-one linear support vector machine evaluated using ranked features extracted from 5- and 1-min segments. Values are presented as the mean percentage ± the standard deviation, obtained after the 10-fold cross-validation. Hypo: hypotension. Normo: normotension. Hyper: hypertension.

True class	**Predicted class**					
	5-min segments			**1-min segments**		
	Hypo	Normo	Hyper	Hypo	Normo	Hyper
Hypo	9.41 ± 1.34	15.68 ± 1.77	8.24 ± 1.59	13.36 ± 1.36	13.39 ± 1.28	6.59 ± 0.90
Normo	10.25 ± 1.76	16.54 ± 1.46	6.54 ± 0.86	10.48 ± 1.29	13.65 ± 1.18	9.21 ± 1.19
Hyper	5.52 ± 1.27	7.16 ± 1.52	20.65 ± 1.69	6.46 ± 1.34	11.71 ± 1.86	15.16 ± 0.85

Table A21: Confusion matrices obtained for the one-vs-one radial-basis support vector machines evaluated using ranked features extracted from 5- and 1-min segments. Values are presented as the mean percentage ± the standard deviation, obtained after the 10-fold cross-validation. Hypo: hypotension. Normo: normotension. Hyper: hypertension. σ: Scale of kernel.

σ	**True class**	**Predicted class**					
		5-min segments			**1-min segments**		
		Hypo	Normo	Hyper	Hypo	Normo	Hyper
0.5	Hypo	2.31 ± 0.89	28.02 ± 1.16	2.99 ± 0.84	9.14 ± 1.24	14.46 ± 0.98	9.73 ± 0.84
	Normo	24.20 ± 1.18	5.19 ± 1.33	3.95 ± 1.06	21.65 ± 0.88	2.86 ± 0.55	8.82 ± 1.04
	Hyper	4.38 ± 1.32	12.87 ± 2.04	16.08 ± 1.47	18.11 ± 0.77	8.23 ± 0.72	7.00 ± 0.66
1.0	Hypo	3.61 ± 1.00	27.69 ± 1.13	2.04 ± 0.49	10.80 ± 0.92	16.25 ± 0.82	6.28 ± 0.74
	Normo	19.81 ± 2.34	12.07 ± 2.05	1.45 ± 0.62	18.94 ± 0.82	5.48 ± 0.62	8.91 ± 1.07
	Hyper	4.23 ± 1.43	11.20 ± 2.20	17.90 ± 1.31	12.40 ± 1.01	9.87 ± 0.66	11.06 ± 0.92
1.5	Hypo	3.64 ± 1.13	27.04 ± 1.22	2.65 ± 0.88	14.93 ± 0.94	13.53 ± 1.02	4.86 ± 0.53
	Normo	14.23 ± 2.50	17.69 ± 2.26	1.42 ± 0.57	18.01 ± 0.60	7.30 ± 0.56	8.02 ± 1.04
	Hyper	3.80 ± 1.20	10.80 ± 1.90	18.73 ± 1.48	10.64 ± 0.88	9.66 ± 0.75	13.03 ± 0.86
2.0	Hypo	3.92 ± 1.08	26.17 ± 1.52	3.24 ± 0.88	17.33 ± 1.27	11.70 ± 1.17	4.31 ± 0.53
	Normo	10.83 ± 1.54	20.68 ± 1.70	1.82 ± 0.64	17.11 ± 0.64	8.52 ± 0.68	7.69 ± 0.91
	Hyper	3.21 ± 1.07	10.90 ± 1.83	19.23 ± 1.53	10.10 ± 1.14	9.31 ± 0.52	13.93 ± 1.04

Table A22: Confusion matrices obtained for the one-vs-one polynomial support vector machines evaluated using ranked features extracted from 5- and 1-min segments. Values are presented as the mean percentage ± the standard deviation, obtained after the 10-fold cross-validation. Hypo: hypotension. Normo: normotension. Hyper: hypertension. n: Order of the polynomial kernel.

n	**True class**	**Predicted class**					
		5-min segments			**1-min segments**		
		Hypo	Normo	Hyper	Hypo	Normo	Hyper
3	Hypo	4.20 ± 1.60	25.43 ± 1.51	3.70 ± 0.80	8.12 ± 4.29	10.69 ± 8.53	14.53 ± 8.82
	Normo	21.60 ± 1.50	7.90 ± 1.37	3.83 ± 0.44	7.29 ± 4.67	9.71 ± 9.05	16.33 ± 9.16
	Hyper	6.02 ± 1.49	8.92 ± 1.24	18.40 ± 1.18	6.39 ± 3.98	9.06 ± 8.87	17.88 ± 9.39
4	Hypo	5.59 ± 2.88	8.70 ± 8.37	19.04 ± 8.19	10.15 ± 15.87	21.75 ± 15.22	1.43 ± 2.75
	Normo	18.61 ± 8.66	2.47 ± 3.49	12.25 ± 8.97	10.05 ± 15.85	21.77 ± 15.23	1.51 ± 2.90
	Hyper	8.43 ± 4.03	3.64 ± 4.14	21.27 ± 5.62	10.04 ± 15.79	21.72 ± 15.19	1.58 ± 3.22
5	Hypo	19.26 ± 15.24	4.17 ± 9.64	9.91 ± 13.73	13.06 ± 16.80	3.58 ± 10.49	16.69 ± 17.39
	Normo	19.69 ± 15.31	3.98 ± 9.33	9.66 ± 13.40	13.25 ± 17.01	3.35 ± 10.44	16.73 ± 17.46
	Hyper	19.75 ± 16.34	3.89 ± 10.06	9.69 ± 14.70	12.91 ± 16.68	3.57 ± 10.33	16.86 ± 17.36

Table A23: Confusion matrices obtained for the k-Nearest Neighbors algorithms evaluated using forward selected features extracted from 5- and 1-min segments. Values are presented as the mean percentage ± the standard deviation, obtained after the 10-fold cross-validation. Hypo: hypotension. Normo: normotension. Hyper: hypertension.

k	**True class**	**Predicted class**					
		5-min segments			**1-min segments**		
		Hypo	Normo	Hyper	Hypo	Normo	Hyper
3	Hypo	14.66 ± 1.26	17.75 ± 1.17	0.93 ± 0.44	22.14 ± 1.02	8.62 ± 1.03	2.57 ± 0.54
	Normo	31.85 ± 0.60	0.86 ± 0.43	0.62 ± 0.36	21.82 ± 1.15	6.10 ± 0.86	5.42 ± 1.20
	Hyper	11.98 ± 1.62	4.04 ± 0.85	17.31 ± 1.38	14.50 ± 0.83	8.09 ± 0.78	10.75 ± 1.01
5	Hypo	16.05 ± 1.68	16.85 ± 1.64	0.43 ± 0.26	22.11 ± 0.90	8.74 ± 0.83	2.49 ± 0.42
	Normo	31.17 ± 0.58	1.94 ± 0.64	0.22 ± 0.25	19.83 ± 0.90	8.00 ± 0.78	5.50 ± 1.01
	Hyper	12.44 ± 1.53	3.83 ± 0.79	17.07 ± 1.37	13.49 ± 0.93	8.96 ± 0.96	10.88 ± 0.87
7	Hypo	13.73 ± 1.63	18.02 ± 1.68	1.57 ± 1.12	20.69 ± 1.18	8.59 ± 0.63	4.05 ± 0.65
	Normo	28.61 ± 1.06	3.27 ± 1.04	1.45 ± 0.80	18.32 ± 0.95	8.28 ± 1.12	6.73 ± 0.85
	Hyper	12.53 ± 2.00	3.80 ± 0.85	17.01 ± 1.58	12.46 ± 0.94	9.09 ± 0.72	11.78 ± 0.86
9	Hypo	14.07 ± 1.61	17.38 ± 1.23	1.88 ± 0.64	19.51 ± 1.08	8.87 ± 1.00	4.96 ± 0.84
	Normo	28.55 ± 1.25	3.58 ± 1.17	1.20 ± 0.42	18.32 ± 1.07	7.97 ± 1.10	7.04 ± 1.03
	Hyper	12.62 ± 1.68	4.32 ± 0.74	16.39 ± 1.04	13.31 ± 0.81	8.57 ± 0.91	11.45 ± 0.72

Table A24: Confusion matrices obtained for the neural networks evaluated using forward selected features extracted from 5- and 1-min segments. Values are presented as the mean percentage ± the standard deviation, obtained after the 10-fold cross-validation. Hypo: hypotension. Normo: normotension. Hyper: hypertension. N: number of neurons in the hidden layer.

N	**True class**	**Predicted class**					
		5-min segments			**1-min segments**		
		Hypo	Normo	Hyper	Hypo	Normo	Hyper
2	Hypo	5.46 ± 4.42	17.10 ± 4.71	10.77 ± 1.51	16.94 ± 2.79	2.94 ± 4.50	13.45 ± 3.16
	Normo	5.93 ± 4.50	18.40 ± 4.62	9.01 ± 1.60	16.20 ± 2.58	2.91 ± 4.11	14.22 ± 3.62
	Hyper	4.63 ± 3.52	9.94 ± 2.74	18.77 ± 1.92	12.87 ± 2.73	2.28 ± 3.24	18.19 ± 3.78
3	Hypo	8.77 ± 5.51	15.68 ± 6.74	8.89 ± 3.49	18.61 ± 3.38	2.70 ± 2.06	12.02 ± 4.07
	Normo	10.03 ± 6.66	15.22 ± 7.26	8.09 ± 4.22	17.34 ± 3.15	3.03 ± 2.28	12.97 ± 3.49
	Hyper	4.78 ± 3.07	7.72 ± 3.34	20.83 ± 1.41	12.36 ± 4.63	2.63 ± 1.94	18.33 ± 4.05
4	Hypo	8.36 ± 4.40	17.22 ± 6.12	7.75 ± 2.24	16.40 ± 3.28	5.97 ± 2.27	10.96 ± 3.95
	Normo	9.07 ± 5.33	17.72 ± 6.27	6.54 ± 3.23	14.98 ± 2.46	5.74 ± 2.98	12.61 ± 3.96
	Hyper	4.60 ± 2.98	8.55 ± 3.79	20.19 ± 2.67	9.84 ± 1.94	4.65 ± 2.13	18.84 ± 2.57
5	Hypo	10.46 ± 3.47	15.86 ± 4.59	7.01 ± 2.01	19.49 ± 3.79	6.20 ± 3.82	7.64 ± 2.14
	Normo	11.14 ± 4.49	16.51 ± 5.47	5.68 ± 2.07	16.27 ± 3.40	7.05 ± 3.84	10.02 ± 2.31
	Hyper	5.03 ± 2.00	7.59 ± 2.31	20.71 ± 1.52	10.96 ± 3.09	5.35 ± 2.93	17.02 ± 1.37
6	Hypo	5.68 ± 1.82	19.91 ± 2.53	7.75 ± 1.80	19.39 ± 3.32	5.26 ± 3.69	8.69 ± 2.09
	Normo	5.83 ± 2.98	21.70 ± 2.81	5.80 ± 1.47	16.89 ± 3.05	5.96 ± 3.46	10.49 ± 2.36
	Hyper	3.27 ± 1.10	9.51 ± 0.65	20.56 ± 1.32	11.45 ± 1.99	5.00 ± 2.57	16.89 ± 1.70

Table A25: Confusion matrices obtained for the neural networks evaluated using forward selected features extracted from 5- and 1-min segments. Values are presented as the mean percentage ± the standard deviation, obtained after the 10-fold cross-validation. Hypo: hypotension. Normo: normotension. Hyper: hypertension. N: number of neurons in the hidden layer.

N	**True class**	**Predicted class**					
		5-min segments			**1-min segments**		
		Hypo	Normo	Hyper	Hypo	Normo	Hyper
7	Hypo	7.50 ± 4.83	16.05 ± 6.61	9.78 ± 2.87	16.30 ± 1.90	8.72 ± 3.23	8.31 ± 2.59
	Normo	7.25 ± 4.24	17.50 ± 6.60	8.58 ± 3.36	13.94 ± 1.87	8.92 ± 3.18	10.48 ± 2.65
	Hyper	3.64 ± 2.59	7.75 ± 2.95	21.94 ± 2.77	9.14 ± 1.64	6.77 ± 2.03	17.42 ± 2.20
8	Hypo	7.31 ± 2.99	18.61 ± 3.43	7.41 ± 1.45	17.85 ± 1.82	7.16 ± 2.04	8.33 ± 1.26
	Normo	8.15 ± 3.25	19.07 ± 3.05	6.11 ± 1.42	14.77 ± 2.14	8.51 ± 2.41	10.05 ± 1.51
	Hyper	3.15 ± 1.21	9.63 ± 1.48	20.56 ± 1.28	9.39 ± 1.26	6.98 ± 2.11	16.97 ± 1.59
9	Hypo	9.57 ± 3.88	15.15 ± 3.94	8.61 ± 1.80	18.16 ± 2.23	6.26 ± 3.24	8.92 ± 1.79
	Normo	9.97 ± 3.90	15.99 ± 3.64	7.38 ± 1.32	14.97 ± 2.86	7.24 ± 3.60	11.13 ± 1.66
	Hyper	4.75 ± 1.95	7.10 ± 2.30	21.48 ± 1.64	9.52 ± 1.78	5.99 ± 2.93	17.83 ± 1.78
10	Hypo	11.23 ± 4.23	14.14 ± 4.88	7.96 ± 1.84	16.61 ± 3.97	7.08 ± 2.84	9.65 ± 2.22
	Normo	12.19 ± 4.65	15.06 ± 4.43	6.08 ± 2.27	13.96 ± 3.31	7.14 ± 2.77	12.23 ± 1.76
	Hyper	5.99 ± 2.14	6.67 ± 2.24	20.68 ± 1.83	9.31 ± 2.54	6.31 ± 2.58	17.72 ± 1.52
11	Hypo	10.83 ± 4.44	14.41 ± 5.20	8.09 ± 1.98	15.60 ± 2.82	9.50 ± 1.97	8.23 ± 1.78
	Normo	11.85 ± 5.30	14.85 ± 5.91	6.64 ± 2.32	13.11 ± 2.94	9.79 ± 1.51	10.43 ± 2.61
	Hyper	6.05 ± 2.89	6.73 ± 2.22	20.56 ± 1.76	8.69 ± 2.52	7.39 ± 1.29	17.26 ± 1.81

Table A26: Confusion matrices obtained for the neural networks evaluated using forward selected features extracted from 5- and 1-min segments. Values are presented as the mean percentage ± the standard deviation, obtained after the 10-fold cross-validation. Hypo: hypotension. Normo: normotension. Hyper: hypertension. N: number of neurons in the hidden layer.

N	**True class**	**Predicted class**					
		5-min segments			**1-min segments**		
		Hypo	Normo	Hyper	Hypo	Normo	Hyper
12	Hypo	6.42 ± 1.39	18.77 ± 1.89	8.15 ± 1.34	16.64 ± 3.44	9.62 ± 3.84	7.08 ± 1.48
	Normo	6.60 ± 2.68	20.28 ± 3.37	6.45 ± 0.97	14.46 ± 3.19	9.76 ± 3.61	9.11 ± 1.33
	Hyper	3.40 ± 1.28	8.89 ± 2.01	21.05 ± 1.90	9.11 ± 2.28	8.35 ± 3.14	15.88 ± 1.42
13	Hypo	11.08 ± 3.69	14.54 ± 4.31	7.72 ± 2.15	17.63 ± 2.42	7.01 ± 2.94	8.69 ± 2.72
	Normo	10.59 ± 3.80	16.27 ± 4.00	6.48 ± 1.44	15.06 ± 1.49	7.61 ± 3.14	10.66 ± 2.77
	Hyper	5.31 ± 2.23	7.84 ± 2.64	20.19 ± 1.80	9.70 ± 1.83	6.33 ± 2.56	17.31 ± 1.93
14	Hypo	10.40 ± 3.27	16.33 ± 3.39	6.60 ± 1.97	17.26 ± 2.98	7.22 ± 2.50	8.85 ± 1.55
	Normo	11.57 ± 2.65	16.79 ± 3.77	4.97 ± 2.22	14.71 ± 2.93	8.04 ± 2.81	10.59 ± 1.99
	Hyper	5.43 ± 1.72	7.59 ± 1.67	20.31 ± 1.70	9.48 ± 1.43	6.33 ± 2.12	17.52 ± 1.83
15	Hypo	10.46 ± 2.36	14.75 ± 2.85	8.12 ± 1.40	17.68 ± 3.28	8.00 ± 3.38	7.65 ± 0.83
	Normo	11.27 ± 3.20	15.49 ± 3.07	6.57 ± 0.85	15.60 ± 3.42	8.21 ± 3.83	9.52 ± 1.62
	Hyper	5.12 ± 1.84	6.79 ± 1.47	21.42 ± 1.64	9.68 ± 1.88	6.73 ± 2.57	16.92 ± 1.30
16	Hypo	7.90 ± 2.47	17.50 ± 3.21	7.93 ± 1.34	16.43 ± 3.17	8.87 ± 3.69	8.04 ± 2.26
	Normo	8.15 ± 3.69	18.80 ± 3.15	6.39 ± 1.32	13.91 ± 3.48	9.48 ± 3.69	9.94 ± 2.86
	Hyper	4.32 ± 1.59	8.02 ± 1.99	20.99 ± 2.04	8.64 ± 2.03	7.65 ± 2.41	17.05 ± 1.37

Table A27: Confusion matrices obtained for the neural networks evaluated using forward selected features extracted from 5- and 1-min segments. Values are presented as the mean percentage ± the standard deviation, obtained after the 10-fold cross-validation. Hypo: hypotension. Normo: normotension. Hyper: hypertension. N: number of neurons in the hidden layer.

N	**True class**	**Predicted class**					
		5-min segments			**1-min segments**		
		Hypo	Normo	Hyper	Hypo	Normo	Hyper
17	Hypo	8.61 ± 2.62	16.54 ± 2.72	8.18 ± 1.26	15.75 ± 3.93	10.49 ± 3.59	7.09 ± 2.48
	Normo	8.92 ± 2.30	17.75 ± 3.42	6.67 ± 1.34	13.39 ± 3.88	10.75 ± 3.46	9.19 ± 1.47
	Hyper	4.41 ± 1.86	7.69 ± 1.41	21.23 ± 1.95	8.72 ± 2.74	8.67 ± 3.65	15.94 ± 2.96
18	Hypo	8.33 ± 3.46	16.70 ± 4.49	8.30 ± 2.62	13.81 ± 5.10	10.18 ± 3.90	9.34 ± 2.00
	Normo	9.85 ± 4.32	16.70 ± 5.02	6.79 ± 2.60	12.12 ± 4.56	9.75 ± 3.26	11.47 ± 1.92
	Hyper	4.69 ± 2.69	7.22 ± 1.79	21.42 ± 1.79	8.00 ± 2.57	7.71 ± 2.51	17.62 ± 1.83
19	Hypo	10.83 ± 2.82	16.54 ± 2.80	5.96 ± 1.12	16.97 ± 2.44	7.84 ± 2.12	8.52 ± 2.10
	Normo	10.43 ± 2.83	18.30 ± 3.27	4.60 ± 1.08	14.53 ± 2.22	8.46 ± 1.33	10.35 ± 1.93
	Hyper	5.40 ± 1.26	7.72 ± 2.31	20.22 ± 1.40	9.45 ± 1.69	6.52 ± 1.68	17.36 ± 2.15
20	Hypo	10.00 ± 3.02	16.05 ± 3.37	7.28 ± 1.07	16.53 ± 1.56	7.89 ± 2.33	8.91 ± 2.00
	Normo	10.00 ± 3.98	16.91 ± 3.70	6.42 ± 1.28	14.27 ± 1.23	8.09 ± 1.86	10.98 ± 1.91
	Hyper	5.03 ± 2.06	7.72 ± 1.87	20.59 ± 1.69	9.21 ± 1.16	6.26 ± 1.32	17.86 ± 1.15

Table A28: Confusion matrices obtained for the one-vs-all linear support vector machine evaluated using forward selected features extracted from 5- and 1-min segments. Values are presented as the mean percentage ± the standard deviation, obtained after the 10-fold cross-validation. Hypo: hypotension. Normo: normotension. Hyper: hypertension.

True class	**Predicted class**					
	5-min segments			**1-min segments**		
	Hypo	Normo	Hyper	Hypo	Normo	Hyper
Hypo	10.83 ± 3.98	8.86 ± 4.16	13.64 ± 4.80	9.82 ± 7.64	7.61 ± 3.49	15.89 ± 5.38
Normo	11.39 ± 5.03	8.61 ± 3.30	13.33 ± 4.85	9.48 ± 8.11	6.56 ± 2.72	17.29 ± 6.44
Hyper	8.77 ± 5.94	5.12 ± 2.64	19.44 ± 5.01	9.89 ± 9.88	5.79 ± 3.74	17.65 ± 8.11

Table A29: Confusion matrices obtained for the one-vs-all radial basis support vector machines evaluated using forward selected features extracted from 5- and 1-min segments. Values are presented as the mean percentage ± the standard deviation, obtained after the 10-fold cross-validation. Hypo: hypotension. Normo: normotension. Hyper: hypertension. σ: Scale of kernel.

σ	**True class**	**Predicted class**					
		5-min segments			**1-min segments**		
		Hypo	Normo	Hyper	Hypo	Normo	Hyper
0.5	Hypo	8.80 ± 1.65	12.90 ± 2.33	11.64 ± 2.50	17.55 ± 1.47	6.73 ± 1.79	9.05 ± 0.88
	Normo	11.98 ± 2.02	10.99 ± 2.36	10.37 ± 1.63	14.51 ± 1.33	7.06 ± 0.99	11.76 ± 0.82
	Hyper	4.78 ± 1.27	5.80 ± 1.80	22.75 ± 1.59	9.42 ± 1.29	6.28 ± 0.89	17.63 ± 0.86
1.0	Hypo	8.18 ± 1.99	11.45 ± 1.85	13.70 ± 1.81	15.63 ± 2.26	6.67 ± 1.19	11.03 ± 1.72
	Normo	9.01 ± 1.87	11.48 ± 2.37	12.84 ± 1.58	12.72 ± 1.68	6.96 ± 1.10	13.65 ± 1.35
	Hyper	4.38 ± 1.39	5.19 ± 1.39	23.77 ± 1.40	8.52 ± 1.06	5.38 ± 0.62	19.42 ± 1.07
1.5	Hypo	8.95 ± 1.91	10.31 ± 2.26	14.07 ± 1.14	14.04 ± 1.18	6.95 ± 1.42	12.35 ± 0.89
	Normo	10.06 ± 2.07	10.59 ± 1.59	12.69 ± 1.60	11.76 ± 0.71	6.38 ± 1.14	15.19 ± 1.37
	Hyper	4.23 ± 1.51	4.78 ± 1.03	24.32 ± 1.70	8.52 ± 1.00	4.42 ± 1.04	20.38 ± 1.37
2.0	Hypo	10.00 ± 2.33	8.21 ± 2.44	15.12 ± 1.75	14.20 ± 1.84	5.55 ± 1.54	13.58 ± 1.21
	Normo	10.77 ± 1.84	8.55 ± 2.52	14.01 ± 1.89	11.34 ± 1.87	6.00 ± 1.59	15.99 ± 1.46
	Hyper	4.51 ± 1.11	4.20 ± 1.77	24.63 ± 1.36	7.56 ± 0.82	4.18 ± 1.03	21.59 ± 1.07

Table A30: Confusion matrices obtained for the one-vs-all polynomial support vector machines evaluated using forward selected features extracted from 5- and 1-min segments. Values are presented as the mean percentage ± the standard deviation, obtained after the 10-fold cross-validation. Hypo: hypotension. Normo: normotension. Hyper: hypertension. n: Order of the polynomial kernel.

n	True class	Predicted class					
		5-min segments			1-min segments		
		Hypo	Normo	Hyper	Hypo	Normo	Hyper
3	Hypo	8.55 ± 2.06	10.96 ± 2.43	13.83 ± 1.20	9.39 ± 2.10	10.40 ± 1.82	13.55 ± 1.02
	Normo	9.32 ± 2.36	11.08 ± 1.64	12.93 ± 1.31	8.51 ± 2.64	9.27 ± 2.08	15.55 ± 1.31
	Hyper	4.78 ± 1.09	4.48 ± 1.37	24.07 ± 1.77	5.47 ± 1.95	7.45 ± 1.64	20.42 ± 0.89
4	Hypo	10.06 ± 2.68	10.22 ± 3.19	13.06 ± 2.01	13.97 ± 7.49	10.15 ± 6.82	9.21 ± 4.26
	Normo	11.05 ± 1.98	10.37 ± 1.88	11.91 ± 1.75	13.60 ± 7.14	9.97 ± 6.29	9.76 ± 4.22
	Hyper	5.06 ± 1.46	4.97 ± 1.19	23.30 ± 1.46	10.92 ± 6.66	7.78 ± 5.76	14.64 ± 4.10
5	Hypo	11.08 ± 8.22	12.10 ± 8.86	10.15 ± 5.76	6.61 ± 8.44	9.78 ± 10.64	16.95 ± 12.38
	Normo	12.50 ± 8.95	12.35 ± 8.68	8.49 ± 4.92	5.73 ± 8.24	9.84 ± 10.64	17.76 ± 12.37
	Hyper	6.11 ± 4.65	6.11 ± 4.84	21.11 ± 3.37	4.90 ± 7.62	7.99 ± 9.07	20.45 ± 10.47

Table A31: Confusion matrices obtained for the one-vs-one linear support vector machine evaluated using forward selected features extracted from 5- and 1-min segments. Values are presented as the mean percentage ± the standard deviation, obtained after the 10-fold cross-validation. Hypo: hypotension. Normo: normotension. Hyper: hypertension.

True class	Predicted class					
	5-min segments			1-min segments		
	Hypo	Normo	Hyper	Hypo	Normo	Hyper
Hypo	10.65 ± 2.70	14.78 ± 3.20	7.90 ± 1.53	10.05 ± 1.18	16.09 ± 1.42	7.19 ± 1.14
Normo	11.94 ± 3.14	15.06 ± 2.85	6.33 ± 0.98	7.48 ± 1.12	18.14 ± 2.08	7.71 ± 1.66
Hyper	5.86 ± 1.79	7.19 ± 1.59	20.28 ± 1.64	4.62 ± 0.95	16.45 ± 1.54	12.27 ± 1.15

Table A32: Confusion matrices obtained for the one-vs-one radial-basis support vector machines evaluated using forward selected features extracted from 5- and 1-min segments. Values are presented as the mean percentage ± the standard deviation, obtained after the 10-fold cross-validation. Hypo: hypotension. Normo: normotension. Hyper: hypertension. σ: Scale of kernel.

σ	**True class**	**Predicted class**					
		5-min segments			**1-min segments**		
		Hypo	Normo	Hyper	Hypo	Normo	Hyper
0.5	Hypo	8.52 ± 1.63	16.76 ± 2.12	8.06 ± 1.34	20.43 ± 2.40	7.03 ± 2.05	5.87 ± 0.85
	Normo	9.26 ± 1.70	17.47 ± 1.97	6.60 ± 1.16	19.73 ± 1.91	6.43 ± 1.42	7.17 ± 1.31
	Hyper	4.26 ± 0.94	8.24 ± 1.67	20.83 ± 1.75	14.09 ± 1.68	5.40 ± 1.53	13.84 ± 0.84
1.0	Hypo	9.17 ± 1.15	15.93 ± 1.60	8.24 ± 1.11	18.42 ± 1.68	10.38 ± 1.32	4.54 ± 1.08
	Normo	9.97 ± 1.10	16.67 ± 2.14	6.70 ± 1.33	15.55 ± 1.43	10.35 ± 1.13	7.43 ± 0.95
	Hyper	4.54 ± 0.68	7.35 ± 1.71	21.45 ± 1.76	10.33 ± 1.48	8.65 ± 1.03	14.35 ± 0.75
1.5	Hypo	8.89 ± 1.69	19.04 ± 1.71	5.40 ± 1.15	19.64 ± 1.68	6.60 ± 1.05	7.09 ± 1.04
	Normo	9.91 ± 1.26	19.75 ± 1.87	3.67 ± 1.04	18.12 ± 1.48	7.34 ± 1.64	7.87 ± 1.28
	Hyper	4.78 ± 0.70	9.29 ± 1.29	19.26 ± 1.32	13.73 ± 1.44	6.34 ± 1.24	13.26 ± 1.16
2.0	Hypo	8.83 ± 2.38	19.94 ± 2.68	4.57 ± 1.22	17.13 ± 1.16	10.30 ± 1.43	5.91 ± 0.91
	Normo	9.51 ± 2.03	21.08 ± 2.28	2.75 ± 0.59	14.38 ± 1.63	11.48 ± 1.42	7.47 ± 1.17
	Hyper	4.85 ± 1.61	9.57 ± 1.25	18.92 ± 1.55	9.11 ± 1.05	9.74 ± 1.14	14.48 ± 0.80

Table A33: Confusion matrices obtained for the one-vs-one polynomial support vector machines evaluated using forward selected features extracted from 5- and 1-min segments. Values are presented as the mean percentage ± the standard deviation, obtained after the 10-fold cross-validation. Hypo: hypotension. Normo: normotension. Hyper: hypertension. n: Order of the polynomial kernel.

n	**True class**	**Predicted class**					
		5-min segments			**1-min segments**		
		Hypo	Normo	Hyper	Hypo	Normo	Hyper
3	Hypo	9.38 ± 1.36	17.50 ± 1.81	6.45 ± 1.17	13.41 ± 1.77	10.80 ± 2.06	9.13 ± 1.04
	Normo	11.17 ± 1.29	17.16 ± 1.78	5.00 ± 0.85	11.14 ± 1.77	10.59 ± 2.18	11.60 ± 1.65
	Hyper	5.31 ± 1.01	8.36 ± 1.66	19.66 ± 1.48	6.74 ± 0.80	8.23 ± 1.03	18.37 ± 0.95
4	Hypo	9.14 ± 3.18	17.10 ± 2.01	7.10 ± 2.24	13.32 ± 11.64	17.39 ± 13.00	2.62 ± 2.48
	Normo	10.65 ± 3.61	17.44 ± 2.26	5.25 ± 2.36	11.75 ± 10.56	17.99 ± 12.08	3.59 ± 3.89
	Hyper	4.63 ± 1.28	8.15 ± 2.05	20.56 ± 1.68	9.47 ± 8.47	16.14 ± 10.12	7.73 ± 3.18
5	Hypo	6.14 ± 1.12	22.62 ± 1.69	4.57 ± 1.13	2.41 ± 2.05	14.71 ± 5.84	16.22 ± 5.73
	Normo	8.09 ± 1.61	22.28 ± 1.91	2.96 ± 0.77	2.39 ± 1.89	12.98 ± 5.12	17.96 ± 5.52
	Hyper	3.92 ± 1.11	10.34 ± 1.18	19.07 ± 1.63	2.10 ± 1.37	8.92 ± 3.73	22.32 ± 4.32

Contributions

The academic contributions made during the time this research was carried out are listed below:

Charlton, P., Kotzen, K., Mejía-Mejía, E., Aston, P., Budidha, K., Mant, J., Pettit, C., Behar, J. & Kyriacou, P. (2022), 'Detecting beats in the photoplethysmogram: benchmarking open-source algorithms', *Physiol Meas* **43**, 085007.

May, J., Mejía-Mejía, E., Nomoni, M., Budidha, K., Choi, C. & Kyriacou, P. (2021), 'Effects of contact pressure in reflectance photoplethysmography in an in vitro tissue-vessel phantom', *Sensors* **21**(24), 8421.

Mejia-Mejia, E., Budidha, K., Abay, T., May, J. & Kyriacou, P. (2020), Heart rate variability and multi-site pulse rate variability for the assessment of autonomic responses to whole-body cold exposure, *in* 'Annu Int Conf IEEE Eng Med Biol Soc', pp. 2618–2621.

Mejía-Mejía, E., Allen, J., Budidha, K., El-Hajj, C., Kyriacou, P. & Charlton, P. (2021), Photoplethysmography signal processing and synthesis, *in* P. Kyriacou & J. Allen, eds, 'Photoplethysmography: Technology, Signal Analysis, and Applications', Elsevier, London, UK, chapter 4, pp. 69–145.

Mejía-Mejía, E., Budidha, K., Abay, T., May, J. & Kyriacou, P. (2020), 'Heart rate variability (hrv) and pulse rate variability (prv) for the assessment of autonomic responses', *Front Physiol* **11**, pp. 779.

Mejía-Mejía, E., Budidha, K., Kyriacou, P. & Mamouei, M. (2022), 'Comparison of pulse rate variability and morphological features of photoplethysmograms in estimation of blood pressure', *Biomed Signal Process Control* **78**, 103968.

Mejía-Mejía, E. & Kyriacou, P. (2022*a*), Outlier management for pulse rate vari-

ability analysis from photoplethysmographic signals, *in* 'Annu Int Conf IEEE Eng Med Biol Soc', pp. 649–652.

Mejía-Mejía, E. & Kyriacou, P. (2022*b*), 'Photoplethysmography-based pulse rate variability and haemodynamic changes in the absence of heart rate variability: An in-vitro study', *Appl Sci* **12**, 7238.

Mejía-Mejía, E. & Kyriacou, P. (2023*a*), 'Duration of photoplethysmographic signals for the extraction of pulse rate variability indices', *Biomed Signal Process Control* **80**, 104214.

Mejía-Mejía, E. & Kyriacou, P. (2023*b*), 'Effects of noise and filtering strategies on the extraction of pulse rate variability from photoplethysmograms', *Biomed Signal Process Control* **80**, 104291.

Mejía-Mejía, E. & Kyriacou, P. (Under review*a*), Pulse rate variability, *in* 'The 2023 wearable photoplethysmography roadmap'.

Mejía-Mejía, E. & Kyriacou, P. (Under review*b*), 'Spectral analysis for pulse rate variability assessment from simulated photoplethysmographic signals'.

Mejía-Mejía, E., May, J., Elgendi, M. & Kyriacou, P. (2021*a*), 'Classification of blood pressure in critically ill patients using photoplethysmography and machine learning', *Comput Meth Prog Bio* **208**, 106222.

Mejía-Mejía, E., May, J. & Kyriacou, P. (2021), Effect of filtering of photoplethysmography signals in pulse rate variability analysis, *in* 'Annu Int Conf IEEE Eng Med Biol Soc', pp. 5500–5503.

Mejía-Mejía, E., May, J. & Kyriacou, P. (2022), 'Effects of using different algorithms and fiducial points for the detection of interbeat intervals, and different sampling rates on the assessment of pulse rate variability from photoplethysmography', *Comput Meth Prog Bio* **218**, 106724.

Mejía-Mejía, E., May, J. M., Elgendi, M. & Kyriacou, P. A. (2021*b*), 'Differential effects of the blood pressure state on pulse rate variability and heart rate variability in critically ill patients', *npj Digit. Med.* **4**, 82.

Mejía-Mejía, E., May, J., Torres, R. & Kyriacou, P. (2020), 'Pulse rate variability in cardiovascular health: A review on its applications and relationship with heart rate variability', *Physiol Meas* **41**, pp. 07TR01.

Bibliography

Abay, T. (2016), Reflectance photoplethysmography for non-invasive monitoring of tissue perfusion, PhD thesis, City, University of London, London, UK.

Abay, T. & Kyriacou, P. (2021), Photoplethysmography in oxygenatiuon and blood volume measurements, *in* P. Kyriacou & J. Allen, eds, 'Photoplethysmography: Technology, Signal Analysis, and Applications', Elsevier, London, UK, chapter 5, pp. 147–187.

Abeysekera, S. & Jaisankar, B. (2015), Photoplethysmographic signal feature extraction using an empirical mode decomposition approach, *in* '2015 10th International Conference on Information, Communications and Signal Processing (ICICS)', pp. 1–5.

Ackermann, S., Laborde, S., Borges, U. & Mosley, E. (2021), 'Commentary: Photoplethysmography for quantitative assessment of sympathetic nerve activity (sna) during cold stress', *Front. Physiol.* **12**, 602745.

Aguirre, N., Grall-Maës, E., Cymberknop, L. & Armentano, R. (2021), 'Blood pressure morphology assessment from photoplethysmogram and demographic information using deep learning with attention mechanism', *Sensors (Basel)* **21**(6), 2167.

Ahmad, S., Bolic, M., Dajani, H. & Groza, V. (2009), Wavelet estimation of pulse rate variability from oscillometric blood pressure measurements, *in* 'International Workshop on Medical Measurements and Applications (MeMeA)', pp. 37–40.

Ahn, J. & Kong, M. (2011), 'The relationship among pulse wave velocity, ankle-brachial pressure index and heart rate variability in adult males', *Korean J. Fam. Med.* **32**, 406–411.

Ahn, J. M. & Kim, J. K. (2020), 'Effect of the ppg sampling frequency of an iir filter on heart rate variability parameters', *Int. J. Sci. Technol. Res.* **9**(3), 1933–1937.

Akar, S., Kara, S., Latifoglu, F. & Bilgic, V. (2015), 'Analysis of heart rate variability during auditory stimulation periods in patients with schizophrenia', *J. Clin. Monit. Comput.* **29**, 153–162.

Akar, S., Kara, S., Latifoğlu, F. & Bilgiç, V. (2013), 'Spectral analysis of photoplethysmographic signals: The importance of preprocessing', *Biomed. Signal Process. Control* **8**, 16–22.

Akl, T., King, T., Long, R., Ericson, M., Wilson, M., McShane, M. & Coté, G. (2012), In vitro performance of a perfusion and oxygenation optical sensor using a unique liver phantom, *in* 'Proc. SPIE 8229, Optical Diagnostics and Sensing XII: Toward Point-of-Care Diagnostics; and Design and Performance Validation of Phantoms Used in Conjunction with Optical Measurement of Tissue IV', p. 822904.

Aksahin, M., Erdamar, A., Firat, H., Ardic, S. & Erogul, O. (2015), 'Obstructive sleep apnea classification with artificial neural network based on two synchronic hrv series', *Biomed. Eng. Appl. Basis Commun.* **27**, 1550011.

Alghoul, K., Alharthi, S., Al Osman, H. & El Saddik, A. (2017), 'Heart rate variability extraction from videos signals: Ica vs. evm comparison', *IEEE Access* **5**, 4711–4719.

Alian, A., Galante, N., Stachenfeld, N., Silverman, D. & Shelley, K. (2011*a*), 'Impact of central hypovolemia on photoplethysmographic waveform parameters in healthy volunteers. Part 1: time domain analysis', *J. Clin. Monit. Comput.* **25**(6), 377–385.

Alian, A., Galante, N., Stachenfeld, N., Silverman, D. & Shelley, K. (2011*b*), 'Impact of central hypovolemia on photoplethysmographic waveform parameters in healthy volunteers part 2: frequency domain analysis', *J. Clin. Monit. Comput.* **25**(6), 387–396.

Alian, A. & Shelley, K. (2014), 'Photoplethysmography', *Best Pract. Res. Clin. Anaesthesiol.* **28**, 395–406.

Alian, A. & Shelley, K. (2021), Ppg in clinical monitoring, *in* P. Kyriacou & J. Allen, eds, 'Photoplethysmography: Technology, Signal Analysis, and Applications', Elsevier, London, UK, chapter 10, pp. 341–358.

Allen, J. (2007), 'Photoplethysmography and its application in clinical physiological measurement', *Physiol. Meas.* **28**, R1–R39.

Allen, J. & Murray, A. (2003), 'Age-related changes in the characteristics of the photoplethysmographic pulse shape at various body sites', *Physiol. Meas.* **21**(2), 297–307.

Alqaraawi, A., Alwosheel, A. & Alasaad, A. (2016*a*), 'Heart rate variability estimation in photoplethysmography signals using bayesian learning approach', *Healthc. Technol. Lett.* **3**, 136–142.

Alqaraawi, A., Alwosheel, A. & Alasaad, A. (2016*b*), Towards efficient heart rate variability estimation in artifact-induced photoplethysmography signals, *in* 'IEEE Canadian Conference on Electrical and Computer Engineering (CCECE)', pp. 1–6.

Alvarado Orellana, S. (2014), Aportes metodológicos en la estimación de tamaños de muestra en estudios poblacionales de prevalencia, PhD thesis, Universitat Autònoma de Barcelona, Cerdanyola del Vallès, Barcelona.

Antali, F., Kulin, D., Lucz, K., Szabó, B., Szucs, L., Kulin, S. & Miklós, Z. (2021), 'Multimodal assessment of the pulse rate variability analysis module of a photoplethysmography-based telemedicine system', *Sensors* **21**, 5544.

Antink, C. H., Mai, Y., Peltokangas, M., Leonhardt, S., Oksala, N. & Vehkaoja, A. (2021), 'Accuracy of heart rate variability estimated with reflective wrist-ppg in elderly vascular patients', *Sci. Rep.* **11**, 8123.

Argüello Prada, E. & Paredes Higinio, A. (2020), 'A low-complexity ppg pulse detection method for accurate estimation of the pulse rate variability (prv) during sudden decreases in the signal amplitude', *Physiol Meas* **41**, 035001.

Arya, A., Singh, M. & Gurwara, A. (2008), 'A comparison of thiopentone sodium, propofol and midazolam for electroconvulsive therapy', *J. Anaesth. Clin. Pharmacol.* **24**, 291–294.

Ash, C., Dubec, M., Donne, K. & Bashford, T. (2017), 'Effect of wavelength and beam width on penetration in light-tissue interaction using computational methods', *Lasers Med. Sci.* **32**, 1909–1918.

Athaya, T. & Choi, S. (2021), 'An estimation method of continuous non-invasive arterial blood pressure waveform using photoplethysmography: A u-net architecture-based approach', *Sensors (Basel)* **21**(5), 1867.

Baek, H., Cho, C., Cho, J. & Woo, J. (2015), 'Reliability of ultra-short-term analysis as a surrogate of standard 5-min analysis of heart rate variability', *Telemed. e-Health* **21**(5), 404–414.

Baek, H. & Cho, J. (2019), 'Novel heart rate variability index for wrist-worn wearable devices subject to motion artifacts that complicate measurement of the continuous pulse interval', *Physiol. Meas.* **40**, 105010.

Baek, H., Shin, J., Jin, G. & Cho, J. (2017), 'Reliability of the parabola approximation method in heart rate variability analysis using low-sampling-rate photoplethysmography', *J. Med. Syst.* **41**, 189.

Barrios, L., Oldrati, P., Santini, S. & Lutterotti, A. (2019), Evaluating the accuracy of heart rate sensors based on photoplethysmography for in-the-wild analysis, *in* 'Proceedings of the 13th EAI International Conference on Pervasive Computing Technologies for Healthcare', p. 251–261.

Bassett, D. (2016), 'A literature review of heart rate variability in depressive and bipolar disorders', *Aust. New Zeal. J. Psychiatry* **50**, 511–519.

Bastos, T., Lampier, L., Goulart, C., Binotte, V., Baldo, G., Valadao, C., Caldeira, E. & Delisle, D. (2021), Development of a socially assistive robot controlled by emotions based on heartbeats and facial temperature of children with autistic spectrum disorder, *in* 'Proceedings of the Future Technologies Conference (FTC) 2020, Volume 3', Vol. 1290.

Beattie, Z., Oyang, Y., Statan, A., Ghoreyshi, A., Pantelopoulos, A., Russell, A. & Heneghan, C. (2017), 'Estimation of sleep stages in a healthy adult population from optical plethysmography and accelerometer signals', *Physiol. Meas.* **38**, 1968–1979.

Beevers, D. & Robertson, J. (2007), *Comprehensive Hypertension*, 1 edn, Mosby Elsevier, Philadelphia, PA, chapter A Short History of the Study of Hypertension, pp. 3–20.

Beh, W., Wu, Y. & Wu, A. (2021), 'Robust ppg-based mental workload assessment system using wearable devices', *IEEE J. Biomed. Health Inform.* .

Bellenger, C., Miller, D., Halson, S., Roach, G. & Sargent, C. (2021), 'Wrist-based photoplethysmography assessment of heart rate and heart rate variability: Validation of whoop', *Sensors* **21**, 3571.

Berntson, G., Jr, J. B., Eckberg, D., Grossman, P., Kaufmann, P., Malik, M., Nagaraja, H., Porges, S., Saul, J., Stone, P. & van der Molen, M. (1997), 'Heart rate variability: Origins, methods and interpretative caveats', *Psychophysiology* **34**, 623–648.

Bian, C., Ma, Q., Si, J., Wu, X., Shao, J., Ning, X. & Wang, D. (2009), 'Sign series entropy analysis of short-term heart rate variability', *Chinese Sci. Bull.* **54**, 4610–4615.

Billman, G. (2013), 'The lf/hf ratio does not accurately measure cardiac sympathovagal balance', *Front. Physiol.* **4**, 26.

Blackford, E., Piasecki, A. & Estepp, J. (2016), Measuring pulse rate variability using long-range, non-contact imaging photoplethysmography, *in* 'Annu. Int. Conf. IEEE Eng. Med. Biol. Soc.', pp. 3930–3936.

Bland, J. & Altman, D. (1986), 'Statistical Methods for Assessing Agreement Between Two Methods of Clinical Measurement', *Lancet* **1**(8476), 307–310.

Bolanos, M., Nazeran, H. & Haltiwanger, E. (2006), Comparison of heart rate variability signal features derived from electrocardiography and photoplethysmography in healthy individuals, *in* 'Conf. Proc. IEEE Eng. Med. Biol. Soc.', pp. 4289–4294.

Bolea, J., Lázaro, J., Gil, E., Rovira, E., Remartínez, J., Laguna, P., Pueyo, E., A, A. N. & Bailón, R. (2017), 'Pulse rate and transit time analysis to predict hypotension events after spinal anesthesia during programmed cesarean labor', *Ann. Biomed. Eng.* **45**, 2253–2263.

Box, G. & Cox, D. (1964), 'An analysis of transformations', *J. R. Stat. Soc. Series B Stat. Methodol.* pp. 211–252.

Bozkurt, M., Uçar, M., Bozkurt, F. & Bilgin, C. (2019), 'In obstructive sleep apnea patients, automatic determination of respiratory arrests by photoplethysmography signal and heart rate variability', *Australas. Phys. Eng. Sci. Med.* **42**, 959–979.

Brefel-Courbon, C., Thalamas, C., Rascol, O., Montastruc, J. & Senard, J. (2000), 'Lack of autonomic nervous dysfunction in progressive supranuclear palsy , a study of blood pressure variability', *Clin. Auton. Res.* **10**, 309–312.

Broucqsault-Dédrie, C., Jonckheere, J. D., Jeanne, M. & Nseir, S. (2016), 'Measurement of heart rate variability to assess pain in sedated critically ill patients: A prospective observational study', *PLoS One* **11**, e0147720.

Budidha, K. (2016), In vivo investigations of photoplethysmograms and arterial oxygen saturation from the auditory canal in conditions of compromised peripheral perfusion, PhD thesis, City, University of London, London, UK.

Budidha, K. & Kyriacou, P. (2019), 'Photoplethysmography for quantitative assessment of sympathetic nerve activity (sna) during cold stress', *Front. Physiol.* **9**, 1863.

Budidha, K. & Kyriacou, P. (2021), Photoplethysmography technology, *in* P. Kyriacou & J. Allen, eds, 'Photoplethysmography: Technology, Signal Analysis, and Applications', Elsevier, London, UK, chapter 3, pp. 43–67.

Budidha, K., Rybynok, V. & Kyriacou, P. (2018), 'Design and development of a modular, multichannel photoplethysmography system', *IEEE Trans. Instrum. Meas.* **67**(8), 1954–1965.

Bulte, C., Keet, S. & Bouwman, R. (2011), 'Level of agreement between heart rate variability and pulse rate variability in healthy individuals', *Eur. J. Anaesthesiol.* **28**, 34–38.

Béres, S. & Hejjel, L. (2021), 'The minimal sampling frequency of the photoplethysmogram for accurate pulse rate variability parameters in healthy volunteers', *Biomed. Signal Process. Control* **68**, 102589.

Béres, S., Holczer, L. & Hejjel, L. (2019), 'On the minimal adequate sampling frequency of the photoplethysmogram for pulse rate monitoring and heart rate variability analysis in mobile and wearable technology', *Meas. Sci. Rev.* **19**, 232–240.

Cai, L., Huang, J., Gao, D., Zeng, S., Tang, S., Chang, Z., Wen, C., Zhang, M., Hu, M. & Wei, G. (2021), 'Effects of mind-body practice on arterial stiffness, central hemodynamic parameters and cardiac autonomic function of college students', *Complement. Ther. Clin. Pract.* **45**, 101492.

Cainelli, E., Vedovelli, L., Bottigliengo, D., Boschiero, D. & Suppiej, A. (2022), 'Social skills and psychopathology are associated with autonomic function in children: a cross-sectional observational study', *Neural Regen. Res.* **17**, 920–928.

Cakmak, A., Alday, E., Poian, G. D., Rad, A., Metzler, T., Neylan, T., House, S., Beaudoin, F., An, X., Stevens, J., Zeng, D., Linnstaedt, S., Jovanovic, T., Germine, L., Bollen, K., Rauch, S., Lewandowski, C., Hendry, P., Sheikh, S., Storrow, A., Musey, P., Haran, J., Jones, C., Punches, B., Swor, R., Gentile, N., McGrath, M., Seamon, M., Mohiuddin, K., Chang, A., Pearson, C., Domeier, R., Bruce, S., O'Neil, B., Rathlev, N., Sanchez, L., Pietrzak, R., Joormann, J., Barch, D., Pizzagalli, D., Harte, S., Elliott, J., Kessler, R., Koenen, K., Ressler, K., Mclean, S., Li, Q. & Clifford, G. (2021), 'Classification and prediction of post-trauma outcomes related to ptsd using circadian rhythm changes measured via wrist-worn research watch in a large longitudinal cohort', *IEEE J. Biomed. Health. Inform.* **25**, 2866–2876.

Calle Uribe, A. (2018), Sistema de Medición Ambulatorio para la Estimación del Tiempo de Tránsito de Pulso con Potencial Uso en Estudios de Hipertensión Arterial, Master's thesis, Universidad EIA, Envigado, Colombia.

Can, Y., Chalabianloo, N., Ekiz, D. & Ersoy, C. (2019), 'Continuous stress detection using wearable sensors in real life: Algorithmic programming contest case study', *Sensors (Basel)* **19**, 1849.

Candia-Rivera, D., Catrambonea, V., Barbieri, R. & Valenza, G. (2021), 'Integral pulse frequency modulation model driven by sympathovagal dynamics: Synthetic vs. real heart rate variability', *Biomed. Signal Process. Control* **68**, 102736.

Canino, M., Dunn-Lewis, C., Proessl, F., LaGoy, A., Hougland, J., Beck, A., Vaughan, G., Sterczala, A., Connaboy, C., Kraemer, W. & Flanagan, S. (2022), 'Finding a rhythm: Relating ultra-short-term heart rate variability measures in healthy young adults during rest, exercise, and recovery', *Auton. Neurosci.* **239**, 102953.

Caro, C., Pedley, T., Schroter, R. & Seed, W. (2012), *The Mechanics of the Circulation*, 2 edn, Cambridge University Press, New York, NY, chapter The systemic arteries, pp. 238–342.

Carthy, E. (2014), 'Autonomic dysfunction in essential hypertension: A systematic review', *Ann Med Surg* **3**(1), 2–7.

Castaldo, R., Melillo, P., Bracale, U., Caserta, M., Triassi, M. & Pecchia, L. (2015), 'Acute mental stress assessment via short term hrv analysis in healthy adults: A systematic review with meta-analysis', *Biomed. Signal Process. Control* **18**, 370–377.

Castillo, J. & Adams, D. (2012), *Primer on the Autonomic Nervous System*, 3 edn, Elsevier, chapter Cardiac Vagal Ganglia, pp. 181–185.

Chakravarthi, K., KS, S., Venumadhav, N., Sharma, A. & Kumar, N. (2014), 'Anatomical variations of brachial artery - its morphology, embryogenesis and clinical implications', *J. Clin. Diagn. Res.* **8**(12), AC17–AC20.

Chan, G., Cooper, R., Hosanee, M., Welykholowa, K., Kyriacou, P., Zheng, D., Allen, J., Abbott, D., Lovell, N., Fletcher, R. & Elgendi, M. (2019), 'Multi-Site Photoplethysmography Technology for Blood Pressure Assessment: Challenges and Recommendations', *J Clin Med* **8**(11), 1827.

Chang, C., Hsiao, T. & Hsu, H. (2014), 'Frequency range extension of spectral analysis of pulse rate variability based on hilbert-huang transform', *Med. Biol. Eng. Comput.* **52**, 343–351.

Chang, C., Hsu, H. & Hsiao, T. (2014), 'The interpretation of very high frequency band of instantaneous pulse rate variability during paced respiration', *Biomed. Eng. Online* **21**, 46.

Charlot, K., Cornolo, J., Brugniaux, J., Richalet, J. & Pichon, A. (2009), 'Interchangeability between heart rate and photoplethysmography variabilities during sympathetic stimulations', *Physiol. Meas.* **30**, 1357–1369.

Charlton, P. H., Mariscal Harana, J., Vennin, S., Li, Y., Chowienczyk, P. & Alastruey, J. (2019), 'Modeling arterial pulse waves in healthy aging: a database for in silico evaluation of hemodynamics and pulse wave indexes', *Am. J. Physiol. Heart Circ. Physiol.* **317**(5), H1062–H1085.

Chatterjee, S. & Kyriacou, P. (2019), 'Monte carlo analysis of optical interactions in reflectance and transmittance finger', *Sensors (Basel, Switzerland)* **19**, 789.

Chen, H., Hu, Y. & Lin, S. (2018), 'Methodological considerations in calculating heart rate variability based on wearable device heart rate samples', *Comput. Biol. Med.* **102**, 396–401.

Chen, J., Wu, H. & Haryadi, B. (2021), 'Reactive hyperemia-triggered wrist pulse analysis for early monitoring of young men with high atherosclerotic risk', *Diagnostics* **11**, 1918.

Chen, X., Chen, T., Luo, F. & Li, J. (2013), Comparison of valley-to-valley and peak-to-peak intervals from photoplethysmographic signals to obtain heart rate variability in the sitting position, *in* '6th International Conference on Biomedical Engineering and Informatics', pp. 214–218.

Chen, X., Huang, Y., Yun, F., Chen, T. & Li, J. (2015), 'Effect of changes in sympathovagal balance on the accuracy of heart rate variability obtained from photoplethysmography', *Exp. Ther. Med.* **10**, 2311–2318.

Chi, H. & Hsiao, T. (2021), 'Extended classifier system with continuous real-coded variables for feature extraction of instantaneous pulse-rate variability and respiration of individuals with gaming disorder', *BioMed. Eng. OnLine* **20**, 93.

Cho, D., Ham, J., Oh, J., Park, J., Kim, S., Lee, N. & Lee, B. (2017), 'Detection of stress levels from biosignals measured in virtual reality environments using a kernel-based extreme learning machine', *Sensors (Basel)* **17**, 2435.

Cho, D., Kim, J., Lee, K. & Kim, S. (2021), 'Reduction of motion artifacts from remote photoplethysmography using adaptive noise cancellation and modified hsi model', *IEEE Access* **9**, 122655–122667.

Choi, A. & Shin, H. (2017), 'Photoplethysmography sampling frequency: pilot assessment of how low can we go to analyze pulse rate variability with reliability?', *Physiol. Meas.* **38**, 586–600.

Choi, K., Kim, J., Kwon, O., Kim, M., Ryu, Y. & Park, J. (2017), 'Is heart rate variability (hrv) an adequate tool for evaluating human emotions? – a focus on the use of the international affective picture system (iaps)', *Psychiatry Res.* **251**, 192–196.

Chon, K., Yang, B., Posada-Quintero, H., Siu, K., Rolle, M., Brink, P., Birzgalis, A. & Moore, L. (2014), 'A novel quantitative method for diabetic cardiac autonomic neuropathy assessment in type 1 diabetic mice', *J. Diabetes Sci. Technol.* **8**, 1157–1167.

Chou, Y., Zhang, A., Wang, P. & Gu, J. (2014), 'Pulse rate variability estimation method based on sliding window iterative dft and hilbert transform', *J. Med. Biol. Eng.* **34**, 347–355.

Chou, Y., Zhang, A. & Yang, B. (2017), 'Age-related alterations in the sign series entropy of shortterm pulse rate variability', *Neurocomputing* **228**, 213–219.

Chou, Y., Zhang, R., Feng, Y., Lu, M., Lu, Z. & Xu, B. (2017), 'A real-time analysis method for pulse rate variability based on improved basic scale entropy', *J. Healthc. Eng.* **2017**, 7406896.

Chuang, S., Liao, J., Chou, C., Chang, C. & Fang, W. (2015), Spectral analysis of photoplethysmography based on eemd method, *in* '2015 IEEE International Conference on Consumer Electronics - Taiwan', pp. 224–225.

Clamor, A., Hartmann, M., Köther, U., Otte, C., Moritz, S. & Lincoln, T. (2014), 'Altered autonomic arousal in psychosis: An analysis of vulnerability and specificity', *Schizophr. Res.* **154**, 73–78.

Clifford, G. (2006), Ecg statistics, noise, artifacts, and missing data, *in* G. Clifford, F. Azuaje & P. McSharry, eds, 'Advanced Methods and Tools for ECG Data Analysis', 1 edn, Artech House, Norwood, MA, pp. 55–99.

CNAP Blood Pressure (2021), Online. **url**: https://www.cnsystems.com/technology/cnap-blood-pressure/.

Coffman, C., Kay, J., Saba, K., Harrison, A., Holloway, J., LaFountaine, M. & Moore, R. (2021), 'Predictive value of subacute heart rate variability for determining outcome following adolescent concussion', *J. Clin. Med.* **10**, 161.

Colimon, K.-M. (2018), *Fundamentos de Epidemiología*, 3 edn, ECOE Ediciones, Bogotá, Colombia.

Conn, N. & Borkholder, D. (2013), Wavelet based photoplethysmogram foot delineation for heart rate variability applications, *in* '2013 IEEE Signal Processing in Medicine and Biology Symposium (SPMB)', pp. 1–5.

Conroy, T., Guzman, J. H., Hall, B., Tsouri, G. & Couderc, J.-P. (2017), 'Detection of atrial fibrillation using an earlobe photoplethysmographic sensor', *Physiol. Meas.* **38**, 1906–1918.

Constant, I., Laude, D., Murat, I. & Elghozi, J. (1999), 'Pulse rate variability is not a surrogate for heart rate variability', *Clin. Sci. (Lond)* **97**, 391–397.

Constantin, E., McGregor, C., Cote, V. & Brouillette, R. (2008), 'Pulse rate and pulse rate variability decrease after adenotonsillectomy for obstructive sleep apnea', *Pediatr. Pulmonol.* **43**, 498–504.

Conti, F. (2011*a*), *Fisiología Médica*, McGraw Hill, chapter Principios de hemodinámica y hemorreología, pp. 883–897.

Conti, F. (2011*b*), *Fisiología Médica*, McGraw Hill, chapter Sangre y hemostasia, pp. 775–818.

Conti, F. (2011*c*), *Fisiología Médica*, McGraw Hill, chapter Actividad mecánica del corazón, pp. 847–882.

Correia, B., Dias, N., Costa, P. & Pêgo, J. (2020), 'Validation of a wireless bluetooth photoplethysmography sensor used on the earlobe for monitoring heart rate variability features during a stress-inducing mental task in healthy individuals', *Sensors* **20**, 3905.

Cosoli, G., Poli, A., Scalise, L. & Spinsante, S. (2021), Heart rate variability analysis with wearable devices: Influence of artifact correction method on classification accuracy for emotion recognition, *in* '2021 IEEE International Instrumentation and Measurement Technology Conference (I2MTC)', pp. 1–6.

Couderc, J., Kyal, S., Mestha, L., Xu, B., Peterson, D., Xia, X. & Hall, B. (2015), 'Detection of atrial fibrillation using contactless facial video monitoring', *Heart Rhythm.* **12**, 195–201.

Cypressvine (2019), 'Cardiac conduction system', Online. **url**: https://commons.wikimedia.org/wiki/File:Cardiac_Conduction_System.jpg.

da Silva, A. F., da Costa de Rezende Barbosa, M. P., Vanderlei, F. M., Christofaro, D. D. & Vanderlei, L. M. (2016), 'Application of heart rate variability in diagnosis and prognosis of individuals with diabetes mellitus: Systematic review', *Ann. Noninvasive. Electrocardiol.* **21**, 223–235.

Dagdanpurev, S., Sun, G., Shinba, T., Kobayashi, M., Kariya, N., Choimaa, L., Batsuuri, S., Kim, S., Suzuki, S. & Matsui, T. (2018), 'Development and clinical application of a novel autonomic transient response-based screening system for major depressive disorder using a fingertip photoplethysmographic sensor', *Front. Bioeng. Biotechnol.* **6**, 64.

de Godoy, M. F. (2016), 'Nonlinear analysis of heart rate variability: A comprehensive review', *Journal of Cardiology and Therapy* **3**, 528–533.

Dehkordi, P., Garde, A., Karlen, W., Petersen, C., Wensley, D., Dumont, G. & Ansermino, J. (2016), 'Evaluation of cardiac modulation in children in response to apnea/hypopnea using the phone oximeter', *Physiol. Meas.* **37**, 187–202.

Dehkordi, P., Garde, A., Karlen, W., Wensley, D., Ansermino, J. & Dumont, G. (2013*a*), Pulse rate variability compared with heart rate variability in children with and without sleep disordered breathing, *in* 'Annu. Int. Conf. IEEE Eng. Med. Biol. Soc.', pp. 6563–6566.

Dehkordi, P., Garde, A., Karlen, W., Wensley, D., Ansermino, J. & Dumont, G. (2013*b*), Pulse rate variability in children with disordered breathing during different sleep stages, *in* 'Computing in Cardiology 2013', pp. 1015–1018.

Dehkordi, P., Garde, A., Karlen, W., Wensley, D., Ansermino, J. & Dumont, G. (2014), Sleep stage classification in children using photoplethysmogram pulse rate variability, *in* 'Computing in Cardiology 2014', pp. 297–300.

Diehl, K., Scott, B. & McCullen, J. (2021), 'Correspondence of parasympathetic-mediated heart rate variability derived from electrocardiogram and photoplethysmography signals in ethnically diverse adolescents', *Int. J. Psychophysiol.* **167**, 7–14.

Ding, X., Wang, Y., Hao, Y., Lv, Y., Chen, R. & Yan, H. (2021), 'A new measure of pulse rate variability and detection of atrial fibrillation based on improved time synchronous averaging', *Comput. Math. Methods Med.* **2021**, 5597559.

Dobbs, W., Fedewa, M., MacDonald, H., Holmes, C., Cicone, Z., Plews, D. & Esco, M. (2019), 'The accuracy of acquiring heart rate variability from portable devices: A systematic review and meta-analysis', *Sports Med.* **49**, 417–435.

Dong, J. (2016), 'The role of heart rate variability in sports physiology (review)', *Exp. Ther. Med.* **11**, 1531–1536.

Dotter, C., Roberts, D. & Steinberg, I. (1950), 'Aortic length: Angiocardiographic measurements', *Circulation* **2**(6), 915–920.

Drew, R. & Sinoway, L. (2012), *Primer on the Autonomic Nervous System*, 3 edn, Elsevier, chapter Autonomic Control of the Heart, pp. 177–180.

El-Hajj, C. & Kyriacou, P. (2020), 'A review of machine learning techniques in photoplethysmography for the non-invasive cuff-less measurement of blood pressure', *Biomed. Signal Process. Control* **58**, 101870.

El-Hajj, C. & Kyriacou, P. A. (2021), 'Deep learning models for cuffless blood pressure monitoring from PPG signals using attention mechanism', *Biomed Signal Process Control* **65**, 102301.

Elgendi, M. (2016), 'Optimal Signal Quality Index for Photoplethysmogram Signals', *Bioengineering (Basel)* **3**(4), 21.

Elgendi, M. (2020), *PPG signal analysis: An Introduction Using MATLAB*, 1 edn, CRC Press, Boca Raton, FL.

Elgendi, M., Fletcher, R., Liang, Y., Howard, N., Lovell, N., Abbott, D., Lim, K. & Ward, R. (2019), 'The use of photoplethysmography for assessing hypertension', *npj Digit. Med.* **2**, 60.

Elgendi, M., Norton, I., Brearley, M., Abbott, D. & Schuurmans, D. (2013), 'Systolic peak detection in acceleration photoplethysmograms measured from emergency responders in tropical conditions', *PLoS One* **8**(10), e76585.

Ernst, G. (2017), 'Heart-rate variability - more than heart beats?', *Front. Public Health* **5**, 240.

Fine, J., Branan, K., Rodriguez, A., Boonya-Ananta, T., Ajmal, Ramella-Roman, J., McShane, M. & Coté, G. (2021), 'Sources of inaccuracy in photoplethysmography for continuous cardiovascular monitoring', *Biosensors* **11**, 126.

Finžgar, M. & Podržaj, P. (2020), 'Feasibility of assessing ultra-short-term pulse rate variability from video recordings', *PeerJ* **8**, e8342.

Fisher, V. & Tahrani, A. (2017), 'Cardiac autonomic neuropathy in patients with diabetes mellitus: Current perspectives', *Diabetes Metab. Syndr. Obes.* **10**, 419–434.

Fong, M. K., Ng, E., Jian, K. E. Z. & Hong, T. (2019), 'Svr ensemble-based continuous blood pressure prediction using multi-channel photoplethysmogram', *Comput. Biol. Med.* **113**, 103392.

Fonseca, P., Weysen, T., Goelema, M., Møst, E., Radha, M., Scheurleer, C. L., van den Heuvel, L. & Aarts, R. (2017), 'Validation of photoplethysmography-based sleep staging compared with polysomnography in healthy middle-aged adults', *Sleep.* **40**.

Fox, S. (2016), *Human Physiology*, 14 edn, McGraw Hill, New York, NY.

Framingham Heart Study (2021), Online. **url**: https://www.framinghamheartstudy.org/.

Fujimoto, K., Ura, M., Yamazaki, H. & Uematsu, A. (2018), 'Instability of parasympathetic nerve function evaluated by instantaneous time-frequency analysis in patients with obstructive sleep apnea', *Sleep Biol. Rhythms* **16**, 323–330.

Fukushima, H., Kawanaka, H., Bhuiyan, S. & Oguri, K. (2013), Cuffless blood pressure estimation using only photoplethysmography based on cardiovascular parameters, *in* 'Annu. Int. Conf. IEEE Eng. Med. Biol. Soc.', pp. 2132–2135.

Gal-On, B., Brown, I. & Nunn, A. (2005), Monitoring and assessment of cardiovascular regulation in spinal cord injured patients, *in* 'Conf. Proc. IEEE Eng. Med. Biol. Soc.', pp. 6859–6862.

Gallardo, J., Bellone, G., Acevedo, R. & Risk, M. (2022), 'Ultra-short-term heart rate variability analysis: comparison between poincare and frequency domain methods', *IEEE Lat. Am. Trans.* **20**(1), 180–188.

Garde, A., Dehkordi, P., Ansermino, J. & Dumont, G. (2017), 'Correntropy-based pulse rate variability analysis in children with sleep disordered breathing', *Entropy* **19**, 282.

Garde, A., Dehkordi, P., Karlen, W., Wensley, D., Ansermino, J. & Dumont, G. (2014), 'Development of a screening tool for sleep disordered breathing in children using the phone oximeter (tm)', *PLoS ONE* **9**, e112959.

Garde, A., Dehkordi, P., Wensley, D., Ansermino, J. & Dumont, G. (2015), Pulse oximetry recorded from the phone oximeter for detection of obstructive sleep apnea events with and without oxygen desaturation in children, *in* 'Annu. Int. Conf. IEEE Eng. Med. Biol. Soc.', pp. 7692–7695.

Garde, A., Dekhordi, P., Ansermino, J. & Dumont, G. (2016), Identifying individual sleep apnea/hypoapnea epochs using smartphone-based pulse oximetry, *in* 'Annu. Int. Conf. IEEE Eng. Med. Biol. Soc.', pp. 3195–3198.

Garde, A., Hoppenbrouwer, X., Dehkordi, P., Zhou, G., Rollinson, A., Wensley, D., Dumont, G. & Ansermino, J. (2019), 'Pediatric pulse oximetry-based osa screening at different thresholds of the apnea-hypopnea index with an expression of uncertainty for inconclusive classifications', *Sleep Med.* **60**, 45–52.

Gaurav, A., Maheedhar, M., Tiwari, V. & Narayanan, R. (2016), Cuff-less ppg based continuous blood pressure monitoring: a smartphone based approach, *in* 'Annu. Int. Conf. IEEE Eng. Med. Biol. Soc.', pp. 607–610.

Gavrilova, E. (2016), 'Heart rate variability and sports', *Hum. Physiol.* **42**, 571–578.

Geary, C. & Rosenthal, S. (2011), 'Sustained impact of mbsr on stress, well-being, and daily spiritual experiences for 1 year in academic health care employees', *J. Altern. Complement. Med.* **17**, 939–944.

Georgiou, K., Larentzakis, A., Khamis, N., Alsuhaibani, G., Alaska, Y. & Giallafos, E. (2018), 'Can wearable devices accurately measure heart rate variability? a systematic review', *Folia Med. (Plovdiv)* **60**, 7–20.

Germán-Salló, Z. & Germán-Salló, M. (2016), 'Non-linear methods in hrv analysis', *Procedia Technology* **22**, 645–651.

Giardino, N., Lehrer, P. & Edelberg, R. (2002), 'Comparison of finger plethysmograph to ecg in the measurement of heart rate variability', *Psychophysiology* **39**, 246–253.

Gil, E., Mendez, M., Vergara, J., Cerutti, S., Bianchi, A. & Laguna, P. (2009), 'Discrimination of sleep-apnea-related decreases in the amplitude fluctuations of ppg signal in children by hrv analysis', *IEEE Trans. Biomed. Eng.* **56**, 1005–1014.

Gil, E., Orini, M., Bail, R., Vergara, J., Mainardi, L. & Laguna, P. (2010), Time-varying spectral analysis for comparison of hrv and ppg variability during tilt table test, *in* 'Annu. Int. Conf. IEEE Eng. Med. Biol. Soc.', pp. 3579–3582.

Gil, E., Orini, M., Bailón, R., Vergara, J., Mainardi, L. & Laguna, P. (2010), 'Photoplethysmography pulse rate variability as a surrogate measurement of heart rate variability during non-stationary conditions', *Physiol. Meas.* **31**, 1271–1290.

Gil, E., Vergara, J. & Laguna, P. (2008), 'Detection of decreases in the amplitude fluctuation of pulse photoplethysmography signal as indication of obstructive sleep apnea syndrome in children', *Biomed. Signal Process. Control* **3**, 267–277.

Goernig, M., Schroeder, R., Roth, T., Truebner, S., Palutke, I., Figulla, H., Leder, U. & Voss, A. (2008), 'Peripheral arterial disease alters heart rate variability in cardiovascular patients', *Pacing Clin. Electrophysiol.* **31**, 858–862.

Goldberger, A., Amaral, L., Glass, L., Hausdorff, J., Ivanov, P., Mark, R., Mietus, J., Moody, G., Peng, C. & Stanley, H. (2000), 'Physiobank, physiotoolkit, and physionet: Components of a new research resource for complex physiologic signals', *Circulation* **101**, e215–e220.

Golińska, A. K. (2012), 'Detrended fluctuation analysis (dfa) in biomedical signal processing: selected examples', *Stud. Logic Gramm. Rhetor.* **29**, 107–115.

Goshvarpour, A., Abbasi, A. & Goshvarpour, A. (2017), 'Fusion of heart rate variability and pulse rate variability for emotion recognition using lagged poincare plots', *Australas. Phys. Eng. Sci. Med.* **40**, 617–629.

Grassi, G. & Seravalle, G. (2012), *Primer on the Autonomic Nervous System*, 3 edn, Elsevier, chapter Sympatho-Vagal Imbalance in Hypertension, pp. 345–348.

Guede-Fernández, F., Ferrer-Mileo, V., Ramos-Castro, J., Fernández-Chimeno, M. & García-González, M. A. (2015), Real time heart rate variability assessment from android smartphone camera photoplethysmography: Postural and device influences, *in* 'Annu. Int. Conf. IEEE Eng. Med. Biol. Soc.', pp. 7332–7335.

Guzman, L., Cazares, A. & Martinez-Torteya, A. (2021), Model for glycemic level detection using heart rate variability in a mexican sample, *in* 'IEEE-EMBS Conference on Biomedical Engineering and Sciences (IECBES)', pp. 505–510.

Haddad, S., Harju, J., Tarniceriu, A., Halkola, T., Parak, J., Korhonen, I., Yli-Hankala, A. & Vehkaoja, A. (2020), Ectopic beat detection from wrist optical signals for sinus rhythm and atrial fibrillation subjects, *in* 'MEDICON 2019, IFMBE Proceedings 76', p. 150–158.

Hamill, R., Shapiro, R. & Vizzard, M. (2012), *Primer on the Autonomic Nervous System*, 3 edn, Elsevier, chapter Peripheral Autonomic Nervous System, pp. 17–26.

Hamilton, J. & Alloy, L. (2016), 'Atypical reactivity of heart rate variability to stress and depression across development: Systematic review of the literature and directions for future research', *Clin. Psychol. Rev.* **50**, 67–79.

Hamilton, P. & Tompkins, W. (1986), 'Quantitative Investigation of QRS Detection Rules Using the MIT/BIH Arrythmia Database', *IEEE Trans Biomed Eng.* **33**(12), 1157–65.

Hao, T., Chang, H., Ball, M., Lin, K. & Zhu, X. (2017), 'chrv uncovering daily stress dynamics usingbio-signal from consumer wearables', *Stud. Health Technol. Inform.* **245**, 98–102.

Hayano, J., Barros, A., Kamiya, A., Ohte, N. & Yasuma, F. (2005), 'Assessment of pulse rate variability by the method of pulse frequency demodulation', *Biomed. Eng. Online* **4**, 62.

Hayano, J. & Yuda, E. (2021), 'Assessment of autonomic function by long-term heart rate variability: beyond the classical framework of lf and hf measurements', *J. Physiol. Anthropol.* **40**, 21.

Heart: function and structure - access revision (n.d.), Online. **url**: https://sites.google.com/site/accessrevision/biology/respiratory-and-circulatorysystems/heart-function-and-structure.

Heathers, J. (2013), 'Smartphone-enabled pulse rate variability: An alternative methodology for the collection of heart rate variability in psychophysiological research', *Int. J. Psychophysiol.* **89**, 297–304.

Heathers, J. (2014), 'Everything hertz: Methodological issues in short-term frequency-domain hrv', *Front. Physiol.* **5**, 177.

Hejjel, L. (2017), 'Comment on 'photoplethysmography sampling frequency: pilot assessment of how low can we go to analyze pulse rate variability with reliability?', *Physiol. Meas.* **38**, 2249–2251.

Hemon, M. & Phillips, J. (2016), 'Comparison of foot finding methods for deriving instantaneous pulse rates from photoplethysmographic signals', *J. Clin. Monit. Comput.* **30**, 157–168.

Hernando, A., Pelaez-Coca, M., Lozano, M., Aiger, M., Izquierdo, D., Sanchez, A., Lopez-Jurado, M., Moura, I., Fidalgo, J., Lazaro, J. & Gil, E. (2019), 'Autonomic nervous system measurement in hyperbaric environments using ecg and ppg signals', *IEEE J. Biomed. Health Inform.* **23**, 132–142.

Hill, L. & Thayer, J. (2019), 'The autonomic nervous system and hypertension: Ethnic differences and psychosocial factors', *Curr. Cardiol. Rep.* **21**, 15.

Holmes, C., Sherman, S., Hornikel, B., Cicone, Z., Wind, S. & Esco, M. (2020), 'Compliance of self-measured hrv using smartphone applications in collegiate athletes', *J. High Technol. Manag. Res.* **31**, 100376.

Holper, L., Seifritz, E. & Scholkmann, F. (2016), 'Short-term pulse rate variability is better characterized by functional near-infrared spectroscopy than by photoplethysmography', *J. Biomed. Opt.* **21**, 091308.

Hosanee, M., Chan, G., Welykholowa, K., Cooper, R., Kyriacou, P., Zheng, D., Allen, J., Abbott, D., Menon, C., Lovell, N., Newton, H., Chan, W., Lim, K., Fletcher, R., Ward, R. & Elgendi, M. (2020), 'Cuffless Single-Site Photoplethysmography for Blood Pressure Monitoring', *J Clin Med* **9**(3), 723.

Hoskins, P. (2017), *Cardiovascular Biomechanics*, Springer International Publishing, Switzerland, chapter Introduction to Cardiovascular Biomechanics, pp. 25–35.

Hoskins, P. & Hardman, D. (2017), *Cardiovascular Biomechanics*, Springer International Publishing, Switzerland, chapter Blood and Blood Flow, pp. 37–63.

Hoskins, P. & Hose, D. (2017), *Cardiovascular Biomechanics*, Springer International Publishing, Switzerland, chapter The Arterial System I: Pressure, Flow and Stiffness, pp. 37–63.

Huikuri, H., Mäkikallio, T., Airaksinen, K., Mitrani, R., Castellanos, A. & Myerburg, R. (1999), 'Measurement of heart rate variability: a clinical tool or a research toy?', *J. Am. Coll. Cardiol.* **34**, 1878–83.

i Caros, J. S. (2011), Continuous non-invasive blood pressure estimation, PhD thesis, ETH Zurich, Zurich, Switzerland.

Izzo, J. (2007), *Comprehensive Hypertension*, 1 edn, Mosby Elsevier, Philadelphia, PA, chapter Hemodynamics of Hypertension, pp. 123–133.

Jaiswal, M., Urbina, E., Wadwa, R., Talton, J., Jr, R. D., Hamman, R., Fingerlin, T., Daniels, S., Marcovina, S., Dolan, L. & Dabelea, D. (2013), 'Reduced heart rate variability is associated with increased arterial stiffness in youth with type 1 diabetes: the search cvd study', *Diabetes care* **36**, 2351–2358.

Jan, H., Chen, M., Fu, T., Lin, W., Tsai, C. & Lin, K. (2019), 'Evaluation of coherence between ecg and ppg derived parameters on heart rate variability and respiration in healthy volunteers with/without controlled breathing', *J. Med. Biol. Eng.* **39**, 783–795.

Jans, O., Brinth, L., Kehlet, H. & Mehlsen, J. (2015), 'Decreased heart rate variability responses during early postoperative mobilization – an observational study', *BMC Anesthesiol.* **15**, 120.

Jensen-Urstad, K., Reichard, P. & Jensen-Urstad, M. (1999), 'Decreased heart rate variability in patients with type 1 diabetes mellitus is related to arterial wall stiffness', *J. Intern. Med.* **245**, 57–61.

Jeyhani, V., Mahdiani, S., Peltokangas, M. & Vehkaoja, A. (2015), Comparison of hrv parameters derived from photoplethysmography and electrocardiography signals, *in* 'Annu Int Conf IEEE Eng Med Biol Soc', pp. 5952–5955.

Jobbágy, A., Majnár, M., Tóth, L. & Nagy, P. (2017), 'Hrv-based stress level assessment using very short recordings', *Period. Polytech. Electr. Eng. Comput. Sci.* **61**, 238–245.

Johnson, A., Pollard, T., Shen, L., Lehman, L., Feng, M., Ghassemi, M., Moody, B., Szolovits, P., Celi, L. & Mark, R. (2016), 'Mimic-iii, a freely accessible critical care database', *Sci. Data* **3**, 160035.

Kamiya, A., Hayano, J., Kawada, T., Michikami, D., Yamamoto, K., Ariumi, H., Shimizu, S., Uemura, K., Miyamoto, T., Aiba, T., Sunagawa, K. & Sugimachi, M. (2005), 'Low-frequency oscillation of sympathetic nerve activity decreases during development of tilt-induced syncope preceding sympathetic withdrawal and bradycardia', *Am. J. Physiol. Heart Circ. Physiol.* **289**, H1758–H1769.

Kaplan, R., Chambers, D. & Glasgow, R. (2014), 'Big data and large sample size: a cautionary note on the potential for bias', *Clin. Transl. Sci.* **7**(4), 342–6.

Karlen, W., Kobayashi, K., Ansermino, J. & Dumont, G. (2012), 'Photoplethysmogram signal quality estimation using repeated Gaussian filters and cross-correlation', *Physiol. Meas.* **33**(10), 1617–1629.

Karmali, S., Sciusco, A., May, S. & Ackland, G. (2017), 'Heart rate variability in critical care medicine: a systematic review', *Intensive Care. Med. Exp.* **5**, 33.

Kechris, C. & Delopoulos, A. (2021), Rmssd estimation from photoplethysmography and accelerometer signals using a deep convolutional network, *in* 'Annu. Int. Conf. IEEE Eng. Med. Biol. Soc.', pp. 228–231.

Keet, S., Bulte, C., Sivanathan, A., Verhees, L., Allaart, C., Boer, C. & Bouwman, R. (2014), 'Cardiovascular autonomic function testing under non-standardised and standardised conditions in cardiovascular patients with type-2 diabetes mellitus', *Anaesthesia* **69**, 476–483.

Kekecs, Z., Szekely, A. & Varga, K. (2016), 'Alterations in electrodermal activity and cardiac parasympathetic tone during hypnosis', *Psychophysiology* **53**, 268–277.

Khalilzadeh, J. & Tasci, A. (2017), 'Large sample size, significance level, and the effect size: Solutions to perils of using big data for academic research', *Tour. Manag.* **62**, 89–96.

Khan, M., Pretty, C., Amies, A., Elliott, R., Shaw, G. & Chase, J. (2015), Investigating the effects of temperature on photoplethysmography, *in* '9th IFAC Symposium on Biological and Medical Systems BMS', pp. 360–365.

Khandoker, A., Karmakar, C., Brennan, M., Palaniswami, M. & Voss, A. (2013), *Poincaré Plot Methods for Heart Rate Variability Analysis*, Springer, Boston, MA.

Khandoker, A., Karmakar, C. & Palaniswami, M. (2011), 'Comparison of pulse rate variability with heart rate variability during obstructive sleep apnea', *Med. Eng. Phys.* **33**, 204–209.

Khoo, M. & Chalacheva, P. (2019), 'Respiratory modulation of peripheral vasoconstriction: a modeling perspective', *J. Appl. Physiol.* **127**, 1177–1186.

Killian, J., Radin, R., Gardner, C., Kasuske, L., Bashirelahi, K., Nathan, D., Keyser, D., Cellucci, C., Darmon, D. & Rapp, P. (2021), 'Alternative devices for heart rate variability measures: A comparative test–retest reliability study', *Behav. Sci.* **11**, 68.

Kim, C. & Kim, K. (2012), *Primer on the Autonomic Nervous System*, 3 edn, Elsevier, chapter Development and Differentiation of Autonomic Neurons, pp. 3–8.

Kim, J. & Ahn, J. (2019), 'Digital iir filters for heart rate variability; a comparison between butterworth and elliptic filters', *Int. J. Sci. Technol. Res.* **8**, 3509–3513.

Kim, J., Seok, H. & Shin, H. (2021), 'Is ultra-short-term heart rate variability valid in non-static conditions?', *Front. Physiol.* **12**, 596060.

King, S., Ahuja, K., Wass, J., Shing, C., Adams, M., Davies, J., Sharman, J. & Williams, A. (2013), 'Effect of whole-body mild-cold exposure on arterial stiffness and central haemodynamics: a randomised, cross-over trial in healthy men and women', *Eur. J. Appl. Physiol.* **113**(5), 1257–69.

Kinnunen, H., Rantanen, A., Kenttä, T. & Koskimäki, H. (2020), 'Feasible assessment of recovery and cardiovascular health: accuracy of nocturnal hr and hrv assessed via ring ppg in comparison to medical grade ecg', *Physiol. Meas.* **41**, 04NT01.

Kleiger, R., Stein, P. & Jr., J. B. (2005), 'Heart rate variability: Measurement and clinical utility', *Ann. Noninvasive Electrocardiol.* **10**, 88–101.

Kobayashi, M., Sun, G., Shinba, T., Matsui, T. & Kirimoto, T. (2017), Simple and objective screening of major depressive disorder by heart rate variability analysis

during paced respiration and mental task conditions, *in* 'Annu. Int. Conf. IEEE Eng. Med. Biol. Soc.', pp. 1316–1319.

Koch, R., Pfeiffer, N., Lang, N., Eskofier, B., Amft, O., Struck, M. & Wittenberg, T. (2020), 'Evaluation of hrv estimation algorithms from ppg data using neural networks', *Curr Dir Biomed Eng* **6**, 505–509.

Koenig, J., Kemp, A., Beauchaine, T., Thayer, J. & Kaess, M. (2016), 'Depression and resting state heart rate variability in children and adolescents - a systematic review and metaanalysis', *Clin. Psychol. Rev.* **46**, 136–150.

Kranjec, J., Begus, S., Gersak, G. & Drnovsek, J. (2014), 'Non-contact heart rate and heart rate variability measurements: A review', *Biomed. Signal Process. Control* **13**, 102–112.

Krishnaswamy, U., Higgins, S., Kosky, C., DeLacy, S. & Williams, A. (2010), 'Diagnosis of plmd from increased pulse rate variability on overnight oximetry', *Nat. Sci. Sleep* **2**, 107–114.

Krivec, U., Salva, M. Q., Constant, I., Ramirez, A., Lofaso, F., Pépin, J. & Fauroux, B. (2012), 'Nocturnal hypoxemia, but not hypercapnia, correlates with sleep quality in children', *Respir. Care.* **57**, 1937–1944.

Krivoshei, L., Weber, S., Burkard, T., Maseli, A., Brasier, N., Kühne, M., Conen, D., Huebner, T., Seeck, A. & Eckstein, J. (2017), 'Smart detection of atrial fibrillation', *Europace* **19**, 753–757.

Królak, A. & Pilecka, E. (2022), Analysis and comparison of heart rate variability signals derived from ppg and ecg sensors, *in* D. Pijanowska, K. Zieliński, A. Liebert & J. Kacprzyk, eds, 'Biocybernetics and Biomedical Engineering – Current Trends and Challenges. Lecture Notes in Networks and Systems', Vol. 293, pp. 9–16.

kumar, C. K., M.Manaswini, Maruthy, K., Kumar, A. S. & kumar, K. M. (2021), 'Association of heart rate variability measured by rr interval from ecg and pulse to pulse interval from photoplethysmography', *Clin. Epidemiol. Glob. Health* **10**, 100698.

Kumar, K., Kirsch, R. & Hornik, C. (2019), *Critical Heart Disease in Infants and Children*, 3 edn, Elsevier, chapter Cardiovascular Physiology for Intensivists, pp. 111–133.e5.

Kyriacou, P. (2021), Introduction to photoplethysmography, *in* P. Kyriacou & J. Allen, eds, 'Photoplethysmography: Technology, Signal Analysis, and Applications', Elsevier, London, UK, chapter 1, pp. 1–15.

Kyriacou, P. & Chatterjee, S. (2021), The origin of photoplethysmography, *in* P. Kyriacou & J. Allen, eds, 'Photoplethysmography: Technology, Signal Analysis, and Applications', Elsevier, London, UK, chapter 2, pp. 17–42.

Kyriacou, P. & May, J. (2021), Photoplethysmography: New trends and future directions, *in* P. Kyriacou & J. Allen, eds, 'Photoplethysmography: Technology, Signal Analysis, and Applications', Elsevier, London, UK, chapter 14, pp. 469–486.

Kyrlagkitsis, S., Papaioannou, T., Gialafos, E., Vavuranakis, M., Siasos, G., Hatzis, G., Kokkou, E., Gatzoulis, K., Karamanou, M., Stefanadis, C. & Tousoulis, D. (2016), 'Relationships between heart rate variability and aortic hemodynamic variables in healthy subjects', *Hellenic J. Cardiol.* **57**, 359–362.

Laborde, S., Mosley, E. & Thayer, J. (2017), 'Heart rate variability and cardiac vagal tone in psychophysiological research - recommendations for experiment planning, data analysis, and data reporting', *Front. Physiol.* **8**, 213.

Lan, K., Raknim, P., Kao, W. & Huang, J. (2018), 'Toward hypertension prediction based on ppg-derived hrv signals: a feasibility study', *J. Med. Syst.* **42**, 103.

Lazaro, J., Gil, E., Vergara, J. & Laguna, P. (2012), Osas detection in children by using ppg amplitude fluctuation decreases and pulse rate variability, *in* '2012 Computing in Cardiology', pp. 185–188.

Lazazzera, R., Deviaene, M., Varon, C., Buyse, B., Testelmans, D., Laguna, P., Gil, E. & Carrault, G. (2021), 'Detection and classification of sleep apnea and hypopnea using ppg and spo¡inline-formula¿¡tex-math notation="latex"¿2¡/tex-math¿¡/inline-formula¿ signals', *IEEE Trans. Biomed. Eng.* **68**, 1496–1506.

Leitner, J., Chiang, P. & Dey, S. (2019), Personalized blood pressure estimation using photoplethysmography and wavelet decomposition, *in* '2019 IEEE International Conference on E-health Networking, Application and Services (HealthCom)', pp. 1–6.

Li, B., Dong, M. & Vai, M. (2010), 'On an automatic delineator for arterial blood pressure waveforms', *Biomed. Signal Process. Control* **5**, 76–81.

Li, K., Rüdiger, H. & Ziemssen, T. (2019), 'Spectral analysis of heart rate variability: Time window matters', *Front. Neurol.* **10**, 545.

Li, Q. & Clifford, G. (2012), 'Dynamic time warping and machine learning for signal quality assessment of pulsatile signals', *Physiol. Meas.* **33**(9), 1491–1501.

Liang, C., Lee, J., Chen, C. & Chang, Y. (2015), 'Reactive heart rate variability in male patients with first-episode major depressive disorder', *Prog. Neuropsychopharmacol. Biol. Psychiatry* **56**, 52–57.

Liang, Y., Abbott, D., Howard, N., Lim, K., Ward, R. & Elgendi, M. (2019), 'How effective is pulse arrival time for evaluating blood pressure? challenges and recommendations from a study using the mimic database', *J. Clin. Med.* **8**, 337.

Liang, Y., Chen, Z., Ward, R. & Elgendi, M. (2018), 'Photoplethysmography and deep learning: Enhancing hypertension risk stratification', *Biosensors (Basel)* **8**(4), 101.

Lin, W., Wu, D., Li, C., Zhang, H. & Zhang, Y. (2014), Comparison of heart rate variability from ppg with that from ecg, *in* 'The International Conference on Health Informatics. IFMBE Proceedings', Vol. 42.

Liu, H., Allen, J., Ghufran Khalid, S., Fei Chen, F. & Zheng, D. (2021), 'Filtering-induced time shifts in photoplethysmography pulse features measured at different body sites: the importance of filter definition and standardization', *Physiol. Meas.* **42**, 074001.

Liu, I., Ni, S. & Peng, K. (2020), 'Enhancing the robustness of smartphone photoplethysmography: A signal quality index approach', *Sensors (Basel)* **20**, 1923.

Liu, S., Teng, J., Qi, X., Wei, S. & Liu, C. (2017), 'Comparison between heart rate variability and pulse rate variability during different sleep stages for sleep apnea patients', *Technol. Health Care.* **25**, 435–445.

Logier, R., Jonckheere, J. D., Dassonneville, A. & Jeanne, M. (2016), Comparison of pulse rate variability and heart rate variability for high frequency content estimation, *in* 'Annu. Int. Conf. IEEE Eng. Med. Biol. Soc.', pp. 936–939.

Lombard, J. & Cowley, A. (2012), *Primer on the Autonomic Nervous System*, 3 edn, Elsevier, chapter Neural Control of Blood Vessels, pp. 187–191.

Lu, G. & Yang, F. (2009), 'Limitations of oximetry to measure heart rate variability measures', *Cardiovasc. Eng.* **9**, 119–125.

Lu, G., Yang, F., Taylor, J. & Stein, J. (2009), 'A comparison of photoplethysmography and ecg recording to analyse heart rate variability in healthy subjects', *J. Med. Eng. Technol.* **33**, 634–641.

Lu, S., Zhao, H., Ju, K., Shin, K., Lee, M., Shelley, K. & Chon, K. (2008), 'Can photoplethysmography variability serve as an alternative approach to obtain heart rate variability information?', *J. Clin. Monit. Comput.* **22**, 23–29.

Lázaro, J., Gil, E., Vergara, J. & Laguna, P. (2014), 'Pulse rate variability analysis for discrimination of sleep-apnea-related decreases in the amplitude fluctuations of pulse photoplethysmographic signal in children', *IEEE J. Biomed. Heal. Informatics* **18**, 240–246.

Magkas, N., Tsioufis, C., Thomopoulos, C., Dilaveris, P., Georgiopoulos, G., Sanidas, E., Papademetriou, V. & Tousoulis, D. (2019), 'Orthostatic hypotension: From pathophysiology to clinical applications and therapeutic considerations', *J Clin Hypertens* **21**(5), 546–554.

Malik, M., Huikuri, H., Lombardi, F. & Schmidt, G. (2017), 'The purpose of heart rate variability measurements', *Clin. Auton. Res.* **27**, 139–140.

Mancia, G. & Grassi, G. (2014), 'The autonomic nervous system and hypertension', *Circ. Res.* **114**, 1804–1814.

Martín-Martínez, D., Casaseca-de-la Higuera, P., Martín-Fernández, M. & Alberola-López, C. (2013), '"stochastic modeling of the ppg signal: A synthesis-by-analysis approach with applications"', *IEEE Trans. Biomed. Eng.* **60**(9), 2432–2441.

Martínez-Rodrigo, A., Fernández-Aguilar, L., Zangróniz, R., Latorre, J., Pastor, J. & Fernández-Caballero, A. (2019), 'Film mood induction and emotion classification using physiological signals for health and wellness promotion in older adults living alone', *Expert Syst.* **37**, e12425.

Mathworks (2022), 'Lilliefors test', Online. **url**: https://www.mathworks.com/help/stats/lillietest.html.

May, J., Mejía-Mejía, E., Nomoni, M., Budidha, K., Choi, C. & Kyriacou, P. (2021), 'Effects of contact pressure in reflectance photoplethysmography in an in vitro tissue-vessel phantom', *Sensors* **21**, 8421–8421.

Mayor, D., Panday, D., Kandel, H., Steffert, T. & Banks, D. (2021), 'Ceps: An open access matlab graphical user interface (gui) for the analysis of complexity and entropy in physiological signals', *Entropy* **23**, 321.

McDuff, D., Gontarek, S. & Picard, R. (2014), 'Improvements in remote cardiopulmonary measurement using a five band digital camera', *IEEE Trans. Biomed. Eng.* **61**, 2593–2601.

McManus, D., Chong, J., Soni, A., Saczynski, J., Esa, N., Napolitano, C., Darling, C., Boyer, E., Rosen, R., Floyd, K. & Chon, K. (2016), 'Pulsesmart: Pulse-based arrhythmia discrimination using a novel smartphone application', *J. Cardiovasc. Electrophysiol.* **27**, 51–57.

Mejía-Mejía, E., Allen, J., Budidha, K., El-Hajj, C., Kyriacou, P. & Charlton, P. (2021), Photoplethysmography signal processing and synthesis, *in* P. Kyriacou & J. Allen, eds, 'Photoplethysmography: Technology, Signal Analysis, and Applications', Elsevier, London, UK, chapter 4, pp. 69–145.

Mejía-Mejía, E., May, J. & Kyriacou, P. (2021), Effect of filtering of photoplethysmography signals in pulse rate variability analysis, *in* 'Annu Int Conf IEEE Eng Med Biol Soc', pp. 5500–5503.

Melchor Rodríguez, A., & Ramos-Castro, J. (2018), 'Video pulse rate variability analysis in stationary and motion conditions', *Biomed. Eng. Online* **17**, 11.

Melinosky, C., Yang, S., Hu, P., Li, H., Miller, C., Khan, I., Mackenzie, C., Chang, W., Parikh, G., Stein, D. & Badjatia, N. (2018), 'Continuous vital sign analysis to predict secondary neurological decline after traumatic brain injury', *Front. Neurol.* **9**, 761.

Messas, E., Pernot, M. & Couade, M. (2013), 'Arterial wall elasticity: State of the art and future prospects', *Diagn. Interv. Imaging* **94**(5), 561–569.

Middleton, P., Tang, C., Chan, G., Bishop, S., Savkin, A. & Lovell, N. (2011), 'Peripheral photoplethysmography variability analysis of sepsis patients', *Med. Biol. Eng. Comput.* **49**, 337–347.

Millán, C., Girón, N. & Lopez, D. (2020), 'Analysis of relevant features from photoplethysmographic signals for atrial fibrillation classification', *Int. J. Environ. Res. Public Health* **17**, 498.

Minassian, A., Geyer, M., Baker, D., Nievergelt, C., O'Connor, D. & Risbrough, V. (2014), 'Heart rate variability characteristics in a large group of active-duty marines and relationship to posttraumatic stress', *Psychosom. Med.* **76**, 292–301.

Minassian, A., Maihofer, A., Baker, D., Nievergelt, C., Geyer, M. & Risbrough, V. (2015), 'Association of predeployment heart rate variability with risk of postdeployment posttraumatic stress disorder in active-duty marines', *JAMA Psychiatry* **72**, 979–986.

Mohapatra, P., Premkumar, P. & Sivaprakasam, M. (2018), 'A yellow – orange wavelength based short-term heart rate variability measurement scheme for wrist-based wearables', *IEEE Trans. Instrum. Meas.* **67**, 1091–1101.

Molkkari, M., Tenhunen, M., Tarniceriu, A., Vehkaoja, A., Himanen, S. & Räsänen, E. (2019), Non-linear heart rate variability measures in sleep stage analysis with photoplethysmography, *in* 'Computing in Cardiology (CinC)', pp. 1–4.

Moody, B., Moody, G., Villarroel, M., Clifford, G. & Silva, I. (2020), 'Mimic-iii waveform database (version 1.0), physionet', Online. **url**: https://doi.org/10.13026/c2607m.

Moreno, E., Lujan, M., Rusinol, M., Fernandez, P., Manrique, P., Trivino, C., Miquel, M., Rodriguez, M. & Burguillos, M. (2017), 'Type 2 diabetes screening test by means of a pulse oximeter', *IEEE Trans. Biomed. Eng.* **64**, 341–351.

Moridani, M., Setarehdan, S., Nasrabadi, A. & Hajinasrollah, E. (2015), 'Analysis of heart rate variability as a predictor of mortality in cardiovascular patients of intensive care unit', *Biocybern. Biomed. Eng.* **35**, 217–226.

Morresi, N., Casaccia, S., Sorcinelli, M., Arnesano, M. & Revel, G. (2020), Analysing performances of heart rate variability measurement through a smartwatch, *in*

‘2020 IEEE International Symposium on Medical Measurements and Applications (MeMeA)’, pp. 1–6.

Mousavi, S., Firouzmand, M., Charmi, M., Hemmati, M., Moghadam, M. & Ghorbani, Y. (2019), ‘Blood pressure estimation from appropriate and inappropriate ppg signals using a whole-based method’, *Biomed. Signal. Process. Control* **47**, 196–206.

Mueck-Weymann, M., Rechlin, T., Ehrengut, F., Rauh, R., Acker, J., Dittmann, R., Czekalla, J., Joraschky, P. & Musselman, D. (2002), ‘Effects of olanzapine and clozapine upon pulse rate variability’, *Depress. Anxiety* **16**, 93–99.

Muhadi, Nasution, S., Putranto, R. & Harimurti, K. (2016), ‘The ability of detecting heart rate variability with the photoplethysmography to predict major adverse cardiac event in acute coronary syndrome’, *Acta Med. Indones.* **48**, 48–53.

Mukkamala, R., Hahn, J., Inan, O., Mestha, L., Kim, C., Töreyin, H. & Kyal, S. (2015), ‘Toward ubiquitous blood pressure monitoring via pulse transit time: Theory and practice’, *IEEE Trans. Biomed. Eng.* **62**, 1879–1901.

Murray, A. (2012), Examining Heart Rate Variability and Alpha-Amylase Levels in Predicting PTSD in Combat-Experienced Marines, PhD thesis, Alliant International University, Alhambra, CA.

Mäki-Petäjä, K., Barrett, S., Evans, S., Cheriyan, J., McEniery, C. & Wilkinson, I. (2016), ‘The role of the autonomic nervous system in the regulation of aortic stiffness’, *Hypertension* **68**(5), 1290–1297.

Nakamura, H. & Tagawa, M. (2019), Pitfall of heart rate variability analyses for autonomic nervous system activity with photoplethysmography, *in* ‘Annu. Int. Conf. IEEE Eng. Med. Biol. Soc.’, pp. 1–4.

Nakao, M., Nomura, K., Karita, K., Nishikitani, M. & Yano, E. (2004), ‘Relationship between brachial-ankle pulse wave velocity and heart rate variability in young japanese men’, *Hypertens. Res.* **27**, 925–931.

Nardelli, M., Greco, A., Vanello, N. & Scilingo, E. (2021), Reliability of pulse rate variability in elderly men and women: an application of cross-mapping approach, *in* ‘Annu. Int. Conf. IEEE Eng. Med. Biol. Soc.’, pp. 492–495.

Nardelli, M., Vanello, N., Galperti, G., Greco, A. & Scilingo, E. (2020), 'Assessing the quality of heart rate variability estimated from wrist and finger ppg: A novel approach based on cross-mapping method', *Sensors (Basel)* **20**, 3156.

Nasr, A. (2012), 'The radial artery and its variations: anatomical study and clinical implications', *Folia Morphol. (Warsz)* **71**(4), 252–262.

Natarajan, A., Pantelopoulos, A., Emir-Farinas, H. & Natarajan, P. (2020), 'Heart rate variability with photoplethysmography in 8 million individuals: a cross-sectional study', *Lancet Digit. Health* **2**, e650–e657.

Nath, R., Thapliyal, H. & Caban-Holt, A. (2018), Towards photoplethysmogram based non-invasive blood pressure classification, *in* '2018 IEEE International Symposium on Smart Electronic Systems (iSES) (Formerly iNiS)', pp. 37–39.

National Health Service (2017), 'Low blood pressure (hypotension)', Online. **url**: https://www.nhs.uk/conditions/low-blood-pressure-hypotension/.

National Health Service (2019*a*), 'High blood pressure (hypertension)', Online. **url**: https://www.nhs.uk/conditions/high-blood-pressure-hypertension/.

National Health Service (2019*b*), 'What is blood pressure?', Online. **url**: https://www.nhs.uk/common-health-questions/lifestyle/what-is-blood-pressure/.

Neshitov, A., Tyapochkin, K., Smorodnikova, E. & Pravdin, P. (2021), 'Wavelet analysis and self-similarity of photoplethysmography signals for hrv estimation and quality assessment', *Sensors* **21**, 6798.

Nichols, W., O'Rourke, M. & Vlachopoulos, C. (2011), *McDonald's Blood Flow in Arteries*, 6 edn, Hodder Arnold, London, UK.

Nitzan, M., Babchenko, A., Khanokh, B. & Landau, D. (1998), 'The variability of the photoplethysmographic signal - a potential method for the evaluation of the autonomic nervous system the variability of the photoplethysmographic signal — a potential method for the evaluation of the autonomic nervous system', *Physiol. Meas.* **19**, 93–102.

Njoum, H. (2017), Investigations of photoplethysmography in the assessment of haemodynamics, vascular mechanics and haemorheology, PhD thesis, City, University of London, London, UK.

Nomoni, M., May, J. & Kyriacou, P. (2019), A pulsatile optical tissue phantom for the investigation of light-tissue interaction in reflectance photoplethysmography, *in* 'Annu Int Conf IEEE Eng Med Biol Soc', pp. 3204–3207.

Nomoni, M., May, J. & Kyriacou, P. (2020), 'Novel polydimethylsiloxane (pdms) pulsatile vascular tissue phantoms for the in-vitro investigation of light tissue interaction in photoplethysmography', *Sensors (Basel)* **20**(15), 4246.

Northcott, C. & Haywood, J. (2007), *Comprehensive Hypertension*, 1 edn, Mosby Elsevier, Philadelphia, PA, chapter Central Nervous System Control of Blood Pressure, pp. 281–290.

Nuuttila, O., Korhonen, E., Laukkanen, J. & Kyröläinen, H. (2022), 'Validity of the wrist-worn polar vantage v2 to measure heart rate and heart rate variability at rest', *Sensors* **22**, 137.

Okkesim, S., Çelik, G., Yildirim, M., Ilhan, M., Karaman, O., Tasan, E. & Kara, S. (2016), 'Comparison of pulse rate variability and heart rate variability for hypoglycemia syndrome', *Methods Inf. Med.* **55**, 250–257.

Orphanidou, C. (2018), *Signal Quality Assessment in Physiological Monitoring*, Springer.

Ostadfar, A. (2016), *Biofluid Mechanics*, 2 edn, Elsevier, Oxford, GB, chapter Macrocirculation System, pp. 61–86.

Owens, A. (2020), 'The role of heart rate variability in the future of remote digital biomarkers', *Front. Neurosci.* **14**, 582145.

Pan, J. & Tompkins, W. (1985), 'A real-time QRS detection algorithm', *IEEE Trans. Biomed. Eng.* **32**(3), 230–6.

Panganiban, F.C. & de Leon, F.A. (2019), Reducing pulse rate variability computational error from a 30 hz photoplethysmography recording, *in* '2019 International Symposium on Multimedia and Communication Technology (ISMAC)', pp. 1–6.

Parasnis, R., Pawar, A. & Manivannan, M. (2015), Multiscale entropy and poincaré plot-based analysis of pulse rate variability and heart rate variability of icu patients, *in* '2015 International Conference on Intelligent Informatics and Biomedical Sciences (ICIIBMS)', pp. 290–295.

Park, Y., Park, Y. & Ko, Y. (2012), 'Relationships of pulse waveform parameters to mood states and chronic fatigue', *J. Altern. Complement. Med.* **18**, 1050–1060.

Pecchia, L., Castaldo, R., Montesinos, L. & Melillo, P. (2018), 'Are ultra-short heart rate variability features good surrogates of short-term ones? state-of-the-art review and recommendations', *Healthc. Technol. Lett.* **5**, 94–100.

Pelaez-Coca, M., Hernando, A., Lazaro, J. & Gil, E. (2022), 'Impact of the ppg sampling rate in the pulse rate variability indices evaluating several fiducial points in different pulse waveforms', *IEEE J. Biomed. Health Inform.* **26**, 539–549.

Pellegrino, P., Schiller, A. & Zucker, I. (2014), 'Validation of pulse rate variability as a surrogate for heart rate variability in chronically instrumented rabbits', *Am. J. Physiol. Heart Circ. Physiol.* **307**, H97–H109.

Peng, R., Zhou, X., Lin, W. & Zhang, Y. (2015), 'Extraction of heart rate variability from smartphone photoplethysmograms', *Comput. Math Methods Med.* **2015**, 516826.

Peralta, E., Lazaro, J., Bailon, R., Marozas, V. & Gil, E. (2019), 'Optimal fiducial points for pulse rate variability analysis from forehead and finger photoplethysmographic signals', *Physiol. Meas.* **40**, 025007.

Pereira, T., Gadhoumi, K., Ma, M., Liu, X., Xiao, R. & Colorado, R. (2020), 'A supervised approach to robust photoplethysmography quality assessment', *IEEE J. Biomed. Health Inform.* **24**(3), 649–657.

Pernice, R., Javorka, M., Krohova, J., Czippelova, B., Turianikova, Z., Busacca, A. & Faes, L. (2018), Reliability of short-term heart rate variability indexes assessed through photoplethysmography, *in* 'Annu. Int. Conf. IEEE Eng. Med. Biol. Soc.', pp. 5610–5513.

Pernice, R., Javorka, M., Krohova, J., Czippelova, B., Turianikova, Z., Busacca, A. & Faes, L. (2019*a*), 'Comparison of short-term heart rate variability indexes evaluated through electrocardiographic and continuous blood pressure monitoring', *Med. Biol. Eng. Comput.* **57**, 1247–1263.

Pernice, R., Javorka, M., Krohova, J., Czippelova, B., Turianikova, Z., Busacca, A. & Faes, L. (2019*b*), 'Comparison of short-term heart rate variability indexes eval-

uated through electrocardiographic and continuous blood pressure monitoring', *Med. Biol. Eng. Comput.* **57**, 1247–1263.

Pernice, R., Javorka, M., Krohova, J., Czippelova, B., Turianikova, Z., Busacca, A. & Faes, L. (2019*c*), A validity and reliability study of conditional entropy measures of pulse rate variability, *in* 'Annu. Int. Conf. IEEE Eng. Med. Biol. Soc.', pp. 5568–5571.

Pi, I., Pi, I. & Wu, W. (2022), 'External factors that affect the photoplethysmography waveforms', *SN Appl. Sci.* **4**, 21.

Pilt, K., Meigas, K., Temitski, K. & Viigimaa, M. (2013), The effect of local cold and warm exposure on index finger photoplethysmographic signal waveform, *in* 'Annu Int Conf IEEE Eng Med Biol Soc.', pp. 2300–2303.

Pinheiro, E., Postolache, O. & Girão, P. (2009), Blood pressure and heart rate variabilities estimation using ballistocardiography, *in* 'Conference on Telecommunications - ConfTele', Vol. 1, pp. 125–128.

Pinheiro, N., Couceiro, R., Henriques, J., Muehlsteff, J., Quintal, I., Goncalves, L. & Carvalho, P. (2016), Can ppg be used for hrv analysis?, *in* 'Annu. Int. Conf. IEEE Eng. Med. Biol. Soc.', pp. 2945–2949.

Poh, M., McDuff, D. & Picard, R. (2011), 'Advancements in noncontact, multiparameter physiological measurements using a webcam', *IEEE Trans. Biomed. Eng.* **58**, 7–11.

Poonam, N., Rajan, K. & Tripta, S. (2013), 'Anatomical considerations and clinical implications of subclavian artery', *J. Evol. Med. Dent. Sci.* **2**(29), 5484–5491.

Posada-Quintero, H.F., Delisle-Rodríguez, D., Cuadra-Sanz, M.B., & Fernández de la Vara-Prieto, R.R. (2013), 'Evaluation of pulse rate variability obtained by the pulse onsets of the photoplethysmographic signal', *Physiol. Meas.* **34**, 179–187.

Prada, E. A. & Maldonado, R. S. (2018), 'A novel and low-complexity peak detection algorithm for heart rate estimation from low-amplitude photoplethysmographic (PPG) signals', *J. Med. Eng. Technol.* **42**(8), 569–577.

Quintana, D. (2017), 'Statistical considerations for reporting and planning heart rate variability case-control studies', *Psychophysiology* **54**, 344–349.

Radha, M., de Groot, K., Rajani, N., Wong, C., Kobold, N., Vos, V., Fonseca, P., Mastellos, N., Wark, P., Velthoven, N., Haakma, R. & Aarts, R. (2019), 'Estimating blood pressure trends and the nocturnal dip from photoplethysmography', *Physiol. Meas.* **40**, 025006.

Rahman, M., Nemati, E., Rahman, M., Nathan, V., Vatanparvar, K. & Kuang, J. (2020), 'Automated assessment of pulmonary patients using heart rate variability from everyday wearables', *Smart Health* **15**, 100081.

Raiko, J., Saari, T., Orava, J., Savisto, N., Parkkola, R., Haaparanta-Solin, M., Nuutila, P. & Virtanen, K. (2021), 'Changes in electrocardiogram parameters during acute nonshivering cold exposure and associations with brown adipose tissue activity, plasma catecholamine levels, and brachial blood pressure in healthy adults', *Physiol. Rep.* **9**, e14718.

Ramesh, J., Solatidehkordi, Z., Aburukba, R. & Sagahyroon, A. (2021), 'Atrial fibrillation classification with smart wearables using short-term heart rate variability and deep convolutional neural networks', *Sensors* **21**, 7233.

Rangayyan, R. (2002), *Biomedical Signal Analysis*, IEEE Press, Calgary, Canada.

Rapalis, A., Petrenas, A., Simaityte, M., Bailón, R. & Marozas, V. (2018), 'Towards pulse rate parametrization during free- living activities using smart wristband', *Physiol. Meas.* **39**, 055007.

Rauh, R., Limley, R., Bauer, R., Radespiel-Troger, M. & Mueck-Weymann, M. (2003), Comparison of heart rate variability and pulse rate variability detected with photoplethysmography, *in* 'Saratov Fall Meeting 2003: Optical Technologies in Biophysics and Medicine V', Vol. 5474, pp. 115–126.

RDocumentation (2022), 'posthoc.friedman.nemenyi.test: Pairwise post-hoc test for multiple comparisons of mean rank sums for unreplicated blocked data (nemenyi-test)', Online. **url**: https://www.rdocumentation.org/packages/PMCMR/versions/4.3/topics/posthoc.friedman.nemenyi.test.

Reddy, V., Choudhury, A., Jayaraman, S., Thokala, N., Deshpande, P. & Kaliaperumal, V. (2017), Perdmcs: Weighted fusion of ppg signal features for robust and efficient diabetes mellitus classification, *in* 'Proceedings of the 10th Interna-

tional Joint Conference on Biomedical Engineering Systems and Technologies - SmartMedDev, (BIOSTEC 2017)', pp. 553–560.

Reisner, A., Clifford, G. & Mark, R. (2006), The physiological basis of the electrocardiogram, *in* G. Clifford, F. Azuaje & P. McSharry, eds, 'Advanced Methods and Tools for ECG Data Analysis', 1 edn, Artech House, Norwood, MA, pp. 1–26.

Ricardo Ferro, B.T., Ramírez Aguilera, A., & Fernández de la Vara Prieto, R.R. (2015), 'Automated detection of the onset and systolic peak in the pulse wave using hilbert transform', *Biomed. Signal Process. Control* **20**, 78–84.

Roth, G.A., et al. (2020), 'Global burden of cardiovascular diseases and risk factors, 1990–2019: Update from the gbd 2019 study', *J. Am. Coll. Cardiol.* **76**(25), 2982–3021.

Rubenstein, D., Yin, W. & Frame, M. (2016), *Biofluid Mechanics*, 2 edn, Elsevier, Oxford, GB, chapter Blood Flow in Arteries and Veins, pp. 161–223.

Rubins, U. (2008), 'Finger and ear photoplethysmogram waveform analysis by fitting with gaussians', *Med. Biol. Eng. Comput* **46**, 1271–1276.

Rybynok, V., May, J., Budidha, K., Njoum, H., Phillips, J. & Kyriacou, P. (2012), Zenppg: A modular multi-channel photoplethysmography system, *in* 'International Symposium of Innovations and Applications of Monitoring Perfusion, Oxygenation and Ventilation (IAMPOV)'.

Saeed, M., Villarroel, M., Reisner, A., Clifford, G., Lehman, L., Moody, G., Heldt, T., Kyaw, T., Moody, B. & Mark, R. (2011), 'Multiparameter intelligent monitoring in intensive care ii (mimic-ii): A public-access icu database', *Crit. Care Med.* **39**, 952–960.

Sakakibara, M., Hayano, J., Oikawa, L., Katsamanis, M. & Lehrer, P. (2013), 'Heart rate variability biofeedback improves cardiorespiratory resting function during sleep', *Appl. Psychophysiol. Biofeedback* **38**, 265–271.

Sakakibara, M., Kanematsu, T., Yasuma, F. & Hayano, J. (2008), 'Impact of real-world stress on cardiorespiratory resting function during sleep in daily life', *Psychophysiology* **45**, 667–670.

Schrödl, E., Kampusch, S., Razlighi, B., Le, V., Széles, J. & Kaniusas, E. (2019), 'Feasibility of pulse rate variability as feedback in closed-loop percutaneous auricular vagus nerve stimulation', *Vibroengineering Procedia* **26**, 35–39.

Schumann, A., Suttkus, S. & Bär, K. (2021), 'Estimating resting hrv during fmri: A comparison between laboratory and scanner environment', *Sensors* **21**, 7663.

Schäfer, A. & Vagedes, J. (2013), 'How accurate is pulse rate variability as an estimate of heart rate variability? A review on studies comparing photoplethysmographic technology with an electrocardiogram', *Int. J. Cardiol.* **166**, 15–29.

Selvaraj, N., Jaryal, A., Santhosh, J., Deepak, K. & Anand, S. (2008), 'Assessment of heart rate variability derived from finger-tip photoplethysmography as compared to electrocardiography', *J. Med. Eng. Technol.* **32**, 479–484.

Semmlow, J. & Griffel, B. (2014), *Biosignal and Medical Image Processing*, 3 edn, CRC Press, Boca Raton, Florida.

Shaffer, F. & Ginsberg, J. (2017), 'An overview of heart rate variability metrics and norms', *Front. Public Health* **5**, 258.

Shahrestani, S., Stewart, E., Quintana, D., Hickie, I. & Guastella, A. (2015), 'Heart rate variability during adolescent and adult social interactions: A meta-analysis', *Biol. Psychol.* **105**, 43–50.

Sheng, Y. & Zhu, L. (2018), 'The crosstalk between autonomic nervous system and blood vessels', *Int J Physiol Pathophysiol Pharmacol* **10**(1), 17–28.

Sheridan, D., Baker, S., Dehart, R., Lin, A., Hansen, M., Tereshchenko, L., Le, N., Newgard, C. & Nagel, B. (2021), 'Heart rate variability and its ability to detect worsening suicidality in adolescents: A pilot trial of wearable technology', *Psychiatry Investig.* **18**, 928–935.

Shi, P., Hu, S. & Zhu, Y. (2008), 'A preliminary attempt to understand compatibility of photoplethysmographic pulse rate variability with electrocardiogramic heart rate variability', *J. Med. Biol. Eng.* **28**, 173–180.

Shi, P., Zhu, Y., Allen, J. & Hu, S. (2009), 'Analysis of pulse rate variability derived from photoplethysmography with the combination of lagged poincaré plots and spectral characteristics', *Med. Eng. Phys.* **31**, 866–871.

Shin, H. (2016), 'Ambient temperature effect on pulse rate variability as an alternative to heart rate variability in young adult', *J. Clin. Monit. Comput.* **30**, 939–948.

Singstad, B., Azulay, N., Bjurstedt, A., Bjørndal, S., Drageseth, M., Engeset, P., Eriksen, K., Gidey, M., Granum, E., Greaker, M., Grorud, A., Hewes, S., Hou, J., Recha, A. L., Matre, C., Seputis, A., Sorensen, S., Thogersen, V., Joten, V., Tronstad, C. & Martinsen, O. (2021), 'Estimation of heart rate variability from finger photoplethysmography during rest, mild exercise and mild mental stress', *J. Electr. Bioimpedance* **12**, 89–102.

Slapničar, G., Luštrek, M. & Marinko, M. (2018), 'Continuous blood pressure estimation from ppg signal', *Informatica (Slovenia)* **42**, 33–42.

Slapničar, G., Mlakar, N. & M, M. L. (2019), 'Blood pressure estimation from photoplethysmogram using a spectro-temporal deep neural network', *Sensors (Basel)* **19**(15), 3420.

Sluyter, J., Camargo, C., Lowe, A. & Scragg, R. (2019), 'Pulse rate variability predicts atrial fibrillation and cerebrovascular events in a large, population-based cohort', *Int. J. Cardiol.* **275**, 83–88.

Sluyter, J., Hughes, A., Lowe, A., Jr, C. C. & Scragg, R. (2016), 'Statin utilisation in a real-world setting: a retrospective analysis in relation to arterial and cardiovascular autonomic function', *Pharma. Res. Per.* **4**, e00276.

Sološenko, A., Petrėnasa, A., Marozasa, V. & Sörnmo, L. (2017), 'Modeling of the photoplethysmogram during atrial fibrillation', *Comput. Biol. Med.* **81**, 130–138.

Souza, H., Philbois, S., Veiga, A. & Aguilar, B. (2021), 'Heart rate variability and cardiovascular fitness: What we know so far', *Vasc. Health Risk Manag.* **17**, 701–711.

Stein, P. & Reddy, A. (2005), 'Non-linear heart rate variability and risk stratification in cardiovascular disease', *Indian Pacing Electrophysiol. J.* **5**, 210–220.

Stuckey, M., Tulppo, M., Kiviniemi, A. & Petrella, R. (2014), 'Heart rate variability and the metabolic syndrome: A systematic review of the literature', *Diabetes Metab. Res. Rev.* **30**, 784–793.

Sun, C., Liu, C., Liu, W., Wu, H., Huang, R. & Liu, A. (2019), 'Compatibility of pulse-pulse intervals with r-r intervals in assessing cardiac autonomic function and its relation to risks of atherosclerosis', *Ci Ji Yi Xue Za Zhi* **32**, 41–46.

Sun, Y., Hu, S., Azorin-Peris, V., Kalawsky, R. & Greenwald, S. (2012), 'Noncontact imaging photoplethysmography to effectively access pulse rate variability', *J. Biomed. Opt.* **18**, 061205.

Sun, Y. & Thakor, N. (2016), 'Photoplethysmography revisited: From contact to noncontact, from point to imaging', *IEEE Trans. Biomed. Eng.* **63**, 463–477.

Suzuki, K., Laohakangvalvit, T., Matsubara, R. & Sugaya, M. (2021), 'Constructing an emotion estimation model based on eeg/hrv indexes using feature extraction and feature selection algorithms', *Sensors* **21**, 2019.

Takahara, M., Mizuno, K., Hirose, K., Sakai, K., Nishii, K., Onozuka, M., Sato, S. & Shirakawa, S. (2008), 'Continuous recording of autonomic nervous activity at nighttime effectively explains subjective sleep reports in postmenopausal women', *Sleep Biol. Rhythms* **6**, 215–221.

Takase, B. (2010), 'Role of heart rate variability in non-invasive electrophysiology: Prognostic markers of cardiovascular disease', *J. Arrhythmia* **26**, 227–237.

Tang, Q., Chen, Z., Allen, J., Alian, A., Menon, C., Ward, R. & Elgendi, M. (2020), 'Ppgsynth: An innovative toolbox for synthesizing regular and irregular photoplethysmography waveforms', *Front Med (Lausanne)* **7**, 597774.

Tang, Q., Chen, Z., Ward, R. & Elgendi, M. (2020), 'Synthetic photoplethysmogram generation using two gaussian functions', *Sci. Rep.* **10**, 13883.

Task Force of the European Society of Cardiology and The North American Society of Pacing and Electrophysiology (1996), 'Heart rate variability: Standards of measurement, physiological interpretation, and clinical use', *Circulation* **93**, 1043–1065.

Tazarv, A., Labbaf, S., Reich, S., Dutt, N., Rahmani, A. & Levorato, M. (2021), Personalized stress monitoring using wearable sensors in everyday settings, *in* 'Annu. Int. Conf. IEEE Eng. Med. Biol. Soc.', pp. 7332–7335.

Thayer, J., Yamamoto, S. & Brosschot, J. (2010), 'The relationship of autonomic imbalance, heart rate variability and cardiovascular disease risk factors', *Int. J. Cardiol.* **141**, 122–131.

Theodorakopoulou, M., Triantafyllou, A., Zafeiridis, A., Boutou, A., Grigoriadou, I., Kintiraki, E., Douma, S., Goulis, D. & Dipla, K. (2021), 'Impaired vagal adaptation to an exercise task in women with gestational diabetes mellitus versus women with uncomplicated pregnancies', *Hormones (Athens)* **20**, 753–760.

Theodoridis, S. & Koutroumbas, K. (2009), *Pattern Recognition*, 4 edn, Academic Press.

Torres-Valencia, C., Álvarez López, M. & Orozco-Gutiérrez, A. (2017), 'Svm-based feature selection methods for emotion recognition from multimodal data', *J. Multimodal User Interfaces* **11**, 9–23.

Trajkovic, I., Scholkmann, F. & Wolf, M. (2011), 'Estimating and validating the interbeat intervals of the heart using near-infrared spectroscopy on the human forehead', *J. Biomed. Opt.* **16**, 087002.

Umair, M., Chalabianloo, N., Sas, C. & Ersoy, C. (2021), 'Hrv and stress: A mixed-methods approach for comparison of wearable heart rate sensors for biofeedback', *IEEE Access* **9**, 14005–14024.

van Gent, P., Farah, H., van Nesb, N. & Arem, B. (2019), 'HeartPy: A novel heart rate algorithm for the analysis of noisy signals', *Transp. Res. F: Traffic Psychol. Behav.* **66**, 368–378.

Vasconcellos, F., Seabra, A., Cunha, F., Montenegro, R., Bouskela, E. & Farinatti, P. (2015), 'Heart rate variability assessment with fingertip photoplethysmography and polar rs800cx as compared with electrocardiography in obese adolescents', *Blood Press. Monit.* **20**, 351–360.

Vazquez, L., Blood, J., Wu, J., Chaplin, T., Hommer, R., Rutherford, H., Potenza, M., Mayes, L. & Crowley, M. (2016), 'High frequency heart-rate variability predicts adolescent depressive symptoms, particularly anhedonia, across one year', *J. Affect. Disord.* **196**, 243–247.

Veloza, L., Jiménez, C., Quiñones, D., Polanía, F., Pachón-Valero, L. & Rodríguez-Triviño, C. (2019), 'Variabilidad de la frecuencia cardiaca como factor predictor de las enfermedades cardiovasculares', *Rev. Colomb. Cardiol.* **26**, 205–210.

Verma, A., Aarotale, P., Dehkordi, P., Lou, J. & Tavakolian, K. (2019), 'Relationship between ischemic stroke and pulse rate variability as a surrogate of heart rate variability', *Brain Sci.* **9**, 162.

Vescio, B., Salsone, M., Gambardella, A. & Quattrone, A. (2018), 'Comparison between electrocardiographic and earlobe pulse photoplethysmographic detection for evaluating heart rate variability in healthy subjects in short- and long-term recordings', *Sensors (Basel)* **18**, 844.

Vila, G., Godin, C., Charbonnier, S. & Campagne, A. (2021), 'Real-time quality index to control data loss in real-life cardiac monitoring applications', *Sensors* **21**, 5357.

Villareal, R., Liu, B. & Massumi, A. (2002), 'Heart rate variability and cardiovascular mortality', *Curr. Atheroscler. Rep.* **4**, 120–127.

Vinik, A., Casellini, C., Parson, H., Colberg, S. & Nevoret, M. (2018), 'Cardiac autonomic neuropathy in diabetes: A predictor of cardiometabolic events', *Front. Neurosci.* **12**, 591.

Volodina, M., Smetanin, N., Lebedev, M. & Ossadtchi, A. (2021), 'Cortical and autonomic responses during staged taoist meditation: Two distinct meditation strategies', *PLoS ONE* **16**, e0260626.

Väliaho, E., Kuoppa, P., Lipponen, J., Hartikainen, J., Jäntti, H., Rissanen, T., Kolk, I., Pohjantähti-Maaroos, H., Castrén, M., Halonen, J., Tarvainen, M., Santala, O. & Martikainen, T. (2021), 'Wrist band photoplethysmography autocorrelation analysis enables detection of atrial fibrillation without pulse detection', *Front. Physiol.* **12**, 654555.

Wan-Hua, L., Zheng, D., Li, G., Zhou, H. & Chen, F. (2022), 'Investigation on pulse wave forward peak detection and its applications in cardiovascular health', *IEEE Trans. Biomed. Eng.* **69**, 700–709.

Wang, H., Jimison, H. & Pavel, M. (2021), Reducing motion artifacts of pulse intervals from photoplethysmogram of a commercial wristband for heart rate variability analysis, *in* 'Annu. Int. Conf. IEEE Eng. Med. Biol. Soc.', pp. 47–51.

Wang, L., Xu, L., Feng, S., Meng, M. Q.-H. & Wang, K. (2013), 'Multi-gaussian fitting for pulse waveform using weighted least squares and multi-criteria decision making method', *Comput. Biol. Med.* **43**(11), 1661–1672.

Watanabe, K., Izumi, S., Yano, Y., Kawaguchi, H. & Yoshimoto, M. (2020), 'Heartbeat interval error compensation method for low sampling rates photoplethysmography sensors', *IEICE Trans. Commun.* **E103-B**, 645–652.

Watanabe, M., Shinohara, H. & Kodama, H. (2015), 'Impact of overnight oximetry findings on cardiac autonomic modulation in women during second trimester of uncomplicated pregnancy', *J. Obstet. Gynaecol. Res.* **41**, 689–696.

Weatherred, T. & Pruett, J. (1995), 'Significance of heart rate variability in cardiovascular disease', *Curr. Opin. Anesthesiol.* **8**, 7–14.

Webster, J. (2010), *Medical instrumentation: Application and design*, 4 edn, John Wiley & Sons, Madison, WI.

Weinschenk, S., Beise, R. & Lorenz, J. (2016), 'Heart rate variability (hrv) in deep breathing tests and 5-min short-term recordings: agreement of ear photoplethysmography with ecg measurements, in 343 subjects', *Eur. J. Appl. Physiol.* **116**, 1527–1535.

Welykholowa, K., Hosanee, M., Chan, G., Cooper, R., Kyriacou, P., Zheng, D., Allen, J., Abbott, D., Menon, C., Lovell, N., Howard, N., Chan, W., Lim, K., Fletcher, R., Ward, R. & Elgendi, M. (2020), 'Multimodal Photoplethysmography-Based Approaches for Improved Detection of Hypertension', *J Clin Med* **9**(4), 1203.

Wieben, O. (1997), Light absorbance in pulse oximetry, *in* J. Webster, ed., 'Design of Pulse Oximeters', CRC Press, Bristol, UK, chapter 4, pp. 44–51.

Wittenberg, T., Koch, R., Pfeiffer, N., Lang, N., Struck, M., Amft, O. & Eskofier, B. (2020), 'Evaluation of hrv estimation algorithms from ppg data using neural networks', *Curr. Dir. Biomed* **6**, 505–509.

Wong, J., Lu, W., Wu, K., Liu, M., Chen, G. & Kuo, C. (2012), 'A comparative study of pulse rate variability and heart rate variability in healthy subjects', *J. Clin. Monit. Comput.* **26**, 107–114.

World Health Organization (2019), 'Hypertension', Online. https://www.who.int/health-topics/hypertension/.

Wu, H., Hsu, P., Sun, C., Wang, H., Liu, C., Chen, H., Liu, A., Tang, C. & Lo, M. (2013), 'Assessment of autonomic dysfunction in patients with type 2 diabetes using reactive hyperemia', *J. Theor. Biol.* **330**, 9–17.

Wulterkens, B., Fonseca, P., Hermans, L., Ross, M., Cerny, A., Anderer, P., Long, X., van Dijk, J., Vandenbussche, N., Pillen, S., van Gilst, M. & Overeem, S. (2021), 'It is all in the wrist: Wearable sleep staging in a clinical population versus reference polysomnography', *Nat. Sci. Sleep.* **13**, 885–897.

Xhyheri, B., Manfrini, O., Mazzolini, M., Pizzi, C. & Bugiardini, R. (2012), 'Heart rate variability today', *Prog. Cardiovasc. Dis.* **55**, 321–331.

Xiaoxiao, S., Liang, Z., Zhaohui, L. & Wenlong, Y. J. Q. (2020), Blood pressure evaluation based on photoplethysmography using deep learning, *in* 'Proc. SPIE 11566, AOPC 2020: Optical Spectroscopy and Imaging; and Biomedical Optics', p. 115660X.

Xu, K., Jiang, X., Ren, H., Liu, X. & Chen, W. (2019), Deep recurrent neural network for extracting pulse rate variability from photoplethysmography during strenuous physical exercise, *in* '2019 IEEE Biomedical Circuits and Systems Conference (BioCAS)', pp. 1–4.

Ye, J., Lee, K., Chou, Y., Sie, H., Huang, R. & Chuang, C. (2018), 'Assessing pain intensity using photoplethysmography signals in chronic myofascial pain syndrome', *Pain Pract.* **18**, 296–304.

Yoshida, S., Izumi, S., Nishikawa, Y., Watanabe, K., Sasai, K., Yano, Y., Kawaguchi, H. & Yoshimoto, M. (2019), A heartbeat interval error compensation method using multiple linear regression for photoplethysmography sensors, *in* '2019 IEEE Biomedical Circuits and Systems Conference (BioCAS)', pp. 1–4.

Yuda, E., Shibata, M., Ogata, Y., Ueda, N., Yambe, T., Yoshizawa, M. & Hayano, J. (2020), 'Pulse rate variability: a new biomarker, not a surrogate for heart rate variability', *J. Physiol. Anthropol.* **39**, 21.

Yuda, E., Yamamoto, K., Yoshida, Y. & Hayano, J. (2020), 'Differences in pulse rate variability with measurement site', *J. Physiol. Anthropol.* **39**, 4.

Zangróniz, R., Martínez-Rodrigo, A., López, M., Pastor, J. & Fernández-Caballero, A. (2018), 'Estimation of mental distress from photoplethysmography', *Appl. Sci.* **8**, 69.

Zanon, M., Kriara, L., Lipsmeier, F., Nobbs, D., Chatham, C., Hipp, J. & Lindemann, M. (2020), A quality metric for heart rate variability from photoplethysmogram sensor data, *in* 'Annu. Int. Conf. IEEE Eng. Med. Biol. Soc.', pp. 706–709.